2
2024
Volume 7
Issue 2
ISSN: 2578-1995(Online)

CHARACTERIZATION AND APPLICATION OF NANOMATERIALS

https://systems.enpress-publisher.com/index.php/CAN

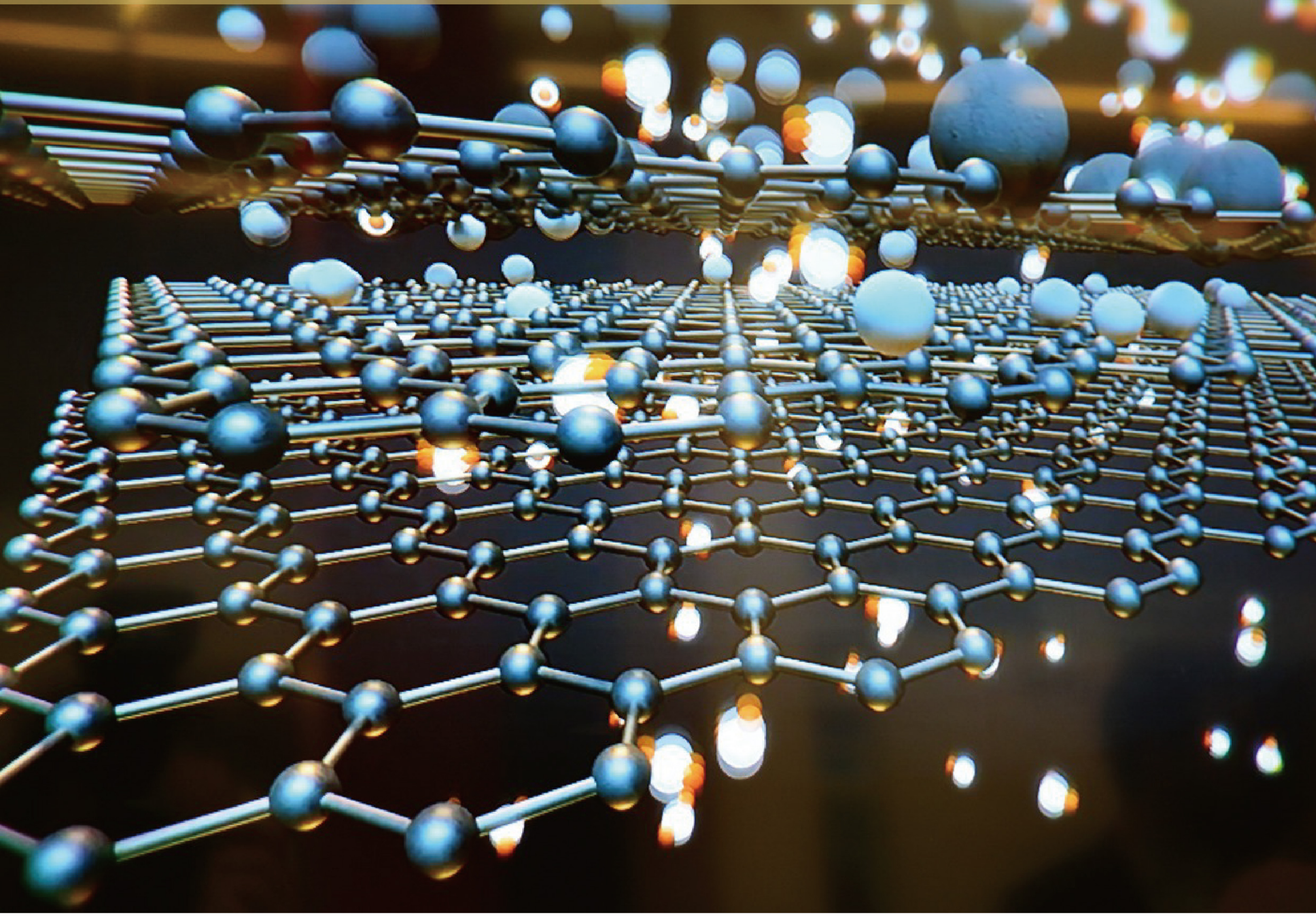

CAN

ISSN 2578-1995
02
9 772578 199073

EnPress Publisher

Editorial Board

Editor-in-Chief

Associate Editor

Editorial Board Members

Samy Mohamed Shaban
Egyptian Petroleum Research Institute
Egypt

Volume 7 Issue 2·2024

Characterization and Application of Nanomaterials

EnPress Publisher

2024 | Volume 7 | Issue 2

Characterization and Application of Nanomaterials

https://systems.enpress-publisher.com/index.php/CAN

Contents

Articles

Reviews

Characterization and Application of Nanomaterials 2024, 7(2), 6240.
https://doi.org/10.24294/can.v7i2.6240

Article

The potency of $AgNO_3$ nanoparticles combined with sweet potato (Ipomea batatas) starch as a sensor for mercury detection in cosmetic products

Esa Ghanim Fadhallah*, Vera Pertiwi, Duwinda, Sugaluh Yulianti, Umi Adila Tsani, Yunita Rachmawati

Department of Agricultural Product Technology, Faculty of Agriculture, Universitas Lampung, Bandar Lampung 35145, Indonesia
*** Corresponding author:** Esa Ghanim Fadhallah, esa.ghanim@fp.unila.ac.id

CITATION

Fadhallah EG, Pertiwi V, Duwinda, et al. The potency of $AgNO_3$ nanoparticles combined with sweet potato (Ipomea batatas) starch as a sensor for mercury detection in cosmetic products. Characterization and Application of Nanomaterials. 2024; 7(2): 6240. https://doi.org/10.24294/can.v7i2.6240

ARTICLE INFO

Received: 6 May 2024
Accepted: 29 May 2024
Available online: 5 July 2024

Abstract: Fraudulence in cosmetic ingredients is becoming increasingly prevalent, alongside the rising demand and utilization of cosmetics within the populace. One of the whitening agents still utilized in cosmetics is mercury, present in forms such as mercury chloramide ($HgNH_2Cl_2$) and mercury chloride ($HgCl_2$). Prolonged mercury exposure can have adverse health effects. To address this issue, alternative mercury analysis methods in samples have been developed, including the utilization of silver nanoparticles amalgamated with sweet potato starch as a stabilizing agent. This paper aims to delve into the roles of silver nanoparticle $AgNO_3$ and sweet potato starch (as a stabilizer) as a sensor for mercury detection, which can be applied in cosmetic products. Detection of mercury utilizing nanoparticles is based on the Surface Plasmon Resonance phenomenon, which endows a high level of selectivity and sensitivity toward the presence of mercury metal ions. When interaction occurs between mercury metal and silver nanoparticles, the liquid undergoes a color change from yellowish-brown to transparent. This phenomenon arises from the oxidation of AgO (yellow) to Ag^+ ions (transparent) by the mercury metal. Consequently, a silver nanoparticle sensor utilizing sweet potato starch as a stabilizing agent exhibits the potential to detect mercury metal within a substance with high efficacy.

Keywords: cosmetic; mercury detection; stabilizer; sweet potato starch

1. Introduction

Commercial whitening creams are widely available and easy to use, at affordable prices. In Indonesia, many cosmetic producers engage in fraudulent practices due to the increasing demand and consumption of cosmetics, driven by the high enthusiasm of the Indonesian population for cosmetics. Consequently, cosmetic producers compete to create products that can quickly brighten and whiten skin at affordable prices, leading to fraudulent practices in cosmetics production. According to the Central Statistics Agency, online transactions increased by 480% during the seven-month pandemic period. Unscrupulous e-commerce sellers exploit this trend to distribute unauthorized (TIE) or illegal and hazardous cosmetic products in various markets. Data on crime vulnerability reported by the Center for Drug and Food Control (POM) from 1 January 2018, to 15 September 2020, revealed several cosmetic products containing harmful whitening agents circulating in Indonesia. Mercury is a commonly used whitening agent in cosmetics, present in forms such as mercury chloride ($HgCl_2$) and mercury amino chloride ($HgNH_2Cl_2$). Prolonged mercury exposure can cause skin discoloration, black spots, allergies, skin irritation, and permanent damage to the nervous system, brain, kidneys, and fetal development. Therefore, there is a need for mercury content analysis in various cosmetics available on the market.

According to Azhar [1], there are several methods for measuring mercury metal concentrations in samples, such as inductive coupled plasma mass spectrometry (ICP-MS) and atomic absorption spectroscopy (AAS). However, the equipment costs for these methods are relatively high, necessitating alternative mercury analysis methods, including the use of silver nanoparticles mixed with starch as a stabilizing agent. Previous studies have utilized starch as a new nanocomposite material containing zinc sulfide quantum dots coated with L-cysteine. Nanocomposites were prepared in the form of potato starch gel and foil embedded with spherical quantum dots sized at 1020 nm. Pb^{2+} and Cu^{2+} ions reduced emission intensity in the photoluminescence spectral band. The described quantum dots were obtained using a simple, safe, and inexpensive method. Due to these properties, alternative sensors for Pb^{2+} and Cu^{2+} can be used in biotechnology and food technology.

Sweet potato is a nutritious tuber, containing fiber 6.33%–9.51%, protein 2.14%–2.86%, and b-carotene 18.83 mg/100 g [2]. However, it is still containing antinutrients such as phytate, oxalate, and tannin [2,3]. Additionally, its starch is widely used for thickening or stabilizing, as it contains 95.26%–96.73% of starch with 18.17%–18.56% of amylose [4]. The native starch from sweet potatoes has previously been reported to have a stable viscosity, with a peak viscosity of 3421.5 cP and a final viscosity of 3447.0 cP [5], making it a potential candidate for use as a stabilizer in mercury detection sensors. Innovation in the utilization of sweet potato starch potentially makes sweet potatoes more widely utilized. Furthermore, with sweet potato starch used as a mercury (Hg) detection sensor, which is more affordable and readily available, it can reduce operational costs in the production of mercury (Hg) detection sensors. With affordable prices and ease of use, it is hoped that many cosmetic producers will be more conscientious in their cosmetic selections, as they can easily utilize these mercury (Hg) detection sensors.

The innovation of sweet potato starch as a stabilizer in the mixing of silver nanoparticles can be beneficial in reducing the production and distribution of cosmetics containing mercury. This concept is also useful in creating a cheap, fast, and effective tool for detecting mercury. The development of sweet potato starch can also increase the productivity of sweet potatoes. The paper aimed to explore the potency of $AgNO_3$ nanoparticles and sweet potato starch (as stabilizers) as a sensor for mercury detection in cosmetic products.

2. Methods

The method used is an effective literature review following the topic. The method of discussion is based on the research results found by previous researchers, which are then integrated with other researchers to get strong results and conclusions.

3. Results and discussion

3.1. Mercury as heavy metals

Heavy metal ions have become a widely discussed environmental pollution issue. Apart from polluting the environment, these metals pose significant risks to human health. One such example of heavy metal is mercury, which is commonly encountered.

Mercury is identified as a hazardous pollutant due to its high toxicity and strong bioaccumulation potential, capable of causing damage to vital organs and tissues in the human body even at low concentrations [6].

Mercury metal sensors are technologies used to detect the presence of mercury in a substance. These sensors are fabricated using AgNO3 nanoparticles stabilized with sweet potato starch. The detection of mercury metal using these nanoparticles is based on the Surface Plasmon Resonance (SPR) effect, wherein the $AgNO_3$ nanoparticles exhibit high selectivity and sensitivity towards the presence of mercury metal ions (Hg) [1]. According to Wahyudi [7], the production of silver nanoparticles requires a stabilizing agent to prevent the colloidal particles from agglomerating. Agglomeration refers to the formation of particle clusters in a solution, leading to colloidal instability in nanoparticles. Starch derived from sweet potatoes is employed as the stabilizing agent in this sensor due to its environmentally friendly nature and non-hazardous properties.

Typically, the preparation of materials for synthesizing silver nanoparticles involves hazardous chemicals, high energy consumption, and complex purification processes [8]. Innovations in nanoparticle synthesis using starch as a stabilizer offer a non-toxic and environmentally friendly chemical development solution, requiring minimal costs for silver nanoparticle synthesis. This is attributed to the abundance of sweet potatoes in Indonesia and their affordable prices. According to data from the Agricultural Data and Information Center of the Ministry of Agriculture in 2022, sweet potato production in Indonesia showed a slight increase of 4.02% from 2020 to 2022. This rise in sweet potato production presents an opportunity for expanding the utilization of sweet potatoes, particularly in non-food applications.

Detection of mercury metal in cosmetics can be conducted on a laboratory scale or implemented by cosmetic resellers to ascertain whether the products being sold are free from mercury. This testing involves mixing the mercury metal sensor solution with the cosmetics under examination, followed by analyzing their absorbance using a UV-VIS spectrophotometer. During this process, a change in the solution's color occurs, enabling the determination of absorbance values.

3.2. Previous study

Previous research studies related to mercury metal sensors using nanoparticles include the research by Winiari and Kurniawan [9], which focused on mercury detection using direct solutions of gold nanoparticles. The results of this study indicated that the sensor activity was demonstrated by a shift in the wavelength towards higher values with increasing concentrations of mercury and gold nanoparticles without modification, which can be utilized for simple, rapid, and practical mercury detection.

Another study relevant to mercury metal sensors utilizing nanoparticles is by Vasileva [10], which explored the application of silver nanoparticles stabilized with starch as a colorimetric sensor for mercury (II) in 0.005 mol/L Nitric Acid. This study highlighted that the presence of 0.005 mol/L nitric acid utilizing starch-coated AgNPs as an optical sensor based on LSPR (Localized Surface Plasmon Resonance) is effective in mercury detection. The procedures conducted were practical, fast, and cost-effective. The mercury metal sensor using nanoparticles in this optical sensor based on LSPR can be applied for drinking water and wastewater.

In the study by Vasileva [8], it was reported that they successfully synthesized silver nanoparticles using environmentally friendly starch as a stabilizing agent. The research revealed that the nanoparticle sensor developed to test hydrogen peroxide exhibited excellent sensitivity and a high response to the presence of hydrogen peroxide in the sample.

3.3. Mercury detection

The detection of mercury has been extensively developed using various methods such as Cold Vapor Atomic Absorption Spectroscopy (CV-AAS), Inductively Coupled Plasma Optical Emission Spectroscopy (ICP-OES), gas chromatography, and others. According to Wang [11], these methods exhibit excellent performance in detecting metals; however, their application requires expensive and sophisticated instruments, complex sample processing, and high analysis costs, hindering their routine application in mercury detection. The increasing mercury metal pollution, particularly in cosmetic products, necessitates routine testing of these products. To reduce the operational costs of mercury detection, cheaper, practical, easy-to-implement, and environmentally friendly technologies are needed. Mercury metal sensors using $AgNO_3$ nanoparticles with sweet potato starch as a stabilizing agent represent an innovative heavy metal detection technology.

In previous research conducted by Wahyudi [7], polyacrylic acid (PAA) was used as the stabilizing agent in the production of silver nanoparticles, while in the study by Khachatryan and Khachatryan [12], potato starch was utilized as the stabilizer in nanocomposites. In this mercury metal sensor, we employ sweet potato starch as an innovation in the use of $AgNO_3$ nanoparticle stabilizers (silver). This innovation is based on the research by Vasileva [10] on the application of nanoparticle particles stabilized with starch for mercury metal detection. **Figure 1** illustrates the reaction that occurs between $AgNO_3$ nanoparticles when reacted with mercury metal (Hg).

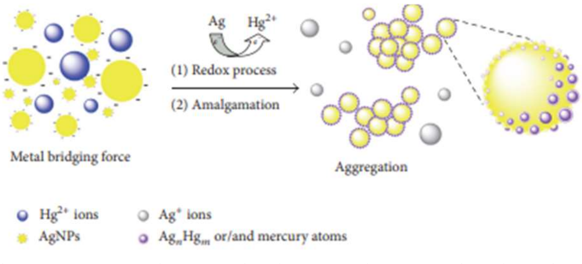

Figure 1. Schematic representation of the interaction mechanism between sweet potato starch-stabilized $AgNO_3$ nanoparticles and mercury.

Source: Vasileva [10].

The interaction between Hg^{2+} and nanoparticles involves electrostatic attraction between negatively charged silver nanoparticles and positively charged Hg^{2+}. This leads to a reduction in the distance between nanoparticles, resulting in aggregation. Hg^{2+} is adsorbed on the surface of AgNPs and reduced to Hg by surface Ag atoms, while simultaneous diffusion of Ag^+ into the solution occurs. The reaction leads to the formation of new mercury atoms combined with surface Ag atoms. This interaction may alter the surface charge of nanoparticles, leading to destabilization and agglomeration.

3.4. Role of $AgNO_3$ nanoparticles with sweet potato starch

The mercury metal sensor is formulated in liquid form, allowing direct application to cosmetics suspected of containing mercury. The production of nanoparticles entails the reduction of AgNO using D-glucose as the reducing agent. A starch solution serves as the capping and stabilizing agent, with the addition of NaOH as a catalyst in the reaction to produce an aqueous dispersion of silver nanoparticles. The schematic diagram of the silver nanoparticle synthesis process with sweet potato starch as the stabilizing agent is illustrated in **Figure 2**.

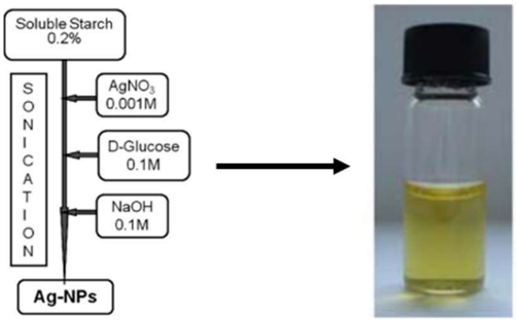

Figure 2. Schematic diagram of the silver nanoparticle synthesis process with sweet potato starch as the stabilizing agent.

The molar ratio of metal to reducer is 1:3, ensuring the complete reduction of Ag^+ ions in the solution into silver metal nanoparticles [10]. As depicted in **Figure 2**, the synthesis process involves stirring a starch solution (0.2% w/v) in a sonication bath for 15 minutes, followed by the addition of 16 mL of 0.0001 mol/L $AgNO_3$ solution. The mixture is stirred for 10 minutes to facilitate the diffusion of metal ions into the starch capping/stabilizing agent. Subsequently, the reducing solution containing D-glucose (0.01 M) is injected under sonication, followed by the addition of 2.4 mL of NaOH solution at 30 °C temperature maintained constant in an ultrasound bath. The reaction is completed within 60 minutes after the color change occurs.

The mercury metal sensor, in the form of silver nanoparticle liquid with starch stabilizer, will react with the tested cosmetic samples. The kinetics of interaction between sweet potato starch-stabilized silver nanoparticles and mercury metal (Hg) are reflected in the color change. According to research by Azhar [1], silver nanoparticles extracted from starfruit are selectively reactive towards mercury metal, indicated by a color change from yellowish-brown to clear. This occurs because mercury metal oxidizes AgO in the yellowish-brown silver nanoparticles to form clear Ag^+ ions. Further characterization of the sensor solution involves measuring the absorbance of the solution via UV-VIS spectrophotometer to determine the effect of mercury on sweet potato starch-stabilized silver nanoparticles. The predicted UV-VIS absorbance graph and color change of the sweet potato starch-stabilized silver nanoparticle liquid with added mercury are illustrated in **Figures 4** and **3**, respectively.

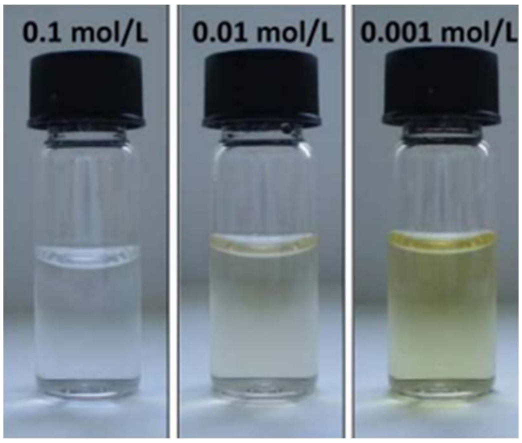

Figure 3. Prediction of mercury metal sensor results using silver nanoparticles with sweet potato starch as the stabilizing agent. Numbers indicated the concentration of mercury.

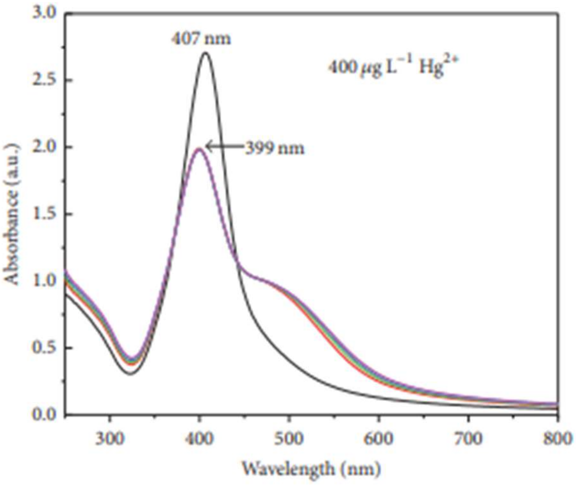

Figure 4. Predicted schematic of UV-VIS absorbance graph for mercury metal sensor using nanoparticles with sweet potato starch as the stabilizing agent.
Source: Vasileva [6].

4. Conclusion

In conclusion, the silver nanoparticle sensor with sweet potato starch as the stabilizing agent shows potential for detecting mercury metal in a substance. This sensor is formulated in liquid form, allowing direct testing on samples suspected of containing mercury, with a color change from yellowish-brown to clear indicating the presence of mercury. The utilization of sweet potato starch for mercury sensor production is expected to enhance the productivity and utilization of sweet potatoes in Indonesia.

Author contributions: Conceptualization, VP, D, SY and UAT; writing the draft in Bahasa, VP, D, SY and UAT; editing to manuscript layout, YR; reviewing the manuscript, EGF; translating article to English, EGF; original draft preparation, EGF; supervision, EGF. All authors have read and agreed to the published version of the manuscript.

Conflict of interest: The authors declare no conflict of interest.

References

1. Azhar FF. Utilization of silver nanoparticles of star fruit extract as colorimetric indicator of mercury metal (Indonesian). Jurnal Ipteks Terapan. 2019; 13(1): 34. doi: 10.22216/jit.2019.v13i1.3614
2. Oloniyo RO, Omoba OS, Awolu OO. Biochemical and antioxidant properties of cream and orange-fleshed sweet potato. Heliyon. 2021; 7(3): e06533. doi: 10.1016/j.heliyon.2021.e06533
3. Gouveia CS, Ganança JF, Lebot V, et al. Changes in oxalate composition and other nutritive traits in root tubers and shoots of sweet potato (*Ipomoea batatas* L. [Lam.]) under water stress. Journal of the Science of Food and Agriculture. 2019; 100(4): 1702-1710. doi: 10.1002/jsfa.10185
4. Babu AS, Parimalavalli R. Effect of starch isolation method on properties of sweet potato starch. Food Technology. 2014; 38(1): 48-63.
5. Babu AS, Parimalavalli R, Jagannadham K, et al. Chemical and structural properties of sweet potato starch treated with organic and inorganic acid. Journal of Food Science and Technology. 2014; 52(9): 5745-5753. doi: 10.1007/s13197-014-1650-x
6. Zhang S, Zhang D, Zhang X, et al. Ultratrace Naked-Eye Colorimetric Detection of Hg^{2+} in Wastewater and Serum Utilizing Mercury-Stimulated Peroxidase Mimetic Activity of Reduced Graphene Oxide-PEI-Pd Nanohybrids. Analytical Chemistry. 2017; 89(6): 3538-3544. doi: 10.1021/acs.analchem.6b04805
7. Wahyudi T, Sugiyana D, Helmy Q. Synthesis of silver nanoparticles and their activity test against bacteria *e. Coli* and *s. Aureus* (Indonesian). Arena Tekstil. 2011; 26(1). doi: 10.31266/at.v26i1.1442
8. Vasileva P, Donkova B, Karadjova I, et al. Synthesis of starch-stabilized silver nanoparticles and their application as a surface plasmon resonance-based sensor of hydrogen peroxide. Colloids and Surfaces A: Physicochemical and Engineering Aspects. 2011; 382(1-3): 203-210. doi: 10.1016/j.colsurfa.2010.11.060
9. Winiari A, Kurniawan F. Direct detection of mercury using gold nanoparticle solution (Indonesian). Jurnal Sains dan Seni Pomits. 2013; 2(1): 1-3.
10. Vasileva P, Alexandrova T, Karadjova I. Application of Starch-Stabilized Silver Nanoparticles as a Colorimetric Sensor for Mercury(II) in 0.005 mol/L Nitric Acid. Journal of Chemistry. 2017; 2017: 1-9. doi: 10.1155/2017/6897960
11. Wang W, Zhang Y, Yang Q, et al. Fluorescent and colorimetric magnetic microspheres as nanosensors for Hg^{2+} in aqueous solution prepared by a sol–gel grafting reaction and host–guest interaction. Nanoscale. 2013; 5(11): 4958. doi: 10.1039/c3nr00580a
12. Khachatryan GC, Khachatryan K. Starch based nanocomposites as sensors for heavy metals – Detection of Cu^{2+} and Pb^{2+} ions. International Agrophysics. 2019; 33: 121-126. doi: 10.31545/intagr/104414

Characterization and Application of Nanomaterials 2024, 7(2), 6031.
https://doi.org/10.24294/can.v7i2.6031

Article

Super-resolution by converting evanescent waves in microsphere to propagating waves and light transmitted from its surface to nano-jet

Y. Ben-Aryeh

Physics Department, Technion-Israel-Institute of Technology, Haifa 32000, Israel; phr65yb@physics.technion.ac.il

CITATION

Ben-Aryeh Y. Super-resolution by converting evanescent waves in microsphere to propagating waves and light transmitted from its surface to nano-jet. Characterization and Application of Nanomaterials. 2024; 7(2): 6031.
https://doi.org/10.24294/can.v7i2.6031

ARTICLE INFO

Received: 26 April 2024
Accepted: 15 May 2024
Available online: 15 July 2024

Abstract: The electro-magnetic (EM) waves transmitted through a thin object with fine structures are observed by a microsphere located above the thin object. The EM radiation transmitted through the object produces both evanescent waves, which include information on the fine structures of the object (smaller than a wavelength), and propagating waves, which include the large image of the object (with dimensions larger than a wavelength). The super-resolutions are calculated by using the Helmholtz equation. According to this equation, evanescent waves have an imaginary component of the wavevector in the z direction, leading the components of the wavevector in the transversal directions to become very large so that the fine structures of the object can be observed. Due to the decay of the evanescent waves, only a small region near the contact point between the thin object and the microsphere is effective for producing the super resolution effects. The image with super-resolution can be increased by a movement of the microsphere over the object or by using arrays of microspheres. Both propagating and evanescent waves arrive at the inner surface of the microsphere. A coupling between the transmitted EM waves and resonances produced in the dielectric sphere, possibly obtained by the Mie method, leads to a product of the EM distribution function with the transfer function. While this transfer function might be calculated by the Mie method, it is also possible to use it as an experimental function. By Fourier transform of the above product, we get convolution between the EM spatial modes and those of the transfer function arriving at the nano-jet, which leads the evanescent waves to become propagating waves with effective very small wavelengths and thus increase the resolution.

Keywords: microsphere; super-resolution; evanescent waves; nano-jet; transfer function; Mie method

1. Introduction

Any microscopic image can be magnified by using a microscope. But observing sub-wavelength structures is difficult because of the Abbe diffraction limit [1], by which light with wavelength λ travelling in medium with refractive index n and aperture angle θ will make a spot with radius.

$$d = \frac{2(n \sin\theta)}{\lambda} \tag{1}$$

The term $n \sin\theta$is called the numerical aperture $(NA)$and the Abbe limit is of order $\lambda/2$.

I analyze in the present article the mechanism by which evanescent waves incident on a microsphere are converted into propagating waves, and by such conversion high resolution is obtained in the image by the microsphere, which is much beyond the Abbe limit. There is much interest in the optical properties of the microsphere system. Many studies on the super-resolution obtained by the microsphere system were described in recent articles [2–10]. The mechanisms by which nan-jets are produced in the microsphere system were analyzed [11–16]. These works and many previous ones led to controversy about the origin of the observed super-resolution effects. In certain works, the super-resolution was related to evanescent waves emitted from the object, which include the fine structures of the object. In these works, the production of the nan-jet was considered a separate effect, not related to super resolution. On the other hand, it was claimed in other works that the super-resolution effects are produced by the same mechanisms that produce the nano-jet, while the evanescent waves might have only minor effect. In the present work, I show that the super-resolution effects are produced in two steps, where in the first step the information on the object's fine structures is obtained by the evanescent waves. In the second step, there is a convolution between the spatial modes of the evanescent waves and the spatial modes of the microsphere, which transforms the evanescent waves into propagating waves with very small effective wavelengths [17].

The super-resolution obtained by the microsphere is like the field of scanning near-field optical microscopy (SNOM), where the resonant effect with the tip detector enhances the super-resolution. We follow in the present analysis the idea that the evanescent wavevectors are coupled to the microsphere by resonances produced by Mie theory analysis [18,19]. Such Mie theory is also used for a good description of the nano-jet [19]. The conversion of evanescent waves to propagating waves, after the transmission through the microsphere surface, is obtained by convolution between the evanescent spatial modes and the transfer function of the microsphere modes [17]. The idea of using such convolution was suggested already in a previous article [20]. My approach to microsphere high resolution will be developed in the next sections by using two steps: 1) In the first step, we use the Helmholtz equation, by which large wave vectors are produced above the object, producing high resolutions. 2) The EM fields of both evanescent waves and propagating waves arriving parallel to the microsphere surface are preserved during transmission through the microsphere surface due to boundary conditions. The enhancement of the conversion of evanescent waves to propagating waves is due to coupling between evanescent waves and resonances, produced in the microsphere, for example, by Mie theory [19]. In the second stage we do not use the Helmholtz equation, and the above coupling is described as a convolution between the spatial modes of the evanescent waves and those of the microsphere modes, described by the transfer function [17]. Although the propagating waves are stronger than those of the evanescent waves, the modulation of the total intensity by the evanescent waves is the source of the high resolutions obtained by the microsphere system.

2. Methods

The use of evanescent waves to increase the resolution beyond the Abbe limit can be related to Helmholtz equation [17]. In homogenous medium this equation is given by

$$(nk_0)^2 = {k_x}^2 + {k_y}^2 + {k_z}^2 \tag{2}$$

where $k_0 = 2\pi/\lambda_0$, λ_9 is the wavelength in vacuum, k_x, k_y, k_z are the wavevector components. The evanescent waves satisfying the relation:

$$k_x{}^2 + k_y{}^2 > (nk_0)^2 \tag{3}$$

are arriving at the microsphere with imaginary k_z. The increase of the components of the wavevector $\vec{k}$ in the plane x, y decreases the "effective" wavelength in this plane, and thus increases the resolution.

As described in **Figure 1**, a dielectric microsphere with radius R and a refractive index n_2 is located above a thin object at a contact point O. The medium between the object and the microsphere has a refractive index n_1. Parallel EM waves are transmitted in a direction perpendicular to a thin planar object, which may be transmitted as "propagation" waves and as "evanescent" waves. But the increase of resolution by the microsphere is related to the conversion of evanescent waves to propagating waves.

We analyze the conversion of evanescent waves to propagating waves at a point P, which is on the microsphere surface. The incident and transmitted angles for the EM waves transmitted into the microsphere at point P are given as Θ_I and Θ_T, respectively. At this point, EM waves with wavevectors $k_x . k_y$ are arriving at the microsphere, where $k_z$is imaginary. The increase in the component of the wavevector $\vec{k}$ in the plane x, y decreases the "effective" wavelength in this plane, and thus increases the resolution. But the evanescent waves decay in the perpendicular z direction, so that to "capture" the fine structure that is available in the evanescent waves, we need that the point P will be near the contact point O, so that its perpendicular distance to the object will be of a wavelength order. According to geometric optics, the microsphere has a spherical symmetry under rotation around the z axis, which connects the center of the microsphere at point C with the contact point O. The line connecting the point C with point P has an angle $\Theta_I$with the symmetric z axis.

As shown in **Figure 1**, the EM waves transmitted through the microsphere are converging into photonic-jet (PJ), where its role in producing the high resolution is controversial. The original work in obtaining high resolution in microsphere imaging was made by Zengo Wang et al. [21]. That analysis was made with a virtual image as follows from the geometric optics description. Since this time, a very large number of papers were published on various effects in the microsphere system. In **Figure 1**, we describe a real image that is produced by using a high-refractive index microsphere (e.g., [22,23]).

The focusing of light in the microsphere system is concentrated in the nano-jet sub-diffraction region, which does not obey the classical laws of geometrical optics. but might be explained by diffraction effects, known as photonic-jet (PJ) (e.g., [24,25]). Exact solutions for non-diffraction beams might be related to the central part of the photonic nano-jet [26,27].

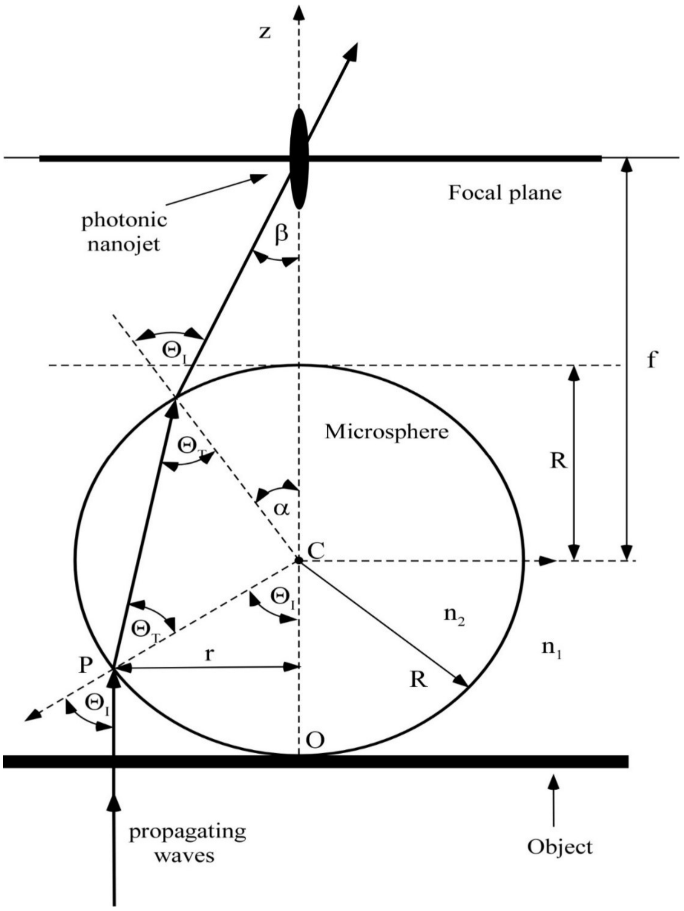

Figure 1. Microsphere and nano-jet.

Propagating EM waves are transmitted through a thin object with a certain structure, whose image is produced by evanescent waves, arriving at the microsphere surface at point P, for example. The EM transmitted through the microsphere is converging into a non-diffraction region known as a photonic jet (PJ).

Rigorous Mie theory predicts the interaction of light with spherical particles, and this theory was used to describe various properties of the PJ's produced by the microsphere system [19]. The exact use of the Mie theory is usually done by numerical calculations, as it is obtained by the sum of many terms that do not give an analytical result. Using Mie theory, optical resonances in microsphere photonic nano-jets were observed [18]. We analyzed the properties of evanescent waves, produced by plane EM waves transmitted through nano-corrugated-metallic thin film, which includes information on its fine structures [28]. A microsphere located above the metallic surface collects the evanescent waves, which are converted to propagating waves. The magnification of the nano-structure images is explained by a geometric optics description, but the high resolution is related to the evanescent wave analysis. Such an approach for explaining the high resolutions obtained by microspheres was developed by using complex Snell's law [29]. Very high resolutions by microspheres were reported also in other works (e.g., [30,31]).

Maslov and Astratov [32,33] studied the origin of super-resolution in microsphere-assisted imaging. The imaging of the nano-jet cannot give a good explanation for the high resolutions obtained in the microsphere system. The evanescent wave source cannot explain the high resolutions obtained by the microsphere system since its effect is too weak. They suggested using a direct approach to Maxwell equations, including optical principles such as point-spread functions, in microspherical imaging. I claim, however, that there are strong arguments that evanescent waves should be included in the theories about high resolutions: a) The propagating distance between the object and the microscope must be small enough to reveal the nanometric features. To generate super-resolution over large areas of the sample, we need to attach the microsphere to a frame, which is scanned on the sample in step-by-step fashion [34] or by using microspheres arrays [6]. b) There is a dependence of the super-resolution on the radius of the microsphere and its index of refraction, which is in good correspondence with the evanescent wave properties [29]. c) The super-resolution is related to information theory, where the information on the fine structures of the object area is available in the evanescent waves. Magnification of the image and optical transforms cannot introduce high resolution if the information on the object's fine structures is not available in such transforms. I find, however, that there is an important mechanism that enhances the transformation of evanescent waves into propagating waves after the microsphere surface, which is beyond classical geometric optics (beyond the use of complex Snell’s law [29]. To explain this new mechanism, it will be helpful to compare the high resolution obtained by the microsphere with the high resolutions obtained in metallic grating [35,36]. It was shown in these works that a thin film of metallic grating with arrays of subwavelength holes can transmit light at certain frequencies, which is order of magnitude larger than the light intensity incident on the area of these holes. Most investigators agree that these experiments, conducted originally by Ebessen et al. [35,36], are related to coupling the light with surface plasmons. I explained these phenomena as transmission enhancement by converting evanescent waves, entering the small holes to propagating waves, due to convolution of the evanescent spatial modes with the plasmon spatial modes, producing high spatial wavevectors with very small “effective” wavelengths [37]. Such effects were described in a similar way by relating the ‘tunelling’ of evanescent waves to propagating waves due to the convolution of the high spatial frequencies of the source with those of the detector [38]. One should consider that in the dielectric sphere we don’t have plasmons, but we have other coupling mechanisms between the evanescent waves and the microsphere EM modes.

3. An analysis for the super resolution, in the microsphere system, obtained in many experiments

In experimental studies on microspheres by other authors [2–23,30,31,34], super resolution effects were observed. These works raised the question: Is the super-resolution related to evanescent waves? or is it related to the existence of the nano-jet? The question led to controversy between the various works. I show in the present theoretical analysis that a combination of two effects produces the high resolution: 1) The evanescent waves produced by the object are incident on the microsphere surface, preserving high resolutions. 2) The same mechanism which produces the nano-jet leads to conversion of the evanescent waves to propagating waves, but with very small wave lengths. The reduction of the wavelength was explained also as a quantum effect

[39,40] where n entangled photons lead to effective wavelength λ/n, and there is a distribution of such effective wavelengths.

We develop the analysis for the microsphere system into two parts: a) In the first part, we describe the propagation of evanescent waves, produced on thin planar objects with fine structures, to the microsphere surface. In this stage, high resolutions of the image are obtained related to the use of the Helmholtz equation. b) In the second part, we consider the propagation of both evanescent and propagating waves produced on the inner surface of the microsphere to the nano-jet. This propagation is described by the convolution of these EM fields with the microsphere modes described by a transfer function [17], which is related to Mie theory, but it is more convenient to use it as an experimental function.

3.1. The use of Helmholtz equation for getting high resolutions by evanescent waves

Let us assume that the planar surface of an object is given by $z = 0$, and the EM field in this plane is given by the Fourier transform

$$U(x,y) = \int_{-\infty}^{\infty}\int_{-\infty}^{\infty} u(k_x,k_y)\, exp\left[-i(k_x x + k_y y)\right] dk_x dk_y \tag{4}$$

where $u(k_x,k_y)$ is the distribution of the EM spatial modes in the x,yplane. Then, the EM waves propagating from the planar surface of the object into homogenous medium in the space $z > 0$ with a refractive index n_1 is given by:

$$U(x,y,z>0) = \int_{-\infty}^{\infty}\int_{-\infty}^{\infty} u(k_x,k_y)\, exp\left[-i(k_x x + k_y y + k_z z)\right] dk_x dk_y \tag{5}$$

Substituting Eq. (5) into the Helmholtz equation we get:

$$(\Delta^2 + k^2)U(\vec{r}) = 0 \tag{6}$$

obtaining the result:

$$\left[k^2 - \left({k_x}^2 + {k_y}^2 + {k_z}^2\right)\right]U(x,y,z>0) = 0 \tag{7}$$

Under the condition $k^2 < {k_x}^2 + {k_y}^2$, $k_z$is imaginary, and for such case we get the evanescent wave solution:

$$U(x,y,z>0) = U(x,y,z=0)\, exp(-\gamma z) \quad ;\gamma = \sqrt{{k_x}^2 + {k_y}^2 - k^2} \tag{8}$$

A dielectric microsphere with refractive index n_2 and radius R is located above a thin film of the object at a contact point O,where the medium between the object and the microsphere has a refraction index n_1. A plane EM wave is transmitted through the thin film of the object in the perpendicular direction and incident on the microsphere at point P. The evanescent waves are incident on the microsphere surface near the contact point O.

For evanescent waves, there is a decay of the wave in the z direction. The resolution obtained by the evanescent waves is limited by the lateral component $k_T$of the wavelength given by:

$$\lambda_T = \frac{2\pi}{k_T} = \frac{2\pi}{\sqrt{{k_x}^2 + {k_y}^2}} \tag{9}$$

As the evanescent waves satisfy the equation $k^2 = k_x{}^2 + k_y{}^2 - \gamma^2$, then Eq. (9) can be written as

$$\lambda_T(evan.) = \frac{2\pi}{\sqrt{k^2 + \gamma^2}} \tag{10}$$

The minimal value of λ_T for propagating waves is given by:

$$\lambda(prop.)\frac{2\pi}{k}_{T,min} \tag{11}$$

since the minimum is obtained when $\vec{k}$ is in the x, y plane.

As by the Abbe limit the resolution is of order $\lambda/2$, the increase of resolution F by using evanescent waves is given by:

$$F = \lambda_T(prop.)/\lambda_T(evan.) = \sqrt{\frac{k^2 + \gamma^2}{k^2}} = \sqrt{1 + \frac{\gamma^2}{n_1{}^2 k_0{}^2}} \tag{12}$$

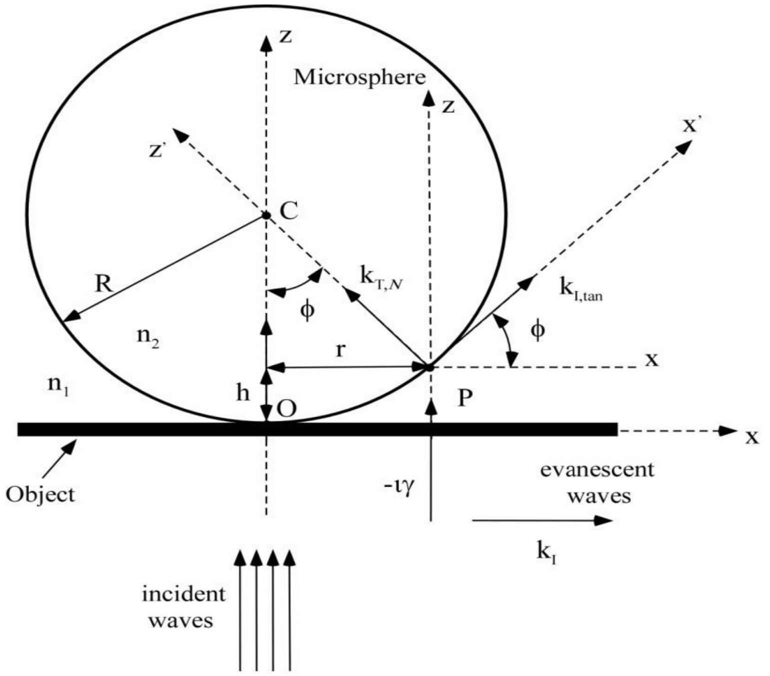

Figure 2. Evanescent waves on microsphere surface.

The distance of the point P from the planar object is given by $h = R(1 - cos\,\phi)$ (see **Figure 2**). For decay constant γ of the evanescent waves, represented in unit $\gamma/n_1 k_0$, the decay of the evanescent wave at point at point P, after transversing the distance h, is given by

$$exp(-\gamma h) = exp\left[-\frac{\gamma}{n_1 k_0} n_1 k_0 R(1 - cos\,\phi\right] = exp\left[-\frac{\gamma}{n_1 k_0} 2\pi(1 - cos\,\phi)\frac{R}{\lambda}\right] \tag{13}$$

We find that this decay increases very much by increasing ϕ, so that only a small region around the contact point O is efficient in obtaining the high resolution by evanescent waves.

3.2. Microsphere imaging by a transfer function from the microsphere surface to the nano-jet

Let us assume that the EM field $E(x,y)_{tan}$, which is tangent to the microsphere surface at the point x, y (of evanescent wave in a small region around the contact point O, plus a propagating wave in a larger region), is given by:

$$E \, cos \, \phi_{tan} \tag{14}$$

where $E(x,y)$ is the EM field before the microsphere surface (see **Figure 2**, and [29]). The EM field E_{tan} is preserved during transmission through the microsphere surface due to boundary conditions, and it includes both the evanescent waves and the propagating waves. The EM field propagating after the microsphere surface is given as

$$E'(x,y) = E_{\tan}(x,y)G(x,y) \tag{15}$$

where the 'transfer function' $G(x,y)$ can be related by Fourier transform [17] to $G(k_x, k_y)$:

$$G(k_x,k_y) = \int_{-\infty}^{\infty}\int_{-\infty}^{\infty} G(x,y) \, exp\big[-i\big(k_x x + k_y y\big)\big] \, dxdy \tag{16}$$

One should notice that $G(k_x, k_y)$ should include both evanescent waves for which ${k_x}^2 + {k_y}^2 > k^2$, and propagating waves for which ${k_x}^2 + {k_y}^2 < k^2$.

Due to the small distance between the points x, y and the contact point O, the evanescent field $E_{tan,\,eva}\ (x,y)$ is approximately parallel to the x, y plane. This EM field is smaller from the evanescent EM field on the thin object, by the factor given approximately by Eq. (13).

The Fourier amplitude $A(k_x, k_y)$ is described by the Fourier inverse of E_{tan}, which is given by:

$$A(k_x,k_y) = \int_{-\infty}^{\infty\int \; exp[-i(k_x x + k_y y)]} \int_{-\infty}^{\infty\int} E(x,y)_{tan} \tag{17}$$

where $k_x . k_y$ are the wavevectors in the x and y directions. The Fourier transform of $E'(x,y)$, (given by the product of Eq. (14)) is obtained by the convolution of the spatial wavevectors $G(k_x, k_y)$ and $A(k_x, k_y)$ [17]:

$$E'(k_x,k_y) = \int_{-\infty}^{\infty}\int_{-\infty}^{\infty} A\big(k'_x, k'_y\big) \, G\big(k_x - k'_x, k_y - k;_y\,\big) dk'_x dk'_y \tag{18}$$

The convolution given by Equation (18) includes spatial wavevectors $k_x - k'_x$ and $k_y - k'_y$which might be very large, so that the corresponding wavelengths can be reduced to very low values. For example, if approximately, $k_x - k'_x = kn$ where n is a large integer, then the effective wavelength will be reduced to λ/n (see the analysis in [39,40]). We use the convolution effect described by Equation (18), to obtain enhancement of the conversion of evanescent waves to propagating waves by reducing the effective wavelength. Although the modulation of the EM waves by evanescent waves is small relative to the total intensity of the EM field, such modulation is effective in producing the high resolution. The spreading of the spatial modes by convolution is like the point spread function used in [32,33], but one should not ignore the super resolution obtained for the object in the first stage of the imaging process, which is related to the use of Helmholtz equation.

The above reduction of the effective wavelength by convolution, was also described as a quantum effect where entanglement between the n photons reduces the effective wavelength to λ/n [39,40]. Such entanglement remains true also after the transformation to propagating waves.

4. Discussions and results

The high resolution obtained in microspheres is due to the following two factors: a) The EM radiation transmitted through the object produces both evanescent waves, which include information on the fine structures of the object (smaller than a wavelength), and propagating waves, which include the large image of the object (with dimensions larger than a wavelength). Evanescent waves lead to a super-resolution, which is better than the Abbe limit, by the factor $F = \sqrt{\left({k_x}^2 + {k_y}^2\right)/k^2} = \sqrt{(k^2 + \gamma^2)/k^2}$ where $k^2 = {k_x}^2 + {k_y}^2 - {k_z}^2$ is the wavevector of the evanescent EM field, $k_z = -i\gamma$ is imaginary, and k_x, k_y are the transversal components. The evanescent waves arrive at the microsphere surface after a decay in the z direction by the factor $exp(-\gamma h)$. where h is the distance from the object to the microsphere surface, and γ is a certain decay constant., so that only the evanescent waves which are near the contact point O of the object are efficient in conserving the fine structure imaging. But one can attach the microsphere to a frame which moves on the object and scans a large image, or to use arrays of microspheres. b) By using boundary conditions, we get on the inner microsphere surface both evanescent waves and propagating waves. The convolution between the EM waves, on the inner surface of the microsphere, and the transfer function, representing the coupling with microsphere EM modes, enables propagation with small effective wavelengths (smaller than a wavelength and correspondingly large wave vectors). This effect is due to the spread of the wavevectors due to the above convolution. The transfer function also includes the wavevectors of the evanescent waves and thus enables them to be transferred to the image without evanescent wave decay. The analytical description of this convolution is given in the article by using Equations (14–18). It is possible to use Mie theory for calculating the transfer function, but such calculations are very complicated and usually give only numerical results. We suggest, therefore, to use the transfer function as an empirical function, which can also be used for a description of the nano-jet.

Figure 1 gives only a geometric optics picture. The incident and transmitted angles θ_I and θ_T are derived by Snell's law, respectively. There are different features in the microsphere system which can be explained by the geometric optics picture. For example, for a small microsphere index of refraction, we get a diverging beam with a virtual image, while if this index of refraction is large, then the beam is converging with a real image, like that in **Figure 1**. The angle β between the beam converging to the nano-jet and the symmetric axis, and the distance r from the point P to the symmetric axis, can be obtained by simple geometric calculations. But the microsphere super-resolutions can be calculated, only by using an analysis, similar to that presented in the present article. Some features of the nano-jet may be described by using Bessel beams [26,27]. **Figure 2** describes the transmittance of both evanescent waves and propagating waves from the object to the inner surface of the microsphere, where the fine structures of the object are included in the evanescent waves.

5. Conclusion

By using the Helmholtz equation, it was shown how the fine structures of the object are transferred by the evanescent EM radiation to the inner surface of the microsphere. The information on the fine structures of the object is included in the evanescent waves, and this information is transferred from the inner microsphere surface to the nano-jet by using the coupling between the EM fields and the EM modes of the microsphere, which might be calculated by Mie theory (e.g., [19]). This coupling leads to transmittance of both the evanescent waves and propagating waves to the nano-jet by using 'transfer functions' (see Equations (14–17) and reference [17]), which lead to a very small 'effective wavelength' for the evanescent waves, although they are not decaying any more. While the propagating waves are stronger than the evanescent waves, the modulation of the total EM radiation intensity in the nano-jet by the evanescent waves is the source of the super-resolutions of the microsphere system. The present analysis solves the controversy about whether the nano-jet or the evanescent waves are the source of the super-resolution effects, as the source of the super-resolution is composed of these two different mechanisms in two different parts of the microsphere system.

Funding: The present study was supported by Technion-Mossad under grant No. 2007256.

Conflict of interest: The author declares no conflict of interest.

References

1. Lipson A, Lipson SG, Lipson H. Optical Physics. Cambridge University Press; 2010. doi: 10.1017/cbo9780511763120
2. Zhang T, Yu H, Li P, et al. Microsphere-Based Super-Resolution Imaging for Visualized Nanomanipulation. ACS Applied Materials & Interfaces. 2020; 12(42): 48093-48100. doi: 10.1021/acsami.0c12126
3. Xie Y, Cai D, Pan J, et al. Chalcogenide Microsphere‐Assisted Optical Super‐Resolution Imaging. Advanced Optical Materials. 2022; 10(6). doi: 10.1002/adom.202102269
4. Li Y, Qiu C, Ji H, et al. Microsphere‐Aided Super‐Resolution Scanning Spectral and Photocurrent Microscopy for Optoelectronic Devices. Advanced Optical Materials. 2023; 11(16). doi: 10.1002/adom.202300172
5. Wu G, Hong M. Optical Microsphere Nano-Imaging: Progress and Challenges. Engineering. 2024; 36: 102-123. doi: 10.1016/j.eng.2023.10.019
6. Zhou J, Lian Z, Zhou C, et al. Scanning microsphere array optical microscope for efficient and large area super-resolution imaging. Journal of Optics. 2020; 22(10): 105602. doi: 10.1088/2040-8986/abb17b
7. Upreti N, Jin G, Rich J, et al. Advances in Microsphere-based Super-resolution Imaging. IEEE Reviews in Biomedical Engineering. 2024; 1-16. doi: 10.1109/rbme.2024.3355875
8. Liu C, Ye A. Microsphere assisted optical super-resolution imaging with narrowband illumination. Optics Communications. 2021; 485: 126658. doi: 10.1016/j.optcom.2020.126658
9. Shang Q, Tang F, Yu L, et al. Super-Resolution Imaging with Patchy Microspheres. Photonics. 2021; 8(11): 513. doi: 10.3390/photonics8110513

10. Jiang W, Wang J, Yang Y, et al. A Review of Microsphere Super-Resolution Imaging Techniques. Sensors. 2024; 24(8): 2511. doi: 10.3390/s24082511
11. Geints YE, E.K. Panina. Surface roughness influence on photonic nanojet parameters of dielectric microspheres. Computer Optics. 2023; 47(4): 559-566. doi: 10.18287/2412-6179-co-1280
12. Gasparic V, Mayerhofer TG, Zopf D, et al. To generate a photonic nanojet outside a high refractive index microsphere illuminated by a Gaussian beam. Optics Letters. 2022; 47(10): 2534. doi: 10.1364/ol.459001
13. Gasparic V, Ristic D, Mayerhofer TG, et al. Photonic nanojet of a Gaussian beam illuminated low refractive index microsphere in air: A comprehensive variation of parameters. Journal of Quantitative Spectroscopy and Radiative Transfer. 2022; 282: 108121. doi: 10.1016/j.jqsrt.2022.108121
14. Darafsheh A. Photonic nanojets and their applications. Journal of Physics: Photonics. 2021; 3(2): 022001. doi: 10.1088/2515-7647/abdb05
15. Mandal A, Tiwari P, Upputuri PK, et al. Characteristic parameters of photonic nanojets of single dielectric microspheres illuminated by focused broadband radiation. Scientific Reports. 2022; 12(1). doi: 10.1038/s41598-021-03610-3
16. Kwon S, Park J, Kim K, et al. Microsphere-assisted, nanospot, non-destructive metrology for semiconductor devices. Light: Science & Applications. 2022; 11(1). doi: 10.1038/s41377-022-00720-z
17. Goodman JW. Introduction to Fourier Optics. Roberts and Company Publishers; 2017.
18. Lee S, Li L, Wang Z. Optical resonances in microsphere photonic nanojets. Journal of Optics. 2013; 16(1): 015704. doi: 10.1088/2040-8978/16/1/015704
19. Lecler S, Perrin S, Leong-Hoi A, et al. Photonic jet lens. Scientific Reports. 2019; 9(1). doi: 10.1038/s41598-019-41193-2
20. Lee S, Li L, Ben-Aryeh Y, et al. Overcoming the diffraction limit induced by microsphere optical nanoscopy. Journal of Optics. 2013; 15(12): 125710. doi: 10.1088/2040-8978/15/12/125710
21. Wang Z, Guo W, Li L, et al. Optical virtual imaging at 50 nm lateral resolution with a white-light nanoscope. Nature Communications. 2011; 2(1). doi: 10.1038/ncomms1211
22. Darafsheh A, Walsh GF, Dal Negro L, et al. Optical super-resolution by high-index liquid-immersed microspheres. Applied Physics Letters. 2012; 101(14). doi: 10.1063/1.4757600
23. Lai HSS, Wang F, Li Y, et al. Super-Resolution Real Imaging in Microsphere-Assisted Microscopy. PLOS ONE. 2016; 11(10): e0165194. doi: 10.1371/journal.pone.0165194
24. Lecler S, Takakura Y, Meyrueis P. Properties of a three-dimensional photonic jet. Optics Letters. 2005; 30(19): 2641. doi: 10.1364/ol.30.002641
25. Horiuchi N. Photonic nanojets. Nature Photonics. 2012; 6(3): 138-139. doi: 10.1038/nphoton.2012.43
26. Durnin J. Exact solutions for nondiffracting beams I The scalar theory. Journal of the Optical Society of America A. 1987; 4(4): 651. doi: 10.1364/josaa.4.000651
27. Ben-Aryeh Y. Nano-jet related to Bessel beams and to super-resolutions in microsphere optical experiments. EPJ Techniques and Instrumentation. 2017; 4(1). doi: 10.1140/epjti/s40485-017-0038-5
28. Ben-Aryeh Y. Superresolution observed from evanescent waves transmitted through nano-corrugated metallic films. Applied Physics B. 2012; 109(1): 165-170. doi: 10.1007/s00340-012-5193-4
29. Ben-Aryeh Y. Increase of resolution by use of microspheres related to complex Snell’s law. Journal of the Optical Society of America A. 2016; 33(12): 2284. doi: 10.1364/josaa.33.002284
30. Yan Y, Li L, Feng C, et al. Microsphere-Coupled Scanning Laser Confocal Nanoscope for Sub-Diffraction-Limited Imaging at 25 nm Lateral Resolution in the Visible Spectrum. ACS Nano. 2014; 8(2): 1809-1816. doi: 10.1021/nn406201q
31. Wu G, Hong M. Optical nano-imaging via microsphere compound lenses working in non-contact mode. Optics Express. 2021; 29(15): 23073. doi: 10.1364/oe.426231
32. Maslov AV, Astratov VN. Origin of the super-resolution of microsphere-assisted imaging. Applied Physics Letters. 2024; 124(6). doi: 10.1063/5.0188450
33. Maslov AV, Astratov VN. Resolution and Reciprocity in Microspherical Nanoscopy: Point-Spread Function Versus Photonic Nanojets. Physical Review Applied. 2019; 11(6). doi: 10.1103/physrevapplied.11.064004
34. Huszka G, Yang H, Gijs MAM. Microsphere-based super-resolution scanning optical microscope. Optics Express. 2017; 25(13): 15079. doi: 10.1364/oe.25.015079
35. Ebbesen TW, Lezec HJ, Ghaemi HF, et al. Extraordinary optical transmission through sub-wavelength hole arrays. Nature. 1998; 391(6668): 667-669. doi: 10.1038/35570

36. Ghaemi HF, Thio T, Grupp DE, et al. Surface plasmons enhance optical transmission through subwavelength holes. Physical Review B. 1998; 58(11): 6779-6782. doi: 10.1103/physrevb.58.6779
37. Ben-Aryeh Y. Transmission enhancement by conversion of evanescent waves into propagating waves. Applied Physics B. 2008; 91(1): 157-165. doi: 10.1007/s00340-008-2945-2
38. Ben-Aryeh Y. Tunneling of evanescent waves into propagating waves. Applied Physics B. 2006; 84(1-2): 121-124. doi: 10.1007/s00340-006-2220-3
39. Ben-Aryeh Y. Nonclassical high resolution optical effects produced by evanescent waves. Journal of Optics B: Quantum and Semiclassical Optics. 2003; 5(6): S553-S556. doi: 10.1088/1464-4266/5/6/002
40. Ben-Aryeh Y. Super resolution of nanomaterials and quantum effects obtained by microspheres. Progress in Materials Science. 2019; 1(3): 1-21. doi:10.21926/rpm.1903003

Characterization and Application of Nanomaterials 2024, 7(2), 6236.
https://doi.org/10.24294/can.v7i2.6236

Article

Reversible logic-based parity generator circuit for nano communication network using QCA

Sravan K. Vittapu*, **Ravichand Sankuru, Ravi Bolimera, Kuruva Madhu Ramudu, Mekala Rameshwar Reddy, Maddula Manasa Reddy**

Department of Electronics and Communication Engineering, Nalla Narasimha Reddy Education Society's Group of Institutions, Hyderabad 500088, Telangana, India
*** Corresponding author:** Sravan K. Vittapu, vsravan91@gmail.com

CITATION

Vittapu SK, Sankuru R, Bolimera R, et al. Reversible logic-based parity generator circuit for nano communication network using QCA. Characterization and Application of Nanomaterials. 2024; 7(2): 6236. https://doi.org/10.24294/can.v7i2.6236

ARTICLE INFO

Received: 6 May 2024
Accepted: 8 July 2024
Available online: 26 July 2024

Abstract: An alternative to CMOS VLSI called Quantum Cellular Automata (QCA) is presently being researched. Although a few basic logical circuits and devices have been examined, very little, if any, research has been done on the architecture of QCA device systems. In the context of nano communication networks, data transmission that is both dependable and efficient is still critical. The technology known as Quantum Dot Cellular Automata (QCA) has shown great promise in the development of nano-scale circuits because of its extremely low power consumption and rapid functioning. This study introduces a unique nano-communication parity-based arithmetic circuit that is reversible, error-detecting, and error-correcting. The minimal outputs are needed for the proposed structure. Based on QCA technology, the proposed nano-communication network makes use of reversible logic gates. The performance increase of the suggested parity generator and checker circuit is significant in terms of clock delay, size, and number of cells.

Keywords: CMOS; nano communications networks; parity generator; parity checker; reversible logic; VLSI

1. Introduction

Given that people must utilise electronics, it is regrettable that common electronic gadgets based on CMOS technology have flaws. There are some significant drawbacks to this technique, such as short-channel effects. As CMOS technology nears its physical limits, issues like power dissipation and the quantum effect are becoming more noticeable. The design complexity increases much further when CMOS technology is down to the nanoscale. Reversibility processing is one of the most important subjects in nanotechnology, the science that complements CMOS technology. This is due to the physical constraints of CMOS technology, which include its larger dimensions compared to QCA. We work on both hardware and software components to attain great efficiency. Power analysis is therefore important since it can assist designers in identifying the positive long-term consequences [1].

On the whole, circuit designers were able to construct new goods utilising QCA technology because the logic value model relies on where electrons are located in each cell of quantum dots. The zero-and-one logic paradigm in CMOS is based on low and high voltages. Irreversible logic generally causes some input data to be lost, which could lead to increased power consumption. When this happens, the output information is not recoverable, so we must retrieve the data from the main memory [2,3]. According to Landauer's research, every bit of information lost results in the loss of KTLn2 joules of heat energy, where T is the operation’s absolute temperature and K is Boltzmann’s constant [4]. A circuit must be made up of reversible gates in order to prevent this energy dissipation [5]. Energy dissipation is decreased by reversible logic, which produces a one-to-one connection between input and output vectors. Reversible computing is limited primarily by minimising the quantum cost, minimising input constants, minimising garbage outputs, and employing the fewest number of gates possible [6,7]. Parity and Feynman diagrams are crucial components of arithmetic computing [8]. This study proposes an optimised reversible Feynman design implementation using parity generators, parity checker gates, and the efficient XOR proposed by Ahmed and Naz [8]. To show expandability, we then create a nano communication design with fewer garbage outputs. Moreover, the proposed nano-communication designs are reversible and provide fault tolerance.

2. Related works

The design of the Nano Communication Network Reversible Based Parity Generator Circuit Using QCA has involved numerous research projects. Below is a discussion of some of them. Numerous issues and inadequacies have been noted in recent decades as a result of the emergence of significant limitations on the complementary metal oxide semiconductor (CMOS) technology’s capacity to scale physically. A few of the challenges that come with this technology are short channel effects and high leakage power consumption. Reversible gates are used in conjunction with a procedural technique in the study of Bagherian Khosroshahy et al. [1] to minimise latency in the system design, which is based on output conformance and a requirements self-checking approach. The reversibility logic will be the focus of the suggested circuit. In comparison to the study of Danehdaran et al. [2], the technique is obtained with enhanced reliability. Since there is no fan-out in the reversible logic gates, there is no power dissipation [3]. The output terms and garbage values are both present in the reversible logic. The relationship between the trash value, the input, and the output [4]. The primary parameters to be discussed in reversible logic are quantum cost, garbage, constant input, and latency. Every circuit needs a delay calculation feature in order to adjust efficiency. The parity generator circuit implements a novel Feynman-based, reversible, and fault-tolerant nano communication arithmetic architecture with several trash outputs [5].

According to Panahi et al.’s research, every bit of information lost results in the loss of KTLn2 joules of heat energy, where T is the operation’s absolute temperature and K is Boltzmann’s constant [6]. Reversibility is crucial for error detection in nano-circuits since it allows for lossless transmission and the absence of data loss. Additionally, latency and cell count are not described independently in the majority of these irreversible circuits. Although their circuits contain more cells and a delay, the parity generator, parity checker, and their nano-communication circuit have been created reversibly using odd parity bits in the study of Panahi et al. [7]. Feynman and parity are crucial components of arithmetic computing in the study of Ahmed and Naz [8]. The suggested Feynman gate uses an XOR gate based on Ahmed and Naz [8], despite certain limitations in cell placement leading to greater overhead areas. Equation [9] can be used to calculate the electrostatic interaction force between each cell's two electrons. QCA technology flaws are mostly associated with the deposition process, which may be classified into four distinct kinds [10–14]. The transmitted data from the parity generator is controlled by the odd parity checker, which verifies its accuracy. An error during transmission will occur if the parity output of the four bits (the three message bits plus the parity bit) is even. As a result, the binary information that was originally transferred was strange [12,15–17]. In the study of Mohaimeed and Rabee [18], new nano composite thin films were fabricated that outperformed TiO_2 films in terms of transmittance and energy gap. In the study of Najm et al. [19], a new technique was employed named solvothermal, which is used for the deposition of nano particles into nano thin films.

Figure 1 shows a high-level representation of a four-dot QCA cell. A square is created by positioning four quantum dots. Little semi-conductor or metal islands known as quantum dots have a diameter that is small enough to cause their fluctuating energy to be more than KBT (where T is the operating temperature and KB is Boltzman's constant). (They will eventually shrink to fit within specifically made molecules.) They will trap individual charge barriers if this is the case.

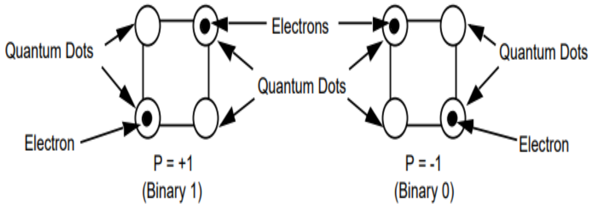

Figure 1. QCA cell polarization and representations of binary 1 and binary 0.

Through electron tunnelling, exactly two mobile electrons are loaded into the cell and are able to travel to various quantum dots within the QCA cell. In 2.1, the lines that join the quantum dots depict the tutoring routes. The electrons will only occupy the corners of the QCA cell due to repulsion, creating two distinct polarisations. There are two types of cells with 90° and 45° rotations that are commonly used in semiconductor QCA technology. Both types can be represented as zero and one logic, but there is a slight variation in the forms of the cells that are placed, even though each cell's computation remains the same. A 90° cell would become a 45° cell if it were rotated by 45°. It is assumed that potential barriers between neighbouring QCA cells, which are raised and lowered by capacitive plates, provide total control over electron tunnelling.

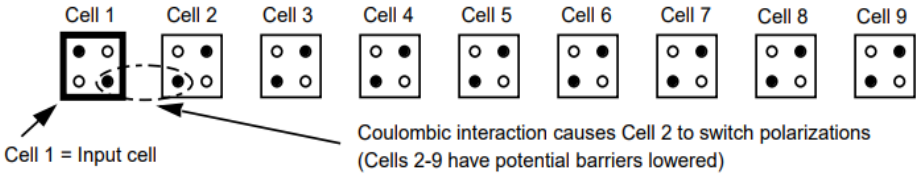

Figure 2. A QCA wire.

A QCA wire depicted in **Figure 2** is created by electrostatic interaction between cells arranged in a row next to one another; any input value can propagate across the wire, and the output cell will have a value equal to the input cell. Because of this, each cell can perform the three important functions of wire, processor, and memory all at once.

Generally speaking, a lot of work has gone into creating an inverter gate, as shown in **Figure 3**. All the gates are identical in terms of functioning, but because they are utilised for distinct purposes, each inverter gate has a unique map and overall design. Random input values are applied to the input cell of every inverter gate. Based on the electrostatic interactions between electrons, any amount of propagation on a gate occurs in between. This is caused by a change in the middle cell's placement, which charges the middle values in the opposite direction. The output cell then provides the reverted value.

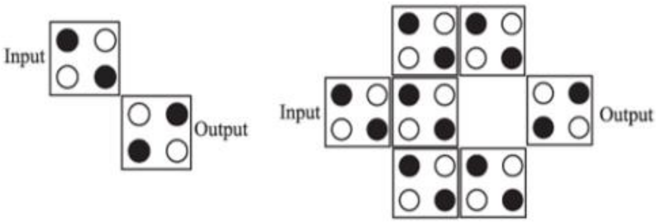

Figure 3. Inverter gate.

Potential barriers (that would be beneath the cell) that can be increased and reduced between neighbouring QCA cells using capacitive plates are considered to be the only means of controlling electron tunnelling.

Majority gate:

The majority and inverter gates are essential gates in QCA technology that designers can utilise to create any kind of new circuit. There should be an odd number of cells in the majority. We now want to talk about a three-input majority gate, which has three inputs, one voter cell, and one output cell—as the name suggests. The function of this gate is indicated in Equation. The majority gate and the inverter gate share the same electrostatic interactions. The structure of the three input majority gates is shown in **Figure 4**.

$$\text{Majority} = AB + BC + AC \tag{1}$$

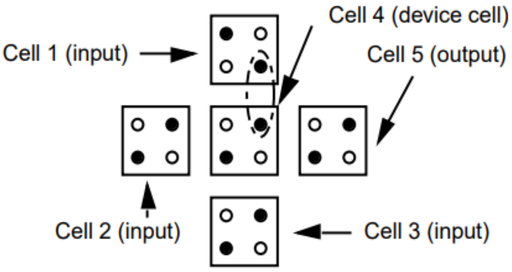

Figure 4. The fundamental QCA logical device—The majority gate.

3. The proposed method

3.1. The reversible Feynman gate

More energy is being used by computers than ever before, with over a billion of them in use globally. Computers with reversible features can use less power in several areas, such as the CPU and memory. To run on a computer, a process has to divide the calculation into smaller units. Reversible hardware ensures that no result is wasted since occasionally, for a process or set of pieces to be completed, it requires the other parts. Therefore, fetching from main memory is not necessary. When a CPU based on reversible hardware executes instructions, for instance, middle registers do not need to keep the results of prior computations; this helps to lower a device's energy consumption and overall calculation time.

Reversible circuit design has generally received far more attention in recent decades [13]; the Feynman gate is one of the most well-known reversible arithmetic logic gates. One of the numerous circuits that can use the Feynman gate is the ALU. The Feynman gate is a two-by-two device with two inputs, A and B, and two outputs, Q and P. The correspondence between the inputs and outputs is one to one. $P = A$ and $Q = (A \oplus B)$ are the respective output equations. When $A = 0$ and B = 0, this gate's functioning would result in $P = 0$ and $Q = 0$ as output. In a similar vein, if $A = 0$ and $B = 1$, the result would be $P = 0$ and $Q = 1$, and the cycle would repeat. The reversible Feynman gate suggested by the QCA layout is depicted in **Figure 5**.

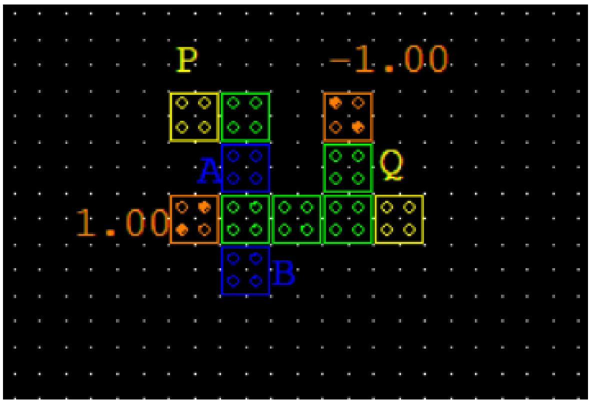

Figure 5. Layout of Feynman gate.

3.2. The reversible odd-parity generator and checker

When designing circuits, the most crucial element is extensibility. A reversible parity generator and checker circuit's complexity is dependent on several variables and necessitates careful evaluation of performance trade-offs. Among the methods most frequently employed for data transmission fault detection is the parity-generating technique. Binary data in digital systems is susceptible to noise during transmission and processing, which can change 0 s (of the data bits) to 1 s and 1 s to 0 s. Below is a block schematic of the parity generator depicted in **Figure 6**.

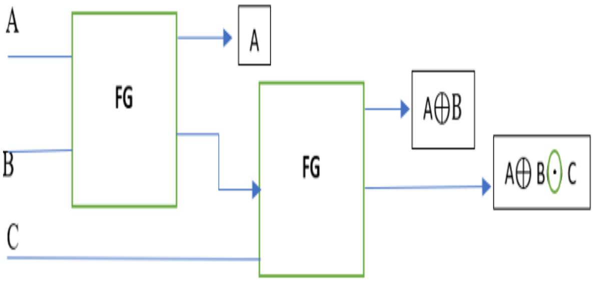

Figure 6. Block diagram of odd-parity generator.

Therefore, to make the number of 1 s even or odd, a parity bit is added to the word containing the data. A new reversible odd-parity generator is shown to illustrate the benefit. It has three inputs, $X1$, $X2$, and $X3$, and one output parity bit. The odd-parity generator's QCA configuration is displayed in **Figure 7**. One way to characterise the suggested 3-bit reversible gate is as follows:

$$X1 = \text{GAR } 1 \tag{2}$$

$$X2 = \text{GAR } 2 \tag{3}$$

$$\text{X3(parity)} = X1 \text{ xor } (X2 \text{ xnor } X3) \tag{4}$$

The schematic of the parity checker is shown in **Figure 8**.

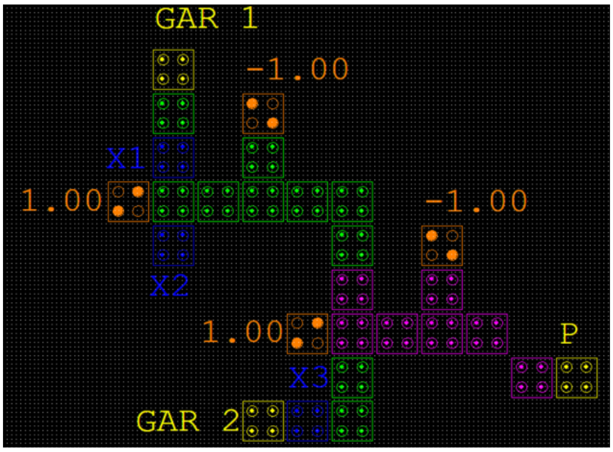

Figure 7. The schematic of the parity generator.

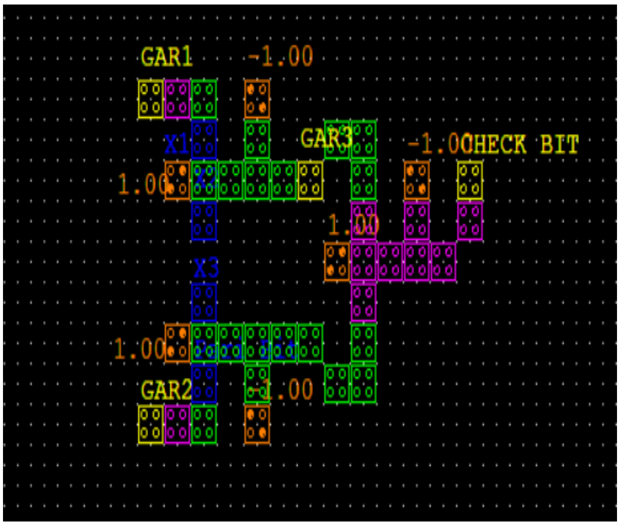

Figure 8. Layout of parity checker.

The odd-parity generator yields GAR1 = 0, GAR2 = 0, and a parity bit of 1 if $X1 = 0$, $X2 = 0$, and $X3 = 0$. On the other hand, the outputs become GAR1 = 0, GAR2 = 0, and parity bit = 0 when the inputs are $X1 = 0$, $X2 = 0$, and $X3 = 1$. The entire set of combinations for this generator is shown in **Table 1**. A circuit known as a parity checker is used to verify the receiver's parity. Check bit = 1 indicates an error occurs when the data word (three input bits plus the parity bit) turns even; check bit = 0 indicates no error occurs. The parity checker generates one output from four inputs

($X1$, $X2$, $X3$, and the parity bit). The mathematics for this circuit, which the parity checker uses, are displayed below.

$$X1 = \text{GAR } 1 \tag{5}$$

$$X2 = \text{GAR } 2 \tag{6}$$

$$X3 = \text{GAR } 3 \tag{7}$$

$$\text{Check bit} = ((X1 \text{ xor } X2)' \text{ xor } (X3 \text{ xor parity bit})')' \tag{8}$$

Table 1. Truth table of the parity generator and parity checker system.

*X*1	*X*2	*X*3	Check bit	Parity bit	GAR1	GAR2
0	0	0	0	1	0	0
0	0	1	0	0	0	0
0	1	0	0	0	0	1
0	1	1	0	1	0	1
1	0	0	0	0	1	0
1	0	1	0	1	1	0
1	1	0	0	1	1	1
1	1	1	0	0	1	1

3.3. The proposed nano-communication system

Generally speaking, vulnerabilities in communications networks can be found by utilising a nano-communication system constructed with checkers and parity producing units. The three proposed components for nano-communication are the transmitter, the transmission medium, and the receiver. We solely used fault-tolerant components when designing the suggested nano-communication system, like fault-tolerant inverters and XOR [11].

- In addition to the three-input message, the transmitter generates a second bit known as the parity bit. The transmitted bit pattern has an odd number of 1s, or odd parity.
- The communication link between the source and the destination is provided by the transmission medium. The transmission medium (communication channel) is used to send the transmission bit pattern that the transmitter generates to the receiver.
- The receiver takes the transmission message word that the transmitter sent, along with the parity bit. At the receiver, the parity bit is examined in order to detect errors. An error has occurred through the transmission medium, indicating that one bit has changed if the received transmission bit pattern contains an even number of 1. If not, there has been no error.

Since actual clocking can lower fabrication costs and simplify the physical design, designing circuits based on it is a crucial component. Implementing QCA circuits based on real clocking has been the subject of numerous attempts; some solutions have been developed in a dynamic approach, while others have been built in a pipeline fashion [14]. Therefore, the pipeline format approach in the study of Jain et al. [14] would be the optimum option in the event of a loop-less circuit where the clock phase placement is sorted in increasing order. This has been taken into consideration in the case of the suggested nano-communication circuits, and the fundamental ideas of our suggested technique readily apply to actual clocking. QCA schematic of the overall nano communication network is shown in **Figure 9**. In **Figures 10–12** show the simulation results of each block as depicted in **Figure 9**.

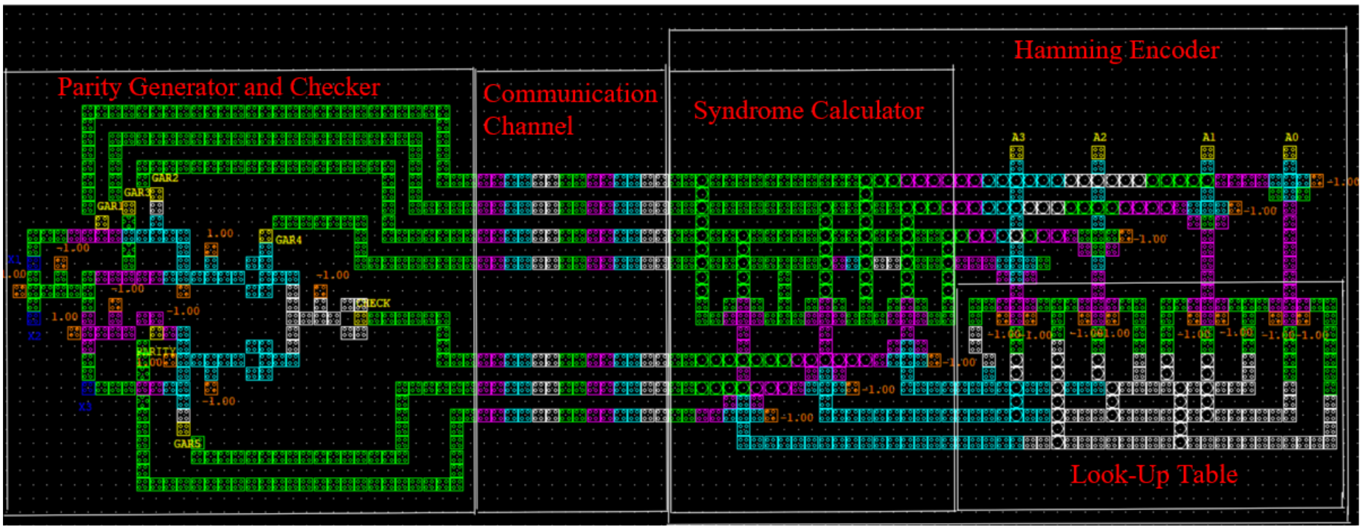

Figure 9. QCA circuit diagram of nano communication circuit.

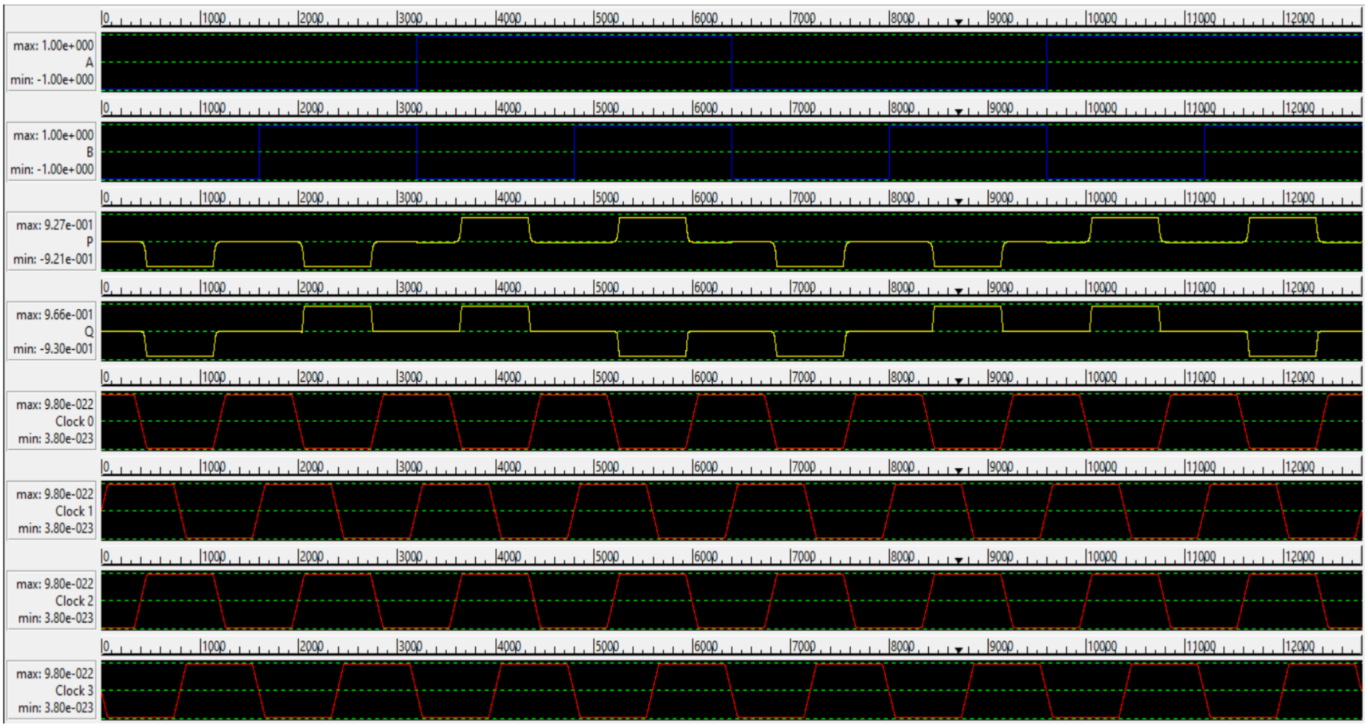

Figure 10. Simulation waveforms of Feynman gate.

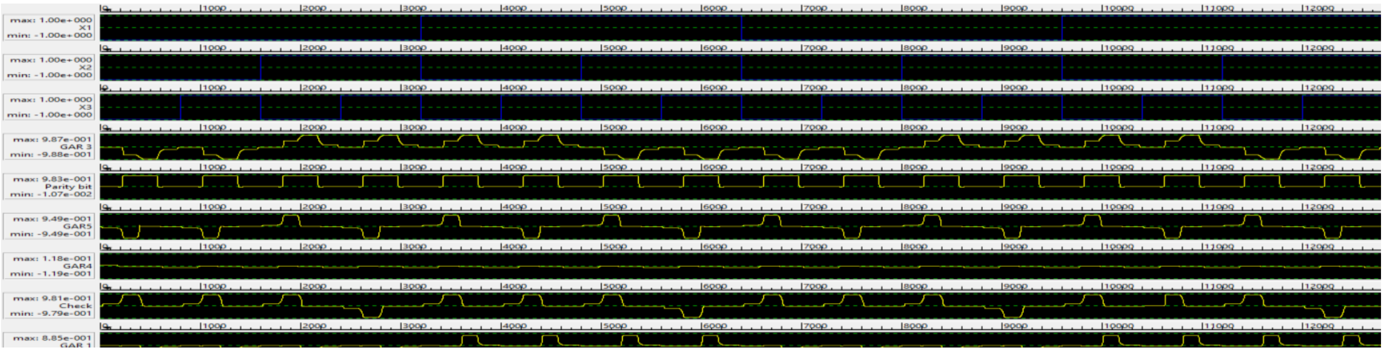

Figure 11. Simulation of parity generator and checker.

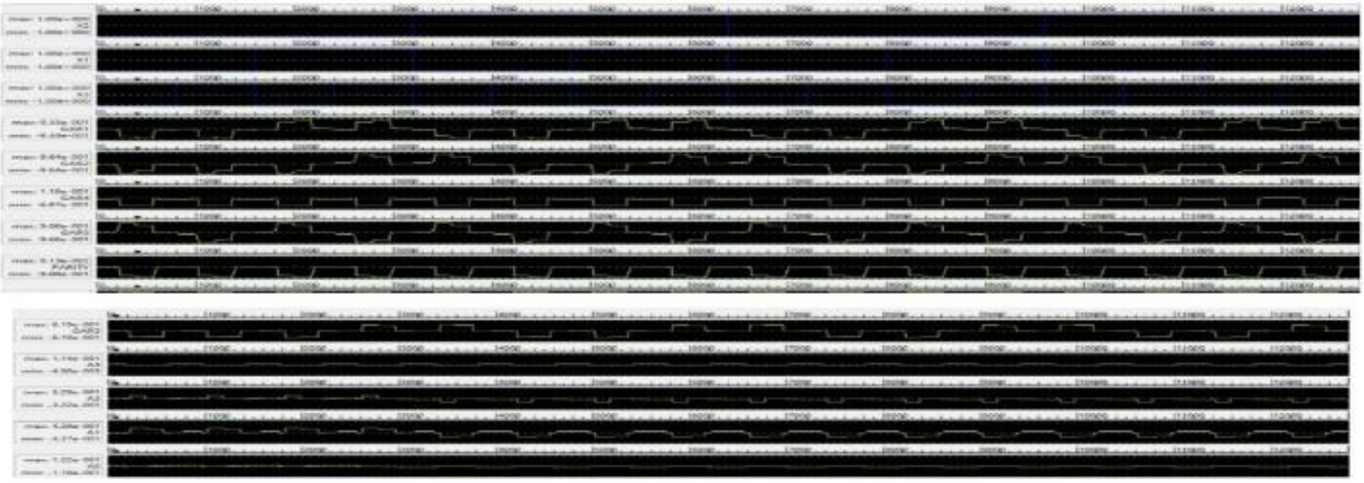

Figure 12. Simulation of nano communication circuit.

4. Experimental results

Performance evaluation and simulation results:

The most potent programme for simulating circuits based on QCA technology is QCA Designer. QCA cell size = 18 nm, quantum dot diameter = 5 nm, number of samples = 50,000, convergence tolerance = 0.001, radius of effect = 65 nm, relative permittivity = 12.9, clock low = 3.8×10^{-23} J, clock high = 9.8×10^{-22} J, clock amplitude factor = 2.000, layer separation = 11.5 nm, and maximum iterations per sample = 100 are some of the simulation parameters for this well-known tool.

5. Conclusion

In summary, a major advancement in the fields of nanotechnology and communication systems has been made with the design of the Nano Communication Network Reversible Based Parity Generator Circuit employing QCA. Through the utilisation of Quantum-dot Cellular Automata (QCA) special features, this circuit presents a viable path towards effective nanoscale data processing and transmission. In addition to guaranteeing low energy consumption (31.2%), its reversible design improves data transmission reliability by enabling error detection through parity creation. This method highlights the potential of nanotechnology to transform a number of industries, such as biomedical devices, the Internet of Things, and more, thereby influencing the direction of communication networks in the future. Building strong, high-performing systems in the nanoscale world requires the integration of

QCA-based circuits, such as the reversible parity generator, as we continue to explore the domain of nano communication.

Author contributions: Conceptualization, SKV and KMR; methodology, SKV, RS and RB; software, KMR, MRR and MMR; validation, SKV, RA and RB; formal analysis, KMR; investigation, SKV; resources, KMR; data curation, SKV and RS; writing—original draft preparation, SKV; writing—review and editing, SKV, RS and RB; visualization, KMR; supervision, SKV; project administration, KMR, MRR and MMR. All authors have read and agreed to the published version of the manuscript.

Conflict of interest: The authors declare no conflict of interest.

References

1. Bagherian Khosroshahy M, Abdoli A, Panahi MM. Novel Feynman-Based Reversible and Fault-Tolerant Nano-communication Arithmetic Architecture Based on QCA Technology. SN Computer Science. 2021; 2(6). doi: 10.1007/s42979-021-00811-5
2. Danehdaran F, Angizi S, Bagherian Khosroshahy M, et al. A combined three and five inputs majority gate-based high performance coplanar full adder in quantum-dot cellular automata. International Journal of Information Technology. 2019; 13(3): 1165-1177. doi: 10.1007/s41870-019-00365-z
3. Ahmad F, John MU, Khosroshahy MB, et al. Performance evaluation of an ultra-high speed adder based on quantum-dot cellular automata. International Journal of Information Technology. 2019; 11(3): 467-478. doi: 10.1007/s41870-019-00313-x
4. Landauer R. Irreversibility and heat generation in the computing process. IBM Journal of Research and Development. 2000; 44(1.2): 261-269. doi: 10.1147/rd.441.0261
5. Bennett CH. Logical Reversibility of Computation. IBM Journal of Research and Development. 1973; 17(6): 525-532. doi: 10.1147/rd.176.0525
6. Panahi MM, Hashemipour O, Navi K. A novel design of a ternary coded decimal adder/subtractor using reversible ternary gates. Integration. 2018; 62: 353-361. doi: 10.1016/j.vlsi.2018.04.014
7. Panahi MM, Hashemipour O, Navi K. A novel design of a multiplier using reversible ternary gates. IEEE.
8. Ahmed S, Naz SF. Notice of Violation of IEEE publication principles: design of cost efficient modular digital QCA circuits using optimized XOR Gate. IEEE Trans Circ Syst II Express Briefs. 2020.
9. Srivastava S, Sarkar S, Bhanja S. Estimation of Upper Bound of Power Dissipation in QCA Circuits. IEEE Transactions on Nanotechnology. 2009; 8(1): 116-127. doi: 10.1109/tnano.2008.2005408
10. Vankamamidi V, Ottavi M, Lombardi F. Two-Dimensional Schemes for Clocking/Timing of QCA Circuits. IEEE Transactions on Computer-Aided Design of Integrated Circuits and Systems. 2008; 27(1): 34-44. doi: 10.1109/tcad.2007.907020
11. Walus K, Dysart TJ, Jullien GA, et al. QCADesigner: A Rapid Design and Simulation Tool for Quantum-Dot Cellular Automata. IEEE Transactions on Nanotechnology. 2004; 3(1): 26-31. doi: 10.1109/tnano.2003.820815
12. Das JC, De D. Quantum-dot cellular automata based reversible low power parity generator and parity checker design for nanocommunication. Frontiers of Information Technology & Electronic Engineering. 2016; 17(3): 224-236. doi: 10.1631/fitee.1500079
13. Thapliyal H, Ranganathan N. Reversible Logic-Based Concurrently Testable Latches for Molecular QCA. IEEE Transactions on Nanotechnology. 2010; 9(1): 62-69. doi: 10.1109/tnano.2009.2025038
14. Jain V, Sharnma DK, Gaur HM, et al. Comprehensive and comparative analysis of QCA-based circuit designs for next-generation computation. ACM Computing Surveys. 2023; 56(53): 1-36.
15. Sardinha LHB, Costa AMM, Neto OPV, et al. NanoRouter: A Quantum-dot Cellular Automata Design. IEEE Journal on Selected Areas in Communications. 2013; 31(12): 825-834. doi: 10.1109/jsac.2013.sup2.12130015
16. Yao F, Zein-Sabatto MS, Shao G, et al. Nanosensor Data Processor in Quantum-Dot Cellular Automata. Journal of Nanotechnology. 2014; 2014: 1-14. doi: 10.1155/2014/259869
17. Kamaraj A, Abinaya, Ramya S. Design of router using Reversible Logic in Quantum Cellular Automata. 2014 International Conference on Communication and Network Technologies. 2014. doi: 10.1109/cnt.2014.7062764

18. Mohaimeed AA, Rabee BH. Influence of Berry dye on some properties of nanocomposite (PVA/TiO2) films. Optical and Quantum Electronics. 2023; 55(3). doi: 10.1007/s11082-022-04523-9
19. Najm AAA, Alshrefi SM, Hadi ZL, et al. Synthesis of Novel [CdO(75%)/VO2(20%)/SiC(4%): p-Si] Heterojunction Composite Thin Films Decorated with Chlorophyll using Solvothermal-Laser Dual Technique for Solar Cell Applications. Silicon. 2024. doi: 10.1007/s12633-024-02997-8

Characterization and Application of Nanomaterials2024, 7(2), 6046.
https://doi.org/10.24294/can.v7i2.6046

Article

Mechanical properties of spinel ($MgCr_2O_4$) phase containing alumino-silicate glass-ceramic

Mrinmoy Garai[1,*], Arianit A. Reka[2], Shibayan Roy[1]

[1] Materials Science Center, Indian Institute of Technology (IIT), Kharagpur 600036, India
[2] Department of Chemistry, Faculty of Natural Sciences and Mathematics, University of Tetova, Tetovo 1200, North Macedonia
*** Corresponding author:** Mrinmoy Garai, mrinmoygarai@iitkgp.ac.in

CITATION

Garai M, Reka AA, Roy S. Mechanical properties of spinel ($MgCr_2O_4$) phase containing alumino-silicate glass-ceramic. Characterization and Application of Nanomaterials. 2024; 7(2): 6046. https://doi.org/10.24294/can.v7i2.6046

ARTICLE INFO

Received: 26 April 2024
Accepted: 9 July 2024
Available online: 1 August 2024

Abstract: This research study explores the addition of chromium (Cr^{6+}) ions as a nucleating agent in the alumino-silicate-glass (ASG) system (i.e., Al_2O_3-SiO_2-MgO-B_2O_3-K_2O-F). The important feature of this study is the induction of nucleation/crystallization in the base glass matrix on addition of Cr^{6+} content under annealing heat treatment (600 ± 10 °C) only. The melt-quenched glass is found to be amorphous, which in the presence of Cr^{6+} ions became crystalline with a predominant crystalline phase, Spinel ($MgCr_2O_4$). Microstructural experiment revealed the development of 200–500 nm crystallite particles in Cr^{6+}-doped glass-ceramic matrix, and such type microstructure governed the mechanical properties. The machinability of the Cr-doped glass-ceramic was thereby higher compared to base alumino-silicate glass (ASG). From the nano-indentation experiment, the Young's modulus was estimated 25(±10) GPa for base glass and increased to 894(±21) GPa for Cr-doped glass ceramics. Similarly, the microhardness for the base glass was 0.6(±0.5) GPa (nano-indentation measurements) and 3.63(±0.18) GPa (micro-indentation measurements). And that found increased to 8.4(±2.3) (nano-indentation measurements) and 3.94(±0.20) GPa (micro-indentation measurements) for Cr-containing glass ceramic.

Keywords: alumino-silicate glass; nucleation; microstructure; microhardness

1. Introduction

Al_2O_3-SiO_2-MgO-B_2O_3-K_2O-F (alumino-silicate-glass) is converted into corresponding glass-ceramic/glass-ceramic composite with typical microstructure-driven mechanical properties [1–3]. In practice, a heat-treatment schedule is followed for converting such silicate-based glass into corresponding glass-ceramic [4,5]. However, the heat treatment requires specified time and electrical energy. It is thus desired to get the glass crystallized with the least energy, i.e., without performing any heat treatment [4,6]. For this purpose, self-nucleation during the glass melting or annealing is desired. K_2O-MgO-B_2O_3-SiO_2-F systems have the ability to incorporate active ions (like chromium, aluminum, lanthanoids, etc.) at various concentrations, making it easier to provide bulk samples compared to crystalline materials. In order to add chromium ions in silicate (SiO_2)-based glasses, it can possess variable oxidation states, viz. +2, +3, +6, etc. Cr^{3+} serves as a modifier, whereas Cr^{6+} (i.e., CrO_4^{2-} structural units) can act as the glass network former [3,4]. Since chromium ions have multi-oxidation states Cr^{n+}($n = 2$–6), the mechanical properties depend on its structural units (i.e., properties of the former and modifier). As the glasses possess no long-range order, the position of Cr-ions can vary depending on the ligand's locations as well as the coordination number and the average distance of the central ion-ligand [6–8]. It is reported that the higher valent chromium ion (i.e., Cr^{6+}) is effective for the crystallization as well as microstructure in boro-silicate/alumino-silicate glass [7–9]. If nucleation in Al_2O_3-SiO_2-MgO-B_2O_3-K_2O-F glass occurs during melting or annealing temperature, glass-ceramic composite-type material is obtained instead of getting superior glass phase [6–8]. In the study on SiO_2-B_2O_3-based glass systems, Aktas et al. [8] demonstrated that 0–1 wt% Cr_2O_3-containing glass is completely amorphous, but Cr_2O_3 contents >1 wt% make those glasses crystalline, i.e., glass-ceramic. However, the effectiveness of such a technique comes from creating a finely structured crystalline phase with random orientation, typically free from pits, dents, voids, micro-cracks, or porosity [7,10]. And such a fine grain type of microstructure can generate the desired mechanical properties in final glass ceramics.

In this report, the substitution of Al^{3+} ions by Cr^{6+} ions in alumino-silicate glass (ASG), i.e., Al_2O_3-SiO_2-MgO-B_2O_3-K_2O-F system, is studied. Due to the Cr^{6+} addition in such glass, the relevant variation of the crystallization features (XRD, FESEM) is interrelated with mechanical properties (microhardness, Youngs modulus, contact depth) [4].

2. Experimental

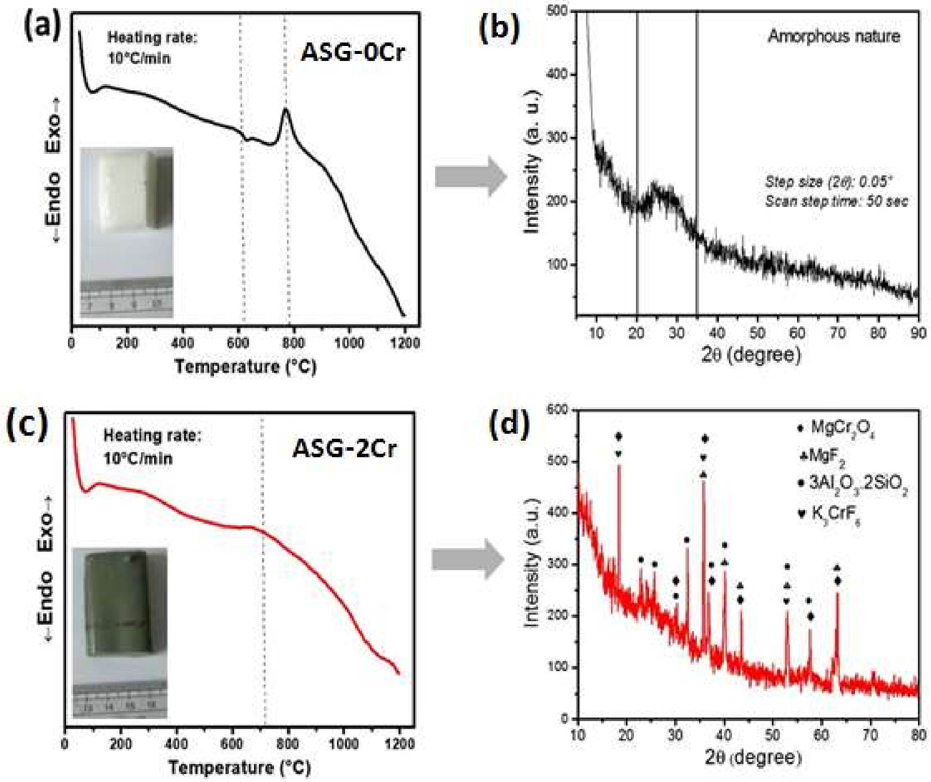

Figure 1. Differential scanning calorimetric (DSC) thermogram of Al_2O_3-SiO_2-MgO-B_2O_3-K_2O-F glass containing. **(a)** 0 mol%; **(c)** 2 mol% chromium content (inset of **Figure 1a,c** shows the photograph of corresponding glasses) and XRD pattern **(b)** 0 mol%; **(d)** 2 mol% Cr-doped glasses [4].

Two alumino-silicate-glass (ASG) of composition (mol%) (i) ASG-0Cr (7K_2O-20MgO-10B_2O_3-44SiO_2-12MgF_2-7Al_2O_3) and (ii) ASG-2Cr (7K_2O-20MgO-10B_2O_3-44SiO_2-12MgF_2-5Al_2O_3-2$K_2Cr_2O_7$) were synthesized by melt-casting using pure chemicals, i.e., SiO_2, $Al(OH)_3$, $Mg(OH)_2$, H_3BO_3,K_2CO_3, MgF_2, and $K_2Cr_2O_7$. The details/purity of reagents are described in a previous report on a similar glass system [4]. The glasses were melted in a platinum (Pt) crucible in an electrically heated furnace at 1570(±10) °C for 2 h, followed by casting in graphite mold and thereafter annealing at 600(±10) °C (2 h). The photographs of the annealed glasses are exhibited in the inset of **Figure 1** that clearly demonstrates the opaque nature [4]. Annealed glass was characterized for microstructural and mechanical properties using the techniques of differential scanning calorimetry (DSC), X-ray diffraction (XRD), field emission scanning electron microscopy (FESEM), energy dispersive X-ray spectroscopy (EDX), nanoindentation, and Vickers microindentation [11–15].

Finely powdered (particle size < 60 µm) ASG samples were subjected to differential scanning calorimetry (DSC SetaramLabsys, Setaram Instrumentation, France) at a heating rate of 10 °C/min to obtain the phase transformation temperature. XRD analysis was recorded using an XPERTPRO MPD diffractometer (PANalytical, Netherlands) operating with Ni-filtered CuKα = 1.5406 Å radiation as the X-ray source. The morphology of the glasses (chemically etched by 2 vol.% aqueous HF solution for 10 min) was examined using a FESEM (model S430i, LEO, CEA, USA). To dictate the elements present in the synthesized glass, qualitative elemental composition analysis was performed using the energy dispersive X-ray spectroscopy (EDX) detector attached to the FESEM microscope [11,12]. Nano-indentation was taken using polished glass samples by the Berkovich indenter tip (radius = 100 nm & angle = 142.3°) Hystron, Model No. TIN 50 Triboindenter, USA. The indentation was carried out with an applied force of 5 mN under a dwell time of 10 s followed by constant unloading. The indentations were obtained from various locations within the specimen surface. For measurement, a total of 20 indentations were taken at any given location following a 4 × 5 square matrix pattern. Standard indentation P-h curves were generated from the load (*P*) controlled nano-indentation tests and the corresponding measurements of indentation depth (*h*). The microhardness (*H*) and Young's modulus (*E*) were determined from the P-h curves based on the Oliver-Pharr method [16]. The Vickers microhardness (microindentation) of the glasses was also estimated (measurement error ± 5%) using a micro-indentation hardness testing instrument (UHL VMHT, Walter UHLTM). For each sample, ten (10) micro-indentions were taken with a constant spacing of 10 µm under identical loading conditions (=500 g) under a 10 s dwell time [4]. The diagonal of different indents was carefully measured using an optical microscope attached to the instrument, and consequently the microhardness values were calculated using the standard Equation (1) for the Vickers geometry.

$$HV = \frac{1.854P}{d^2} \tag{1}$$

where *HV* is the Vickers hardness number (VHN) in Kg/mm^2. *P* is the normal load in g, *d* is the average diagonal length of the indentation in mm. Here, the *HV* value obtained/100.1 = Vickers hardness in GPa.

3. Results and discussion

In order to ensure the nucleation of chromium (Cr^{6+}) with respect to phase transformation phenomena in Al_2O_3-SiO_2-MgO-B_2O_3-K_2O-F system, a non-isothermal differential scanning calorimetric (DSC) study was conducted, and the representative thermograms are shown in **Figure 1** [4]. The DSC pattern of ASG-0Cr glass exhibited in **Figure 1a** is very different compared to the chromium-doped one, i.e., the ASG-2Cr system (exhibited in **Figure 1c**). As seen from **Figure 1a**, the characteristic endothermic hump corresponding to the glass transition region is initiated at 580–590 °C and ended towards the minimum at 625–627 °C. From the onset of that endothermic hump, the glass transition temperature (Tg) is estimated at 610 ± 2 °C for ASG-0Cr glass. In the case of the chromium-doped system, the appearance of the glass transition hump (DSC) presented in **Figure 1c** is very different compared to ASG-0Cr. The hump for ASG-2Cr in **Figure 1c** is insignificant to define those as amorphous material; however, the minor endothermic hump that appeared is the indication of residual Al_2O_3-SiO_2-MgO-B_2O_3-K_2O-F glassy phase [1,2]. As mentioned in the experimental section, after melting, the as-quenched glass was annealing heat-treated. After annealing, ASG-2Cr found crystallized. In the present system, the ASG-0Cr glass is not crystallized upon annealing temperature. It is a well-established fact that nucleation is the process by which atoms or molecules come together to form a new phase or structure, and such a process is the initial stage in the formation of a crystal and involves the formation of a small cluster of atoms or molecules, i.e., a nucleus. Hence, it can be elucidated that ASG-0Cr is practically glass, but ASG-2Cr is not glass; it can be a glass-ceramic composite [8,9], and the pattern of exothermic peak broadening in **Figure 1c** is due to a minor residual glass phase. In a similar study on boro-silicate systems, Aktas et al. [8] argued that 0–1 wt% Cr_2O_3 containing silicate glass is completely amorphous, but Cr_2O_3 contents >1 wt% make those glass crystalline. For ASG-0Cr glass, the exothermic maximum (peak) is estimated at 768 ± 2 °C, which is corresponding to crystallization temperature [9]. Lin et al. [3] similarly studied DSC on Cr-doped alumino-silicate glass and argued that the incorporation of Cr-ion, as a modifier, can break the glass network and finally result in the decreased glass phase (i.e., Si-O-Si) stability. Thus, from DSC it is pointed out that the ASG-0Cr is glass but the ASG-2Cr contains crystallinity [4].

The nucleation phenomena of chromium (Cr^{6+}) doped Al_2O_3-SiO_2-MgO-B_2O_3-K_2O-F glass predicted from the DSC study were further confirmed from the X-ray diffraction (XRD) study [17]. XRD analysis revealed the formation of spinel phases at nucleation temperatures. As is evident from **Figure 1b** (i.e., ASG-0Cr glass), the broad hump that appeared at (2θ) 20°–35° signifies the amorphous nature. In view of the DSC experiment (**Figure 1**), it is pointed out that the catalyzed nucleation for initiating the crystallization process occurred in chromium-containing glass. Thus, crystalline nature is demonstrated by ASG-2Cr, as depicted in **Figure 1d**. As evident from **Figure 1d**, the crystalline peaks that appeared at (2θ) 18°, 30°, 36°, 37°, 44°, 58° and 63° are attributed to the crystalline planes (111), (220), (311), (222), (400), (511) and (531) of the spinel phase, $MgCr_2O_4$; JCPDS-PDF file number = 82–1529, FCC lattice [5]. The characteristic peaks appeared at (2θ) 18°, 30°, 36°, and 53° and are attributed to the formation of crystalline planes (101), (200), (202), and (312) of K_3CrF_6; JCPDS-PDF file number = 27–1354, tetragonal BCC lattice. ASG-2Cr is hence a glass-ceramic or glass-ceramic composite of multi-crystalline nature [4]. During the annealing at 600(±10) °C, MgF_2 crystals are precipitated as primary crystalline phase, and the characteristic peaks (2*θ*) 36°, 40°, 44°, 53°, and 63° are ascribed to the (101), (111), (210), (211), and (310) crystalline planes of MgF_2, JCPDS-PDF file number = 72–2231. Another Al- and Si-enriched crystalline phase is also developed in these glasses during annealing at 600(±10) °C. The crystalline peaks formed at (2*θ*) 23°, 26°, 30°, 33°, 37°, 40° and 58° correspond to the crystalline planes (200), (120), (001), (220), (130), (121) and (041) of mullite ($3Al_2O_3{\cdot}2SiO_2$), JCPDS-PDF file number = 82–0037 [4]. For the ASG-2Cr system, the crystalline peak that appeared at (2*θ*) 36° is associated with the highest intensity, and that peak is ascribed to the development of the spinel phase ($MgCr_2O_4$) [4,16]. Thus, from XRD, it can be clarified that through the annealing heat treatment in such Al_2O_3-SiO_2-MgO-B_2O_3-K_2O-F system, the spinel phase, i.e., $MgCr_2O_4$ can be predominately obtained when using Cr^{6+} as a nucleation agent [6–9].

The Cr-controlled nucleation at annealing temperature was caused by chromium ions in the ASG-2Cr system, and thus the microstructures (FESEM) developed in such chromium-doped glass ceramic were studied. **Figure 2** presents the results of experimental investigation on microstructure (size and morphology of crystalline phases) [4]. As observed in **Figure 2a**, the randomly distributed crystallite particles throughout the matrix gathered to develop a colony-like arrangement. Under higher magnification, i.e., from **Figure 2b**, it is seen that rock-like 200-500 nm-sized crystalline particles are dispersed throughout the ASG system and further lead to a compact microstructure. From the EDX pattern (inset of **Figure 2b**), the elements present in the ASG-2Cr matrix are made out as K, O, Cr, Mg, Al, and Si, and it confirms the development of the predominant spinel phase ($MgCr_2O_4$), as already pointed out from XRD. Such fine-grained compact microstructure developed in the ASG-2Cr system significantly controls the mechanical parameters (microhardness, Young's mudulus, etc.) as analyzed from nanoindentation and microindentation studies [17,18].

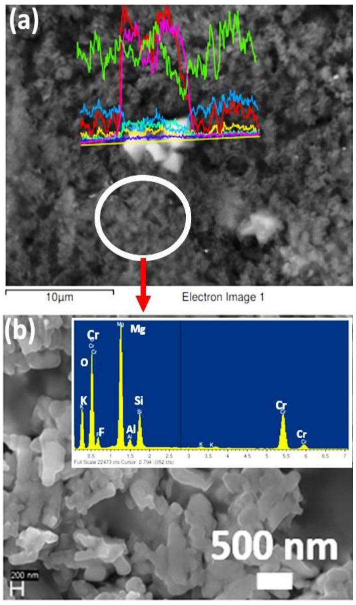

Figure 2. FESEM photomicrograph of Al_2O_3-SiO_2-MgO-B_2O_3-K_2O-F glass-ceramic (ASG-2Cr) in **(a)** 10 µm; **(b)** 500 nm scale (inset of **Figure 2b** presents the EDX pattern of ASG-2Cr system) [4].

The load-displacement curves and loading-unloading P-h curves from the nano-indentation tests on the studied glasses are presented in **Figures 3** and **4**, respectively. As pointed out from XRD and FESEM observations, the base Al_2O_3-SiO_2-MgO-B_2O_3-K_2O-F glass (Cr-0) is an amorphous system, which, on addition of chromium, was converted into the glass-ceramic, and such a similar observation is further evidenced from the load-displacement study exhibited in **Figure 3**.

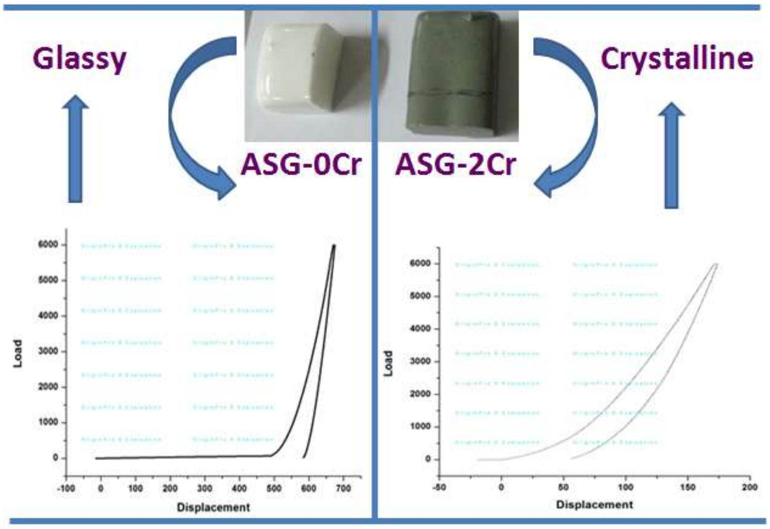

Figure 3. Load-displacement curves exhibiting ASG-0Cr as glass and CSG-2Cr as glass-ceramic.

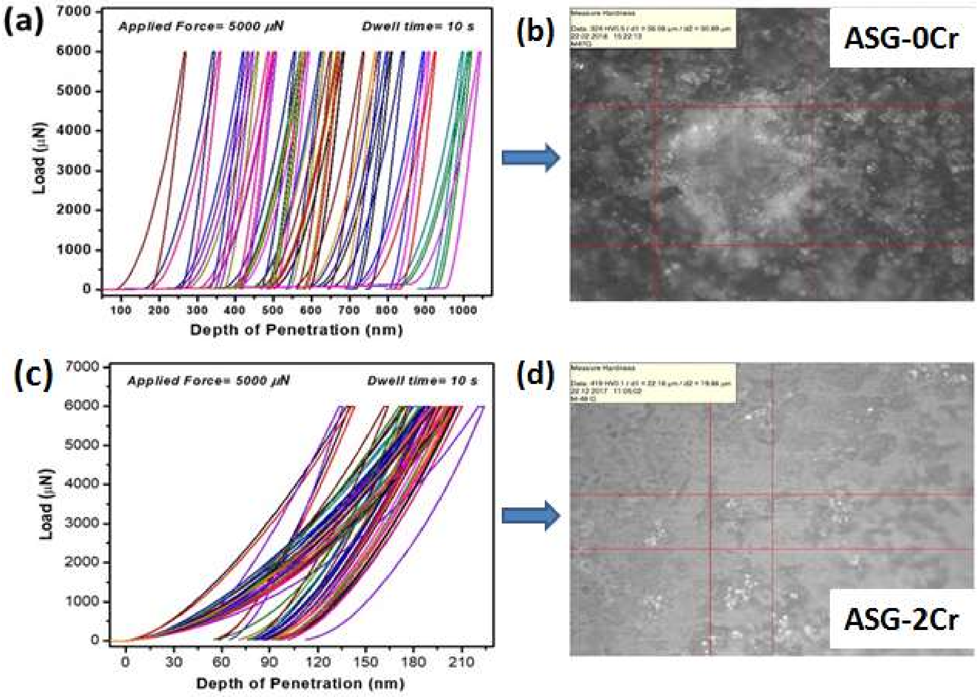

Figure 4. P-h curves from nano-indentation tests using Berkovich indenter tip from Al_2O_3-SiO_2-MgO-B_2O_3-K_2O-F glasses i.e., **(a)** ASG-0Cr; **(c)** ASG-2Cr. Photograph of Vickers microhardness indentation impression on; **(b)** ASG-0Cr; **(d)** ASG-2Cr glasses showing the increasing crystallinity with chromium content [4].

Figure 4a thus represents loading-unloading P-h curve characteristics for ASG-0Cr glass with a much higher depth of penetration for the constant load of 5 mN [4]. The low depth of penetration for ASG-2Cr glass-ceramics (**Figure 4c),** on the other hand, suggests higher strength due to correspondingly higher crystallinity and compactness of the microstructures [4]. The load-displacement curve also demonstrates the trend of increasing elastic modulus. The contact depth is the depth of indenter in contact with the ASG glass samples under used load P (constant load of 5 mN). When under the same load (P), a higher contact depth occurs, which means the sample is not so hard (comparatively), i.e., lower microhardness is observed [16,18]. For the ASG-0Cr system (glass), the depth of penetration reached to ~950 nm, whereas for ASG-2Cr glass-ceramics, it is ~200–250 nm. Interestingly, Young's modulus and microhardness both found to increase when Cr-ion was added to the base ASG glass (**Table 1),** and that is ascribed to the change in morphology of the crystal phases.

Table 1. Depth of penetration (h), Young's modulus and microhardness measured from the nano-indentation tests on Al_2O_3-SiO_2-MgO-B_2O_3-K_2O-F glasses with and without $K_2Cr_2O_7$ [4].

Sample	Contact depth (nm)	Young's modulus (GPa)	Microhardness (GPa)
ASG-0Cr	619 ± 195	25 ± 10	0.6 ± 0.5
ASGr-2Cr	139 ± 16	94 ± 21	8.4 ± 2.3

Microhardness Microhardness of glass/glass-ceramic materials is largely dependent on strength, crystallinity, as well as residual glass phase in the microstructure [17]. Vicker's microhardness indentation impression for the studied glasses is presented in **Figures 4b,d**. For ASG-0Cr glass, the microhardness is estimated at 3.63 (±0.18) GPa, and for chromium-containing systems, it is higher due to the crystalline nature [18]. The ASG-2Cr matrix (**Figure 2**) is composed of 200–500 nm-sized crystals dispersed randomly, and such arrangements are the reason for the microhardness value of 3.94 (±0.20) GPa [12,16].

Thus, the addition of Cr-ion caused self-nucleation and, moreover, a significant change in the microstructure and hence the mechanical properties, i.e., contact depth, modulus, and hardness value, of the ASG-2Cr system [18–20]. The residual glass phase in ASG-2Cr is directly related to the mechanical properties of such Al_2O_3-SiO_2-MgO-B_2O_3-K_2O-F glass ceramics [17,20]. This fact led to the suitability of ASG-2Cr glasses as a machinable glass-ceramic (MACOR) due to their specific microstructure-driven mechanical properties, including a microhardness of 3.94 ± 0.20 GPa [15–18].

4. Conclusions

In presence of chromium ion (Cr^{6+}), self-nucleation of Al_2O_3-SiO_2-MgO-B_2O_3-K_2O-F glass occurred at annealing heating 600 ± 10 °C only. From the XRD pattern, it is confirmed that the base glass is amorphous, whereas chromium-doped glass is crystalline with predominant phases of spinel ($MgCr_2O_4$). Dense and compact microstructure containing 200–500 nm crystallites is obtained in chromium-doped Al_2O_3-SiO_2-MgO-B_2O_3-K_2O-F glass ceramic. From nano-indentation, the hardness and Young's modulus for base glass were estimated 0.6(±0.5) and 25(±10) GPa, respectively, which increased in the case of chromium-doped glass ceramics. Vicker's microhardness for the base glass was 3.63(±0.18) GPa which was also increased to 3.94(±0.20) GPa for chromium-containing glass ceramic. In brief, the hexavalent chromium ion (Cr^{6+}) doping in alumino-silicate glass Al_2O_3-SiO_2-MgO-B_2O_3-K_2O-F imposed nucleation at annealing temperature and was thereby effective for improving the machinability.

Author contributions: Conceptualization, MG; methodology, MG; data curation, MG and AAR; writing—original draft preparation, MG and AAR; writing—review and editing, SR. All authors have read and agreed to the published version of the manuscript.

Funding: The author is thankful to B. Karmakar, Former Head, GSTS, CSIR-Central Glass and Ceramic Research Institute, Kolkata for his guidance (PhD thesis) to carry out this work. MG thankfully acknowledges DST-SERB for financial support under the National Post Doctoral Fellowship (N-PDF) scheme (Ref No: PDF/2016/003799) at Indian Institute of Technology (IIT), Kharagpur. AAR is thankful for the partial support form University of Tetova.

Conflict of interest: The authors declare no conflict of interest.

References

1. Zarabi Golkhatmi S, Asghar MI, Lund PD. A review on solid oxide fuel cell durability: Latest progress, mechanisms, and study tools. Renewable and Sustainable Energy Reviews. 2022; 161: 112339. doi: 10.1016/j.rser.2022.112339
2. Beall GH. Milestones in Glass-Ceramics: A Personal Perspective. International Journal of Applied Glass Science. 2014; 5(2): 93-103. doi: 10.1111/ijag.12063
3. Lin C, Liu J, Han L, et al. Study on the structure, thermal and optical properties in Cr_2O_3-incorporated MgO-Al_2O_3-SiO_2-B_2O_3 glass. Journal of Non-Crystalline Solids. 2018; 500: 235-242. doi: 10.1016/j.jnoncrysol.2018.08.004
4. Garai M, Karmakar B, Roy S. Cr^{6+} Controlled Nucleation in SiO_2-MgO-Al_2O_3-K_2O-B_2O_3-F Glass Sealant (SOFC). Frontiers in Materials. 2020; 7: 57. doi: 10.3389/fmats.2020.00057
5. Pingale SS, Patil SF, Vinod MP, et al. Mechanism of humidity sensing of Ti-doped $MgCr_2O_4$ ceramics. Materials Chemistry and Physics. 1996; 46(1): 72-76.
6. Bremm S, Dölling S, Becker W, et al. A methodological contribution to failure prediction of glass ceramics sealings in high-temperature solid oxide fuel cell stacks. Journal of Power Sources. 2021; 507: 230301. doi: 10.1016/j.jpowsour.2021.230301
7. Sun, T, Chi Z, Feng Z, et al. Mixed CaO/MgO effect on microstructure, mechanical properties and crystallization behaviour of Li_2O-Al_2O_3-SiO_2-ZrO_2-P_2O_5 glass. Journal of Non-Crystalline Solids. 2023; 616: 122457. doi: doi.org/10.1016/j.jnoncrysol.2023.122457
8. Aktas B, Yalcin S, Dogru K, et al. Structural and radiation shielding properties of chromium oxide doped borosilicate glass. Radiation Physics and Chemistry. 2019; 156: 144-149. doi: 10.1016/j.radphyschem.2018.11.012
9. Timurkutluk C, Toruntay F, Onbilgin S, et al. Development of ceramic fiber reinforced glass ceramic sealants for microtubular solid oxide fuel cells. Ceramics International. 2022; 48(11): 15703-15710. doi: 10.1016/j.ceramint.2022.02.105
10. Garai M, Reka AA, Karmakar B, et al. Microstructure–mechanical properties of Ag0/Au0 doped K–Mg–Al–Si–O–F glass-ceramics. RSC Advances. 2021; 11(19): 11415-11424. doi: 10.1039/d0ra10519h
11. Das, S, Madheshiya A, Das S, et al. Mechanical, surface morphological and multi-objective optimization of tribological properties of V_2O_5 doped lead calcium titanate borosilicate glass ceramics. Ceramics International. 46(11): 19170-19180. doi: 10.1016/j.ceramint.2020.04.252
12. Karamanov A, Pisciella P, Pelino M. The effect of Cr_2O_3 as a nucleating agent in iron-rich glass-ceramics. Journal of European Ceramic Society. 1999; 19: 2641-2645. doi: 10.1016/S0955-2219(99)00047-3

13. Hubert M, Faber AJ, Akmaz F, et al. Stabilization of divalent chromium Cr(II) in soda-lime-silicate glasses. Journal of Non-Crystalline Solids. 2014; 403: 23-29. doi: 10.1016/j.jnoncrysol.2014.06.015
14. Singh K, Walia T. Review on silicate and borosilicate-based glass sealants and their interaction with components of solid oxide fuel cell. International Journal of Energy Research. 2021; 45(151): 20559-20582. doi: https://doi.org/10.1002/er.7161
15. Rezvani M, Eftekhari-Yekta B, Solati-Hashjin M, et al. Effect of Cr_2O_3, Fe_2O_3 and TiO_2 nucleants on the crystallization behaviour of SiO_2-Al_2O_3-CaO-MgO(R_2O) glass-ceramics. Ceramics International. 2005; 31(1): 75-80. doi: 10.1016/j.ceramint.2004.03.037
16. Oliver WC, Pharr GM. An improved technique for determining hardness and elastic modulus using load and displacement sensing indentation experiments. Journal of Materials Research. 1992; 7(6): 1564-1583. doi: 10.1557/jmr.1992.1564
17. Garai M, Murthy TSRCH, Karmakar B. Microstructural characterization and wear properties of silver and gold nanoparticle doped K-Mg-Al-Si-O-F glass-ceramics. Ceramics International. 2018; 44(18): 22308-22317. doi: 10.1016/j.ceramint.2018.08.356
18. Jahanshahi M, Mofidian R, Hosseini SS, et al. Investigation of mechanical properties of granular γ-alumina using experimental nano indentation and nano scratch tests. SN Applied Sciences. 2023; 5(6). doi: 10.1007/s42452-023-05388-7
19. Garai M, Singh CK, Rout SK. Crystallization and microstructure in K_2O substituted SiO_2-MgO-Al_2O_3-Li_2O-$AlPO_4$ glass-ceramics. Solid State Communications. 2022; 350: 114758. doi: 10.1016/j.ssc.2022.114758
20. Serbena FC, Mathias I, Foerster CE, et al. Crystallization toughening of a model glass-ceramic. Acta Materialia. 2015; 86: 216-228. doi: 10.1016/j.actamat.2014.12.007

Characterization and Application of Nanomaterials 2024, 7(2), 6414.
https://doi.org/10.24294/can.v7i2.6414

Article

Micro/nanoscaled cellulose from coffee pods do not impact HT-29 cells while improving viability and endosomal compartment after *C. jejuni* CDT intoxication

Daniele Lopez[1,2], Giovanna Panza[1], Pietro Gobbi[1], Michele Guescini[1], Laura Valentini[1], Stefano Papa[1], Vieri Fusi[2], Eleonora Macedi[2], Daniele Paderni[2], Mariele Montanari[1], Barbara Canonico[1,*]

[1] Department of Biomolecular Sciences, University of Urbino Carlo Bo, 61029 Urbino, Italy
[2] Department of Pure and Applied Sciences (DiSPeA), University of Urbino Carlo Bo, 61029 Urbino, Italy
*** Corresponding author:** Canonico Barbara, barbara.canonico@uniurb.it

CITATION

Lopez D, Panza G, Gobbi P, et al. Micro/nanoscaled cellulose from coffee pods do not impact HT-29 cells while improving viability and endosomal compartment after *C. jejuni* CDT intoxication. Characterization and Application of Nanomaterials. 2024; 7(2): 6414. https://doi.org/10.24294/can.v7i2.6414

ARTICLE INFO

Received: 15 May 2024
Accepted: 28 June 2024
Available online: 1 August 2024

Abstract: The food industry progressively requires innovative and environmentally safe packaging materials with increased physical, mechanical, and barrier properties. Due to its unique properties, cellulose has several potential applications in the food industry as a packaging material, stabilizing agent, and functional food ingredient. A coffee pod is a filter of cellulosic, non-rigid, ready-made material containing ground portions and pressed coffee prepared in dedicated machines. In our study, we obtained, with homogenization and sonication, cellulose micro/nanoparticles from three different coffee pods. It is known that nanoparticulate systems can enter live cells and, if ingested, could exert alterations in gastrointestinal tract cells. Our work aims to investigate the response of HT-29 cells to cellulose nanoparticles from coffee pods. In particular, the subcellular effects between coffee-embedded nanocellulose (CENC) and cellulose nanoparticles (NC) were compared. Finally, we analysed the pathologic condition (Cytolethal Distending Toxin (CDT) from *Campylobacter jejuni*) on the same cells conditioned by NC and CENC. We evidenced that, for the cellular functional features analysed, NC and CENC pre-treatments do not worsen cell response to the *C. jejuni* CDT, also pointing out an improvement of the autophagic flux, particularly for CENC preconditioning.

Keywords: coffee embedded nanocellulose; nanocellulose; *C. jejuni* CDT; HT-29 intestinal cells; vacuolar compartment; biological improving responses; mitochondrial damage

1. Introduction

Cellulose materials are "generally regarded as safe" (GRAS) as binders and thickeners in food products. However, nanocellulose materials have unique properties that can improve food quality and safety and have not received US Food and Drug Administration (FDA) approval as food ingredients. Because of their unique properties, nanoscale fibrillated cellulose and crystals have additional potential applications in the food industry as 1) packaging materials, 2) stabilizing agents, and 3) functional food ingredients [1–3]. Moreover, several studies have been published regarding the use of the material to produce edible films, act as a stabilizer, and be used as an emulsifying agent, among others [4–12].

In vitro and in vivo toxicological studies of ingested nanocellulose revealed minimal cytotoxicity and no subacute in vivo toxicity. However, ingested materials may modulate gut microbial populations or alter aspects of intestinal function not elucidated by toxicity testing, which could have significant health implications [3].

Nanocellulose may have applications in modulating digestion and the absorption of nutrients and other ingested substances. Nanocellulose materials are also potentially applicable as a non-caloric fibre source to reduce the energy density of foods like chocolate, hamburgers, and dough-based products [13,14]. In addition, some studies have suggested that using nanocellulose as a source of dietary fibres may offer a range of health benefits and assist in reducing the risk of chronic diseases [2,14].

Although cellulose, widely used as a thickener and filler in foods and drugs, has been designated as GRAS [15], as cited, nanocellulose (NC) has yet to be designated as GRAS. Several researchers found that ingested NC has slightly acute toxicity and is likely non-hazardous after small quantities of ingestion [16]. From a toxicological point of view, cellulose-based ingredients have shown excellent biocompatibility, particularly NC, which exhibits minimal cytotoxicity in a wide range of human and animal cells. Cellulose nanocrystals are employed as drug carriers in medicine [17], and their cellular uptake was demonstrated. A coffee pod is a filter of cellulosic, non-rigid, ready-made material containing portions of ground and pressed coffee prepared in dedicated machines through boiling water under pressure. Coffee is the most widely known and popular beverage globally, with more than 500 billion cups consumed annually [18]. The function of the paper filter is to store the coffee powder and allow for coffee brewing. Commercially available paper filters have characteristics corresponding to the preferences and needs of the consumer, such as size, which enables the preparation of larger or smaller volumes of coffee. The coffee pods contain a precise amount of coffee between two cellulose layers. The international coffee pod market has shown rapid growth due to consumers' inclinations towards innovation, convenience, and lifestyle changes, which have, in turn, driven the global adoption of coffee pod machines (**Figure 1A**) [19]. Even with homemade coffee pods, you can get a cup of coffee with a good yield, just like with professional espresso machines.

Recently published studies [20–23] tested how many nano plastics (NP) are released when coffee cups (or other plastic disposables) are exposed to hot water. Indeed, Hernandez and co-workers found recently that plastic teabags release billions of microparticles and nanoparticles into tea [21]. Although cellulose is a renewable, sustainable, inexpensive, eco-friendly, and safely employable polymer compared to plastics, it was recently reported that water swelling has a negative impact on cellulosic material applications in packaging [24,25] and as composite additives [26]. Indeed, this cellulose response may be temperature dependent [25] and could induce some nanoparticle release, impacting the behaviour of NC along the gastrointestinal tract and its influence on food digestion and nutrient absorption [27]. Generally, the uptake of nanoparticles by the cellular system occurs through a process known as endocytosis. It is influenced by the physicochemical characteristics of nanoparticles, such as size, shape, surface chemistry, and the employed experimental conditions [28]. Nanoparticulate systems can enter live cells, often through several endocytic pathways. Considering that passive penetration of the plasma membrane may occur as an alternative route, in that case, the internalized nanomaterials are directly transferred into the cytoplasm [28,29].

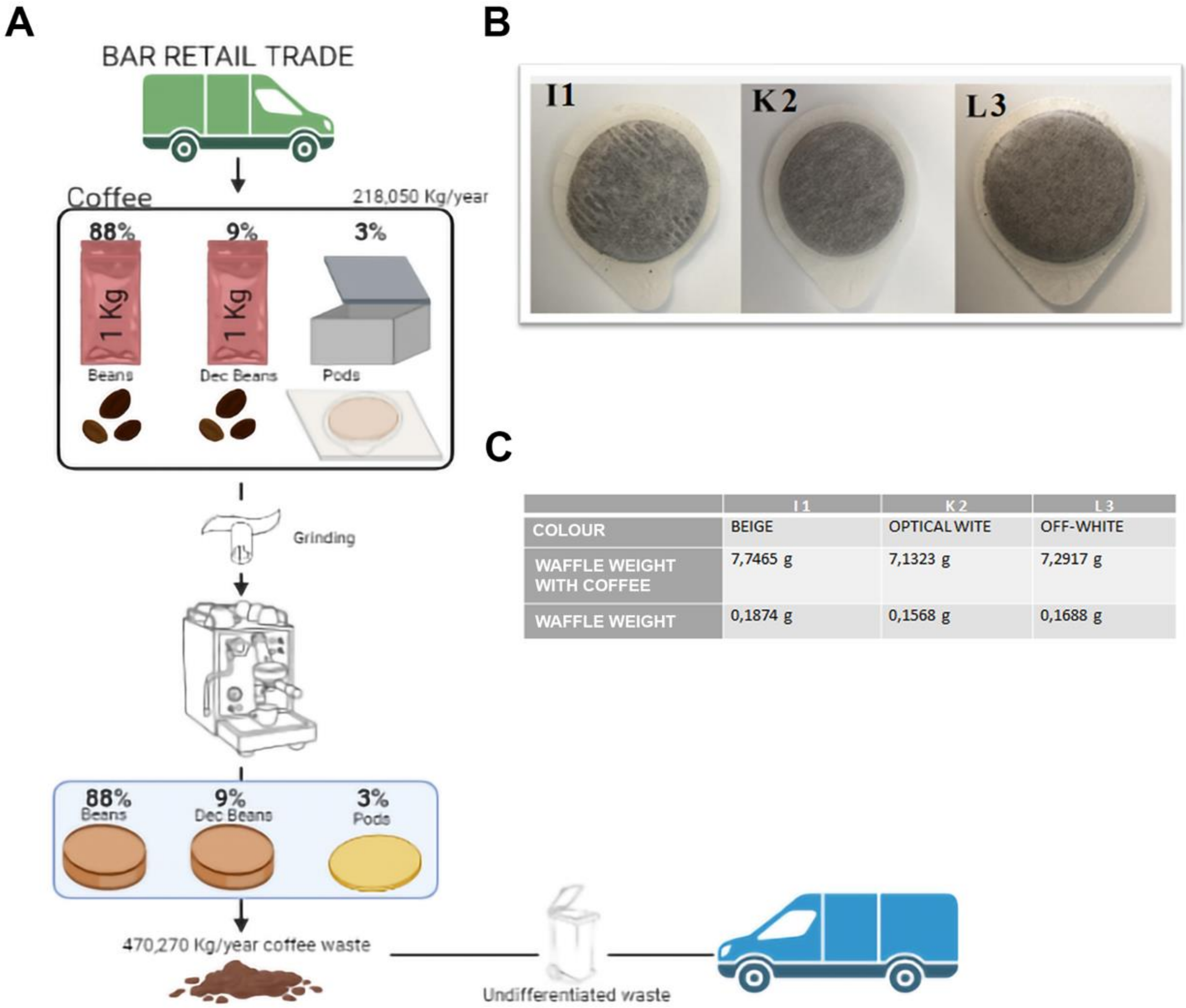

	I 1	K 2	L 3
COLOUR	BEIGE	OPTICAL WITE	OFF-WHITE
WAFFLE WEIGHT WITH COFFEE	7,7465 g	7,1323 g	7,2917 g
WAFFLE WEIGHT	0,1874 g	0,1568 g	0,1688 g

Figure 1. (A) Scheme of the path of coffee from producer to the consumer up to the disposal of the pods and highlight the relative percentages for each type (created in Biorender.com); **(B)** photos illustrating the different coffee pods we used, I1, K2, and L3; **(C)** table explaining the characteristics of paper filters, such as the color and weight of the individual waffle containing and not containing coffee.

Intestinal mucus is the first barrier for ingested nanoparticles (NPs) [30,31]. Small NPs penetrate more quickly than large ones [31]. Recently, Cao and co-workers [14] analysed the effects of cellulose nanocrystals (CNC) in different food models. They measured the volume-weighted particle size distributions in food models and oral, gastric, and small intestinal phases of digestion, exposing a tricultured small intestinal epithelium to this obtained nanoparticulate matter. They demonstrated that CNC is relatively non-cytotoxic in a triculture of human intestinal epithelium under the tested experimental conditions. Moreover, CNC in the employed food models had little impact on the triculture proteome. Therefore, several authors agree that nanocellulose's applications in the food industry need future investigations to determine its potential implications for human health.

Foodborne pathogens (bacteria, parasites, etc.) are biological agents that cause food poisoning [32], and foodborne disease is divided into two categories: infection and intoxication. Foodborne infection is associated with a prolonged incubation period; therefore, the onset of symptoms in foodborne intoxication is shorter than in foodborne infection [33]. Gram-negative *Campylobacter jejuni* is a major cause of foodborne gastroenteritis in humans worldwide. The cytotoxic effects of *Campylobacter* have been mainly ascribed to the actions of the Cytolethal Distending Toxin (CDT) [34]. CDT is a tripartite genotoxin composed of CdtA, CdtB, and CdtC subunits [35–37]. Among them, CdtB has deoxyribonuclease activity and induces double-strand breaks (DSBs). DSB stimulates spontaneous activation of DNA damage responses, leading to cell cycle arrest. CdtB has been shown to arrest the cell cycle in the G2/M phase [37]. Indeed, we previously demonstrated [38] that CDT-treated HeLa cells increase their endolysosomal compartment because of toxin internalization, in addition to simultaneous and partial lysosomal destabilization. Indeed, in human-isolated monocytes, we found that mitochondria and lysosomes were targeted differently by CDTs from different *C. jejuni* strains [39].

We investigated the response of HT-29 cells, representing a model of goblet intestinal cells, to cellulose nanoparticles from three different typologies of coffee pods. Besides evaluating possible cytotoxic effects, we detailed the mitochondrial network and vacuolar compartment (endosome-lysosomes). Indeed, since we are investigating effects induced by cellulose from coffee pods, we treated HT-29 cells with homogenates obtained without coffee brewing (eliminating coffee powder) and homogenates of pods after coffee brewing to consider the peculiar impact of coffee embedding. The comparison of the subcellular effects between cellulose nanoparticles (NC) and coffee-embedded nanoparticles (CENC) was performed, mixing the three pod typologies, for a better interpretation of the data.

Finally, we analysed the impact (on the same endosomal-lysosomal routes) of *C. jejuni* CDT on HT-29 intestinal cells conditioned by micro/nanoscaled cellulose from coffee pods. This step enables us to verify possible differences between CENC and NC treatments in physiological conditions (w/o CDT exposure) and pathological conditions (during CDT exposure). Our work highlights that micro/nanoscaled cellulose from coffee pods does not significantly impact the viability and functions of HT-29 cells but even improves cell status/condition and endosomal compartment after *C. jejuni* CDT intoxication.

2. Materials and methods

2.1. Nanocellulose obtainment from coffee pods: I1, K2 and L3

We selected three coffee pods of the most famous brands of coffee present in Italy, to which we have assigned the acronyms I1, K2, and L3.

Coffee Embedded Nano Cellulose (CENC): coffee was prepared, taking care to recover the waffles, deprived of their coffee content prior to the homogenization of cellulose. For Nano Cellulose (NC) we used the coffee pod border (not brewing coffee). For the extraction of micro- and nanoparticles of cellulose, we used the homogenization technique through MediMachine II (CTSV, Torino) and serial filtration (**Figure S1**). For sonication, we took 7 mL of homogenate containing micro- and nanoparticles of cellulose and sonicated at 30 kHz with 100 W power for 1 h and 30 min with a UP200S Hielscher Ultrasonic Technology (Teltow, Germany) in an ice/water bath.

2.2. Growth conditions of bacterial strains and cell lysate preparation

jejuni ATCC 33291 were grown at 37 ℃ in a microaerobic chamber (Don Whitley Scientific, Shipley, United Kingdom) containing 85% N_2, 10% CO_2, and 5% O_2, either on blood agar (BA) plates containing Columbia agar base (Oxoid, Basingstoke, United Kingdom) supplemented with 7% (v/v) horse blood (TCS Microbiology, United Kingdom) and Campylobacter Selective Supplement (Oxoid) or in Brucella broth (Oxoid) with shaking at 75 rpm. *C. jejuni* strain was grown on BA plates for 24 h prior to use in all assays, unless otherwise stated. *C. jejuni* strain was grown in 50 mL Brucella broth (Oxoid) at 37 ℃ in a shaking incubator under microaerophilic conditions for 48 h. The bacterial suspensions were centrifuged at 4000 rpm for 10 min and the pellets were resuspended in 20 mL of Dulbecco's modified eagle medium (D-MEM) (Sigma-Aldrich, St Louis, MO, USA). Then, bacterial suspensions were adjusted spectrophotometrically to approximately 108 bacteria/mL and lysed by sonication (2 × 30 s bursts with 30 s intervals between each burst) by using a sonicator (Sonifier 450, Branson, Danbury, CT, USA). Cell debris and unlisted bacterial cells were then removed by centrifugation at 4000 rpm for 10 min. Aliquots of each lysate were sterilised by a 0.22-µm membrane filter (Millipore, Milano, Italy) and stored at −20 ℃ before use [40].

2.3. ESEM -EDS characterisation

Morphological characterisation of the micro- and nanoparticles was carried out using an Environmental Scanning Electron Microscope-Energy Dispersive Spectrometer (ESEM-EDS). A FEI Quanta 200 microscope (FEI, Hillsboro, OR, USA), equipped with an energy dispersive X-ray spectrometer (Edax Inc., Mahwah, NJ, USA), was used to evaluate the elemental composition of the sample. Observations were made on samples prepared in non-demineralized distilled water without any subsequent treatment after air drying at low vacuum (0.2−1.2 Torr) at a working distance of 10 mm using secondary and back-diffused electrons with a variable acceleration voltage of 12 to 25 kV. For elemental mapping, a real-time count of 100 s was used with spot mode—focused beam on discrete points of the sample, repeating the analysis 3–5 times per measurement.

2.4. NTA characterisation

For NanoSight tracking analysis (NTA), the homogenate underwent an additional 0.22 µm filtration to discriminate nanoparticles from micro particles. NTA measurements were performed with a NanoSight LM10 (NanoSight, Malvern Instruments Ltd., UK), equipped with a sampling chamber with a 640 nm laser and a Viton O-ring fluoroelastomer. The samples were injected into the sample chamber with sterile syringes until the liquid reached the tip of the nozzle. All measurements were made at room temperature (RT).

2.5. In vitro acute exposure of HT-29 cells

The HT-29 cell line is a human colorectal adenocarcinoma cell line and was cultured in RPMI 1640 Medium (Sigma-Aldrich, St Louis, MO, USA) supplemented with 10% Heat-Inactivated Foetal Bovine Serum (FBS; Gibco; Thermo Fisher

Scientific, Inc., Waltham, MA, USA), 1% L-glutamine (Sigma-Aldrich, St Louis, MO, USA), and 1% penicillin/streptomycin (Sigma-Aldrich, St Louis, MO, USA) at 37 °C in humidified air with 5% CO_2. Regarding experimental assays, cells were seeded in 6-well plates at a density of 1.5×10^5 cells per well. CENC and NC were added to the medium at a dilution of 1:10 for I1 and K2, and 1:9 for L3 samples, and incubated for 24 h, 48 h, 72 h and 96 h. For the negative control, the cells were incubated with medium only.

2.6. Treatment of HT-29 cells with *C. jejuni* lysates

HT-29 cells after pre-treatment with CENC and NC were incubated with 2 mL of media enriched with *C. jejuni* cell lysates (1:50 dilution) from ATCC 33291 strains previously prepared for 24 h and 72 h. Treated cells were analysed by means of flow cytometry and confocal microscopy to evaluate different cellular parameters. For the negative control, cells were incubated with media only.

2.7. Flow cytometric analyses

Cytometric experiments were performed with a FACSCanto II (BD) flow cytometer equipped with an argon laser (Blue, Ex 488 nm), a helium neon laser (Red, Ex 633 nm), and a solid-state diode laser (Violet, Ex 405 nm). The analyses were performed with the FACSDiva TM (BD) software. At least 10,000 cellular events were acquired for each sample.

Cell viability was assessed by means of Propidium Iodide (PI; Sigma-Aldrich, St Louis, MO, USA) or 7-AAD staining. The cells were incubated for 10 min in the dark with PI 1 mg/mL or with 7-AAD (Beckman Coulter, USA). We detected the percentage of PI or 7-AAD-positive events. Mitochondrial characteristics were investigated through TMRE staining. Tetra-methylrodamine ethyl ester perchlorate (TMRE) (Sigma-Aldrich, St. Louis, MO, USA) is a cationic dye that can penetrate the mitochondria, generating a red-orange fluorescence as intense as the mitochondrial membrane potential. TMRE 40 nm was added to the sample 15 min before the acquisition time. The samples were analysed by flow cytometry using the appropriate fluorescence channel [41]. LysoTracker Green or Deep Red (LTG/LTDR) dye (Thermo Fisher Scientific, USA) was used to mark and trace the lysosomes. The LysoTracker is an acidotropic and fluorescent probe that serves to monitor acidic organelles in living cells. The amount of fluorescence obtained by LysoTracker staining is directly proportional to the volume of lysosomes in the cell. LysoTracker 100 nm was used to mark the lysosomes, and after 30 min of incubation, the green or red lysosomal fluorescence was detected by flow cytometry and confocal microscopy [42]. To study the autophagic machinery, the cells were incubated with 50 μm monodansylcadaverine MDC (Sigma-Aldrich, St. Louis, MO, USA) in order to evaluate the autophagolysosomes (autophagic vacuoles). The generation of reactive oxygen species was determined by the cytometric analysis of cells labelled with CM-H2DCFDA (Thermo Fisher Scientific, USA), which can detect the generation of intracellular H_2O_2. The 5-(e-6)-chloromethyl-2,7-dichlorodihydrofluorescein diacetate acetyl ester (CM-H2DCFDA) fluorescent probe is a membrane-permeable compound that is converted into a fluorescent, impermeable compound, H2DCF, by intracellular esterases. DCF (dichlorofluorescein) is a highly fluorescent compound produced by the oxidation of H2DCF by hydrogen peroxide. The amount of peroxide produced affects the intensity of DCF fluorescence inside the cells. CM-H2DCFDA was solubilized in dimethyl sulfoxide (DMSO) (Sigma-Aldrich, USA) and then diluted in Phosphate-buffered saline (PBS) and used at a final concentration of 5 μm for 30 min at 37 ℃ [43,44]. A new fluorescent probe for vesicular trafficking, the 1,7-bis-(7-nitrobenzo[1,2,5]oxadiazole-4-yl)-4,10-dimethyl-1,4,7,10-tetraazacyclododecane, called AJ2NBD [45], was used. AJ2NBD was dissolved in DMSO at the final concentration of 15 mm. Cells were incubated at 37 ℃ with 500 nm (f.c.) of AJ2NBD for 20 min [46]. In order to quantify the vesicular trafficking in treated cells, HT-29 cells were incubated in complete culture medium and stained at different time points from 0 to 1 day with the specific probe AJ2NBD (500 nm for 20 min).

2.8. Confocal microscopy

To evaluate the behaviour of different probes, the cells were grown on MatTek glass bottom chambers (MatTek Corporation) and then stained with fluorescent probes. To evaluate the vesicular trafficking in treated cells, HT-29 cells were incubated in complete culture medium with the specific probe AJ2NBD (500 nm for 20 min), and the vesicular compartment was studied by confocal microscopy at different time points from t0 (after incubation of AJ2NBD) up to 1 day. To evaluate the lysosomal formation, the cells were stained with LysoTracker Deep Red (LTDR) at 100 nm. The images were acquired by a Leica TCS SP5 II confocal microscope (Leica Microsystem, Germany) with 488, 543, and 633 nm illumination and oil-immersed objectives and averaged in real time using a line average to reduce random noise. The images were further processed and analysed in ImageJ software (National Institutes of Health, Bethesda, MD, USA).

2.9. Statistical analyses

Data are shown as the mean (or percentage, as indicated) ± standard deviation (SD) of at least three independent experiments. The means of two groups were compared using a *t* test. The *p* values less than 0.05 were considered statistically significant. Analysis of variance (ANOVA) approaches were used to compare values among more than two different experimental groups for data that met the normality assumption. One-way ANOVA or two-way ANOVA were followed by a Bonferroni post-hoc test. The *p* values less than 0.05 were considered statistically significant. Bonferroni's multiple comparison test revealed statistical significance: * = $p < 0.05$, ** = $p < 0.01$, *** = $p < 0.001$, **** = $p < 0.0001$. All statistical analyses were performed using GraphPad Prism 9.0.0 (GraphPad software, San Diego, CA, USA).

3. Results

3.1. Nanocellulose evaluation by ESEM and NanoSight characterisation

We selected three types of coffee pods (I1, K2, L3). A first evaluation of the pods was made macroscopically based on the physical and morphological characteristics of the coffee waffle, in particular the size (weight) and the colour (**Figure 1C**). As reported in the materials and methods section, we obtained two types of nanocellulose: Coffee Embedded Nano Cellulose (CENC) and Nano Cellulose (NC). We characterized 1) the presence of micro- and cellulose nanoparticles, and then 2) we evaluated whether the use of sonication improved the yield of nanoparticles. ESEM data show the best morphological uniformity in the homogenate samples than in the homogenization + sonication procedure (**Figure 2A**). Consequently, we continue the analyses on the nanoparticles obtained by the unique homogenization step. We evaluated the size and morphology of cellulose nanoparticles by NTA (**Figure 2B**). From NTA and ESEM, the average size of the nanoparticles obtained by the homogenization technique is 80 nm (**Figures 2A** and **2B).** The ESEM-EDS elemental analysis peaks showed the presence of sulfur (S) (**Figure 2C**). Hydrochloric and sulfuric acids have been extensively used to obtain cellulose from wood [47]. Sulfuric acid hydrolysis of native cellulose fibres causes the breakdown of the fibres into rod-like fragments [48]. During the hydrolysis by sulfuric acid, negatively charged sulfate groups will be introduced on the cellulose chain through the esterification of hydroxyls [47]. For this reason, the presence of sulphur must be considered normal based on wood treatment to obtain cellulose. We evaluated each homogenate's dry weight (**Figure 2D**) to gain further knowledge of the concentration of our homogenates. The results obtained (**Figure 2E**) were assessed as a value of μg/mL. However, besides such quantitative assessment, we performed the nanoparticle counts employing NTA (**Figure 2F)**, obtaining the particle concentration/mL that we equally administered to HT-29 cells.

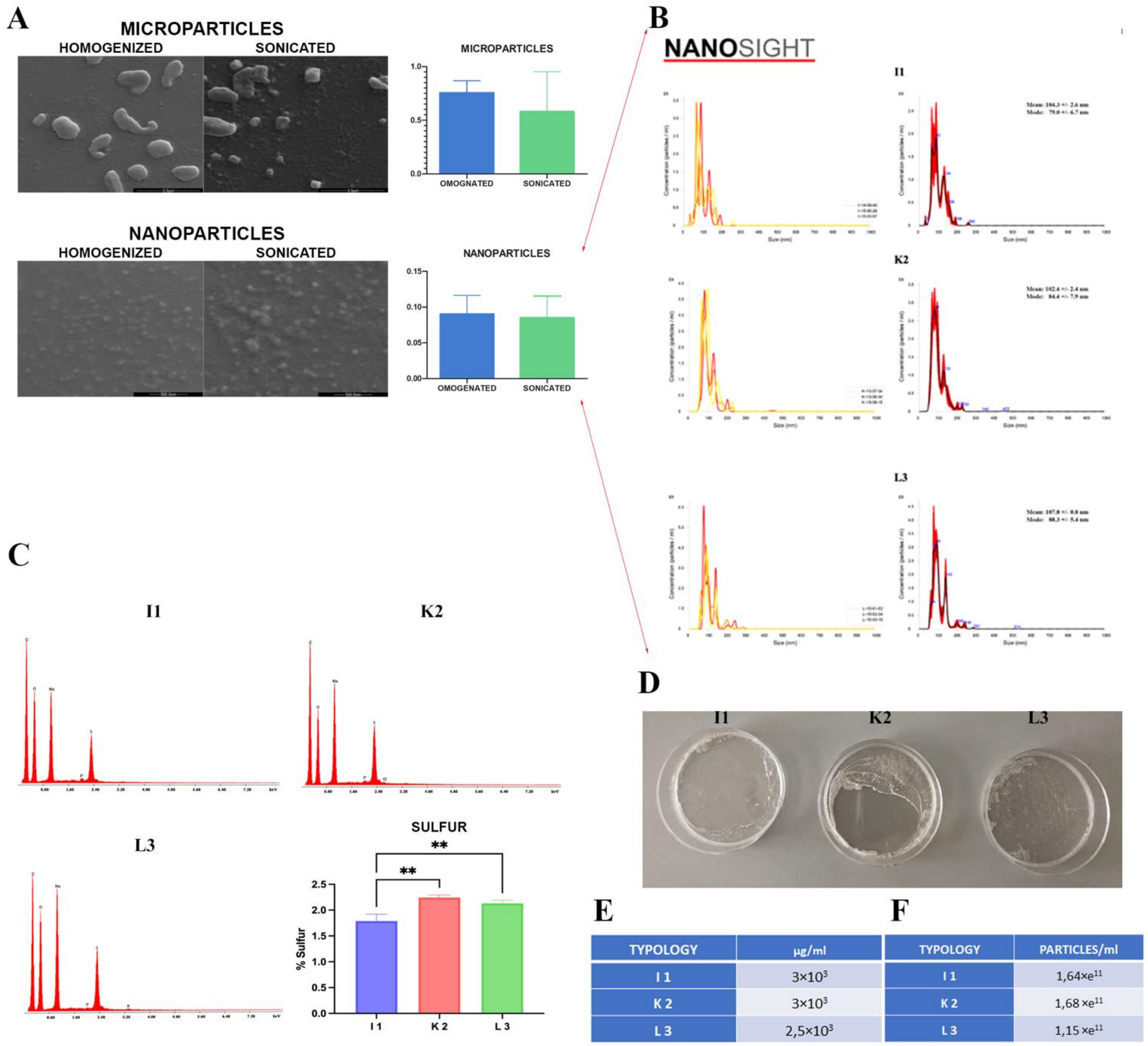

TYPOLOGY	μg/ml
I 1	3×10^3
K 2	3×10^3
L 3	$2{,}5\times10^3$

TYPOLOGY	PARTICLES/ml
I 1	$1{,}64\text{xe}^{11}$
K 2	$1{,}68\ \text{xe}^{11}$
L 3	$1{,}15\ \text{xe}^{11}$

Figure 2. (A) ESEM analysis of microparticles and nanoparticles obtained by homogenization and by homogenization and sonication. Histograms reveal the size of microparticles and nanoparticles with the *T*-test assessments (*P* value to two tails); **(B)** NTA of the size distribution of the different types of pods (I1, K2, L3); **(C)** EDS spectra for homogenates I1, K2, L3 and histogram evaluating the percentage of Sulphur present in homogenates. One-way ANOVA with Bonferroni's multiple comparison tests revealed a significant difference: ** = $p < 0.01$; **(D)** photos of the homogenates of micro- and nanoparticles/fibrils in Petri dishes following complete evaporation of the liquid medium (fore dry weight of micro- and nanoparticles/fibrils); **(E)** table reporting the concentration in μg/mL for each type of micro and nanoparticles/fibrils analyzed by the dry weight; **(F)** table reporting the number of particles per mL by NanoSight.

3.2. Intestinal cell response to nanosized cellulose (NC) and to coffee embedded nanosized cellulose (CENC)

The most important factors influencing recognition, uptake, and cellular response include nanocellulose size, length of fibres, shape, surface area and charge, degree of agglomeration in biological media, source, and type of nanocellulose [49]. In our model, all these features are identical for CENC and NC samples, varying only for the presence of the imbibition of the cellulose by coffee brewing.

Cell viability

Although nanocellulose is largely considered non-toxic in its bulk form, different authors reported that chronic cell exposure to high concentrations of nanocellulose may result in an apoptotic cellular response [50]; moreover, coffee has the ability to trigger apoptosis by modulating multiple components of the apoptotic response [51,52]. Cell death was assessed using supravital propidium iodide (supravital PI). We did not detect any relevant cell death induction or significant differences in CENC and NC-treated cells with respect to control (**Figure 3A**,**C**), (**Figure 3B**,**D**) for the investigated time points. In detail, after 24 h of exposure, CENC-treated cells (I1, K2, L3) appear to maintain viable conditions as in the control. The analyses showed that, compared with control cells, the treatment with CENC and NC did not cause any significant increase in the percentage of PI-positive cells. Indeed, CENC-treated HT-29 cells revealed, after 24 h and 72 h, lower PI positivity than control samples (**Figure 3B**).

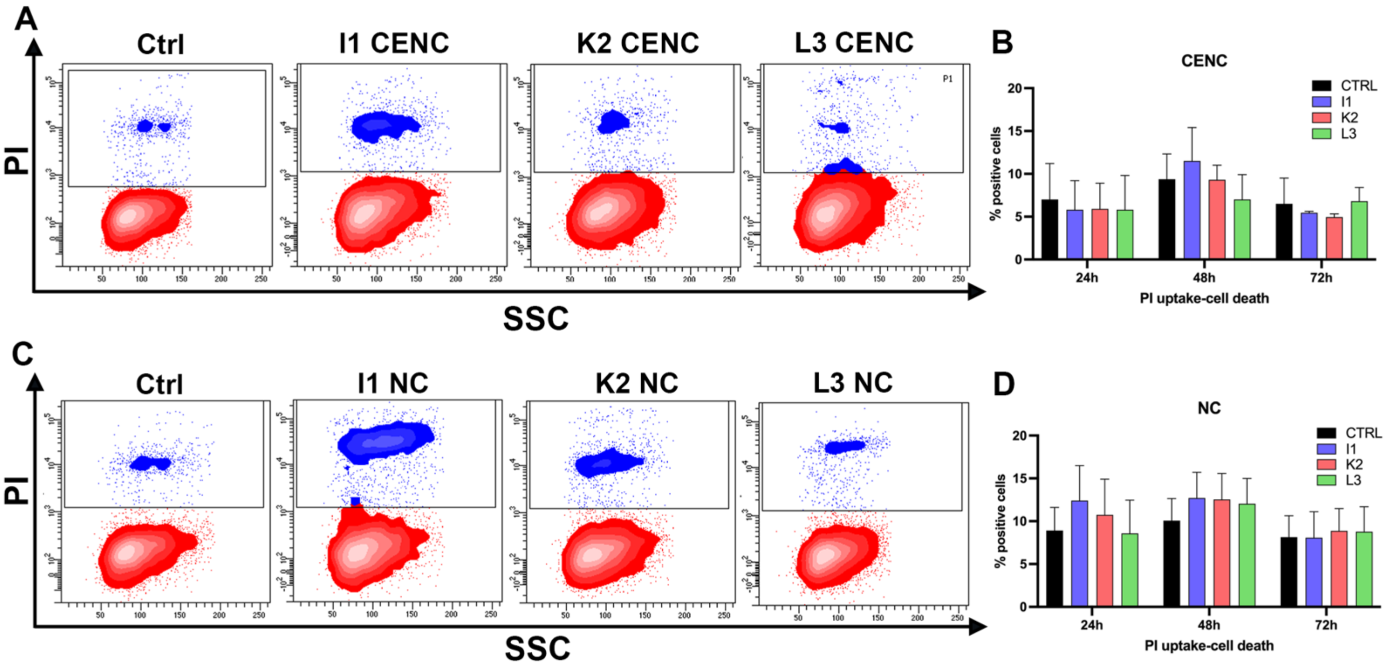

Figure 3. (A) Contour plot SSC vs PI from HT-29 control cells, I1 CENC HT-29 treated cells, K2 CENC HT-29 treated cells, L3 CENC HT-29 treated cells at 48 h. The rectangular region identifies events with high PI uptake (cell death); **(B)** percentages of PI-positive HT-29 cells for each CENC experimental condition from 24 h to 72 h; **(C)** contour plot SSC vs. PI from HT-29 control cells, I1 NC HT-29 treated cells, K2 NC HT-29 treated cells, and L3 NC HT-29 treated cells at 48 h. High PI uptake reveals cell death; **(D)** percentages of PI-positive HT-29 cells for each NC experimental condition from 24 h to 72 h.

3.3. Mitochondrial oxidative stress and autophagolysosome modulation in cells treated by the tree different CENC and NC types of pods

Mitochondrial membrane potential was investigated through TMRE staining, a cationic dye able to penetrate the mitochondria and generate a red-orange fluorescence as intense as the mitochondrial membrane potential (MMP). **Figure 4** highlights a comparison between HT-29 cell MMP after administration of the three typologies of nanosized cellulose (NC) and coffee embedded nanosized cellulose (CENC). We did not observe relevant and significant differences between exposure to NC and CENC, except for L3 at the longest times (72 h and 96 h, **Figure 4A**,**D**, respectively), revealing a significant increase in mitochondria hyperpolarization in NC samples.

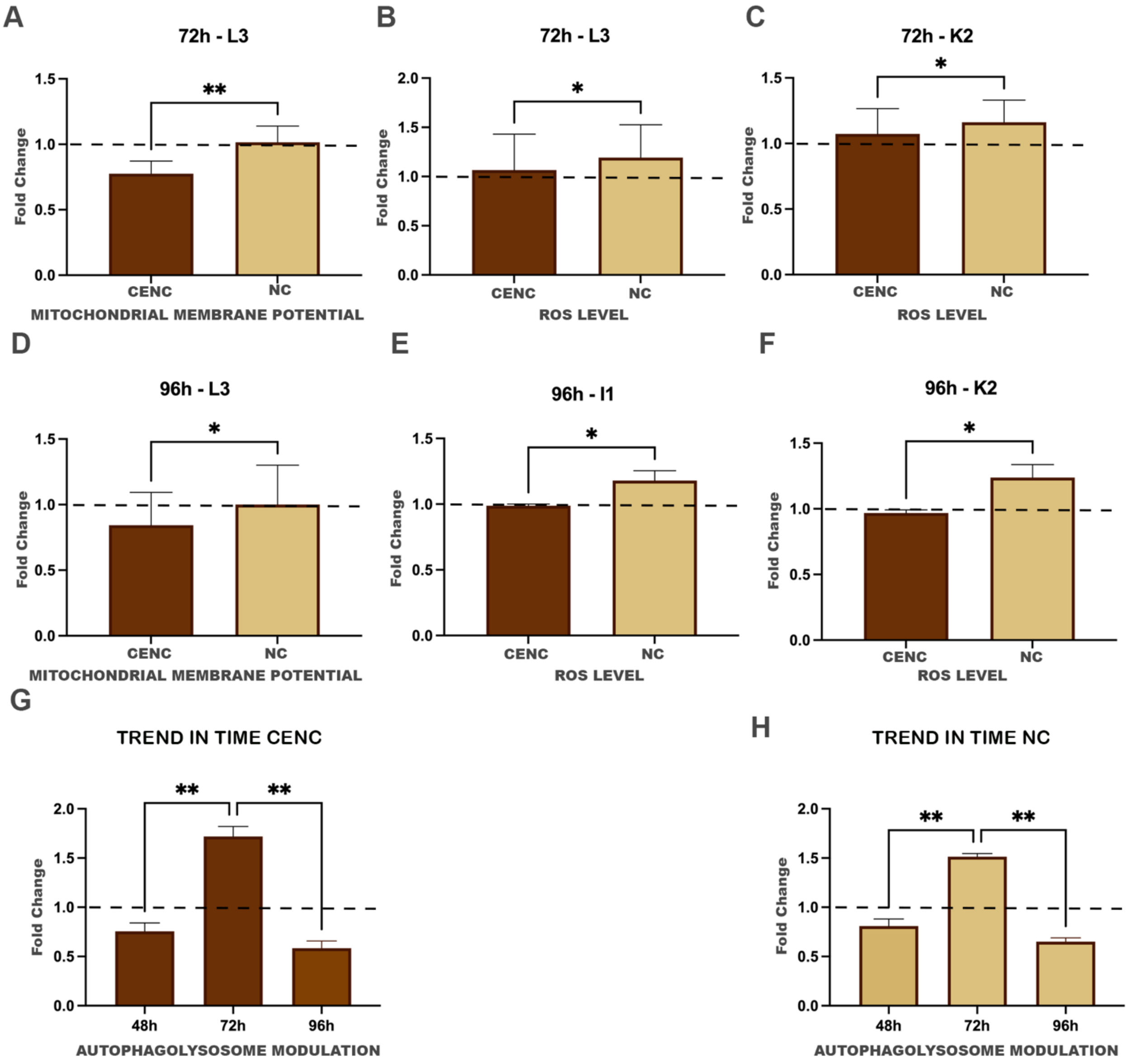

Figure 4. Fold change of: **(A)** TMRE intensity relative to untreated HT-29 cells (ctrl) for L3 CENC-treated HT-29 cells and L3 NC-treated HT-29 cells at 72 h; **(B)** DCF intensity relative to untreated HT-29 cells for L3 CENC-treated HT-29 cells and L3 NC-treated HT-29 cells at 72 h; **(C)** DCF intensity relative to untreated HT-29 cells for K2 CENC-treated HT-29 cells and K2 NC-treated HT-29 cells at 72 h; **(D)** TMRE intensity relative to untreated HT-29 cells for L3 CENC-treated HT-29 cells and L3 NC-treated HT-29 cells at 96 h; **(E)** DCF intensity relative to untreated HT-29 cells for I1 CENC-treated HT-29 cells and I1 NC-treated HT-29 cells at 96 h; **(F)** DCF intensity relative to untreated HT-29 cells for K2 CENC-treated HT-29 cells and K2 NC-treated HT-29 cells at 96 h. Fold change of autophagic-like vacuoles (MDC) intensity relative to untreated HT-29 cells (ctrl) for CENC-treated HT-29 cells; **(G)** NC-treated HT-29 cells **(H)** 48 h to 96 h. T-test and One-way ANOVA with Bonferroni’s multiple comparison tests revealed significant differences * = $p < 0.05$, ** = $p < 0.01$.

To evaluate changes in the amount of intracellular reactive oxygen species (ROS), H_2O_2 was targeted by means of CM-H2DCFDA (DCF). These evaluations are further coupled with data on MMP, in agreement with the findings of several researchers [53–56].

Histograms B and C in **Figure 4** show higher hydrogen peroxide concentrations in specific NC samples, lacking in CENC samples, in agreement with the antioxidant activity of coffee. Higher ROS amounts were registered for L3 and K2 NC-treated cells after 72 h (**Figure 4B**,**C**), whereas after 96 h, H_2O_2 increased significantly in I1 NC-treated cells.

The two major cellular sites of ROS production are the electron transport chain in mitochondria and endosomes via the NOX2-oxidase enzyme [57]. Therefore, to verify possible modulations of autophagic-like vacuoles, we investigated the intracellular presence of autophagosomes with Monodansylcadaverine (MDC). Our data show that CENC and NC-treated cells show a progressive increase of autophagic-like vacuoles at 72 h (**Figure 4G**,**H**). Of note, at 96 h, both CENC and NC-treated cells show a decrease in MDC fluorescence, suggesting that cells were able to clear the excess of autophagosomes. We did not detect any significant differences in time trends of CENC and NC samples, revealing that autophagic vacuole increase is mainly primed by nanocellulose internalisation and the modulation is essentially dependent on time and not coffee.

Autophagy is a lysosome-mediated intracellular biological degradation process [58]. For this reason, we also investigated lysosome networks. Indeed, the cellular uptake of CENC and NC particles in HT-29 cells may lead to direct lysosome damage. To assess lysosome integrity, we used a lysosomotropic dye (Lysotracker Deep Red, LTDR), analysed by flow cytometry and confocal microscopy (**Figure 5**). Moreover, we coupled these analyses to AJ2NBD (**Figure 5C**), useful in intracellular vesicular organelle detection [46]. AJ2NBD is a new dye containing the 7-nitrobenzo[1,2,5]oxadiazole-4-yl (NBD) fluorophore [59] synthesised (and patented) by Fusi and co-workers [45].

Flow cytometry highlights a not-significantly lower MFI (Mean Fluorescence Intensity) registered for K2 and L3-treated samples in respect to controls, whereas confocal images illustrate in detail AJ2NBD and LTDR co-staining.

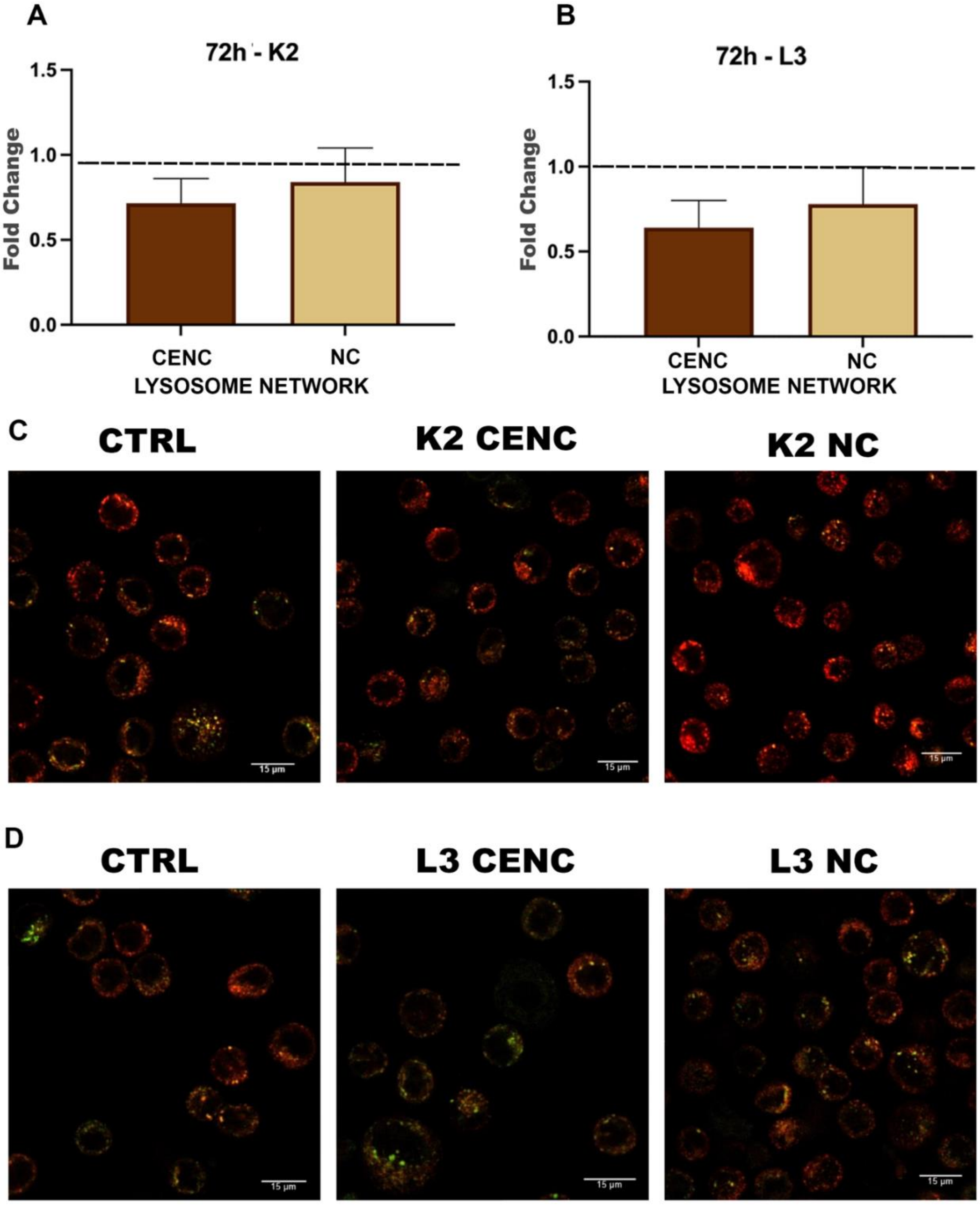

Figure 5. (A) Fold change of: LTDR intensity relative to untreated HT-29 cells (ctrl) for K2 CENC-treated HT-29 cells and K2 NC-treated HT-29 cells at 72 h; **(B)** LTDR intensity relative to untreated HT-29 cells (ctrl) for L3 CENC-treated HT-29 cells and L3 NC-treated HT-29 cells at 72 h; **(C)** Confocal images of AJ2NBD (green) and Lysotracker Deep Red (LTDR, red) fluorescence from HT-29 control cells (CTRL), K2 CENC-treated HT-29 cells and K2 NC-treated HT-29 cells, after 72 h of treatments. Scale bar: 15 µm; **(D)** Confocal images of AJ2NBD (green) and Lysotracker Deep Red (LTDR, red) fluorescence from HT-29 control cells (CTRL), L3 CENC-treated HT-29 cells and L3 NC-treated HT-29 cells, after 72 h of treatments. Scale bar: 15 µm.

3.4. Evaluation of DNA content and cell cycle profiles in cells treated by CENC and NC preparations

Finally, we evaluated the DNA content of samples treated with the three different coffee pod types (**Figure 6**). The statistical evaluation of S and G2/M phases at 72 h for both CENC and NC treatments did not highlight significant differences, except for

K2 treatments. In detail, after K2-CENC treatment, HT-29 cells revealed a mild but significant increase in S phase events, whereas after K2-NC treatment, G2/M phase events appeared to have mildly increased. This finding could arise from the highest sulphur content detected in these specific coffee pods, as shown in **Figure 2C**. In fact, different authors [60] published on the biologic effects of sulphur compounds that can inhibit or delay the cell cycle progression [61]. The overall data suggest that ingested NC has negligible toxicity, even at the massive concentrations used in our study. Moreover, coffee embedding demonstrates that it can further modulate the NC effects, even improving the baseline condition of the control, as demonstrated by the PI data as well as by other studies on coffee biologic effects [62]. Coffee includes a wide array of components that can have potential implications for health. In particular, the vast array of components included in the brewed product and the varied effects of each compound drastically limit the understanding of its physiological effects. A scheme of the most represented compounds is shown in **Figure S2**. Nevertheless, we want to underline that in our model, coffee is present in scarce amounts, derived from cellulose embedding.

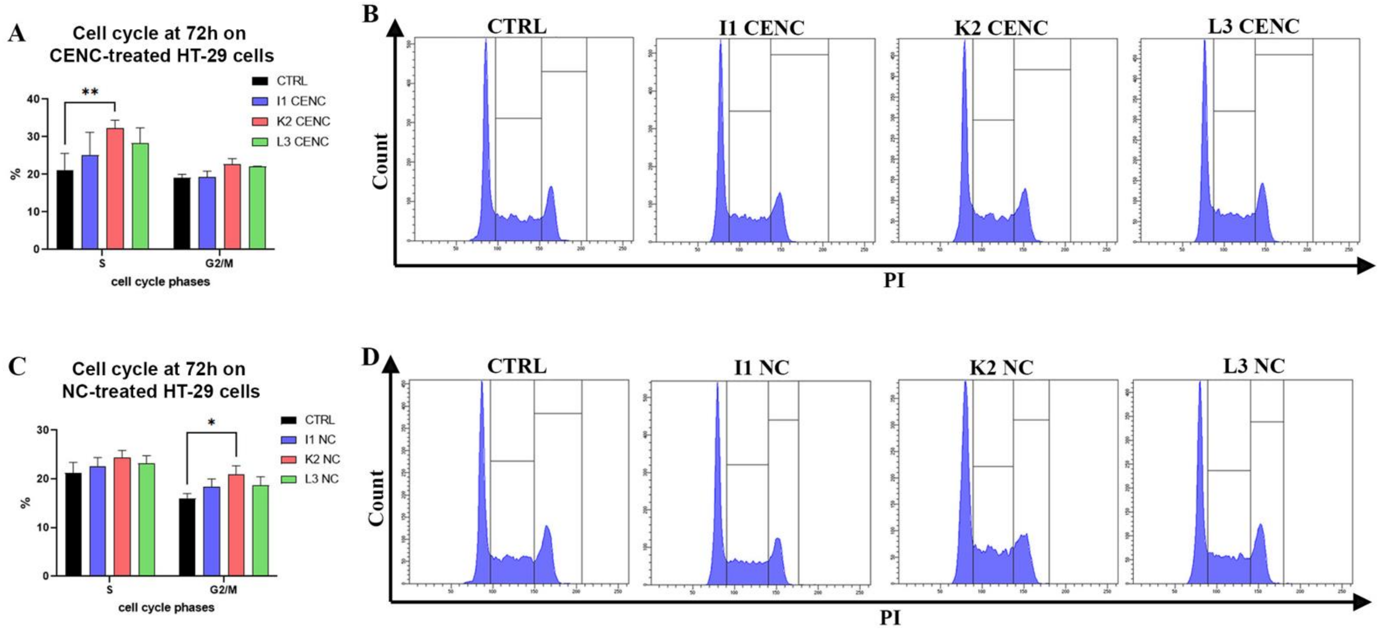

Figure 6. (A) Statistical histogram of the cell cycle phases was calculated by FC via PI staining at 72 h for HT-29 control cells and I1, K2, and L3 CENC HT-29 treated cells; **(B)** FC histograms representing the HT-29 cell population in the S and G2/M phases of the cell cycle after 72 h of I1, K2, L3 CENC administration; Two-way ANOVA with a Bonferroni's multiple comparison test revealed a significant difference (**$p < 0.01$); **(C)** Statistical histogram of the cell cycle phases at 72 h for HT-29 control cells, I1/K2/L3 NC HT-29 treated cells; Two-way ANOVA with a Bonferroni's multiple comparison test revealed a significant difference (*$p < 0.05$); **(D)** FC markers represent the HT-29 cell population in the S and G2/M cell cycle phases after 72 h of I1, K2, and L3 NC administration.

3.5. Cell response to CDT in mixed NC- and CENC-treated intestinal cells

3.5.1. Evaluation of cell viability during the time course

In this step of the study, we considered the exposure of intestinal cells to *C. jejuni* CDT-containing lysate. We mixed the homogenates from the three different coffee pods in a unique formulation to correlate only two main groups (NC and CENC). This mixing is also justified by the lack of striking differences between the three different coffee pods (I1, K2, L3). Our data did not reveal any significant cytotoxic effects of the NC and CENC treatments; indeed, positive PI events after 24 h of NC administration were even lower than in control cells (**Figure 7A**). At 72 h the cells treated with CENC and NC show a slight increase in dead cells but are still not significant (**Figure 7B**). As observed in other cell lines [34,38,39,63], the ATCC lysate did not induce in HT-29 cells an important necrotic/apoptotic effect after 24 h (**Figure 7**); however, previous conditioning with CENC treatment showed a reduction in cell death percentages (**Figure 7C**).

After 72 h, we found a mild, although significant, increase in cell death after ATCC CDT lysate administration (**Figure 7D**), observing a decrease in dead cells in NC and CENC pretreated samples. In agreement with our previous research [34,38,39,63] and literature [64–67], the type and timing of CDT-induced cell death depend on the cell type, requiring at least 24 h to be observed.

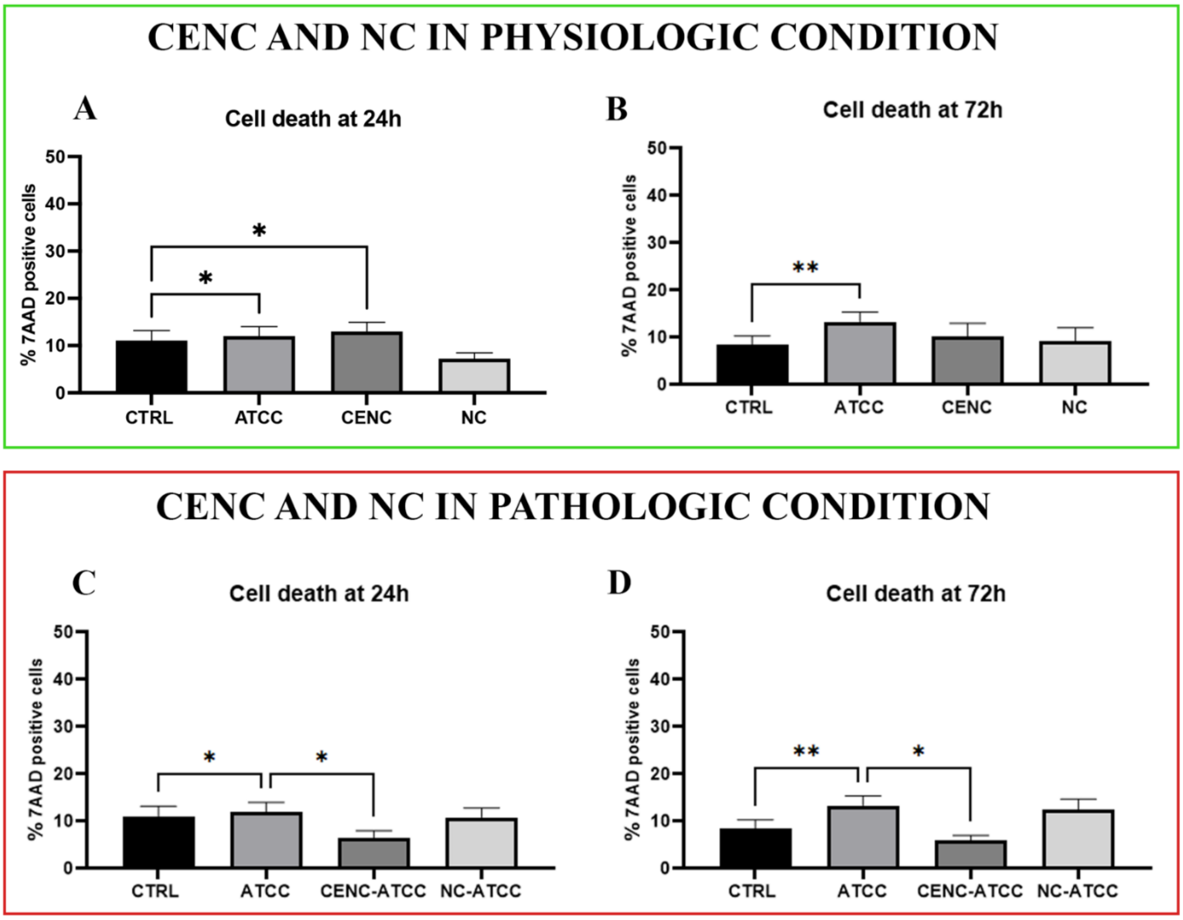

Figure 7. In the green square, % dead cells in physiological condition: **(A)** statistical histogram at 24 h on HT-29 untreated cells (CTRL), ATCC treated cells, CENC, NC; **(B)** statistical histogram at 72 h on HT-29 untreated cells (CTRL), ATCC treated cells, CENC, NC. In the red square, % dead cells in pathological condition: **(C)** statistical histogram at 24 h on HT-29 untreated cells (CTRL), ATCC treated cells, ATCC + CENC, and ATCC + NC; **(D)** statistical histogram at 72 h on HT-29 untreated cells (CTRL), ATCC treated cells, ATCC + CENC, and ATCC + NC; One-way ANOVA with Bonferroni's multiple comparison test revealed significant differences (*$p < 0.05$, **$p < 0.01$, ***$p < 0.001$).

3.5.2. Short term analyses of subcellular effects: 24 h

We evaluated intracellular ROS levels, mainly hydrogen peroxide, as shown in **Figure 8A**,**C**. Since mitochondria are one of the main producers of ROS, we contemporary assessed the MMP (**Figure 8B**). HT-29 intestinal cells slightly decrease MMP to a similar extent after NC and CENC treatment, in both groups, i.e., with and without CDT-containing lysate exposure (**Figure 8,D**).

Cellulose conditioning slightly decreases MMP, to a similar extent for control and CDT-poisoned cells **(Figure 8B**,**D)** [68]. Indeed, the possible impact of nanocellulose on MMP has been reported by Ventura et al. [69], describing the entry of nanoparticles and nanofibers into the mitochondrial outer membrane, causing an initial disturbance in mitochondrial activity [70].

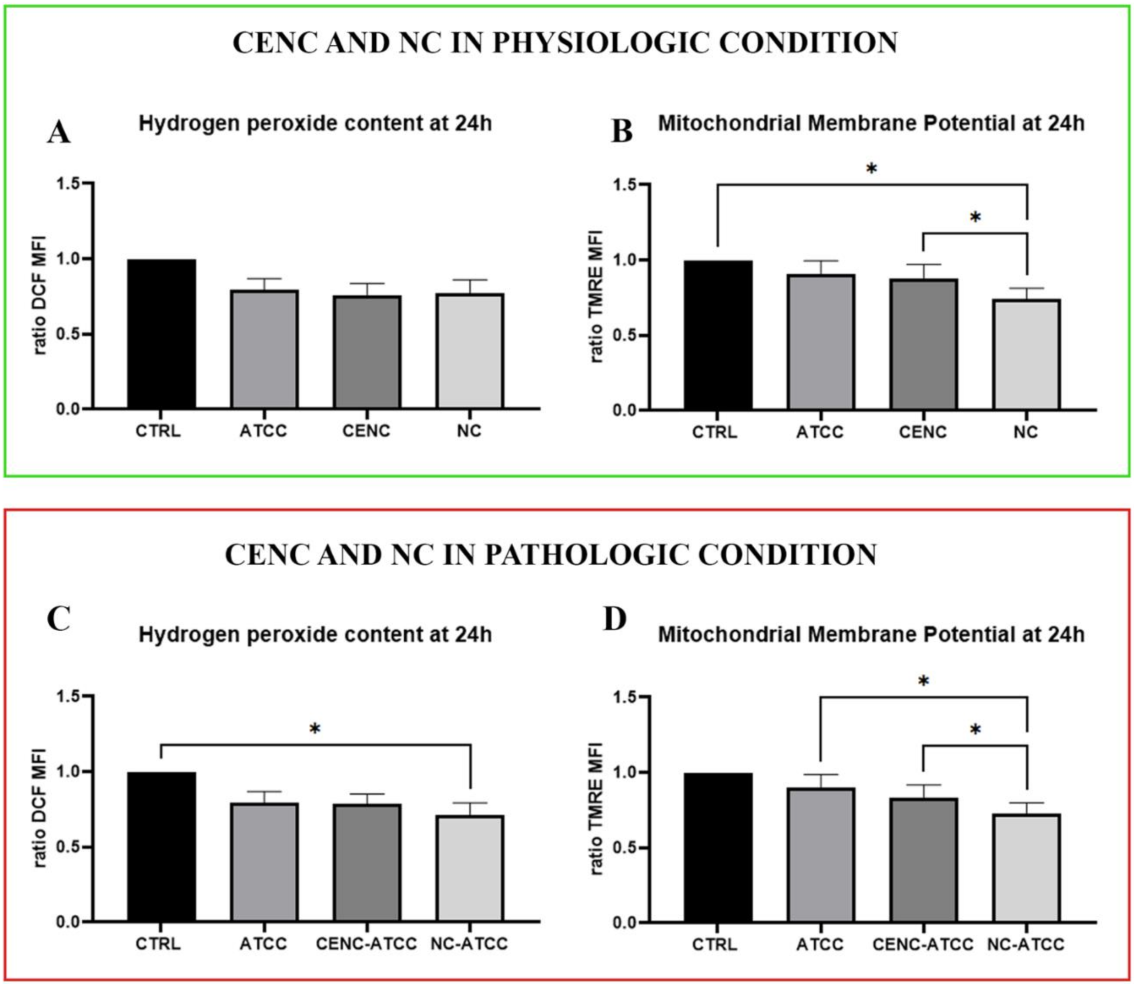

Figure 8. In the green square, the status of MMP and ROS levels in physiological conditions: **(A)** statistical histogram of ROS levels at 24 h on HT-29 untreated cells (CTRL), ATCC treated cells, CENC, and NC; expressed as fold of change of treated cells/CTRL cells of DCF MFI; **(B)** statistical histogram of MMP levels at 24 h on HT-29 untreated cells (CTRL), ATCC treated cells, CENC, and NC.; expressed as fold of change of treated cells/CTRL cells of TMRE MFI In the red square, the status of MMP and ROS levels in pathological conditions; in the red square, the status of MMP and ROS levels in pathological condition: **(C)** statistical histogram of ROS levels at 24 h on HT-29 untreated cells (CTRL), ATCC treated cells, ATCC+CENC, and ATCC+NC; **(D)** statistical histogram of MMP levels at 24 h on HT-29 untreated cells (CTRL), ATCC treated cells, ATCC+CENC, and ATCC+NC. One-way ANOVA with Bonferroni's multiple comparison tests revealed significant differences (*$p < 0.05$, **$p < 0.01$, ***$p < 0.001$).

Finally, autophagic-like vesicles, labelled by means of an MDC probe, did not show any relevant modifications among CENC, NC, and the untreated cells during short-term analyses (**Figure 9A**). To evaluate the autophagic features, we coupled lysosomal network detection to intracellular vesicle determination by means of LTDR and AJ2NBD (a new patented dye), respectively, in both NC and CENC-treated cells, with and without CDT infection (**Figure 9**).

Cytometric data report conditions similar to control cells in NC and CENC-treated cells, both for autophagosomes (**Figure 9A**) and lysosomes (**Figure 9B**). In **Figure 9C,** the AJ2NBD labelling highlights only a slight but significant decrease in ATCC-treated HT-29 cells. Contemporary findings showed that the ATCC CDT lysate induced an accumulation of autophagic-like vacuoles (**Figure 9A**,**D).** In pathological conditions, treatment with NC appears to weakly and significantly counteract the effects of CDT. Statistical histograms revealed that the lysosomal compartment decreased after ATCC CDT administration; on the contrary, NC conditioning limited this phenomenon (**Figure 9E**). Vesicular trafficking does not appear altered in NC and CENC samples (**Figure 9F**). Confocal images of AJ2NBD and LTDR co-labelling show a similar distribution of green vesicles in untreated cells and cells treated by CENC and NC (**Figure 9G**, upper). After ATCC conditioning, clustered and perinuclear green vesicles are visible, and LTDR RED fluorescence almost disappears; indeed, no colocalization is appreciable (**Figure 9G**). Of note, as quantified by flow cytometry, CENC and NC pretreatment rescue cells from lysosome acidity loss, and yellow fluorescence (merging green and red organelles) suggests a priming of the AJNBD+ vesicles towards lysosomal features.

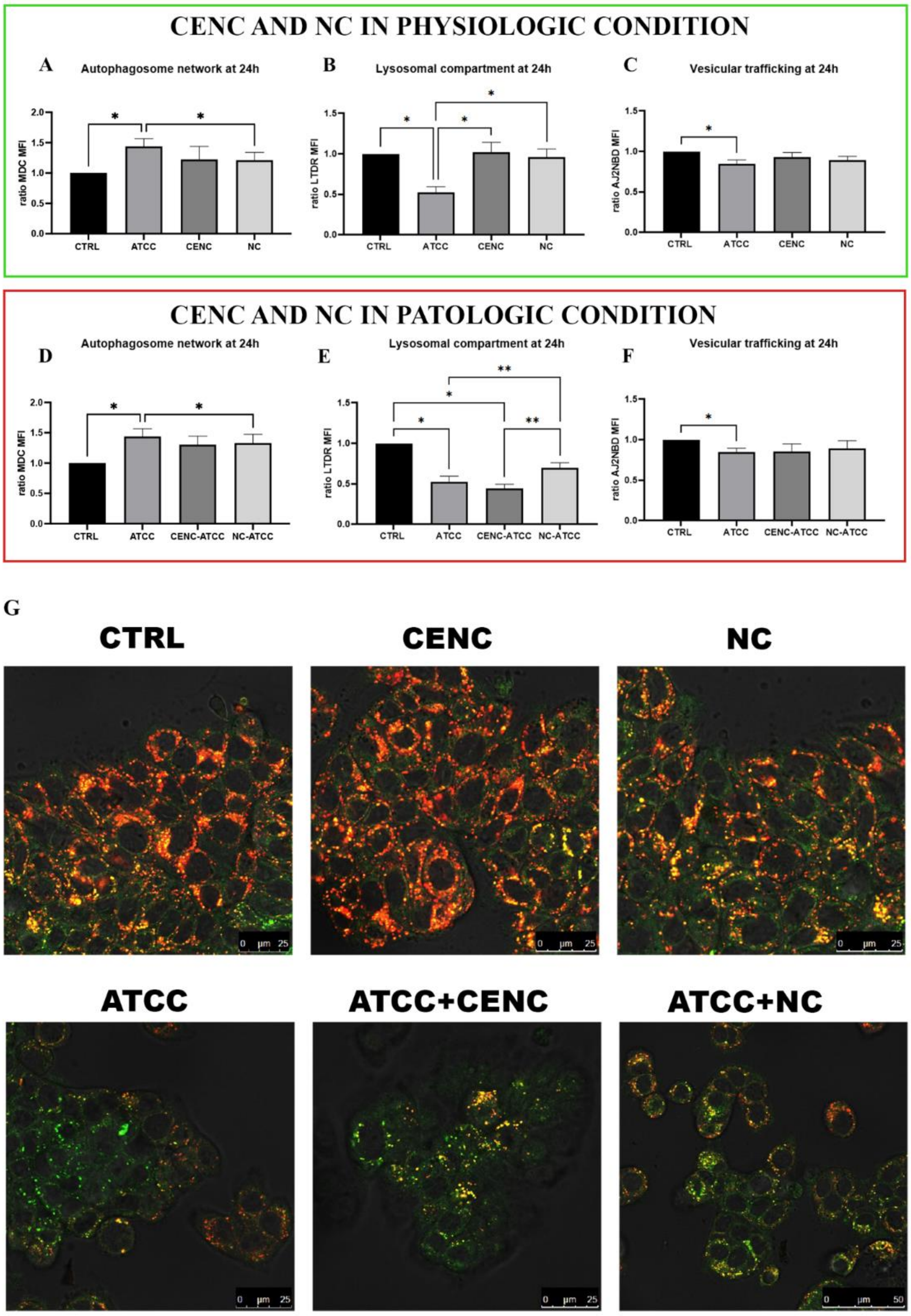

Figure 9. In the green square, the status of lysosomal and vesicular compartment in physiological conditions: **(A)** statistical histogram of autophagic-like vacuole at 24 h on HT-29 untreated cells (CTRL), ATCC treated cells, CENC, and NC; expressed as fold of change of treated cells/CTRL cells of MDC MFI; **(B)** statistical histogram of the lysosomal compartment at 24 h on HT-29 untreated cells (CTRL), ATCC treated cells, CENC, and NC; expressed as fold of change of treated cells/CTRL cells of LTDR MFI; **(C)** statistical histogram of vesicular compartments at 24 h on HT-29 untreated cells (CTRL), ATCC treated cells, CENC, and NC.; expressed as fold of change of treated cells/CTRL cells of AJ2NBD MFI; In the red square, the status of lysosomal and vesicular compartment in pathological conditions: **(D)** statistical histogram of autophagic-like vacuole at 24 h on HT-29 untreated cells (CTRL), ATCC treated cells, CENC, and NC; **(E)** statistical histogram of the lysosomal compartment at 24 h on HT-29 untreated cells (CTRL), ATCC treated cells, CENC, and NC; **(F)** statistical histogram of vesicular compartments at 24 h on HT-29 untreated cells (CTRL), ATCC treated cells, ATCC + CENC, and ATCC + NC. One-way ANOVA with Bonferroni's multiple comparison tests revealed significant differences (*$p < 0.05$, **$p < 0.01$, ***$p < 0.001$); **(G)** confocal images of AJ2NBD (green) and Lysotracker Deep Red (LTDR, red) fluorescence on HT-29 untreated cells (ctrl), cells in physiological condition treated with CENC, NC, ATCC, and cells in pathological condition ATCC + CENC and ATCC + NC after 24 h of treatments.

3.5.3. Long term analyses of subcellular effects: 72 h

After 72 h, ROS levels demonstrated a significant reduction between untreated, control, and ATCC-CDT-infected cells. Unexpectedly, CENC-ATCC samples (**Figure 10**) revealed ROS rising at 72 h, whereas no increase in ROS was detected in NC-ATCC-infected HT-29 cells. This finding propelled us to consider the properties of coffee [71,72]. It is known that coffee exhibits antioxidant and pro-oxidant properties [73]. Coffee varieties also influence the antioxidant/pro-oxidant capacities. Several bioactive molecules are present in coffee; among these, caffeine displays significant antioxidant activity, protecting membranes from oxidative damage [74] at millimolar concentrations, whereas there is no antioxidant activity present in caffeine at micromolar concentrations [75]. Furthermore, it is important to consider that the coffee traces act directly on intestinal cells without the insertion of an oral phase (as normally happens in the case of regular coffee consumption). Our data appear in agreement with [76], describing the prooxidative action of regular coffee samples during the intestinal phase.

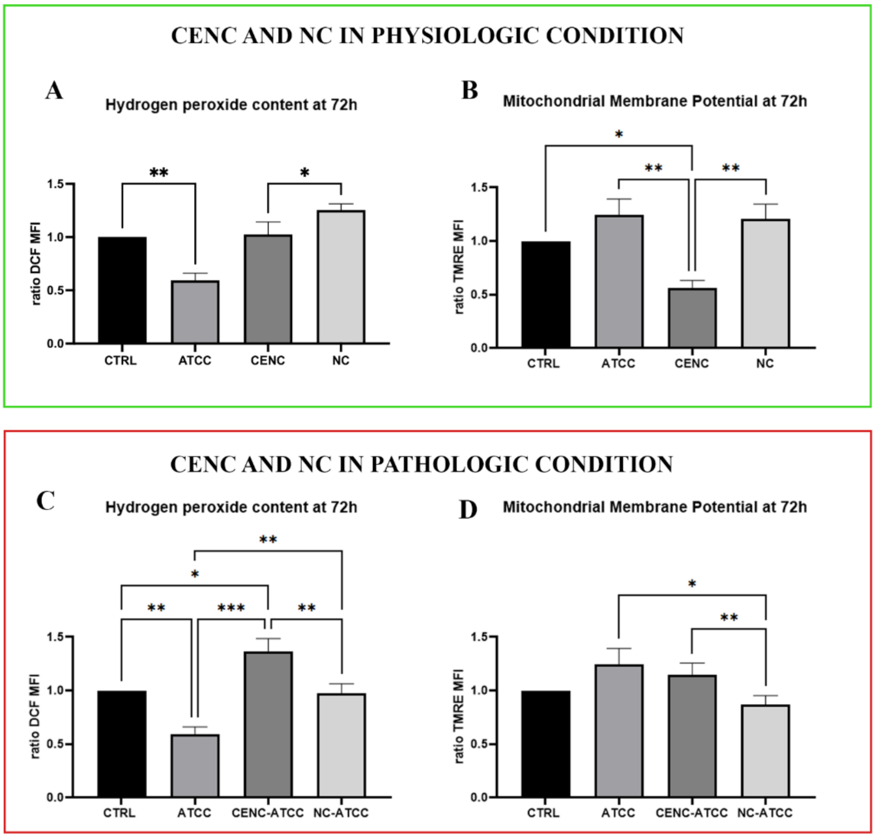

Figure 10. In the green square, ROS levels and MMP in physiological conditions: **(A)** statistical histogram of ROS levels at 72 h on HT-29 untreated cells (CTRL), ATCC treated cells, CENC and NC; expressed as fold of change of treated cells/CTRL cells of DCF MFI; **(B)** statistical histogram of MMP levels at 72 h on HT-29 untreated cells (CTRL), ATCC treated cells, CENC, and NC; expressed as fold of change of treated cells/CTRL cells of TMRE MFI. In the red square, ROS levels and MMP in pathological conditions: **(C)** statistical histogram of ROS levels at 72 h on HT-29 untreated cells (CTRL), ATCC treated cells, ATCC + CENC, and ATCC + NC; **(D)** statistical histogram of MMP levels at 72 h on HT-29 untreated cells (CTRL), ATCC treated cells, ATCC + CENC, and ATCC + NC. One-way ANOVA with Bonferroni's multiple comparison tests revealed significant differences (*$p < 0.05$, **$p < 0.01$, ***$p < 0.001$).

MMP highlighted a different response after CENC and NC administration in physiological conditions: a decrease and an increase, respectively (**Figure 10**). The pathologic condition panel highlights CENC and NC being able to lower the MMP rise induced by ATCC: the decrease is mild and not significant in CENC samples and more relevant and significant in NC samples.

Autophagic-like vesicles, actors of the autophagic process strictly linked to mitochondrial functions and ROS production [77], are traced by MDC labelling and quantified by flow cytometry. Our data did not point out any significant difference between the control, CENC, and NC samples; of note, the MFI increase observable in ATCC CDT-treated cells is reduced by both CENC and NC conditioning, reaching values like controls (**Figure 11A**,**D**).

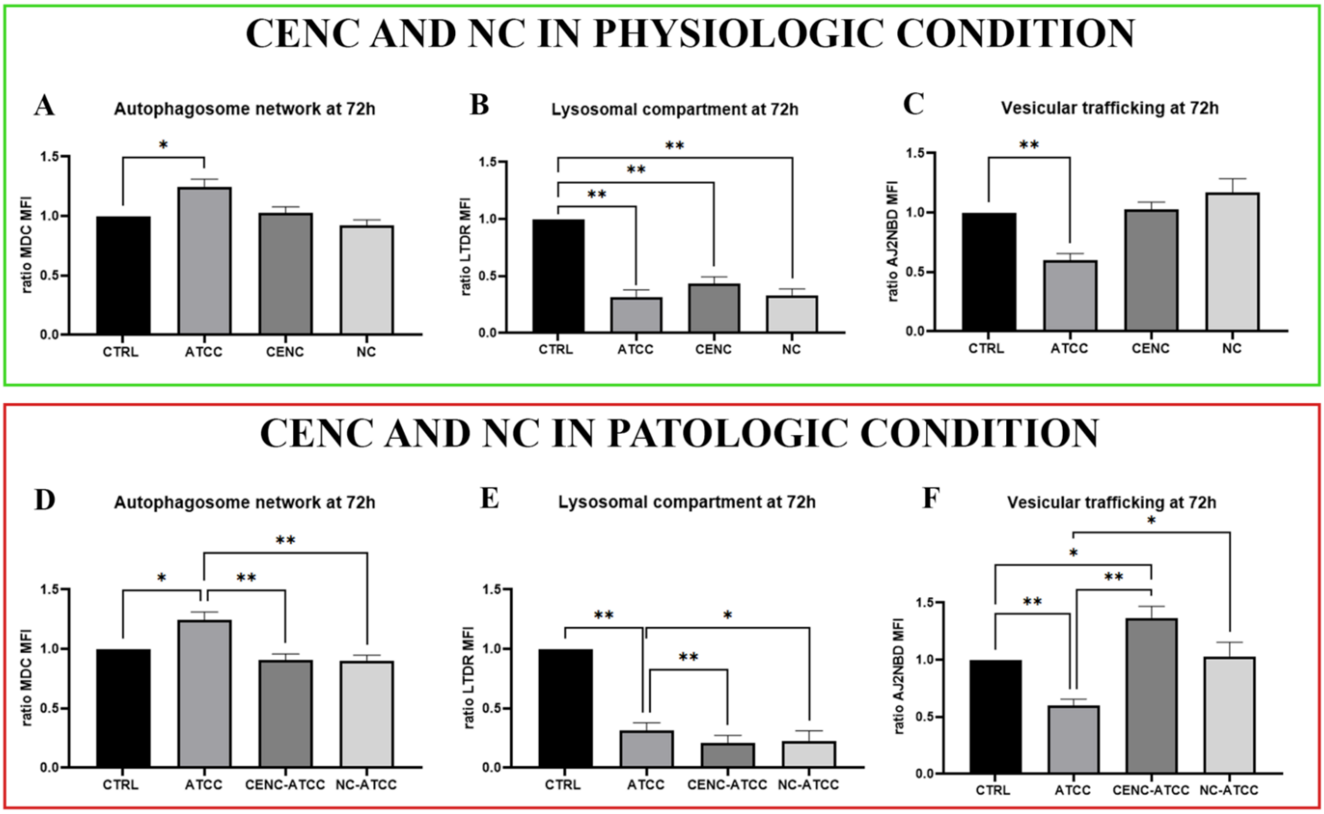

Figure 11. In the green square, the status of lysosomal and vesicular compartment in physiological conditions: **(A)** statistical histogram of autophagic-like vacuole at 72 h on HT-29 untreated cells (CTRL), ATCC treated cells CENC and NC; expressed as fold of change of treated cells/CTRL cells of MDC MFI; **(B)** statistical histogram of the lysosomal compartment at 72 h on HT-29 untreated cells (CTRL), ATCC treated cells, CENC and NC; expressed as fold of change of treated cells/CTRL cells of LTDR MFI; **(C)** statistical histogram of vesicular compartments at 72 h on HT-29 untreated cells (CTRL), ATCC treated cells, CENC and NC; expressed as fold of change of treated cells/CTRL cells of AJ2NBD MFI; In the red square, the status of lysosomal and vesicular compartment in pathological conditions; **(D)** statistical histogram of autophagic-like vacuole at 72 h on HT-29 untreated cells (CTRL), ATCC treated cells, CENC and NC; **(E)** statistical histogram of the lysosomal compartment at 72 h on HT-29 untreated cells (CTRL), ATCC treated cells, CENC and NC; **(F)** statistical histogram of vesicular compartments at 72 h on HT-29 untreated cells (CTRL), ATCC treated cells, ATCC + CENC, and ATCC + NC. One-way ANOVA with Bonferroni’s multiple comparison tests revealed significant differences (*$p < 0.05$, **$p < 0.01$, ***$p < 0.001$).

We found significant differences for NC and CENC treatments in physiological conditions for lysosomes (LTDR MFI): both nanocellulose conditioning induced a relevant decrease compared to control and ATCC CDT-treated samples (**Figure 11B**,**E**). Given the high interconnectivity of endosomal, lysosomal, and autophagosomal pathways, dysfunctions in one of these systems may trigger alterations in another [78]. Briefly, the more acidic vacuoles, such as lysosomes, progressively decreased, from 24 h to 72 h in each ATCC CDT-treated sample, whereas after CENC treatments we observed an initial lysosome number/function increase (at 24 h), followed by a subsequent decrease (at 72 h). This finding is in agreement with other researchers [79,80] at least for the bioactive compound caffeine. Regarding non-acidic vacuoles targeted by AJ2NBD, a drop was detected after the 72 h treatment with ATCC, whereas CENC and NC seem to contribute, at any time points, to restoring the vesicle compartment (and trafficking) altered by ATCC CDT (**Figure 11C**,**F**).

The following scenario emerges from the data: i) after 24 h, NC and CENC treatments did not produce any relevant and significant modification; ii) ATCC-treated cells, as expected, revealed perturbations in the autophagic flux (increased autophagolysosomes and decreased acidic, mature lysosomes); iii) CENC and NC preconditioning restored autophagic vacuoles to the values of control cells, revealing a partial improvement of the perturbed autophagic flux.

4. Discussion and conclusion

Nanocellulose in food packaging applications, like any other food contact material, raises potential safety concerns [81]. Several review studies on NC have shown that toxicity studies remain scarce and knowledge gaps remain. Studies of nanocellulose exposure in various in vitro cell lines and animal models are limited, and no evidence of significant toxicity has been found [82], but certain studies have shown diverging results [83]. Our study is then useful to identify the properties of coffee-embedded nanocellulose and nanocellulose from coffee pods in an in vitro model represented by HT-29 intestinal cells.

The in vitro toxicological endpoints evaluated in this study consider cell death, ROS production (often an early precursor of cytotoxicity), mitochondria membrane potential, lysosomes, and autophagosomes. These approaches allowed to detect: i) mitochondrial damage, a crucial event in particulate matter (PM)-induced cytotoxicity [84]; ii) lysosomal network impairment; and iii) endosome and autophagosome alteration. In fact, endocytosis and autophagy are two major pathways for cellular homeostasis, and although endosomal and autophagy are discrete pathways, there is extensive crosstalk between these vesicular compartments.

The initial response to PM is a decrease in mitochondrial membrane potential and increased oxygen radical production, followed by inner mitochondrial membrane damage [85]. Our data reveal a mild decrease in MMP of CENC-treated cells after 72, but with CDT administration, MMP restores to the control level. These findings confirm that, also in our model and at the massive concentrations employed, both CENC and NC are non-cytotoxic. Furthermore, the three different interrelated intracellular vacuole/vesicle compartments analysed highlight the improvement of the autophagic flux due to CENC and NC conditioning, suggesting the increase of non-acidic vacuoles (i.e., endosomes). In conclusion, the micro/nanoscaled cellulose in both CENC and NC formats from coffee pods does not significantly impact the viability and functions of HT-29 intestinal cells but does indeed improve the viable status and endosomal compartment after *C. jejuni* CDT intoxication.

However, results obtained from in vitro studies cannot often be used directly to predict the biological responses of organisms to chemical exposure in vivo. Therefore, further studies are needed, including chronic in vivo feeding studies and assessments of other potential endpoints.

Supplementary materials: Figures S1 and **S2** can be downloaded at Supplementary material.

Author contributions: Conceptualization, BC, MM and DL; methodology, DL, MM, BC, GP, MG, PG, LV, EM and DP; validation, DL, GP, MM and BC; formal analysis, DL, BC and MM; investigation, DL, BC, GP, EM and MM; resources, VF, SP and BC; data curation, DL, GP, MM, BC, LV and MG; writing—original draft preparation, DL, MM, BC and GP; writing—review and editing, DL, PG, MG, VL, EM, BC and MM; visualization, BC and DL; supervision, BC, DL and MM; project administration, BC and DL; funding acquisition, VF, SP and BC. All authors have read and agreed to the published version of the manuscript.

Acknowledgments: We want to thank CTSV for providing us the newly developed MediMachineII, Medicons, Foodcons and Filcons and to have supplied Foodcons by their early days of marketing. We want to acknowledge Doctor Caterina Ciacci for her excellent assistance for confocal microscope analysis.

Conflict of interest: The authors declare no conflict of interest.

References

1. Athinarayanan J, Periasamy VS, Alsaif MA, et al. Presence of nanosilica (E551) in commercial food products: TNF-mediated oxidative stress and altered cell cycle progression in human lung fibroblast cells. Cell Biology and Toxicology. 2014; 30(2): 89-100. doi: 10.1007/s10565-014-9271-8
2. Gómez HC, Serpa A, Velásquez-Cock J, et al. Vegetable nanocellulose in food science: A review. Food Hydrocolloids. 2016; 57: 178-186. doi: 10.1016/j.foodhyd.2016.01.023
3. Khare S, DeLoid GM, Molina RM, et al. Effects of ingested nanocellulose on intestinal microbiota and homeostasis in Wistar Han rats. NanoImpact. 2020; 18: 100216. doi: 10.1016/j.impact.2020.100216
4. Onyango C, Unbehend G, Lindhauer MG. Effect of cellulose-derivatives and emulsifiers on creep-recovery and crumb properties of gluten-free bread prepared from sorghum and gelatinised cassava starch. Food Research International. 2009; 42(8): 949-955. doi: 10.1016/j.foodres.2009.04.011
5. Pereda M, Amica G, Rácz I, et al. Structure and properties of nanocomposite films based on sodium caseinate and nanocellulose fibers. Journal of Food Engineering. 2011; 103(1): 76-83. doi: 10.1016/j.jfoodeng.2010.10.001
6. Boluk Y, Lahiji R, Zhao L, et al. Suspension viscosities and shape parameter of cellulose nanocrystals (CNC). Colloids and Surfaces A: Physicochemical and Engineering Aspects. 2011; 377(1-3): 297-303. doi: 10.1016/j.colsurfa.2011.01.003
7. Kalashnikova I, Bizot H, Cathala B, et al. New Pickering Emulsions Stabilized by Bacterial Cellulose Nanocrystals. Langmuir. 2011; 27(12): 7471-7479. doi: 10.1021/la200971f
8. Zhao GH, Kapur N, Carlin B, et al. Characterisation of the interactive properties of microcrystalline cellulose-carboxymethyl cellulose hydrogels. International Journal of Pharmaceutics. 2011; 415(1-2): 95-101. doi: 10.1016/j.ijpharm.2011.05.054

9. Tang L, Huang B, Lu Q, et al. Ultrasonication-assisted manufacture of cellulose nanocrystals esterified with acetic acid. Bioresource Technology. 2013; 127: 100-105. doi: 10.1016/j.biortech.2012.09.133
10. Paunonen SV, Hong RY. The many faces of assumed similarity in perceptions of personality. Journal of Research in Personality. 2013; 47(6): 800-815. doi: 10.1016/j.jrp.2013.08.007
11. Alves JS, dos Reis KC, Menezes EGT, et al. Effect of cellulose nanocrystals and gelatin in corn starch plasticized films. Carbohydrate Polymers. 2015; 115: 215-222. doi: 10.1016/j.carbpol.2014.08.057
12. Nsor-Atindana J, Chen M, Goff HD, et al. Functionality and nutritional aspects of microcrystalline cellulose in food. Carbohydrate Polymers. 2017; 172: 159-174. doi: 10.1016/j.carbpol.2017.04.021
13. Robson AA. Tackling obesity: can food processing be a solution rather than a problem? Agro Food Industry Hi-Tech. 2012; 23(2): 10-11.
14. Cao X, Zhang T, DeLoid GM, et al. Cytotoxicity and cellular proteome impact of cellulose nanocrystals using simulated digestion and an in vitro small intestinal epithelium cellular model. NanoImpact. 2020; 20: 100269. doi: 10.1016/j.impact.2020.100269
15. Li Q, Wu Y, Fang R, et al. Application of Nanocellulose as particle stabilizer in food Pickering emulsion: Scope, Merits and challenges. Trends in Food Science & Technology. 2021; 110: 573-583. doi: 10.1016/j.tifs.2021.02.027
16. DeLoid GM, Cao X, Molina RM, et al. Toxicological effects of ingested nanocellulose in in vitro intestinal epithelium and in vivo rat models. Environmental Science: Nano. 2019; 6(7): 2105-2115. doi: 10.1039/c9en00184k
17. Karimian A, Parsian H, Majidinia M, et al. Nanocrystalline cellulose: Preparation, physicochemical properties, and applications in drug delivery systems. International Journal of Biological Macromolecules. 2019; 133: 850-859. doi: 10.1016/j.ijbiomac.2019.04.117
18. Lanfranchi M, Giannetto C, Dimitrova V. Evolutionary aspects of coffee consumers' buying habits: Results of a sample survey. Bulgarian Journal of Agricultural Science. 2016; 22(5): 705-712.
19. Abuabara L, Paucar-Caceres A, Burrowes-Cromwell T. Consumers' values and behaviour in the Brazilian coffee-in-capsules market: promoting circular economy. International Journal of Production Research. 2019; 57(23): 7269-7288. doi: 10.1080/00207543.2019.1629664
20. Chen H, Xu L, Yu K, et al. Release of microplastics from disposable cups in daily use. Science of The Total Environment. 2023; 854: 158606. doi: 10.1016/j.scitotenv.2022.158606
21. Corlett D, Stock Phot A. Nanoplastic should be better understood. Nature Nanotechnology. 2019; 14(4): 299-299. doi: 10.1038/s41565-019-0437-7
22. Cox KD, Covernton GA, Davies HL, et al. Human Consumption of Microplastics. Environmental Science & Technology. 2019; 53(12): 7068-7074. doi: 10.1021/acs.est.9b01517
23. Zangmeister CD, Radney JG, Benkstein KD, et al. Common Single-Use Consumer Plastic Products Release Trillions of Sub-100 nm Nanoparticles per Liter into Water during Normal Use. Environmental Science & Technology. 2022; 56(9): 5448-5455. doi: 10.1021/acs.est.1c06768
24. Rodríguez-Fabià S, Torstensen J, Johansson L, et al. Hydrophobisation of lignocellulosic materials part I: physical modification. Cellulose. 2022; 29(10): 5375-5393. doi: 10.1007/s10570-022-04620-8
25. Torstensen J, Ottesen V, Rodríguez-Fabià S, et al. The influence of temperature on cellulose swelling at constant water density. Scientific Reports. 2022; 12(1). doi: 10.1038/s41598-022-22092-5
26. Dagnon KL, Shanmuganathan K, Weder C, et al. Water-Triggered Modulus Changes of Cellulose Nanofiber Nanocomposites with Hydrophobic Polymer Matrices. Macromolecules. 2012; 45(11): 4707-4715. doi: 10.1021/ma300463y
27. Liu L, Kong F. The behavior of nanocellulose in gastrointestinal tract and its influence on food digestion. Journal of Food Engineering. 2021; 292: 110346. doi: 10.1016/j.jfoodeng.2020.110346
28. Salatin S, Yari Khosroushahi A. Overviews on the cellular uptake mechanism of polysaccharide colloidal nanoparticles. Journal of Cellular and Molecular Medicine. 2017; 21(9): 1668-1686. doi: 10.1111/jcmm.13110
29. Wang T, Bai J, Jiang X, et al. Cellular Uptake of Nanoparticles by Membrane Penetration: A Study Combining Confocal Microscopy with FTIR Spectroelectrochemistry. ACS Nano. 2012; 6(2): 1251-1259. doi: 10.1021/nn203892h
30. Crater JS, Carrier RL. Barrier Properties of Gastrointestinal Mucus to Nanoparticle Transport. Macromolecular Bioscience. 2010; 10(12): 1473-1483. doi: 10.1002/mabi.201000137
31. Bergin IL, Witzmann FA. Nanoparticle toxicity by the gastrointestinal route: evidence and knowledge gaps. International Journal of Biomedical Nanoscience and Nanotechnology. 2013; 3(1/2): 163. doi: 10.1504/ijbnn.2013.054515

32. Suvarna V, Nair A, Mallya R, et al. Antimicrobial Nanomaterials for Food Packaging. Antibiotics. 2022; 11(6): 729. doi: 10.3390/antibiotics11060729
33. Bintsis T. Foodborne pathogens. AIMS Microbiology. 2017; 3(3): 529-563. doi: 10.3934/microbiol.2017.3.529
34. Canonico B, Cesarini E, Montanari M, et al. Rapamycin Re-Directs Lysosome Network, Stimulates ER-Remodeling, Involving Membrane CD317 and Affecting Exocytosis, in Campylobacter Jejuni-Lysate-Infected U937 Cells. International Journal of Molecular Sciences. 2020; 21(6): 2207. doi: 10.3390/ijms21062207
35. Pickett CL, Pesci EC, Cottle DL, et al. Prevalence of cytolethal distending toxin production in Campylobacter jejuni and relatedness of Campylobacter sp. cdtB gene. Infection and Immunity. 1996; 64(6): 2070-2078. doi: 10.1128/iai.64.6.2070-2078.1996
36. Lara-Tejero M, Galán JE. A Bacterial Toxin That Controls Cell Cycle Progression as a Deoxyribonuclease I-Like Protein. Science. 2000; 290(5490): 354-357. doi: 10.1126/science.290.5490.354
37. Zhang Y, Huang R, Jiang Y, et al. The role of bacteria and its derived biomaterials in cancer radiotherapy. Acta Pharmaceutica Sinica B. 2023; 13(10): 4149-4171. doi: 10.1016/j.apsb.2022.10.013
38. Canonico B, Campana R, Luchetti F, et al. Campylobacter jejuni cell lysates differently target mitochondria and lysosomes on HeLa cells. Apoptosis. 2014; 19(8): 1225-1242. doi: 10.1007/s10495-014-1005-0
39. Canonico B, Di Sario G, Cesarini E, et al. Monocyte Response to Different Campylobacter jejuni Lysates Involves Endoplasmic Reticulum Stress and the Lysosomal-Mitochondrial Axis: When Cell Death Is Better Than Cell Survival. Toxins. 2018; 10(6): 239. doi: 10.3390/toxins10060239
40. Jongsma MLM, Berlin I, Wijdeven RHM, et al. An ER-Associated Pathway Defines Endosomal Architecture for Controlled Cargo Transport. Cell. 2016; 166(1): 152-166. doi: 10.1016/j.cell.2016.05.078
41. Nasoni MG, Carloni S, Canonico B, et al. Melatonin reshapes the mitochondrial network and promotes intercellular mitochondrial transfer via tunneling nanotubes after ischemic-like injury in hippocampal HT22 cells. Journal of Pineal Research. 2021; 71(1). doi: 10.1111/jpi.12747
42. Canonico B, Cangiotti M, Montanari M, et al. Characterization of a fluorescent 1,8-naphthalimide-functionalized PAMAM dendrimer and its Cu(ii) complexes as cytotoxic drugs: EPR and biological studies in myeloid tumor cells. Biological Chemistry. 2022; 403(3): 345-360. doi: 10.1515/hsz-2021-0388
43. Salucci S, Burattini S, Battistelli M, et al. Tyrosol prevents apoptosis in irradiated keratinocytes. Journal of Dermatological Science. 2015; 80(1): 61-68. doi: 10.1016/j.jdermsci.2015.07.002
44. Fiorani M, De Matteis R, Canonico B, et al. Temporal correlation of morphological and biochemical changes with the recruitment of different mechanisms of reactive oxygen species formation during human SW872 cell adipogenic differentiation. BioFactors. 2021; 47(5): 837-851. doi: 10.1002/biof.1769
45. Fusi V, Formica M, Giorgi L, et al. Preparation of heterocyclic compounds as fluorescent probes for detection in biological systems. Available online: https://ora.uniurb.it/handle/11576/2675836.2 (accessed on 5 January 2023).
46. Canonico B, Giorgi L, Nasoni MG, et al. Synthesis and biological characterization of a new fluorescent probe for vesicular trafficking based on polyazamacrocycle derivative. Biological Chemistry. 2021; 402(10): 1225-1237. doi: 10.1515/hsz-2021-0204
47. Tayeb A, Amini E, Ghasemi S, et al. Cellulose Nanomaterials—Binding Properties and Applications: A Review. Molecules. 2018; 23(10): 2684. doi: 10.3390/molecules23102684
48. Roman M, Winter WT. Effect of Sulfate Groups from Sulfuric Acid Hydrolysis on the Thermal Degradation Behavior of Bacterial Cellulose. Biomacromolecules. 2004; 5(5): 1671-1677. doi: 10.1021/bm034519
49. Čolić M, Tomić S, Bekić M. Immunological aspects of nanocellulose. Immunology Letters. 2020; 222: 80-89. doi: 10.1016/j.imlet.2020.04.004
50. Pereira MM, Raposo NRB, Brayner R, et al. Cytotoxicity and expression of genes involved in the cellular stress response and apoptosis in mammalian fibroblast exposed to cotton cellulose nanofibers. Nanotechnology. 2013; 24(7): 075103. doi: 10.1088/0957-4484/24/7/075103
51. Oh JH, Lee JT, Yang ES, et al. The coffee diterpene kahweol induces apoptosis in human leukemia U937 cells through down-regulation of Akt phosphorylation and activation of JNK. Apoptosis. 2009; 14(11): 1378-1386. doi: 10.1007/s10495-009-0407-x
52. Jabir NR, Islam MT, Tabrez S, et al. An insight towards anticancer potential of major coffee constituents. BioFactors. 2018; 44(4): 315-326. doi: 10.1002/biof.1437

53. Prasanthi JRP, Dasari B, Marwarha G, et al. Caffeine protects against oxidative stress and Alzheimer’s disease-like pathology in rabbit hippocampus induced by cholesterol-enriched diet. Free Radical Biology and Medicine. 2010; 49(7): 1212-1220. doi: 10.1016/j.freeradbiomed.2010.07.007
54. Ko J, Kim JY, Kim J, et al. Anti-oxidative and anti-adipogenic effects of caffeine in an in vitro model of Graves’ orbitopathy. Endocrine Journal. 2020; 67(4): 439-447. doi: 10.1507/endocrj.ej19-0521
55. Silvério A dos SD, Pereira RGFA, Duarte SM da S, et al. Coffee beverage reduces ROS production and does not affect the organism s response against Candida albicans. Revista de Ciências Farmacêutica Básica e Aplicadas—RCFBA. 2020; 41. doi: 10.4322/2179-443x.0684
56. Castaldo L, Toriello M, Sessa R, et al. Antioxidant and Anti-Inflammatory Activity of Coffee Brew Evaluated after Simulated Gastrointestinal Digestion. Nutrients. 2021; 13(12): 4368. doi: 10.3390/nu13124368
57. To EE, Erlich JR, Liong F, et al. Therapeutic Targeting of Endosome and Mitochondrial Reactive Oxygen Species Protects Mice from Influenza Virus Morbidity. Frontiers in Pharmacology. 2022; 13: 870156. doi: 10.3389/fphar.2022.870156
58. Zeng Q, Ma X, Song Y, et al. Targeting regulated cell death in tumor nanomedicines. Theranostics. 2022; 12(2): 817-841. doi: 10.7150/thno.67932
59. Amatori S, Ambrosi G, Borgogelli E, et al. Modulating the Sensor Response to Halide Using NBD-Based Azamacrocycles. Inorganic Chemistry. 2014; 53(9): 4560-4569. doi: 10.1021/ic5001649
60. Miękus N, Marszałek K, Podlacha M, et al. Health Benefits of Plant-Derived Sulfur Compounds, Glucosinolates, and Organosulfur Compounds. Molecules. 2020; 25(17): 3804. doi: 10.3390/molecules25173804
61. Xie J, Liao B, Tang RY. Functional Application of Sulfur-Containing Spice Compounds. Journal of Agricultural and Food Chemistry. 2020; 68(45): 12505-12526. doi: 10.1021/acs.jafc.0c05002
62. Cano-Marquina A, Tarín JJ, Cano A. The impact of coffee on health. Maturitas. 2013; 75(1): 7-21. doi: 10.1016/j.maturitas.2013.02.002
63. Montanari M, Guescini M, Gundogdu O, et al. Extracellular Vesicles from Campylobacter jejuni CDT-Treated Caco-2 Cells Inhibit Proliferation of Tumour Intestinal Caco-2 Cells and Myeloid U937 Cells: Detailing the Global Cell Response for Potential Application in Anti-Tumour Strategies. International Journal of Molecular Sciences. 2022; 24(1): 487. doi: 10.3390/ijms24010487
64. Hickey TE, Majam G, Guerry P. Intracellular Survival of Campylobacter jejuni in Human Monocytic Cells and Induction of Apoptotic Death by Cytholethal Distending Toxin. Infection and Immunity. 2005; 73(8): 5194-5197. doi: 10.1128/iai.73.8.5194-5197.2005
65. Alzheimer M, Svensson SL, König F, et al. A three-dimensional intestinal tissue model reveals factors and small regulatory RNAs important for colonization with Campylobacter jejuni. PLOS Pathogens. 2020; 16(2): e1008304. doi: 10.1371/journal.ppat.1008304
66. Martin OCB, Frisan T. Bacterial Genotoxin-Induced DNA Damage and Modulation of the Host Immune Microenvironment. Toxins. 2020; 12(2): 63. doi: 10.3390/toxins12020063
67. Balta I, Butucel E, Stef L, et al. Anti-Campylobacter Probiotics: Latest Mechanistic Insights. Foodborne Pathogens and Disease. 2022; 19(10): 693-703. doi: 10.1089/fpd.2022.0039
68. Athinarayanan J, Alshatwi AA, Subbarayan Periasamy V. Biocompatibility analysis of Borassus flabellifer biomass-derived nanofibrillated cellulose. Carbohydrate Polymers. 2020; 235: 115961. doi: 10.1016/j.carbpol.2020.115961
69. Ventura C, Pinto F, Lourenço AF, et al. On the toxicity of cellulose nanocrystals and nanofibrils in animal and cellular models. Cellulose. 2020; 27(10): 5509-5544. doi: 10.1007/s10570-020-03176-9
70. Wang X, Qiu Y, Wang M, et al. Endocytosis and Organelle Targeting of Nanomedicines in Cancer Therapy. International Journal of Nanomedicine. 2020; 15: 9447-9467. doi: 10.2147/ijn.s274289
71. López-Galilea I, De Peña MP, Cid C. Correlation of Selected Constituents with the Total Antioxidant Capacity of Coffee Beverages: Influence of the Brewing Procedure. Journal of Agricultural and Food Chemistry. 2007; 55(15): 6110-6117. doi: 10.1021/jf070779x
72. Acidri R, Sawai Y, Sugimoto Y, et al. Phytochemical Profile and Antioxidant Capacity of Coffee Plant Organs Compared to Green and Roasted Coffee Beans. Antioxidants. 2020; 9(2): 93. doi: 10.3390/antiox9020093
73. Andueza S, Cid C, Cristina Nicoli M. Comparison of antioxidant and pro-oxidant activity in coffee beverages prepared with conventional and “Torrefacto” coffee. LWT—Food Science and Technology. 2004; 37(8): 893-897. doi: 10.1016/j.lwt.2004.04.004

74. Cui WQ, Wang ST, Pan D, et al. Caffeine and its main targets of colorectal cancer. World Journal of Gastrointestinal Oncology. 2020; 12(2): 149-172. doi: 10.4251/wjgo.v12.i2.149
75. Lee C. Antioxidant ability of caffeine and its metabolites based on the study of oxygen radical absorbing capacity and inhibition of LDL peroxidation. Clinica Chimica Acta. 2000; 295(1-2): 141-154. doi: 10.1016/S0009-8981(00)00201-1
76. Soares MJ, Sampaio GR, Guizellini GM, et al. Regular and decaffeinated espresso coffee capsules: Unravelling the bioaccessibility of phenolic compounds and their antioxidant properties in milk model system upon in vitro digestion. LWT. 2021; 135: 110255. doi: 10.1016/j.lwt.2020.110255
77. Filomeni G, De Zio D, Cecconi F. Oxidative stress and autophagy: the clash between damage and metabolic needs. Cell Death & Differentiation. 2014; 22(3): 377-388. doi: 10.1038/cdd.2014.150
78. Roosen DA, Cookson MR. LRRK2 at the interface of autophagosomes, endosomes and lysosomes. Molecular Neurodegeneration. 2016; 11(1). doi: 10.1186/s13024-016-0140-1
79. Farias-Pereira R, Park CS, Park Y. Mechanisms of action of coffee bioactive components on lipid metabolism. Food Science and Biotechnology. 2019; 28(5): 1287-1296. doi: 10.1007/s10068-019-00662-0
80. Al-Bari MdAA, Ito Y, Ahmed S, et al. Targeting Autophagy with Natural Products as a Potential Therapeutic Approach for Cancer. International Journal of Molecular Sciences. 2021; 22(18): 9807. doi: 10.3390/ijms22189807
81. Silva FAGS, Dourado F, Gama M, et al. Nanocellulose Bio-Based Composites for Food Packaging. Nanomaterials. 2020; 10(10): 2041. doi: 10.3390/nano10102041
82. Bhattacharya K, Kiliç G, Costa PM, Fadeel B. Cytotoxicity screening and cytokine profiling of nineteen nanomaterials enables hazard ranking and grouping based on inflammogenic potential. Nanotoxicology. 2017; 11(6): 809-826. doi: 10.1080/17435390.2017.1363309
83. Stoudmann N, Schmutz M, Hirsch C, et al. Human hazard potential of nanocellulose: quantitative insights from the literature. Nanotoxicology. 2020; 14(9): 1241-1257. doi: 10.1080/17435390.2020.1814440
84. Hiura TS, Li N, Kaplan R, et al. The Role of a Mitochondrial Pathway in the Induction of Apoptosis by Chemicals Extracted from Diesel Exhaust Particles. The Journal of Immunology. 2000; 165(5): 2703-2711. doi: 10.4049/jimmunol.165.5.2703
85. Teodoro JS, Simões AM, Duarte FV, et al. Assessment of the toxicity of silver nanoparticles in vitro: A mitochondrial perspective. Toxicology in Vitro. 2011; 25(3): 664-670. doi: 10.1016/j.tiv.2011.01.004

Characterization and Application of Nanomaterials 2024, 7(2), 6414.
https://doi.org/10.24294/can.v7i2.6414

Article

Micro/nanoscaled cellulose from coffee pods do not impact HT-29 cells while improving viability and endosomal compartment after *C. jejuni* CDT intoxication

Supplementary materials

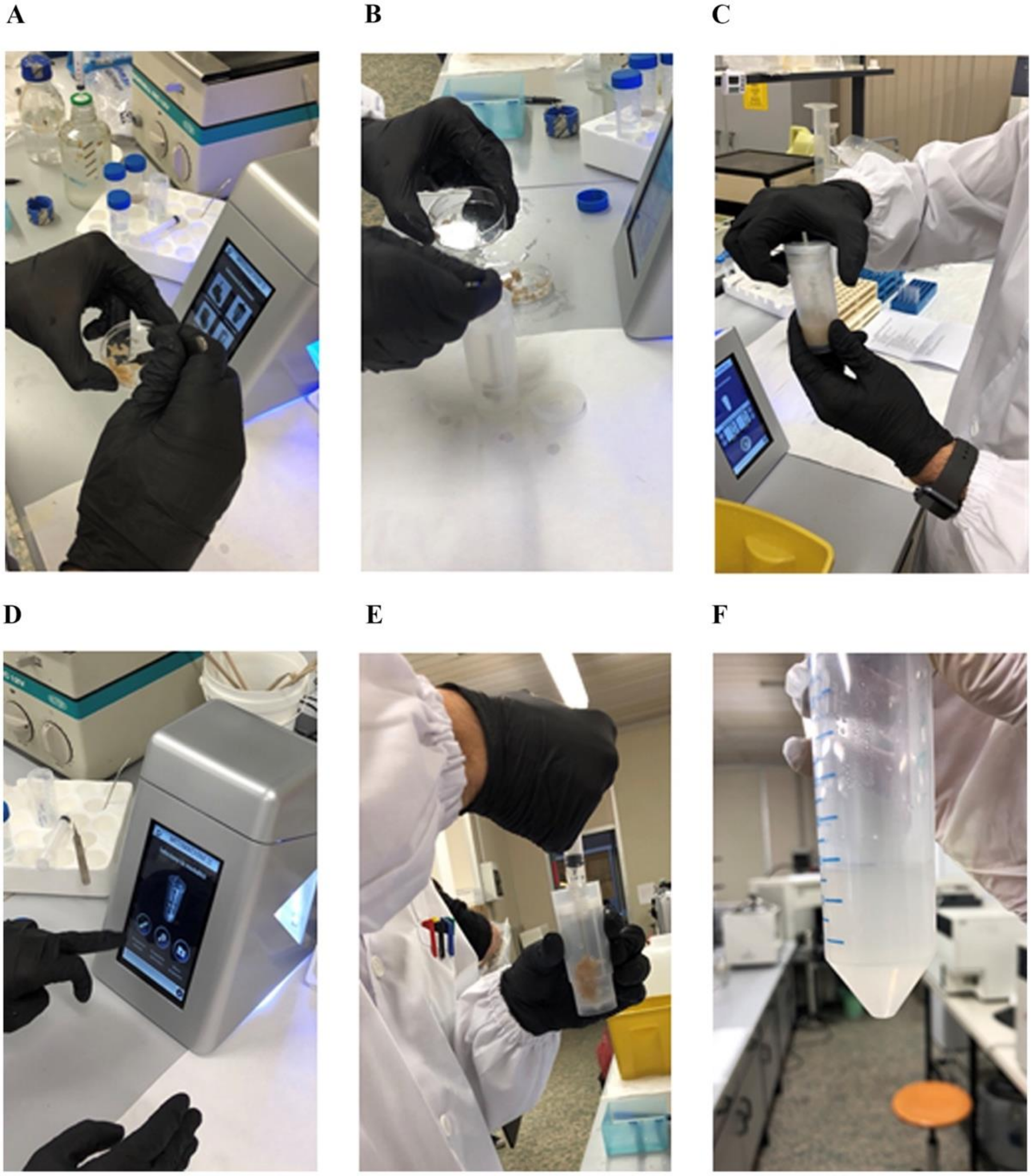

Figure S1. The images represent the sequence of NC extraction from coffee pods using Medimachine II. **(A)** dissecting the coffee pod into 2 mm × 2 mm squares; **(B)** insertion inside the Foodcon holder and the addition of PBS; **(C)** the closure of the holder; **(D)** setting the procedure of the program on the instrument; **(E)** the sampling with a sterile syringe of the NC-containing homogenate; **(F)** the NC-containing solution after filtration through Filcons.

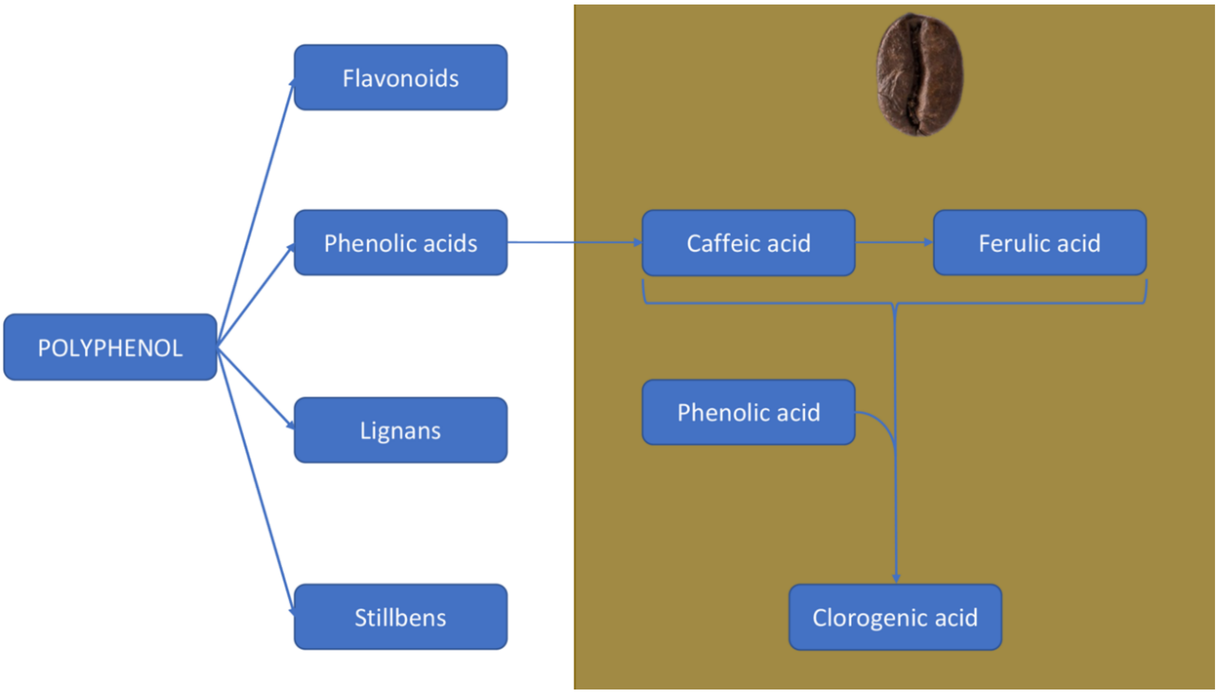

Figure S2. Scheme of Dietary polyphenols known subclasses and Phenolic compounds of coffee bean. Coffee contains high amounts of phenolic compounds: Phenolic acids are the highly abundant polyphenols in coffee, in particular Caffeic acid, that may be transformed into ferulic acid. Nonetheless, the most frequent is chlorogenic acid.

Characterization and Application of Nanomaterials 2024, 7(2), 7007.
https://doi.org/10.24294/can.v7i2.7007

Article

Ajwa date seed mediated green synthesis of alginate-silver nanocomposite beads and films for antibacterial and catalytic degradation applications

Naba Almukharraq†**, Marwa Almarzooqi**†**, Hasan Ruyan**†**, Fatima AlHannan, Praveen Kumar, Fryad Henari, G. Roshan Deen***

Materials for Medicine Research Group, School of Medicine, Royal College of Surgeons in Ireland (RCSI), Medical University of Bahrain, Busaiteen 228, Kingdom of Bahrain
*** Corresponding author:** G. Roshan Deen, rdeen@rcsi.com

† Equal contribution to this work and share first author status.

CITATION

Almukharraq N, Almarzooqi M, Ruyan H, et al. Ajwa date seed mediated green synthesis of alginate-silver nanocomposite beads and films for antibacterial and catalytic degradation applications. Characterization and Application of Nanomaterials. 2024; 7(2): 7007. https://doi.org/10.24294/can.v7i2.7007

ARTICLE INFO

Received: 11 June 2024
Accepted: 3 July 2024
Available online: 1 August 2024

Abstract: Alginate-silver nanocomposites in the form of spherical beads and films were prepared using a green approach by using the aqueous extract of Ajwa date seeds. The nanocomposites were fabricated by in situ reduction and gelation by ionotropic crosslinking using calcium ions in solution. The rich phytochemicals of the date seed extract played a dual role as a reducing and stabilizing agent in the synthesis of silver nanoparticles. The formation of silver nanoparticles was studied using UV-Vis absorption spectroscopy, and a distinct surface plasmon resonance peak at 421 nm characteristic of silver nanoparticles confirmed the green synthesis of silver nanoparticles. The morphology of the nanocomposite beads and film was compact, with an even distribution of silver nanoclusters. The catalytic property of the nanocomposite beads was evaluated for the degradation of 2-nitrophenol in the presence of sodium borohydride. The degradation followed pseudo-first-order kinetics with a rate constant of 1.40×10^{-3} s^{-1} at 23 °C and an activation energy of 18.45 kJ mol^{-1}. The thermodynamic parameters, such as changes in enthalpy and entropy, were evaluated to be 15.22 kJ mol^{-1} and −197.50 J mol^{-1} K^{-1}, respectively. The nanocomposite exhibited properties against three clinically important pathogens (gram-positive and gram-negative bacteria).

Keywords: Ajwa dates seed; silver nanoparticles; green synthesis; alginate beads; degradation; 2-nitrophenol; antibacterial activities

1. Introduction

Water contamination from toxic organic chemical waste from pharmaceutical, textile, and electrochemical industries and their adverse effects on human and aquatic life have received tremendous attention in recent years. Exposure to chemicals above the threshold limits leads to skin discoloration, damage to the nervous system and organs, and developmental effects [1]. The toxic chemicals include nitrophenols, azo dyes, and heavy metals, and water containing these needs to be treated before it is safely discharged into waterbodies or land. Various approaches have been employed in the removal of harmful pollutants, such as adsorption, ion exchange, solvent extraction, photochemical reactions, etc. [2], and among these techniques, adsorption using activated carbon is widely used as the process is economical and effective in the removal of various pollutants. However, this method allows for the adsorption of pollutants but not their degradation to non-toxic substances.

In recent years, photocatalysis or photodegradation methods using metallic and metal oxide nanoparticles such as silver, gold, platinum, palladium, copper, nickel, cobalt, iron, zinc oxide (ZnO), and titanium dioxide (TiO_2) have gained much research attention for the complete reduction of toxic chemical waste to non-toxic substances in water [3–7]. Nanoparticles on solid polymer supports such as polysulfone, polypropylene, poly(vinylidene fluoride), polyamide, cellulose acetate, and sodium alginate offer improved catalytic properties along with material sustainability, as these materials can be used repeatedly [7–9]. Silver nanoparticles supported on various inorganic and organic substrates such as zeolite, silica or fiber glass, carbon materials, natural macro-porous materials, and polymers have been recognized as effective photocatalysts and antimicrobial agents. Nanocomposite beads based on the natural polymers sodium alginate and silver nanoparticles offer extended physical and chemical properties and are currently being considered for point-of-use drinking water disinfection [8–10].

Sodium alginate is a linear polysaccharide found in marine brown algae and is composed of irregular blocks of b-D-mannuronic acid (M) and a-L-guluronic residues (G). Due to their non-toxicity, degradability, and bio-compatibility alginate-based gels have attracted numerous biomedical applications, such as drug and protein delivery, wound dressing, 3D bioprinting for tissue engineering, scaffolds for cell growth and organoid morphogenesis, and flexible electronics for health monitoring [11–15].

Silver nanoparticles synthesized by green chemistry using the extracts of plants or plant products have been used in the fabrication or engineering of alginate-nanocomposite beads. The phytochemicals present in the extract act both as reducing agents for the reduction of silver salt to silver nanoparticles and as stabilizing the resulting nanoparticles against aggregation [16,17]. Date palm, commonly known as *Phoenix dactylifera*, is one of the oldest cultivated varieties of date palm trees with nutritional, economic, and environmental benefits. There are about 5000 varieties of date palm that are grown in different regions of the world, and the nutritional and phytochemical values vary among the dates. Among these, Ajwa dates are widely cultivated in the Al Madinah and surrounding regions of Saudi Arabia. This type of date has high sugar (34.5% glucose, 25.6% fructose, and 0.5% sucrose) and mineral (3%) content compared to other varieties of dates [18,19]. These date seeds are a rich source of polyphenols, flavonoids, glycosides, phenolic acids, proteins, and carbohydrates and demonstrate antioxidant, anti-inflammatory, antimicrobial, and anti-tumor properties. The extract of the Ajwa date seed in methanol and acetone exhibits reasonable antibacterial properties against gram-positive and gram-negative bacteria [19,20].

In this study, we have developed reusable alginate-based silver nanocomposite beads by in situ chemical reduction and gelation methods for the quick reduction of 2-nitrophenol. The silver nanoparticles were first synthesized by green chemistry using the extract of Ajwa date seeds as an efficient source for reduction and stabilization, and then incorporated into alginate beads by ionotropic crosslinking using calcium ions. To the best of our knowledge, this is the first study on the fabrication of alginate-silver nanocomposite beads using the extracts of Ajwa date seed.

2. Experimental

2.1. Materials

Ajwa date (*Phoenix dactylifera*) seed powder was purchased from a grocery store in Hoora, Bahrain. Silver nitrate ($AgNO_3$), sodium alginate ($NaC_6H_7O_6$), sodium hydroxide (NaOH), sodium borohydride ($NaBH_4$), 2-nitrophenol (2-NP), Congo red (CR), and calcium chloride ($CaCl_2$) were purchased from sigma and used as received. Deionized water collected from a Millipore system (Elix Technology, Germany) with a conductivity of 18.2 MW cm^{-1} was used for all aqueous sample preparations. The antibacterial properties of the synthesized nanoparticles, nanocomposite beads, and films were evaluated against three different types of bacteria: *Staphylococcus aureus* (*S. aureus*), *Escherichia coli* (*E. coli*), and *Salmonella typhimurium* (*S. typhimurium*). The bacteria were obtained from the Ministry of Health, Kingdom of Bahrain (MOH, Bahrain, Microbiologiscs, France).

2.2. Preparation of date seeds extract

About 1.00 g of the date seed powder was added to 100 mL of water in a beaker and boiled for 30 min under magnetic stirring. The mixture was air-cooled and centrifuged for 10 min at an rpm of 4200 to remove any suspended materials. The clear extract was used fresh in the synthesis of silver nanoparticles.

2.3. Green synthesis of silver nanoparticles

Silver nanoparticles were synthesized by reducing the silver nitrate in the freshly prepared date seed extract as follows: $AgNO_3$ (1 mm, 5 mL) was placed in a screw-capped glass vial and stirred gently using a magnetic stirring bar. Freshly prepared date seed extract (1 mL) was added dropwise into the vial with continuous stirring. After about 5 min, NaOH (0.5 M, 50 mL) was added dropwise, and the mixture was stirred overnight for the completion of the reaction. Upon addition of NaOH, the color of the solution turned pale yellow and finally to brown (after 24 h). The observed color changes are an indication of the formation of nanoparticles. The solution containing the nanoparticle was centrifuged (rpm 10,000) for 10 min, and the sedimented nanoparticles were washed repeatedly with water and dried in an oven at 70 ℃.

2.4. Synthesis of alginate-silver nanocomposite beads

Alginate beads containing silver nanoparticles were prepared by the sequential chemical reduction and gelation method as described as follows: In this method, silver nanoparticles were first synthesized using the date seed extract and then incorporated into the alginate beads during the gelation. A silver nitrate solution of concentration 1 mm was first prepared by dissolving 0.0175 g of the salt in 100 mL of water. To this solution, 20 mL of fresh date seed extract was added under magnetic stirring, followed by the addition of 1 mL of 0.5 M NaOH. Upon addition of sodium hydroxide, the solution turned pale gray and then pale brown, indicating the onset of the formation of silver nanoparticles. The solution was continuously stirred for an additional 24 h for the completion of the reaction, followed by the addition of 2.20 g of sodium alginate. The solution was heated to 60 ℃ and continuously stirred for another 24 h for the complete dissolution of sodium alginate, resulting in a homogenous mixture. The solution was air-cooled and then stored in the refrigerator to remove any air bubbles. The prepared alginate-silver nanoparticle solution was injected into 200 mL of a 5 wt% calcium chloride solution using a plastic syringe of 20 mL capacity at a rate of 20 drops per minute. The resulting black-colored beads were washed thoroughly with water and dried at 70 ℃ until a constant weight was maintained.

2.5. Synthesis of peelable alginate-silver nanocomposite films

Peelable alginate-silver nanocomposite film was prepared by a mist spray gelation method as described as follows: A 10 mL alginate-silver nanoparticle solution described in the previous section was placed in a clean glass petri dish and mist sprayed with $CaCl_2$ solution (5 wt%). The petri dish was covered and left overnight at room temperature for the completion of gelation. The dark brown film was carefully peeled off from the petri dish, washed repeatedly with water, and dried at 50 ℃ until a constant weight was maintained.

2.6. UV-Vis absorption spectroscopy

The formation of silver nanoparticles was confirmed by measuring the absorbance of the silver nanoparticle solution using a double-beam Shimadzu UV-1800 spectrophotometer. The solution (3 mL) was placed in a quartz cuvette (Helma) of 1 cm path length, and the absorption spectrum was recorded in the wavelength range 250–1000 nm with a resolution of 1 mm. Water was used as the blank reference for all measurements.

2.7. Scanning electron microscopy (SEM)

The size and morphology of the alginate-silver nanocomposite beads were characterized using a scanning electron microscope operating at a voltage of 10 kV (Inovenso, IEM-11). The samples were sputtered with gold for 15 s using an Inovenso SPT-20 coater.

2.8. Catalytic degradation studies of 2-nitrophenol (2-NP)

The catalytic degradation of 2-NP by the alginate-silver nanocomposite beads was followed using a UV-Vis spectrophotometer. A solution of 2-NP (0.13 mm, 2.5 mL) was placed in a quartz cuvette of 1 cm path length, and the absorbance was recorded. After this, 0.5 mL of freshly prepared $NaBH_4$ (0.1 M) was added to the solution, and the absorbance was recorded again. About 10 nanocomposite beads were then added to the solution, and the change in absorbance was recorded at intervals of 3 min for a period of 15 min. The percentage degradation of 2-NP was calculated using the following equation,

$$\text{Degradation (\%)} = \frac{A_0 - A_t}{A_0} \times 100 \tag{1}$$

where, A_0 and A_t are the absorbance at time zero and absorbance at time t, respectively.

2.9. Antibacterial activity

The antibacterial activity of the synthesized silver nanoparticles against different types of gram-positive and gram-negative bacteria, such as *S. aureus*, *E. coli*, and *S. typhimurium*, was carried out using the Kirby-Bauer disk diffusion susceptibility test method. The bacteria strains were spread on a nutrient agar (LB agar) medium using a sterile spreader in all directions. The filter paper discs were loaded with silver nanoparticles with aseptic precautions, and then the agar plate was incubated at 37 °C for 24 h. The zone of inhibition was observed and measured after 24 h of incubation.

3. Results and discussion

3.1. Ajwa date seeds mediated green synthesis of silver nanoparticles

Plant extract-mediated synthesis of metallic nanoparticles is a desired method as it is environmentally friendly and toxic reagents are not used in the process. The formation of silver nanoparticles using the aqueous extract of Ajwa date seeds was studied by visual observation and spectrophotometry. Upon the addition of the date seed extract to the silver nitrate solution, a color change to pale brown was observed, which indicates the in situ chemical reduction of silver ions (Ag^+) to silver nanoparticles (Ag^0). The formation of silver nanoparticles was quantified using UV-Vis absorption spectroscopy, and a distinct surface plasmon resonance (SPR) peak centered at 421 nm confirmed the presence of silver nanoparticles in the solution, as shown in **Figure 1**.

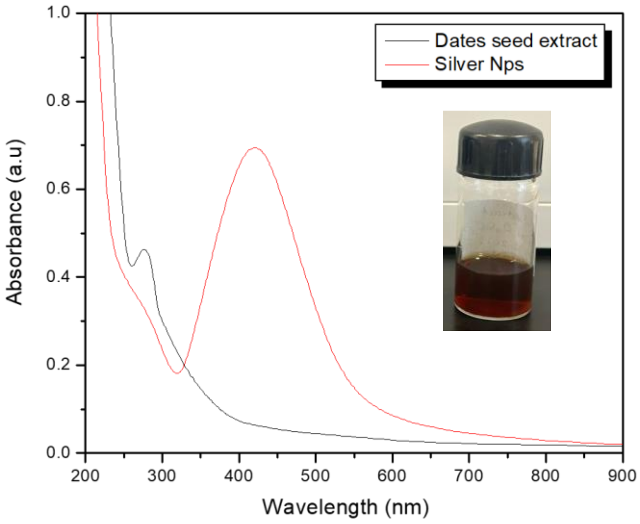

Figure 1. UV-Vis absorption spectra of colloidal silver nanoparticles synthesized using Ajwa dates seeds (insert: digital image of colloidal silver nanoparticles).

This peak arises due to collective oscillations of conduction electrons in the electromagnetic field of the incident light [16,17]. The Ajwa date seeds are rich in phytochemicals such as polyphenols, flavonoids including rutin, catechins, iso-flavonoids, and lignans [18–20]. These phytochemicals present in the extract of Ajwa date seeds are responsible for the chemical reduction and subsequent stabilization of the resulting silver nanoparticles. The peak at 276 nm for the date seeds is attributed to the active phytochemicals that are responsible for the chemical reduction. The absence of this peak in the spectrum of the silver nanoparticles correlates to the reaction and the reduction in concentration of the active phytochemical. The nanoparticles were stable against aggregation for more than a month, with no obvious change in the position (401 nm) and intensity of the SPR peak observed in the absorption spectrum.

3.2. Formation and morphology of alginate beads and film

Silver particles encapsulated in alginate beads were prepared by ionotropic crosslinking with divalent cations such as calcium ions (Ca^{2+}). The divalent cations bind to the guluronate blocks of the sodium alginate chains, as the blocks allow a high degree of coordination with the cations. The guluronate blocks of one polymer then form physical junctions (crosslink points) with the guluronate blocks of adjacent polymer chains. This type of crosslinking and formation of a gel is termed the egg-box model of crosslinking [21].

The alginate beads containing silver particles prepared in this study were pale brown in color in their hydrated state and black when completely dry, as shown in **Figure 2a**,**b.** The dry beads were close to spherical in shape, with an average size of 1.2 mm, as shown by the SEM micrograph in **Figure 2c**. The surface of the nanocomposite beads was compact, with dense particulate clusters of silver in the form of plates (**Figure 2d**). To verify the presence of silver nanoparticles, the alginate beads were soaked in a phosphate buffer solution and dissociated.

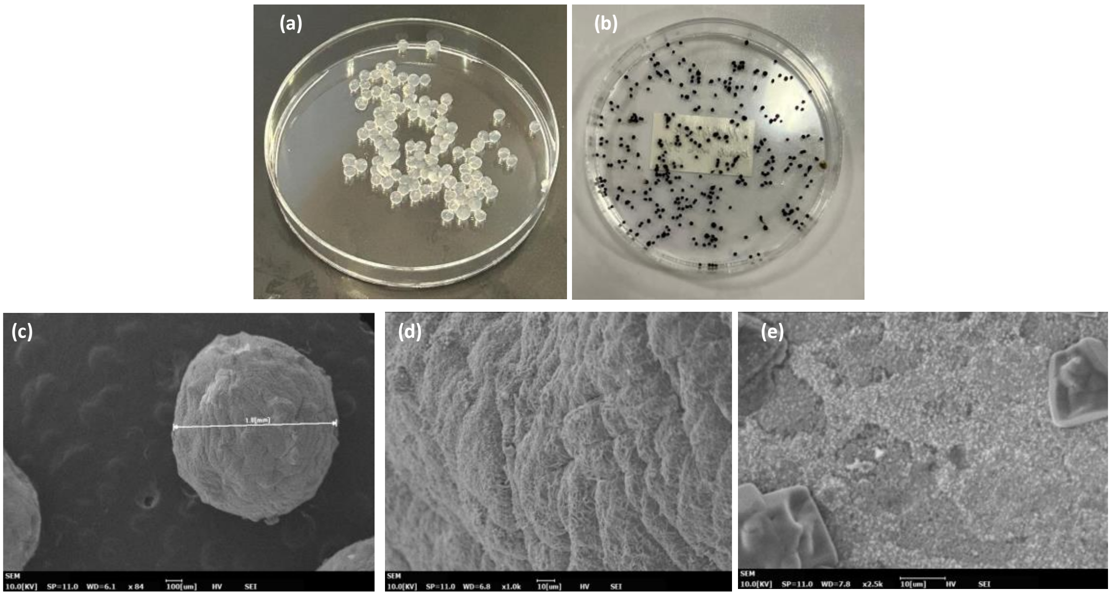

Figure 2. Images of alginate beads; **(a)** wet alginate beads; **(b)** dry alginate-silver nanocomposite beads; **(c)** SEM image of nanocomposite bead; **(d)** high magnification SEM image of nanocomposite bead; **(e)** SEM image of nanocomposite film.

The dissociation causes chelation of Ca^{2+} by PO_4^{-} and HPO_4^{2-} ligands, releasing the alginate and silver nanoparticles in solution. The resulting viscous solution was analyzed by UV-Vis absorption spectroscopy. A strong SPR peak around 420 nm confirmed the presence of silver nanoparticles in the alginate-nanocomposite beads. The nanocomposite film does not show any significant morphology, and the silver nanoparticles were evenly distributed on the surface of the film, as observed in **Figure 2e**.

3.3. Catalytic degradation of 2-nitrophenol (2-NP)

Effluents from the dye and pesticide industries contain 2-NP, which is an environmental hazard and is known to cause methemoglobinemia. The reduced product of 2-NP is 2-amino phenol (2-AP), which is a non-toxic product. The catalytic activity of the alginate-silver nanocomposite beads in the degradation of 2-NP in the presence of $NaBH_4$ was studied using UV-Vis absorption spectroscopy. The time-dependent change in absorbance during the degradation of 2-NP is shown in **Figure 3a**. The absorption peak at 351 nm corresponds to 2-NP, and this shifts to 416 nm due to the formation of a 2-nitrophenolate ion (due to deprotonation of the −OH group) upon the addition of $NaBH_4$ as observed in **Figure 3a**. The reduction in the absorption of the 2-nitrophenolaote ion corresponds to the formation of 2-AP; however, this reaction has a large kinetic barrier due to the large potential difference between the reducing agent ($NaBH_4$) and 2-NP [22]. As a result, a catalyst is required to overcome the large energy barrier associated with this reduction process at room temperature.

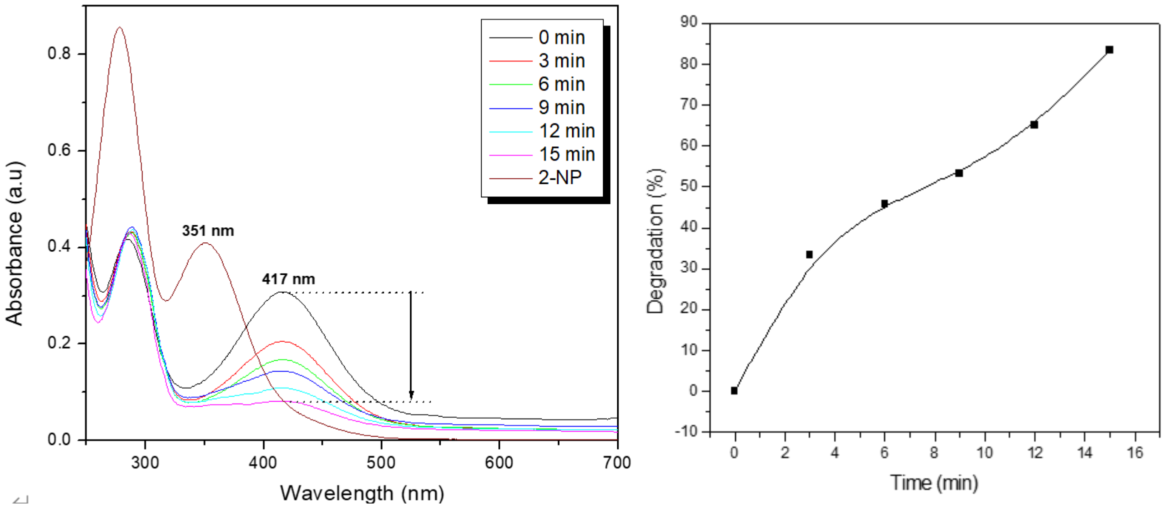

(a) **(b)**

Figure 3. Degradation of 2-NP in the presence of alginate-silver nanocomposite beads in the presence of $NaBH_4$; **(a)** UV-Vis absorption spectra showing the degradation; **(b)** plot of percent degradation as function of reaction time.

Upon addition of the nanocomposite beads (10 beads) into the solution, the initial absorption (0.30) at 416 nm decreased significantly, reaching 0.05 in 15 min. This decrease corresponds to about 83% of the of the degradation of 2-NP. At the same time, the intensity of the absorption peak at 300 nm increased, which indicates the formation of 2-AP and the reaction being accelerated by the silver nanoparticles present in the nanocomposite. The degradation kinetics are shown in **Figure 3b**, and a degradation of 83% is observed in just 15 min of the reaction.

The rate of reaction could be shortened by improving the surface morphology of the nanocomposite beads by making them more porous, which would allow higher diffusion of the 2-nitrophenolate ion into the beads for a faster reaction with the active proton species, or by increasing the number of beads. In the absence of the nanocomposite beads, the degradation reaction was extremely slow (more than 3 days), confirming the major catalytic role of the silver nanoparticles. The degradation reaction mechanism [21–23] in the presence of the nanocomposite takes place in four steps, such as: (i) adsorption of 2-NP onto the nanocomposite bead; (ii) diffusion of 2-NP to the active site; (iii) reaction of 2-NP to form the adsorbed product; and (iv) desorption of the product from the nanocomposite. A schematic representing the degradation of 2-NP in the presence of the strong reducing agent, $NaBH_4$, is shown in **Figure 4**, according to literature reports [22,23].

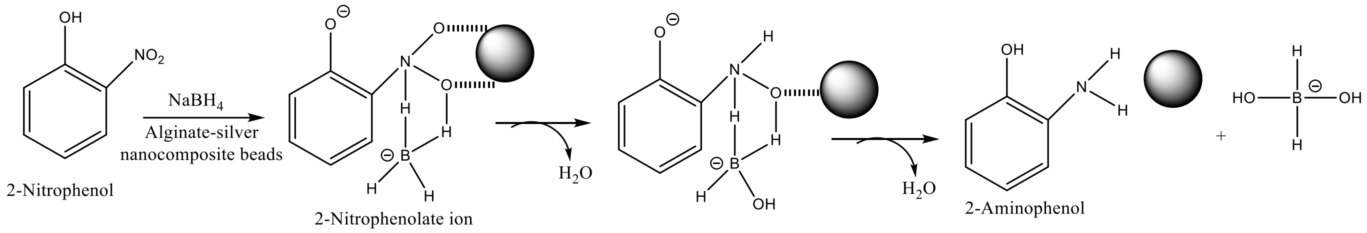

Figure 4. Mechanism of degradation of 2-NP in the presence of alginate-silver nanocomposite beads and $NaBH_4$.

The rate constant (k) of the degradation was determined from the linear plot of $\ln(A_t/A_0)$ versus reaction time (t) in min (**Figure 5**) according to the following linear equation,

$$\ln\frac{C_t}{C_0} = \ln\frac{A_t}{A_0} = -kt \tag{2}$$

where C_t and C_0 are the concentration of 2-NP, and A_t and A_0 are the absorbances at time t, and $t = 0$, respectively, k (min^{-1}) is the rate constant of the reaction.

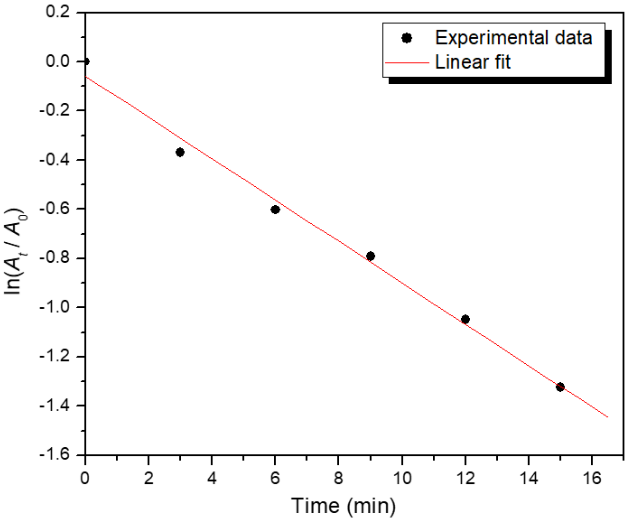

Figure 5. Plot of $\ln(A_t/A_0)$ versus time for the reduction of 2-NP in the presence of $NaBH_4$ at 23 °C.

The degradation reaction follows a pseudo-first order reaction kinetics with respect to the alginate-silver nanocomposite beads because the concentration of $NaBH_4$ (10 mm) was much higher than that of 2-NP (1 mm). The rate constant for the degradation reaction was determined to be 1.40×10^{-3} s^{-1}. The reaction kinetics and the rate constant obtained agree with reported values for catalytic reduction of nitrophenol compounds by green synthesized silver and gold nanoparticles and polymer nanocomposites [21,23–25].

3.4. Catalytic performance of alginate-silver nanocomposite beads

The activation energy (E_a) for the degradation process was determined from the gradient of a plot of ln(k) versus 1/T according to Arrhenius equation as [26],

$$\ln(k) = \left(\frac{E_a}{R}\right)\frac{1}{T} + \ln(A)$$

where A = frequency factor or Arrhenius constant, R = 8.314 J K^{-1} mol^{-1}, T = absolute temperature in Kelvin, and k = rate constant.

From a linear plot of ln(k) versus 1/T, the E_a and A were determined from the gradient and intercept as 18.45 kJ mol^{-1} and 5.19 s^{-1}, respectively (**Figure 6**).

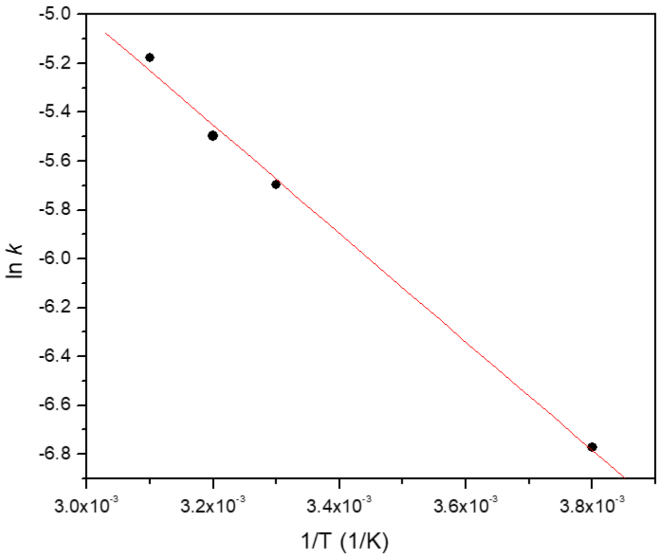

Figure 6. Effect of temperature on the pseudo-first order rate constant and determination of activation energy.

An activation energy of 17 kJ mol^{-1} has been reported for the degradation of 2-NP using calcium alginate beads containing iron-silver bimetallic nanoparticles [5]. Our results agree with this, confirming the excellent catalytic properties of the nanocomposite beads. The results indicate that the catalytic reduction has a low potential barrier and that the catalytic reduction reactions occur via surface catalysis. In comparison to 4-NP (E_a = 10.51 kJ mol^{-1}), the obtained activation energy for 2-NP is higher by a factor of about 1.5, and this increase is attributed to the steric hinderance of 2-NP. The thermodynamic parameters of degradation reaction, such as enthalpy change, (ΔH), and entropy change (ΔS) were determined using the Eyring equation as [5,27],

$$\ln\frac{k}{T} = \ln\frac{k_B}{h} + \frac{\Delta S}{R} - \frac{\Delta H}{R}\left(\frac{1}{T}\right) \tag{3}$$

where k_B is the Boltzmann constant (1.381×10^{-23} JK^{-1}), h is the Planck's constant (6.626×10^{-34} J·s), R is the ideal gas constant, and T is the absolute temperature in Kelvin.

From a linear plot of ln(k/T) versus $1/T$ (**Figure 7**), the enthalpy (ΔH) and entropy (ΔS) changes for the degradation of 2-NP were determined to be 15.22 kJ mol^{-1} and −197.50 J mol^{-1} K^{-1}, respectively. These values agree with reported values of ΔH = 12.77 kJ mol^{-1} and ΔS = −198.42 J mol^{-1} K^{-1} for the degradation of 2-NP using alginate nanocomposite beads containing iron and silver nanoparticles [5]. The negative entropy values indicate that the randomness on the interface between the nanocomposite bead and 2-NP decreases during the degradation process. The kinetic and thermodynamic parameters for the catalytic reduction of 2-NP by the alginate-silver nanocomposite beads are summarized in **Table 1**.

Table 1. Kinetic and thermodynamic parameters for catalytic degradation of 2-NP by the alginate-silver nanocomposite beads.

Temperature (K)	k (s^{-1})	E_a (kJ mol^{-1})	ΔH (kJ mol^{-1})	ΔS (J mol^{-1} K^{-1})
296	1.400×10^{-3}	18.45	12.77	−198.42
303	3.528×10^{-3}			
308	4.101×10^{-3}			
318	5.650×10^{-3}			

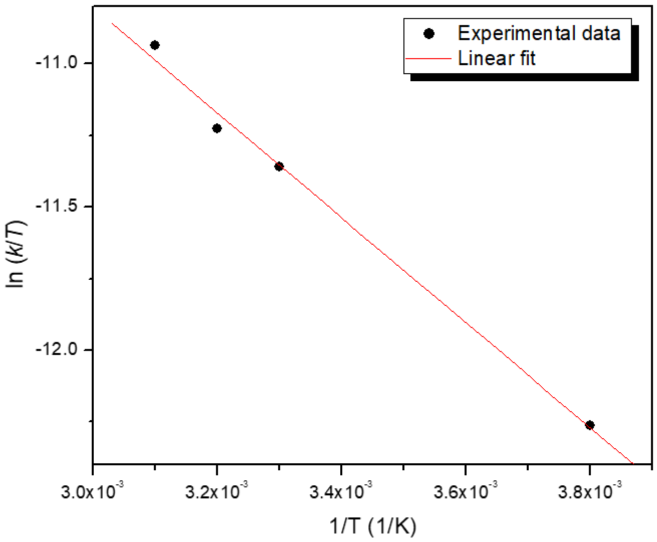

Figure 7. Eyring plot to determine the thermodynamic parameters for the degradation reaction.

The conversion efficiency of the alginate-silver nanocomposite beads was also evaluated for five successive cycles, and the results are shown in **Figure 8**.

After the first cycle of 2-NP degradation, the beads were removed from the solution, washed repeatedly with water, and then placed into a fresh solution containing 2-NP and NaBH$_4$. The conversion efficiency of the nanocomposite beads was constant within the range of 80%–83% up to five successive cycles, which indicates good catalytic efficiency on repeated usage. During this process, no leaching of silver nanoparticles from the beads was observed.

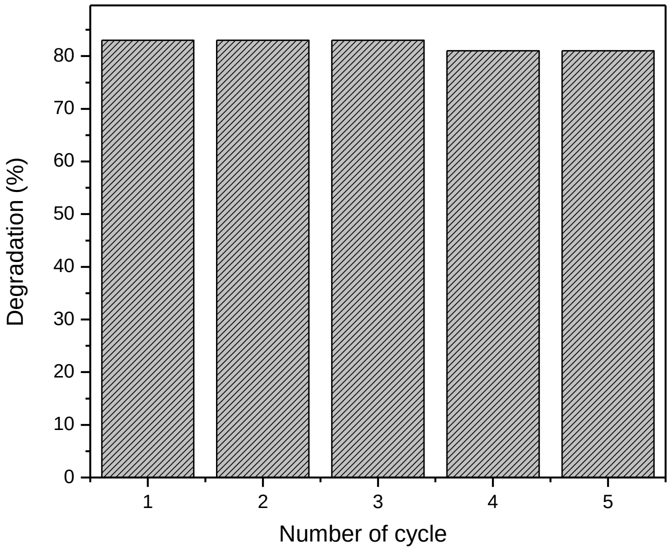

Figure 8. Plot showing the degradation efficiency of the alginate-silver nanocomposite beads for 5 reaction cycles.

3.5. Antibacterial properties

The silver nanoparticles (No. 7), alginate-silver nanocomposite beads (No. 3), and alginate-silver nanocomposite film (No. 2) exhibited weak to good antibacterial properties against *E. coli*, *S. aureus*, and *S. typhimurium*. The bacterial agar plates with the zone of inhibition for a concentration of 10 mm $AgNO_3$ are shown in **Figure 9**. The Ajwa seed extract (No. 5) showed a very weak antibacterial effect against all three types of bacteria, and interestingly, the neat alginate beads (No. 4) showed a comparable effect. The silver nanoparticles (No. 2) were effective against all three types of bacteria, and the antibacterial effect of silver nanoparticles is well known. However, a higher susceptibility was observed for *S. typhimurium*. The alginate-silver nanocomposite beads exhibited a larger zone of inhibition relative to the neat alginate beads, which indicates the synergistic antibacterial effect of the nanocomposites. Similar synergistic effects have been observed for many green-synthesised silver nanocomposites [28].

Figure 9. The antibacterial activity of silver nanoparticles, alginate-silver nanocomposite films and alginate-silver nanocomposite beads on different pathogenic bacteria.

The mechanism of interaction of silver nanoparticles with bacteria is mainly ionic. The silver nanoparticles and silver ions (released from the nanoparticles) can accumulate in the pits of the cell wall, which leads to denaturation of the cell membrane [29]. In addition, the silver nanoparticles could penetrate the cell membrane, leading to denaturation and rupture of organelles, resulting in lysis.

Further, the silver nanoparticles can disrupt bacterial signal transduction, leading to cell apoptosis and the termination of bacterial cell multiplication.

4. Conclusion and future perspectives

Alginate-silver nanocomposites in the form of spherical beads and thin films were successfully fabricated using silver nanoparticles synthesized using the extract of Ajwa date seed. The nanocomposite beads were effective in the catalytic degradation of 2-nitrophenol, and 80% degradation was achieved in 15 min. The beads showed good reusability, with no appreciable decrease in their degradation capacity even after five successive cycles of operation. The degradation followed pseudo-first-order reaction kinetics. The nanocomposite exhibited antibacterial effects against three clinically important pathogens, with a higher susceptibility to *S. typhimurium*. Overall, this study has laid the foundation for a new, effective strategy as an alternative to high-cost commercial catalysis for the detoxification of organic pollutants. The new material developed through the eco-friendly green approach, in addition to its catalytic properties, has the potential to treat hospital wastewater in the future.

Author contributions: Conceptualization, RD; methodology, RD, NA, MA and HR; software, RD; validation, RD and FH; formal analysis, RD, NA and HR; investigation, RD, NA, MA, HR, FA and PK; resources, FA; data curation, RD; writing—original draft preparation, RD; writing—review and editing, RD, NA, MA and HR; supervision, RD and FH; project administration, RD; funding acquisition, RD. All authors have read and agreed to the published version of the manuscript

Conflict of interest: The authors declare no conflict of interest.

Abbreviations

CR	Congo red
NP	2-nitrophenol
SEM	Scanning Electron Microscopy
SPR	Surface Plasmon Resonance
UV-Vis	Ultraviolet-Visible

References

1. Niaz A, Fischer J, Barek B, et al. A novel voltametric method for the determination of maleic acid using silver amalgam paste electrode. Electroanalysis. 2009; 21(15): 1719-1722. doi: 10.1002/elan.200904655
2. Ganapuram BR, Alle M, Dadigala R, et al. Catalytic reduction of methylene blue and Congo red dyes using green synthesized gold nanoparticles capped by Salmalia malabarica gum. International Nano Letters. 2015; 5(4): 215-222. doi: 10.1007/s40089-015-0158-3
3. Gola D, Kriti A, Bhatt N, et al. Silver nanoparticles for enhanced dye degradation. Current Research in Green and Sustainable Chemistry. 2021; 4: 100132. doi: 10.1016/j.crgsc.2021.100132
4. Choudhary MK, Kataria J, Sharma S. Evaluation of the kinetic and catalytic properties of biogenically synthesized silver nanoparticles. Journal of Cleaner Production. 2018; 198: 882-890. doi: 10.1016/j.jclepro.2018.09.015
5. Gupta VK, Yola ML, Eren T, et al. Catalytic activity of Fe@Ag nanoparticle involved calcium alginate beads for the

reduction of nitrophenols. Journal of Molecular Liquids. 2014; 190: 133-138. doi: 10.1016/j.molliq.2013.10.022

6. Augustine R, Kalarikkal N, Thomas S. A facile and rapid method for the black pepper leaf mediated green synthesis of silver nanoparticles and the antimicrobial study. Applied Nanoscience. 2013; 4(7): 809-818. doi: 10.1007/s13204-013-0260-7
7. Kastner C, Thunemann F. Catalytic reduction of 4-nitrophenol using silver nanoparticles with adjustable activity. Langmuir. 2016; 32(29): 7383-7391. doi: 10.1021/acs.langmuir.6b01477
8. Lin S, Huang R, Cheng W, et al. Silver nanoparticle-alginate composite beads for point-of-use drinking water disinfection. Water Research. 2013; 47(12): 3959-3965. doi: 10.1016/j.watres.2012.09.005
9. Mthombeni NH, Mpenyana-Monytasi I, Onyango, MS, et al. Breakthrough analysis for water disinfection using silver nanoparticles coated resin beads in fixed-bed column. Journal of Hazardous Materials. 2012; 217-218: 133-140. doi: 10.1016/j.jhazmat.2012.03.004
10. Lv Y, Lou H, Wang Z, et al. Silver nanoparticle-decorated porous ceramic composite for water treatment. Journal of Membrane Science. 2009; 331(1-2): 50-56. doi: 10.1016/j.memsci.2009.01.007
11. Saha S, Pal A, Kundu S, et al. Photochemical green synthesis of calcium-alginate-stabilised Ag and Au nanoparticles and their catalytic application to 4-nitrophenol reduction. Langmuir. 2009; 26(4): 2885-2893. doi: 10.1021/la902950x
12. Martinez-Gómez F, Guerrero J, Matsuhiro B, et al. In vitro release of metformin hydrochloride from sodium alginate/polyvinyl alcohol hydrogels. Carbohydrate Polymers. 2017; 155: 182-191. doi: 10.1016/j.carbpol.2016.08.079
13. Albalwi H, El Fadl FIA, Ibrahim MM, et al. Catalytic activity of silver nanocomposite beads for degradation of basic dye: kinetic and isothermal study. Applied Organometallic Chemistry. 2021; 36(1). doi: 10.1002/aoc.6490
14. Fagieh TM, Bakhsh EM, Khan SB, et al. Alginate/banana waste beads supported metal nanoparticles for efficient water remediation. Polymers. 2021; 13(23): 4054-4071. doi: 10.3390/polym13234054
15. Wang Y, Lu Y. Sodium alginate-based functional materials towards sustainability applications: Water treatment and energy storage. Industrial Engineering and Chemistry Research. 2023; 62: 11279-11304. doi: 10.1021/acs.iecr.3c01082
16. Alomar A, Qassim T, AlNajjar Y, et al. Green nanotechnology and phytosynthesis of metallic nanoparticles: The green approach, mechanism, biomedical applications and challenges. World Scientific Annual Review of Functional Materials. 2024; 1: 2430001-2430023.
17. Deen GR, Alhannan F, Henari F, et al. Effects of different parts of the okra plant (Abelmoschus esculentus) on the phytosynthesis of silver nanoparticles: Evaluation of synthesis conditions, nonlinear optical and antibacterial properties. Nanomaterials. 2022; 12(23): 4174-4185. doi: 10.3390/nano12234174
18. Mostafa H, Airouyuwa JO, Maqsood S. A novel strategy for producing nanoparticles from date seeds and enhancing their phenolic content and antioxidant properties using ultrasound-assisted extraction: A multivariate based optimization study. Ultrasonics Sonochemistry. 2022; 87: 106017. doi: 10.1016/j.ultsonch.2022.106017
19. Khalid S, Khalid N, Khan RS, et al. A review on chemistry and pharmacology of Ajwa dates fruit and pit. Trends in Food Science & Technology. 2017; 63: 60-69. doi: 10.1016/j.tifs.2017.02.009
20. Eid N, Osmanova H, Natchez C, et al. Impact of palm date consumption on microbiota growth and large intestinal health: A randomized, controlled, cross-over human intervention study. British Journal of Nutrition. 2015; 114(8): 1226-1236. doi: 10.1017/s0007114515002780
21. Cao PL, Lu W, Mata A, et al. Egg-box model-based gelation of alginate and pectin: A review. Carbohydrate Polymers. 2020; 242: 116389. doi: 10.1016/j.carbpol.2020.116389
22. Gangula A, Podila R, Karanam L, et al. Catalytic reduction of 4-nitrophenol using biogenic gold and silver nanoparticles derived from Breynia rhamnoides. Langmuir. 2011; 27(24): 15268-15274. doi: 10.1021/la2034559
23. Jiang ZJ, Liu CY, Sun LW. Catalytic properties of silver nanoparticles supported on silica spheres. The Journal of Physical Chemistry B. 2005; 109(5): 1730-1735. doi: 10.1021/jp046032g
24. Kumar I, Gangwar C, Yaseen B, et al. Kinetic and mechanistic studies of the formation of silver nanoparticles by nicotinamide as a reducing agent. ACS Omega. 2022; 7(16): 13778-13788. doi: 10.1021/acsomega.2c00046
25. Khan SB, Ahmad S, Kamal T, et al. Metal nanoparticles decorated sodium alginate-carbon nitride composite beads as effective catalyst for the reduction of organic pollutants. International Journal of Biological Macromolecules. 2020; 164: 1087-1098. doi: 10.1016/j.ijbiomac.2020.07.091
26. Shimoga G, Palem RR, Lee SH, et al. Catalytic degradability of p-nitrophenol using ecofriendly silver nanoparticles. Metals. 2020; 10(12): 1661. doi: 10.3390/met10121661
27. Meija YR, Bogireddy NKR. Reduction of 4-nitrophenol using green-fabricated metal nanoparticles. RSC Advances. 2022;

12(29): 18661-18675. doi: 10.1039/d2ra02663e

28. Farazin A, Mohammadimehr M, Ghasemi AM, et al. Design, preparation and characterization of CS/PVA/SA hydrogels modified with mesoporous Ag_2O/SiO_2 and curcumin nanoparticles for green, biocompatible, and antibacterial biopolymer film. RSC Advances. 2021; 11(52): 32775-32791. doi: 10.1039/d1ra05153a
29. Cittrarasu V, Kaliannan D, Dharman K, et al. Green synthesis of selenium nanoparticles mediated from Ceropegia bulbosa Roxb extract and its cytotoxicity, antimicrobial, mosquitocidal and photocatalytic activities. Scientific Reports. 2021; 11(1): 1032-1046. doi: 10.1038/s41598-020-80327-9

Characterization and Application of Nanomaterials 2024, 7(2), 6401.
https://doi.org/10.24294/can.v7i2.6401

Article

QCA-based design of polar encoder circuit

Sravan Kumar Vittapu, Ravichand Sankuru, Chepuri Rakshana, Beeradhar Mahesh*, Amudha Naga Teja

Department of ECE, Nalla Narasimha Reddy Education Society's Group of Institutions, Chowdariguda, Hyderabad 500088, Telangana, India
*** Corresponding author:** Beeradhar Mahesh, beeradharmahesh@gmail.com

CITATION

Vittapu SK, Sankuru R, Rakshana C, et al. QCA-based design of polar encoder circuit. Characterization and Application of Nanomaterials. 2024; 7(2): 6401.
https://doi.org/10.24294/can.v7i2.6401

ARTICLE INFO

Received: 14 May 2024
Accepted: 8 July 2024
Available online: 26 July 2024

Abstract: In the last few decades, nano-electronic devices have been manufactured using VLSI technology. Over the past four decades, IC technology has been growing by using CMOS technology successfully, but this CMOS technology has a scaling limitation. To overcome this scaling limitation, QCA (quantum dot cellular automata) emerges as an alternative. This work is the implementation of the design of a polar encoder using QCA technology. This design is a single-layered and even bottom-up approach technique. The Polar code is more efficient and has less energy dissipation compared to the turbo code and conventional codes (CC). This design explores (8:4). A Polar encoder is designed to have fewer cells and area compared to the turbo encoder and conventional encoder. The proposed design is implemented using the QCA designer tool.

Keywords: ALU; CMOS; nano technology; polar encoder; QCA; VLSI

1. Introduction

The IC technology is growing faster and is using VLSI technology successfully. However, the scaling limitation of the CMOS technology is the main disadvantage. This leads to a switch to an alternative approach. QCA is a nano technology that has emerged as an alternative to CMOS technology. An encoder is an electronic digital circuit that compares the inputs and outputs. An encoder is used in error correction and communication networks. At the nanoscale level, quantum-dot cellular automata (QCA) is an emerging computing technology beyond the current paradigm. QCA uses charge to encode binary values. Information is processed with the aid of the intercellular coupling mechanism and the QCA cell's configuration or magnetization. In comparison to CMOS devices, QCA might provide high device density, high integration, and high switching speed with extremely low energy dissipation. Up until now, QCA has been used to design and implement a large number of sequential and combinational logic circuits. In addition, a simple processor design strategy and complex arithmetic circuits demonstrate the QCA's efficiency as a viable nano computer. Inherent shift-register capacity in QCA, as opposed to conventional characteristics of logic circuits, results in cyclic 4-phase clocking in QCA devices. Circuits have been investigated in a number of studies. The key design element for storage is "memory-in-motion" and for computation, it is "logic-in-wire", in order to achieve high performance and device density. The issue of "layout = timing" in QCA design is illustrated by using variables like wire length, clock zone width, wasted space, and physical feedback.

These factors are taken into account when designing QCA circuits in an effective and dependable manner. Additionally, a number of design guidelines are put forth by the researchers to accomplish dependable and effective nano-scale digital circuit design in QCA. In QCA, nano communication has drawn interest from a broad spectrum of researchers. Numerous nano communication architectures based on QCA have previously been documented by scholars. However, there are still many different domains in which to construct a QCA-based architecture for nano communication. This study investigates the design.

2. Related work

To build the QCA architectures for nano communication, several works have been proposed [1–28]. To maximize channel utilization, a multiplexer (MUX) and demultiplexer (DEMUX)-based router architecture was created in QCA, as proposed by Tirthji Maharaja Jagadguru [1]. The computational fidelity for channels composed of QCA devices in nanocomputing has been calculated by Van Loan [2]. An array of QCA cells is used as the noisy channel for the estimation. The random flaw in the array has been taken into account during measurement. A nano-router circuit employing DEMUX, PISO converter, and crossbar architecture is suggested by Hashemi and Navi [3] in contrast to the method presented by Das and De [4]. A detailed description is given of how well this nano-router routes information. A 4-bit data processor circuit was implemented in QCA by Sardinha et al. [5]. That data processor can be used for various multifunctional tasks, including sigmoid function creation and information preprocessing. Sayedsalehi et al. [6] presented a strong QCA architecture with serial communication capabilities. This design includes a SIPO converter, a PISO converter, a parity checker, and a hamming code generator. The turbo encoder design process and its implementation in QCA are illustrated by Yao et al. [7]. The use of reversible logic in QCA and its application in the design of nano communication architecture are discussed.

To further achieve security during nano communication, a number of cryptographic and steganographic architectures have been developed by Kamaraj et al. [8], Kianpour et al. [9], and Angizi et al. [10]. An enhanced arithmetic logic unit (ALU) design in QCA has been demonstrated in Zhang et al. [11]. The ALU is made up of a 1-bit full adder, a 2:1 MUX, and a two-input XOR gate. Additionally, it has been explained in Sheikhfaal et al. [12] how those I/O interfaces can be used to solve the issue with conventional tri-state gates. Sayedsalehi et al. [13], an effective. QCA SRAM cell implementation has been investigated. One 3-input MV, one 5-input MV, and a 2:1 MUX are included in this design. Accurate descriptions are also provided for energy efficiency and structural strength. A brand-new programmable QCA circuit is shown in Ahmad et al. [14]. Crossbar architecture is used in the design of the circuit. You can use this proposed circuit to build any type of Boolean logic. The architecture helps create and model area-efficient, stable, and consistent QCA circuits. A synchronous counter with a reliable and effective architecture is described in Kalogeiton et al. [15], Das and De [16,17]. Dflip-flip and edge-to-level converter circuits make up the design. A proposed efficient Fredkin gate with QCA implementation can be found in Das and De [18] and Chandra Das and De [20]. The Fredkin gate is then used to create an authenticator circuit that uses the user's password to identify the authorized user. Compared to previous QCA-Fredkin gates, this one has a lower cell count, latency, and device area. In order to investigate circuit stability, the computational functionality under thermal randomization is also assessed. By Zhang et al. [21], the QCA design of a block cipher employing an electronic code book (ECB) is demonstrated, and QCA technology is used to implement it. A proposed encoder circuit with dual functionality as a decoder circuit is able to construct block ciphers.

Polar code

A polar code is an error-correcting code. Polar code uses recursive cascading, which converts the physical medium into a virtual medium. The main advantage of the polar code is that there is less polarization. A polar code has 4 tuples (i.e., N, R, A, UA). Here, N represents the block length; R represents the code rate; A is the bit position; and UA is the fixed rate.

This polar code has K inputs and N outputs. This design explorer (8:4) In the polar encoder, the code rate is calculated by (K/N). The code rate of this proposed design is (1/2), which is the code rate. A polar code, often known as an error-correcting code, is a kind of linear block code that ranges from 23 to 25. Cascaded recursively over the short kernel code is employed in the creation of the polar code, which transforms the tangible medium into a virtual one by Azimi et al. [22] and Zhang et al. [23]. For a high quantity of repeat. The information bits are allocated to the most dependable virtual medium based on whether the virtual medium has low or high polarization during the simulation process. With polynomial dependence by Premananda et al. [24] on the gap to capacity, it was built to achieve the capacity of symmetric binary-input discrete memory-less channels (B-DMC). In formal terms, a polar code is defined as a 4-tuple (N, R, A, UA), in which N is the block length (i.e., the length of information bit travelled via the communication channel) by Teen et al. [25].

The code is represented by $R \in [0,1]$. A polar code, often known as error-correcting code, is a kind of linear block code that ranges from 23 to 25 by Dehbozorgi et al. [26] and Siddaiah et al. [27]. It cascaded recursively over the short kernel code.

3. Proposed work

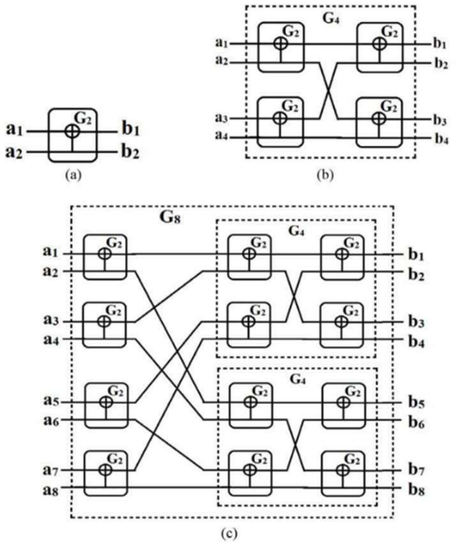

Figure 1. Block diagrams of **(a)** G2; **(b)** G4; **(c);** G8 [9].

The proposed polar encoder has 4 inputs and 8 outputs, which represents the (8:4) polar encoder. This encoder has G8 and 'a' be the input (ai = a1, a2, a3, a4, …, an) and the 'b' the output (bi = b1, b2, b3, b4, …, bn).

Actually, this encoder is given 8 inputs, of which 4 are frozen or fixed with values, and the remaining 4 are for giving inputs. So, here, a1, a2, a3, and a5 are frozen inputs, and a4, a6, a7, and a8 are given inputs, as shown in **Figure 1**.

3.1. Construction of G8

The G8 structure can be denoted by GN. To achieve the construction of G8, firstly, the construction of G2 is made. By using G2, the G4 is made, and lastly, by using G4, the construction of the G8 is made. One way to define it is by using a simple recursive rule. This section deals with the construction of G8. To attain the structure of G8, first the building of G2 has been completed. After that, G4 was constructed using the structure of G2. Lastly, employ G2 and G4, the building blocks of G8.

3.1.1. Design of G2

The outputs of G2 are two (b1, b2) and two inputs (a1, a2). **Figure 2** (where ⊕ indicates the XOR operation and the input-output mapping is displayed) and **Figure 3** demonstrate that the output b2 is equal to the input a2, and the output b1 is the XOR value of the inputs a1 and a2. Therefore, building the structure of G2 just requires a single XOR operation.

b1 = a1 ⊕ a2
b2 = a2

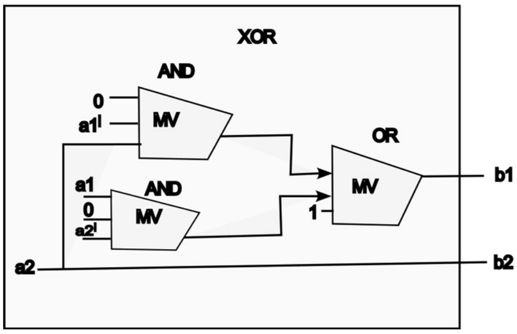

Figure 2. Design of G2.

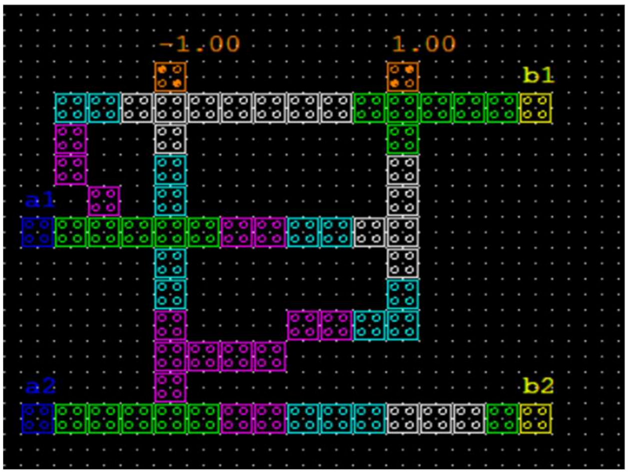

Figure 3. Implementation of G2 design.

3.1.2. Design of G4

The structure of G4 can be easily created by concatenating four copies of G2, as FIG-4 illustrates. It maps inputs (a1, a2, a3, and a4) to outputs (b1, b2, b3, and b4).

$b1 = a1 \oplus a2 \oplus a3 \oplus a4$

$b2 = a3 \oplus a4$

$b3 = a2 \oplus a4$

$b4 = a4$

As said, one XOR operation is needed for the production of G2. As a result, to complete the QCA implementation of G2, corresponding to **Figure 3**, as illustrated in **Figure 4**, one QCA XOR circuit is sufficient. **Figure 5** displays the QCA layout.

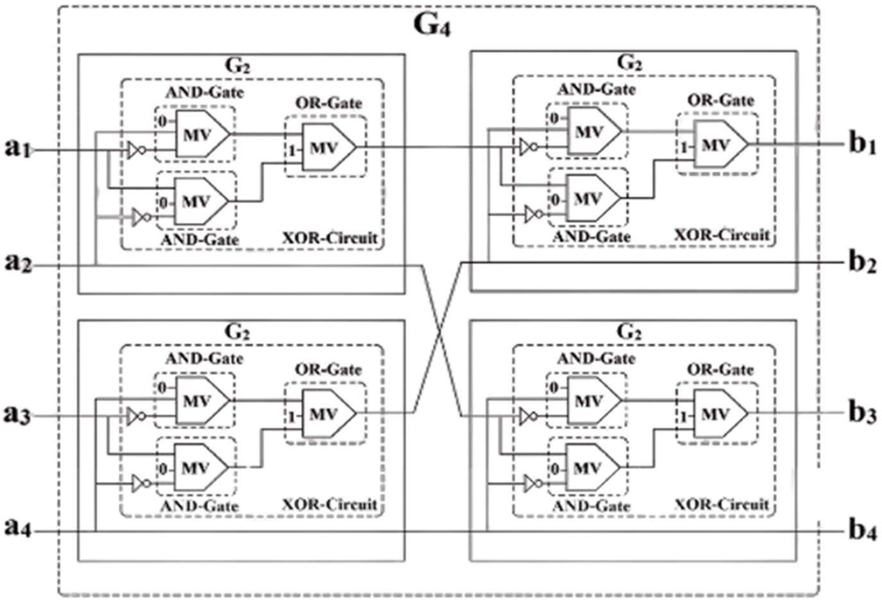

Figure 4. Design of G4 [9].

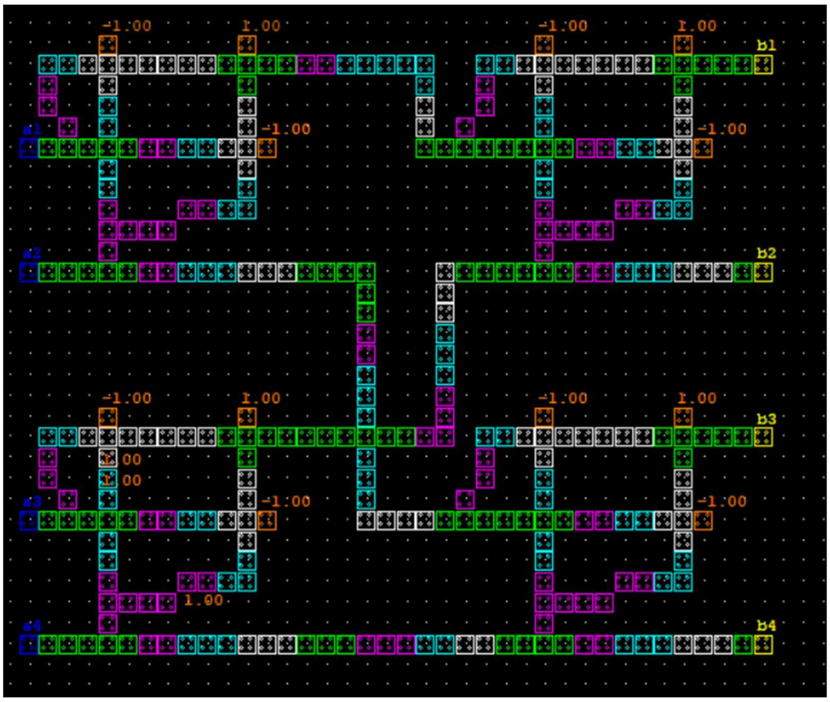

Figure 5. Implementation of G4.

3.1.3. Design of G8

The construction of G8 includes 4 blocks of G2 design and two blocks of G4 design, as shown in **Figure 6**. It has 8 inputs (a1, a2, a3, a4, a5, a6, a7, a8) and 8 outputs (b1, b2, b3, b4, b5, b6, b7, b8). **Figure 7** illustrates the implementation of G8.

$b1 = a1 \oplus a2 \oplus a3 \oplus a4 \oplus a5 \oplus a6 \oplus a7 \oplus a8$

$b2 = a5 \oplus a6 \oplus a7 \oplus a8$

$b3 = a3 \oplus a4 \oplus a7 \oplus a8$

$b4 = a7 \oplus a8$

$b5 = a2 \oplus a4 \oplus a6 \oplus a8$

$b6 = a6 \oplus a8$

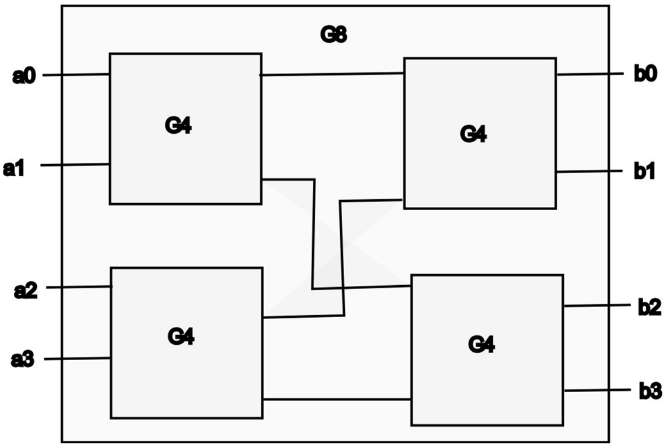

Figure 6. Design of G8.

Figure 7. Implementation of G8.

4. Experimental results

The design of G8 has no fixed cells and has (8:4). The G8 design has fixed polarized input cells, and 36 are fixed polarized QCA cells. Totally, the G8 design consists of 40 fixed polarized cells. The design is simulated using the QCA Designer program. The QCA implementation of G2 is accomplished by using the wire crossing technique suggested by Abedi et al. To implement single-layer wire crossing in QCA, the four-phase clocking approach of QCA Designer, with its benefit of two clock zones, is helpful. It is demonstrated by Angizi et al. [10] that clock zones 0 and 2 can be combined to build a wire cross. The same thing Plotting the simulation result corresponds to **Figure 6**. The legitimate outputs are displayed in a rectangle box. **Figure 6** illustrates that when a1 = 0 and a2 = 0, the resulting values are b1 = 0 and b2 = 0. The results are b1 = 1 and b2 = 1 for a1 = 0 and a2 = 1. In a similar vein, every output appears in accordance with every input. This outcome validates the theoretical values, demonstrating the accuracy of the design. Another interesting finding from **Figure 6** is that the output appears during the second clock cycle, meaning that it is delayed by one clock cycle after the input. In the work of Vangala et al. [28], algorithms for polar encoders were proposed, and in the work of Babar et al. [29], polar encoder types were designed using QCA.

Two G2 copies are needed for the production of G4. As seen in **Figure 4,** the QCA implementation of G4 will thus be done utilizing two QCA circuits in G2. **Figure 8** displays the QCA layout from **Figure 9**. The design is simulated using QCA.

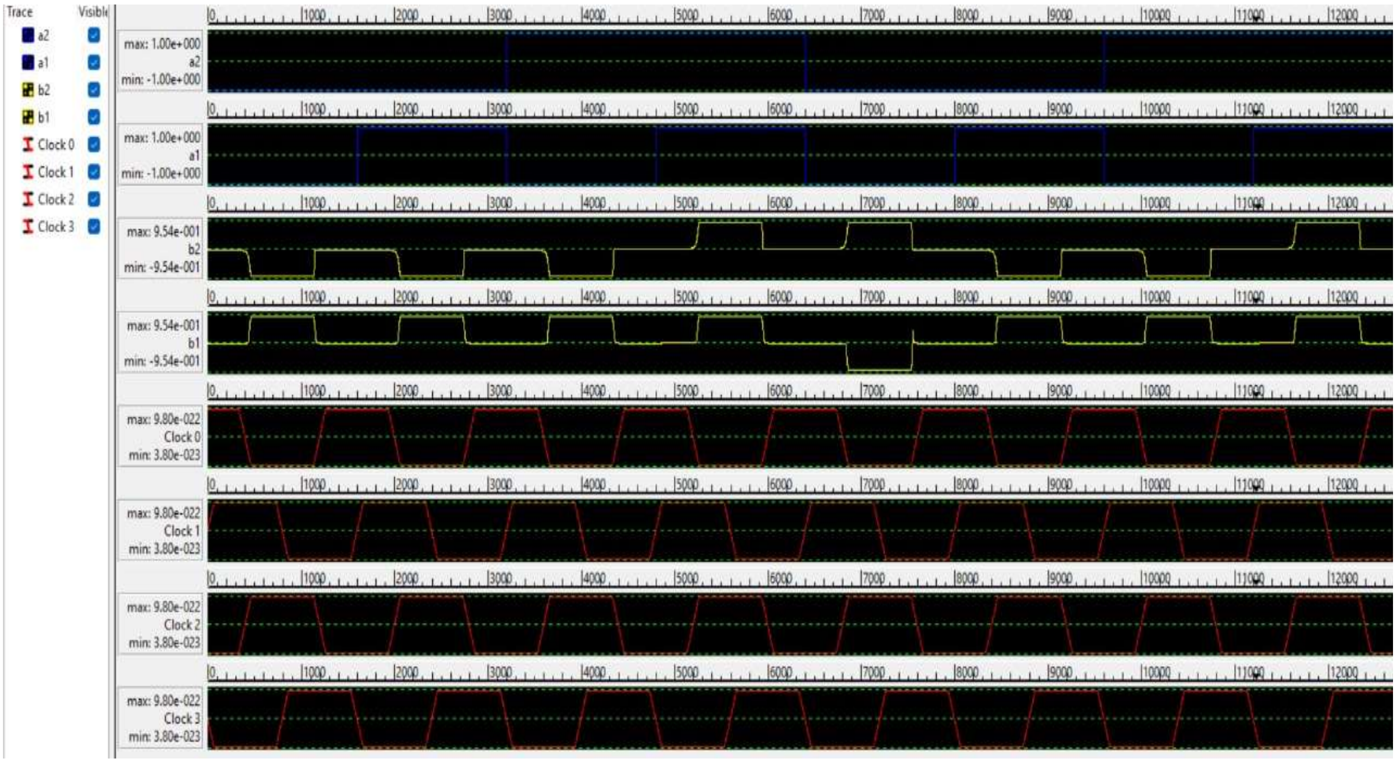

Figure 8. Output waveform of G2.

Figure 9. Output waveform of G4.

Figure 10 displays the simulation results that correlate. The legitimate outputs are displayed in a rectangle box. As can be seen from **Figure 6c**, the output is b1 = 0, b2 = 0, b3 = 0, and b4 = 0 when a1 = 0, a2 = 0, a3 = 0, and a4 = 0. The result is b1 = 1, b2 = 1, b3 = 1, and b4 = 1 when a1 = 0, a2 = 0, a3 = 0, and a4 = 1. In a similar manner, the input combinations determine how each output appears. Therefore, the outcome validates the theory.

Figure 10. Output waveform of G8.

Figure 10 describes the simulation result corresponding to the (8:4) polar encoder as it is displayed in **Figure 7**. The valid results are displayed using the rectangle box. According to **Figure 8b**, the outputs for data bits a4 = 0, a6 = 0, a7 = 0, and a8 = 0 are b1 = 0, b2 = 0, b3 = 0, b4 = 0, b5 = 0, b6 = 0, b7 = 0, and b8 = 0. This is because all of the frozen bits (i.e., a1, a2, a3, and a5) are set to zero. The outputs are b1 = 1, b2 = 1, b3 = 1, b4 = 1, b5 = 1, b6 = 1, b7 = 1, and b8 = 1 for the data bits a4 = 0, a6 = 0, a7 = 0, and a8 = 1. In the same vein, every output appears in accordance with the data bits. As a result, the outcome validates the theoretical values, proving the design's accuracy. **Figure 10** also shows that the output is six clock cycles behind the input; that is, the legitimate output appears at the eleventh clock cycle. The performance comparison of the proposed schematic with the existing one is shown in **Table 1**. From **Table 1**, it is clear that the proposed schematic outperforms the existing [11] in terms of cell count, area, and complexity.

Table 1. Comparison of proposed vs. existing [11].

Parameters	**Existing [11]**	**Proposed**
Cells count	2275	1188
Area (um^2)	5.4320	1.915
Complexity	More	Less

5. Conclusion

In this work, the (8:4) polar encoder circuit is designed for nano scale communication and implemented using the QCA platform. Here, the bottom-up approach is used to reduce the complexity, and it is performed by a single layer, which reduces the complexity even during the physical device fabrication. The code proposed has a lower cell count and less area compared to other encoders that use turbo and cc codes [11]. The top-down method has been taken into consideration to simplify the design. The implementation is done in a single layer, which helps lower complexity while fabricating devices. The communication procedure with the Polar encoder is depicted in the communication architecture. It is helpful to give fault-free design with the stuck-at-fault effect analysis. The suggested test vectors are robust enough to enable 100% fault coverage. The simulation result validates the encoder circuit's design accuracy. Device area and circuit latency demonstrate the quicker speed at which the Polar Encoder circuit may work at the nanoscale. The low dissipated energy of the proposed Polar encoder circuit is verified through energy dissipation estimation.

Author contributions: Conceptualization, SKV and CR; methodology, CR, BM and ANT; software, CR; validation, SKV and RS; formal analysis, CR; investigation, SKV, RS; resources, CR; data curation, CR; writing—original draft preparation, SKV and CR; writing—review and editing, SKV and CR; visualization, CR, BM and ANT; supervision, SKV; project administration, CR, BM and ANT. All authors have read and agreed to the published version of the manuscript.

Conflict of interest: The authors declare no conflict of interest.

References

1. Tirthji Maharaja Jagadguru SSBK. Vedic Mathematics. Motilal Banarsidas; 1986.
2. Van Loan CF. The ubiquitous Kronecker product. Journal of computational and applied mathematics. 2000; 123(1-2): 85-100. doi: 10.1016/S0377-0427(00)00393-9
3. Hashemi S, Navi K. New robust QCA D flip flop and memory structures. Microelectronics Journal. 2012; 43(12): 929-940. doi: 10.1016/j.mejo.2012.10.007
4. Das S, De D. Nanocommunication using QCA: A data path selector cum router for efficient channel utilization. In: Proceedings of the 2012 International Conference on Radar, Communication and Computing (ICRCC); 21-22 December 2012; Tiruvannamalai, India. pp. 43-47. doi: 10.1109/icrcc.2012.6450545
5. Sardinha LHB, Costa AMM, Neto OPV, et al. NanoRouter: A Quantum-dot Cellular Automata Design. IEEE Journal on Selected Areas in Communications. 2013; 31(12): 825-834. doi: 10.1109/jsac.2013.sup2.12130015
6. Sayedsalehi, Samira, Moaiyeri MH, and Navi K. Design of efficient and testable n-input logic gates in quantum-dot cellular automata. Journal of Computational and Theoretical Nanoscience. 2013; 10(10): 2347-2353.
7. Yao F, Zein-Sabatto MS, Shao G, et al. Nanosensor Data Processor in Quantum-Dot Cellular Automata. Journal of Nanotechnology. 2014; 2014: 1-14. doi: 10.1155/2014/259869
8. Kamaraj A, Abinaya, Ramya S. Design of router using Reversible Logic in Quantum Cellular Automata. In: Proceedings of the 2014 International Conference on Communication and Network Technologies; 18-19 December 2014; Sivakasi, India. pp. 249-253. doi: 10.1109/cnt.2014.7062764
9. Kianpour M, Sabbaghi-Nadooshan R, Navi K. A novel design of 8-bit adder/subtractor by quantum-dot cellular automata. Journal of Computer and System Sciences. 2014; 80(7): 1404-1414. doi: 10.1016/j.jcss.2014.04.012
10. Angizi S, Moaiyeri MH, Farrokhi S, et al. Designing quantum-dot cellular automata counters with energy consumption analysis. Microprocessors and Microsystems. 2015; 39(7): 512-520. doi: 10.1016/j.micpro.2015.07.011
11. Zhang M, Cai L, Yang X, et al. Design and Simulation of Turbo Encoder in Quantum-Dot Cellular Automata. IEEE Transactions on Nanotechnology. 2015; 14(5): 820-828. doi: 10.1109/tnano.2015.2449663
12. Sheikhfaal S, Angizi S, Sarmadi S, et al. Designing efficient QCA logical circuits with power dissipation analysis. Microelectronics Journal. 2015; 46(6): 462-471. doi: 10.1016/j.mejo.2015.03.016
13. Sayedsalehi S, Rahimi Azghadi M, Angizi S, et al. Restoring and non-restoring array divider designs in Quantum-dot Cellular Automata. Information Sciences. 2015; 311: 86-101. doi: 10.1016/j.ins.2015.03.030
14. Ahmad F, Bhat GM, Khademolhosseini H, et al. Towards single layer quantum-dot cellular automata adders based on explicit interaction of cells. Journal of Computational Science. 2016; 16: 8-15. doi: 10.1016/j.jocs.2016.02.005
15. Kalogeiton VS, Papadopoulos DP, Liolis O, et al. Programmable Crossbar Quantum-Dot Cellular Automata Circuits. IEEE Transactions on Computer-Aided Design of Integrated Circuits and Systems. 2017; 36(8): 1367-1380. doi: 10.1109/tcad.2016.2618869
16. Das JC, De D. User Authentication Based on Quantum-Dot Cellular Automata Using Reversible Logic for Secure Nanocommunication. Arabian Journal for Science and Engineering. 2015; 41(3): 773-784. doi: 10.1007/s13369-015-1870-z
17. Das JC, De D. Circuit switching with Quantum-Dot Cellular Automata. Nano Communication Networks. 2017; 14: 16-28. doi: 10.1016/j.nancom.2017.09.002
18. Das JC, De D. Nanocommunication network design using QCA reversible crossbar switch. Nano Communication Networks. 2017; 13: 20-33. doi: 10.1016/j.nancom.2017.06.003
19. Abutaleb MM. Robust and efficient quantum-dot cellular automata synchronous counters. Microelectronics Journal. 2017; 61: 6-14. doi: 10.1016/j.mejo.2016.12.013
20. Chandra Das J, De D. QCA based secure nanocommunication block cipher design based on electronic code book. Malaysian Journal of Computer Science. 2018; 31(2): 130-142. doi: 10.22452/mjcs.vol31no2.3
21. Zhang Y, Xie G, Cheng X, et al. The Implementation of I/O Interface in Quantum-dot Cellular Automata. Optik. 2018; 166: 177-188. doi: 10.1016/j.ijleo.2018.04.020
22. Azimi S, Angizi S, Moaiyeri MH. Efficient and Robust SRAM Cell Design Based on Quantum-Dot Cellular Automata. ECS Journal of Solid State Science and Technology. 2018; 7(3): Q38-Q45. doi: 10.1149/2.0281803jss
23. Zhang Y, Xie G, Han J. Serial concatenated convolutional code encoder in quantum-dot cellular automata. Nano Communication Networks. 2019; 22: 100268. doi: 10.1016/j.nancom.2019.100268

24. Premananda BSC, Skanda, Srivatsa B. Area and energy efficient QCA based decoder. In: Proceedings of the 2021 6th International Conference on Communication and Electronics Systems (ICCES); 8-10 July 2021; Coimbatre, India. pp. 7-12. doi: 10.1109/ICCES51350.2021.9489011
25. Teen YPA, Subha M, Shabeer SH, et al. Programmable multiplier circuit designed for quantum-dot cellular automata devices. Materials Today: Proceedings. 2021; 37: 1295-1300. doi: 10.1016/j.matpr.2020.06.464
26. Dehbozorgi L, Sabbaghi-Nadooshan R, Kashaninia A. Realization of processing-in-memory using binary and ternary quantum-dot cellular automata. The Journal of Supercomputing. 2021; 78(5): 6846-6874. doi: 10.1007/s11227-021-04152-1
27. Siddaiah, Premananda B, Megha P, Nagavika K. Compact and Energy Efficient QCA Based Hamming Encoder for Error Detection and Correction. Advances in Electrical and Electronic Engineering. 2023; 21(2): 120-126.
28. Vangala H, Hong Y, Viterbo E. Efficient Algorithms for Systematic Polar Encoding. IEEE Communications Letters. 2016; 20(1): 17-20. doi: 10.1109/lcomm.2015.2497220
29. Babar Z, Kaykac Egilmez ZB, Xiang L, et al. Polar Codes and Their Quantum-Domain Counterparts. IEEE Communications Surveys & Tutorials. 2020; 22(1): 123-155. doi: 10.1109/comst.2019.2937923

EnPress Publisher

Characterization and Application of Nanomaterials 2024, 7(2), 4768.
https://doi.org/10.24294/can.v7i2.4768

Article

Non-enzymatic detection of 17β-estradiol in real samples using PANI@CeO_2 nanocomposite

Aditya Dam, Tanu Rajput, Sakshi Verma, Devendra Kumar*

Department of Applied Chemistry, Delhi Technological University, Delhi 110042, India
*** Corresponding author:** Devendra Kumar, dkumar@dce.ac.in

CITATION

Dam A, Rajput T, Verma S, Kumar D. Non-enzymatic detection of 17β-estradiol in real samples using PANI@CeO_2 nanocomposite. Characterization and Application of Nanomaterials. 2024; 7(2): 4768. https://doi.org/10.24294/can.v7i2.4768

ARTICLE INFO

Received: 20 February 2024
Accepted: 22 July 2024
Available online: 19 August 2024

Abstract: Herein, we developed a non-enzymatic biosensing platform using polyaniline (PANI) polymer matrix grafted with CeO_2. The one-pot synthesized nanocomposite has been used for the detection of 17β-estradiol (E2). The homogeneous distribution of CeO_2 onto the PANI matrix leads to an increase in surface area, conductivity, and effectiveness of the synthesized nanocomposite PANI@CeO_2. The PANI@CeO_2 nanocomposite was characterized using structural and morphological techniques. Further, the electrode fabrication was performed electrophoretically by depositing the PANI@CeO_2 nanocomposite onto the ITO electrode. The PANI@CeO_2/ITO showed enhanced electrochemical behavior as compared to PANI/ITO. Detection of E2 was carried out using the differential pulse voltametric technique (DPV). Linearity has been observed through the detection range of 1 μM–100 μM with LOD = 2.15 μM. The developed biosensor has been found to be stable and selective towards E2. It has been successfully utilized for the detection of E2 in real samples like tap water and human urine samples. Thus, this research encourages its use for more applications in clinical diagnosis and biomedical sciences.

Keywords: polyaniline; 17β-estradiol; biosensor; tap water; urine; CeO_2

1. Introduction

The excessive use of steroid growth hormones has resulted in the widespread presence of 17β-estradiol (E2) in food commodities such as meat and dairy products. These hormones are excreted by animals into the environment, serving as prevalent forms of environmental endocrine disruptors [1]. At low concentrations, the abuse of steroid growth hormones can mimic the effects of female sex hormones in the human body and disrupt hormone actions through different mechanisms. This interference with the endocrine system can lead to adverse effects such as infertility, diabetes, birth defects, PCOD, and reproductive dysfunctions in humans. Exceeding a certain threshold concentration, exogenous E2 can disturb the balance within the human body. It has been reported that elevated levels of E2 lead to an increased incidence of prostate cancer in men and breast cancer in women [2,3].

During the last decade, many analytical methods have been reported for the determination of E2, such as HPLC, LC-MS, GC-MS, etc. These methodologies use expensive instruments, require intricate operation, extended assay time, and personnel with specialized training. Some alternative methods that have been introduced for detecting E2 are surface plasmon resonance biosensors, surface molecular imprinting techniques, colorimetric methods, and enzyme-linked immunosorbent assays. Despite the appreciable sensitivity of these newly developed methods for detecting E2, most of them still require expensive instruments, similar to chromatography techniques. As a result, they are not suitable for on-site detections due to cost and instrument dependency limitations [4–6]. Also, the detection of hormones based on enzyme immobilization mobility is gaining popularity due to its high selectivity, easy fabrication, and rapid response. Despite this popularity, this technique comes with various limitations, like high cost, low sensitivity, and leaking of enzyme from the transducer surface. Therefore, there is a strong demand for reliable, rapid, and user-friendly biosensors that can effectively detect low concentrations of E2 in samples [7,8].

Conducting polymers (CP) due to their electrochemical activity, mechanical elasticity, biocompatibility, electrical conductivity, and environmental stability are the most liable to be used as sensing elements in analytical and bioanalytical systems. Electrochemical biosensors based on enzymatic and non-enzymatic methods have gained tremendous attention throughout the world. However, enzymatic methods are known to have some drawbacks, such as thermal and storage stability, environmental selectivity, etc. [9,10]. Hence, scientists have been more focused on the development of non-enzymatic biosensors in the last decade because of their high selectivity and lower cost than enzymatic ones. The most common among them is the MIP-based sensors, which do not require any biologically recognized element. The principle for these nonenzymatic biosensors for the detection of E2 is based on the direct oxidation of the hydroxyl group. The sensing properties of CP's can be modified by alternating their surface and morphology, such as by developing a metal-based structure grafted with conducting polymer. N-type inorganic semiconductors such as CeO_2, ZnO, TiO_2, and WO_3 can be used efficiently with conducting polymers as a sensing material [11,12].

Polyaniline (PANI) displays exceptional advantages, including easy synthesis, superior electrical conductivity, and reversible redox behavior. Despite the numerous positive characteristics of the polymer, PANI-based chemical sensors can face limitations in terms of sensitivity, linearity, selectivity, or stability. One way to overcome these limitations is by incorporating a secondary material into the PANI, resulting in the formation of a polymeric composite. The integration of PANI with a secondary nanocomponent, such as metallic nanoparticles, metal oxide nanoparticles, carbon compounds, or polymers, leads to enhanced functionality and improved performance, providing an effective design approach [13,14]. The synergistic interactions between the constituents in nanocomposites of PANI and metal oxides such as CeO_2 result in improved properties, making them highly valuable for applications such as sensors and biosensors, photovoltaics, and batteries. Nanocomposites of PANI with CeO_2 have been extensively explored for sensing applications. The enhanced sensor response of these composites can be attributed to the formation of electron-conducting pathways within the material, leading to improved device efficiency. The inclusion of semiconductor metal oxide CeO_2 into polymer matrices PANI has been shown to improve the mechanical, thermal, dielectric, and optical properties of polymers, enabling high carrier mobilities [15]. This research work reveals the biosensory fabrication of electrodes using synthesized PANI@CeO_2 nanocomposite, which acts as an effective sensing platform for E2 detection (**Figure 1**). The performance of PANI@CeO_2 composite as a sensing platform has been analysed in real samples, i.e., human urine and tap water.

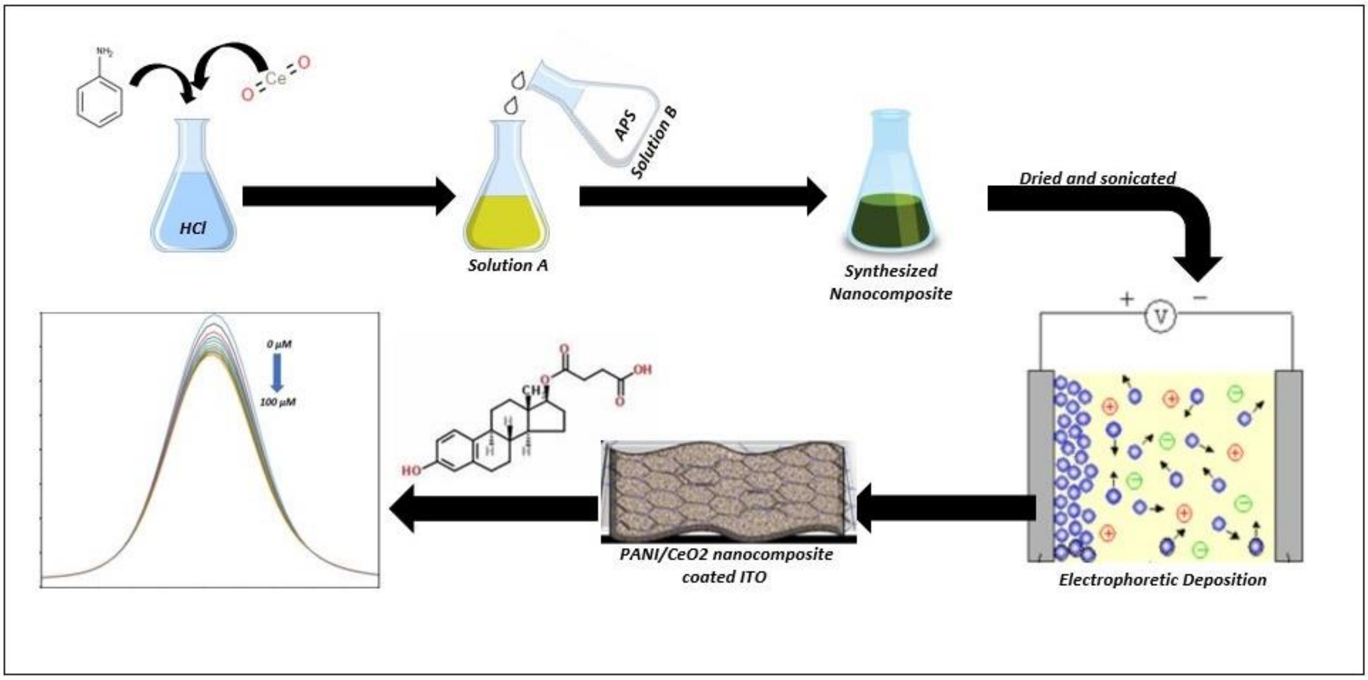

Figure 1. Schematic diagram of the synthesis of PANI@CeO_2 and its deposition on ITO.

2. Materials and methods

2.1. Materials required

For synthesizing the PANI, CeO_2, and PANI@CeO_2 nanocomposite, we used aniline and ammonium persulfate, bought from Central Drug House (Pvt), [$Ce(NO_3)_3 \cdot 6H_2O$], 99% trace metal basis, procured from Sigma Aldrich (France), hydrochloric acid (HCl, 25%), and liquor ammonia (25% ammonia) procured from Thermofisher Scientific, India. Other chemicals, i.e., di-sodium hydrogen orthophosphate dihydrate, potassium ferrocyanide, sodium dihydrogen orthophosphate, and potassium ferricyanide, were purchased from Qualigens Fine Chemicals for preparing PBS and Ferro-Ferri solution (pH = 7.4). The cleaning was done using 100% acetone and 99.9% ethanol, which were purchased from central drug house (Pvt).

2.2. Synthesis of polyaniline

For the synthesis of PANI, we took 1 mL aniline and mixed it with 15 mL HCl (1 M) to get solution-A. Then solution B was prepared by dissolving ammonium persulfate in 15 mL HCl (1 M). The molar ratio of aniline with respect to ammonium persulfate was taken to be 1:1.15, respectively. In an ice bath maintaining 0–5 ℃, solution-b was added dropwise into solution-a, followed by 3 h of stirring under the same condition. At last, the resultant solution was kept overnight in the refrigerator and rinsed with acetone and distilled water the next day to remove impurities. The obtained product was then left to dry in an oven at 60 ℃ to get dark green-colored PANI [16].

2.3. Synthesis of CeO_2

For the preparation of CeO_2 nanoparticles, 1.5 m mol of Cerium (III) nitrate hexahydrate was dissolved in distilled water (50 mL) with the addition of 1.5 mL of liquid ammonia. The resulting solution was stirred for around 30 min using a magnetic stirrer. Following this, the solution mixture was shifted to an autoclave (120 mL) (Teflon-lined stainless steel) and left at 180 ℃ in an oven for 24 h. The obtained stagnant was then cooled at room temperature, rinsed with both distilled water and ethanol repeatedly for the excretion of excessive ammonium hydroxide, and left at 60 ℃ for 24 h to get the dry, desired pale-yellow, white-colored product.

2.4. Synthesis of PANI@CeO_2 nanocomposite

For synthesis of PANI@CeO_2 nanocomposite, 40% (w/w) of synthesized CeO_2 was mixed with 1 mL of aniline in 15 mL of HCl (1 M) to get solution-a, followed by the same procedure as mentioned in Synthesis of PANI.

2.5. Electrophoretic deposition (EPD) on electrode

A GX300C (Genetix) electrophoretic unit was used to carry out the process of electrophoretic deposition, where platinum was used as the counter electrode. We deposited all three synthesized compounds on an ITO (indium tin oxide) coated glass electrode. For that, we mixed 1 mg of each compound with 10 mL of distilled water separately and ultrasonicated them for 3–4 h. The EPD process was conducted at a constant voltage of 10 V provided via a DC power supply for stable and efficient deposition and optimized at 7 s for PANI and cerium (IV) oxide suspension, and for PANI@CeO_2 nanocomposite suspension, it was optimized at 15 s. After EPD, the electrodes were removed from the suspension and stored in a refrigerator for further use.

2.6. Characterization

For the study of X-ray diffraction of the synthesized materials, Cu Kα radiations with a wavelength of λ = 1.5406 Å based on a Bruker D-8 Advance X-ray diffractometer (XRD) have been used. For the study of the presence of functional groups and saturation in materials, the Perkin Elmer Fourier transform infrared (FTIR) spectrum (model spectrum 2) has been used. We used a Zeta potential analyzer (Malvern Instruments Ltd.) for analysing the charge of the materials. TGA 4000, PerkinElmer, was used in the range of 0–600 ℃ in an atmosphere of nitrogen with a constant heating rate of 10 ℃/min for studying the degradation of materials with temperature. Similarly, DSC 8000, Perkin Elmer, was used for differential scanning calorimetry for the analysis of thermal characteristics. For electrochemical studies, we used autolab potentiostat/galvanostat (Eco-Chemie, the Netherlands), which is a three-electrode cell having ITO, platinum, and Ag/AgCl as a working, inert, and auxiliary electrode in phosphate buffered saline (PBS; pH 7.4; 100 mM) mixed with ferrocyanide and ferricyanide $[Fe(CN)_6]^{3-/4-}$ of 5 mM concentration each.

3. Results and discussion

3.1. X-ray diffraction study

The powder XRD pattern of CeO_2 and PANI@CeO_2 nanocomposite and PANI has been shown in **Figure 2A** and **Figure S1**. It has been observed that CeO_2 shows clearly distinct XRD peaks at 2θ = 28.5°, 33.1°, 47.7°, 57.1°, 59.3°, 69.6°, 77.0° and 79.2° respectively. No other peaks are obtained, which indicates the successful synthesis of CeO_2. The observed X-ray patterns of the synthesized CeO_2 satisfied the fluorite-type crystal cubic phase of CeO_2 (JC-PDS card no 01-075-8371) [17].

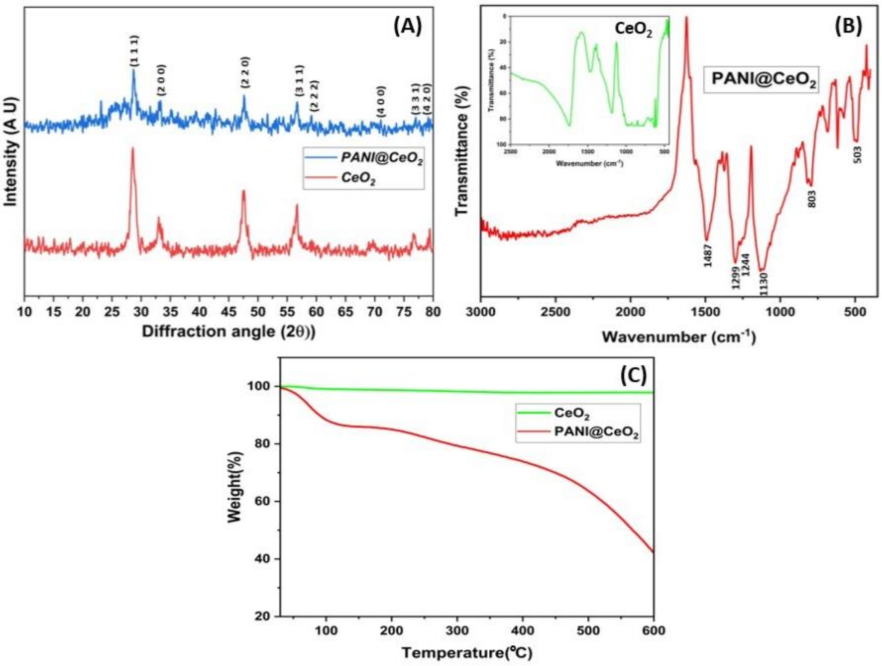

Figure 2. (A) XRD spectra; **(B)** FT-IR spectra; **(C)** TGA plot of PANI@CeO_2 and CeO_2.

The results here indicate that both the compounds maintained its characteristic in the composite mixture.

In the XRD pattern of PANI@CeO_2 nanocomposite, it was observed that the diffraction peaks of PANI and CeO_2 overlapped with each other. Both the PANI and PANI@CeO_2 nanocomposite show a wide peak located at 2θ = 26° satisfying the amorphous (semi-crystalline) nature of PANI. The synthesized PANI@CeO_2 nanocomposite shows its peaks at 2θ = 28.5°, 33.1°, 47.7°, 57.1°, 59.3°, 69.6°, 77.0° and 79.2° respectively which resembled the (111), (200), (220), (311), (222), (400), (331) and (420) Bragg's crystal plane reflections [18].

3.2. Fourier transform infrared study

The FTIR spectra of CeO_2, PANI@CeO_2 nanocomposite, and PANI are shown in **Figure 2B** and **Figure S2**. The vibration peaks of the as-prepared PANI@CeO_2 nanocomposite sample appear at 503, 689, 803, 1130, 1299, 1244, 1487, and 2822 (cm^{-1}). The C–N stretching of a secondary aromatic amine is responsible for a minor, distinct peak observed at 1299 cm^{-1}. The wide and sharp peaks at 1130 cm^{-1}

correspond to the bending vibration of C–H. The very small and clear peaks at 803 cm^{-1} indicate the metal-oxygen bands. The minor peak at 1244 cm^{-1} showed the C–N stretching and C–C stretching bands of PANI. The sharp peak at 1487 cm^{-1} showed the Benzenoid ring stretching of PANI. The broad peak at 503 cm^{-1} corresponds to the metal-oxygen stretching frequency. As the percentage of CeO_2 in the PANI@CeO_2 composite increases, the intensity also increases. For pure CeO_2 this peak was observed at 496 cm^{-1}, and moved at 503 cm^{-1} in the case of PANI@CeO_2 which illustrates the weak interaction between CeO_2 and PANI, while other prominent peaks of pure CeO_2 are 619, 1126, 1356, and 1569 (cm^{-1}) attributes to the stretching band of the metal-oxygen bond [17,19–21].

3.3. Thermogravimetric analysis study

From the TGA of CeO_2 and PANI@CeO_2 as shown in **Figure 2C**, it is observed that pure CeO_2 crystals are superiorly stable and thermally resistant in the temperature range of 20–600 °C whereas PANI@CeO_2 nanocomposite shows a loss in its mass in two steps. The first decrease in mass of about 10% occurs in the range of 40–100 °C owing to the deprivation of water from PANI chains. In the second step, loss of mass occurs in the range of 250–600 °C, corresponding to the breaking of polymeric chains. It is observed that when the CeO_2 to aniline ratio is about 40% in the PANI@CeO_2 nanocomposite, it shows highest thermal stability. The higher the content of CeO_2 in the composite, the more strengthening occurs between the polymeric chains and CeO_2 and the thermal decomposition of the chains is restricted accordingly [22–24].

3.4. Morphological studies

The surface morphology of PANI and PANI@CeO_2 was analysed using scanning electron microscopy (SEM), as shown in **Figure 3A,B**, respectively. The morphology of PANI appeared as a grain-like structure that contains some pores and voids. From the morphology of PANI@CeO_2 nanocomposites, it was observed that PANI@CeO_2 has some spherical and irregularly shaped grains with diameters in the nanorange, where the CeO_2 nanoparticles are homogeneously compacted in the PANI matrix, leading to homogeneous morphology and the higher conductivity of PANI@CeO_2 nanocomposite.

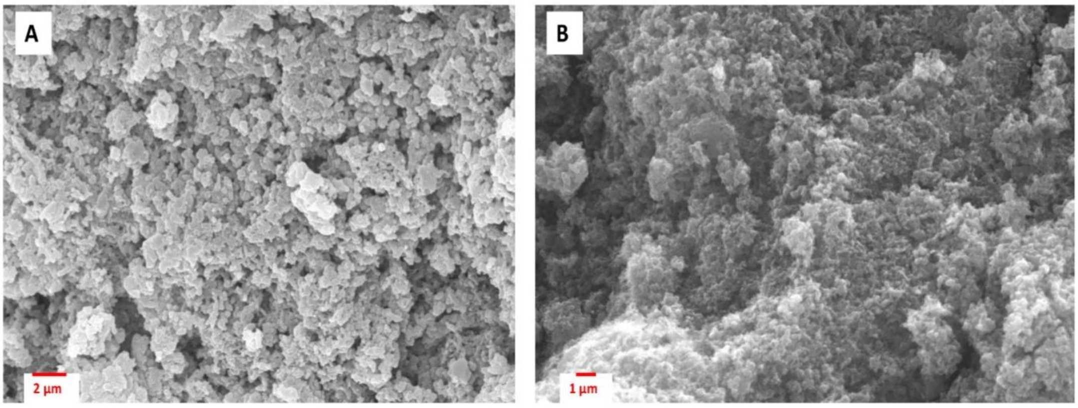

Figure 3. (A) SEM images of PANI; **(B)** SEM images of PANI@CeO_2 nanocomposite. Indicating more homogeneously compacted morphology of the nanocomposite.

4. Electrochemical studies

4.1. Electrochemical studies of electrodes

Electrochemical studies of the PANI/ITO and PANI@CeO_2/ITO electrodes have been performed using Cyclic Voltammetry (CV) technique in PBS (pH—7.4; 100 mM) carrying $[Fe(CN)_6]^{3-/4-}$ solution of 5 mM concentration. At 50 mV/s, it was noticed that PANI@CeO_2 electrode exhibits higher current with respect to the PANI/ITO electrode, which illustrates the better electron conduction ability of the PANI@CeO_2/ITO electrode (**Figure 4A**).

A scan rate study has also been performed for both electrodes, as shown in **Figure 4B** and **Figure S3**. It is observed that the anodic peak potential rises from 10 mV/s to 300 mV/s and the cathodic peak potential collapses with an increase in the scanning rate for both the PANI and PANI@CeO_2 modified ITO electrodes. This led to a linear relation between the cathodic and anodic peak potentials (E_{pa} and E_{pc}) of PANI and PANI@CeO_2 with respect to logarithmic scan rate ($\log v$) (**Figure 4D**) [Equations (1)–(4)] [25].

A linear correlation between the cathodic and anodic peak currents (I_{pa} and I_{pc}) with respect to the square root of scan rates ($v^{1/2}$) has also been observed from the scan rate studies of PANI and PANI@CeO_2 grafted ITO electrodes (**Figure 4C**) and has been depicted by Equations (5)–(8).

$$E_{pa}\ [\text{PANI@CeO}_2\text{/ITO}]\ (V)= 0.04968 \log(v) + 0.148;\ R^2 = 0.9492 \quad (1)$$

$$E_{pc}\ [\text{PANI@CeO}_2\text{/ITO}]\ (V) = -0.0708 \log(v) + 0.183;\ R^2 = 0.9710 \quad (2)$$

$$E_{pa}\ [\text{PANI/ITO}]\ (V) = 0.1075 \log(v) + 0.1187;\ R^2 = 0.9833 \quad (3)$$

$$E_{pc}\ [\text{PANI/ITO}]\ (V) = -0.2257 \log(v) + 0.3403;\ R^2 = 0.8701 \quad (4)$$

$$I_{pa}\ [\text{PANI@CeO}_2\text{/ITO}]\ (A) = 2.75 \times 10^{-5} \times v^{1/2} + 4.483 \times 10^{-5};\ R^2 = 0.994 \quad (5)$$

$$I_{pc}\ [\text{PANI@CeO}_2\text{/ITO}]\ (A) = -1.77 \times 10^{-5} \times v^{1/2} - 7.008 \times 10^{-5};\ R^2 = 0.978 \quad (6)$$

$$I_{pa}\ [\text{PANI/ITO}]\ (A) = 1.66 \times 10^{-5} \times v^{1/2} + 5.6315 \times 10^{-5};\ R^2 = 0.9905 \quad (7)$$

$$I_{pc}\ [\text{PANI/ITO}]\ (A) = -9.31 \times 10^{-6} \times v^{1/2} - 6.422 \times 10^{-5};\ R^2 = 0.9855 \quad (8)$$

The value of electron transfer co-efficient (α) for both PANI and PANI@CeO_2 grafted ITO electrodes was obtained to be 0.9138 and 0.8874, respectively (Equation S1). Using the value of (α) and the Equation (S2), the value of the charge transfer rate constant (K_s) is found to be 0.1804 s^{-1} and 0.8185 s^{-1} for PANI and PANI@CeO_2 respectively. Further, the value of average surface coverage (λ) is to be calculated using Equation S3, which is found to be 1.515×10^{-4} m^{-2} and 2.07×10^{-4} m^{-2} for PANI and PANI@CeO_2 respectively. The value of diffusion coefficient for $[Fe(CN)_6]^{3-/4-}$ solution (D) and effective surface area of electrodes (A) are calculated using the gradient of lines established by the linear connection between I_p and $v^{1/2}$, using the Randles-Sevcik equation as shown in Equation (S4).

The effective surface area of PANI having $D = 4.964 \times 10^{-4}$ m^2 s^{-1} and PANI@CeO_2 having $D = 9.5 \times 10^{-4}$ m^2 s^{-1} is found to be 5.22×10^{-7} m^2 and 6.32×10^{-7} m^2 respectively. The values of D and A are greater for PANI@CeO_2 nanocomposite than PANI because PANI@CeO_2 performs better diffusion of redox ions through its active detection area and electrode interface [26,27]. All the parameters have been summarized in **Table 1**.

Table 1. Comparison of the electrochemical behaviour of the PANI/ITO and PANI@CeO$_2$/ITO electrodes.

Modified electrodes	**Electron transfer co-efficient (α)**	**Charge transfer rate constant (K_s) (s^{-1})**	**Average surface coverage (λ) (m^{-2})**	**Diffusion co-efficient (D) (m^2s^{-1})**	**Effective surface area (A) (m^2)**
PANI/ITO	0.9138	0.1804	1.515×10^{-4}	4.964×10^{-4}	5.22×10^{-7}
PANI@CeO$_2$/ITO	0.8874	0.8184	2.07×10^{-4}	9.5×10^{-4}	6.32×10^{-7}

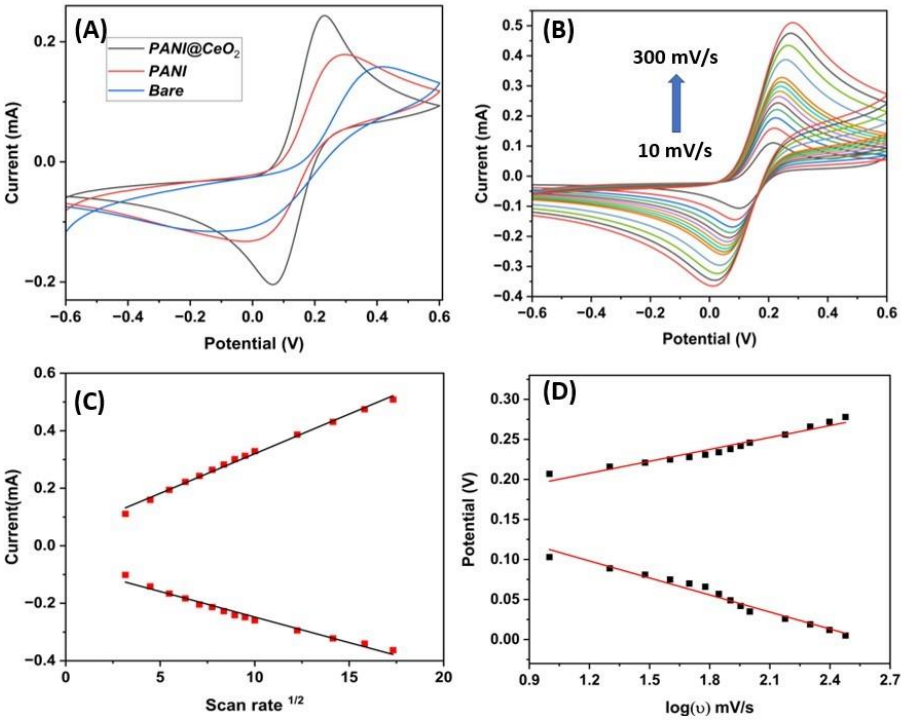

Figure 4. (A) CV studies of PANI@CeO$_2$, PANI and bare electrode demonstrating the higher conduction ability of PANI@CeO$_2$; **(B)** different scan rates with PANI@CeO$_2$ electrode (10–300 mV/s); **(C)** Plot of I_{pa}, I_{pc} vs. square root of scan rate for PANI@CeO$_2$ electrode; **(D)** plot of potential vs. logarithm of scan rate for pani@CeO$_2$ electrode.

4.2. Optimization of pH parameter

For an effective sensing methodology of the electrodes, it is mandatory to optimize the value of pH of the electrolyte solution, as the pH affects the sensitivity of the electrode towards the analyte. Thus, we performed the optimization of buffer solution from pH 5.5 to pH 8.5 using the DPV. Maximum current has been observed at pH 7.4, and thus we used pH 7.4 buffer for all the sensing studies (**Figure S4**). This can be attributed to the fact that the rate of deprotonation of phenols declines with the rise in pH of the solution. Also, human body serum has an optimum pH of 7.4, hence this pH is favourable for clinical studies as well [8].

4.3. Electrochemical biosensing of E2

The electrochemical sensing of E2 was performed using the DPV technique in PBS (pH 7.4) carrying 5 mM $[Fe(CN)_6]^{-3/-4}$ solution, as shown in **Figure 5A**. It was noticed that the peak current declined linearly with the concentration of the E2 as analyte (1–100 µM). This can be justified as, with an increase in concentration, the analyte tends to bind with iron coming from $[Fe(CN)_6]^{-3/-4}$ solution to make an iron complex, which retards the analyte from getting onto the electrode surface of the

PANI@CeO_2 modified ITO electrode [28]. The linear correlation between the concentration and peak current of the analyte is illustrated in **Figure 5B**, which follows the equation:

$$I\,(A) = 7.6 \times 10^{-5} - 9.012 \times 10^{-8}\,[E2];\ R^2 = 0.9865$$

From the slope of the equation, the sensitivity of the biosensor obtained is 142.6 $\mu A\ \mu M^{-1}\ m^{-2}$. The fabricated electrode offers an LOD of 21.53 µM towards E2 with reference to the equation: LOD = $3\sigma/S$. (σ = standard deviation, S = sensitivity, which is determined from the slope of the calibration curve) [29]. The aromatic ring of E2 consists of the hydroxy group, which is liable to make phenoxyl radicals in an aqueous medium during the process of oxidation. The radical on further oxidation leads to the formation of commensurate ketone derivatives, which conclude the effective electrocatalytic direct oxidation of E2 using PANI@CeO_2 [30].

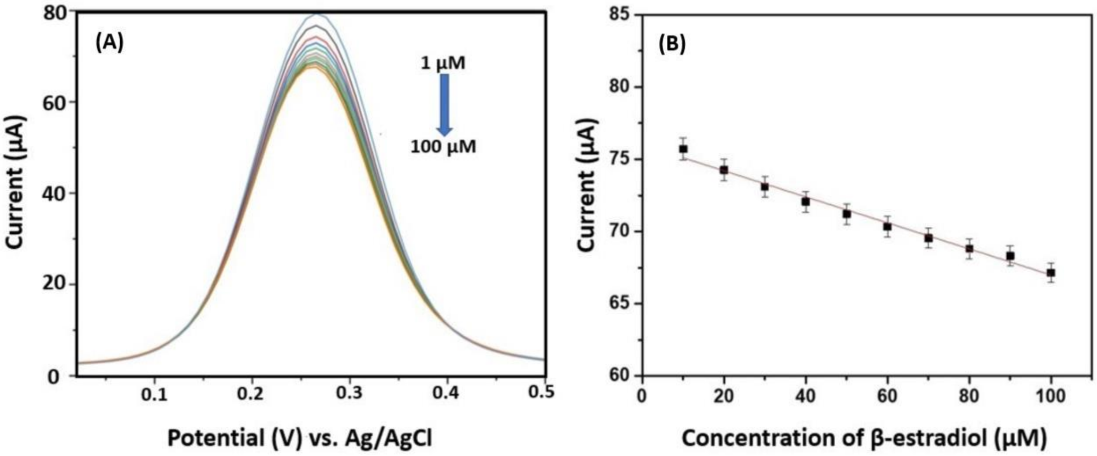

Figure 5. (A) DPV response for PANI@CeO_2 electrode with increase in concentration of E2 as an analyte (1–100 µM); **(B)** Calibration plot between magnitude of current response vs. Concentration of the analyte where linearity is observed.

4.4. Interference, shelf life and stability study

To understand the specificity for analyte E2, an interference study has been performed by testing E2 (100 µM) in the presence of equal amounts of interferants like ascorbic acid (100 µM), glucose, NaCl, urea, estriol, and uric acid, which might restrict the sensing of E2 while its detection in urine and water samples. It has been observed from the current response for different interferants that the target analyte maintained its specificity in different interferants (**Figure 6A**).

Further, the shelf life of the developed electrode was examined for 21 days in the interval of 7 days. From this study, no change in the current response is observed till 14 days. Whereas a sudden diminution in peak current of around 12.1% is noticed on the 21st day of this study. Therefore, we confirm the good stability of the developed biosensor for a period of up to 15 days (**Figure 6B**). However, the stability of the biosensing electrode has been confirmed by repeating each result thrice.

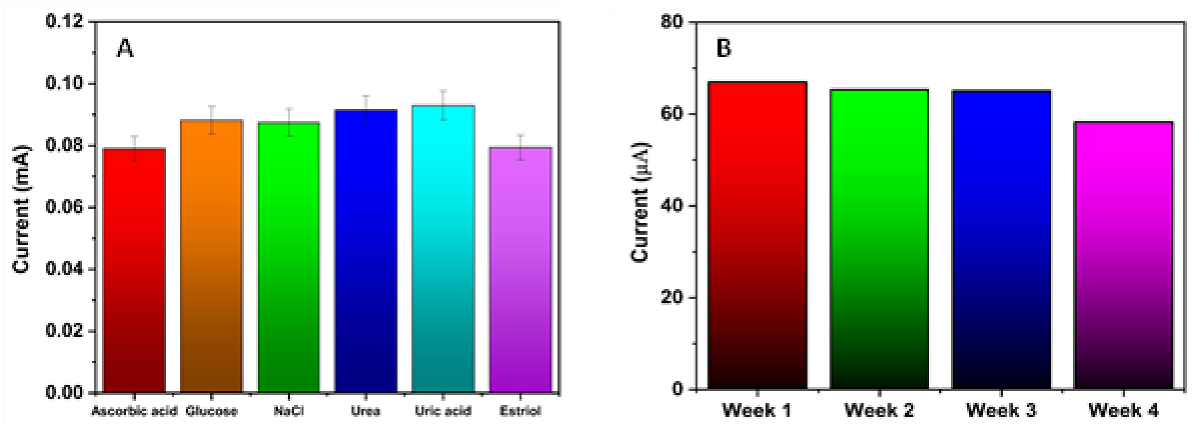

Figure 6. (A) Interference study for different analytes indicating the specificity of E2 analyte; **(B)** Shelf study of the PANI@CeO_2 modified electrode in 7.4 pH PBS containing 5 mM $[Fe(CN)_6]^{3-/4-}$ for 100 µM E2; from this result, we confirmed a shelf life of up to 15 days for the developed biosensor.

4.5. Real sample analysis

To examine the precision and practical applicability of our biosensor, we performed electrochemical analysis in two different samples, viz., human urine (healthy female) and tap water (DTU, Delhi). For analysis, each real sample was infused with different concentrations of E2 (1–100 µM) [31]. From the above analysis, we observed recovery of E2 in the range of 98.3%–99.7% for human urine and 97.1%–98.1% for tap water which validates the good productivity and effectuality of the PANI@CeO_2 electrode (**Table 2**).

Table 2. Recovery percentage data of E2 in real samples.

Sample	Added amount (µM)	Found amount (µM)	Recovery (%)
Human urine	10	9.85	98.5
	40	39.88	99.7
	60	59.64	99.4
	100	98.3	98.3
Tap water	10	9.71	97.1
	40	38.92	97.3
	60	58.86	98.1
	100	97.6	97.6

5. Conclusion

In this study, a method was incorporated to detect E2 using a non-enzymatic approach. We synthesized and characterized a PANI@CeO_2 nanocomposite, which was then electrophoretically deposited onto an ITO substrate. The electrochemical behaviour of the PANI@CeO_2 modified electrode was compared to a PANI modified electrode.

After considering the results, this work can be summarized as:

a) The incorporation of CeO_2 in the conducting polymer (PANI), forming PANI@CeO_2 acts as an effective sensing platform for E2. PANI matrix grafted with CeO_2 increases the surface area, density, electrical conductivity, and sensitivity of nanocomposite.

b) PANI@CeO_2 modified electrode persisting higher current as compared to PANI modified electrode has been depicted, indicating better diffusion of redox ions.

c) The study also included a quantitative analysis of three important parameters: sensitivity (275.4 mA $(\mu M)^{-1}$), linear range (1–100 μM), and limit of detection (2.15 μM). These results demonstrated the reliability and performance of the developed biosensor in terms of sensitivity, range, and detection limit. The experiments showed good repeatability, stability, and reproducibility, further validating the effectiveness of the non-enzymatic biosensor for detecting E2.

d) For better evaluation, the applicability of the biosensor is demonstrated by conducting the analysis in real samples, viz., human urine and tap water, which showcase the practicality and potential of the biosensor in real-world scenarios.

Supplementary materials: Consists of supporting equations, XRD and FTIR pattern of PANI, and pH optimization results.

Author contributions: Conceptualization, AD, and TR; methodology, SV; software, AD; validation, SV and DK; formal analysis, SV; investigation, AD and TR; resources, AD; data curation, TR; writing—original draft preparation, AD and TR; writing—review and editing, SV; visualization, SV; supervision, DK. All authors have read and agreed to the published version of the manuscript.

Funding: Authors thank Dept. of Physics, DTU, Delhi India for the XRD facility. S. Verma acknowledges UGC for the JRF Award (NOV 2017-139082).

Data availability: The data that has been used is confidential.

Conflict of interest: The authors declare no conflict of interest.

References

1. Wang Y, Zhao X, Zhang M, et al. A fluorescent amplification strategy for high-sensitive detection of 17 β-estradiol based on EXPAR and HCR. Analytica Chimica Acta. 2020; 1116: 1-8. doi: 10.1016/j.aca.2020.04.010
2. Pu H, Huang Z, Sun DW, et al. Recent advances in the detection of 17β-estradiol in food matrices: A review. Critical Reviews in Food Science and Nutrition. 2019; 59(13): 2144-2157. doi: 10.1080/10408398.2019.1611539
3. Orozco-Hernández L, Gómez-Oliván LM, Elizalde-Velázquez A, et al. 17-β-Estradiol: Significant reduction of its toxicity in water treated by photocatalysis. Science of The Total Environment. 2019; 669: 955-963. doi: 10.1016/j.scitotenv.2019.03.190
4. Minopoli A, Sakač N, Lenyk B, et al. LSPR-based colorimetric immunosensor for rapid and sensitive 17β-estradiol detection in tap water. Sensors and Actuators B: Chemical. 2020; 308: 127699. doi: 10.1016/j.snb.2020.127699
5. Yao X, Wang Z, Dou L, et al. An innovative immunochromatography assay for highly sensitive detection of 17β-estradiol based on an indirect probe strategy. Sensors and Actuators B: Chemical. 2019; 289: 48-55. doi: 10.1016/j.snb.2019.03.078
6. Triviño JJ, Gómez M, Valenzuela J, et al. Determination of a natural (17β-estradiol) and a synthetic (17α-ethinylestradiol) hormones in pharmaceutical formulations and urine by adsorptive stripping voltammetry. Sensors and Actuators B: Chemical. 2019; 297: 126728. doi: 10.1016/j.snb.2019.126728
7. Goswami B, Mahanta D. Fe3O4-Polyaniline Nanocomposite for Non-enzymatic Electrochemical Detection of 2,4-Dichlorophenoxyacetic Acid. ACS Omega. 2021; 6(27): 17239-17246. doi: 10.1021/acsomega.1c00983
8. Paneru S, Kumar D. A Novel Electrochemical Biosensor Based on Polyaniline-Embedded Copper Oxide Nanoparticles for High-Sensitive Paraoxon-Ethyl (PE) Detection. Applied Biochemistry and Biotechnology. 2023; 195(7): 4485-4502. doi: 10.1007/s12010-023-04350-y

9. Ramanavicius S, Ramanavicius A. Conducting Polymers in the Design of Biosensors and Biofuel Cells. Polymers. 2020; 13(1): 49. doi: 10.3390/polym13010049
10. Petruleviciene M, Juodkazyte J, Savickaja I, et al. BiVO4-based coatings for non-enzymatic photoelectrochemical glucose determination. Journal of Electroanalytical Chemistry. 2022; 918: 116446. doi: 10.1016/j.jelechem.2022.116446
11. Emir G, Dilgin Y, Ramanaviciene A, et al. Amperometric nonenzymatic glucose biosensor based on graphite rod electrode modified by Ni-nanoparticle/polypyrrole composite. Microchemical Journal. 2021; 161: 105751. doi: 10.1016/j.microc.2020.105751
12. Adeosun WA, Asiri AM, Marwani HM, et al. Enzymeless Electrocatalytic Detection of Uric Acid Using Polydopamine/Polypyrrole Copolymeric film. ChemistrySelect. 2020; 5(1): 156-164. doi: 10.1002/slct.201903628
13. Ashwini IS, Pattar J, Anjaneyulu P, et al. Synthesis and electrical properties of polyaniline–cerium oxide composites. Synthetic Metals. 2020; 270: 116588. doi: 10.1016/j.synthmet.2020.116588
14. Rossignatti BC, Vieira AP, Barbosa MS, et al. Thin Films of Polyaniline-Based Nanocomposites with CeO2 and WO3 Metal Oxides Applied to the Impedimetric and Capacitive Transducer Stages in Chemical Sensors. Polymers. 2023; 15(3): 578. doi: 10.3390/polym15030578
15. Sharma SS, Palatty S. Advances in functionalized polyaniline nanocomposites for electrochemical sensing and energy storage applications. Applications of Multifunctional Nanomaterials. 2023; 2023: 177-196. doi: 10.1016/b978-0-12-820557-0.00004-7
16. Beygisangchin M, Abdul Rashid S, Shafie S, et al. Preparations, Properties, and Applications of Polyaniline and Polyaniline Thin Films—A Review. Polymers. 2021; 13(12): 2003. doi: 10.3390/polym13122003
17. Hussein MA, Khan A, Alamry KA. A highly efficient electrochemical sensor containing polyaniline/cerium oxide nanocomposites for hydrogen peroxide detection. RSC Advances. 2022; 12(49): 31506-31517. doi: 10.1039/d2ra05041b
18. Lei Y, Qiu Z, Tan N, et al. Polyaniline/CeO2 nanocomposites as corrosion inhibitors for improving the corrosive performance of epoxy coating on carbon steel in 3.5% NaCl solution. Progress in Organic Coatings. 2020; 139: 105430. doi: 10.1016/j.porgcoat.2019.105430
19. Parvatikar N, Jain S, Bhoraskar SV, et al. Spectroscopic and electrical properties of polyaniline/CeO2 composites and their application as humidity sensor. Journal of Applied Polymer Science. 2006; 102(6): 5533-5537. doi: 10.1002/app.24636
20. Li C, Wang J, Wen Y, et al. Polyaniline/CeO2 Nanofiber Composite Membrane as a Promoter of Pt for Formic Acid Electro-Oxidation. ECS Electrochemistry Letters. 2012; 2(1): H1-H4. doi: 10.1149/2.001302eel
21. Saranya J, Sreeja BS, Padmalaya G, et al. Ultrasonic Assisted Cerium Oxide/Graphene Oxide Hybrid: Preparation, Anti-proliferative, Apoptotic Induction and G2/M Cell Cycle Arrest in HeLa Cell Lines. Journal of Inorganic and Organometallic Polymers and Materials. 2020; 30(7): 2666-2676. doi: 10.1007/s10904-019-01403-w
22. Huang H, Guo ZC. Preparation and Characterization of Conductive Polyaniline/Cerium Dioxide Composites. Materials Science Forum. 2010; 663-665: 686-689. doi: 10.4028/www.scientific.net/msf.663-665.686
23. Wang S, Huang Z, Wang J, et al. Thermal stability of several polyaniline/rare earth oxide composites (I): polyaniline/CeO2 composites. Journal of Thermal Analysis and Calorimetry. 2011; 107(3): 1199-1203. doi: 10.1007/s10973-011-1777-1
24. Ramezanzadeh B, Bahlakeh G, Ramezanzadeh M. Polyaniline-cerium oxide (PAni-CeO2) coated graphene oxide for enhancement of epoxy coating corrosion protection performance on mild steel. Corrosion Science. 2018; 137: 111-126. doi: 10.1016/j.corsci.2018.03.038
25. Elgrishi N, Rountree KJ, McCarthy BD, et al. A Practical Beginner's Guide to Cyclic Voltammetry. Journal of Chemical Education. 2018; 95(2): 197-206. doi: 10.1021/acs.jchemed.7b00361
26. Laviron E. General expression of the linear potential sweep voltammogram in the case of diffusionless electrochemical systems. Journal of Electroanalytical Chemistry and Interfacial Electrochemistry. 1979; 101: 19-28. doi: 10.1016/S0022-0728(79)80075-3
27. Jalil O, Pandey CM, Kumar D. Highly sensitive electrochemical detection of cancer biomarker based on anti-EpCAM conjugated molybdenum disulfide grafted reduced graphene oxide nanohybrid. Bioelectrochemistry. 2021; 138: 107733. doi: 10.1016/j.bioelechem.2020.107733
28. Li J, Liu S, Yu J, et al. Electrochemical immunosensor based on graphene-polyaniline composites and carboxylated graphene oxide for estradiol detection. Sensors and Actuators B: Chemical. 2013; 188: 99-105. doi: 10.1016/j.snb.2013.06.082

29. Verma S, Pandey CM, Kumar D. A highly efficient rGO grafted MoS2 nanocomposite for dye adsorption and electrochemical detection of hydroquinone in wastewater. New Journal of Chemistry. 2022; 46(44): 21190-21200. doi: 10.1039/d2nj04285a
30. Li J, Jiang J, Zhao D, et al. Facile synthesis of Pd/N-doped reduced graphene oxide via a moderate wet-chemical route for non-enzymatic electrochemical detection of estradiol. Journal of Alloys and Compounds. 2018; 769: 566-575. doi: 10.1016/j.jallcom.2018.08.016
31. Supchocksoonthorn P, Alvior Sinoy MC, de Luna MDG, et al. Facile fabrication of 17β-estradiol electrochemical sensor using polyaniline/carbon dot-coated glassy carbon electrode with synergistically enhanced electrochemical stability. Talanta. 2021; 235: 122782. doi: 10.1016/j.talanta.2021.122782

EnPress Publisher

Characterization and Application of Nanomaterials 2024, 7(2), 4768.
https://doi.org/10.24294/can.v7i2.4768

Article

Non-enzymatic detection of 17β-estradiol in real samples using PANI@CeO$_2$ nanocomposite

Supplementary materials

Equations:

$$Epa = \frac{RT}{(1-\alpha)nF} \quad \text{(S1)}$$

$$\ln(Ks) = \alpha\ln(1-\alpha) + (1-\alpha)\ln\alpha - \ln\{RT/nF\upsilon\} - \alpha(1-\alpha)nF\frac{\Delta Ep}{RT} \quad \text{(S2)}$$

$$I_{pa}/\upsilon = n^2F^2A\lambda/4RT \quad \text{(S3)}$$

$$I_p = 2.99 \times 10^5 \times \alpha^{1/2}n^{3/2}ACD^{1/2}v^{1/2} \quad \text{(S4)}$$

where R = gas constant, T is 298 K, ΔE_p = difference in the peak potential, n = number of electrons transferred and F = Faraday's constant, S = Sensitivity ($I_p/v^{1/2}$), C = Concentration of $[\mathrm{Fe(CN)_6}]^{3-/4-}$ solution.

Figure:

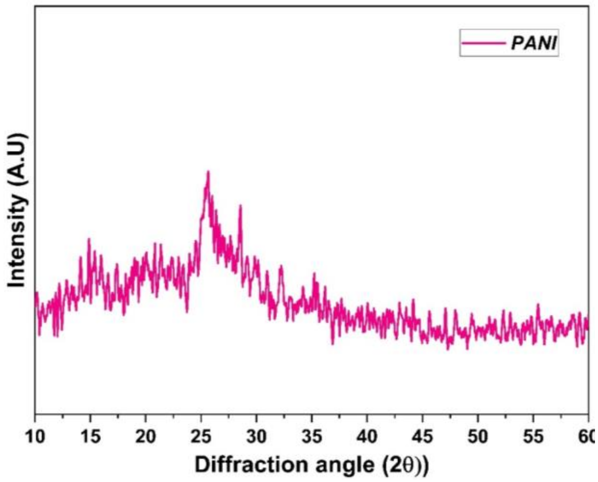

Figure S1. S1-XRD spectra of PANI.

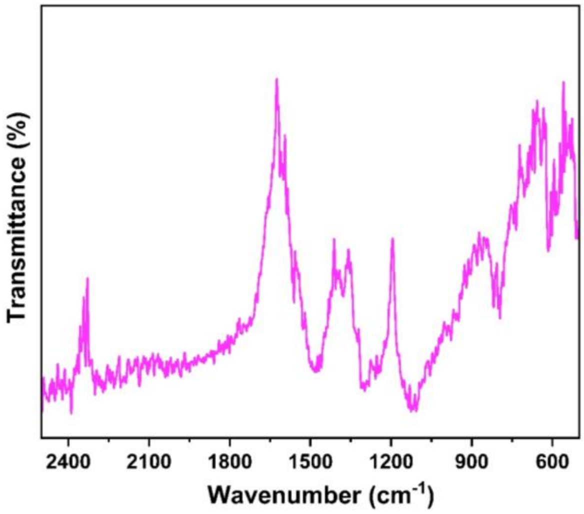

Figure S2. FT-IR spectra of PANI.

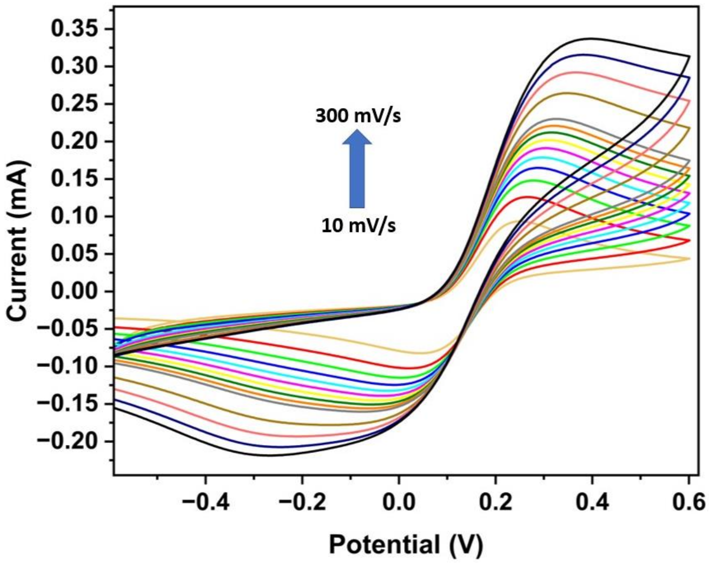

Figure S3. Cyclic Voltammetry at different scan rates (10–300 mV/S) for PANI/ITO electrode.

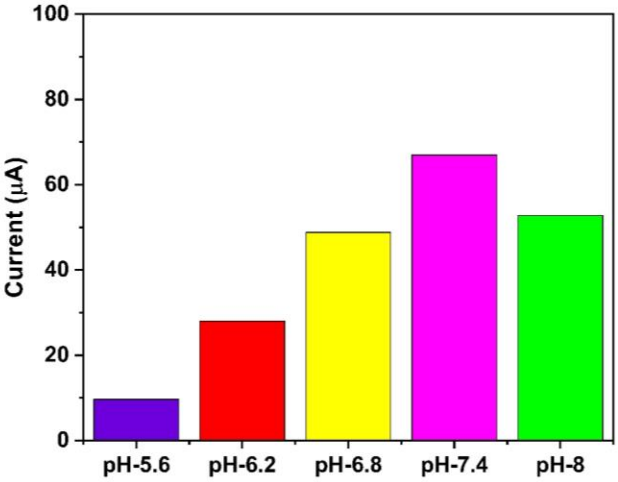

Figure S4. Optimization of pH.

Characterization and Application of Nanomaterials 2024, 7(2), 4682.
https://doi.org/10.24294/can.v7i2.4682

Article

PVA/MB-ssDNA/MXene hydrogel synthesized by freeze thawing process with the effect of MB-ssDNA

Elham Ghazizadeh[1,*], **Sahar Aghayani**[2]

[1] Department of Bioinspired Materials and Biosensor Technologies, Institute of Materials Science, Faculty of Engineering, Kiel University, 24103 Kiel, Germany
[2] Department of Chemistry, Catalysis Division, University of Isfahan, Isfahan 83431, Iran
*** Corresponding author:** Elham Ghazizadeh, elhamgenetic@gmail.com

CITATION

Ghazizadeh E, Aghayani S. PVA/MB-ssDNA/MXene hydrogel synthesized by freeze thawing process with the effect of MB-ssDNA. Characterization and Application of Nanomaterials. 2024; 7(2): 4682.
https://doi.org/10.24294/can.v7i2.4682

ARTICLE INFO

Received: 19 February 2024
Accepted: 4 March 2024
Available online: 22 October 2024

Abstract: Freeze-thawing plays a vital role in enhancing materials in medicines. Here, we describe the F-T process of synthesis of Poly (vinyl alcol)- Methylene blue single strand-Mxene (PVA–MB-ssDNA –Mxene), which may be effective for gen delivery applications. The PVA –MB-ssDNA –Mxene hydrogel was formed using 1,3,5 consecutive cycles. We also demonstrated that PVA –MB-ssDNA –Mxene hydrogel can be formed by the affection of DNA with PVA and the MXene network. The F-T process shows the new intra molecular bond of PVA-PVA, compared to the non F-T hydrogel which formed by a biologic crosslinking as MB-ssDNA. Scanning electron microscopy reported that the microstructure. The differential scan shows three endothermic peaks at 70, 180, and 300 °C for water loss and decomposition. The swelling behavior rapidly increased due to the PVA chains in the F-T methods and then became stable. With a high concentration of MB-DNA, the tensile strength was slightly high, and the swelling behavior was low. Our results indicated that the PVA –MB-ssDNA –Mxene hydrogel using F-T process would have more suitable structural features as gene hydrogel carrier which need greater mechanical strength and stability in body analyses.

Keywords: hydrogel; MXene; MB-ssDNA; freeze thawing; physical crosslinking

1. Introduction

Freeze thawing is a critical process used extensively in the fields of medicine and healthcare. This technique involves freezing a substance, followed by thawing at a later stage [1]. This cycle is repeated multiple times, allowing for the preservation and utilization of various medical components such as proteins, cells, tissues, and organs [2]. The freeze–thaw technique has been employed to develop hydrogels for medical materials. The advantages of this freeze-thaw technique compared to the conventional technique are that it does not require a high temperature or any extra chemicals as crosslinking agents that may cause toxicity [3,4]. On the hand, one of the important challenges in using gene delivery is protecting DNA during the delivery process, optimal control of DNA release from carriers, and proper cellular uptake of DNA. This technique allows for the enhanced delivery, protection, controlled release, and cellular uptake of DNA [5,6]. DNA hydrogels are three-dimensional networks formed by self-assembling DNA strands. These materials exhibit exceptional biocompatibility, biodegradability, and programmability, making them an ideal choice for various biomedical applications. However, to fully harness their potential, it is essential to optimize their structure and properties. This is where the freeze-thaw method comes into play. In this article, we will explore the significance of freeze-thawing PVA –MB-ssDNA –Mxene in the medical field. Zhao et al. prepared a flame-retardant

PVA/PA/MXene hydrogel coating via a freeze–thaw cycle [7]. This coating showed excellent self-healing properties and high water retention (water content ≥ 90%) owing to the increased number of hydrogen bonds with the introduction of MXene. Many studies have been conducted on PVA-based hydrogels using the freeze-thaw process in the medical industry. Waresindo et al. showed that a polyvinyl alcohol (PVA) hydrogel loaded with guava leaf extract (GLE) could be fabricated by freeze–thaw (F-T) method as a wound dressing with good antibacterial activity [8]. In 2008, the effect of DNA on the mechanical properties of nanofiber hydrogels was demonstrated. PVA nanofiber gels incorporating double-stranded deoxyribonucleic acid DNA were fabricated without the aid of cross-linkers using electrospinning. Unlike the weak connection between DNA and PVA, the elastic modulus of the DNA/PVA gels was higher than that of the PVA gel [9]. In this study, we synthesized a PVA –MB-ssDNA –Mxene hydrogel using the freeze-thawing method, which can be used as an effective hydrogel approaches carrier in gene delivery research using single-stranded DNA (ss-DNA). So, we investigated PVA –MB-ssDNA –Mxene synthesis using the F-T method to study the structural, morphological, and thermal properties of this hydrogel compared to the synthesis hydrogel of PVA –MB-ssDNA –Mxene without F-T method. Due to the fact that biological cross-linking as MB-ssDNA is used in both methods, we have tried to investigate the effect of freeze-thaw cycles on the structure and increasing the tensile strength of the hydrogel. The results show that the samples were successfully prepared during different F-T processes (1, 3, and 5 cycles). The PVA –MB-ssDNA –Mxene hydrogel synthesized by the F-T method was also stronger than PVA –MB-ssDNA –Mxene without F-T Methods The. Our study also showed the effect of MB-ssDNA on the increasing the tensile strength and reducing the swelling properties of PVA –MB-ssDNA –Mxene hydrogel structure synthesized by freeze-thawing method. As a result, we introduced the novel synthesis of PVA –MB-ssDNA –Mxene hydrogel structure by the F-T method, which was influenced of biological (MB-ssDNA) and physical cross-linking which can be used as a future reliable gene carrier based hydrogel in medical purposes.

2. Experimental

2.1. Chemicals and reagents

Lithium fluoride (LiF), Ti_3AlC_2 (powder, 200 mesh), Tris Buffer, Poly (vinyl alcohol), and borax (sodium tetraborate decahydrate, purity > 99.5%, $Na_2B_4O_7$, $10H_2O$, Mw = 381.37 g/mol) ammonia water were purchased from Sigma-Aldrich. All the chemicals were used directly without further purification. Single-strand DNA such as MB-ssDNA; 5'- Atto MB_2-TCA ACA TCA GTC TGA TAA GCT A –(OH) 3’ was synthesized from Metabion (German).

2.2. Methods

2.2.1. Preparation of Ti_3C_2Tx MXene Nanosheets

$Ti_3C_2T_x$ MXene nanosheets were prepared by modified hydrofluoric acid etching. In brief, 2 g Ti_3AlC_2 powder and 2 g LiF were dissolved in 20 mL HCl solution (9 M), injected with nitrogen for deoxygenation, and sealed in an oven at 200 °C for 24 h.

The resulting suspension was collected and washed again. Ti_3C_2 was collected by centrifugal washing. Finally, the supernatant was freeze-dried to obtain MXene (Ti_3C_2) nanosheets.

2.2.2. Preparation of PVA –MB-ssDNA –Mxene nanocomposite hydrogel

The synthesized was modified by PVA–Mxene- borax protocol [10]. After completely dissolved 0.6 g PVA (10%w/v) at 90 °C for about 4 h, 6 mg/mL of ss-MB-DNA were dissolved in 16 mL distilled water and stirred continuously at 30 °C until DNA was completely dissolved without denaturation. Subsequently, a certain amount of MXene was added to the solution and stirred for 5 h. The mixture was cast onto a petri dish, followed by freezing at −20 °C for 18 h, and thawed at room temperature for 6 h. The experiment was conducted for 1, 3 and 5 consecutive cycles, respectively (**Figure 1**). The hydrogel was stored in a desiccator to prevent moisture adsorption. In parallel, we synthesized non F-T PVA –MB-ssDNA –Mxene hydrogel as described above but without the consecutive cycles.

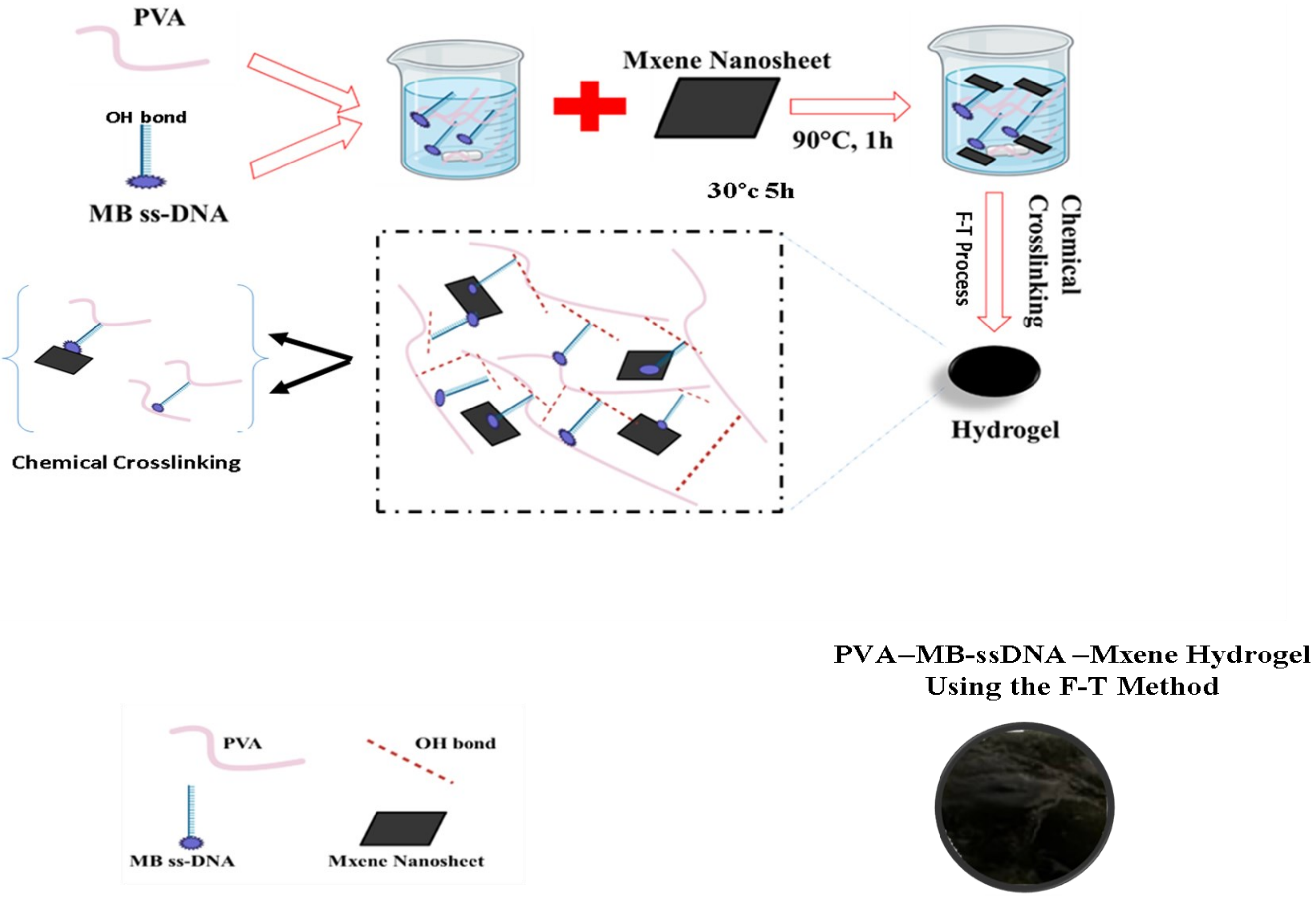

Figure 1. Step-wise preparation of PVA –MB-ssDNA –Mxene hydrogel using the freeze thaw process.

2.2.3. Swelling behavior

To investigate the swelling behavior of the synthesized of PVA –MB-ssDNA –Mxene with freeze thawing method, the samples were cut into 1 cm^2 × 1 cm^2 pieces with the same weight (W_d) and immersed in deionized water (DI) for 24 h. Samples were removed from the solution, dried with filter paper to remove excess water, and weighed (W_w). The samples were then investigated using the following equation, and the data were reported as the statistical average and standard deviation.

$$Swelling\ (\%) = \frac{Ww - Wd}{\mathrm{wd}} \times 100$$

where W_w is the weight of the swollen sample and W_d is the initial weight of the hydrogel.

2.2.4. Fourier transform infrared (F-TIR) characterization of the samples

A Fourier-transform infrared spectrometer (SPECTRUM ONE, Perkin Elmer, USA) was used to determine the chemical structure. The sample was scanned from 400 cm^{-1} to 4000 cm^{-1} at room temperature in air mode at a resolution of 4 cm^{-1}.

2.2.5. Scanning electron microscope (SEM)

The morphology was determined by scanning electron microscopy. In detail, the micromorphology of PVA –MB-ssDNA-MXene hydrogel by freeze thawing processes and non-freeze thawing process composite hydrogel was analyzed by FEI Inspect F50 scanning electron microscope (SEM, Quanta 250 microscope, Japan). Hydrogels were treated with liquid nitrogen to expose the inner structure. Then, hydrogel samples were rapidly dropped onto a gold-coated high purity copper block cooled in liquid nitrogen due to entering the rapid freezing to minimize compression of the hydrogel samples. In the following, we used as the airlock transfer adapter to remove the hydrogel sample from liquid nitrogen immersion and transferred to the sample preparation airlock precooled to −175 °C.

2.2.6. Differential scanning calorimetry (DSC)

Thermal behavior of PVA –MB-ssDNA –Mxene hydrogel was determined using DSC (NETZSCH DSC 204 F1 Phoenix, Germany). The samples were placed in aluminum pans at a flow rate of 40 $mL \cdot min^{-1}$. The temperature was fixed at 30 °C to 350 °C at a flow rate of 10 $°C \cdot min^{-1}$. The data are presented as the glass transition temperature, melting temperature, and specific heat capacity. By passing a nitrogen gas stream from 0–600 °C at a heating rate of 20 °C/min, samples were scanned and thermograms were collected.

2.2.7. Tensile testing

The samples (1 mm thickness) for the tensile tests were cut with a dumbbell cutter (Analyzer Texture XT2i, Iran). The speed of the test was 10 mm/min to obtain the tensile stress (r)–strain (DL/L_0) curve, where r was calculated using the cross-sectional area of the unreformed gel. DL and L_0 indicate the deformation of the gel and initial length before deformation, respectively.

3. Results and discussion

PVA –MB-ssDNA –Mxene hydrogel was successfully prepared using the freeze-thaw technique. It exhibits a reformable shape. **Figure 2** illustrates the F-TIR spectra of the PVA –MB-ssDNA –Mxene hydrogel prepared by the freeze-thaw technique. No significant changes in the functional groups of the hydrogels were observed based on the variation of consecutive cycles in the freeze-thaw process. The functional groups of the hydrogels were similar for all compositions of hydrogel PVA –MB-ssDNA –Mxene without the F-T process based on the F-TIR analysis that was used to qualitatively analyze the presence of functional groups in the hydrogels. In **Figure 2**, the characteristic peak at 3445 cm^{-1}was observed. This indicates the presence of an OH-stretching group (hydroxyl group). It refers to the presence of polyvinyl alcohol, MXene, and MB-DNA. This was in agreement with our work for synthesizing MXene-PVA hydrogel without F-T processes. It also clearly showed the major peaks related to freeze-thawed PVA (10). Another peak was attributed to the C–H stretching vibrations at 1410 cm^{-1} and 2911 cm^{-1}. F-TIR peaks at 2225 cm^{-1} and 1600 cm^{-1} were observed sequentially for the C–N stretching and C=O stretching groups. This can be created by the adsorption of MB on MXene and PVA. This is in agreement with a previous study by Zhang on MB adsorption on MXene based on electrostatic forces [11]. Another peak at 1579 cm^{-1} and the C–H bond can imply the bond between MB and PVA or MXene. In this study, the F-TIR peaks at 500 cm^{-1} and 1350 cm^{-1}and 1575 cm^{-1} were related to C–O, C–N, and N–H bonds of DNA. Generally, our results showed that there is no significant change on functional group of hydrogels during on variation of consecutive cycle in F-T process. As F-TIR analysis indicated the qualitatively analyze the existence of functional group of hydrogels, it can be concluded that functional group of hydrogels was still similar for all compositions of hydrogel. On the hand, F-T hydrogel results were also similar to the Non F-T MXene-PVA/MB-ssDNA hydrogel, with the difference in the shifting of the C-C and CH$_2$ at 800 cm^{-1}and 900 cm^{-1}. On the hand, results indicated F-TIR peaks at 1220 cm^{-1}at the C-O-C bond between the intramolecular PVA chains with the highlighting of the new peaks at 1141 cm^{-1} and 2882 cm^{-1}, which indicate the intra-or intermolecular bonds of PVA. These results showed that the existence of a physical process besides cross-linking (MB-ssDNA) can lead to the formation of more intra- and intermolecular PVA networks., in comparison with the conventional hydrogel methods of MXene-PVA/MB-ssDNA.

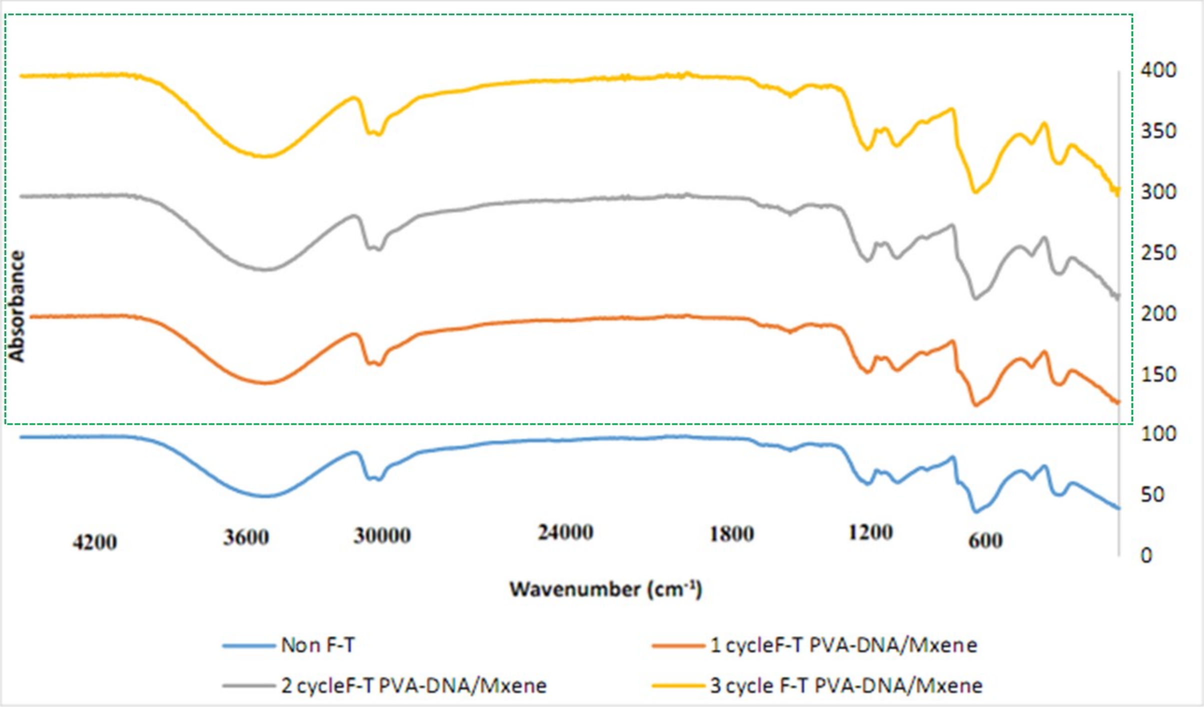

Figure 2. F-TIR spectra of PVA –MB-ssDNA –Mxene hydrogel prepared with/out F-T process.

Figure 3 shows the morphological properties of the PVA –MB-ssDNA –Mxene hydrogel could prepared using also the freeze-thaw technique. Our results revealed a porous structure. It was remarkable to note that all microstructural images presented the porous structure about forming of hydrogel by F-T methods similar non F-T method.

The pores are interconnected and regularly distributed. The pores were mostly caused by the F-T process which can show the existence of more obvious pores than non F-T method. Moreover, it seems that with three and five consecutive cycles, the number of pores was less than that with one consecutive cycle. The surface became homogenous when compared to that of the control. This implies that the hydrogel was well packed. With a high number of consecutive cycles of freeze thawing, the crosslinking reaction between DNA and MXene or PVA was successfully prepared. Our results may provide a reliable method for synthesizing DNA hydrogel carriers. Also, our results show that the presence of porous and dense structures of PVA –MB-ssDNA –Mxene using without freeze-thaw technique is more than the consecutive cycles of freeze-thaw technique. This is in agreement with a study by Sornkamnerd et al. on synthesize the tough and porous hydrogels by simple lyophilization of LC gels [12].

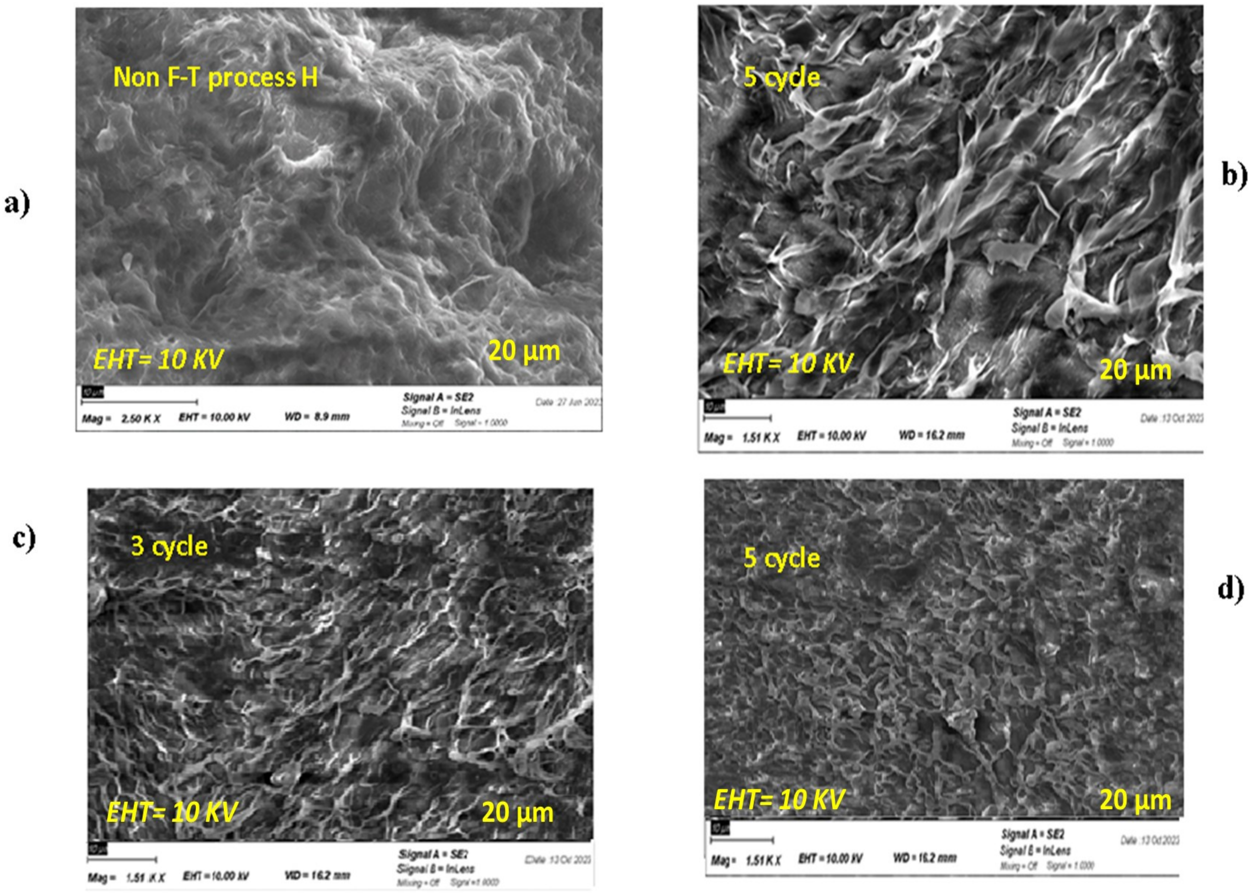

Figure 3. Morphological properties of PVA –MB-ssDNA –Mxene hydrogels. **(a)** PVA –MB-ssDNA –Mxene hydrogels synthesized without F-T methods; **(b–c)** PVA –MB-ssDNA –Mxene hydrogels synthesized with F-T processes.

Differential scanning calorimetry was performed to detect the presence of water molecules in the hydrogel network owing to the large amount of water in the hydrogel. These results showed the water state change in the MXene - and PVA-based hydrogel networks in previous studies. **Figure 4** showed the DSC measurements of DNA, polyvinyl alcohol, and the MXene hydrogel prepared by the freeze–thaw technique. Various compositions of DNA, PVA, and MXene were evaluated based on 1, 3, and 5 consecutive freeze-thaw cycles. All curves were reported in a similar form. The DSC thermogram of of MXene-PVA/MB-ssDNA hydrogel showed a small peak at 70 ℃ and then two large endothermic at approximately 180 ℃ and 300 ℃. DSC characterization confirmed the formation of the new hydrogel. Crosslinked matrices of PVA –MB-ssDNA –Mxene revealed higher thermal stability than MB-DNA. The DSC peaks at 70 ℃ indicate the water loss from the matrices, which was followed by decomposition at approximately 180 ℃ and 300 ℃. Clearly, our hydrogel fabrication method yields thermally stable cross-linked matrices of MB-DNA. DSC results also slightly shifted to 330 ℃ for three and five consecutive cycles. The presence of more PVA-PVA network may enhance the compactness of the hydrogel by the freeze–thaw process. These findings are in good agreement with the F-TIR results.

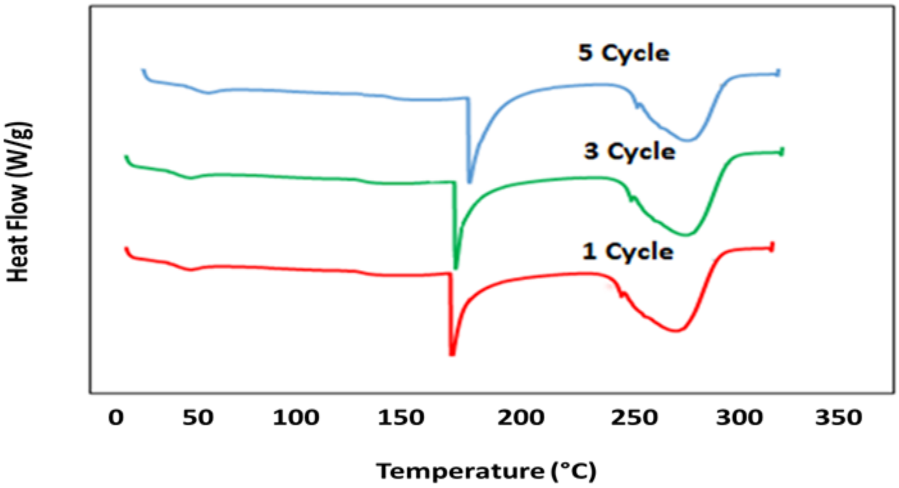

Figure 4. Thermal properties of PVA –MB-ssDNA –Mxene hydrogel composite prepared by freeze thaw process.

Figure 5 showed the swelling characteristics of the PVA –MB-ssDNA –Mxene hydrogel composite. The swelling ratio of the hydrogel structure was observed within 200 min. Subsequently, the swelling ratio remained constant. The swelling behavior can be explained by the hydrophilicity of PVA located inside the hydrogel network. They can adsorb water molecules from the system. These results are consistent with those of a study by Asy-Syifa [13]. As MB-ssDNA contains methylene blue, it can affect the swelling behavior of the PVA –MB-ssDNA –Mxene hydrogel. Martinez et al. showed the swelling and adsorption of MB in a poly (*N*, *N*-dimethylacrylamide-*co*-2-hydroxyethyl methacrylate) hydrogel [14]. MB-ssDNA, as a crosslinker, can reduce the swelling ratio. Our results showed that, as the concentration of MB-ssDNA increased, the swelling rate of the PVA –MB-ssDNA –Mxene hydrogel decreased (**Figure 6**).

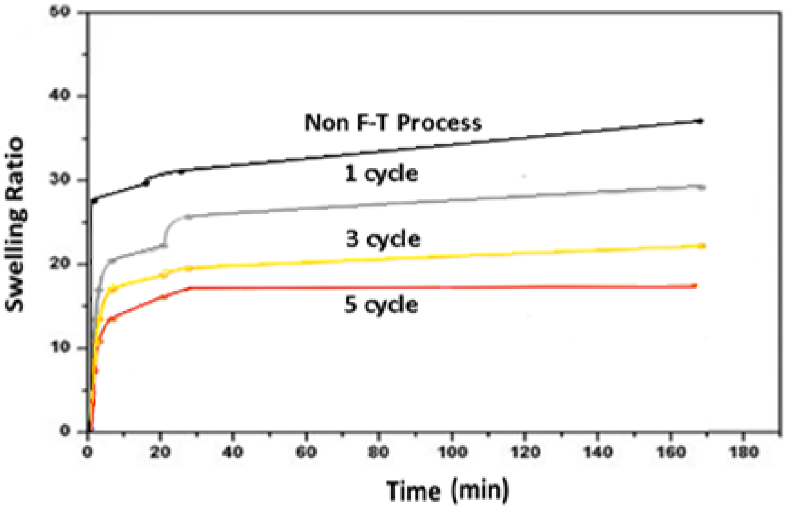

Figure 5. Swelling behavior of PVA –MB-ssDNA –Mxene hydrogel composite prepared by freeze thaw process compare to Non F-T process.

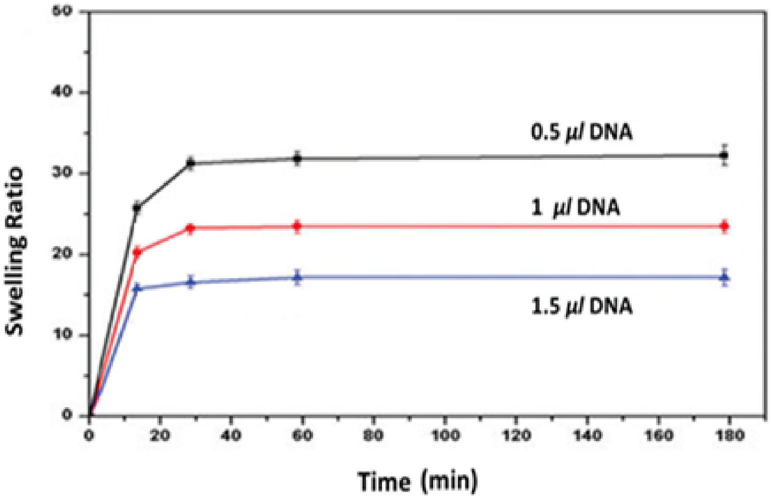

Figure 6. Swelling behavior of PVA –MB-ssDNA –Mxene hydrogel prepared by freeze thaw process with the effecting of MB-ssDNA.

Generally, the swelling behavior is associated with the interconnected porous structure in the hydrogel network, as suggested by Yu et al. [15]. Our results agree with those of the SEM analysis. In addition, the swelling (%) increased as the number of cycles increased to five. At a higher number of cycles (five), the swelling (%) rapidly increased within 30 min and reached equilibrium in approximately 50 min. The blockage of active sites on PVA chains results in a decrease in hydrophilic groups [16]. On the one hand, the swelling ratio of the hydrogel synthesized by non F-T process was lower than the nonporous hydrogels prepared by freeze–thawing of the original hydrogels. This is also in agreement with a study by Sornkamnerd [12].

Analysis of the mechanical properties of hydrogels for medical use is very important. **Figure 7** showed the tensile strength of the PVA –MB-ssDNA –Mxene hydrogel composite. Our measurements were tested, and the data were reported. A uniform structure of PVA –MB-ssDNA –Mxene was prepared by F-T processes, as shown in **Figure 2**. We tested the four measurements and the datas were also evaluated by statistical average and standard deviation.

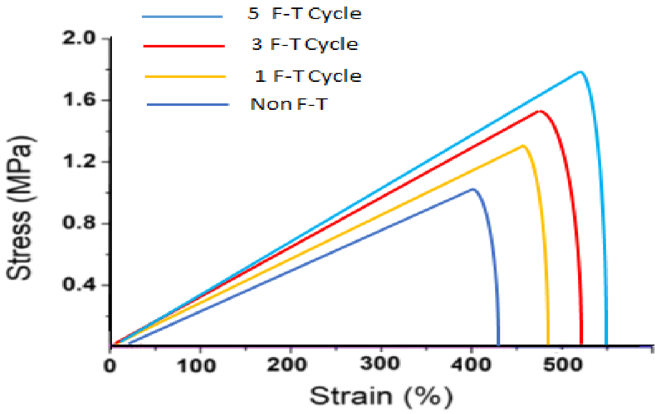

Figure 7. Tensile strength of MB-ssDNA hydrogel prepared by freeze thaw process with the effecting of MB-ssDNA.

Here, the level of tensile strength for all hydrogels by the F-T process in three cycles was in the region of 2.1 MPa to 2.5 MPa. This indicates that the PVA –MB-ssDNA –Mxene hydrogel can be prepared using the F-T technique. Based on our parallel study, it has been shown that MB-DNA can act as a biological cross-linkage which it could increase the tensile strength. As a result of the current study, the F-T process was also influenced by MB-DNA. This indicated that the hydrogel structure with the F-T method was stronger than that without the F-T method. On the hand, the tensile stress can be affected by an increase in the MB-ssDNA concentration, indicating that MB-ssDNA plays a significant role in the enhancement of mechanical strength. In fact, the PVA –MB-ssDNA –Mxene gel was robust, for example, 2 µL MXene-PVA / MB-ssDNA (**Figure 8**).

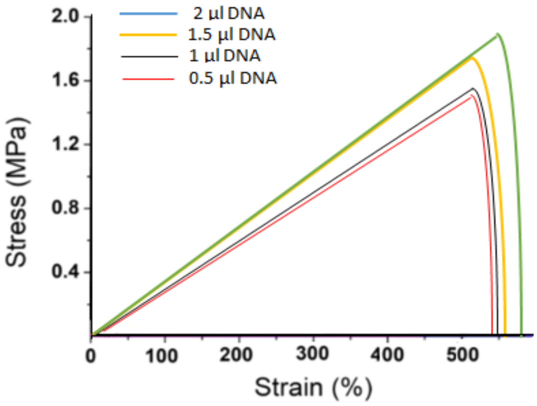

Figure 8. Tensile strength of MB-ssDNA hydrogel prepared by freeze thaw process.

4. Conclusions

The freeze-thawing method is a versatile and straightforward technique for synthesizing hydrogels. This method offers flexibility in terms of tailoring the properties of the hydrogel according to specific requirements, making it highly suitable for various biomedical applications [17,18]. DNA hydrogels are three-dimensional structures composed of crosslinked DNA molecules. These materials possess unique properties such as high water content, biocompatibility, and the ability to respond to external stimuli like temperature variations. However, obtaining hydrogels with precise characteristics and performance remains a challenge. This is where the freeze-thawing method comes into play [19]. In this report, we successfully synthesized the PVA –MB-ssDNA –Mxene hydrogel using the freeze-thaw technique in addition to the effect of MB-ssDNA. Five consecutive freeze-thaw cycles were optimal for hydrogel formation compared to the conventional methods. Fourier transform infrared spectroscopy confirmed that hydrogen bonding resulted in a new inter-and intramolecular network of PVA-PVA throughout the hydrogel network by the OH group affected by MB-ssDNA. Scanning electron microscopy revealed the microstructure of the hydrogel. It presented as a porous network with an increase in DNA concentration, the swelling rate decreased, whereas relatively increase the tensile stress behavior occurred. Also, we showed that freeze-thaw processes can form stronger hydrogels of PVA –MB-ssDNA –Mxene with less swelling behavior compare the non F-T processes. Generally, the PVA –MB-ssDNA –Mxene hydrogel prepared with F-T method exhibited extraordinary properties for use as a medical material.

Authors contributions: Provide draft and methodology, EG; provide some of methodology and editing, SA. All authors have read and agreed to the published version of the manuscript.

Acknowledgments: The authors acknowledge the support of the Alexander von Humboldt Foundation for Elham Ghazizadeh via the Post-Doctoral Research Fellowship

Conflict of interest: The authors declare no conflict interest.

References

1. Bernal-Chávez SA, Romero-Montero A, Hernández-Parra H, et al. Enhancing chemical and physical stability of pharmaceuticals using freeze-thaw method: challenges and opportunities for process optimization through quality by design approach. Journal of Biological Engineering. 2023; 17(1). doi: 10.1186/s13036-023-00353-9
2. Oyama T. Cross-linked polymer synthesis. In: Encyclopedia of polymeric nanomaterials. Berlin, Heidelberg: Springer Berlin Heidelberg; 2014. pp. 1-11.
3. Figueroa-Pizano MD, Vélaz I, Peñas FJ, et al. Effect of freeze-thawing conditions for preparation of chitosan-poly (vinyl alcohol) hydrogels and drug release studies. Carbohydrate Polymers. 2018; 195: 476-485. doi: 10.1016/j.carbpol.2018.05.004
4. Adelnia H, Ensandoost R, Shebbrin Moonshi S, et al. Freeze/thawed polyvinyl alcohol hydrogels: Present, past and future. European Polymer Journal. 2022; 164: 110974. doi: 10.1016/j.eurpolymj.2021.110974
5. Zhong R, Talebian S, Mendes BB, et al. Hydrogels for RNA delivery. Nature Materials. 2023; 22(7): 818-831. doi: 10.1038/s41563-023-01472-w
6. Duran-Mota JA, Yani JQ, Almquist BD, et al. Polyplex-Loaded Hydrogels for Local Gene Delivery to Human Dermal Fibroblasts. ACS Biomaterials Science & Engineering. 2021; 7(9): 4347-4361. doi: 10.1021/acsbiomaterials.1c00159
7. Zhao X, Tian M, Wei R, et al. Facile fabrication of a novel self-healing and flame-retardant hydrogel/MXene coating for wood. Scientific Reports. 2023; 13(1). doi: 10.1038/s41598-023-28228-5
8. Waresindo WX, Luthfianti HR, Edikresnha D, et al. A freeze–thaw PVA hydrogel loaded with guava leaf extract: physical and antibacterial properties. RSC Advances. 2021; 11(48): 30156-30171. doi: 10.1039/d1ra04092h
9. Shin MK, Kim SH, Jung S il, et al. The effect of DNA on mechanical properties of nanofiber hydrogels. Applied Physics Letters. 2008; 93(17). doi: 10.1063/1.3009204
10. Waresindo WX, Luthfianti HR, Edikresnha D, et al. A freeze–thaw PVA hydrogel loaded with guava leaf extract: physical and antibacterial properties. RSC Advances. 2021; 11(48): 30156-30171. doi: 10.1039/d1ra04092h

11. Lim S, Kim JH, Park H, et al. Role of electrostatic interactions in the adsorption of dye molecules by Ti3C2-MXenes. ACS Omega. 2017; 2(8): 5304-5314.
12. Sornkamnerd S, Okajima MK, Kaneko T. Tough and Porous Hydrogels Prepared by Simple Lyophilization of LC Gels. ACS Omega. 2017; 2(8): 5304-5314. doi: 10.1021/acsomega.7b00602
13. Asy-Syifa N, Kusjuriansah, Waresindo WX, et al. The Study of the Swelling Degree of the PVA Hydrogel with varying concentrations of PVA. Journal of Physics: Conference Series. 2022; 2243(1): 012053. doi: 10.1088/1742-6596/2243/1/012053
14. Hernandez-Martínez AR, Lujan-Montelongo JA, Silva-Cuevas C, et al. Swelling and methylene blue adsorption of poly(N,N-dimethylacrylamide-co-2-hydroxyethyl methacrylate) hydrogel. Reactive and Functional Polymers. 2018; 122: 75-84. doi: 10.1016/j.reactfunctpolym.2017.11.008
15. Guo Y, de Vasconcelos LS, Manohar N, et al. Highly Elastic Interconnected Porous Hydrogels through Self-Assembled Templating for Solar Water Purification. Angewandte Chemie International Edition. 2021; 61(3). doi: 10.1002/anie.202114074
16. Muangsri R, Chuysinuan P, Thanyacharoen T, et al. Utilization of freeze thaw process for polyvinyl alcohol/sodium alginate (PVA/SA) hydrogel composite. Journal of Metals, Materials and Minerals. 2022; 32(2): 34-41. doi: 10.55713/jmmm.v32i2.1257
17. Szekalska M, Sosnowska K, Wróblewska M, et al. Does the Freeze–Thaw Technique Affect the Properties of the Alginate/Chitosan Glutamate Gels with Posaconazole as a Model Antifungal Drug? International Journal of Molecular Sciences. 2022; 23(12): 6775. doi: 10.3390/ijms23126775
18. Waresindo WX, Luthfianti HR, Priyanto A, et al. Freeze–thaw hydrogel fabrication method: basic principles, synthesis parameters, properties, and biomedical applications. Materials Research Express. 2023; 10(2): 024003. doi: 10.1088/2053-1591/acb98e
19. Adelnia H, Ensandoost R, Shebbrin Moonshi S, et al. Freeze/thawed polyvinyl alcohol hydrogels: Present, past and future. European Polymer Journal. 2022; 164: 110974. doi: 10.1016/j.eurpolymj.2021.110974

Characterization and Application of Nanomaterials 2024, 7(2), 4946.
https://doi.org/10.24294/can.v7i2.4946

Review

Modernizations of graphene nanocomposites using synthesis strategies—State-of-the-art

Ayesha Kausar[1,2,*], **Ishaq Ahmad**[1,2]

[1] NPU-NCP Joint International Research Center on Advanced Nanomaterials and Defects Engineering, Northwestern Polytechnical University, Xi'an 710072, China
[2] UNESCO-UNISA Africa Chair in Nanosciences/Nanotechnology, iThemba LABS, Somerset West 7129, South Africa
*** Corresponding author:** Ayesha Kausar, dr.ayeshakausar@yahoo.com

CITATION

Kausar A, Ahmad I. Modernizations of graphene nanocomposites using synthesis strategies—State-of-the-art. Characterization and Application of Nanomaterials. 2024; 7(2): 4946. https://doi.org/10.24294/can.v7i2.4946

ARTICLE INFO

Received: 1 March 2024
Accepted: 6 May 2024
Available online: 1 July 2024

Abstract: Graphene has been ranked among one of the most remarkable nanostructures in the carbon world. Graphene modification and nanocomposite formation have been used to expand the practical potential of graphene nanostructure. The overview is an effort to highlight the indispensable synthesis strategies towards the formation of graphene nanocomposites. Consequently, graphene has been combined with useful matrices (thermoplastic, conducting, or others) to attain the desired end material. Common fabrication approaches like the in-situ method, solution processing, and melt extrusion have been widely involved to form the graphene nanocomposites. Moreover, advanced, sophisticated methods such as three- or four-dimensional printing, electrospinning, and others have been used to synthesize the graphene nanocomposites. The focus of all synthesis strategies has remained on the standardized graphene dispersion, physical properties, and applications. However, continuous future efforts are required to resolve the challenges in synthesis strategies and optimization of the parameters behind each technique. As the graphene nanocomposite design and properties directly depend upon the fabrication techniques used, there is an obvious need for the development of advanced methods having better control over process parameters. Here, the main challenging factors may involve the precise parameter control of the advanced techniques used for graphene nanocomposite manufacturing. Hence, there is not only a need for current and future research to resolve the field challenges related to material fabrication, but also reporting compiled review articles can be useful for interested field researchers towards challenge solving and future developments in graphene manufacturing.

Keywords: graphene; nanocomposite; synthesis; technique; in situ; melt extrusion

1. Introduction

Due to the technical utilization of graphene nanostructures, considerable literature has been reported on the structure and synthesis methods [1]. Particularly, matrix-nanofiller compatibility has been found important to enhance the optical, electronic, thermal, mechanical, and other important properties of the graphene nanocomposites [2,3]. Consequently, the miscibility effects in the nanocomposite nanostructure resulted in synergistic property improvements in the high-tech nanomaterial [4]. The interfacial interactions in the matrix-nanofiller system greatly depend on the synthesis strategies used [5]. In this context, choice of an appropriate synthesis method may lead to advanced nanocomposite with superior physical features [6]. Traditional methods used to form the polymer/graphene nanocomposites include the in situ, solution, and melt methods [7]. In addition, various efficient advanced processes have been used to form the graphene nanocomposites, like printing, spinning lithography, and several others [8,9]. Consequently, thermoplasts, thermosets, and conjugated matrices have been filled with graphene nanoparticles to attain superior properties and applications [10–12]. The resulting graphene nanocomposites have enhanced physical properties due to suitable processing techniques applied to gain improved interfacial aspects of these nanomaterials [13].

Hence, noteworthy chemical and physical properties of graphene have been widely inspected by the researchers over the past decades. Graphene has been used in numerous potential fields due to its high surface area and excellent electrical, mechanical, thermal, and other structural and physical characteristics. Consequently, graphene has been found applicable for energy devices, electronics, sensors, nanocomposites, biomedical devices, drug delivery, and tissue engineering. To enhance the practical use of graphene nanocomposite in technical fields, it has been found important to fabricate the graphene-based materials by opting for appropriate synthesis strategies. Advanced fabrication techniques have well-controlled parameters to attain specific properties of graphene nanocomposites for desired end applications.

This review focuses on the designs and synthesis strategies for the high-performance graphene nanocomposites. According to analysis, this article is novel to present manufacturing approaches of novel graphene-derived nanocomposites. For graphene nanocomposites, various traditional and modified methods have been used. Developments in the synthesis techniques of graphene nanocomposites can enhance the technical potential of these nanomaterials. Consequently, the designing, features, and appropriate processes for the graphene nanocomposites have been explained here. Literature research reports so far have been observed on the fabrication of graphene-based nanomaterials using appropriate synthesis strategies. However, no compiled review article is seen on technical fabrication techniques and comprehensive debates towards structural developments using modified methods and controlled parameters. The aim or objective of this review is to develop a comprehensive article on the most frequently used methods for graphene nanomaterial synthesis. Accordingly, the resulting graphene nanocomposites have been discussed under numerous categories of solution, melt, and other fabrication techniques in this article. Then, the design, characteristics, and applications of the nanocomposites have been explained with respect to the fabrication methods used. Thus, such a specific overview on graphene nanocomposite fabrication has not been seen in literature before, with well-explained recent literature and an outline. Despite the advancements so far, devoted future research efforts are still required on the fabrication of high-performance nanocomposite to overcome the related design and parameter control challenges.

2. Graphene

Graphene is a two-dimensional single nanosheet of sp^2 hybridized carbons [14]. Detection of graphene is linked back to 2004 [15]. Graphene has been formed using many technical approaches, like exfoliation approaches, laser methods, chemical vapor deposition, and chemical synthesis approaches [16]. Graphene has been explored for a range of structural and physical features [17]. Graphene has countless enhanced features, including a very high Young’s modulus of 1 TPa, electron mobilization of 3000–5000 W/mK, and thermal conductivity of around 200,000

$cm^2V^{-1}s^{-1}$ [18]. Essential properties of graphene have been found to be dependent on the graphene nanostructure [19]. Owing to van der Waals forces, the nanosheet displays wrinkling effects [20]. To augment the structural features of graphene, the nanosheet has been functionalized to introduce oxygen-bearing groups on the surface [21]. Such a surface functional graphene nanosheet with hydroxyl, carbonyl, epoxide, carboxylic acid, etc. groups has been often termed graphene oxide. Graphene and some linked nanostructures are shown in **Figure 1**. Graphene and derivative nanostructures own fine electronic, mechanical, thermal, and chemical characters [22]. Consequently, applications of graphene have been observed towards electronics as well as energy devices and countless other technological sectors [23,24].

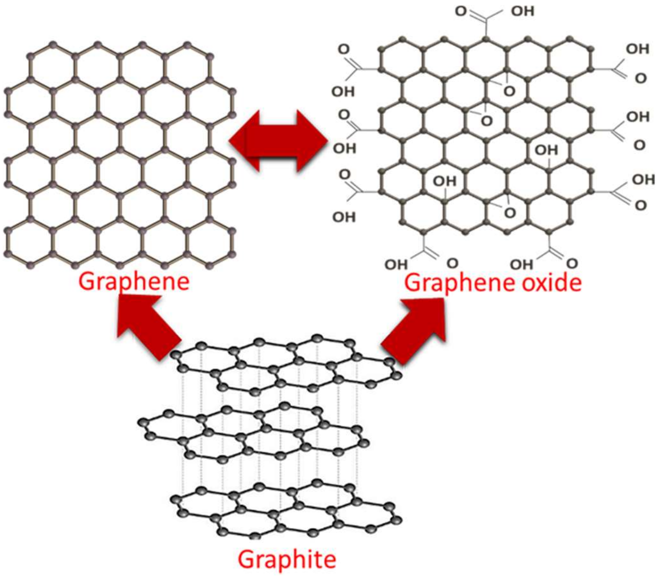

Figure 1. Graphite to graphene and graphene oxide and interconversions.

3. In situ technique towards graphene nanocomposites

One of the simple and efficient methods for the formation of graphene nanocomposites is the in situ polymerization, or in situ method [25]. This synthesis strategy has been found effective for better graphene dispersion [26]. Fine nanoparticle scattering in turn generated better interactions in matrix-nanofiller phases [27]. The main benefits of the in situ synthesis strategy include the environmental friendliness, use of non-toxic solvents, room-temperature processing, and one-step processes involved to form the graphene nanocomposites [28]. Subsequently, countless graphene nanocomposite designs have been reported using the in situ synthesis strategy [29]. The in situ technique is a facile, low-cost, and environmentally benign method to physically or covalently functionalize graphene nanosheets. In this method, monomers are in situ polymerized in the presence of graphene or graphene oxide to form the nanocomposites. In situ polymerization has been used as a common method for the polymerization of ε-caprolactam monomer to form the polyamide 6 backbone [30]. Adding 1–2 vol.% graphene contents along with ε-caprolactam monomer during in situ polymerization resulted in a reasonable electrical conductivity of ~0.028 Sm^{-1}. In addition, the resulting in situ polymerized polyamide 6/graphene nanocomposites have revealed the superior thermal conductivity of around 0.27 $Wm^{-1}K^{-1}$ [31,32]. In situ synthesis strategy has also led to enhanced mechanical properties of the polyamide 6/graphene nanocomposites [33]. Elevated tensile strength and Young's modulus were found with a 0.1 wt.% graphene nanofiller addition. The improved properties were accredited to the mutual interactions between the matrix and nanofillers leading to compatibility effects. Xu et al. [33] synthesized the polyamide 6 and graphene-derived nanocomposites using the in situ polymerization method. The caprolactam monomer was in situ polymerized by the ring-opening polymerization reaction [34]. The reaction was carried out in the presence of graphene oxide nanoparticles to follow the in situ process (**Figure 2**). This method involved the use of 6 aminocaproic acid for an in situ process. This technique caused fine dispersion of monomers as well as graphene nanoparticles in solvent medium, followed by the in situ polymerization to form the polyamide 6/graphene nanocomposite. **Figure 3** displays the stress strain curves of unfilled polyamide 6 as well as 0.01 and 0.1 wt.% nano-additive reinforced graphene nanocomposites. The 0.01 and 0.1 wt.% graphene-loaded nanocomposite had tensile strengths of 84 and 123 MPa, respectively, relative to the neat matrix (56 MPa). Hereafter, the mechanical properties of the nanocomposites were found to be more than 50% higher than the unfilled matrix. Hence, this method has been suggested to minimize the nanoparticle dispersion responsible for improved features of the nanomaterials.

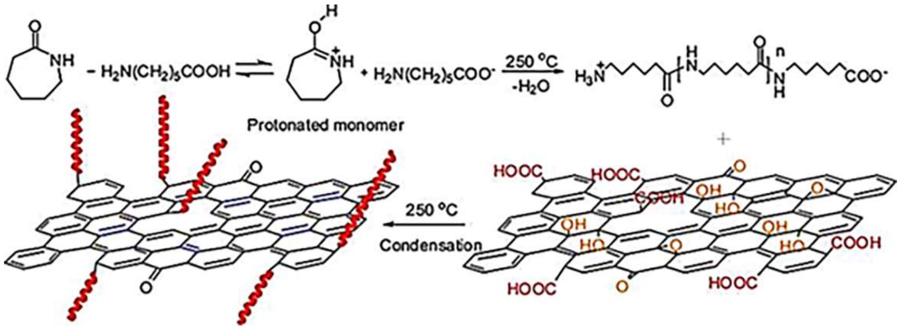

Figure 2. In situ synthesis strategy of graphene nanocomposite by in situ ring opening polymerization of caprolactam occurring in the presence of graphene oxide [33]. Reproduced with permission from ACS.

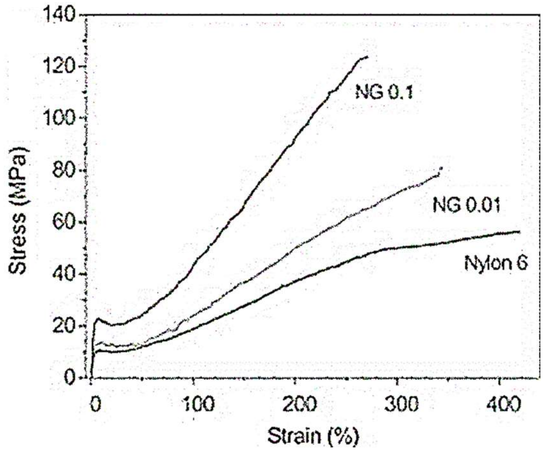

Figure 3. Stress strain curves of neat polyamide 6 and nano-graphene (NG) nanocomposites with 0.01 and 0.1 wt.% graphene additions [33]. Reproduced with permission from ACS.

Polystyrene, another commodity thermoplastic, has also been polymerized by in situ technique [35,36]. In the presence of styrene monomer and graphene dispersion, the in situ polymerization method is applied using surfactants [37,38]. Styrene monomer is absorbed on graphene surface and then polymerized, leading to fine dispersion of nanoparticles and compatibility with the matrix [39,40]. In this way, in situ-produced nanocomposite had fine interactions leading to high electron conduction, heat stabilization, glass transition, and other improved properties [41,42]. Poly(methyl methacrylate) and graphene-derived nanocomposites have also been formed using the in situ method and polymerizing the methyl methacrylate monomers [43,44]. Physical as well as covalent bindings have been observed between the poly(methyl methacrylate) and graphene nanoparticles [45]. Reports on waterborne polyurethane and graphene-based in situ-formed nanomaterials have also been found in the literature [46,47]. Here again, interfacial interactions between matrix and nanofiller led to enhanced performance, thus depicting the efficiency of the in situ technique [48].

4. Solution strategies for graphene nanocomposites

Another common synthesis strategy to form graphene nanocomposites is solution casting, solution synthesis, or solvent-based processing approaches [49,50]. The solvent method is facile and low-cost for the formation of graphene nanocomposites [51]. In this technique, polymers are dissolved in a suitable solvent, and graphene nanosheets are also dispersed in an appropriate solvent [52]. Both the dispersions are mixed and stirred to form a homogeneous nanocomposite mixture (**Figure 4**). The nanocomposite formation occurs through the solvent evaporation step. Numerous thermoplastic polymers have been successfully formed by solution technique [53,54]. For example, polystyrene and graphene-based nanocomposites have been prepared using solution processing [55]. N-methyl-2-pyrrolidinone was used as a solvent to dissolve polystyrene and disperse graphene nanoparticles. The addition of 10 wt.% nanofiller enhanced the electrical conductivity of the polystyrene matrix to 1.5×10^{-7} Sm^{-1} [56]. In this concern, the microstructure and matrix-nanofiller interactions in solution-formed nanomaterials have been investigated [57].

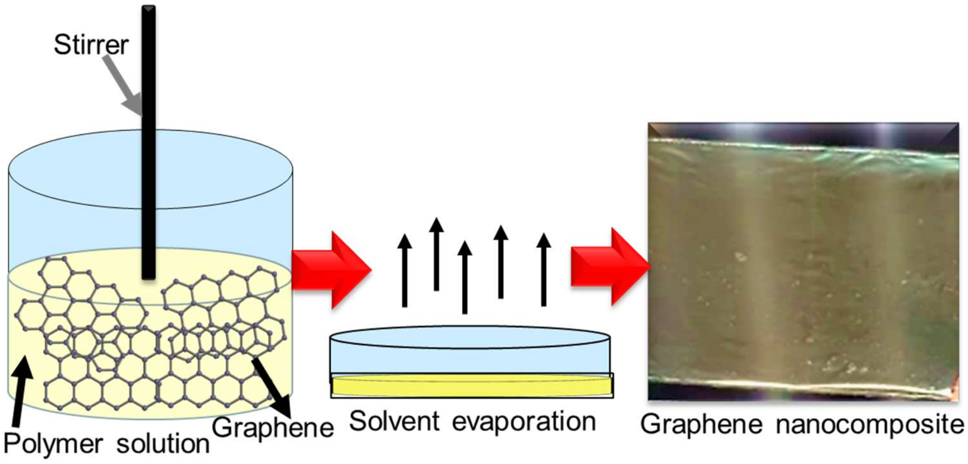

Figure 4. A simple route of solution method.

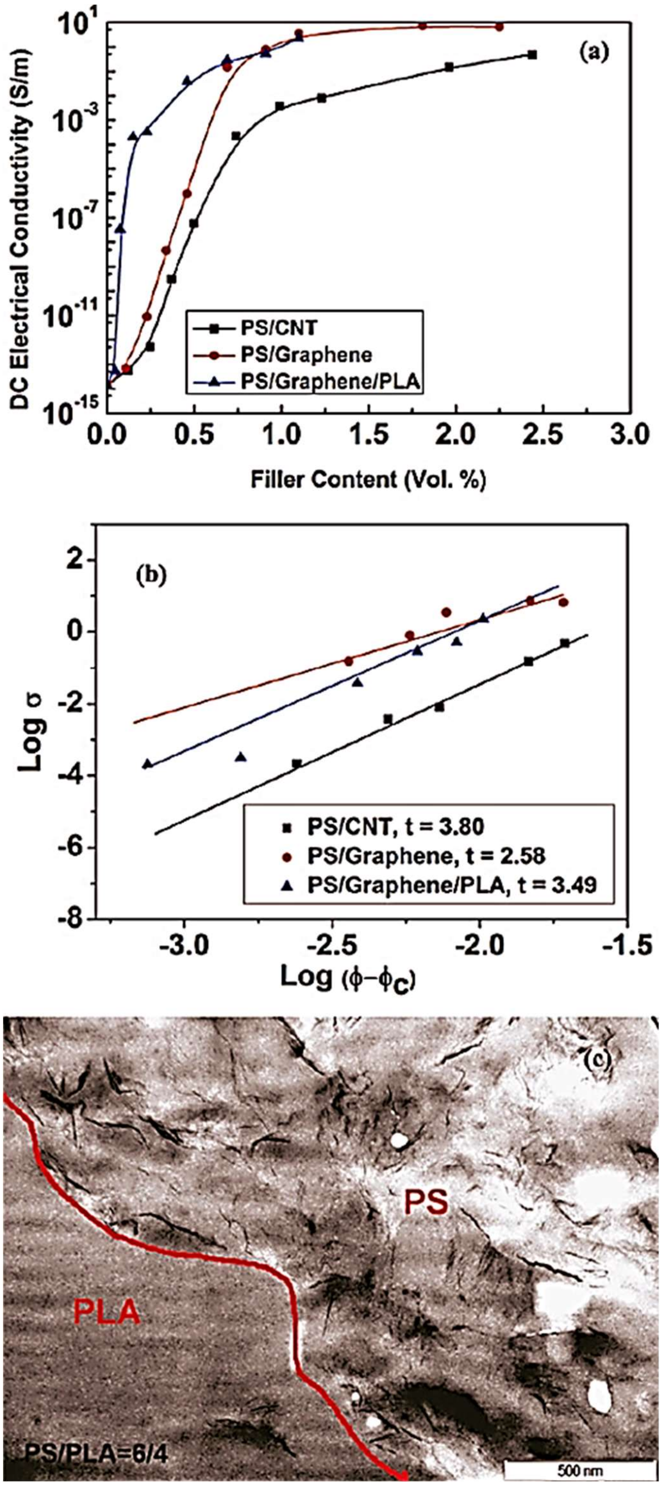

Figure 5. (a) Electrical conductivity versus filler content for neat polystyrene (PS) and its nanocomposites; **(b)** Double-logarithmic plot of electrical conductivity versus ϕ-ϕ_c, where ϕ is the filler volume fraction and ϕ_c is the percolation threshold; and **(c)** Transmission electron microscopy image of PS:PLA (6:4) composite with ~0.46 vol.% (~1.0 wt.%) graphene additives. The selective localization of graphene in the polystyrene region is evident from the image [58]. PS/CNT = polystyrene/carbon nanotube; PS = polystyrene; PLA = poly (lactic acid); PS/PLA = polystyrene/poly (lactic acid). Reproduced with permission from ACS.

Qi et al. [58] synthesized polystyrene/graphene, polystyrene/graphene/poly (lactic acid), and polystyrene/carbon nanotube nanocomposites using solution strategy. **Figure 5** demonstrates an increase in the electrical conductivity of the polystyrene/graphene nanocomposites with the addition of 0.1 to 0.69 vol.% nanofiller. High electrical conductivity of 3.49 Sm^{-1} was observed with 1.1 vol.% graphene contents. Nanoparticle dispersion formed a conducting network in the matrix to improve the electrical conductivity values at the percolation threshold. Furthermore, double-logarithmic plots of the polystyrene/graphene (0.33 vol.%) and polystyrene/carbon nanotube (0.50 vol.%) nanocomposites depicted values at 3.80 and 2.58, respectively. Transmission electron microscopy image of polystyrene/poly(lactic acid) blend showed two-phase morphology. Graphene nanoparticles can be seen dispersed in the polystyrene matrix.

Poly (methyl methacrylate) and graphene-based nanocomposites have been reported using the solution technique [59]. These nanomaterials have been studied for morphology, electrical conductivity, and mechanical characters [60]. The poly(methyl methacrylate) filled with 2.0 wt.% graphene contents had a high electrical conductivity of 0.04 Sm^{-1}. Enhancement in electrical conductivity was attributed to the formation of interlinked graphene networks in the matrix [61]. Polyethylene and graphene based nanocomposites were also formed using the solution method [62,63]. Similarly, poly(vinyl alcohol) and graphene-based nanomaterials have been developed using the solvent method [64]. Inclusion of 6.5 vol.% graphene to the matrix led to a high conductivity of 0.06 Scm^{-1}. In addition, the Young's modulus of poly(vinyl alcohol) was enhanced by 58% [65]. Consequently, the low-cost, simple, and ecofriendly solution technique has been applied to a variety of thermoplastics and graphene nanofillers. The resulting high-performance nanocomposites have superior dispersion, electrical and thermal conductivity, glass transition temperature, thermal stability, and mechanical strength performances [66,67].

5. Melt strategy for graphene nanocomposites

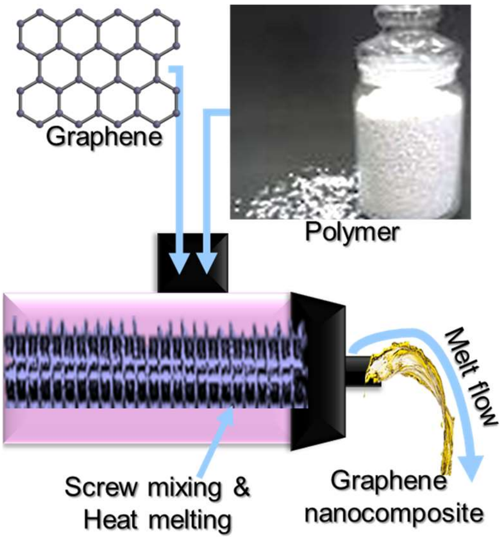

Figure 6. Schematic of melt strategy.

Subsequently, numerous thermoplastic matrices have been melt processed with graphene nanoparticles [75]. Polystyrene and graphene-based nanocomposites have been developed using melt blending [76,77]. These nanomaterials have revealed fine dispersion and electron conduction features. Shen and colleagues [78] industrialized the polystyrene and graphene derivative nanocomposites through melt blending. **Figure 7** shows a schematic for the development of π-π stacking interactions in melt blending of polystyrene/graphene nanomaterials. Due to high shear forces, polymer chains are inserted between the graphene nanosheets. **Figure 8** reveals the thermogravimetric analysis of the polystyrene/functional graphene nanocomposites. Inclusion of 5 to 60 wt.% nanofiller considerably boosted the thermal stability of the polystyrene matrix.

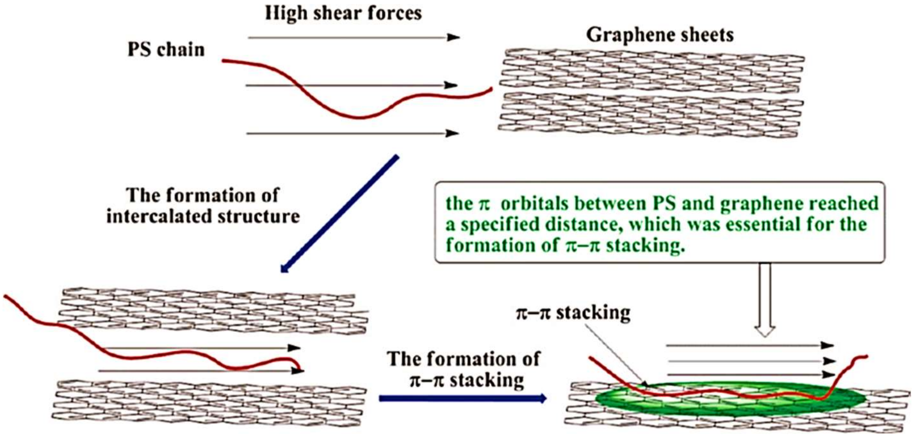

Figure 7. Schematic for the formation of π-π stacking during melt blending [78]. PS = polystyrene. Reproduced with permission from ACS.

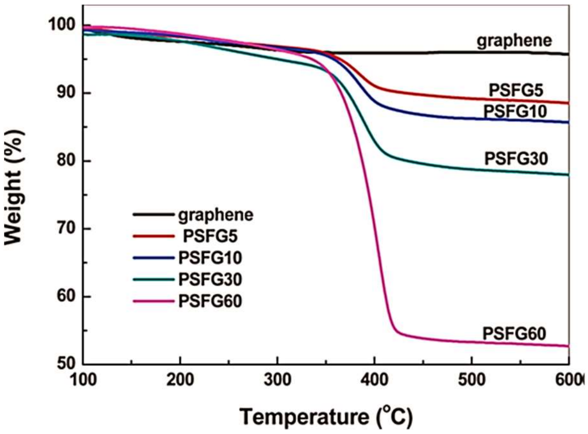

Figure 8. Thermogravimetric analysis curves of nanocomposites. PSFG = polystyrene/functional graphene. 5, 10, 30, 60 = nanofiller contents in designations [78]. Reproduced with permission from ACS.

The graphene-filled polypropylene nanocomposites were processed using the melt blending technique for enhanced electrical, thermal, and mechanical features [79]. The elevated performance was attributed to the interfacial interactions in the matrix-nanofiller [80]. Melt-processed graphene-filled polyethylene and polyethylene terephthalate nanocomposites have been developed with elevated strength features [81,82]. The poly(methyl methacrylate) nanocomposites with graphene have also been prepared through melt blending practice [83]. The melt strategy has been found facile, low-cost, and large-scale processable [84,85]. Controlling the reaction temperature, time, and shear and extrusion rate may define fine dispersion in the polymeric matrices [86,87].

6. More synthesis strategies

For graphene nanocomposites, solution approaches have been applied as effective methods; however, complex posttreatments must be used for solvent evaporation [88]. A range of other synthesis strategies have been found effective for the formation of graphene nanocomposites. Essential processing techniques include three- or four-dimensional printing approaches [89]. Among printing methods, stereolithography [90], inkjet printing [91], selective laser sintering [92], direct ink writing [93], fused deposition modeling [94], and others have been used. Printing techniques have been used to enhance the dispersion as well as the end properties and performances of the graphene nanomaterials [95,96]. Choice of a particular printing technique has been found critical to form the desired material and properties. Accordingly, the performance of printed material relies on the polymer type, nanoparticle dispersion, interactions, and printing parameters. The direct three-dimensional printing involves the extrusion of viscous material from the pressurized syringe to form the three-dimensional shapes. The fused deposition modeling printing performs with controlled filament extrusion. By controlling the printing parameters, product quality can be managed. The selective laser sintering uses high power lasers to fuse the powder, and product resolution depends upon the powder specifications, laser power, and scan speed. Electrospinning has also been adopted as an efficient and sophisticated method to form the high-tech nanomaterials [97,98]. By using electrospinning, finely reinforced graphene nanocomposites have been designed [98,99]. This technique may include a syringe, spinneret, collector, and voltage-based system [100,101]. Resulting electrospun graphene nanocomposite nanofibers have been tested for high electrical, mechanical, thermal, and other advanced technical features [102]. **Table 1** displays essential details of some literature-reported graphene-filled nanocomposite designs formed using efficient synthesis strategies. Hence, the manufacturing technique relies on the inherent features of graphene nanomaterials.

Table 1. Specs of graphene nanocomposites thru various synthesis strategies.

Matrices	Nanofiller	Manufacturing	Ref.
Polystyrene	Graphene	In situ polymerization	[35]
Polyamide 6	Graphene	In situ polymerization	[31]
Polyamide 6	Graphene	In situ polymerization	[32]
Polystyrene	Graphene	Solution method	[56]
Poly (methyl methacrylate)	Graphene	Solution method	[60]
Poly (methyl methacrylate)	Graphene	Solution method	[61]
Poly (vinyl alcohol)	Graphene	Solution method	[64]
Polystyrene, polycarbonate, polypropylene, high density polyethylene, low density polyethylene	Graphene	Melt compounding	[75]
Poly (methyl methacrylate), polystyrene, polybutyl acylate	Graphene	Atom transfer radical polymerization	[103]
Polystyrene, poly (methyl methacrylate), poly (vinyl fluoride)	Graphene	Colloid method	[104]

7. Scenarios and conclusions

Graphene nanocomposites have been designed using several simple and sophisticated synthesis strategies (**Figure 9**) [105]. Choice of a particular technique always relies on the cost, ease of processing, and opportunities for large-scale production [106,107]. Accordingly, graphene dispersion, matrix-nanofiller interactions, and interface developments were influenced. Consequently, suitable synthesis technique has been found important to improve the nanocomposite features and end uses of the graphene nanocomposites [108]. Here, each synthesis method owns relevant advantages and disadvantages towards the formation of graphene nanomaterials [109].

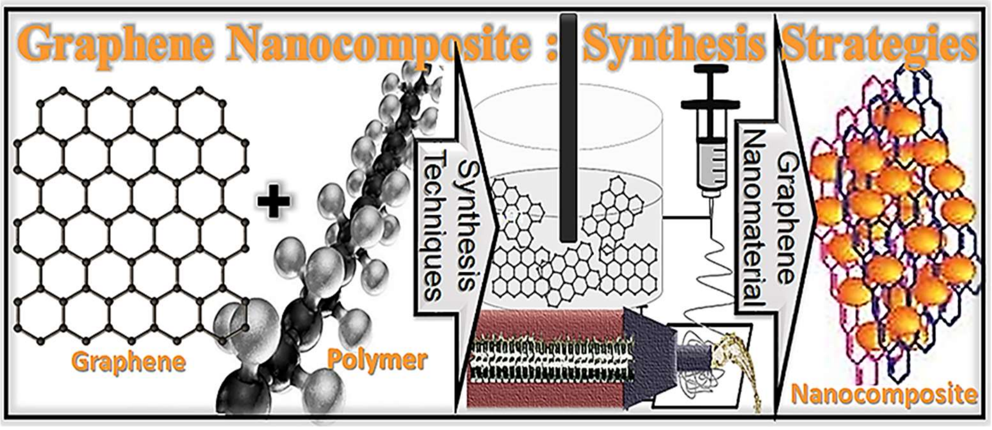

Figure 9. Synthesis strategies for graphene nanocomposites.

Solution synthesis is a simple method; however, this may include the drawback of using toxic solvents. The in situ technique, on the other hand, has resolved this issue by using environmentally friendly solvents [110]. The melt method has also been found beneficial, avoiding the use of any toxic solvent. Sometimes the melt extrusion method may have the drawback of poor graphene dispersion in the nanocomposites. Therefore, the nanofiller dispersion depends on the type of synthesis strategy used. Sophisticated techniques like printing and electrospinning have been found effective to form well-dispersed high-performance graphene nanocomposites [111]. However, these techniques have drawbacks of high cost and limitations for large scale processing [112,113]. Moreover, nanoparticle aggregation has been found challenging in sophisticated techniques like coating and prating [114]. Beside studying the experimentally processed graphene nanocomposites, theoretical approaches like molecular dynamics or simulation must be applied for graphene nanomaterials [115]. Henceforth, research efforts have focused on the use of appropriate synthesis techniques and controlled processing parameters to attain high-performance graphene nanocomposites. Main application areas recognized for the well-processed graphene nanocomposites include batteries, supercapacitors, solar cells, fuel cells, coatings, membranes, engineering structures, space, automobiles, and other transportation sectors.

In short, this article summarizes the synthesis strategies widely used for the formation of graphene nanocomposites. Most importantly, in situ strategy, solution processing, melt blending, printing, spinning, and numerous other methods can be adopted for the development of efficient graphene-filled nanomaterials. Here, a suitable method may reveal fine graphene dispersion, matrix-nanofiller associations, and physical property enhancements. In this context, important microstructure, electrical, thermal, and mechanical features were improved with the graphene additions. Consequently, the nanocomposite performance was enhanced by controlling the parameters of the synthesis strategies used. Future progress on the processing of graphene nanocomposites may lead to the development of advanced next-level approaches for the formation of high-tech nanomaterials.

Conflict of interest: The authors declare no conflict of interest.

References

1. Kausar A, Ahmad I, Lam TD. High-tech graphene oxide reinforced conducting matrix nanocomposites—Current status and progress. Characterization and Application of Nanomaterials. 2023; 6(1). doi: 10.24294/can.v6i1.2637
2. Kausar A, Ahmad I. Graphene and nanocomposites—Imprints on environmentally sustainable production and applications based on ecological aspects. Characterization and Application of Nanomaterials. 2024; 7(1): 4226. doi: 10.24294/can.v7i1.4226
3. Kausar A, Ahmad I. Cutting-edge conjugated nanocomposites—Fundamentals and anti-corrosion significance. Characterization and Application of Nanomaterials. 2023; 6(2): 3361. doi: 10.24294/can.v6i2.3361
4. Idumah CI. Phosphorene polymeric nanocomposites for biomedical applications: a review. International Journal of Polymeric Materials and Polymeric Biomaterials. 2022; 73(4): 292-309. doi: 10.1080/00914037.2022.2158333
5. Cai C, Liu L, Fu Y. Processable conductive and mechanically reinforced polylactide/graphene bionanocomposites through interfacial compatibilizer. Polymer Composites. 2017; 40(1): 389-400. doi: 10.1002/pc.24663
6. Potts JR, Dreyer DR, Bielawski CW, et al. Graphene-based polymer nanocomposites. Polymer. 2011; 52(1): 5-25. doi: 10.1016/j.polymer.2010.11.042
7. Tripathy DB, Gupta A. Nanocomposites as sustainable smart materials: A review. Journal of Reinforced Plastics and Composites. 2024. doi: 10.1177/07316844241233162
8. Yousefi N, Gudarzi MM, Zheng Q, et al. Self-alignment and high electrical conductivity of ultralarge graphene oxide–polyurethane nanocomposites. Journal of Materials Chemistry. 2012; 22(25): 12709. doi: 10.1039/c2jm30590a
9. Goyal M, Singh K, Bhatnagar N. Conductive polymers: A multipurpose material for protecting coating. Progress in Organic Coatings. 2024; 187: 108083. doi: 10.1016/j.porgcoat.2023.108083
10. Yan Y, Han M, Jiang Y, et al. Electrically Conductive Polymers for Additive Manufacturing. ACS Applied Materials & Interfaces. 2024; 16(5): 5337-5354. doi: 10.1021/acsami.3c13258
11. Balaji KV, Shirvanimoghaddam K, Naebe M. Multifunctional basalt fiber polymer composites enabled by carbon nanotubes and graphene. Composites Part B: Engineering. 2024; 268: 111070. doi: 10.1016/j.compositesb.2023.111070
12. Lee SH, Luvnish A, Su X, et al. Advancements in polymer (Nano)composites for phase change material-based thermal storage: A focus on thermoplastic matrices and ceramic/carbon fillers. Smart Materials in Manufacturing. 2024; 2: 100044. doi: 10.1016/j.smmf.2024.100044
13. Abbasi H, Antunes M, Velasco JI. Recent advances in carbon-based polymer nanocomposites for electromagnetic interference shielding. Progress in Materials Science. 2019; 103: 319-373. doi: 10.1016/j.pmatsci.2019.02.003
14. Gao Y, Zhang Y, Chen P, et al. Toward Single-Layer Uniform Hexagonal Boron Nitride–Graphene Patchworks with Zigzag Linking Edges. Nano Letters. 2013; 13(7): 3439-3443. doi: 10.1021/nl4021123
15. Berger C, Song Z, Li X, et al. Electronic Confinement and Coherence in Patterned Epitaxial Graphene. Science. 2006; 312(5777): 1191-1196. doi: 10.1126/science.1125925
16. Wei C, Negishi R, Ogawa Y, et al. Turbostratic multilayer graphene synthesis on CVD graphene template toward improving electrical performance. Japanese Journal of Applied Physics. 2019; 58(SI): SIIB04. doi: 10.7567/1347-4065/ab0c7b
17. Narayanam PK, Botcha VD, Ghosh M, et al. Growth and photocatalytic behavior of transparent reduced GO–ZnO nanocomposite sheets. Nanotechnology. 2019; 30(48): 485601. doi: 10.1088/1361-6528/ab3ced

18. Zandiatashbar A, Lee GH, An SJ, et al. Effect of defects on the intrinsic strength and stiffness of graphene. Nature Communications. 2014; 5(1). doi: 10.1038/ncomms4186
19. Shen X, Zeng X, Dang C. Graphene Composites. In: Celasco E, Chaika AN, Stauber T, et al.(editors). Handbook of Graphene Set. Scrivener Publishing; 2019. pp. 1-25. doi: 10.1002/9781119468455.ch53
20. Zhou Q, Xia G, Du M, et al. Scotch-tape-like exfoliation effect of graphene quantum dots for efficient preparation of graphene nanosheets in water. Applied Surface Science. 2019; 483: 52-59. doi: 10.1016/j.apsusc.2019.03.290
21. Pei S, Cheng HM. The reduction of graphene oxide. Carbon. 2012; 50(9): 3210-3228. doi: 10.1016/j.carbon.2011.11.010
22. Lee H, Lee KS. Interlayer Distance Controlled Graphene, Supercapacitor and Method of Producing the Same. US20150103469A1, 26 February 2019.
23. Tang C, Titirici MM, Zhang Q. A review of nanocarbons in energy electrocatalysis: Multifunctional substrates and highly active sites. Journal of Energy Chemistry. 2017; 26(6): 1077-1093. doi: 10.1016/j.jechem.2017.08.008
24. Panwar N, Soehartono AM, Chan KK, et al. Nanocarbons for Biology and Medicine: Sensing, Imaging, and Drug Delivery. Chemical Reviews. 2019; 119(16): 9559-9656. doi: 10.1021/acs.chemrev.9b00099
25. Sen Gupta R, Mandal S, Malakar A, et al. Graphene oxide offers precise molecular sieving, structural integrity, microplastic removal, and closed-loop circularity in water-remediating membranes through a covalent adaptable network. Journal of Materials Chemistry A. 2024; 12(1): 321-334. doi: 10.1039/d3ta04539k
26. Owji E, Ostovari F, Keshavarz A. Influence of the chemical structure of diisocyanate on the electrical and thermal properties of in situ polymerized polyurethane–graphene composite films. Physical Chemistry Chemical Physics. 2022; 24(46): 28564-28576. doi: 10.1039/d2cp03826a
27. Ajaj Y, AL-Salman HNK, Hussein AM, et al. Effect and investigating of graphene nanoparticles on mechanical, physical properties of polylactic acid polymer. Case Studies in Chemical and Environmental Engineering. 2024; 9: 100612. doi: 10.1016/j.cscee.2024.100612
28. Yang C, Gede M, Abdulhamid MA, et al. Solvent and material selection for greener membrane manufacturing. In: Basile A, Favvas EP (editors). Current Trends and Future Developments on (Bio-) Membranes: Modern Approaches in Membrane Technology for Gas Separation and Water Treatment. Elsevier; 2024. pp. 249-293. doi: 10.1016/b978-0-323-99311-1.00016-7
29. Itapu B, Jayatissa A. A Review in Graphene/Polymer Composites. Chemical Science International Journal. 2018; 23(3): 1-16. doi: 10.9734/csji/2018/41031
30. Zheng D, Tang G, Zhang HB, et al. In situ thermal reduction of graphene oxide for high electrical conductivity and low percolation threshold in polyamide 6 nanocomposites. Composites Science and Technology. 2012; 72(2): 284-289. doi: 10.1016/j.compscitech.2011.11.014
31. Chen J, Chen X, Meng F, et al. Super-high thermal conductivity of polyamide-6/graphene-graphene oxide composites through in situ polymerization. High Performance Polymers. 2016; 29(5): 585-594. doi: 10.1177/0954008316655861
32. Ding P, Su S, Song N, et al. Influence on thermal conductivity of polyamide-6 covalently-grafted graphene nanocomposites: varied grafting-structures by controllable macromolecular length. RSC Advances. 2014; 4(36): 18782. doi: 10.1039/c4ra00500g
33. Xu Z, Gao C. In situ Polymerization Approach to Graphene-Reinforced Nylon-6 Composites. Macromolecules. 2010; 43(16): 6716-6723. doi: 10.1021/ma1009337
34. Wang S, Zhang L, Zeng Q, et al. Designing Polymer Electrolytes via Ring-Opening Polymerization for Advanced Lithium Batteries. Advanced Energy Materials. 2023; 14(3). doi: 10.1002/aenm.202302876
35. Lu Y, Wang X, Chen D, et al. Polystyrene/graphene composite electrode fabricated by in situ polymerization for capillary electrophoretic determination of bioactive constituents in Herba Houttuyniae. Electrophoresis. 2011; 32(14): 1906-1912. doi: 10.1002/elps.201100162
36. Muthukumar J, Kandukuri VA, Chidambaram R. A critical review on various treatment, conversion, and disposal approaches of commonly used polystyrene. Polymer Bulletin. 2023; 81(4): 2819-2845. doi: 10.1007/s00289-023-04851-0
37. Babaie B, Najafi M, Ataeefard M. Designing an optimised formulation for in situ emulsion polymerization: printing ink production by response surface methodology. Pigment & Resin Technology. 2024. doi: 10.1108/prt-10-2023-0091
38. Wang Y, Lu Q, Xie H, et al. In-situ formation of nitrogen doped microporous carbon nanospheres derived from polystyrene as lubricant additives for anti-wear and friction reduction. Friction. 2023; 12(3): 439-451. doi: 10.1007/s40544-023-0766-2

39. Wang X, Hu Y, Song L, et al. In situ polymerization of graphene nanosheets and polyurethane with enhanced mechanical and thermal properties. Journal of Materials Chemistry. 2011; 21(12): 4222. doi: 10.1039/c0jm03710a
40. Milani MA, González D, Quijada R, et al. Polypropylene/graphene nanosheet nanocomposites by in situ polymerization: Synthesis, characterization and fundamental properties. Composites Science and Technology. 2013; 84: 1-7. doi: 10.1016/j.compscitech.2013.05.001
41. Patole AS, Patole SP, Kang H, et al. A facile approach to the fabrication of graphene/polystyrene nanocomposite by in situ microemulsion polymerization. Journal of Colloid and Interface Science. 2010; 350(2): 530-537. doi: 10.1016/j.jcis.2010.01.035
42. Hu H, Wang X, Wang J, et al. Preparation and properties of graphene nanosheets–polystyrene nanocomposites via in situ emulsion polymerization. Chemical Physics Letters. 2010; 484(4-6): 247-253. doi: 10.1016/j.cplett.2009.11.024
43. Wang J, Hu H, Wang X, et al. Preparation and mechanical and electrical properties of graphene nanosheets–poly(methyl methacrylate) nanocomposites via in situ suspension polymerization. Journal of Applied Polymer Science. 2011; 122(3): 1866-1871. doi: 10.1002/app.34284
44. Ahmed MAM, Jurczak KM, Lynn NS, et al. Rapid prototyping of PMMA-based microfluidic spheroid-on-a-chip models using micromilling and vapour-assisted thermal bonding. Scientific Reports. 2024; 14(1). doi: 10.1038/s41598-024-53266-y
45. Salam MA, Alsultany FH, Al-Bermany E, et al. Impact of graphene oxide nanosheets and polymethyl methacrylate on nano/hybrid-based restoration dental filler composites: ultrasound behavior and antibacterial activity. Journal of Ultrasound. 2024. doi: 10.1007/s40477-023-00855-8
46. Lee YR, Raghu AV, Jeong HM, et al. Properties of Waterborne Polyurethane/Functionalized Graphene Sheet Nanocomposites Prepared by an in situ Method. Macromolecular Chemistry and Physics. 2009; 210(15): 1247-1254. doi: 10.1002/macp.200900157
47. Yang L, Huang R, Yuan J, et al. High thermal conductive polyurethane composite films with a three-dimensional boron nitride network in-situ constructed by multi-folding and multi-laminating. Composites Science and Technology. 2024; 245: 110326. doi: 10.1016/j.compscitech.2023.110326
48. Mishra SK, Tripathi SN, Choudhary V, et al. SPR based fibre optic ammonia gas sensor utilizing nanocomposite film of PMMA/reduced graphene oxide prepared by in situ polymerization. Sensors and Actuators B: Chemical. 2014; 199: 190-200. doi: 10.1016/j.snb.2014.03.109
49. Ganguly S. Preparation/processing of polymer-graphene composites by different techniques. In: Rahaman M, Nayak L, Hussein IA, Das NC (editors). Polymer Nanocomposites Containing Graphene: Preparation, Properties, and Applications. Elsevier; 2022. pp. 45-74. doi: 10.1016/b978-0-12-821639-2.00015-x
50. Ali Z, Yaqoob S, Yu J, et al. Advancements in Graphene-Based Hybrid Filler Polymer Composites: A Comprehensive Survey of Processing, Properties, and Influential Factors. Available online: https://www.preprints.org/manuscript/202402.1412/v1 (accessed on 1 March 2024).
51. Wu K, Tan J, Liu Z, et al. Incombustible solid polymer electrolytes: A critical review and perspective. Journal of Energy Chemistry. 2024; 93: 264-281. doi: 10.1016/j.jechem.2024.01.013
52. Zhang J, Liang B, Long J. Preparation and characteristics of composite films with functionalized graphene/polyimide. Journal of Applied Polymer Science. 2023; 141(10). doi: 10.1002/app.55045
53. Hu K, Kulkarni DD, Choi I, et al. Graphene-polymer nanocomposites for structural and functional applications. Progress in Polymer Science. 2014; 39(11): 1934-1972. doi: 10.1016/j.progpolymsci.2014.03.001
54. Panzer F, Dyson MJ, Bakr H, et al. A Unified Picture of Aggregate Formation in a Model Polymer Semiconductor during Solution Processing. Advanced Functional Materials. 2024. doi: 10.1002/adfm.202314729
55. He F, Lam KH, Fan J, et al. Improved dielectric properties for chemically functionalized exfoliated graphite nanoplates/syndiotactic polystyrene composites prepared by a solution-blending method. Carbon. 2014; 80: 496-503. doi: 10.1016/j.carbon.2014.08.089
56. Yu YH, Lin YY, Lin CH, et al. High-performance polystyrene/graphene-based nanocomposites with excellent anti-corrosion properties. Polym Chem. 2014; 5(2): 535-550. doi: 10.1039/c3py00825h
57. Zhao F, Zhang G, Zhao S, et al. Fabrication of pristine graphene-based conductive polystyrene composites towards high performance and light-weight. Composites Science and Technology. 2018; 159: 232-239. doi: 10.1016/j.compscitech.2018.02.013

58. Qi XY, Yan D, Jiang Z, et al. Enhanced Electrical Conductivity in Polystyrene Nanocomposites at Ultra-Low Graphene Content. ACS Applied Materials & Interfaces. 2011; 3(8): 3130-3133. doi: 10.1021/am200628c
59. Kausar A, Bocchetta P. Poly(methyl methacrylate) Nanocomposite Foams Reinforced with Carbon and Inorganic Nanoparticles—State-of-the-Art. Journal of Composites Science. 2022; 6(5): 129. doi: 10.3390/jcs6050129
60. Zeng X, Yang J, Yuan W. Preparation of a poly(methyl methacrylate)-reduced graphene oxide composite with enhanced properties by a solution blending method. European Polymer Journal. 2012; 48(10): 1674-1682. doi: 10.1016/j.eurpolymj.2012.07.011
61. Balasubramaniyan R, Pham VH, Jang J, et al. A one pot solution blending method for highly conductive poly (methyl methacrylate)-highly reduced graphene nanocomposites. Electronic Materials Letters. 2013; 9(6): 837-839. doi: 10.1007/s13391-013-6025-3
62. Kuila T, Bose S, Hong CE, et al. Preparation of functionalized graphene/linear low density polyethylene composites by a solution mixing method. Carbon. 2011; 49(3): 1033-1037. doi: 10.1016/j.carbon.2010.10.031
63. Chen M, Peng B, Guo X, et al. Polyethylene interfacial dielectric layer for organic semiconductor single crystal based field-effect transistors. Chinese Chemical Letters. 2024; 35(4): 109051. doi: 10.1016/j.cclet.2023.109051
64. Vadukumpully S, Paul J, Mahanta N, et al. Flexible conductive graphene/poly(vinyl chloride) composite thin films with high mechanical strength and thermal stability. Carbon. 2011; 49(1): 198-205. doi: 10.1016/j.carbon.2010.09.004
65. Kausar A, Rafique I, Anwar Z, et al. Perspectives of Epoxy/Graphene Oxide Composite: Significant Features and Technical Applications. Polymer-Plastics Technology and Engineering. 2015; 55(7): 704-722. doi: 10.1080/03602559.2015.1098700
66. Chen W, Weimin H, Li D, et al. A critical review on the development and performance of polymer/graphene nanocomposites. Science and Engineering of Composite Materials. 2018; 25(6): 1059-1073. doi: 10.1515/secm-2017-0199
67. Hu T, Ye H, Luo Z, et al. Efficient exfoliation of UV-curable, high-quality graphene from graphite in common low-boiling-point organic solvents with a designer hyperbranched polyethylene copolymer and their applications in electrothermal heaters. Journal of Colloid and Interface Science. 2020; 569: 114-127. doi: 10.1016/j.jcis.2020.02.068
68. Gill YQ, Ehsan H, Mehmood U, et al. A novel two-step melt blending method to prepare nano-silanized-silica reinforced crosslinked polyethylene (XLPE) nanocomposites. Polymer Bulletin. 2022; 79(11): 10077-10093. doi: 10.1007/s00289-021-03989-z
69. Kaczor DP, Bajer K, Raszkowska-Kaczor A, et al. Screw Extrusion as a Scalable Technology for Manufacturing Polylactide Composite with Graphene Filler. Advances in Science and Technology Research Journal. 2024; 18(2): 226-237. doi: 10.12913/22998624/184152
70. Tan B, Thomas NL. A review of the water barrier properties of polymer/clay and polymer/graphene nanocomposites. Journal of Membrane Science. 2016; 514: 595-612. doi: 10.1016/j.memsci.2016.05.026
71. Liu Y, Davies R, McCutchion P, et al. Fabrication of functionalised graphene-PAEK nanocomposites for different manufacturing processes. Virtual and Physical Prototyping. 2023; 19(1). doi: 10.1080/17452759.2023.2283884
72. Scaffaro R, Maio A. A green method to prepare nanosilica modified graphene oxide to inhibit nanoparticles re-aggregation during melt processing. Chemical Engineering Journal. 2017; 308: 1034-1047. doi: 10.1016/j.cej.2016.09.131
73. Yan D, Zhang HB, Jia Y, et al. Improved Electrical Conductivity of Polyamide 12/Graphene Nanocomposites with Maleated Polyethylene-Octene Rubber Prepared by Melt Compounding. ACS Applied Materials & Interfaces. 2012; 4(9): 4740-4745. doi: 10.1021/am301119b
74. Kausar A. In-situ modified graphene reinforced polyamide 1010/poly(ether amide): mechanical, thermal, and barrier properties. Materials Research Innovations. 2017; 23(4): 191-199. doi: 10.1080/14328917.2017.1409392
75. Mittal V, Chaudhry AU. Polymer – graphene nanocomposites: effect of polymer matrix and filler amount on properties. Macromolecular Materials and Engineering. 2015; 300(5): 510-521. doi: 10.1002/mame.201400392
76. Shen B, Zhai W, Tao M, et al. Enhanced interfacial interaction between polycarbonate and thermally reduced graphene induced by melt blending. Composites Science and Technology. 2013; 86: 109-116. doi: 10.1016/j.compscitech.2013.07.007
77. Mohammadsalih ZG, Uddin Siddiqui V, Sapuan SM. The role of organic solvent and nano-additives loading in preparing and characterizing graphene oxide based polystyrene nanocomposites. Polymer-Plastics Technology and Materials. 2024; 63(9): 1175-1186. doi: 10.1080/25740881.2024.2325431
78. Shen B, Zhai W, Chen C, et al. Melt Blending In situ Enhances the Interaction between Polystyrene and Graphene through π–π Stacking. ACS Applied Materials & Interfaces. 2011; 3(8): 3103-3109. doi: 10.1021/am200612z

79. El Achaby M, Arrakhiz F, Vaudreuil S, et al. Mechanical, thermal, and rheological properties of graphene-based polypropylene nanocomposites prepared by melt mixing. Polymer Composites. 2012; 33(5): 733-744. doi: 10.1002/pc.22198
80. Ryu SH, Shanmugharaj AM. Influence of hexamethylene diamine functionalized graphene oxide on the melt crystallization and properties of polypropylene nanocomposites. Materials Chemistry and Physics. 2014; 146(3): 478-486. doi: 10.1016/j.matchemphys.2014.03.056
81. Istrate OM, Paton KR, Khan U, et al. Reinforcement in melt-processed polymer–graphene composites at extremely low graphene loading level. Carbon. 2014; 78: 243-249. doi: 10.1016/j.carbon.2014.06.077
82. Maiti S, Suin S, Shrivastava NK, et al. Low percolation threshold in polycarbonate/multiwalled carbon nanotubes nanocomposites through melt blending with poly(butylene terephthalate). Journal of Applied Polymer Science. 2013; 130(1): 543-553. doi: 10.1002/app.39168
83. Jiang S, Gui Z, Bao C, et al. Preparation of functionalized graphene by simultaneous reduction and surface modification and its polymethyl methacrylate composites through latex technology and melt blending. Chemical Engineering Journal. 2013; 226: 326-335. doi: 10.1016/j.cej.2013.04.068
84. Anwar Z, Kausar A, Rafique I, et al. Advances in Epoxy/Graphene Nanoplatelet Composite with Enhanced Physical Properties: A Review. Polymer-Plastics Technology and Engineering. 2015; 55(6): 643-662. doi: 10.1080/03602559.2015.1098695
85. Papageorgiou DG, Kinloch IA, Young RJ. Mechanical properties of graphene and graphene-based nanocomposites. Progress in Materials Science. 2017; 90: 75-127. doi: 10.1016/j.pmatsci.2017.07.004
86. Mittal V. Functional Polymer Nanocomposites with Graphene: A Review. Macromolecular Materials and Engineering. 2014; 299(8): 906-931. doi: 10.1002/mame.201300394
87. Du J, Cheng H. The Fabrication, Properties, and Uses of Graphene/Polymer Composites. Macromolecular Chemistry and Physics. 2012; 213(10-11): 1060-1077. doi: 10.1002/macp.201200029
88. Diniz FLJ, Lima TBS, Araujo ES, et al. Graphene-Based Flexible and Eco-Friendly Wearable Electronics and Humidity Sensors. Materials Research. 2024; 27. doi: 10.1590/1980-5373-mr-2023-0480
89. Wu JJ, Huang LM, Zhao Q, et al. 4D Printing: History and Recent Progress. Chinese Journal of Polymer Science. 2017; 36(5): 563-575. doi: 10.1007/s10118-018-2089-8
90. Kafle A, Luis E, Silwal R, et al. 3D/4D Printing of Polymers: Fused Deposition Modelling (FDM), Selective Laser Sintering (SLS), and Stereolithography (SLA). Polymers. 2021; 13(18): 3101. doi: 10.3390/polym13183101
91. Guo Y, Patanwala HS, Bognet B, et al. Inkjet and inkjet-based 3D printing: connecting fluid properties and printing performance. Rapid Prototyping Journal. 2017; 23(3): 562-576. doi: 10.1108/rpj-05-2016-0076
92. Shirazi SFS, Gharehkhani S, Mehrali M, et al. A review on powder-based additive manufacturing for tissue engineering: selective laser sintering and inkjet 3D printing. Science and Technology of Advanced Materials. 2015; 16(3): 033502. doi: 10.1088/1468-6996/16/3/033502
93. Wan X, Luo L, Liu Y, et al. Direct Ink Writing Based 4D Printing of Materials and Their Applications. Advanced Science. 2020; 7(16). doi: 10.1002/advs.202001000
94. Ponnamma D, Yin Y, Salim N, et al. Recent progress and multifunctional applications of 3D printed graphene nanocomposites. Composites Part B: Engineering. 2021; 204: 108493. doi: 10.1016/j.compositesb.2020.108493
95. Ul Hassan R, Sharipov M, Ryu W. Electrohydrodynamic (EHD) printing of nanomaterial composite inks and their applications. Micro and Nano Systems Letters. 2024; 12(1). doi: 10.1186/s40486-023-00194-7
96. Park SS, Park Y, Repo E, et al. Three-dimensionally printed scaffold coated with graphene oxide for enhanced heavy metal adsorption: Batch and fixed-bed column studies. Journal of Water Process Engineering. 2024; 57: 104658. doi: 10.1016/j.jwpe.2023.104658
97. Che H, Yuan J. Recent advances in electrospinning supramolecular systems. Journal of Materials Chemistry B. 2022; 10(1): 8-19. doi: 10.1039/d1tb02304g
98. Tiwari SK, Sahoo S, Wang N, et al. Electrospinning of Graphene. Springer International Publishing; 2021. doi: 10.1007/978-3-030-75456-3
99. Han Z, Wang J, Liu S, et al. Electrospinning of Neat Graphene Nanofibers. Advanced Fiber Materials. 2021; 4(2): 268-279. doi: 10.1007/s42765-021-00105-8
100. Li Y, Dong T, Li Z, et al. Review of advances in electrospinning-based strategies for spinal cord regeneration. Materials Today Chemistry. 2022; 24: 100944. doi: 10.1016/j.mtchem.2022.100944

101. Reneker DH, Yarin AL. Electrospinning jets and polymer nanofibers. Polymer. 2008; 49(10): 2387-2425. doi: 10.1016/j.polymer.2008.02.002
102. Gopiraman M, Fujimori K, Zeeshan K, et al. Structural and mechanical properties of cellulose acetate/graphene hybrid nanofibers: Spectroscopic investigations. Express Polymer Letters. 2013; 7(6): 554-563. doi: 10.3144/expresspolymlett.2013.52
103. Lee SH, Dreyer DR, An J, et al. Polymer Brushes via Controlled, Surface-Initiated Atom Transfer Radical Polymerization (ATRP) from Graphene Oxide. Macromolecular Rapid Communications. 2010; 31(3): 281-288. doi: 10.1002/marc.200900641
104. Zhao W, Wu F, Wu H, et al. Preparation of Colloidal Dispersions of Graphene Sheets in Organic Solvents by Using Ball Milling. Journal of Nanomaterials. 2010; 2010: 1-5. doi: 10.1155/2010/528235
105. Ganesan V, Jayaraman A. Theory and simulation studies of effective interactions, phase behavior and morphology in polymer nanocomposites. Soft Matter. 2014; 10(1): 13-38. doi: 10.1039/c3sm51864g
106. Gupta T, Ratandeep, Dutt M, et al. Graphene-based nanomaterials as potential candidates for environmental mitigation of pesticides. Talanta. 2024; 272: 125748. doi: 10.1016/j.talanta.2024.125748
107. Banglani TH, Chandio I, Khilji MUN, et al. Graphene-based nanocomposites for gas sensors: challenges and opportunities. Reviews in Inorganic Chemistry. 2024; 0(0). doi: 10.1515/revic-2023-0033
108. Saeed M, Haq RSU, Ahmed S, et al. Recent advances in carbon nanotubes, graphene and carbon fibers-based microwave absorbers. Journal of Alloys and Compounds. 2024; 970: 172625. doi: 10.1016/j.jallcom.2023.172625
109. Wypych G. Graphene: Important Results and Applications. ChemTec Publishing; 2019.
110. Seyedjamali H, Pirisedigh A. Well-dispersed polyimide/TiO_2 nanocomposites: in situ sol–gel fabrication and morphological study. Colloid and Polymer Science. 2012; 290(7): 653-659. doi: 10.1007/s00396-012-2599-9
111. Wang B, Chen X, Ahmad Z, et al. 3D electrohydrodynamic printing of highly aligned dual-core graphene composite matrices. Carbon. 2019; 153: 285-297. doi: 10.1016/j.carbon.2019.07.030
112. Levchenko I, Ostrikov K, Zheng J, et al. Scalable graphene production: perspectives and challenges of plasma applications. Nanoscale. 2016; 8(20): 10511-10527. doi: 10.1039/c5nr06537b
113. Zhong YL, Tian Z, Simon GP, et al. Scalable production of graphene via wet chemistry: progress and challenges. Materials Today. 2015; 18(2): 73-78. doi: 10.1016/j.mattod.2014.08.019
114. Yan H, Tao X, Yang Z, et al. Effects of the oxidation degree of graphene oxide on the adsorption of methylene blue. Journal of Hazardous Materials. 2014; 268: 191-198. doi: 10.1016/j.jhazmat.2014.01.015
115. Rissanou A, Power A, Harmandaris V. Structural and Dynamical Properties of Polyethylene/Graphene Nanocomposites through Molecular Dynamics Simulations. Polymers. 2015; 7(3): 390-417. doi: 10.3390/polym7030390

EnPress Publisher

Characterization and Application of Nanomaterials 2024, 7(2), 4945.
https://doi.org/10.24294/can.v7i2.4945

Review

Fullerene in water remediation nanocomposite membranes—Cutting edge advancements

Ayesha Kausar[1,2]

[1] NPU-NCP Joint International Research Center on Advanced Nanomaterials and Defects engineering, Northwestern Polytechnical University, Xi'an 710072, China; dr.ayeshakausar@yahoo.com
[2] UNESCO-UNISA Africa Chair in Nanosciences/Nanotechnology, iThemba LABS, Somerset West 7129, South Africa

CITATION

Kausar A. Fullerene in water remediation nanocomposite membranes—Cutting edge advancements. Characterization and Application of Nanomaterials. 2024; 7(2): 4945. https://doi.org/10.24294/can.v7i2.4945

ARTICLE INFO

Received: 1 March 2024
Accepted: 1 April 2024
Available online: 1 July 2024

Abstract: Among carbon nanoparticles, fullerene has been observed as a unique zero-dimensional hollow molecule. Fullerene has a high surface area and exceptional structural and physical features (optical, electronic, heat, mechanical, and others). Advancements in fullerene have been observed in the form of nanocomposites. Application of fullerene nanocomposites has been found in the membrane sector. This cutting-edge review article basically describes the potential of fullerene nanocomposite membranes for water remediation. Adding fullerene nanoparticles has been found to amend the microstructure and physical features of the nanocomposite membranes in addition to membrane porosity, selectivity, permeation, water flux, desalination, and other significant properties for water remediation. Variations in the designs of fullerene nanocomposites have resulted in greater separations between salts, desired metals, toxic metal ions, microorganisms, etc. Future investigations on ground-breaking fullerene-based membrane materials may overcome several design and performance challenges for advanced applications.

Keywords: fullerene; nanocomposite; membranes; water remediation; permeation

1. Introduction

Benefits of membrane skills have been observed for technical utilization due to low cost, efficient working, low energy consumption, and scaled-up processing [1]. In traditional membrane technologies, pressure-driven membrane assemblies have been used for filtration [2]. Developments in this field have led to the implication of polymer-based membranes and materials. Consequently, numerous polymers have been used as filtration membranes to enhance their robustness, selectivity, permeability, and desalination performance at low pressure [3,4]. Polymeric membranes have been fabricated using a range of techniques, such as simple solution casting, phase inversion, sol-gel procedures, and efficient electrospinning techniques [5–7]. The efficiency of polymeric membranes has been found to be reliable on the surface area, microstructure, porosity, crystallinity, hydrophilicity, etc., enhancing flux, fouling resistance, and desalination performances [8–10]. In this regard, applying nanocomposite membranes instead of pristine polymeric membranes has been found advantageous [11]. Consequently, carbon nanostructures like graphene, carbon nanotubes, nanofibers, etc. have been employed to develop nanocomposite membranes [12,13]. Most competent fullerene nanoparticles have been applied to polymeric membranes [14]. Hence, water remediation has been investigated using polymer- and fullerene-derived nanocomposite membranes [15–17].

This state-of-the-art article presents fullerene-filled nanocomposite membranes for water purification. Inclusion of fullerene in filtration membranes caused significant effects on the separation performances owing to the high surface area, pore size, porosity, surface roughness, and other surface properties [18]. Fullerene-based membranes revealed fine potential to overcome the performance challenges of the filtration of unwanted pollutants [19].

2. Fullerene

Fullerene is a hollow, symmetrical carbon nano-allotrope with sp^2 hybridization [20,21]. Owing to structural features, π conjugation has been observed in the fullerene molecule [22]. This cage-shaped nanostructure has a size of about 1 nm. Its discovery dates back to 1985 [23]. Fullerene molecules have been found as C_{20}, C_{24}, C_{60}, C_{70}, C_{120}, etc., depending upon the number of carbon atoms in the hollow ball-like ring structure (**Figure 1**) [24]. Fullerene C_{60} is the most frequently adopted form, known as buckminsterfullerene. This marvelous molecule has been studied for its optical, electronic, mechanical, thermal, and biomedical properties [25]. A number of techniques have been used to form the fullerene molecules, like the plasma method, chemical vapor deposition, arc discharge, and many others [26,27]. Advancements in fullerene research have been observed in the form of nanocomposite structures [28,29]. For nanocomposite formation, the solubility of fullerene molecules has been considered [30]. Various solvents like water, poly(vinylpyrrolidone), and organic solvents have been used for fullerene molecules [31]. Consequently, better-processed fullerene nanomaterials have been applied for photovoltaics, optoelectronics, sensors, and biomedical applications [32–35]. Furthermore, high-performance fullerene-based nanocomposite membranes have been designed. The membrane performance was dependent upon the type of fullerene molecules, dispersions, and interactions with the matrix materials used [36].

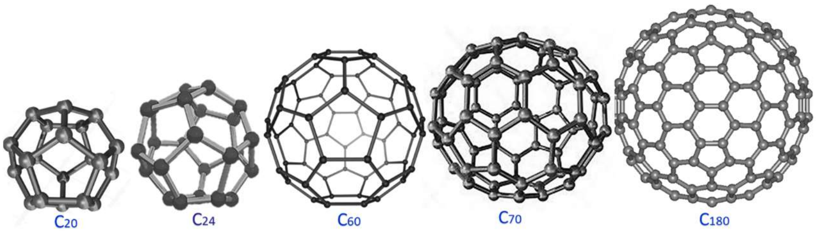

Figure 1. Some fullerene molecules.

3. Nanocomposite membranes

Various technological sectors have focused on the application of membranes [37,38]. In this regard, membranes have been effectively applied for the removal of environmental contaminants from water [39]. Most importantly, polymer-based nanocomposite membranes have been designed with numerous potential benefits for water separation [40]. Accordingly, the pollutants from ground, domestic, sea, and industrial water have been removed using the advanced membranes [41]. The membrane filtration efficiency definitely relies on the permeability and selectivity features [42]. Moreover, nanocomposite membranes have been explored for improved physicochemical properties [43,44]. Important membrane features studied in this regard include porosity, hydrophilicity, selectivity, fouling, mechanical, and heat stability [45]. A range of different filtration nanocomposite membranes have been prepared, such as microfiltration, nanofiltration, ultrafiltration, reverse osmosis, mixed matrix, and so on [46,47]. The membrane properties also depend on the nanofiller type, quantity, and dispersion features of the polymeric systems [48]. For nanocomposite membrane formation, various nanocarbon nanoparticles have been used, including graphene, carbon nanotubes, nanodiamonds, etc. [49,50]. Similarly, wide-ranging polymers have been adopted to form efficient membranes [51]. For example, reports on polysulfone- and graphene-based nanocomposite membranes have been observed [52,53]. The polysulfone/graphene nanocomposite membranes were fabricated using the phase inversion technique [54]. These membranes have been investigated for crystallinity, morphology, and matrix-nanofiller interactions, enhancing their physical properties and water remediation performance [55]. Similarly, countless polymer/nanocarbon nanomaterials have been reported for membrane applications.

4. Fullerene in nanocomposite membranes for water remediation

Fullerene-filled nanocomposite membranes have been prepared and examined for membrane properties like desalination, toxic ion removal, metal ion removal or recovery, and microorganism separation from water [56]. Various toxic metals like lead, mercury, arsenic, etc. have been removed using the efficient fullerene-filled membranes [57–59]. The separation performance of these membranes relies on the porosity and surface defects of these membranes [60,61]. Perera and colleagues [62] reported on fullerene-based reverse osmosis membranes. The membranes revealed a high water flux of 26.1 L/m^{2}h and salt rejection properties. The nanocomposite membranes were effectively used to separate the lithium ions from seawater [63].

Polyamide is a commodity thermoplastic polymer with amide bonds in the main chain [64,65]. Polyamide has been effectively adopted for membrane application [66,67]. Plisko and co-researchers [68] designed the polyamide and hydroxy functional fullerene-derived nanocomposite membranes for water remediation. Adding 5 wt.% nanofiller aided the antifouling properties. In addition, the removal of organic matter has been observed for the nanocomposite membranes. Dmitrenko et al. [69] used polyamide polyphenylene isophthalamide and filled it with fullerene nanoparticles along with other carbon fillers. The mixed matrix pervaporation membranes have been fabricated through the solid-phase synthesis method. **Figure 2** displays a simple route for the formation of polyphenylene isophthalamide/C$_{60}$ pervaporation membranes. The inclusion of nanofiller increased the transport properties of the nanocomposite membranes. The membranes were tested for the transport properties of an azeotropic methanol-toluene mixture. Adding fullerene nanoparticles has considerably improved the permeation flux of the membranes [70]. Here, permeation flux was observed in the range of 0.084–0.214 kg/(m^{2}h) with 5 wt.% fullerene contents. In addition, a selectivity of 96 wt.% was observed. The porosity, permeability, and selectivity of the pervaporation membranes were dependent on the fullerene contents and interactions with the polymers [71,72].

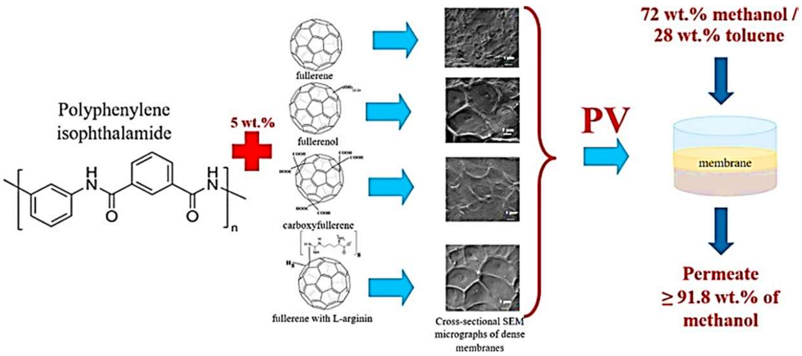

Figure 2. Graphical representation of development of novel polyphenylene isophthalamide pervaporation (PV) membranes modified with various types of C_{60} derivatives [72]. Reproduced with permission from MDPI.

Liu et al. [73] reported on epoxy-derived nanocomposite membranes filled with fullerene C_{60} and graphene oxide. The resulting membranes have been studied for their ion permeation and desalination properties. **Figure 3** shows a transmission electron microscopy micrograph of fullerene and graphene oxide-based nanomaterials. The interlayer spacing between the fullerene-grafted graphene nanosheets was found to be around 100 nm due to the insertion of 0.7–1 nm fullerene nanoparticles. Due to interlayer spacing, a low permeation rate was observed. **Figure 4** expresses the fabrication and water desalination setup for the formation of water permeation membranes of epoxy and fullerene-grafted graphene nanoparticles. Including fullerene molecules led to a high water flux of up to 10.85 L/m^{2}hbar. Better desalination and water permeation have been observed. **Figure 5** displays the variations in ion concentrations on permeation vs. time for the fullerene-based membranes. The stability features of the nanocomposite membranes were found to affect the desalination performance [74]. **Table 1** exhibits examples of some fullerene-filled nanocomposites-based filtration membranes.

Table 1. Specifications of few polymeric membranes with fullerene nanofiller for water purification.

Nanoparticles	**Fullerene nanoparticle size (nm)**	**Membrane pore size**	**Filtration (L/m^{2}h.bar)/LMH.bar**	**Ref**
C_{60}	14–59	34 to 55 nm	-	[68]
Functional C_{60}	~1	0.86 to 0.59 nm	26.1 LMH	[62]
Polyhydroxylated C_{60}	-	0.64 nm	6.7 LMH.bar	[63]
C_{60}	0.14	-	-	[75]
C_{60}	-	Large pore size	-	[76]
C_{60}	-	17 nm	-	[77]
C_{60}	9–15	5 wt.% nanoparticles small pores	0.084–0.214 kg/(m^{2}h)	[69]
C_{60}	0.375	-	-	[78]

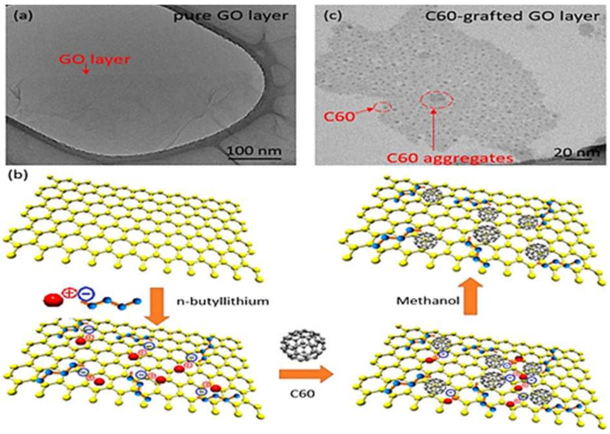

Figure 3. (a) Transmission electron microscopy (TEM) image of pure GO layer (very thin layer with a little folding edge represents GO layer, at scale bar of 100 nm); **(b)** Schematic illustration of grafting C_{60} on GO layer through lithiation reaction; and **(c)** TEM image of C_{60} grafted GO layer (smooth layer with irregular shape represents GO layer and dark dots represent C_{60} nanoparticles, at scale bar 20 nm). The GO layer is around 150 nm, whereas the C_{60} nanoparticles are 1–2 nm) [73]. GO = graphene oxide; C_{60} = fullerene. Reproduced with permission from ACS.

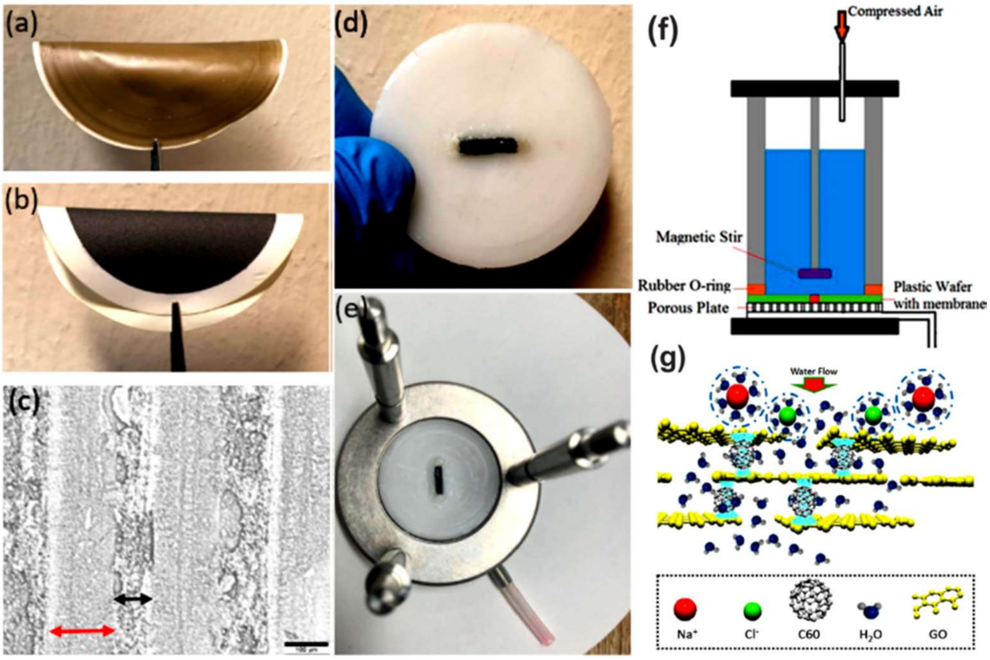

Figure 4. Fabrication process and water desalination setup using C_{60} grafted graphene oxide membranes. The photograph shows: **(a)** graphene oxide membrane without C_{60}; **(b)** C_{60} grafted graphene oxide membrane; **(c)** optical micrograph of cross-sectional area with scale bar 100 µm. The micrograph shows 148 µm thick graphene oxide laminates embedded in 81 µm thick epoxy; **(d)** graphene oxide-C_{60} membrane encapsulated with epoxy in plastic disk of 47 mm; **(e)** graphene oxide-C_{60} membrane inside water desalination setup; **(f)** and **(g)** are schematic setup of flat membrane made of graphene oxide and C_{60} hybrid for water desalination [73]. GO = graphene oxide; C_{60} = fullerene; Reproduced with permission from ACS.

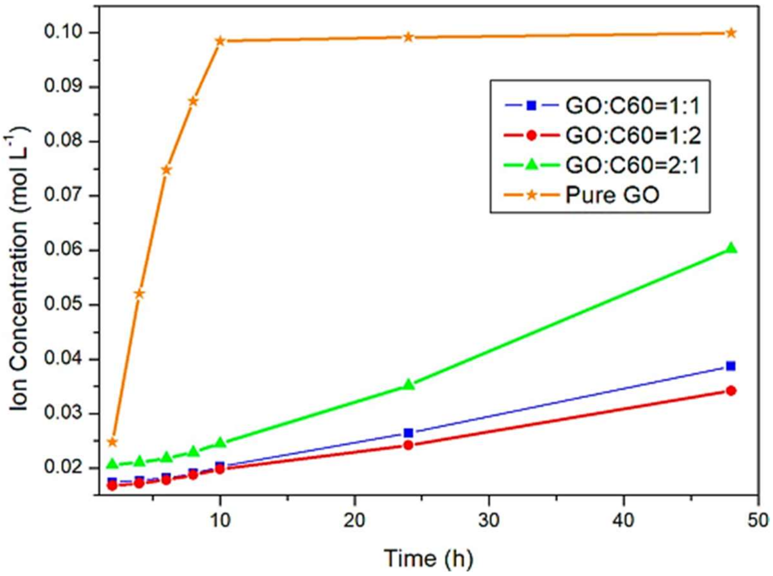

Figure 5. Ion concentration on the permeation side through GO/C_{60} membrane over time period (the red, blue, and green lines indicate the feed ratios of GO:C60 = 1:2, 1:1, and 2:1, respectively) [73]. GO = graphene oxide; C_{60} = fullerene. Reproduced with permission from ACS.

Polysulfone is a marketable thermoplastic polymer commonly used [79]. Polysulfone has several advantageous features, like chemical, mechanical, and thermal robustness. Polysulfone has been used to form membranes, coatings, and other practical nanostructures for methodological fields [80]. Penkova and colleagues [81] reported on polysulfone and fullerene-derived mixed-matrix membranes. Adding 5 wt.% fullerene C_{60} enhanced the membrane transport features, especially pervaporation of the ethyl acetate-water mixture [82]. Including fullerene nanofiller also elevated the membrane surface area and hydrophilicity. The solution-diffusion processes were used to promote pervaporation through the membrane [83]. Consequently, mass transfer and permeability were found to increase through the membranes.

Nafion is another important matrix for membrane formation [84,85]. Nafion-based commercial membranes have been widely adopted for environmental, energy, and energy/electronics applications [86,87]. Here, fullerene-filled nafion membranes have been produced [88]. The antimicrobial properties of the nanocomposite membranes were considered. Tasaki and colleagues [89] formed the nafion/fullerene nanocomposite membrane using the solution casting method. The solvent technique was efficient in forming compatible fullerene-filled membranes [15]. The membranes were studied using molecular dynamic simulations, and fine fullerene nanoparticle dispersion was deliberated. Layon et. al. [90] developed fullerene nanocomposites using poly(vinyl pyrrolidone) as well as different solvent media. The resulting membranes were used for wastewater remediation. **Figure 6** shows that the sonication technique better dispersed the fullerene nanoparticles in the medium relative to aqueous dispersion and in tetrahydrofuran. Fullerene nanoparticles had a size of 30–100 nm. In poly(vinyl pyrrolidone), aggregated fullerene nanoparticles have been observed [91]. The effects of minimal inhibitory concentrations on aggregate surface area can be seen in **Figure 7**. There was no linear relationship between the minimal inhibitory concentrations and aggregate surface area. However, enhanced surface area increased membrane performance due to better interactions.

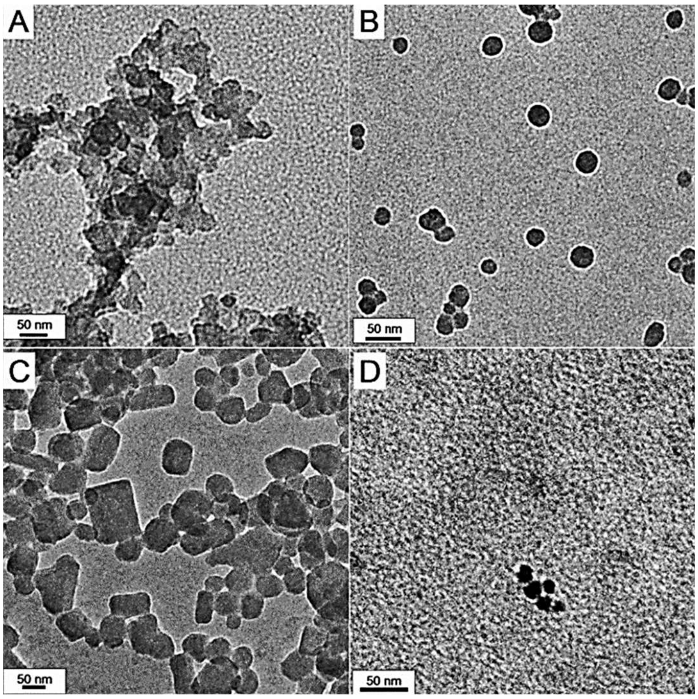

Figure 6. Transmission electron microscopy micrographs of **(A)** aq/nC$_{60}$; **(B)** son/nC$_{60}$; **(C)** THF/nC$_{60}$; and **(D)** PVP/nC$_{60}$ [90]. Reproduced with permission from ACS.

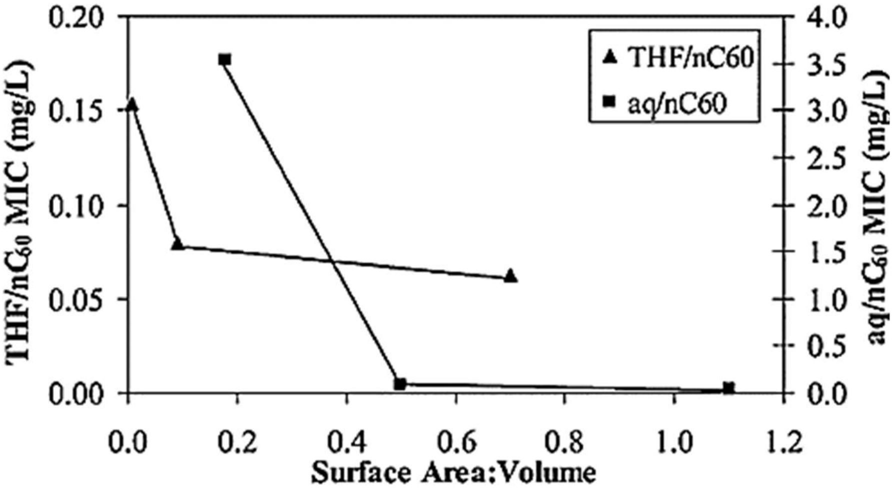

Figure 7. Relationship between Minimal inhibitory concentrations (MIC) and aggregate surface area. There is no linear relationship between the mean MIC and the surface area to volume ratio calculated, indicating that the difference in surface area alone does not account for the difference in MIC between the small and large aggregates [90]. Reproduced with permission from ACS.

5. Prospects and conclusions

Fullerene nanostructures have brought about revolutions in a range of methodological industries, including organic photovoltaics, energy, biomedical purposes, biopharmaceuticals, etc. [92–94]. Fullerene nanocomposite membranes have been widely used in filtration systems. Other water decontamination strategies have also been considered, such as sedimentation, distillation, biological processes, flocculation, chlorination, ultraviolet light, etc. [95]. Various combinations and types of polymer/fullerene membranes have been developed (**Figure 8**). In fullerene-based membranes, remarkable morphology, mechanical, and barrier features have significantly contributed towards water remediation [96]. Fullerene molecules have contributed to the matrix-nanofiller interactions, enhancing the compatibility of these nanostructures. The main challenging aspect has been recognized as nanoparticle dispersion in polymeric membranes [97].

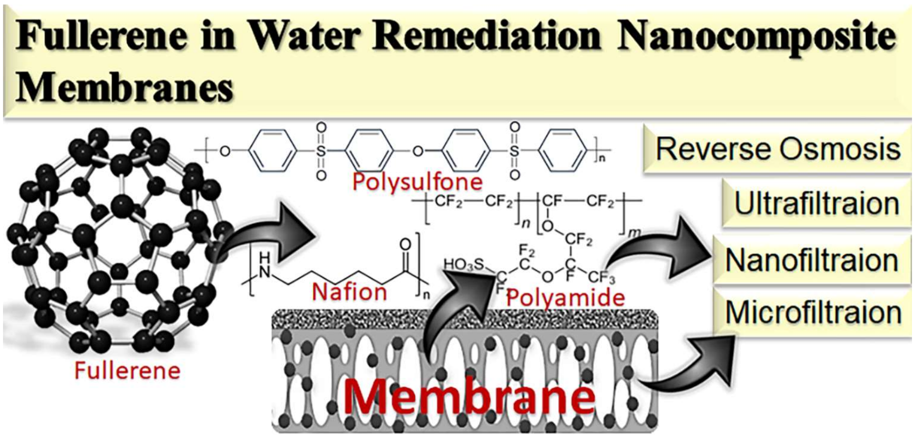

Figure 8. Design of fullerene-based membranes.

Better fullerene dispersion throughout the membrane ultimately defines the controlled pore size or structure, morphology, surface roughness, and wettability of efficient membranes. In this regard, separation mechanisms need to be explored to further improve the fullerene membrane-based filtration processes. Theoretical studies on fullerene nanocomposite membranes may also help to resolve the performance challenges. In the future, variations in membrane designs may also bring about revolutions in this field.

This cutting-edge review presents an analysis of applying fullerene nanocomposite membranes for water purification purposes. Polymer-based nanocomposite membranes with fullerene nanoparticles have been found to transform waste water remediation. Efforts on fullerene nanocomposite membranes have led to improved surface properties, permeability, selectivity, separation, antifouling, and other features. These membranes have a low price and lasting stability for large-scale filtration. Further research may lead to a number of enhanced membrane parameters to overcome these drawbacks.

Conflict of interest: The author declares no conflict of interest.

References

1. Kausar A, Ahmad I. Graphene and nanocomposites—Imprints on environmentally sustainable production and applications based on ecological aspects. Characterization and Application of Nanomaterials. 2024; 7(1): 4226. doi: 10.24294/can.v7i1.4226

2. Shah MP. Sustainable Industrial Wastewater Treatment and Pollution Control. Springer Nature Singapore; 2023. doi: 10.1007/978-981-99-2560-5
3. Bardhan A, Subbiah S, Mohanty K, et al. Feasibility of Poly (Vinyl Alcohol)/Poly (Diallyldimethylammonium Chloride) Polymeric Network Hydrogel as Draw Solute for Forward Osmosis Process. Membranes. 2022; 12(11): 1097. doi: 10.3390/membranes12111097
4. Hallinan DT, Minelli M, Oparaji O, et al. Effect of Polystyrene Synthesis Method on Water Sorption and Glass Transition. Membranes. 2022; 12(11): 1059. doi: 10.3390/membranes12111059
5. Lu X, Elimelech M. Fabrication of desalination membranes by interfacial polymerization: history, current efforts, and future directions. Chemical Society Reviews. 2021; 50(11): 6290-6307. doi: 10.1039/d0cs00502a
6. Lalia BS, Kochkodan V, Hashaikeh R, et al. A review on membrane fabrication: Structure, properties and performance relationship. Desalination. 2013; 326: 77-95. doi: 10.1016/j.desal.2013.06.016
7. Dong X, Lu D, Harris TAL, et al. Polymers and Solvents Used in Membrane Fabrication: A Review Focusing on Sustainable Membrane Development. Membranes. 2021; 11(5): 309. doi: 10.3390/membranes11050309
8. Ng ZC, Lau WJ, Matsuura T, et al. Thin film nanocomposite RO membranes: Review on fabrication techniques and impacts of nanofiller characteristics on membrane properties. Chemical Engineering Research and Design. 2021; 165: 81-105. doi: 10.1016/j.cherd.2020.10.003
9. Zhang Y, Wang H, Wang W, et al. Engineering covalent organic framework membranes for efficient ionic/molecular separations. Matter. 2024; 7(4): 1406-1439. doi: 10.1016/j.matt.2024.01.028
10. Yang Y, Chai W, Zhang L, et al. A mini-review of polymeric porous membranes with vertically penetrative pores. Journal of Polymer Science. 2023; 62(3): 492-507. doi: 10.1002/pol.20230501
11. Subaer S, Fansuri H, Haris A, et al. Pervaporation Membranes for Seawater Desalination Based on Geo–rGO–TiO_2 Nanocomposites: Part 2—Membranes Performances. Membranes. 2022; 12(11): 1046. doi: 10.3390/membranes12111046
12. Kausar A, Bocchetta P. Polymer/Graphene Nanocomposite Membranes: Status and Emerging Prospects. Journal of Composites Science. 2022; 6(3): 76. doi: 10.3390/jcs6030076
13. Tufail S, Sherwani MA, Shamim Z, et al. 2D nanostructures: Potential in diagnosis and treatment of Alzheimer's disease. Biomedicine & Pharmacotherapy. 2024; 170: 116070. doi: 10.1016/j.biopha.2023.116070
14. Teow YH, Ooi BS, Ahmad AL, et al. Investigation of Anti-fouling and UV-Cleaning Properties of PVDF/TiO_2 Mixed-Matrix Membrane for Humic Acid Removal. Membranes. 2020; 11(1): 16. doi: 10.3390/membranes11010016
15. Jatoi AS, Ahmed J, Bhutto AA, et al. Recent advances and future perspectives of carbon-based nanomaterials for environmental remediation. Brazilian Journal of Chemical Engineering. 2024. doi: 10.1007/s43153-024-00439-x
16. Silah H, Unal DN, Selcuk O, Uslu B. Applications of zero-dimensional carbon nanomaterials in water treatment. In: Joseph K, Wilson R, George G, Appukuttan S (editors). Zero-Dimensional Carbon Nanomaterials. Elsevier; 2024. pp. 577-609. doi: 10.1016/b978-0-323-99535-1.00018-4
17. Jatoi AS, Hashmi Z, Usman T, et al. Role of carbon nanomaterials for wastewater treatment—A brief review. In: Dehghani MH, Karri RR, Mubarak NM (editors). Water Treatment Using Engineered Carbon Nanotubes. Elsevier; 2024. pp. 29-62. doi: 10.1016/b978-0-443-18524-3.00016-7
18. Aydin D, Gübbük İH, Ersöz M. Recent advances and applications of nanostructured membranes in water purification. Turkish Journal of Chemistry. 2024; 48(1): 1-20. doi: 10.55730/1300-0527.3635
19. Balakumar S, Mahesh N, Kamaraj M, et al. Customized carbon composite nanomaterials for the mitigation of emerging contaminants: a review of recent trends. Carbon Letters. 2024; 34: 1091-1114. doi: 10.1007/s42823-024-00715-3
20. Jehoulet C, Obeng YS, Kim YT, et al. Electrochemistry and Langmuir trough studies of fullerene C60 and C70 films. Journal of the American Chemical Society. 1992; 114(11): 4237-4247. doi: 10.1021/ja00037a030
21. Chen Z, Zhu J, Yang D, et al. Isomerization strategy on a non-fullerene guest acceptor for stable organic solar cells with over 19% efficiency. Energy & Environmental Science. 2023; 16(7): 3119-3127. doi: 10.1039/d3ee01164j
22. Radford CL, Mudiyanselage PD, Stevens AL, et al. Heteroatoms as Rotational Blocking Groups for Non-Fullerene Acceptors in Indoor Organic Solar Cells. ACS Energy Letters. 2022; 7(5): 1635-1641. doi: 10.1021/acsenergylett.2c00515
23. Montellano López A, Mateo-Alonso A, Prato M. Materials chemistry of fullerene C60derivatives. Journal of Materials Chemistry. 2011; 21(5): 1305-1318. doi: 10.1039/c0jm02386h
24. Blanter MS, Borisova PA, Brazhkin VV, et al. The influence of metals on the phase transformations of fullerenes at high pressure and high temperatures. Materials Letters. 2022; 318: 132199. doi: 10.1016/j.matlet.2022.132199

25. Akasaka T, Wakahara T, Nagase S, et al. Structural Determination of the La@C82 Isomer. The Journal of Physical Chemistry B. 2001; 105(15): 2971-2974. doi: 10.1021/jp003930d
26. Gupta RK. NanoCarbon: A Wonder Material for Energy Applications. Springer Nature Singapore; 2024. doi: 10.1007/978-981-99-9935-4
27. Ghosh T, Banerji P, Das NC. Synthesis methods for the preparation of fullerenes. In: Joseph K, Wilson R, George G, Appukuttan S (editors). Zero-Dimensional Carbon Nanomaterials. Elsevier; 2024. pp. 135-151.
28. Dmitruk NL. Effect of chemical modification of thin C_{60} fullerene films on the fundamental absorption edge. Semiconductor Physics, Quantum Electronics and Optoelectronics. 2010; 13(2): 180-185. doi: 10.15407/spqeo13.02.180
29. Wang W, Hanindita F, Hamamoto Y, et al. Fully conjugated azacorannulene dimer as large diaza[80]fullerene fragment. Nature Communications. 2022; 13(1): 1498. doi: 10.1038/s41467-022-29106-w
30. Pesado-Gómez C, Serrano-García JS, Amaya-Flórez A, et al. Fullerenes: Historical background, novel biological activities versus possible health risks. Coordination Chemistry Reviews. 2024; 501: 215550. doi: 10.1016/j.ccr.2023.215550
31. Baskar AV, Benzigar MR, Talapaneni SN, et al. Self-Assembled Fullerene Nanostructures: Synthesis and Applications. Advanced Functional Materials. 2021; 32(6). doi: 10.1002/adfm.202106924
32. Heredia DA, Durantini AM, Durantini JE, et al. Fullerene C_{60} derivatives as antimicrobial photodynamic agents. Journal of Photochemistry and Photobiology C: Photochemistry Reviews. 2022; 51: 100471. doi: 10.1016/j.jphotochemrev.2021.100471
33. Chae SR, Therezien M, Budarz JF, et al. Comparison of the photosensitivity and bacterial toxicity of spherical and tubular fullerenes of variable aggregate size. Journal of Nanoparticle Research. 2011; 13(10): 5121-5127. doi: 10.1007/s11051-011-0492-y
34. Modi A, Koratkar N, Lass E, et al. Miniaturized gas ionization sensors using carbon nanotubes. Nature. 2003; 424(6945): 171-174. doi: 10.1038/nature01777
35. Gallo M, Favila A, Glossman-Mitnik D. DFT studies of functionalized carbon nanotubes and fullerenes as nanovectors for drug delivery of antitubercular compounds. Chemical Physics Letters. 2007; 447(1-3): 105-109. doi: 10.1016/j.cplett.2007.08.098
36. Djordjevic A, Srdjenovic B, Seke M, et al. Review of Synthesis and Antioxidant Potential of Fullerenol Nanoparticles. Journal of Nanomaterials. 2015; 2015: 1-15. doi: 10.1155/2015/567073
37. Molinari R, Palmisano L, Drioli E, et al. Studies on various reactor configurations for coupling photocatalysis and membrane processes in water purification. Journal of Membrane Science. 2002; 206(1-2): 399–415 doi: 10.1016/S0376-7388(01)00785-2
38. Zhu Q, Cai Z, Zhou P, et al. Recent progress of membrane technology for chiral separation: A comprehensive review. Separation and Purification Technology. 2023; 309: 123077. doi: 10.1016/j.seppur.2022.123077
39. Choi JY, Ho-Bum P. Separation Membrane Including Graphene. US 9,713,794, 25 July 2017.
40. Adeola AO, Nomngongo PN. Advanced Polymeric Nanocomposites for Water Treatment Applications: A Holistic Perspective. Polymers. 2022; 14(12): 2462. doi: 10.3390/polym14122462
41. Valladares Linares R, Li Z, Sarp S, et al. Forward osmosis niches in seawater desalination and wastewater reuse. Water Research. 2014; 66: 122-139. doi: 10.1016/j.watres.2014.08.021
42. Zhang X, Huang Q, Deng F, et al. Mussel-inspired fabrication of functional materials and their environmental applications: Progress and prospects. Applied Materials Today. 2017; 7: 222-238. doi: 10.1016/j.apmt.2017.04.001
43. Sri Abirami Saraswathi MS, Nagendran A, Rana D. Tailored polymer nanocomposite membranes based on carbon, metal oxide and silicon nanomaterials: a review. Journal of Materials Chemistry A. 2019; 7(15): 8723-8745. doi: 10.1039/c8ta11460a
44. Dashti A, Harami HR, Rezakazemi M. Accurate prediction of solubility of gases within H 2 -selective nanocomposite membranes using committee machine intelligent system. International Journal of Hydrogen Energy. 2018; 43(13): 6614-6624. doi: 10.1016/j.ijhydene.2018.02.046
45. Pishnamazi M, Nakhjiri AT, Ghadiri M, et al. Computational fluid dynamics simulation of NO_2 molecular sequestration from a gaseous stream using NaOH liquid absorbent through porous membrane contactors. Journal of Molecular Liquids. 2020; 313: 113584. doi: 10.1016/j.molliq.2020.113584
46. Kausar A. Efficiency of polymer/nanocarbon-based nanocomposite membranes in water treatment techniques. Journal of the Chinese Advanced Materials Society. 2018; 6(4): 508-526. doi: 10.1080/22243682.2018.1515659

47. Mashhadikhan S, Ahmadi R, Ebadi Amooghin A, et al. Breaking temperature barrier: Highly thermally heat resistant polymeric membranes for sustainable water and wastewater treatment. Renewable and Sustainable Energy Reviews. 2024; 189: 113902. doi: 10.1016/j.rser.2023.113902
48. Jhaveri JH, Murthy ZVP. Nanocomposite membranes. Desalination and Water Treatment. 2015; 57(55): 26803-26819. doi: 10.1080/19443994.2015.1120687
49. Sacco LN, Vollebregt S. Overview of Engineering Carbon Nanomaterials Such as Carbon Nanotubes (CNTs), Carbon Nanofibers (CNFs), Graphene and Nanodiamonds and Other Carbon Allotropes inside Porous Anodic Alumina (PAA) Templates. Nanomaterials. 2023; 13(2): 260. doi: 10.3390/nano13020260
50. Sreeramareddygari M, Sureshkumar K, Thippeswamy R, et al. Various properties of zero-dimensional carbon nanomaterials–reinforced polymeric matrices. In: Joseph K, Wilson R, George G, Appukuttan S (editors). Zero-Dimensional Carbon Nanomaterials. Elsevier; 2024. pp. 357-384. doi: 10.1016/b978-0-323-99535-1.00012-3
51. Elrasheedy A, Nady N, Bassyouni M, et al. Metal Organic Framework Based Polymer Mixed Matrix Membranes: Review on Applications in Water Purification. Membranes. 2019; 9(7): 88. doi: 10.3390/membranes9070088
52. Ammar A, Al-Enizi AM, AlMaadeed MA, et al. Influence of graphene oxide on mechanical, morphological, barrier, and electrical properties of polymer membranes. Arabian Journal of Chemistry. 2016; 9(2): 274-286. doi: 10.1016/j.arabjc.2015.07.006
53. Ganesh BM, Isloor AM, Ismail AF. Enhanced hydrophilicity and salt rejection study of graphene oxide-polysulfone mixed matrix membrane. Desalination. 2013; 313: 199-207. doi: 10.1016/j.desal.2012.11.037
54. Abdolmaleki A, Mohamadi Z, Fashandi H, et al. Synergistic contribution of sulfonated poly(ether sulfone) and iminodiacetic acid functionalized-graphene oxide nanosheets towards enhancing cationic dye wastewater purification using nanocomposite membranes. Chemical Engineering Journal. 2024; 481: 148622. doi: 10.1016/j.cej.2024.148622
55. Arahman N. Fabrication of Polyethersulfone membranes using nanocarbon as additive. International Journal of GEOMATE. 2018; 15(50). doi: 10.21660/2018.50.95424
56. Brunet L, Lyon DY, Hotze EM, et al. Comparative Photoactivity and Antibacterial Properties of C_{60} Fullerenes and Titanium Dioxide Nanoparticles. Environmental Science & Technology. 2009; 43(12): 4355-4360. doi: 10.1021/es803093t
57. Zhang BT, Zheng X, Li HF, et al. Application of carbon-based nanomaterials in sample preparation: A review. Analytica Chimica Acta. 2013; 784: 1-17. doi: 10.1016/j.aca.2013.03.054
58. Burakov AE, Galunin EV, Burakova IV, et al. Adsorption of heavy metals on conventional and nanostructured materials for wastewater treatment purposes: A review. Ecotoxicology and Environmental Safety. 2018; 148: 702-712. doi: 10.1016/j.ecoenv.2017.11.034
59. Samonin VV, Nikonova VYu, Podvyaznikov ML. Carbon adsorbents on the basis of the hydrolytic lignin modified with fullerenes in producing. Russian Journal of Applied Chemistry. 2014; 87(2): 190-193. doi: 10.1134/s1070427214020116
60. Yashas SR, Shahmoradi B, Wantala K, et al. Potentiality of polymer nanocomposites for sustainable environmental applications: A review of recent advances. Polymer. 2021; 233: 124184. doi: 10.1016/j.polymer.2021.124184
61. Ma J, Guo Q, Gao HL, et al. Synthesis of C_{60}/Graphene Composite as Electrode in Supercapacitors. Fullerenes, Nanotubes and Carbon Nanostructures. 2014; 23(6): 477-482. doi: 10.1080/1536383x.2013.865604
62. Perera MGN, Galagedara YR, Ren Y, et al. Fabrication of fullerenol-incorporated thin-film nanocomposite forward osmosis membranes for improved desalination performances. Journal of Polymer Research. 2018; 25(9). doi: 10.1007/s10965-018-1593-4
63. Shen Q, Xu S, Xu Z, et al. Novel thin-film nanocomposite membrane with water-soluble polyhydroxylated fullerene for the separation of Mg^{2+}/Li^{+} aqueous solution. Journal of Applied Polymer Science. 2019; 136(41). doi: 10.1002/app.48029
64. Vojdani M., and Giti R. Polyamide as a denture base material: A literature review. Journal of Dentistry, 2015; 16(1 Suppl): 1-9
65. Shrivastava A, Chakraborty M, Singh AK. Biocomposites with polyamide fibers (nylons and aramids). In: Karak N (editors). Advances in Biocomposites and their Applications. Elsevier; 2024. pp. 121-147. doi: 10.1016/b978-0-443-19074-2.00004-6
66. Tan X fei, Liu Y guo, Gu Y ling, et al. Biochar-based nano-composites for the decontamination of wastewater: A review. Bioresource Technology. 2016; 212: 318-333. doi: 10.1016/j.biortech.2016.04.093
67. Fang Y, Zhu C, Yang H, et al. Polyamide nanofiltration membranes by vacuum-assisted interfacial polymerization: Broad universality of Substrate, wide window of monomer concentration and high reproducibility of performance. Journal of Colloid and Interface Science. 2024; 655: 327-334. doi: 10.1016/j.jcis.2023.11.002

68. Plisko TV, Liubimova AS, Bildyukevich AV, et al. Fabrication and characterization of polyamide-fullerenol thin film nanocomposite hollow fiber membranes with enhanced antifouling performance. Journal of Membrane Science. 2018; 551: 20-36. doi: 10.1016/j.memsci.2018.01.015
69. Dmitrenko ME, Penkova AV, Kuzminova AI, et al. Development and investigation of novel polyphenylene isophthalamide pervaporation membranes modified with various fullerene derivatives. Separation and Purification Technology. 2019; 226: 241-251. doi: 10.1016/j.seppur.2019.05.092
70. Taheri M. Advances in Nanohybrid Membranes for Dye Reduction: A Comprehensive Review. Global Challenges. 2023; 8(1). doi: 10.1002/gch2.202300052
71. Inamuddin, Khan A. Sustainable Materials and Systems for Water Desalination. Springer International Publishing; 2021. doi: 10.1007/978-3-030-72873-1
72. Jani M, Arcos-Pareja JA, Ni M. Engineered Zero-Dimensional Fullerene/Carbon Dots-Polymer Based Nanocomposite Membranes for Wastewater Treatment. Molecules. 2020; 25(21): 4934. doi: 10.3390/molecules25214934
73. Liu Y, Phillips B, Li W, et al. Fullerene-Tailored Graphene Oxide Interlayer Spacing for Energy-Efficient Water Desalination. ACS Applied Nano Materials. 2018; 1(11): 6168-6175. doi: 10.1021/acsanm.8b01375
74. Yang H, Dong G, Qin L, et al. Polyamide nanofiltration membranes mediated by mesoporous silica nanosheet interlayers display substantial desalination performance enhancement. Journal of Membrane Science. 2024; 693: 122387. doi: 10.1016/j.memsci.2023.122387
75. Alekseeva OV, Bagrovskaya NA, Noskov AV. Sorption of heavy metal ions by fullerene and polystyrene/fullerene film compositions. Protection of Metals and Physical Chemistry of Surfaces. 2016; 52(3): 443-447. doi: 10.1134/s2070205116030035
76. Jin X, Hu JY, Tint ML, et al. Estrogenic compounds removal by fullerene-containing membranes. Desalination. 2007; 214(1-3): 83-90. doi: 10.1016/j.desal.2006.10.019
77. Sudareva NN, Penkova AV, Kostereva TA, et al. Properties of casting solutions and ultrafiltration membranes based on fullerene-polyamide nanocomposites. Express Polymer Letters. 2012; 6(3): 178-188. doi: 10.3144/expresspolymlett.2012.20
78. Penkova AV, Polotskaya GA, Toikka AM, et al. Structure and Pervaporation Properties of Poly(phenylene-iso-phthalamide) Membranes Modified by Fullerene C_{60}. Macromolecular Materials and Engineering. 2009; 294(6-7): 432-440. doi: 10.1002/mame.200800362
79. Serbanescu OS, Voicu SI, Thakur VK. Polysulfone functionalized membranes: Properties and challenges. Materials Today Chemistry. 2020; 17: 100302. doi: 10.1016/j.mtchem.2020.100302
80. Esfahani MR, Aktij SA, Dabaghian Z, et al. Nanocomposite membranes for water separation and purification: Fabrication, modification, and applications. Separation and Purification Technology. 2019; 213: 465-499. doi: 10.1016/j.seppur.2018.12.050
81. Penkova AV, Dmitrenko ME, Sokolova MP, et al. Impact of fullerene loading on the structure and transport properties of polysulfone mixed-matrix membranes. Journal of Materials Science. 2016; 51(16): 7652-7659. doi: 10.1007/s10853-016-0047-9
82. John N. Fullerene and nanodiamond-based polymer nanocomposite membranes and their pervaporation performances. Polymer Nanocomposite Membranes for Pervaporation. Published online 2020: 153-173. doi: 10.1016/b978-0-12-816785-4.00007-0
83. Aryafard E, Rahmatmand B, Rahimpour MR. Application of computational fluid dynamics technique in pervaporation processes. Current Trends and Future Developments on (Bio-) Membranes. Published online 2022: 247-268. doi: 10.1016/b978-0-12-822294-2.00012-6
84. Karimi MB, Mohammadi F, Hooshyari K. Recent approaches to improve Nafion performance for fuel cell applications: A review. International Journal of Hydrogen Energy. 2019; 44(54): 28919-28938. doi: 10.1016/j.ijhydene.2019.09.096
85. Peron J, Mani A, Zhao X, et al. Properties of Nafion® NR-211 membranes for PEMFCs. Journal of Membrane Science. 2010; 356(1-2): 44-51. doi: 10.1016/j.memsci.2010.03.025
86. Maiti TK, Singh J, Majhi J, et al. Advances in polybenzimidazole based membranes for fuel cell applications that overcome Nafion membranes constraints. Polymer. 2022; 255: 125151. doi: 10.1016/j.polymer.2022.125151
87. Wan YH, Sun J, Jian QP, et al. A Nafion/polybenzimidazole composite membrane with consecutive proton-conducting pathways for aqueous redox flow batteries. Journal of Materials Chemistry A. 2022; 10(24): 13021-13030. doi: 10.1039/d2ta01746f

88. Li Y, He G, Wang S, et al. Recent advances in the fabrication of advanced composite membranes. Journal of Materials Chemistry A. 2013; 1(35): 10058. doi: 10.1039/c3ta01652h
89. Tasaki K, Gasa J, Wang H, et al. Fabrication and characterization of fullerene–Nafion composite membranes. Polymer. 2007; 48(15): 4438-4448. doi: 10.1016/j.polymer.2007.05.049
90. Lyon DY, Adams LK, Falkner JC, et al. Antibacterial Activity of Fullerene Water Suspensions: Effects of Preparation Method and Particle Size. Environmental Science & Technology. 2006; 40(14): 4360-4366. doi: 10.1021/es0603655
91. Alshammari AH, Alshammari M, Ibrahim M, et al. Processing polymer film nanocomposites of polyvinyl chloride – Polyvinylpyrrolidone and MoO3 for optoelectronic applications. Optics & Laser Technology. 2024; 168: 109833. doi: 10.1016/j.optlastec.2023.109833
92. Hu X, Zhang Z, Gholizadeh M, et al. Coke Formation during Thermal Treatment of Bio-oil. Energy & Fuels. 2020; 34(7): 7863-7914. doi: 10.1021/acs.energyfuels.0c01323
93. Zheng T, Fan L, Zhou H, et al. Engineering of Electron Extraction and Defect Passivation via Anion-Doped Conductive Fullerene Derivatives as Interlayers for Efficient Invert Perovskite Solar Cells. ACS Applied Materials & Interfaces. 2020; 12(22): 24747-24755. doi: 10.1021/acsami.0c04315
94. Djordjević A, Bogdanović GM, Dobrić S. Fullerenes in biomedicine. Journal of the Balkan Union of Oncology. 2006; 11(4): 391-404
95. Kundu D, Dutta D, Joseph A, et al. Safeguarding drinking water: A brief insight on characteristics, treatments and risk assessment of contamination. Environmental Monitoring and Assessment. 2024; 196(2). doi: 10.1007/s10661-024-12311-z
96. Amooghin AE, Sanaeepur H, Pedram MZ, et al. New advances in polymeric membranes for CO_2 separation. Polymer Science: Research Advances, Practical Applications and Educational Aspects. Formatex Research Center; 2016. pp. 354-368
97. Vladisavljević GT. Preparation of microparticles and nanoparticles using membrane-assisted dispersion, micromixing, and evaporation processes. Particuology. 2024; 84: 30-44. doi: 10.1016/j.partic.2023.03.003

Characterization and Application of Nanomaterials 2024, 7(2), 5454.
https://doi.org/10.24294/can.v7i2.5454

Review

Boron and tungsten carbides based and related nanodispersed composites—A review

Otar Tsagareishvili[1], Levan Chkhartishvili[1,2,*], Marina Matcharashvili[2], Shorena Dekanosidze[2]

[1] Ferdinand Tavadze Metallurgy and Materials Science Institute, Semiconducting and Powder Composite Materials Laboratory, Tbilisi 0186, Georgia
[2] Engineering Physics Department, Georgian Technical University, Tbilisi 0160, Georgia
*** Corresponding author:** Levan Chkhartishvili, levanchkhartishvili@gtu.ge

CITATION

Tsagareishvili O, Chkhartishvili L, Matcharashvili M, Dekanosidze S. Boron and tungsten carbides based and related nanodispersed composites—A review. Characterization and Application of Nanomaterials. 2024; 7(2): 5454. https://doi.org/10.24294/can.v7i2.5454

ARTICLE INFO

Received: 26 March 2024
Accepted: 4 June 2024
Available online: 18 July 2024

Abstract: Boron and tungsten carbides, B_4C and WC, are hard materials widely used in modern technologies. Further improvement of their performance characteristics involves the development of new B_4C and WC-based and/or related composites in a nanodispersed state. This article provides a review of available literature research on B-C-W systems, which would be useful in future studies in this direction.

Keywords: boron carbide; tungsten carbide; B-C-W system; composite; nanodispersed state

1. Introduction

Boron and tungsten carbides, B_4C and WC, are well-known hard materials widely used in modern technologies. Improvement of their performance characteristics involves the development of new composites with B_4C and WC matrices in a nanodispersed state. Good examples of this kind are the boron carbide-titanium diboride B_4C-TiB_2 quasieutetic and tungsten carbide-cobalt WC-Co ceramic alloys. In nanodispersed form, some additional attractive physical-mechanical properties are exhibited (for example, see the research of Chkhartishvili et al. [1,2] and Shabalin [3]) by more complex composites containing both boron and tungsten carbides, which serve as matrix and modifying components, respectively, or vice versa. This makes the development of newer boron and tungsten carbide-based and/or related composites very promising (for example, see the recent reviews of Manzar et al. [4] and Singh et al. [5] on various techniques for the development of hard boron carbon nitride nanoscale coatings on metal surfaces).

The present article aims to give only a short review of available in the literature research on B-C-W systems not illustrated with self-drawn or reproduced figures and tables and not provide criticism towards the described results. Authors are not claiming to provide exhaustive information about the huge number of publications in this field. Nevertheless, we believe that the data presented here are representative and thus will be useful in future studies on boron and tungsten carbide-based composite materials.

2. B-W systems

Using the tungsten coatings saturated with boron of compositions W-(13wt.%-23wt.%)B to substrates from austenitic steel was found [6] to be suitable. Obtained structures revealed much more resistance to corrosion and wear losses in material mass than uncoated steel. The beta-WB and W_2B (tungsten boride high-temperature phases) coatings of titanium Ti and steel surfaces containing tungsten can be formed [7] applying the shaped charge explosion technique. Microhardness of coated material achieved 42 GPa. The hardness and stability of the highest tungsten borides, when they are built of tungsten atoms separated by borophene layers, were studied in the study of Gonzalez Szwacki [8].

Shift of so-called DBTT (Ductile-to-Brittle Transition Temperature) in tungsten foil was found by studying the neutron irradiation effect. Processing techniques, possible applications, as well as some physical characteristics of multilayered materials (ceramic-C and ceramic-metal structures) with an operating temperature higher than 1200 °C were considered in the study of Sorokin et al. [9]. This problem is of interest because of the applicability of boron compound-tungsten compound composites as effective neutron-shield materials.

Aiming to increase the physical-mechanical properties of tungsten tetraboride WB_4 (which is a lower-cost transition-metal boride), its solid solutions with metals, namely, chromium Cr, manganese Mn, and tantalum Ta, were synthesized and characterized [10]. And the concentrations of these transition metals up to 50.0at.% were tested. The listed solutions, which are the refractory compounds, were obtained from component elements by arc melting method. Samples chemical composition was examined using X-ray EDS (Energy-Dispersive Spectroscopy). The XRD (X-ray diffraction) results indicated that the solubility limits of Cr, Mn, and Ta in WB_4 are <10at.%, <20at.% and >20at.%, respectively. Vickers hardness optimized values measured by microindentation were of 53.5, 53.7, and 52.8 GPa when WB_4 was added with 10at.%, 4at.% and 2at.% of Cr, Mn, and Ta, respectively. It was also produced the tungsten tetraboride-based ternary solid solution with a Ta concentration fixed at 2at.%, while varying Mn and Cr concentrations. The values of hardness measured for $W_{0.93}Ta_{0.02}Cr_{0.05}B_4$ and $W_{0.94}Ta_{0.02}Mn_{0.04}B_4$ compositions equal to 57.3 and 55.8 GPa, respectively. According to the high-pressure (<65 GPa) in situ XRD measurements, for the hardest WB_4-based solid solution, $W_{0.93}Ta_{0.02}Cr_{0.05}B_4$, the bulk modulus is 335 GPa, and a phase transition induced by pressure, which is observable in pure tungsten tetraboride, was suppressed.

Obtaining of powder tungsten tetraboride by reactive HPV (hot pressing in vacuum) method from powders of its component chemical elements (amorphous boron a-B and tungsten W) was systematically investigated [11] in dependence on temperature of synthesis, molar ratio between boron and tungsten in charge, applied pressure, and duration of phase formation. Metastable WB_4 was obtained at a molar ratio of B:W = 8:1 and a temperature of 1350 °C under uniaxial pressure of 30 MPa for 1 h. Both SEM (Scanning Electron Microscopy) and TEM (Transmission Electron Microscopy) studies revealed that particles of the obtained powder tend to agglomerate. Besides, a-B trace was detected in the product. At the same time, XRD pattern analysis of the as-synthesized powders conforms formation of the WB_4 crystalline phase.

3. C-W systems

In general, hard alloys are the wear-resistant metal materials that can retain their advanced properties at 900–1200 °C and are mainly made from carbides of tungsten, titanium, tantalum, or/and chromium and bonded with metal binders with varying cobalt or nickel content. Hard alloys produced by industry can be divided into four groups according to the metal carbides present in them: tungsten, titanium-tungsten, titanium-tantalum-tungsten, and tungsten-free alloys [12]. One can see that the tungsten carbide presence is critical.

- The first group consists of alloys of the tungsten carbide-cobalt (WC-Co) system. They can be marked with the letters WCo and a number indicating the cobalt content as wt.%; for example, WCo10 alloy contains 10wt.% Co and the rest (up to 100wt.%) is WC. These alloys are characterized by maximum strength but reduced hardness. They are heat-resistant up to temperatures of 800 °C. As the content of cobalt increases, impact toughness increases as well, but wear resistance decreases. Alloys of the WCo-group are used for processing workpieces made of brittle metals such as cast iron, bronze, and other non-ferrous metals and alloys, as well as some non-metallic materials.
- The second group is formed by alloys of the tungsten carbide-titanium carbide-cobalt (WC-TiC-Co) system. They can be marked with the letters Ti and Co and numbers. The numbers after the letters Ti and Co mean the wt.% of TiC and Co, respectively, and the rest (up to 100wt.%) is WC. For example, the Ti5Co10 alloy contains 5wt.%, 10wt.% and 85wt.% of TiC, Co, and WC, respectively. Alloys in this group are more wear-resistant but less durable. As the TiC content increases, wear resistance increases, but strength decreases. The heat resistance of TiCo-group alloys is higher, about 900–1000 °C. The heat resistance performance increases as the amount of TiC increases. Tools made from alloys of this group provide higher cutting speeds. They are most often used for processing carbon and alloy steels.
- The third group is formed by alloys of the tungsten carbide-titanium carbide-tantalum carbide-cobalt (WC-TiC-TaC-Co) system. These alloys are usually marked with the letters TiTa and Co. The numbers after the letters TiTa and Co indicate the wt.% of titanium and tantalum carbides together, TiC-TaC and Co, and the rest (up to 100wt.%) is tungsten carbide WC. For example, the TiTa5Co15 alloy contains 5wt.%, 15wt.%, and 80wt.% TiC-TaC, Co, and WC, respectively. These alloys differ in greater strength and better resistance to vibration and chipping. Alloys of this group are used under the most severe cutting conditions—roughing of steel ingots, castings, and forgings.
- To rationally use scarce tungsten, a fourth group of tungsten-free hard alloys was developed. They contain titanium carbides (TiC) and titanium carbonitrides (TiCN) bonded with a nickel-molybdenum (NiMo) metallic alloy. Their manufacturing technologies are quite similar to the above-listed hard alloys containing tungsten; however, they have lower bending and impact strengths and, because of lower thermal conductivity, are more sensitive to changes in temperature. Their advantages are: higher (up to 1000 °C) heat resistance and lower adhesion during cutting and, consequently, not prone to buildup to materials being processed. This is why tools made from tungsten-free hard alloys are recommended for finishing turning and milling processes.

Thus, according to the chemical composition, hard alloys are divided into tungsten-cobalt (WCo), titanium-tungsten-cobalt (TiCo), and titanium-tantalum-tungsten-cobalt (TiTaCo) alloys. As for the production method, such classification of hard alloys divides them into two groups: sintered and casted alloys. Products from sintered hard alloys are manufactured by powder metallurgy, and they can be processed by physical or chemical methods (dispersing and grinding, treatment with US (UltraSound) and laser, etching in acids, etc.) and, most perfectly, by electrical erosion. Casted hard alloys intended for surfacing tools can be subjected to mechanical and thermal treatments (annealing, hardening, aging, etc.).

Finally, the ISO (International Organization for Standardization) standards classify the hard alloys according to their intended purpose:

- P: steel castings and materials, processing of which forms the drain chips;
- M: processing difficult-to-cut materials (for example, stainless steel);
- K: processing cast iron Fe;
- N: processing aluminum Al, other non-ferrous metals and metallic alloys;
- S: processing heat-resistant alloys and titanium-based alloys; and
- H: hardened steel.

In hard alloys, as a result of combining their matrix and reinforcing modifiers, a complex of properties of the composition is formed, which not only reflects the initial characteristics of components but also includes properties that the isolated components do not possess. In particular, the presence of interfaces between reinforcing components and matrix significantly increases the crack resistance of the material, and in hard composites, unlike homogeneous metals, an increase in static strength does not lead to a decrease but, as a rule, to an increase in fracture toughness characteristics.

Hard alloy tools have high hardness and heat resistance, typically of 80–90 HRA and 800–1000 °C, because of refractory metal carbide components. Products made from them can be processed at several times higher speeds in comparison with the characteristic speeds of cutting high-carbon steels. The main disadvantages of hard alloys are fragility and difficulty in machining their products. They have reduced bending strength, 1000–1500 MPa, and very low impact toughness. Due to their high hardness, hard alloys are low-tech. For example, it is impossible to shape tools from them. In addition, hard alloys can be ground to a limited extent—only with a diamond tool. In this regard, frequently there are used their plates, either soldered or fixed to the tool holders.

As entropy is a key characteristic of thermodynamic systems, its calculation allows studying the equilibrium state, in particular, component contact interaction, when the composite is formed. A study by Syrovatko [13] introduced such calculations for tungsten carbide phases WC-W_2C eutectic by statistically processing the digitalized photos of scanned component phases. Entropies of WC and W_2C phases were found to be 29.22 and 58.38 J/mol·K, respectively, which are in satisfactory agreement with reference data [14]: 32.21 and 56.28 J/mol·K, respectively. Ultrafast compacting possibility for tungsten carbide WC without adding any binder phase was explored [15] for a technology combining sintering processes assisted with uniaxial pressure and limited AC (alternating current).

In modern production, WC-Co hard alloy parts are mainly made either by casting or powder metallurgy methods. Therefore, details with complex geometry often require further mechanical processing, which is associated with difficulties due to the high hardness of the material. So-called additive manufacturing technology was proposed [16] for producing details of small dimensions and complex configurations.

It includes SLM (Selective Laser Melting), SEBM (Selective Electron Beam Melting), inkjet additive production of binder, gel 3D printing, and melting stages. Product properties depend on WC particle size and Co amount in the composite. Due to the uneven distribution of energy, the microstructures of samples obtained by SLM- and SEBM-methods are not uniform. For this reason, their properties are unstable. In addition, in the samples obtained by SLM, due to the high energy density, Co and C are burned. These losses lead to cracked and brittle samples, and if the energy density is reduced, the cobalt cannot melt completely and the samples turn out to be porous.

Using the method of obtaining nanocrystalline tungsten carbide with Co component developed in Gachechiladze et al.'s study [17], the ultradispersed WC-Co alloys were synthesized from the precursor in the form of a suspension of ethyl alcohol solution of tungsten chloride $WCl_6 \cdot 6H_2O$ and a mixture of aqueous solution of cobalt chloride $CoCl_2 \cdot 6H_2O$ and an alcohol solution of urotropin $C_6H_{12}N_4$. It is known that in the process of synthesizing tungsten carbide, the presence of some intermediate complex carbides, mainly W_3Co_3C and W_6Co_6C, in the final product is expected, which cause degradation of the material's physical-mechanical properties. However, optimizing the technological parameters made it possible to obtain the final product without these intermediate carbides.

A systematic analysis of WC-Co alloys was carried out [18] on samples obtained under identical conditions. Namely, the influences of WC matrix particle size, Co binder content, and temperature on their complex mechanical properties were studied. By determining the mechanical characteristics during bending tests, the three temperature intervals with different mechanisms of plastic deformation, temperatures of ductile-brittle transition, and strain hardening coefficients, as well as their indicators, were established. Impact toughness increases and hardness decreases with increasing both Co content and average WC grain size, with some exceptions, where impact toughness and, consequently, cracking resistance can be increased at hardness expense and, thus, wear resistance. The maximum strength limit is reached when the average WC grain size varies in the range of 1.4–5.3 μm, and the Co amount in the alloy is 6 wt.%. The maximum compressive strength is achieved when the average WC grain size changes in the range of 1.4–1.7 μm. As for the bending strength limit, it practically does not change with further reduction of the average grain size.

Tungsten carbide compound produced by powder metallurgy methods, which is widely used to develop the tool materials necessary for high-speed processing, consists of carbide particles—usually tungsten carbide WC itself and a relatively soft metal binder. Currently, hundreds of WC-based alloys are known, most of which use cobalt Co, nickel Ni, and chromium Cr as binders, as well as other binders with various metallic and non-metallic additives. At room temperature, tungsten carbide WC is characterized by high hardness, which is largely maintained at higher temperatures. But it lacks sufficient high-temperature strength, the cutting tool's key property. To maintain the high hardness of tungsten carbide while increasing its toughness, the special metal binders should be used. The composite obtained in this way must have a much higher hardness than high-speed steel and a higher rate of service life as well. An increase in the amount of metal binder in the WC-Co alloy leads to a decrease in its hardness. The hardness of this material also depends on the size of the tungsten carbide particles; the hardness of the alloy decreases with the increase in the carbide grain size [19].

The work of Pereira et al. [20] presents the WC-based composites with various binder metal systems: WC-Co, WC-CoNi, WC-Ni, WC-CoCr, WC-CoNiCr, WC-NiCr, and WC-NiCrMo. Wear in such samples was studied, and it has been determined that chromium-containing metal binders are characterized by higher wear resistance compared to other investigated composites.

The operational properties of hard alloys are improved not only by the influence of carbide additives but also by optimizing the composition of the cementing metal components. In this sense, the partial or complete replacement of cobalt in the WC-Co alloy still seems like a relevant task. Complex metal alloys have been proposed not only to replace cobalt but also to improve the high-temperature characteristics of the alloy. It is worth noting the creation of a cementitious multi-component metal alloy FeNiCoCr [21], in which the chromium content exceeds 8 wt.%. The characteristics of the WC-FeNiCoCr composite depend on the grain size of the matrix material, i.e., WC. In it, compared to WC-Co of the corresponding composition, the hardness value is essentially preserved and the toughness is reduced by 25%.

The WC-TiC-Co system alloys of various compositions are widely used in practice. Such compositions are characterized by high hardness, chemical stability at high temperatures, and wear resistance. It has been established that obtaining WC-TiC-Co systems in an ultradispersed state and maintaining such a state after compaction significantly improves the physical-mechanical and operational characteristics of the material. WC-TiC-Co systems can be obtained in a nanocrystalline state by sputtering liquid charge and chemical and mechanical methods. If the composition of the alloy is fixed, then the important factors that lead to the improvement of the material's mechanical characteristics are the size of the particles, the degree of homogeneity of the structure, and the purity of the initial powder. Thus, it is recommended that the sizes of the carbides, WC and TiC, which make up the WC-TiC-Co system, should be as small as possible—ultradispersed and their mixture—homogeneous. The sputtering method can be considered promising for obtaining high-purity nanopowders for industrial purposes. However, its application is hindered by the problem related to the titanium dioxide TiO_2 reduction in the WC-TiC-Co nanostructured system preparation process. A mechanical-chemical method was successfully used to obtain an ultra-dispersed WC-TiC-Co composite. In particular, its powder with 200 nm particle size was obtained [22] in this way.

The effect of TiC on WC-Co was studied [23], when it replaced WC by 5 wt.%–20 wt.%. This composite was consolidated by isostatic HTP (High-Temperature Pressing) at a temperature of 1350 °C and a pressure of 50–150 MPa. When replacing with 5wt.% and 20wt.% TiC, the required pressures were 50 and 150 MPa, respectively. It led hardness to increase from 1050 up to 1330 and 1600 HV. Such a high rate should be not only due to the addition of TiC but also to the reduction of porosity during high-pressure compaction. Young’s modulus, on the contrary, decreases with the addition of TiC. When the Young’s modulus of WC-Co was equal to 570 MPa, it became 420–490 MPa with the addition of TiC. The impact toughness and composite density also decrease slightly with the addition of TiC.

By discussing [24] the heat treatment processes in two-carbide, WC, and TiC alloys and the laser impulse effect on their structure, as well as operational mode parameters, it has been established that the microcracks in the surface layers of Ti15Co6 alloy increase by 150–200 units due to laser-pulse impact. Such strengthening is associated with structural and phase transformations caused by electrical-physical effects: a new phase W_2C is formed in the surface layers, and the binding cobalt phase is saturated with tungsten and titanium carbides. In addition, laser heat treatment increases the operational characteristics of $Ti_{15}Co_6$ alloy by 2–3 times.

Physical-mechanical properties and structure of tungsten-cobalt WC-Co hardmetals, which contained different amounts of cobalt and alloyed tantalum and vanadium carbides (TaC and VC), were investigated in the work of Falkovsky et al. [25]. It was shown that the addition of 0.5 wt.%–2 wt.% TaC increases the hardness, while the bending strength remains practically unchanged. Then the content of TaC was kept at the constant level of 5 wt.%, while the VC amount changed from 0.4 wt.% to 10 wt.%. If the VC amount was less than its solubility in Co, the materials showed structure with basic carbide phase (WC) ultrafine grains: 0.2–0.5 μm. At 6 wt.% and 10 wt.% of Co, typical physical-mechanical parameters of these hardmetals were: hardness of 93.5 and 93.0 kgf/mm^2, bending strength of 1670 and 1870 MPa, cracking coefficient of 11 and 16 $MPa \cdot m^{1/2}$ and coercive force of 417 and 383 Oe, respectively. A process was developed [26] to produce WC in nanopowder form applying a plasma-chemical reduction method. The carbide grain size value was adjustable from 0.01 to 0.05 μm. Two more routes were suggested as alternatives to obtain WC-Co ultrafine-grade powder mixtures. Depending on the sintering mode variable parameters, the size of carbide phase grains was kept in ranges of 0.1–0.2 or 0.3–0.4 μm. The hardness of these hardmetals proved sharply increased, while their strength rose by 25%–30%.

It has been shown in the research of Ruziev et al. [27] that the addition of 1wt.%–12wt.% vanadium carbide VC in the WC-6wt.%Co alloy slightly, no more than by 3%, increases the hardness of the material, but significantly, by 33%–50%, improves its wear resistance, compared to unmodified WC-6wt.%Co. Also, properties and characteristics of WC-6wt.%Co hard alloy separately modified with VC and rhenium carbide ReC were discussed. In particular, with the addition of ReC to 5 wt.%, the wear efficiency of WC-6 wt.%Co increases to 66.3%, while the working resource of the tool made from it increases to 35.0%.

The WC-13 wt.%Co composite with added iron Fe can be obtained [28] by pressureless sintering. Material structure, porosity, and size of grains, as well as mechanical properties, were studied using SEM, XRD, X-ray EDS, and Vickers hardness tests. The Fe atoms position, when they are added in component phases, was determined: in eutectic, at 2 wt.%–4 wt.%, it exists both in low-carbon eta- and binder phases. In the eta-phase lattice, Fe atoms occupy the Co sites, being uniformly distributed in the binder simple cubic lattice. Tungsten boride growth in melted iron was found to be strongly limited. In W-C-Co-Fe systems, WC grain size increases up to 1.14–1.21 μm, when iron content increases to 4 wt.%. Thus, the WC growth process in melted CoFe metallic alloy should differ from that in melted iron and be closer to that in melted cobalt. When both 2 wt.% Fe and 1 wt.% C are added, the sample possesses the optimal combination of hardness/toughness: hardness is increased up to 1070 HV (from 980 HV for the sample without Fe and C additives) at a slight increase in toughness.

Interface models of DCCC (Diamond-Coated Cemented Carbide) WC-Co, with interface terminals TiC, TiN, CrN, and SiC but without intermediate layers, were suggested in Yang et al.'s study [29]. According to the conducted calculations, adding four corresponding intermediate layers increases the work of interface adhesion. Interface adhesion improvement of this DCCC could be ranked as: SiC > CrN > TiC > TiN. Adding the intermediate layer changes the interface junction charge distribution and forms a more stable chemical bond as a result of interface junction electron cloud overlapping. In the energy overlapping area, an additional intermediate layer increases the interface atoms DoS (density-of-states). And the DCCC interface bonding enhances as well. The most obvious should be diamond/$SiC_{C\text{-}Si}$/WC-Co interface interatomic electron cloud overlapping. Corresponding bond length was found to be the shortest: 1.62 Å, while the energy resonance peak-forming region was the largest, from −5 to +20 eV, and bonding was the strongest. At the diamond/TiN_{Ti}/WC-Co interface, on the contrary, these characteristics were the longest: 4.11 Å, the smallest from −5 to +16 eV, and the weakest, respectively. Among the considered intermediate layers, the best and the worst for improving the DCCC interface bonding were SiC and TiN, respectively.

4. B-C-W systems

WC tool cutting edges treated by LD (Laser Doping) of boron nitride BN revealed extra-long cutting distance. In view of this, WC-Co, the base material of the tool, was processed [30] similarly to the study, resulting in changes in crystal structure. X-ray and electron backscatter diffractions allow to observe the effect in the near-surface 50 nm thick LD: increased by ~11.7% strength at maintained WC structure.

Some physical-mechanical and tribological properties of WC-TiB_2 composites, as well as their microstructure, at sliding (against stainless steel-201) conditions were studied in Zhang et al.'s study [31]. Mechanical properties and relative density improved, while concentration of microstructural defects decreased when the TiB_2 component increased from 10 wt.% to 30 wt.%. As for the friction coefficient, it decreased both with increasing applied load and sliding speed. As the fracture effect is important for composite coatings contact surfaces, it led to the formation of abrasive and adhesive wear mechanisms. For WC-TiB_2 compositions, the rate of specific wear increased with increasing sliding velocity and normal load. In particular, the sample of intermediate composition WC-30wt.%TiB_2 possessed better tribological properties than WC-10 wt.%TiB_2 and WC-20 wt.%TiB_2 ones.

Tool materials from TiB_2-WC compositions can be produced [32] using the HPV technique with sintering additives such as Co and Ni metals and NiMo metallic alloys as well. SEM-, XRD-, and EDS analyses showed that TiB_2-WC ceramic composites microstructure consisted of TiB_2 uniform and WC fine grains. In composition TiB_2-WC-Ni, there are observed few pores and Ni_3B_4 brittle phase inclusions. As for the composition TiB_2-WC-Co, it contains a lot of pores and Co_2B and W_2CoB_2 brittle phases. Coarse-grained TiB_2 phase and pores are formed as a result of the reaction consuming the liquid cobalt. Coarse-grained components, brittle phase inclusions, and pores in significant volume fractions were harmful to the TiB_2-WC compositions mechanical properties and density. Using NiMo alloy as a sintering additive had significantly improved these characteristics. The accompanying process of $MoNi_4$

intermetallic compound formation not only inhibited NiMo liquid phase consumption and related coarse grains and pores growth but also strengthened the WC/TiB_2 interface interaction between grains of different components. As grains were fine, the relative density of TiB_2-WC-NiMo composite in average was up to 99.1%. Material Vickers hardness, flexural strength, and fracture toughness were of 22.7 GPa, 1307 MPa, and 8.2 MPa·$m^{1/2}$, respectively.

Boron carbide and its different nanocomposites manufacturing parameters were studied [33] for an effective two-stage technology. At the first stage, the combustion method is used to obtain boron carbide in nanopowder form, and then, at the second stage, metalceramic-ceramic nanocomposites on the basis of boron carbide are produced in the process of joint melting, milling, and sintering. At well-adjusted composition B_4C-25wt.%TiB_2-10wt.%(WC-10wt.%Co), the boron carbide-titanium diboride-tungsten carbide-cobalt nanocomposites powder morphology shows the reduction of B_4C particles in size from 500–5000 to 200–600 nm.

The synthesized composite powder XRD pattern proves the presence of all the target phases: B_4C, TiB_2, WC, and Co. WC peaks are of relatively low intensity, which can be explained by some transformations taking place in the WO_3 reagent phase. The obtained product may contain graphite with ultrafine grains, a mixture of various tungsten borides with “amorphous” structure, and trace phases as well. The different B:C:Ti:Co ratios according to the charge composition and experimentally obtained from the EDS spectra showed the combination of carbon reduction and cobalt evaporation yielding the ultrafine-grained tungsten borides formation. Such a mixture behaves as an amorphous-like inclusion. From XRD- and EDS-analyses, it can be concluded that the synthesized fine-grained powders contain both ceramic B_4C-TiB_2 and ceramic WC-Co components of the target composite; however, there are also some amorphous-like trace phases that are not visible on the XRD patterns. To find the sources, it is suitable to analyze chemical reactions taking place in the system at elevated, >1500 ℃, temperatures. To examine the corresponding reaction, a test process was conducted with a powder mixture of B_4C-TiB_2-(WC-Co) at 1800 ℃. The presence of crystalline B_4C, TiB_2, W_2B_5 and graphite traces is clearly visible on the product XRD pattern. Therefore, the sintering temperature of powders synthesized in this way should not exceed 1600 ℃, as tungsten boride W_2B_5 is expected to form at higher temperatures.

A wet chemical method can be used [34] to prepare preceramic precursors for low-temperature synthesis of ultrafine powders of tungsten boride composite with boron carbide matrix ceramics. That technique includes the thermal treatment of ammonium paratungstate-zirconium oxide-cobalt acetate tetrahydrate-sucrose-amorphous boron mixture viscous paste in air at 200 ℃ and then in argon at 600 ℃ for 2 h, grinding of the intermediate powder product, and its additional thermal treatment at 800–1500 ℃. These complex ceramic powders were pressed at 1000–1700 ℃ by using the SPS (Spark-Plasma Sintering). Phases WO_{3-x}, Co_3O_4, CoO, and amorphous carbon were formed at 600 ℃. XRD-analysis data confirmed the relatively low-temperature (800–1000 ℃) formation of WC-Co, B_4C, and metal boride (ZrB_2 and W_2B_5) phases. Finally, WC was completely converted into W_2B_5.

For boron carbide-based composites production, the ultradispersed powders of preceramic precursors were obtained [35] by their relatively low-temperature (200–

1000 °C) synthesis from liquid charge consisting of commercially available compounds (oxides and salts). These ceramics with boron carbide matrix were consolidated by their SPS at 1500–1700 °C. The XRD peaks of monoclinic zirconia ZrO_2 and WC phases visible in the preceramic precursors disappeared when the SPS process was conducted at 1500 °C. It was demonstrated that additive compounds of tungsten and cobalt promoted not only ceramic components low-temperature synthesis in powder form but also their sintering processes. According to the EDS analysis, the ceramic products contain a small amount of Co (0.8 wt%–2 wt%). The cobalt-containing ceramic B_4C-ZrB_2-W_2B_5-Co density exceeds that of Co-free ceramics (such as B_4C-ZrB_2-W_2B_5).

5. B_4C-W systems

Compositions B_4C-W with 5 vol.%, 10 vol.%, 15 vol.%, and 20 vol.% W were synthesized [36] by SPS in vacuum at uniaxial pressure of 40 MPa and temperature of 1500–1600 °C for 4 min (at a heating rate of 100 °C/min). For initial materials served the commercial powders of B_4C and W with particle sizes of 0.7 and 60 μm and purity of 99.5% and 99.8%, respectively. The initial mixture of these powders was prepared by milling for 24 h in ethanol with WC balls. Tungsten pentaboride W_2B_5 formed as the result of a reaction between particles of the B_4C and W component phases. When the tungsten amount increased, part of the carbon remained unbounded, forming the graphite phase inclusions. On the one hand, the free carbon presented in these composite materials deteriorated their physical-mechanical properties. But, on the other hand, metallic tungsten addition improved some technological properties of initial powder mixtures, in particular, their sinterability. Besides, it densifies the matrix like boron carbide samples with almost theoretical densities. Studies of neutron- and gamma-radiation attenuation by carbide-tungsten composites lead to the conclusion that increasing the tungsten concentration in the B_4C-W system yields the higher gamma-attenuation property of this composite, whereas it provides a lower neutron shielding capacity than that of pure B_4C.

For B_4C-based ceramics, pressureless sintering of powders can be considered an industry method. However, it possesses a disadvantage as well: the impossibility to sinter to high density without densification additives. Parts of sintering additives, tungsten among them, and appropriate methods of sintering are described in the review [37].

From B_4C-W-WC system powders, it was obtained [38] WC-WB-W_2B composites using reactive hot pressing, which initiated energization by a solid-state reaction between B_4C and W components. At 76.9 mol.% WC in the starting powder, phases of WB and WC were formed in the reaction $B_4C + 5W + x\text{WC} = \text{WB} + (1 + x)\text{WC}$. These two plus W_2B phases were produced at 85.4 mol.% WC. Pure WC in densely sintered state was not obtained. As for WC-WB-W_2B compositions obtained at (5.4 mol.%–95.6 mol.% WC), they were fully consolidated, having high mechanical characteristics (Young’s modulus, Vickers hardness, and fracture toughness) comparable with pure WC.

Toughness, hardness, and crack density of fine-grained WC-Co compositions were investigated in Tamizifar et al.’s [39] work. Namely, about 30 experimental and commercial hard metal grades with different additives, such as boron B_4C, vanadium VC, chromium Cr_3C_2, and silicon carbides SiC, were obtained in an HPV commercial isostatic sintering furnace. Microstructural and physical-mechanical properties were investigated to construct a representative hardness/crack density measurement band useful to estimate the most effective temperature for sintering, as well as amounts of additives. Comparison of grain growth inhibitors effect in optimal conditions showed that B_4C- and VC-doped grades for growth inhibitors exhibit the maximal hardness. However, addition of Cr_3C_2 is found to favor the toughness improvement.

Boron carbide coatings can be synthesized using the method of an RF (Radio Frequency) plasma source and an external magnetic field [40]. The nanohardness of steel surfaces coated in this way was 14.0–16.6 GPa. Such B_4C coatings were found to have the hardness 1.73–3.89 times higher than uncoated (bare) steel surfaces served as targets. This technique would be useful for coating tungsten substrates with boron carbide.

Due to the high cross section of (epi)thermal neutrons captured by boron ^{10}B isotope nuclei, all-boron and boron-rich systems—compounds and composites—are widely used as materials that intensively interact with neutron radiation. In the fine-dispersive form, they have the improved performance characteristics. Preparation methods of some fine-dispersive important boron-containing B_4C-W composites useful in neutron shielding were reported in the studies of Chkhartishvili et al. [41,42].

Using the spin coating technique on the B_4C surface, first a WO_3 layer was deposited to reduce it to metallic α-W at a temperature of 600–800 °C under a hydrogen atmosphere. Usually, such α-W layer was weakly attached to the boron carbide. The sandwich composites can be effectively obtained by SPS at 1300–2000 °C. For this purpose, the method by which previously tungsten-contained multicomponent ceramics with boron carbide matrix were synthesized was modified. The substrates used were compacted by SPS at temperatures of 1500–2000 °C from ultradispersive boron carbide powders prepared from liquid charge systems like amorphous boron-carbohydrates-water and boron acid-organic compound-water. During heating at temperatures exceeding 1300 °C, in these sandwich structures, it starts the formation of tungsten pentaboride W_2B_5, while at >1600 °C it converts into a new sandwich composite B_4C-W_2B_5. From two-component sandwiches, applying the SPS, one is able to manufacture similar multicomponent structures: B_4C-W-B_4C-W, W-B_4C-W-B_4C, and the like.

Monolithic B_4C-W samples were obtained from B_4C and W powders in SPS processes as well. First, the powder of metallic W was compacted and placed in a graphite press mold with a graphitic foil lining. Then B_4C powder was sprinkled on the W layer. After leveling the surface, again the graphitic foil was placed on it. During the described method, including rapid heating together with applying a certain pressure, powder consolidates and a sandwich composite is obtained. The SEM and EDS investigations showed the presence of the fracturing on the contact interface between B_4C and W consolidated in the sandwich structure. There are the opposite directions of diffusion of B and W atoms, and an intermediate-phase W_2B_5 forms. The thickness of layers can be adjusted within wide limits. After removing metallic tungsten and tungsten boride layers, the sample sintered at 1600 °C revealed the relative density of boron carbide as 87%–92% of the theoretical value. XRD patterns of the cleaned surface unambiguously confirmed boron carbide presence, as well as metallic tungsten removal from the sandwich surface. To obtain similar composites using tungsten plates instead of their powders, a new method was developed. Conclusion was made that heating and pressing of the boron carbide powder-metallic tungsten foil structure leads to the intermediate phase W_2B_5 formation and provides a strong bonding between these phases.

Based on theoretical simulations [43–45], B_4C-W thin-layered sandwich compositions are considered effective shield materials containing both low- and high-Z atoms (here Z denotes the atomic number), boron and tungsten, serving as effective absorbers for, respectively, (epi)thermal neutrons and secondary gamma-quanta, which accompany the neutrons captured by ^{10}B nuclei.

The thin film materials based on W and B and including B_4C, WC, and WB_3 phases can display too high a hardness. Compounds of composition WB_{3+x} were shown to have Vickers hardness approaching 40 GPa for relatively small x. Thin film materials based on W and B and including B_4C, WC, and WB_3 display very high hardness. Also, borophene doped with W was found to exhibit superior hardness. In Martin's [46] study, $W_{1-y}B_{3+x}$ structures elastic properties were summarized. Among them, only the stoichiometric WB_3 phase can be considered as superhard material. Contamination with extra B-atoms is energetically unfavorable and affects the hardness: it lowers the shear modulus while maintaining the bulk modulus, effectively leading to a softer material. The W-vacancies, e.g., in $W_{0.75}B_{3+x}$ composition, form structures with hardness less sensitive to variations in boron content.

Interface roughness influences the B_4C-W multilayer reflectivity and varies with bilayer number N [47]. In particular, multilayers of B_4C-W composition with equal design period thickness (2.5 nm), a real-structure model can be used to calculate the variation of reflectivity with N (N = 50, 100, 150, and 200). DC (Direct Current) magnetron sputtering system was used to fabricate such multilayers. The XRD measurement of their reflectivity and scattering intensity indicates that the reflectivity is a function of bilayer number, and interface roughness slightly increases from layer to layer during the growth of the multilayer.

6. B_4C-WB_2 systems

From B_4C and WB_2 as initial raw materials, the densified compositions B_4C-WB_2 were produced by the HPV method at a temperature of 1950 ℃ [48]. The B_4C-68.7 vol.%WB_2 composition obtained in this way demonstrated a quite good set of physical-mechanical properties such as superior hardness of 34.8 GPa, high flexural strength of 696 MPa, acceptable fracture toughness of 3.3 $MPa \cdot m^{1/2}$ and low density of 5.59 g/cm^3. These compositions, in addition, showed good electrical conductivity of 3.3×10^5 S/m, which, together with the above mechanical properties, make them interesting for various applications, e.g., as armor protection and cutting tool materials.

Based on the explored B_4C-TiB_2 compositions fine microstructure, it was proposed [49] an overall evolution picture of their microstructure, starting from the processing of raw powders to sintering and compacting. It was found that structures with small-scale grain and their local mechanical properties (measured applying the nanoindentation method) are correlated and thus provide a trend in their mechanical behavior. In particular, dense ceramics can be typified by the core-shell structure development in titanium boride grains, where shells comprise two-component solid solution TiB_2-WB_2 with different assemblage and variable (in dependence on the technological route) content of tungsten atoms, i.e., guest cations. Analyses conducted by TEM revealed some morphological and chemical differences that can be related to the densification mechanisms. To extract the composite and component phases (core TiB_2, shell WB_2, and matrix B_4C) properties, it was used the nanoindentation highlighting modulus and hardness variations as functions of lattice perturbation from nominally pure boride coarse to shell regions.

7. B_4C-W_2B_5 systems

To understand the WC and TiC additions effect on mixtures of compositions B_4C-B-Si on the sintering process and final product mechanical properties, a special investigation was undertaken [50]. In the process of milling in attrition, the starting component powders are alloyed with WC, TiC, and Co phases by the hard metal spheres. In the case of long milling, the rate of material wear decreased strongly. Powder products milled for 2 and 4 h, respectively, contained 39 wt.% and 47 wt.% WC-TiC. During the heating, the components of the starting powder milled for 2 h (B, B_4C, Si, Co, WC, and TiC) reacted to form B_4C, TiB_2, and W_2B_5. Some chemical reactions took place in the temperature range of 800–1500 °C.

The W_2B_5 boride phase started formation at 1100 °C and its maximum amount is reached at 1600–1800 °C. The content of W_2B_5 phase very strongly decreases at higher temperatures. The TiB_2 phase started its formation at 1050 °C and at further heating the system up to a temperature of 1200 °C its content increased. Within the temperature range of 1200–1800 °C, the TiB_2 phase amount remains almost unchanged, and when temperature is higher than 1800 °C, a strong increase in the TiB_2 amount takes place.

Increasing in TiB_2 amount and decreasing in W_2B_5 amount at same temperatures lead to the conclusion that the solubility of W in TiB_2 increases with temperature. It is why the three different phases in form of boron compounds are observable. These are boron carbide, tungsten pentaboride, and titanium diboride. The grain size of these boron compounds is about 1 μm.

The 72 vol.%, 20 vol.% and 8 vol.% of component phases B_4C, TiB_2 and W_2B_5, respectively, contained the alloy compositions prepared by powder attrition milling for 2 h. The material porosity was less than 3 vol.%. The increase in temperature causes the decrease in density because of W_2B_5 dissolution and subsequent formation of the diboride system TiB_2-WB_2. This reaction lowers both the hardness and bending strength of the material after its compacting. The above-presented observations can be summarized as follows: Attrition milling of mixtures containing B_4C, B, and Si powders with WC-TiC-Co spheres decreases the hot-pressing temperature and increases the strength of boron-carbide-based hard material. During heating, the starting components reacted and formed boron carbide and TiB_2 and W_2B_5 boride phases, which are more stable than corresponding carbides.

Pure boron carbide and boron carbide-based composite ceramics B_4C-W_2B_5 were prepared [51] by the hot-pressing method. Their microstructure and chemical and phase compositions were characterized by means of XRD, TEM, and EPMA (Electron

Probe MicroAnalysis). Measuring results of their electrical conductivity and Seebeck coefficient temperature dependences in the range of 300–1500 K showed that the B_4C-W_2B_5 composite electrical conductivity strongly exceeds that for pure boron carbide, while the composite Seebeck coefficient is somewhat lower if compared with that for the B_4C ceramic. Note that both of these characteristics increase with temperature. The figure-of-merit of this composite ceramic was found to be higher than that of the B_4C, though its thermal conductivity is somewhat higher in comparison with that of boron carbide.

Two, WB and W_2B_5, tungsten borides, were experimentally prepared [52] by the SHS (self-propagating high-temperature synthesis) process, during which borothermic reduction of tungsten oxide WO_3 and interaction between B and W proceeded concurrently. Two series of molar proportions, WO_3:B:W = 1:5.5:x with $x = 1.16$–2.50 and 1:7.5:y with $y = 0.50$–1.33, were adopted for powder mixtures to produce WB and W_2B_5 phases, respectively. The reactants compact starting stoichiometry substantially affected the combustion regime and the final product composition. Increasing in tungsten and boron contents reduced the overall exothermicity of the reaction, which leads to some decrease in both reaction front velocity and combustion temperature. The initial composition of the reactant compact should be optimized for the predominant synthesis of WB or W_2B_5. The compact WO_3-5.50B-2.00W powder system dominantly produced WB together with small amounts of W_2B and W_2B_5 additive phases. As for the W_2B_5 phase optimal formation, it was observed from the initial system of WO_3-7.50B-0.85W composition. Excess in boron amount about 10 mol.%–13 mol.% was experimentally found to be favorable for the formation of mentioned WB and W_2B_5 trace phases.

Pressureless sintering at 2150 °C can be used [53] to compact boron carbide-based ceramic powders to a relative density of 96.1% with the co-incorporation of tungsten carbide WC and pyrolytic carbon C phases. The specific surface of as-batched boron carbide powder was 7.89 m^2/g. In the BW-6C composite, the fracture toughness value of 5.80 $MPa \cdot m^{1/2}$ was achieved. As for the sintering aids for tungsten boride and carbon, they were formed in an in-situ reaction. The observed improvement in material toughness should be attributed to the residual thermal stresses as well as the presence of W_2B_5 phase platelets. Thus, B_4C-W_2B_5 composites have the potential to be used as structural materials.

Boron carbide matrix graphite-containing composites and in situ-formed W_2B_5 were obtained [54] by the SPS method. Starting powders of B_4C containing 5 vol.%W were shaped into the composite bulk. The sintering was conducted under vacuum at 1500, 1550, and 1600 °C. Sintering temperature and tungsten addition influences on material microstructural and phase properties, densification degree, hardness, and fracture toughness were examined by XRD and SEM in-Lens mode, as well as Vickers indentation technique and Palmqvist method. Results showed that these composites possess high hardness and improved fracture toughness.

The ceramic compositions B_4C-(WC-TiC) containing different amounts of WC-TiC solid solution were obtained in the work of Deng et al. [55] by the hot-pressing method. A chemical reaction taking place during the process resulted in B_4C-TiB_2-W_2B_5 composite with high density and mechanical properties improved in comparison with monolithic boron carbide. Addition of WC-TiC solution affects the rates of densification of the composite. Increasing in WC-TiC content increased the densification rate, while the B_4C-(WC-TiC)C composites sintering temperature was lowered to 1850 ℃ from that of 2150 ℃ for monolithic boron carbide. With an increase in WC-TiC content up to 50 wt.%, the composite material's hardness decreased while its flexural strength and fracture toughness increased continuously.

The boron carbide matrix composites B_4C-(TiB_2-ZrB_2)-W_2B_5 and their cobalt Co additive can be obtained from commercially available initial compounds on the basis of preparing corresponding precursor pastes and their processing in controlled thermal regimes [56]. All the component phases (B_4C, TiB_2, ZrB_2, W_2B_5 and Co) can be synthesized at relatively low temperatures (around 1000 ℃) from cobalt-containing liquid charges. Note that from cobalt-free precursors only zirconium diboride formation can be observed under the same conditions. Maintaining the initial grain size by inhibiting their SPS growth in boron carbide matrix composite powders with cobalt additive is one more advantage of this approach.

8. W layers

Surfaces of different types coated with metallic tungsten are widely used in DRA (Dynamic Random Access) and flash memories, microprocessors, image sensors, and a number of other modern technologies. The thin-layer coatings of semiconducting surfaces with W are mainly carried out applying CVD (Chemical Vapor Deposition) technique using for precursor materials WF_6, SiH_4 and H_2. Maintaining the vacuum in the reaction chamber at pressure within the range of 20–760 Torr increases both the tungsten deposition rate and reflectivity of the produced W-surface [57].

Using the LPCVD (Low Pressure CVD) method, thin W film was deposited [58] (see Plyushcheva et al.'s [59] work as well) on Si(100) substrate. WF_6 and SiH_4 were used for source and tungsten-reducing (from WF_6) gases, respectively. The deposited tungsten thin film was formed either on SiH_4 or Si substrates by the WF_6 reduction in cold wall conditions and by the SiH_4 reduction under the hot wall conditions. The nm-layer tungsten silicide W_5Si_3 was formed at the W-Si interface only during the gas phase deposition. Growth of other tungsten silicide WSi_2 layers commences at 700 ℃ for CVD layers and above 750 ℃ for plasma-chemically deposited films. This drastic increase increases the material's electrical resistance: under optimal conditions, W-films with a resistivity of 8×10^{-6} Ohm·cm can be obtained.

Dissolving of tungsten in hydrogen peroxide and subsequent evaporating the residual solvent yielded [60] the water-soluble powder of tungsten-IPA (Inorganic Peroxopolytungstic Acid). The obtained W-IPA solution was mixed with organic solvent and spin-coated on wafer. Films of metallic tungsten were formed by the reduction process. Appropriate selection of organic solvent and UV (ultraviolet) irradiating leads to the film with remarkably decreased sheet resistance.

Frequently obtained tungsten powders are nanosizes. Reduction of WO_3 at 600 ℃ by using in situ produced hydrogen gas [61] could be considered for a W nanopowder production route. According to the XRD patterns, the final product's alpha- and beta-W phases are presented in nanostructured form. DTA (Differential Thermal Analysis) showed that phase transition from beta-W to alpha-W takes place at a temperature of 435 ℃. Pastes and suspensions of powders of this type were used for coating various surfaces. Tungsten alpha-W layer can be formed by reducing WO_3 oxide layer preliminary formed by spin coating in hydrogen at a temperature of 600–800 °C [62]. Applying the $WO_x(OH)_y$ chemical vapor transport, the morphology of the tungsten surface can be transformed into star-shaped cracking, floret, irregularly fibrous, rod-like, and spherical particles.

Technologies of tungsten deposition on different metal substrates are also used [63]. Commonly applied metals are aluminum, copper, and titanium. PNL (Pulsed Nucleation Layer) and ALD (Atomic Layer Deposition) methods can be used to grow layers of tungsten nucleation. The ultrafine tungsten powder reduction industrial process evolution is described in Gao et al.'s [64] study. In industrial push furnaces, the blue oxides of tungsten were used for reduction in hydrogen counter-current flow. Reduction was carried out according to the following scheme: $WO_{2.9} \rightarrow WO_{2.72} \rightarrow WO_2 \rightarrow W$. Quite often, the pure tungsten films are deposited using PVD (Physical Vapor Deposition) or evaporation/sputtering and CVD. The HWALD (Hot Wire-assisted ALD) method, which was developed in Yang et al.'s [65] work, forms a tungsten layer from W-filament heated up to a temperature of 1700–2000 °C. Atomic hydrogen generated by molecular hydrogen dissociation can react with WF_6 at the substrate to form the deposit. Typically, nucleation CVD layers are deposited in argon carrier gas from SiH_4 and WF_6. A cheap and, at the same time, practical method is the metallic tungsten coating on the ceramic surface, which uses the applicability of chemical solution deposition to form films on the alumina tubules inner surfaces. This approach includes the tungsten oxide layer preparation from PTA (PeroxoTungstic Acid) precursor solutions and subsequent reduction to tungsten under hydrogen [66].

The patent [67] proposes a technological route of formation of the sandwich structures, namely, a method of metallization of boron carbide ceramics. This invention describes the four-step process: Step 1: Mixing of metal powder containing 10 wt.%–40 wt.% Mo, Ni, and W (according to wt.% ratio) during ball milling and 300-mesh sieving; Step 2: Mixing the obtained in the Step 1 metal powder with 5 wt.% ethylcellulose solution in wt.% ratios of (100–120):30 to prepare the metalized paste; Step 3: Printing the obtained in the Step 2 metalized paste on the boron carbide ceramic part to be metalized to a layer of thickness of 20–30 μm and its drying; and Step 4: Metalizing the obtained in the Step 3 dried boron carbide part by its placement for metallization into a sintering furnace and for 30–35 min at temperature from the range of 1650–1680 °C in hydrogen, keeping the dew point at 0–10 °C and cooling along with the furnace. The proportioned MoNiW metallic alloy layer is close to the boron carbide thermal expansion system. Its bonding strength is high, while the metalized stress is small. Due to the sub-μm network structure, the formed metal layer is not prone to falling off after brazing.

The spin coating allows to reduce the previously formed WO_3 tungsten oxide layer to an alpha-W layer at a temperature of 600–800 °C in hydrogen [68]. Hardness and wear resistance of such tungsten layers, when they are sequentially implanted with boron B (and carbon C as well) 60 keV ions at temperatures of 300–350 K, were investigated. For sample hardness testing, they were modified by fluences of 1×10^{15}–3×10^{15} and 1×10^{16}–3×10^{17} ion/cm^2. Nano- and micro-indentations showed that hardness and wear resistance of obtained composites are improved with 1.3–4.5- and 2.0–6.7-times, respectively.

The superior mechanical properties characteristic of tungsten foils at room temperature can be expanded [69] by fabricating the metallic laminate composites containing tungsten.

9. Utilization of W-containing waste

As mentioned, tungsten-containing alloys are widely used in modern technologies. For this reason, the demand for this type of material is increasing day by day. The scarcity of tungsten led to its removal from tool scrap and reuse to make hard instruments. Methods for extracting tungsten from tungsten-containing scrap have been developed for decades. A number of methods implemented in practice have certain strengths and weaknesses. In general, when selecting ways to process such waste, it is important to take into account the productivity and simplicity of the technological process, its environmental friendliness, and also low energy costs. The description of main ways of processing wastes of tungsten-containing hard materials is given in the book of Panov and Chuvilin [70].

Here are listed the main methods used to recycle such kind of waste in the production of tungsten-containing hard alloys.

- Crude dispersion of sintered waste with different types of crushers and then grinding of the obtained mixtures into finely dispersed fractions (a version of this method is to extract cobalt from waste by heating it to 2300–2500 °C and dispersing the rest material);
- Complete decomposition of waste by chemical-metallurgical methods in a special furnace with strong oxidizers—alkaline nitrates and nitrites, product pouring, crushing, and leaching in hot water;
- Selective separation of cobalt from the solution by heating and treating it with acid or alkali;
- Multistep chlorination in the presence of carbon dioxide to obtain tungsten and cobalt chlorides and their separation in distillation columns, purification, conversion into oxides, and reducing;
- Heating to 1100 °C, oxidizing it in air, and reducing WO_3 together with forming cobalt tungstate hampering complete removal of tungsten;
- Oxidizing and then chlorinating to trap the tungsten chloride and leave the cobalt dioxide in the chlorinator;
- Electrochemical processing of solutions of ammonia, alkaline, and salts;
- Hydro-/pyrometallurgical sawdust processing;
- Processing with regenerators, including fine-grained grinding with a high-energy air stream, quenching of hard alloys in ice water at 1300–1400 °C and crushing the forged mass;
- Dissolution with sodium hydroxide, precipitation in hydrochloric acid, precipitation and purification of ammonium paratungstate with ammonia, and reduction to tungsten with hydrogen;
- Thermal regeneration as an oxidation-reduction-carbidization process; and
- Cobalt extraction with zinc and vacuum distillation.

A comparative economic analysis [71] of different regeneration technologies of producing the metalceramic alloys demonstrated the ability of shock-wave processing as a stimulating factor for powder products (of any configuration) destruction to obtain high-quality powder for further molding and sintering to produce tools of various purposes, eco-friendly technology of processing superhard materials, as well as metalceramic components of obsolete military equipment. Industrial tests of rock destroying tool batches, die-blanks for non-ferrous metallic drawing pipes, and mandrel-blanks confirmed the high quality, effectiveness, and feasibility of the developed technology.

An analysis of available methods to study the tungsten waste regeneration from hard alloys containing cobalt was conducted. These are chemical (chlorine and zinc) and thermochemical and hydro- and pyrometallurgical methods, as well as technology based on explosive energy consumption. Metalceramic solid alloys are heterogeneous mixtures, in bulk of which there are surfaces with gaps in any microscopic parameter values.

Industrial technology development solves the superhard alloys and scrap materials recycling problem and also helps in their subsequent rehabilitation and, respectively, significant savings of expensive raw materials.

The regeneration process of hard alloys under the influence of shock waves is also processed. Through the direct regeneration of secondary raw materials, this highly efficient production technology allows, without thermochemical and metallurgical processes, obtaining the powders of hard alloys useful to create the tools. This technology differs from the existing ones in terms of high technical and economic indicators, high performance, low energy consumption, and environmental friendliness. The recovery of the tungsten-containing mixture is carried out under conditions of high-pressure gradients and delivery velocities in cylindrical reaction ampoules subjected to the impact caused by the detonation of an axially symmetric explosive charge.

10. Conclusions

In summary, there is a review of scientific publications on boron and tungsten carbide-based and related nanodispersed composites, the hard materials, with a perspective of wide technological applications. It covers a class of hard materials such as boron-tungsten B-W, carbon-tungsten C-W, boron-carbon-tungsten B-C-W, boron carbide-tungsten B_4C-W, boron carbide-tungsten diboride B_4C-WB_2 and boron carbide-tungsten pentaboride B_4C-W_2B_5 systems, as well as tungsten W layers. Especially is discussed one of the related important tasks: utilization of the W-containing waste to reduce tungsten, an expensive metal, for its reusing in hard instrument production.

Conflict of interest: The authors declare no conflict of interest.

References

1. Chkhartishvili L, Mikeladze A, Chedia R, et al. Synthesizing fine-grained powders of complex compositions B_4C-TiB_2-WC-Co. Solid State Sciences. 2020; 108: 106439. doi: 10.1016/j.solidstatesciences.2020.106439
2. Chkhartishvili L, Mikeladze A, Tsagareishvili O, et al. Advanced boron carbide matrix nanocomposites obtained from liquid-charge: Focused review. Condensed Matter. 2023; 8(2): 37. doi: 10.3390/condmat8020037

3. Shabalin IL. Refractory Carbides III (W Carbides). In: Ultra-High Temperature Materials IV. Cham, Springer Nature; 2022. doi: 10.1007/978-3-031-07175-1
4. Manzar R, Saeed M, Shahzad U, et al. Recent advancements in boron carbon nitride (BNC) nanoscale materials for efficient supercapacitor performances. Progress in Materials Science. 2024; 144: 101286. doi: 10.1016/j.pmatsci.2024.101286
5. Singh M, Singh H, Sharma Y, et al. Review on various techniques for the development of thin film boron nitride coating on metal surfaces. AIP Conference Proceedings. 2024; 2986: 020024. doi: 10.1063/5.0192656
6. Mallia B, Dearnley PA. Exploring new W-B coating materials for the aqueous corrosion-wear protection of austenitic stainless steel. Thin Solid Films. 2013; 549: 204-215. doi: 10.1016/j.tsf.2013.09.035
7. Gromilov SA, Kinelovskii SA, Alekseev AV, et al. Investigation of W_2B and β-WB high-temperature phases in coatings produced by a shaped charge explosion. Journal of Structural Chemistry. 2010; 51(6): 1126-1131. doi: 10.1007/s10947-010-0171-3
8. Gonzalez Szwacki N. The structure and hardness of the highest boride of tungsten, a borophene-based compound. Scientific Reports. 2017; 7(1). doi: 10.1038/s41598-017-04394-1
9. Sorokin OY, Kuznetsov BY, Lunegova YU, et al. High-temperature composites with a multi-layered structure (Review) (Russian). Proceedings of VIAM. 2020; 88(4-5): 42-53. doi: 10.18577/2307-6046-2020-0-45-42-53
10. Mohammadi R, Xie M, Lech AT, et al. Toward inexpensive superhard materials: Tungsten tetraboride-based solid solutions. Journal of the American Chemical Society. 2012; 134(51): 20660-20668. doi: 10.1021/ja308219r
11. Ma K, Cao X, Yang H, et al. Formation of metastable tungsten tetraboride by reactive hot-pressing. Ceramics International. 2017; 43(12): 8551-8555. doi: 10.1016/j.ceramint.2017.03.059
12. Sharapova VA. Special Composite Materials (Russian). Available online: http://elar.urfu.ru/handle/10995/93470 (accessed on 19 March 2024).
13. Syrovatko YV. Calculation of the entropy of the eutectic phases WC and W_2C in alloy W-C by the method of statistical processing of photo-images (Russian). Ukrainian Applied Physics. 2020; 4: 79-84.
14. Pankratz LB. Thermodynamic Properties of Carbides, Nitrides, and Other Selected Substances. Available online: https://digital.library.unt.edu/ark:/67531/metadc12836/ (accessed on 19 March 2024).
15. Mazo I, Molinari A, Sglavo VM. Electrical resistance flash sintering of tungsten carbide. Materials & Design. 2022; 213: 110330. doi: 10.1016/j.matdes.2021.110330
16. Yang Y, Zhang C, Wang D, et al. Additive manufacturing of WC-Co hardmetals: A review. The International Journal of Advanced Manufacturing Technology. 2020; 108(5-6): 1653-1673. doi: 10.1007/s00170-020-05389-5
17. Gachechiladze A, Kandelaki A, Mikadze O, et al. Method for Reception of Nanocrystalline Solid Materials on the Basis of Tungsten Carbide. Available online: https://www.sakpatenti.gov.ge/en/publications/?subject=OfficialBulletinsofIndustrialProperty (accessed on 19 March 2024).
18. Goncharuk VA. Influence of Structural Factors on the Mechanical Properties of High-Strength Composite Materials Based on Refractory Compounds (Ukrainian). Available online: http://www.materials.kiev.ua/abstract/67/Autoref_Goncharuka.pdf (accessed on 19 March 2024).
19. Mannesson K, Borgh I, Borgenstam A, et al. Abnormal grain growth in cemented carbides—Experiments and simulations. International Journal of Refractory Metals and Hard Materials. 2011; 29(4): 488-494. doi: 10.1016/j.ijrmhm.2011.02.008
20. Pereira P, Vilhena LM, Sacramento J, et al. Abrasive wear resistance of WC-based composites, produced with Co or Ni-rich binders. Wear. 2021; 482-483: 203924. doi: 10.1016/j.wear.2021.203924
21. Soria-Biurrun T, Lozada-Cabezas L, Navarrete-Cuadrado J, et al. Densification of WC-Fe-Ni-Co-Cr cemented carbides processed by HIP after sintering: Effect of WC powder particle size. International Journal of Refractory Metals and Hard Materials. 2023; 110: 105994. doi: 10.1016/j.ijrmhm.2022.105994
22. Ha GH, Li GG, Yan MC, et al. Synthesis of WC-TiC-Co nanopowder by mechano-chemical process. In: Euro PM Conference Proceedings. Shrewsbury; 2006. pp. 97-102.
23. Dutkiewicz J, Rogal L, Bobrowski P, et al. The effect of substitution of WC by TiC in WC-Co composite tool materials on microstructure and mechanical properties. Chiang Mai Journal of Science. 2017; 44(4): 1714-1721.
24. Bogodukhov SI, Kozik ES, Svidenko EV. Thermal hardening of hard alloy T15K6. Industrial Laboratory Diagnostics of Materials. 2017; 83(12): 38-42. doi: 10.26896/1028-6861-2017-83-12-38-42
25. Falkovsky VA, Klyachko LI, Glushkov VN, et al. Multi-carbide hardmetals. In: Kneringer G, Rodhammer P, Wildner H (editors). Powder Metallurgical High Performance Materials, Proceedings of the 15th International Plansee Seminar 2001;

Reutte, Austria; Plansee Holding AG; 2011. pp. 29-34.

26. Falkovsky V, Ebiagoveschenski Y, Glushkov V, et al. Nanocrystalline WC-Co hardmetals produced by plasmochemical method. In: Kneringer G, Rodhammer P, Wildner H (editors). Powder Metallurgical High Performance Materials, Proceedings of the 15th International Plansee Seminar 2001; Reutte, Austria; Plansee Holding AG; 2011. pp. 91-96.
27. Ruziev UN, Guro VP, Safarov YT, et al. Doping of hard alloy VK-6 with vanadium carbide (Russian). Universum: Chemistry and Biology. 2019; 8(62).
28. Li X, Zhang J, Zhang Q, et al. Microstructure Evolution and Hardness Improvement of WC-Co Composites sintered with Fe substituting part of Co binder. Coatings. 2023; 13(1): 116. doi: 10.3390/coatings13010116
29. Yang J, Yue Y, Lv H, et al. Effect of adding intermediate layers on the interface bonding performance of WC-Co diamond-coated cemented carbide tool materials. Molecules. 2023; 28(16): 5958. doi: 10.3390/molecules28165958
30. Tanaka Y, Sato H, Eryu O. Structural modification of WC-Co cutting tools by laser doping treatment. Heliyon. 2023; 9(9): e19930. doi: 10.1016/j.heliyon.2023.e19930
31. Zhang C, Song J, Jiang L, et al. Fabrication and tribological properties of WC-TiB_2 composite cutting tool materials under dry sliding condition. Tribology International. 2017; 109: 97-103. doi: 10.1016/j.triboint.2016.12.029
32. Song J, Huang C, Zou B, et al. Effects of sintering additives on microstructure and mechanical properties of TiB_2-WC ceramic-metal composite tool materials. International Journal of Refractory Metals and Hard Materials. 2012; 30(1): 91-95. doi: 10.1016/j.ijrmhm.2011.07.008
33. Chkhartishvili L, Mikeladze A, Chedia R, et al. Combustion synthesis of boron carbide matrix for superhard nanocomposites production. In: Advances in Combustion Synthesis and Technology. Bentham Science Publishers; 2022. pp. 66-95. doi: 10.2174/9789815050448122010007
34. Barbakadze N, Chkhartishvili L, Mikeladze A, et al. Method of obtaining multicomponent fine-grained powders for boron carbide matrix ceramics production. Materials Today: Proceedings. 2022; 51: 1863-1871. doi: 10.1016/j.matpr.2021.08.013
35. Chkhartishvili L, Mikeladze A, Jalabadze N, et al. New low-temperature method of synthesis of boron carbide matrix ceramics ultra-dispersive powders and their spark plasma sintering. Solid State Phenomena. 2022; 331: 173-184. doi: 10.4028/p-8n6hzy
36. Ozer SC, Buyuk B, Tugrul AB, et al. Gamma and neutron shielding behavior of spark plasma sintered boron carbide-tungsten based composites. In: TMS 145th Annual Meeting & Exhibition. Cham, Springer International Publishing; 2016. pp. 449-456. doi: 10.1007/978-3-319-48254-5
37. Zhang W, Yamashita S, Kita H. Progress in pressureless sintering of boron carbide ceramics—A review. Advances in Applied Ceramics. 2019; 118(4): 222-239. doi: 10.1080/17436753.2019.1574285
38. Sugiyama S, Taimatsu H. Preparation of WC-WB-W_2B composites from B_4C-W-WC powders and their mechanical properties. Materials Transactions, 2002; 43(5): 1197-1201. doi: 10.1016/S0955-2219(03)00253-X
39. Tamizifar H, Hadian AM, Tamizifar M. The comparison between boron carbide (B_4C) with other common inhibitors on physical and mechanical properties of WC/Co. International Journal of Modern Physics: Conference Series. 2012; 05: 102-110. doi: 10.1142/s2010194512001900
40. Taran AV, Garkusha IE, Taran VS, et al. Structure and properties of B_4C coatings obtained by RF sputtering with external magnetic field. In: Nanomaterials and Nanocomposites, Nanostructure Surfaces, and Their Applications. Cham, Springer Nature; 2021. pp. 51-57. doi: 10.1007/978-3-030-51905-6_5
41. Chkhartishvili L, Chedia R, Tsagareishvili O, et al. Preparation of neutron-capturing boron-containing nanosystems. In: Proceedings of the 9th International Conference & Exhibition on Advanced and Nanomaterials; 24-26 October 2022; Victoria, Canada. pp. 1-15.
42. Chkhartishvili L, Makatsaria S, Gogolidze N. Boron-containing fine-dispersive composites for neutron-therapy and neutron-shielding. In: Proceedings of the International Scientific-Practical Conference "Innovations and Modern Challenges 2022"; 18-19 November 2022; Tbilisi, Georgia. pp. 221-226.
43. Nabakhtiani G, Chkhartishvili L, Gigineishvili A, et al. Attenuation of gamma-radiation concomitant neutron-absorption in boron-tungsten composite shields. Nano Studies. 2013; 8: 259-266.
44. Evans BR, Lian J, Ji W. Evaluation of shielding performance for newly developed composite materials. Annals of Nuclear Energy. 2018; 116: 1-9. doi: 10.1016/j.anucene.2018.01.022
45. Chkhartishvili L. Boron-contained nanostructured materials for neutron-shields. In: Nanostructured Materials for the Detection of CBRN. Dordrecht, Springer Science; 2018. pp. 133-154. doi: 10.1007/978-94-024-1304-5_11

46. Martin PM. Active thin films: Applications for graphene and related materials. Vacuum Technology & Coating. 2018; 19(11): 6-14.
47. Dai M, Zhang Z, Zhu J, et al. Influence of interface roughness on reflectivity of tungsten/boron-carbide multilayers with variable bi-layer number by X-ray reflection and diffuse scattering. Chinese Optics Letters. 2009; 7(8): 738-740. doi: 10.3788/col20090708.0738
48. Ma K, Shi X, Cao X, et al. Mechanical, electrical properties and microstructures of hot-pressed B_4C-WB_2 composites. Ceramics International. 2022; 48(14): 20211-20219. doi: 10.1016/j.ceramint.2022.03.300
49. Silvestroni L, Failla S, Gilli N, et al. Disclosing small scale length properties in core-shell structured B_4C-TiB_2 composites. Materials & Design. 2021; 197: 109204. doi: 10.1016/j.matdes.2020.109204
50. Hofmann H, Petzow G. Structure and properties of reaction hot-pressed B_4C-TiB_2-W_2B_5 materials. Journal of the Less-Common Metals. 1986; 117(1-2): 121-127. doi: 10.1016/0022-5088(86)90020-2
51. Cai KF, Nan CW. The influence of W_2B_5 addition on microstructure and thermoelectric properties of B_4C ceramic. Ceramic International. 2000; 26: 523-527. doi: 10.1016/S0272-8842(99)00089-9
52. Yeh CL, Wang HJ. Preparation of tungsten borides by combustion synthesis involving borothermic reduction of WO_3. Ceramic International. 2011; 37: 2597-2601. doi: 10.1016/j.ceramint.2011.04.006
53. Yin J, Huang Z, Liu X, et al. Microstructure, mechanical and thermal properties of in situ toughened boron carbide-based ceramic composites co-doped with tungsten carbide and pyrolytic carbon. Journal of the European Ceramic Society. 2013; 33(10): 1647-1654. doi: 10.1016/j.jeurceramsoc.2013.01.009
54. Ozer SC, Turan S, Sahin FC. Mechanical and microstructural properties of spark plasma sintered B_4C-W_2B_5 composites. In: Proceedings of the 18th International Metallurgy and Materials Congress - IMMC 2016; 29 September-1 October 2016; Istanbul, Turkey. pp. 62-66.
55. Deng J, Zhou J, Feng Y, Ding Z, Microstructure and mechanical properties of hot-pressed B_4C/(W,Ti)C ceramic composites. Ceramic Interational. 2002; 28(4): 425-430. doi: 10.1016/S0272-8842(01)00113-4
56. Chkhartishvili L, Mikeladze A, Tsagareishvili O, et al. Effect of cobalt additive on phases formation in boron carbide matrix composites B_4C-(Ti,Zr)B_2-W_2B_5. Solid State Sciences. 2023; 145: 107339. doi: 10.1016/j.solidstatesciences.2023.107339
57. Chang M, Leung C, Wang DN, et al. Process for CVD Deposition of Tungsten Layer on Semiconductor Wafer. US Patent 5028565, 2 July 1991.
58. Kim SH. Deposition of tungsten thin film on silicon surface by low pressure chemical vapor deposition method. Journal of Korean Chemical Society. 1994; 38(7): 473-479.
59. Plyushcheva SV, Mikhailov GM, Shabel'nikov LG, et al. Tungsten thin-film deposition on a silicon wafer: The formation of silicides at W-Si interface. Inorganic Materials. 2009; 45(2): 140-144. doi: 10.1134/s002016850902006x
60. Kim HJ, Lee JH, Sohn IH, et al. Preparation of tungsten metal film by spin coating method. Korea-Australia Rheology Journal. 2002; 14(2): 71-76.
61. Singla G, Singh K, Pandey OP. Structural and thermal properties of in-situ reduced WO_3 to W powder. Powder Technology. 2013; 237: 9-13. doi: 10.1016/j.powtec.2013.01.008
62. Wang Y, Long BF, Liu CY, et al. Evolution of reduction process from tungsten oxide to ultrafine tungsten powder via hydrogen. High Temperature Materials and Processes. 2021; 40(1): 171-177. doi: 10.1515/htmp-2021-0017
63. Yu ML, Ahn KY, Joshi RV. Surface reactions in the chemical vapor deposition of tungsten using WF_6 and SiH_4 on Al, PtSi, and TiN. Journal of Applied Physics. 1990; 67(2): 1055-1061. doi: 10.1063/1.345791
64. Gao J, Chan LH, Wongsenakhum P. Methods for Improving Uniformity and Resistivity of Thin Tungsten Films. US Patent 7655567B1, 2 February 2010.
65. Yang M, Aarnink AAI, Kovalgin AY, et al. Comparison of tungsten films grown by CVD and hot-wire assisted atomic layer deposition in a cold-wall reactor. Journal of Vacuum Science & Technology A: Vacuum, Surfaces, and Films. 2015; 34(1). doi: 10.1116/1.4936387
66. Dippel AC, Schneller T, Lehmann W, et al. Tungsten coatings by chemical solution deposition for ceramic electrodes in fluorescent tubes. Journal of Materials Chemistry. 2008; 18(29): 3501. doi: 10.1039/b802686f
67. Cao P, Cao JP, Cao JH. Boron carbide ceramic metallization preparation method (Chinese). China Patent CN110981550B, 7 December 2021.
68. Guldamashvili A, Nardaya Y, Nebieridze T, et al. Mechanical properties of tungsten implanted with boron and carbon ions. Journal of Materials Science and Engineering A. 2017; 7(3/4): 82-88. doi: 10.17265/2161-6213/2017.3-4.003

69. Zinovev A, Terentyev D, Chang CC, et al. Effect of neutron irradiation on ductility of tungsten foils developed for tungsten-copper laminates. Nuclear Materials and Energy. 2022; 30: 101133. doi: 10.1016/j.nme.2022.101133
70. Panov VS, Chuvilin AM. Technology and Properties of Sintered Alloys and Products Made from Them (Russian). Available online: http://www.materialscience.ru/subjects/materialovedenie/knigi/tehnologiya_i_svoystva_spechennih_tverdih_splavov_i_izdeliy_iz_nih_uchebnoe_posobie_dlya_vuzov__panov_vs_chuvilin_am__m_misis_2001__432_s_07_02_2010/ (accessed on 19 March 2024).
71. Shapoval AA, Dragobetskii VV, Savchenko IV. Analysis of processes of shock-wave regeneration of solid alloys (Russian). Kharkiv National Technical University Bulletin. 2018; 31(1306): 100-105.

Characterization and Application of Nanomaterials 2024, 7(2), 2539.
https://doi.org/10.24294/can.v7i2.2539

Review

Nanorobots in drug delivery systems and treatment of cancer

Mudavath Hanuma Naik[1,*], **Jala Satyanarayana**[2], **Raj Kumar Kudari**[3]

[1] Department of pharmaceutics, St Mary's College of Pharmacy, Guntur 522212, Andhra Pradesh, India
[2] Department of pharmacology, St Mary's College of Pharmacy, Guntur 522212, Andhra Pradesh, India
[3] Principal & Professor Department of pharmaceutical Analysis, St Mary's college of pharmacy, Guntur 522212, Andhra Pradesh, India
*** Corresponding author:** Mudavath Hanuma Naik, m.hanumanaik7@gmail.com

CITATION

Naik MH, Satyanarayana J, Kudari RK. Nanorobots in drug delivery systems and treatment of cancer. Characterization and Application of Nanomaterials. 2024; 7(2): 2539. https://doi.org/10.24294/can.v7i2.2539

ARTICLE INFO

Received: 22 April 2024
Accepted: 16 June 2024
Available online: 28 August 2024

Abstract: Cancer is the 3rd leading cause of death globally, and the countries with low-to-middle income account for most cancer cases. The current diagnostic tools, including imaging, molecular detection, and immune histochemistry (IHC), have intrinsic limitations, such as poor accuracy. However, researchers have been working to improve anti-cancer treatment using different drug delivery systems (DDS) to target tumor cells more precisely. Current advances, however, are enough to meet the growing call for more efficient drug delivery systems, but the adverse effects of these systems are a major problem. Nanorobots are typically controlled devices made up of nanometric component assemblies that can interact with and even diffuse the cellular membrane due to their small size, offering a direct channel to the cellular level. The nanorobots improve treatment efficiency by performing advanced biomedical therapies using minimally invasive operations. Chemotherapy's harsh side effects and untargeted drug distribution necessitate new cancer treatment trials. The nanorobots are currently designed to recognize 12 different types of cancer cells. Nanorobots are an emerging field of nanotechnology with nanoscale dimensions and are predictable to work at an atomic, molecular, and cellular level. Nanorobots to date are under the line of investigation, but some primary molecular models of these medically programmable machines have been tested. This review on nanorobots presents the various aspects allied, i.e., introduction, history, ideal characteristics, approaches in nanorobots, basis for the development, tool kit recognition and retrieval from the body, and application considering diagnosis and treatment.

Keywords: nanorobots; atherosclerosis; cancer; nano sensors; nanoscale

1. Introduction

Cancer is the 3rd leading cause of death globally, as almost every six deaths is caused by it. By 2030, it's expected to be 26 million new cases of cancer, with almost 17 million deaths per year. The countries with low-to-middle income account for most cancer cases that are expected to be 61% by 2050. In 1965, the International Agency for Research on Cancer (IARC) was established with the mission of conducting multidisciplinary investigations into the causes of human cancers. After conducting several studies, particularly on the structure of genes, experts have concluded that changes in human lifestyle, diet, and environmental factors have resulted in an increased number of cancer cases. The current diagnostic tools, including imaging, molecular detection, and immune histochemistry (IHC), have intrinsic limitations, such as poor accuracy. However, researchers have been working to improve anti-cancer medication delivery systems so that they can target tumor cells more precisely and create fewer adverse effects than chemotherapy. Current advances, however, will not be enough to meet the growing demand for more efficient drug delivery systems.

Nanorobots, an emerging technology, are nano-devices developed to perform specific tasks with precision at the nanoscale (1–100 nm). To perform these specific tasks, nanorobots are designed to work at cellular levels in medical fields. These are machines with nanoscale intelligence and information that can sense, signal, respond, and process. For the synthesis of nanorobots, the mainly used element is carbon due to its inertness, high thermal conductivity, and strength. Moreover, the externally passive diamond coating is performed to elude host immune system attack.

Recent advancement in this field leads to the development of nanorobotic drug delivery systems, including surgical and cellular repair nanorobots. First of all, in 1986, Eric Drexler presented the idea of inserting medical nanorobots into the human body. In these nanorobots, artificial mechanical RBCs (respirocytes), WBCs (microbivores), and platelets (clottocytes) were used. A group of scientists in Korea led by designed a nanorobot that can diffuse a cancer cell’s outer surface and then destroy the cell from the inside. These machine nanoparticles are gold-made and frequently fold and unfold to destroy a cell without any anti-cancer drug. DNA-based cancer-fighting nanobots are being utilized to cure tumors. Similarly, in another study, a new cancer treatment idea is proposed in which nanorobots formed from fragments of DNA (deoxyribonucleic acid) can not only eradicate cancer cells in the body but also kill them. Nanorobots, however, have certain drawbacks, including expensive design and development, high complexity, and invisibility. It becomes harder for drug-loaded nanorobots to travel through blood arteries due to the high blood viscosity; however, researchers are working to address this issue.

The use of nanodevices with higher complexity and possible uses in cancer treatment is the most current challenge in nanotechnology. These nanorobots can support or improve treatment efficiency by performing advanced biomedical therapies using minimally invasive operations. Chemotherapy’s harsh side effects and untargeted drug distribution necessitate new cancer treatment trials. The nanorobots are currently designed to recognize 12 different types of cancer cells. Furthermore, the molecular motors in this equipment can alter their response to UV light and pass through cellular layers to cause necrosis and medications to target specific areas.

The nanorobots, or nanoparticles, are made with a mixture of a polymer and a protein called transferring, which has the capacity of detecting tumor cells because of its molecular particularities. Once they are in the cells, the chemical sensor gives the order to dissolve, and when nanoparticles are dissolved, they let loose some substances that act on the RNA of each cell, disabling the gene responsible for the cancer. Specifically, what the nanoparticles deactivate is the ribonucleic redacts, the protein associated with the cancer growth that is fabricated by the disabled gene. Cancer can be successfully treated with current stages of medical technologies and therapy tools. However, a decisive factor to determine the chances for a patient with cancer to survive is: how earlier it was diagnosed; what means, if possible, a cancer should be detected at least before the metastasis has begun. Another important aspect of achieving a successful treatment for patients is the development of efficient targeted drug delivery to decrease the side effects from chemotherapy. Considering the properties of nanorobots to navigate as bloodborne devices, they can help on such extremely important aspects of cancer therapy. Nanorobots with embedded chemical biosensors can be used to perform detection of tumor cells in early stages of development inside the patient's body. Integrated nano sensors can be utilized for such a task in order to find the intensity of E-adhering signals. Therefore, a hardware architecture based on nano-bioelectronics is described for the application of nanorobots for cancer therapy [1–4].

2. History of nanorobots

1980's by Nobel Prize laureate Richard Smalley. Smalley has extended his vision to carbon nanotubes, discovered by Sumio Iijima, which he envisions as the next super interconnection for ultra-small electronics. The term nanotechnology has evolved to mean the manipulation of the elements to create unique and hopefully useful structures [4].

Beginnings: 1981: Gerd Binnig and Heinrich Rohrer of IBM Zürich invented the Scanning Tunneling Microscope (STM). Used for imaging surfaces at the atomic level and identifying some properties (i.e., energy). 1985: Discovery of fullerenes (molecules composed entirely of carbon). They have many applications in materials science, electronics, and nanotechnology. 1991: discovering carbon nanotubes (cylindrical fullerenes) as a direct result of the fullerenes. Exhibit high tensile strength, unique electrical properties, and efficient thermal conductivity. Their electrical properties make them ideal circuit components (i.e., transistors or sand ultra-capacitors). Recently, research in chemical and biomedical engineering has used carbon nanotubes as a vessel for delivering drugs into the body [5].

Contents: 1991: Invention of the Atomic Force Microscope (AFM). One of the foremost tools for imaging, measuring, and manipulating matter at the nanoscale. It performs sit functions by feeling the surface with a mechanical probe. Since it allows for precision interaction with materials on the nanoscale, it is considered a nanorobot. 2000: The United States National Nanotechnology Initiative is founded to coordinate federal research and development in nanotechnology. Marks the start of a serious effort in nanotechnology research. 2000: The company Nano Factory Collaboration is founded. Developing a research agenda for building a nano factory capable of building nanorobots for medical purposes. Currently, DNA machines (nucleic acid robots) are being developed. Performs mechanical-like movements, such as switching, in response to certain stimuli (inputs). Molecular-sized robots and machines paved the way for nanotechnology by creating smaller and smaller machines and robots.

3. Ideal characteristics

It will communicate with the doctor by encoding messages to acoustic signals at carrier wave frequencies of 1–100 MHz. It might produce multiple copies of it to replace worn-out units, a process called self-replication. After the completion of the task, it can be retrieved by allowing it to excuse itself via the usual human excretory channel, so it can also be removed by active scavenger systems. Nanorobots must have a size between 0.5 and 3 microns large with 1–100 nm parts. It will prevent itself from being attacked by the immune system by having a passive, diamond exterior [6].

3.1. Advantages of nanorobots

Nanotechnology enables us to create functional materials, devices, and systems by controlling matter at the atomic and molecular scales, and exploiting novel properties and phenomena.

- Cost benefit ration is great.
- Environmentally friendly.
- Little pollution from production.
- No wasted materials.
- Very durable.
- Can complete work faster than larger robots.
- Nanorobots can be programmed to self-replicate.
- As the nanorobot does not generate any harmful activities there is no side effect. It operates at specific sites only.
- It has no side effect.

3.2. Disadvantages of nanorobots

- The initial design cost is very high [7].
- The design of the nanorobot is a very complicated one.
- Electrical systems can create stray fields, which may activate bioelectric-based molecular recognition systems in biology.
- Electrical nanorobots are susceptible to electrical interference from external sources such as RF or electric fields, EMP pulses, and stray fields from other in vivo electrical devices.
- Hard to interface, customize, and design; complex.
- Nanorobots can cause a brutal risk in the field of terrorism. Terrorism and anti-groups can make use of nanorobots as a new form of torturing the communities, as nanotechnology also has the capability of destructing the human body at the molecular level.
- Privacy is the other potential risk involved with nanorobots. As nanorobots deal with the design of compact and minute devices, there are chances for more eavesdropping than that already exists in nanorobots.
- The nanorobot should be very accurate; otherwise, harmful effects may occur.

4. Nanorobots and drug delivery systems

Predictions about the use of nanorobots considered applications in the Central Nervous System (CNS), cancer treatment, body surveillance, delicate surgeries, and endoscopy, among others. Challenges such as limitations of nanotechnology and few studies focused on the fundamental understanding of behavior in the nanoworld, difficult handling, and construction of these nanomachines. In nanomedicine, it has been explored in DDS, which acts directly on target points of the human body. Researchers develop systems able to deliver drugs in specific locations, also controlling the dosage and frequency of this release. Drug delivery systems can be applied in the treatment of articular diseases, dental, diabetes, cancer, and others. Diseases such as neoplasms, hepatitis, diabetes, pulmonary, dentistry, and cancer can be used nanorobot technology as a means of implementing the DDS. One of the advantages of this technology is the diagnosis and treatment of diseases with minimum prejudice to the healthy cells, lowering the risk of unfavorable effects, and directing healing and reconstructive treatment at the cellular and subcellular levels [8–21].

5. Technology applied in nanorobots for use as DDS

Recent improvements in drug delivery turn up higher quality in targeted drug delivery that identifies the specific cells with the self of nano sensors and regulates the discharge by use of smart drugs. Some researchers classify nanorobots in drug delivery and therapeutics according to their application, which is described below: Pharmacy: Classified as medical nanorobots with a size of 1–2 µm able to carry up to 1 µm3 of a given drug in the tanks. They are controlled using mechanical systems for sorting pumps. Depending on the situation, the weight is discharged into the extracellular fluid or cytosol (the aqueous component of the cytoplasm of a cell). They are provided with molecular markers or chemotactic sensors that guarantee full targeting accuracy. Glucose and oxygen extracted from the local environment, such as blood, intestinal fluid, and cytosol, are the onboard power supplies. After the nanorobot completes tasks, they can be removed or recovered by centrifuge nan apheresis [22–28].

Diagnosis and imaging: The authors cite microchips that are overlaid with human molecules. The chip is projected to send an electrical signal when the molecules detect disease. Gives an example of special sensor nanorobots that can be introduced into the blood under the skin, where they verify blood contents and notify of any possible diseases. They can also be used to monitor the sugar level in the blood. The advantages are the low price to produce and ease of manipulation [26–32].

Reciprocates: It’s about an artificial red blood cell, which is a blood-borne spherical 1 µm diamondoid 1000 atmosphere pressure vessel with reversible molecules and selective pumps. The power is obtained by endogenous serum glucose. This artificial cell can give 236 times more oxygen to the tissues per unit volume than RBCs (Red Blood Cells) and to administer acidity. The nanomachine is constructed with 18 billion atoms justly organized in a diamondoid pressure tank that is pumped full of up to 3 billion oxygen (O_2) and carbon dioxide (CO_2) molecules. It is impossible to release these gases from the tank. Gas concentration sensors on the outside will signal when it is time to discharge O_2 and unload CO_2 [26,27].

Clottocytes: This nanorobot is classified with a unique biological capability: “instant” hemostasis using clottocytes, or artificial mechanical platelets. It is known that platelets are roughly spheroidal nucleus-free blood cells measuring approximately 2 µm in diameter. Platelets join at a place of bleeding. There they are activated, becoming tacky and lumping together to form a tampon that aids in stamping the blood vessel and stopping the bleeding. They also deliver substances that help promote coagulation. Another interesting feature is its ability to perform phagocytosis of foreign particles and killing of microfilariae larval parasites. A complete functional design is elaborate, but the work of Freitas focuses on the purely mechanical aspects of the hemostatic function of platelets and reports the function in a small in vivo population of medical nanorobotic devices [33].

Microbivores: It is an oblate spheroidal device for biomedical applications with 3.4 µm in diameter along its major axis and 2.0 µm in diameter along its minor axis.

Composed precisely organized of 610 billion atoms in a 12.1 μm 3 geometric volume. The nanobot can continuously consume up to 200 PW. This power is used to digest trapped microbes. Microbivores have different characteristics of natural or antibiotic-assisted biological phagocytic defenses, acting approximately up to 1000 times faster. Another distinctive feature is related to the ability to phagocyte approximately 80 times more efficiently than macrophage agents in terms of volume/sec digested per unit volume of phagocytic agent. Thus, according to the existing technological proposals, nanorobots are an efficient and innovative way for applications in nanomedicine, including DDS and therapeutics (diagnostic and therapeutic) [34]. Searching keywords "drug delivery systems" in the database Periodic CAPES, it was obtained 176,511 publications. Only 0.21% is related to nanorobots, and in this amount of work, only 8% have a relationship between "drug delivery systems and nanorobots". Another database searched was Web of Science [35,36].

The results were 113,896 publications with the keyword "drug delivery" and 201 for nanorobots. The survey also showed that only 0.02% was published with the correlation "drug delivery and nanorobots". Before the number of published papers, it is noted that much more should be done so that nanomedicine can grow apace with the help of nanorobots in treating diseases, in particular cancer.

6. Drug delivery systems for anticancer drugs

The therapeutic index of most anticancer drugs is narrow, causing toxicity to normal stem cells, hematological adverse effects, and gastrointestinal effects, among others. Doxorubicin is used in several types of cancer, such as HD (Hodgkin's disease), in which treatment is administered in combination with other antineoplastic agents in order to reduce their toxicity [37]. Paclitaxel is administered by intravenous infusion and plays a role in the treatment of breast cancer.

Among the adverse effects encountered, some serious, are bone marrow suppression and cumulative neurotoxicity [38]. Cisplatin is an alkylating agent that causes intra-DNA-binding filaments. Some of its side effects are nausea and severe vomiting, as well as being nephrotoxic. Camptothecin is used in the treatment of neoplasias due to the inhibition of type I topoisomerases, an essential enzyme for the cellular replication of genetic material. Several efforts have been implemented to use nanotechnology to develop DDS that can minimize the harmful effects of conventional therapies. Clinical trials are studies in humans to measure the parameters of safety and efficacy of new drugs; they are essential for the arrival of new therapeutic alternatives in the market [39]. Anyway, just a few DDS reached more advanced stages of clinical evaluation, such as those consisting of doxorubicin, paclitaxel, camptothecin, and platinum complexes [40]. Doxorubicin was stacked on the surface of Single-Walled Carbon Nanotubes (SWNTs) [41]. Doxorubicin was employed as a polymer prodrug/collagen hybrid in metastatic tumor cells. The use of polymeric prodrug nanotechnology applied to the treatment of neoplasia shows up as a new development in this area boundary [42]. Super Paramagnetic Nanoparticles of Iron Oxide (SPIONs) loaded with doxorubicin were coated with modified inulin and evaluated for potential use in anti-neoplastic therapy [43].

This arch for biocompatible materials that can serve as a drug delivery system is always the focus of nanotechnology. Nanoparticles HA (hydroxyapatite)—a major constituent of bone and teeth—were used to carry Paclitaxel (tax), an antineoplastic agent, and the results suggest good expectations with treatment starting from hydrophobic drugs [44]. Searching carbon materials, nanoscale graphene oxide was tested as a drug carrier of anti-cancer [45].

Another possible application area of the drug delivery system is especially important in the intrathecal route of administration for the relief of pain related to certain types of cancer. The application drug delivery system intrathecal may be useful in refractory pain to others of administration or even in cases of persistent pain [46]. Again, observing the research with the themes “drug delivery systems and cancer” found a total of 31,134 publications. As noted in recent years, the interest increases in DDS have been directly associated with the need for alternative conventional chemotherapeutics, which possess some serious side effects for the patient [47].

6.1. Limitations of chemotherapy

Conventional chemotherapeutic agents work by destroying rapidly dividing cells, which is the main property of neoplastic cells. This is why chemotherapy also damages normal healthy cells that divide rapidly, such as cells in the bone marrow, macrophages, digestive tract, and hair follicles [48]. Conventional chemotherapy is that it cannot give selective action only to the cancerous cells. This results in common side effects of most chemotherapeutic agents, which include myelosuppression (decreased production of white blood cells causing immunosuppression), mucositis (inflammation of the lining of the digestive tract), alopecia (hair loss), organ dysfunction, and even anemia or thrombocytopenia. These side effects sometimes impose dose reduction, treatment delay, or discontinuance of the given therapy [49]. Furthermore, chemotherapeutic agents often cannot penetrate and reach the core of solid tumors, failing to kill the cancerous cells [50]. Traditional chemotherapeutic agents often get washed out from the circulation being engulfed by macrophages. Thus, they remain in circulation for a very short time and cannot interact with the cancerous cells, making the chemotherapy completely ineffective. The poor solubility of the drugs is also a major problem in conventional chemotherapy, making them unable to penetrate the biological membranes [51]. Another problem is associated with P-glycoprotein, a multidrug resistance protein that is overexpressed on the surface of cancerous cells, which prevents drug accumulation inside the tumor, acts as the efflux pump, and often mediates the development of resistance to anticancer drugs. Thus, the administered drugs remain unsuccessful or cannot bring the desired output [52–60].

6.2. Drug delivery and nanorobots in cancer treatment

The clinical use of nanorobots for diagnosis, therapeutic, and surgical purposes should be done with intravenous injection. Therefore, the nanorobots can be released directly into the patient’s bloodstream. The major cancer treatment cycle for chemotherapy pharmacokinetics includes absorption and metabolism, plus a break for the body’s re-establishment before the next chemotherapy session. Patients are normally treated in cycles of every 2 weeks for small tumors. As an initial time threshold for medical purposes, nanorobots should be able to analyze and provide a body diagnosis within one week through the use of proteomic-based sensors. The uptake kinetics of a low molecular weight using a magnetic resonance contrast agent can predict the delivery of protein drugs to solid tumors. Hence, a similar approach is useful to verify in vivo nanorobot biosensor activation through targeted detection.

The test and diagnosis are an important part of the research on nanorobots. It enables rapid testing and diagnosis at the first visit, so without the need for a follow-up visit after the lab test, and the detection of diseases at an earlier stage. The limitation in vivo use of nanorobots is the need for energy for propulsion. Higher levels of energy are required since "low inertia and high viscous forces are coupled with low efficiency and low convective motion". The fuels of chemically powered nanomotors were toxic. The availability of alternative sources of energy, such as sound waves and light, has led to an increase in the research on in vivo use of nanorobots, which resulted in more patent applications. One study of nanomotors is the acoustic propulsion of nanorod motors inside living cells" [61–67].

Which was a result of the development of ultrasonic-wave-powered minerals, which are safe for living systems. 65 reported an in vivo model of artificial micromotors in a living organism. The model examines the distribution, retention, cargo delivery, and acute toxicity role of synthetic motors in mouse stomachs via oral administration. This work is anticipated to significantly advance the emerging field of nano/micromotors and to open the door to in vivo evaluation and clinical applications of these synthetic motors. This development may be an important step for the possibility of in vivo applications of drug delivery for cancer treatment with decreasing the side effects of chemotherapy. Juul et al. published a paper on their research into nanorobots that contain medicine that can be opened and closed based on the surrounding temperatures. Recently, reported bacteria-based microrobots (bacteriology) as a new type of active drug delivery system. In the study, genetically modified non-toxic Salmonella typhi-murium (flagellar bacteria), which is attracted to chemicals released by cancer cells, is used. Perault and Shih from the Wyss Institute for Biologically Inspired Engineering at Harvard University introduced virus-inspired enveloped DNA nanostructures as a design strategy for biomedical applications. Recent studies revealed that nanotechnology, DNA engineering of molecular-scale devices with superb control over geometry, and site-specific functionalization promise fascinating advantages in advancing nanomedicine. However, instability in biological environments and innate immune activation remain obstacles for in vivo application. After nanorobots cross cellular membranes for targeted delivery, drug retention in the tumor will determine the therapeutic efficiency.

The chemotherapy is influenced by drug transfer processes from plasma to tissue in achieving more effective tumor chemotherapy based on its composition. Thus, the major advantage of nanorobots for cancer drug delivery is to minimize chemotherapy side effects. As the best approach, the nanorobot architecture incorporates CNT (carbon nanotubes) and DNA, which are recent candidates for new forms of nanoelectronics.

ACMOS (Complementary Metal Oxide Semiconductor) for constructing circuits with features in the tens of nanometers as a hybrid biosensor with single-chain antigen-binding proteins. This process uses activation based on proteomics and bioelectronics signals for formation release. Therefore, each time the nanorobot detects predefined changes in protein gradients, nanoactuators are activated to manipulate drug delivery. Changes to chemical and thermal signals are applicable conditions directly related to major medical target identification. Some examples of changing protein concentrations inside the body near a medical target under pathological circumstances are NOS (Nitric Oxide Synthase), E-cadherin, and BCL-2 [68,69].

7. Approaches in nanorobots

Biochip: The joint use of nanoelectronics, photolithography, and new biomaterials provides a possible approach to manufacturing nanorobots for common medical applications, such as surgical instrumentation, diagnosis, and drug delivery [69]. Biochips not only consist of immobilized molecules spatially addressed on planar surfaces but also contain biomolecules fixed in microchannels or microcells or on an array of beads or sensors. Nanotechnology has made biochips more applicable for commercialization purposes where biochips could be implanted inside the body to dynamically transmit information and monitor any biological changes in vivo [70].

Nubot: Nubot is an abbreviation for “nucleic acid robot”. They are organic molecular machines [71]. DNA structure can provide means to assemble 2D and 3D nanomechanical devices. DNA-based machines can be activated using small molecules, proteins, and other molecules of DNA [72]. Nubots have DNA structures used for targeting drug delivery as a carrier.

Bacteria-based: This approach proposes the use of biological microorganisms, like the bacterium Escherichia coli. Thus, the model uses a flagellum for propulsion purposes. Electromagnetic fields normally control the motion of this kind of biologically integrated device.

Open technology: A document with a proposal for nanobiotech development using open technology approaches has been addressed to the United Nations General Assembly. According to the document sent to the UN, in the same way that open source has in recent years accelerated the development of computer systems, a similar approach should benefit society at large and accelerate nanorobots development.

Nanobearing and nanogears: To establish the feasibility of molecular manufacturing, it is first necessary to create and analyze possible designs for nanoscale mechanical parts that could, in principle, be manufactured [73]. “Ability to model molecular machines (systems and devices) of specific kinds, designed in part for ease of modeling, has far out run our ability to make them. Design calculations and computational experiments enable the theoretical studies of these devices, independent of the technologies needed to implement them.” The simple structure and operation of molecular bearings make it the most convenient class of components to be designed. OneofthesimplestexamplesisDrexler’soverlap-repulsionbearingdesign.

Medical nanorobot architecture: The main parameters used for the medical nanorobot architecture and its control activation, as well as the required technological background that may lead to manufacturing hardware for molecular machines, are described next.

Manufacturing technology: The ability to manufacture nanorobots may result from current trends and new methodologies in fabrication, computation, transducers, and manipulation. Depending on the case, different gradients on temperature, the concentration of chemicals in the bloodstream, and electromagnetic signature are some of the relevant parameters for diagnostic purposes [74].

CMOS VLSI (Very Large Scale Integration) systems designed using deep ultraviolet lithography provide high precision and a commercial way of manufacturing early nanodevices and nanoelectronics systems. The CMOS industry may successfully drive the pathway for the assembly processes needed to manufacture nanorobots, where the joint use of nano photonics and nanotubes may even accelerate further the actual levels of resolution ranging from 248 nm to 157 nm devices [75]. To validate designs and achieve a successful implementation, the use of VHDL (Verification Hardware Description Language) has become the most common methodology utilized in the integrated circuit manufacturing industry [76].

Chemical sensor: Manufacturing silicon-based chemical- and motion-sensor arrays using a two-level system architecture hierarchy has been successfully conducted in the last 15 years. Applications range from the automotive and chemical industry with detection of air to water element pattern recognition through embedded software programming to biomedical uses. Through the use of nanowires, the existing significant costs of energy demand for data transfer and circuit operation can be decreased by up to 60%. CMOS-based biosensors using nanowires as materials for circuit assembly can achieve maximal efficiency for applications regarding chemical changes, enabling new medical treatments [77]. Chemical nano sensors can be embedded in the nanorobot to monitor E-cadherin gradients. Thus, nanorobots programmed for such tasks can make a detailed screening of the patient's whole body. In our medical nanorobotic architecture, the mobile phone is applied to retrieve information about the patient's conditions [78,79]. For that, it uses electromagnetic waves to command and detect the current status of nanorobots inside the patient. New materials, such as strained channels with relaxed Si Gelayer scan, reduce self-heating and improve performance. Recent developments in 3D circuits and FinFET double-gates have achieved astonishing results, and according to the semiconductor roadmap, they should improve even more [80]. To further advance manufacturing techniques, Silicon-On-Insulator (SOI) technology has been used to assemble high-performance logic sub90nm circuits. Circuit design approaches to solve problems with bipolar effects and hysteretic variations based on SOI structure have been demonstrated successfully [81]. Thus, already-feasible 90nm and 45nm CMOS devices represent breakthrough technology devices that are already being utilized in products.

Power supply: The use of CMOS for active telemetry and power supply is the most effective and secure way to ensure energy as long as necessary to keep the nanorobot in operation. The same technique is also appropriate for other purposes, like digital bit-encoded data transfer from inside a human body [82]. Thus, nanocircuits with resonant electric properties can operate as a chip, providing electro-magnetic energy supplying 1.7 mA at 3.3 V for power, allowing the operation of many tasks with few or no significant losses during transmission [83]. Radio frequency-based telemetry procedures have demonstrated good results in patient monitoring and power transmission with the use of inductive coupling [84] using well-established techniques already widely used in commercial applications of RFID (Radio Frequency Identification Device). The energy received can also be saved in ranges of 1 μW while the nanorobot stays in inactive modes, just becoming active when signal patterns require it to do so. Some typical nanorobotic tasks may require the device only to spend low power amounts once it has been strategically activated. For communication, sending RF signals 1 mW is required. A practical way to achieve easy implementation of this architecture will obtain both energy and data transfer capabilities for nanorobots by employing mobile phones in such a process [85]. The mobile phone should be uploaded with the control software that includes the communication and energy transfer protocols.

Data transmission: The application of devices and sensors implanted inside the human body to transmit data about the health of patients can provide great advantages in continuous medical monitoring [86]. Most recently, the use of RFID for in vivo data collection and transmission was successfully tested for electroencephalograms. For communication in liquid workspaces, depending on the application, acoustic, light, RF, and chemical signals may be considered as possible choices for communication and data transmission. Chemical signaling is quite useful for nearby communication among nanorobots for some teamwork coordination [87]. Work with RFID has been developed as an integrated circuit device for medicine [88,89]. Using integrated sensors for data transfer is the better answer to reading and writing data in implanted devices. Teams of nanorobots may be equipped with single-chip RFID CMOS-based sensors. CMOS with a submicron system-on-chip design could be used for extremely low power and longer distances through acoustic sensors. For the nanorobot, active sonar communication frequencies may reach up to 20 µW @ 8 Hz at resonance rates with a 3V supply [90]. In our molecular machine architecture, to successfully set an embedded antenna with a 200 nm size for the nanorobot RF communication, a small loop planar device is adopted as an electromagnetic pick-up having a good matching on low noise amplifier; it is based on gold nanocrystal with 1.4 nm, CMOS, and nano electronic circuit technologies [91]. Frequencies ranging from 1 to 20 MHz can be successfully used for biomedical applications without any damage.

Targets it and their communication with the machines [92]: The nanorobot design includes integrated nano electronics which involves the use of mobile phones. It uses an RFID (CMOS transponder system) for in vivo positioning, using a well-established communication protocol that allows tracking information about its positioning. There are three approaches to recognizing the target site: first, as a point of comparison, the scientists use nanorobots with small Brownian motions to find the target by random search. In a second method, it monitors for chemical concentration significantly above the background level.

After detecting the signal, it estimates the concentration gradient and moves toward higher concentrations until it reaches the target. In the third approach, nanorobots at the target release another chemical, which others use as an additional guiding signal to the target. With these signal concentrations, only it passes within a few microns of the target is likely to detect the signal. Most recently, the use of RFID for in vivo data collection and transmission was successfully tested for electroencephalograms. For communication in liquid workspaces, depending on the application, acoustic, light, RF, and chemical signals may be considered as possible choices for communication and data transmission. One of the simplest ways to send broadcast-type messages into the body, to be received by in vivo nanorobots, is aural messaging. A device similar to an ultrasound probe would encode messages on aural carrier waves at frequencies between 1–10 MHz. Thus, the supervising physician can easily send new commands or parameters to nanorobots already at work inside the body. Each nanorobot has its own power supply, computer, and sensorium; thus, it can receive the physician's messages via aural sensors, then compute and implement the appropriate response. The other half of the process is getting messages back out of the body, from the working nanodevices out to the physician [93].

Applications-diagnosis and treatment [92–94]: Medical nanorobots can perform a vast array of diagnostic, testing, and monitoring functions, both in tissues and in the blood stream. These devices could continuously record and report all vital signs, including temperature, pressure, chemical composition, and immune system activity, from all different parts of the body.

Cancer therapy: Nanorobots with embedded chemical biosensors can be used to perform the detection of tumor cells in the early stages of development inside the patient's body. These nanorobots would search out and identify the cancer-affected cells using certain molecules as they could be introduced into the bloodstream. Medical nanorobots would then destroy these cells.

Nanorobots with chemical nano biosensors can be programmed to detect different levels of E-cadherin and beta-catenin as medical targets in primary and metastatic phases, helping target identification and drug delivery. Integrated nano sensors can be utilized for such a job to find the intensity of E-cadherin signals. Nanorobots could also carry the chemicals used in chemotherapy to treat cancer directly at the site.

Diabetes: The protein sodium-dependent glucose co-transporter system has an important influence in maintaining proper gastrointestinal cholinergic nerve and skeletal muscle function activities, regulating extracellular glucose concentration. The hSGLT3 molecule can serve to define glucose levels and serves as a sensor to identify glucose for diabetes patients. For glucose monitoring, the nanorobot uses an embedded chemo sensor that involves the modulation of hSGLT3 protein glucose sensor activity. Through its onboard chemical sensor, the nanorobot can thus effectively determine if the patient needs to inject insulin or take any further action, such as any medication clinically prescribed. They flow with the RBCs through the blood stream, detecting the glucose levels. In the medical nanorobot architecture, the significant measured data can be then transferred automatically through the RF signals to the mobile phone carried by the patient. At any time, if the glucose achieves critical levels, the nanorobot emits an alarm through the mobile phone.

8. Surgery

Surgical nanorobots could be introduced into the body through the vascular system or at the ends of catheters into various vessels and other cavities in the human body. A surgical nanorobot, programmed or guided by a human surgeon, could act as a semiautonomous on-site surgeon inside the human body. It performs various functions, such as searching for pathology and then diagnosing and correcting lesions by nanomanipulation, coordinated by an onboard computer while maintaining contact with the supervising surgeon via coded ultrasound signals. The earliest forms of cellular nano surgery are already being explored today.

8.1. As an artificial oxygen carrier

The artificial mechanical red cell, the respirocyte, is an imaginary nanorobot that floats all along in the bloodstream. The respirocyte is a tiny pressure tank that can be pumped full of oxygen (O_2) and carbon dioxide (CO_2) molecules. These gases can be released from the tiny tank in a controlled manner. When the nanorobot passes through the lung capillaries, O_2 partial pressure is high and CO_2 partial pressure is low, so the onboard computer tells the sorting rotors to load the tanks with oxygen and dump the CO_2. When the device later finds itself in the oxygen-starved peripheral tissues, the sensor readings are reversed. CO_2 partial pressure is relatively high and O_2 partial pressure is relatively low, so the onboard computer commands the sorting rotors to release O_2 and absorb CO_2. Respirocytes mimic the action of the natural hemoglobin-filled red blood cells and can deliver 236 times more oxygen per unit than a natural red cell.

8.2. As artificial phagocyte(microbivore)

Microbivore is an artificial mechanical phagocyte of microscopic size whose primary function is to destroy microbiological pathogens found in the human bloodstream using the “digest and discharge” protocol. The chief function of microbes is to wipe out microbiological pathogens found in the human bloodstream using the “digest and discharge” procedure. Microbivores, upon given intravenously (I.V.), would achieve complete clearance of the most severe septicemic infections in hours or less, far better than the weeks or months needed for antibiotic-assisted natural phagocytic defenses. The nanorobots do not boost the risk of sepsis or septic shock because the pathogens are completely digested into harmless simple sugars, mono-residue amino acids, mononucleotides, free fatty acids, and glycerol, which are the biologically inactive effluents from the nanorobot.

8.3. As artificial neurons

Nanorobots can be employed in replacing every neuron in one’s brain with a nanorobot that is designed to function just like normal, natural neurons. The nanotech neurons are functionally equivalent. They connect to the same synapse of the original neuron, and they perform the same functional roles.

Atherosclerosis: Medical nanorobots can locate atherosclerotic lesions in blood vessels, mainly in the coronary circulation, and treat them either mechanically, chemically, or pharmacologically.

Cell repair and lysis: An interesting utilization of nanorobots may be their attachment to transmigrating inflammatory cells or white blood cells to reach swollen tissues and assist in their healing process. Mobile cell-repair nanorobot is capable of limited vascular surface travel into the capillary bed of the targeted tissue or organ, followed by extravasations, histation, cyto-penetration, and complete chromatin replacement in the nucleus of one target cell, and ending with a return to the bloodstream and subsequent extraction of the device from the body, completing the cell repair mission.

Hemophilia: One particular kind of nanorobot is the choanocyte or artificial platelet. The choanocyte carries a small mesh net that dissolves into a sticky membrane upon contact with blood plasma. According to Freitas RA, the man who designed the choanocyte, clotting could be up to 1000 times faster than the body's natural clotting mechanism.

Gout: Gout is a situation where the kidneys lose the ability to remove waste from the breakdown of fats from the bloodstream. This waste sometimes crystallizes at points near joints like the knees and ankles. A nanorobot could break up the crystalline structures at the joints, providing relief from the symptoms, though it wouldn't be able to reverse the state permanently.

Kidney stones: Kidney stones can be intensely painful; the larger the stone, the more difficult it is to pass. An nanorobot could break up kidney stones using a small laser.

Cleaning wounds: Nanorobots could help remove debris from wounds, decreasing the likelihood of infection. They would be particularly useful in cases of puncture wounds, which can be difficult to treat using more conventional methods.

Gene therapy: Medical nanorobots can readily treat genetic diseases by comparing the molecular structures of both DNA and proteins found in the cell to known or desired reference structures. Any irregularities can then be corrected, or desired modifications can be edited in place. In some cases, chromosomal replacement therapy is more efficient than cyto repair.

Conflict of interest: The authors declare no conflict of interest.

References

1. WHO. Cancer. Available online: https://www.who.int/news-room/fact-sheets/detail/cancer (accessed on 3 February 2022).
2. Thun MJ, De Lancey JO, Center MM, et al. The global burden of cancer: Priorities for prevention. Carcinogenesis. 2010; 31(1): 100-110. doi: 10.1093/carcin/bgp263
3. Bray F, Møller B. Predicting the future burden of cancer. Nature Reviews Cancer. 2006; 6(1): 63-74. doi: 10.1038/nrc1781
4. Blackadar CB. Historical review of the causes of cancer. World Journal of Clinical Oncology. 2016; 7(1): 54-86. doi: 10.5306/wjco.v7.i1.54
5. GIZMODO, Egyptian mummy had prostate cancer; lots more ancient peeps probably did too. Available online: https://gizmodo.com/egyptian-mummy-had-prostate-cancerlots-more-ancient-p-5854019 (accessed on 3 February 2022).
6. N.C. Institute, Risk factors for cancer. Available online: https://www.cancer.gov/about-cancer/causes-prevention/risk (accessed on 3 February 2022).
7. Liu M, Yu X, Chen Z, et al. Aptamer selection and applications for breast cancer diagnostics and therapy. Journal of Nanobiotechnology. 2017; 15(1): 1-16. doi: 10.1186/s12951-017-0311-4
8. Chen T, Ren L, Liu X, et al. DNA nanotechnology for cancer diagnosis and therapy. International Journal of Nanomedicine. 2018; 19(6): 1671. doi: 10.3390/ijms19061671
9. Aeran H, Kumar V, Uniyal S, Tanwer P, et al. Nanodentistry: Is just a fiction or future. Journal of Oral Biology and Craniofacial Research. 2015; 5(3): 207-211. doi: 10.1016/j.jobcr.2015.06.012
10. Sarath KS, Nasim BP, Abraham E. Nanorobots a future device for diagnosis and treatment. Journal of Pharmacy and Pharmaceutics. 2018; 5(1): 44-49. doi: 10.15436/2377-1313.18.1815
11. Neto AMJC, Lopes IA, Pirota KR. A review on nanorobots. Journal of Computational and Theoretical Nanoscience. 2010; 7(10): 1870-1877. doi: 10.1166/jctn.2010.1552
12. Sivasankar M, Durairaj RB. Brief review on nano robots in bio medical applications. Advances in Robotics & Automation. 2012; 1(1): 101. doi: 10.4172/2168-9695.1000101
13. Manjunath V, Kishore V. The promising future in medicine: Nanorobots. Biomedical Science and Engineering. 2014; 2(2): 42-47. doi: 10.12691/bse-2-2-3
14. Jeong Y, Jin S, Palanikumar L, et al. Stimuli-responsive adaptive nanotoxin to directly penetrate the cellular membrane by

molecular folding and unfolding. Journal of the American Chemical Society. 2022; 144(12): 5503-5516. doi: 10.1021/jacs.2c00084

15. Desrosiers A, Derbali RM, Hassine S, et al. Programmable self-regulated molecular buffers for precise sustained drug delivery. Nature Communications. 2022; 13(1): 1-13. doi: 10.1038/s41467-022-33491-7
16. Harroun SG, Prévost-Tremblay C, Lauzon D, et al. Programmable DNA switches and their applications. Nanoscale. 2018; 10: 4607-4641. doi: 10.1039/C7NR07348H
17. Lenaghan SC, Wang Y, Xi N, et al. Grand challenges in bioengineered nanorobots for cancer therapy. IEEE Transactions on Bio-Medical Engineering. 2013; 60(3): 667-673. doi: 10.1109/TBME.2013.2244599
18. Paul S. A brief insight into nanorobots. In: Bhattacharyya S, Das N, Bhattacharjee D (editors). Handbook of Research on Recent Developments in Intelligent Communication Application. IGI Global; 2017. pp. 23-74.
19. Ricotti L, Cafarelli A, Iacovacci V, et al. Advanced micro-nano-bio systems for future targeted therapies. Current Nanoscience. 2015; 11(2): 144-160. doi: 10.2174/1573413710666141114221246
20. Giri G, Maddahi Y, Zareinia K. A brief review on challenges in design and development of nanorobots for medical applications. Applied Sciences. 2021; 11(21): 10385. doi: 10.3390/app112110385
21. Vartholomeos P, Fruchard M, Ferreira A, Mavroidis C. MRI-Guided nanorobotic systems for therapeutic and diagnostic applications. Annual Review of Biomedical Engineering. 2011; 13: 157-184. doi: 10.1146/annurev-bioeng-071910-124724
22. Ungaro F, d'Angelo I, Miro A, et al. Engineered PLGA nano-and micro- carriers for pulmonary delivery: Challenges and promises. The Journal of Pharmacy and Pharmacology. 2012; 64(9): 1217-1235. doi: 10.1111/j.2042-7158.2012.01486.x
23. Pappu P, Madduru D, Chandrasekharan M, et al. Next generation sequencing analysis of lung cancer datasets: A functional genomics perspective. Indian Journal of Cancer. 2016; 53(1): 1-8. doi: 10.4103/0019-509X.180832
24. Verma SK, Chauhan R. Nanorobots in dentistry—A review. Indian Journal of Dentistry. 2014; 5: 62-70. doi: 10.1016/j.ijd.2012.12.010
25. Dixon KL. The radiation biology of radioimmunotherapy. Nuclear Medicine Communications. 2003; 24(9): 951-957. doi: 10.1097/00006231-200309000-00002
26. Reza KH, Asiwarya G, Radhika G, Bardalai D. Nanorobots: The future trend of drug delivery and therapeutics. International Journal of Pharmaceutical Sciences Review and Research. 2011; 10(1): 60-68.
27. Freitas RA. Medical nanorobots: The long-term goal for nanomedicine. Available online: http://www.nanomedicine.com/Papers/ArtechChapter2009.pdf (accessed on 3 February 2022).
28. Freitas RA. Pharmacytes: An ideal vehicle for targeted drug delivery. Journal of Nanoscience and Nanotechnology. 2006; 6(9-10): 2769-2775. doi: 10.1166/jnn.2006.413
29. Manjunath A, Kishore V. The promising future in medicine: Nanorobots. Biomedical Science and Engineering. 2014; 2(2): 42-47. doi: 10.12691/bse-2-2-3
30. Karan S, Banerjee B, Tripathi A, Majumder DD. Nanorobots control systems design—A new paradigm for healthcare system. In: Satapathy SC, Govardhan A, Raju KS, Mandal JK (editors). Emerging ICT for Bridging the Future, Proceedings of the 49th Annual Convention of the Computer Society of India (CSI); 12-14 December 2014; Hyderabad, Telangana, India. Springer; 2014. Volume 1.
31. Bhowmik D, Bhattacharjee C, Jayakar B. Role of nanotechnology in novel drug delivery system. Journal of Pharmaceutical Science and Technology. 2009; 1(1): 20-35.
32. Freitas RB. IMM report number 18: Nanomedicine. Clottocytes: Artificial mechanical platelets. Available online: http://www.imm.org/reports/rep018/ (accessed on 3 February 2022).
33. Dabbs DJ, Thompson LDR. Diagnostic Immunohistochemistry: Theranostic and Genomic Applications, 4th ed. Saunders; 2013.
34. Web of science. Available online: http://apps.webofknowledge.com/UA_GeneralSearch_input.do?product=UA&search_mode=GeneralSearch&SID=3DCzfvN7XkKHGA5i9Hu&preferencesSaved (accessed on 3 February 2022).
35. Golan DE, Tashjian AH, Armstrong EJ. Armstrong AW. Principles of Pharmacology: The Pathophysiologic Basis of Drug Therapy, 3rd ed. Lippincott Williams & Wilkins; 2011.
36. Ritter JM, Rang HP, Flower R, Henderson G. Rang & Dale's Pharmacology, 8th ed. Churchill Livingstone; 2015.
37. National Health Surveillance Agency—An visa (Portuguese). Available online: http://portal.anvisa.gov.br/wps/content/anvisa+portal/anvisa/sala+de+imprensa/menu+-

+noticias+anos/2015/publicadas+novas+normas+para+pesquisa+clinica (accessed on 3 February 2022).

38. Kratz F, Warnecke A. Finding the optimal balance: Challenges of improving conventional cancer chemotherapy using suitable combinations with nano-sized drug delivery systems. Journal of Controlled Release. 2012; 164(2): 221-235. doi: 10.1016/j.jconrel.2012.05.045
39. Zeeshan MA, Pané S, Youn SK, et al. Graphite coating of iron nanowires for nanorobotic applications: Synthesis, characterization and magnetic wireless manipulation. Advanced Functional Materials. 2012; 23(7): 823-831. doi: 10.1002/adfm.201202046
40. Kojima C, Suehiro T, Watanabe K, et al. Doxorubicin-conjugated dendrimer/collagen hybrid gels for metastasis-associated drug delivery systems. Acta Biomaterialia. 2013; 9(3): 5673-5780. doi: 10.1016/j.actbio.2012.11.013
41. Scialabba C, Licciardi M, Mauro N, et al. Inulin-based polymer coated SPIONs as potential drug delivery systems for targeted cancer therapy. European Journal of Pharmaceutics and Biopharmaceutics. 2014; 88(3): 695-705. doi: 10.1016/j.ejpb.2014.09.008
42. Watanabe K, Nishio Y, Makiura R, et al. Paclitaxel-loaded hydroxyapatite/collagen hybrid gels as drug delivery systems for metastatic cancer cells. International Journal of Pharmaceutics. 2013; 446(1-2): 81-86. doi: 10.1016/j.ijpharm.2013.02.002
43. Liu Z, Robinson JT, Tabakman SM, et al. Carbon materials for drug delivery & cancer therapy. Materials Today. 2011; 14(7-8): 316-323. doi: 10.1016/S1369-7021(11)70161-4
44. Health Quality Ontario. Intrathecal drug delivery systems for cancer pain: A health technology assessment. Ontario Health Technology Assessment Series. 2016; 16(1): 1-51.
45. Sutradhar KB, Amin L. Nanotechnology in cancer drug delivery and selective targeting. International Scholarly Research Notices. 2014; 2014: 939378. doi: 10.1155/2014/939378
46. Zhao G, Rodriguez BL. Molecular targeting of liposomal nanoparticles to tumor microenvironment. International Journal of Nanomedicine. 2013; 8: 61-71. doi: 10.2147/IJN.S37859
47. Coates A, Abraham S, Kaye SB, et al. On the receiving end-patient perception of the side-effects of cancer chemotherapy. European Journal of Cancer& Clinical Oncology. 1983; 19(2): 203-308. doi: 10.1016/0277-5379(83)90418-2
48. Tannock IF, Lee CM, Tunggal JK, et al. Limited penetration of anticancer drugs through tumor tissue: A potential cause of resistance of solid tumors to chemotherapy. Clinical Cancer Research. 2002; 8(3): 878-884.
49. Mousa SA, Bharali DJ. Nanotechnology-based detection and targeted therapy in cancer: Nano-bio paradigms and applications. Cancers. 2011; 3(3): 2888-2903. doi: 10.3390/cancers3032888
50. Links M, Brown R. Clinical relevance of the molecular mechanisms of resistance to anti-cancer drugs. Expert Reviews in Molecular Medicine. 1999; 1(15):1-21. doi: 10.1017/S146239949900109X
51. World Health Organization. Cancer. Available online: http://www.who.int/cancer/en/ (accessed on 3 February 2022).
52. Mutoh K, Tsukahara S, Mitsuhashi J, et al. Estrogen-mediated post transcriptional down-regulation of P-glycoprotein in MDR_1-transduced human breast cancer cells. Cancer Science. 2006; 97(11): 1198-1204. doi: 10.1111/j.1349-7006.2006.00300.x
53. Lagzi I. Chemical robotics—Chemotactic drug carriers. Central European Journal of Medicine. 2013; 8(4): 377-382. doi: 10.2478/s11536-012-0130-9
54. Xu X, Kim K, Fan D. Tunable release of multiplex biochemicals by plasmonically active rotary nanomotors. Angewandte Chemie (International Edition). 2015; 54(8): 2525-2529. doi: 10.1002/anie.201410754
55. Couvreur P, Gref R, Andrieux K, Malvy C. Nanotechnologies for drug delivery: Application to cancer and autoimmune diseases. Progress in Solid State Chemistry. 2006; 34(2-4): 231-235. doi: 10.1016/j.progsolidstchem.2005.11.009
56. Janda E, Nevolo M, Lehmann K, et al. Raf plus TGFβ-dependent EMT is initiated by endocytosis and lysosomal degradation of E-cadherin. Oncogene. 2006; 25(54): 7117-7130. doi: 10.1038/sj.onc.1209701
57. Osterlind K. Chemotherapy in small cell lung cancer. European Respiratory Journal. 2001; 18(6): 1026-1043. doi: 10.1183/09031936.01.00266101
58. Artemov D, Solaiyappan M, Bhujwalla ZM. Magnetic resonance pharmacoangiography to detect and predict chemotherapy delivery to solid tumors. Cancer Research. 2001; 61(7): 3039-3044.
59. Cavalcanti A, Shirinzadeh B, Freitas RA, Hogg T. Nanorobot architecture for medical target identification. Nanotechnology. 2007; 19(1): 015103. doi: 10.1088/0957-4484/19/01/015103
60. Sharma NN, Mittal RK. Nanorobot movement: Challenges and biologically inspired solutions. International Journal on Smart Sensing and Intelligent Systems2008; 1(1): 87-109. doi: 10.21307/ijssis-2017-280

61. Wang W, Li S, Mair L, et al. Acoustic propulsion of nanorod motors inside living cells. Angewandte Chemie (International Edition). 2014; 53(12): 3201-3204. doi: 10.1002/anie.201309629
62. Gao W, Dong R, Thamphiwatana S, et al. Artificial micromotors in the mouse's stomach: A step toward in vivo use of synthetic motors. ACS Nano. 2015; 9(1): 117-123. doi: 10.1021/nn507097k
63. Juul S, Iacovelli F, Falconi M, et al. Temperature-controlled encapsulation and release of an active enzyme in the cavity of a self-assembled DNA nanocage. ACS Nano. 2013; 7(11): 9724-9734. doi: 10.1021/nn4030543
64. Ahmad A, Kamal A, Ashraf F, Ansari AF. A review on current scenario in the field of nanorobotics. International Journal of Engineering Sciences & Research Technology (IJESRT). 2014; 3(6): 578-584.
65. Fisher B. Biological research in the evolution of cancer surgery: A personal perspective. Cancer Research. 2008; 68(24): 10007-10020. doi: 10.1158/0008-5472
66. Cavalcanti A, Shirinzadeh B, Zhang M, Kretly LC. Nanorobot hardware architecture for medical defense. Sensors. 2008; 8(5): 2932-2958. doi: 10.3390/s8052932
67. Wong PC, Wong K, Foote H. Organic data memory using the DNA approach. Communications of the ACM. 2003; 46(1): 95-98. doi: 10.1145/602421.602426
68. Seeman NC. From genes to machines: DNA nanomechanical devices. Trends in Biochemical Sciences. 2005; 30(3): 119-125. doi: 10.1016/j.tibs.2005.01.007
69. Drexler KE. Nanosystems: Molecular Machinery, Manufacturing, and Computation, 1st ed. Wiley; 1992.
70. Hogg T, Kuekes PJ. Mobile microscopic sensors for high resolution in vivo diagnostics. Nanomedicine: Nanotechnology, Biology, and Medicine. 2006; 2(4): 239-247. doi: 10.1016/j.nano.2006.10.004
71. Bogaerts W, Baets R, Dumon P, et al. Nanophotonic waveguides in silicon-on-insulator fabricated with CMOS technology. Journal of Lightwave Technology. 2005; 23(1): 401-412. doi: 10.1109/JLT.2004.834471
72. Kubista PB. Creating Standard VHDL Test Environments. U.S. Patent 6,813,751, 2 November 2004.
73. Curtis ASG, Dalby M, Gadegaard N. Cell signaling arising from nanotopography: Implications for nanomedical devices. Nanomedicine. 2006; 1(1): 67-72. doi: 10.2217/17435889.1.1.67
74. Ahuja SP, Myers JR. A survey on wireless grid computing. Journal of Supercomputing. 2006; 37(1): 3-21. doi:10.1007/s11227-006-3845-z
75. Hanada E, Antoku Y, Tani S, et al. Electromagnetic interference on medical equipment by low-power mobile telecommunication systems. IEEE Transactions on Electromagnetic Compatibility. 2000; 42(4): 470-476. doi: 10.1109/15.902316
76. Sauer C, Stanacevic M, Cauwenberghs G, Thakor N. Power harvesting and telemetry in CMOS for implanted devices. IEEE Transactions on Circuits and Systems I: Regular Papers. 2005; 52(12): 2605-2613. doi: 10.1109/TCSI.2005.858183
77. Bernstein K, Chuang CT, Joshi R, Puri R. Design and CAD challenges in sub-90nm CMOS technologies. In: Proceedings of the International Conference on Computer Aided Design (ICCAD 2003); 9-13 November 2003; San Jose, CA, USA. pp. 129-136.
78. Mohseni P, Najafi K. Wireless multichannel biopotential recording using an integrated FM telemetry circuit. In: Proceedings of the 26th Annual International Conference of the IEEE Engineering in Medicine and Biology Society; 1-5 September 2004; San Francisco, CA, USA.
79. Eggers T, Marscher C, Marschner U, et al. Advanced hybrid integrated low-power telemetric pressure monitoring system for biomedical application. In: Proceedings of the IEEE Thirteenth Annual International Conference on Micro Electro Mechanical Systems (MEMS 2000); 23-27 January 2000; Miyazaki, Japan. pp. 23-37.
80. Ricciardi L, Pitz I, AI-Sarawi S, et al. Investigation into the future of RFID in biomedical applications. In: Proceedings of the Microtechnologies for the New Millenium 2003; 19-21 May 2003; Maspalomas, Gran Canaria, Spain.
81. Cavalcanti B, Shirinzadeh B, Freitas RA, Kretly LC. Medical nanorobot architecture based on nanobioelectronics. Recent Patents on Nanotechnology. 2007; 1(1): 1-10. doi: 10.2174/187221007779814745
82. Hogg T. Coordinating microscopic robots in viscous fluids. Autonomous Agents and Multi-Agent Systems. 2007; 14(3): 271-305. doi: 10.1007/s10458-006-9004-3
83. Horiuchi TK, Etienne-Cummings R. A time-series novelty detection chip for sonar. International Journal of Robotics and Automation. 2004; 19: 171-177.
84. Hamad-Schifferli K, Schwartz JJ, Santos AT, et al. Remote electronic control of DNA hybridization through inductive coupling to an attached metal nanocrystal antenna. Nature. 2002; 415(6868): 152-155. doi: 10.1038/415152a

85. Cavalcanti A, Shirinzadeh B, Zhang M. Nanorobot hardware architecture for medical defense. Sensors. 2008; 8: 2932-2958. doi: 10.3390/s8052932
86. Kharwade M, Nijhawan M, Modani S. Nanorobots: A future medical device in diagnosis and treatment. Research Journal of Pharmaceutical, Biological and Chemical Sciences. 2013; 4(2): 1299-1307.
87. Venkatesan M, Jolad B. Nanorobots in cancer treatment. In: Proceedings of the International Conference on Emerging Trends in Robotics and Communication Technologies (INTERACT 2010); 3-5 November 2010; Chennai, India. pp. 258-264.
88. Cavalcanti A, Shirinzadeh B, Kretly LC. Medical nanorobotics for diabetes control. Nanomedicine: Nanotechnology, Biology and Medicine. 2008; 4(2): 127-138. doi: 10.1016/j.nano.2008.03.001
89. Freitas RA. Nanotechnology, nanomedicine and nanosurgery. International Journal of Surgery. 2005; 3(4): 243-246. doi: 10.1016/j.ijsu.2005.10.007
90. Diez-Sampedro A, Wright EM, Hirayama BA. Residue 457 controls sugar binding in the Na^+/glucose cotransporter*. Journal of Biological Chemistry. 2001; 276(52): 49188-49194. doi: 10.1074/jbc.M108286200
91. Patil M, Mehta DS, Guvva S. Future impact of nanotechnology on medicine and dentistry. Journal of Indian Society of Periodontology. 2008; 12(2): 34-40. doi: 10.4103/0972-124X.44088
92. Cavalcanti A, Rosen L, Kretly LC, et al. Nanorobotic challenges in biomedical applications, design and control. In: Proceedings of the 11th IEEE International Conference on Electronics, Circuits and Systems (ICECS 2004); 13-15 December 2004; Tel Aviv, Israel.
93. Freitas RA. Computational tasks in medical nanorobotics. In: Eshaghian-Wilner MM (editor). Bio-Inspired and Nanoscale Integrated Computing. Wiley; 2009
94. Gupta J. Nanotechnology applications in medicine and dentistry. Journal of Investigative and Clinical Dentistry. 2011; 2: 81-88. doi: 10.1111/j.2041-1626.2011.00046.x

Characterization and Application of Nanomaterials 2024, 7(2), 6348.
https://doi.org/10.24294/can.v7i2.6348

Review

Synthesis, technological prospects and applications of MXene in biomedicine, supercapacitors and sensors: A review

Nujud Badawi M.[1,*], M. Bhuyan[2,*], Namrata Agrawal[3], Yogesh Kumar[4]

[1] University of Hafr Al-Batin College of Science, Hafer Al-Batin 39921, Saudi Arabia
[2] Institute of Physics, Sachivalaya marg, Bhubaneswar 751005, India
[3] Department of Physics, Swami Shraddhanand College, University of Delhi, New Delhi 110036, India
[4] Department of Physics, ARSD College, University of Delhi, Delhi 110021, India
*** Corresponding authors:** Nujud Badawi M., nujuds@uhb.edu.sa; M. Bhuyan, bunuphy@um.edu.my

CITATION

Badawi M. N, Bhuyan M, Agrawal N, Kumar Y. Synthesis, technological prospects and applications of MXene in biomedicine, supercapacitors and sensors: A review. Characterization and Application of Nanomaterials. 2024; 7(2): 6348. https://doi.org/10.24294/can.v7i2.6348

ARTICLE INFO

Received: 11 May 2024
Accepted: 27 May 2024
Available online:14 September 2024

Abstract: MXenes are one of the most important classes of materials discussed worldwide by many researchers of diverse fields for diverse applications in recent years. It is a nanomaterial with a wide range of applications due to its multiple forms and structures with fascinating properties, for example, high surface area and porosity, biocompatibility, ease of fictionalizing with various active chemical moieties, benefit of high metallic conductivity, activated metallic hydroxide sites, and sensitivity to moisture. MXenes have great chances for potential applications in environmental issues, water purification, biological applications, and energy storage devices and sensors. MXenes show great selectivity towards the absorption of heavy metals and a good capability to reduce chemical and biological pollutants present in the water. The present review article critically analyzed advancements in water purification using the adsorption and reduction abilities of MXenes and their composites. The mechanism of various procedures, important challenges, and associated problems using MXene and their composites are discussed in detail. The future research directions can be extracted from this article efficiently and comprehensively. The energy storage issues of rechargeable lithium-ion batteries, batteries other than lithium-ion batteries, and electrochemical capacitors are also discussed in detail.

Keywords: 2D materials; MXene; energy storage; batteries; capacitors

1. Introduction

In 2011, a new type of two-dimensional substance called MXene was discovered for the first time. The MXene family sparked intense interest in research across many disciplines due to its diverse chemical composition and excellent physical and chemical properties, particularly in the areas of energy storage, the environment, catalysis, and biomedical applications, the latter of which, in particular, is experiencing rapid growth. Since graphene's exfoliation [1,2], a lot of attention has been paid to other 2D layered materials [3,4] because of their exceptional electrical, mechanical, and optical capabilities. Most studied examples of 2D materials other than graphene include transition metal dichalcogenides [4,5], phosphorene [6,7], and their derivatives. In recent years [6], a family of 2D-layered compounds known as "MXenes" has attracted a great deal of interest from the scientific community due to their unusual structural and electrical properties, which make them applicable to a wide range of fields.

MXenes are compounds produced by the chemical delamination of ternary (or quaternary) layered carbides or nitrides. The unique properties of the MXene family are due to their electrical structures, atomic stacking, synthetic methods, surface terminal groups, and peculiar bonding, which consists of metallic and covalent connections. Despite MXenes rising star power, there is a dearth of comprehensive information on them.

Many sensors [2–4], as well as portable and wearable electronic devices [5–7], have emerged to sense and interact with physical worlds to foster the development of a smarter life with the vigorous rise of the internet of things (IoT) and the great improvement of the reliability of wireless communication protocols [1]. Despite this, a reliable power supply [8–10] requires the successful integration of on-chip energy-storage units with novel electronic devices due to the intermittent nature of renewable resources (wind [11], solar [12], tidal [13], and geothermal energy [14]). Conventional micro-batteries have a high energy density [15] and can keep devices running for a while, but they are unable to meet the requirement of rapid power delivery in applications where battery replacement is impractical [16]. Micro-supercapacitors (MSCs) have gained widespread interest as a micro-battery substitute because of their fascinating long lifetime, high power density, and fast charging rate [17]. However, their progress in microelectronics is hampered by their low power and energy density [18].

With the rapid development of biomedicine and the attractive physiochemical properties of two-dimensional materials, many researchers have focused on the biomedical applications of two-dimensional materials, such as hexagonal boron nitrides (h-BN), graphene and its derivatives, transition metal oxides (TMOs), layered double hydroxides (LDHs), and MXenes. MXenes have more functional groups on their surface, allowing for greater versatility in modification than most other 2D materials. MXenes are useful for biomedical applications due to their hydrophilicity, compositional versatility, and the presence of full metal atomic layers. Another advantage is that MXenes can be mass-produced at low cost. Bioimaging, antimicrobials, biosensors, drug delivery, tissue engineering, and a wide range of therapeutics are just some of the ways MXenes have been put to use in the medical field so far (**Figure 1a**) [19]. Because of their high near-infrared light absorption and conversion efficiency, MXenes have found applications in photothermal therapy for tumour ablation. This form of treatment is highly effective in targeting cancer cells while causing minimal collateral damage to healthy tissue. In addition, bioimaging can be used in real-time to track the tumour's location as contrast chemicals are administered during cancer treatment. In addition, the modified MXenes can also carry anticancer medications and release pharmaceuticals in a specific manner. Photothermal therapy, chemotherapy, and real-time bioimaging monitoring have considerably increased the success rate of cancer treatment thus far. As a bonus, MXenes are proving to be promising raw materials for developing biocompatible tools for easy, rapid detection of biological events [19].

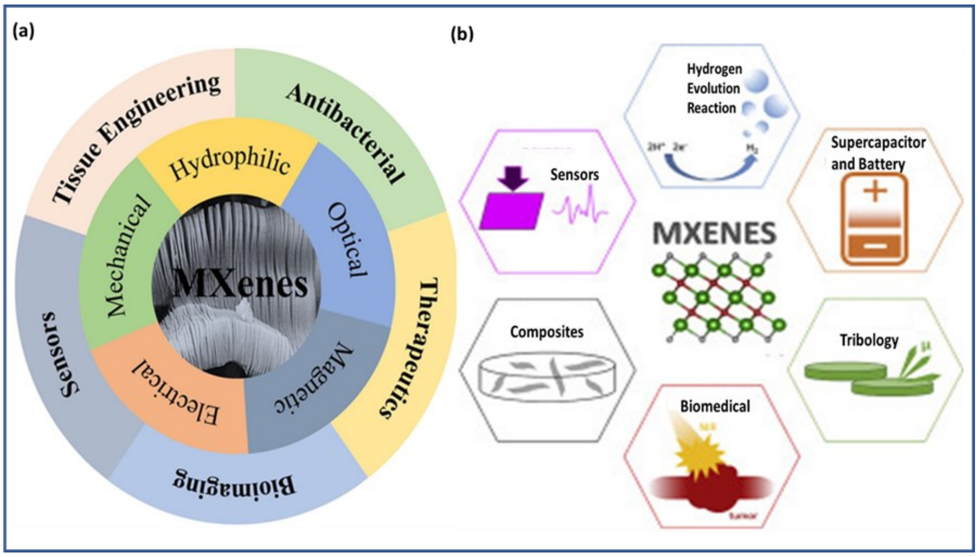

Figure 1. (a) Properties and biomedical applications of MXenes [19]; **(b)** MXenes in a wide range of applications [20].

The purpose of this study was to analyze and remark on the most important basic and technological aspects of MXenes about their structure, electronics, properties, applications, and devices (see **Figure 1b**) [20]. The history of MXenes' creation is presented first, followed by examples of MXene production, structure, and characteristics, surface modification schemes, biomedical applications, cytotoxicity, and biocompatibility. We have examined the key features and properties of MXenes. The present status, trends and future possibilities in various fields, such as energy, electronics, biomedicine, etc., have been critically examined. Finally, current challenges and future potential applications of MXene have been discussed.

2. Logic of MXene

New 2D transition metal carbides, nitrides, and carbonitrides called MXenes (pronounced "machines") were first fabricated by wind [11], solar [12], tidal [13], and geothermal energy [14]. Hydrofluoric acid (HF) was used at room temperature to selectively etch the "A" (Al atoms) in layered hexagonal ternary carbide, Ti_3AlC_2, to produce the first MXene made of 2D titanium carbide (Ti_3C_2). From the precursor MAX phase ($M_{n+1}AX_n$), MXenes can be constructed with the general formula $M_{n+1}X_nT_x$ (n = 1–3), where M is an early transition metal, X is carbon and/or nitrogen, A is an element from groups 12 to 16, T is the surface termination groups like fluorine (–F), oxygen (=O), chlorine (–Cl), and hydroxyl (–OH), and x is the number of surface functionalities [21]. There is a strong M-X bond and a comparatively weak M-A bond in the MAX phase, where an A layer is sandwiched by octahedral $M_{n+1}X_n$ [22]. Elements that produce MAX phases ($M_{n+1}AX_n$) are denoted in bold in **Figure 2** [23]. Depending on the n value in MXenes ($M_{n+1}X_nT_x$), the interlayer spacing can be anywhere from 0.1 to 1.0 nm [8].

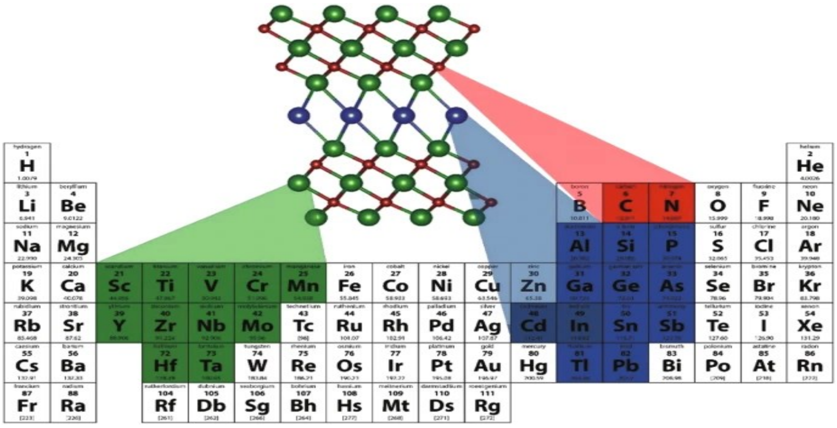

Figure 2. Elements in the periodic table that are known to form $M_{n+1}AX_n$phases. Reprinted with the permission from Ref [23].

3. Synthesis methodologies of MXene: Procedures and structures

About 30 different compositions of MXenes have been described in the literature, all of which have been synthesized from MAX phase precursors, with the addition of two or more transition metals to the M layers as the primary route to do so [20]. In particular, MXenes based on titanium, such as $Ti_3C_2T_x$ and Ti_2CT_x, are widely used for ecological purposes [1,17]. Other MXene structures, such as those including nitride and carbonitride, have also found use outside of the realm of carbides [23]. MXenes' distinct layered structures and 2D morphology make them an ideal candidate for use in composites, which can be utilized to improve the properties of other materials [8]. Preparing a sample for synthesis involves taking a few parameters into account, like safety, cost, procedures, instruments (such as monitors and gauges), and control systems. Etching, exfoliation, and chemical vapour deposition (CVD) are the three most common approaches to MXene production. Etching and exfoliation are examples of top-down processes, while chemical vapour deposition, the template method, and plasma-enhanced pulsed laser deposition are examples of bottom-up techniques.

The most popular method for synthesizing 2D MXenes is the top-down etching of 'A' from MAX phases ($M_{n+1}AX_n$), where M is an early transition metal; A is one of numerous elements (Al, Si, P, S, Ga, Ge, As, Cd, In, Sn, Tl, or Pb); X is C, N or both; and *n* is 1–4. Metallic bonds are typical between *M* and *A*, but covalent, ionic, or metallic bonds can exist between M and X [19]. As a result, it is difficult to break the M-A connection using mechanical shearing or direct exfoliation. Etchants, such as HF, can, however, etch it selectively. Two processes are required in the synthesis of MXenes [20,24] (**Figure 3**) [25]: First, selective etching of the A element from a precursor (MAX phases or other layered ceramics); second, delamination to obtain a single-layer MXene. However, the manufacturing of MXenes for energy storage applications has not been thoroughly addressed using these methods. The processes of MXene manufacturing are explained in greater detail below. Each MXene has a mother MX phase from which it is created, where "M" represents an early transition metal, "A" represents a group 13 or 14 element, "X" represents carbon or nitrogen, and "*n*" ranges from 1 to 3 [21].

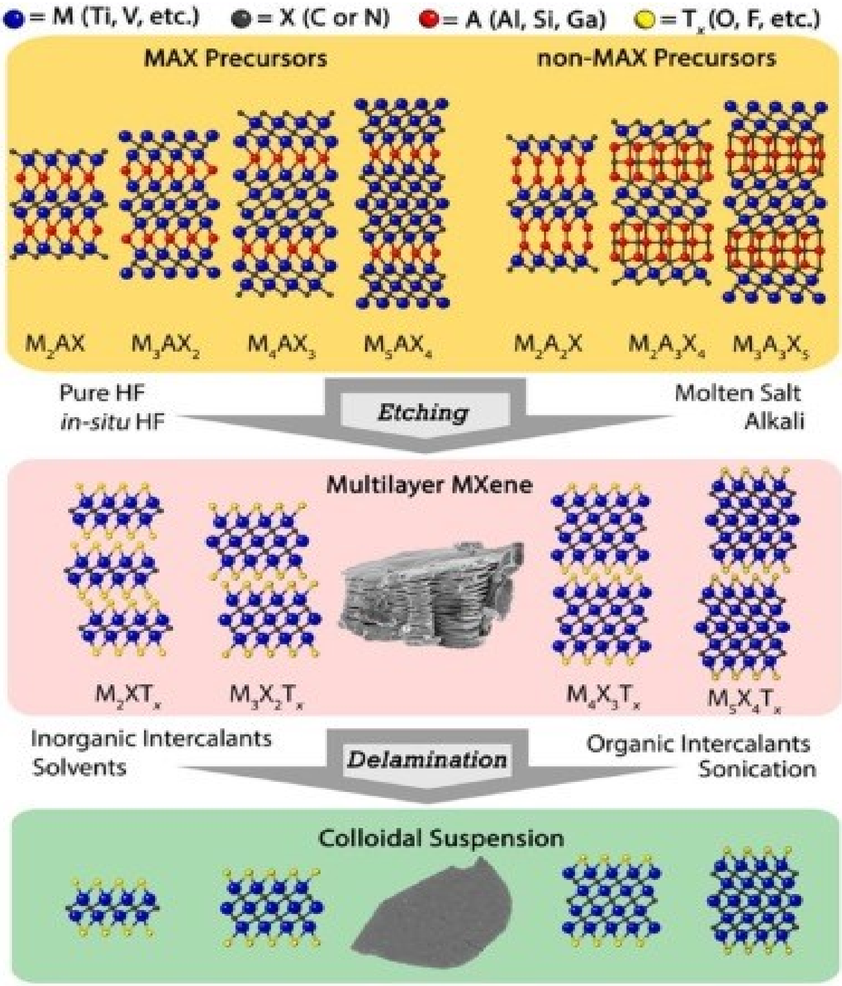

Figure 3. Synthesis of Mxene—selective etching of MAX and non-MAX phases to form multilayered MXenes, followed by delamination (chemical/mechanical) to produce a colloidal suspensionof single-layered MXene [25].

MXenes. In the top-down process, MXenes were synthesized from the bulk by a two-stage procedure: chemical etching and delamination [8,26]. To remove the interleaved layers of ‘A’ atoms from the bulk ceramic, an etchant is utilized to cleave the M-A metallic connection. The aggregated nanosheets are then delaminated via liquid-phase exfoliation [8], tetrapropylammonium hydroxide (TPAOH) intercalation [27,28], or ultrasonication [26]. In **Figure 4a** [29], a schematic depicting the steps involved in creating MXene is given. To prevent the dangers of fluorine-based etchants, fluorine-free techniques are also used [30]. Bottom-up methods often employ CVD technology, which works upwards from the atomic or molecular level [31]. Both top-down synthesis and bottom-up approaches can be used to create

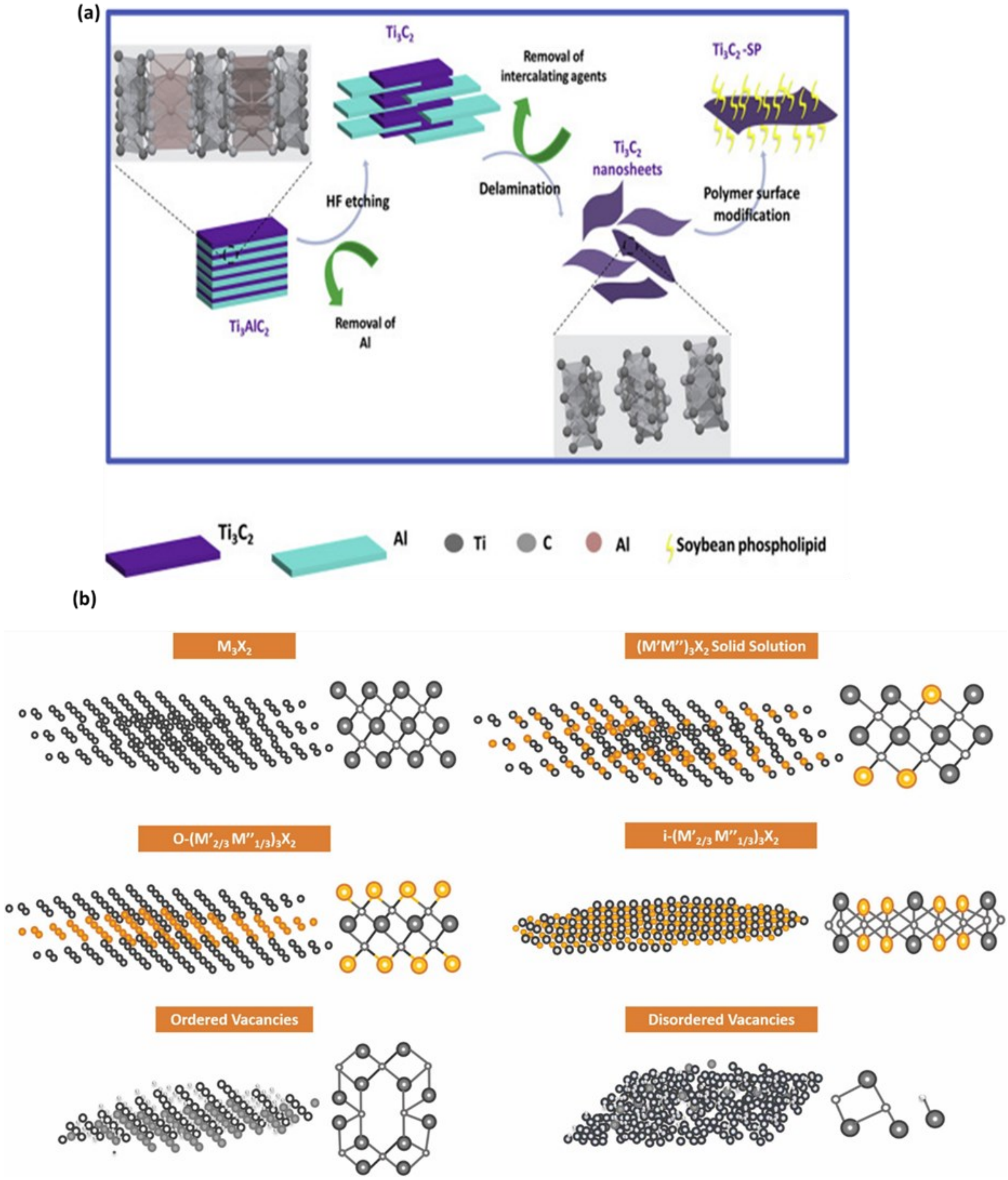

Figure 4. (a) Fabrication of 2D ultrathin Ti_3C_2 nanosheets by etching, delamination, and surface modification along with its crystal structure [29]; **(b)** different structures of MXenes [27].

4. Simulation-based studies on MXene structures

To complement experimental studies and get a more in-depth understanding of MXene structures, computer simulations are frequently used. MXenes typically end with surface groups, including –F, –OH, and –O, following exfoliation from the MAX phase. The usefulness of such structures is determined by the relationships among their features and characteristics [26]. There are three possible configurations of MXenes, all of which correspond to the parent MAX phases and have a single metal in the M site: M_2C, M_3C_2, and M_4C_3, where M is an early transition metal, A is a particular element from groups 13 or 14, X is carbon or nitrogen, and n is a number from one to four. The A element must be carefully removed from a MAX phase or other stacked precursor (such as MO_2Ga_2C). In MAX phases, X atoms fill octahedral sites in an otherwise hexagonally stacked M layer with P63/MMC symmetry. As a result, the A and M elements form metallic bonds. $M_{n+1}X_n$ layers and MXenes containing ordered double-transition metals, like (Cr_2V) C_2 and (MO_2Ti_2) C_3, are interwoven throughout the “A” element [29]. Computer modelling has helped disclose the structures of MXenes and has also aided in the discovery of new, stable MXenes. There are six distinct MXene structures: (1) Nb_4C_3 and Ti_2C are examples of mono-M components; (2) $(Cr, V)_3C_2$ and $(Ti, V)_3C_2$ are examples of solid solutions; (3) ordered out-of-plane two-fold M components have one transition metal (typically Cr and Mo) filling the outer layers and the other the focus layers (Ta and Nb); (4) ordered in-plane two-fold M components have the distinguishing M components arranged in the basal plane, such as in [22,27,29–32]. Structures of different MXenes are shown in **Figure 4b**.

The surface terminations (–F, –OH, and –O) group linked to M atoms give MXene its chemical formula, $M_{n+1}X_nT_z$ (1 n 3). **Figure 5a** [22] depicts the steps required to prepare MXene. A typical schematic diagram is depicted in **Figure 5b** [33], representing the process of synthesizing MXenes from MAX phases.

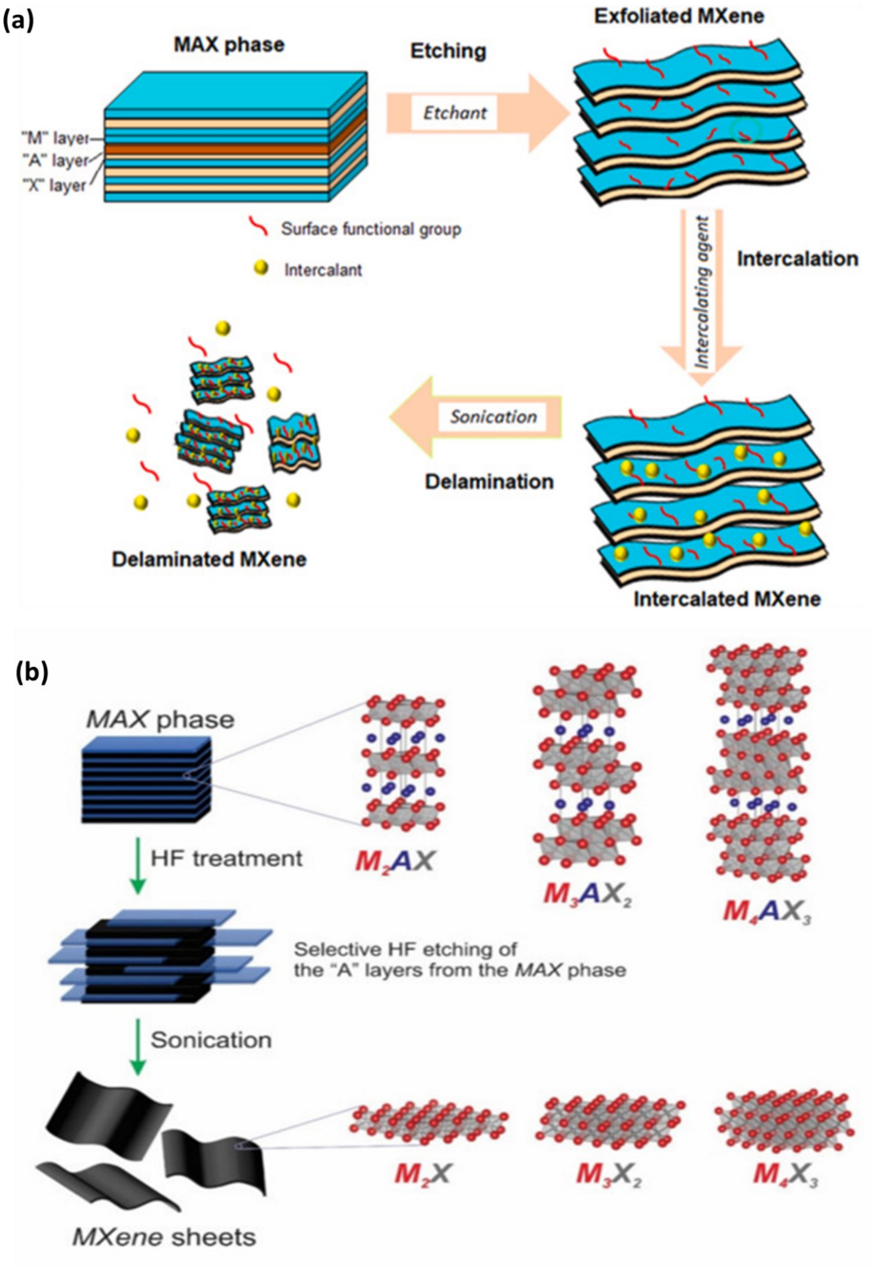

Figure 5. (a) MXenes, derived from the parent layered solids MAX phases [22]; **(b)** the schematic diagram represents the process of synthesizing MXenes from MAX phases. Reproduced with permission from [33].

5. Applications

5.1. Prospects of MXenes in biological applications

The promising results of MXenes in stem cell-based tissue treatments and the material sciences make it reasonable to expect future multi-tasking biomedical therapies to be based on their unique properties [33]. Titanium carbide (Ti_3C_2) MXene nanofibers were used to create smart biomaterials for tissue engineering and cell culture in one study. Fabrication of hydrophilic composite nanofibers via electrospinning and doping was carried out by Chen et al. [34]. The MXene nanofiber composites' surface functional groups were considered to foster healthy cellular environments. Bone marrow-derived mesenchymal stem cells (BMSCs) were used to analyse the biochemically representative characteristics, and the resulting MXene composite nanofibers showed good biocompatibility and significantly improved cellular activity, as well as boosting BMSC differentiation to osteoblasts.

Smart biomaterials, which have many desirable biological characteristics, are very useful in tissue engineering and repair procedures [35]. Because of their immunomodulatory properties, which selectively reduced the activation of human CD4+IFN-+ T-lymphocytes while stimulating the expansion of immunosuppressive CD_4+CD_{25}+$FoxP_3$+regulatory T-cells in a stimulated lymphocyte population, two-dimensional structures with BMSC biocompatibility could stimulate fibroblasts derived from bone marrow-derived stem cells (BMSCs) for post-injury tissue repair. [35,36]. The incorporation of Ti_3C_2MXene QDs (quantum dots (MQDs) sensor) into a chitosan hydrogel resulted in the creation of a 3D platform with enhanced physicochemical characteristics, which can facilitate stem cell trafficking and tissue restoration. The resultant composite hydrogel was both injectable and thermos-sensitive, and it showed excellent conductivity [37]. In a similar line, biocompatible Ti_3C_2Tz-enhanced poly (lactic acid) nanocomposite membranes were created by mediating the interface between the hydrophobic poly (lactic acid) matrix and the Ti_3C_2Tz nanosheets. These membranes achieved an optimized tensile strength of 72 MPa, which is approximately 33% greater than a pure poly (lactic acid) membrane [37,38]. Therefore, Ti_3C_2Tz insertion into the membrane might improve its biological characteristics, including osteogenic differentiation, proliferation, and in vitro adhesion of MC3T3-E1 murine preosteoblasts.

MXenes' exceptional properties, which include hydrophilicity, high electronic conductivity, and adsorptive, reductive, and antibacterial properties, make them well-suited for a wide range of ecological uses. The adaptability of MXenes makes them desirable for a wide range of uses. Their chemical stability, ion intercalation, and adjustable bang gaps suggest catalysis and energy storage applications like fuel cells, hydrogen storage, and lithium-ion batteries (LIBs), while their high Young's modulus, good electrical conductivity, and surface chemistry alteration are appealing for the creation of composites.

5.2. MXenes for environmental and water treatment applications

5.2.1. H_2O_2 oxidation activated by MXene-based materials

Hydrogen peroxide (H_2O_2) oxidation has attracted much attention in the removal of pollutants [36], where Fe^{2+} can act as a catalyst to form free radicals [36,39]. 2D MXene has a layered structure and surface electronegativity. Metal particles can be loaded onto the surface and layered surfaces of 2D MXene [24,40]. In addition, 2D MXene can also degrade metal nanoparticles and inhibit the aggregation of metal nanoparticles [41]. Interestingly, metal particle-loaded 2D MXene has a larger surface area and better pore structure than pure 2D MXene. The pores in the composite can serve as microreactors for H_2O_2 activation. Magnetic nanoscale zero-valent iron particles (nZVI)@Ti_3C_2 nanosheets could remove 91.1% of ranitidine in 30 min [42]. Therefore, 2D MXene-supported metal particles can be considered a good catalyst to activate H_2O_2 to degrade organic pollutants.

Wu et al. [43] developed a nanoplatform based on multimodal TMO connecting ultrathin Ti_3C_2 nanosheets to self-assembled $MnFe_2O_4$ nanoparticles using chitosan as a chemical cross-linking agent to form an interfacial Schottky junction, Ti_3C_2@Chitosan-$MnFe_2O_4$(TC@Ch-MFO). This led to an improvement in reactive oxygen species (ROS) production and optimization of biocompatibility. This heterojunction could control the catalysis of H_2O_2 to produce O_2 and deplete excess glutathione levels in the hypoxic tumor microenvironment, so that under near-infrared stimulation, the cyclization was completed by the Fenton reaction. TC@ChMFO also provided a multifunctional nanoplatform for photothermal therapy by introducing an effective photothermal agent, Ti_3C_2. Additionally, it integrated visualization with T1- and T2-weighted magnetic resonance imaging simultaneously (see **Figure 6a**) [43]. As the toxicity of TC@ChMFO to normal tissues is negligible, this platform might provide new insights into the development of multimodal synergistic nanoplatforms for biological applications.

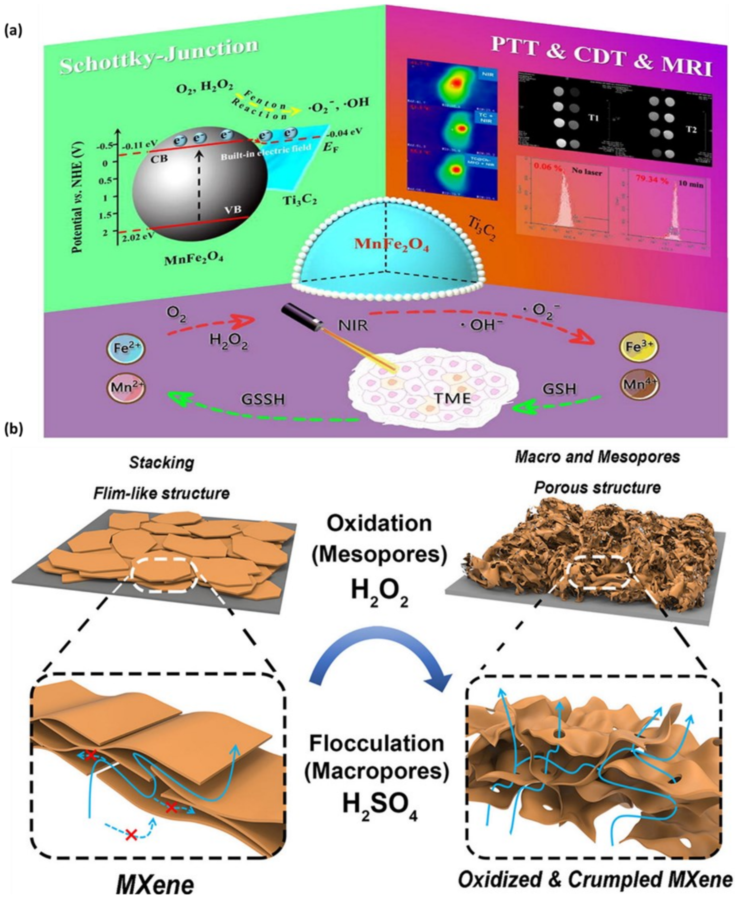

Figure 6. (a) MXene-based Schottky junctions self-assembled transition metal oxides for near-infrared radiation to modify the tumor microenvironment and enhance CDT/PTT/MRI activation [43]; **(b)** oxidized MXene co-wrinkled multi scale porous structure [44].

Lee et al. [44] proposed a new method to produce MXene oxidative wrinkled multiscale porous structures through a sequential process involving partial oxidation with H_2O_2 as agglomeration in acid (see **Figure 6b**). These processes lead to the simultaneous formation of mesopores caused by oxidation and macropores due to shrinkage patterns. The specific surface area of oxidatively co-degraded MXene (72 m^2/g) was found to be five times that of pure MXene. The efficiency of the performance (307 F/g at 20 mV/s in 1 M H_2SO_4) and the capacity of the scan (225 F/g at 100 mV/s) were also found to be better than in pure MXene. Additionally, 87.6% of capacity was retained after 6000 cycles. This was due to the structure of porous, oxidized, folded MXene. Here, the diffusion of ions through mesopores was promoted, while folded macropores prevented restacking.

The performance and mechanism of Ti_3C_2 MXene-modified Fe^{3+}/hydrogen peroxide system in dark light and visible light were compared in detail, and a new standard for coating Fe^{3+} reactions and reductions of MXene was proposed by Xu et al. [45]. Taking Bisphenol A (BPA) as the target pollutant, the degradation effect of BPA in the Fe^{3+}/H_2O_2 system was improved after adding MXene in the dark. The degradation of BPA in 12.5 min under visible light was ≥95%, which was 6 times higher than in the dark. Fe^{2+} was identified as a useful element for the activation of H_2O_2 to form OH. It was found that MXene formed a complex with Fe^{3+}. MXene reacted with Fe^{3+}, breaking the TiC bond and activating the Fe^{3+}/Fe^{2+} cycle. MXene used photogenerated electrons to promote chemical reactions under light. OH and O_2 were found to be the main reactive oxygen species in light, while OH was the main reactive oxygen species in light (see **Figure 7a**). Thus, MXene could utilize O_2 to produce O_2 and promote the Fe^{3+}/Fe^{2+} cycle in light. This work provided a theoretical basis for the combination of visible light catalysis and the higher oxidation process of Ti_3C_2 MXene.

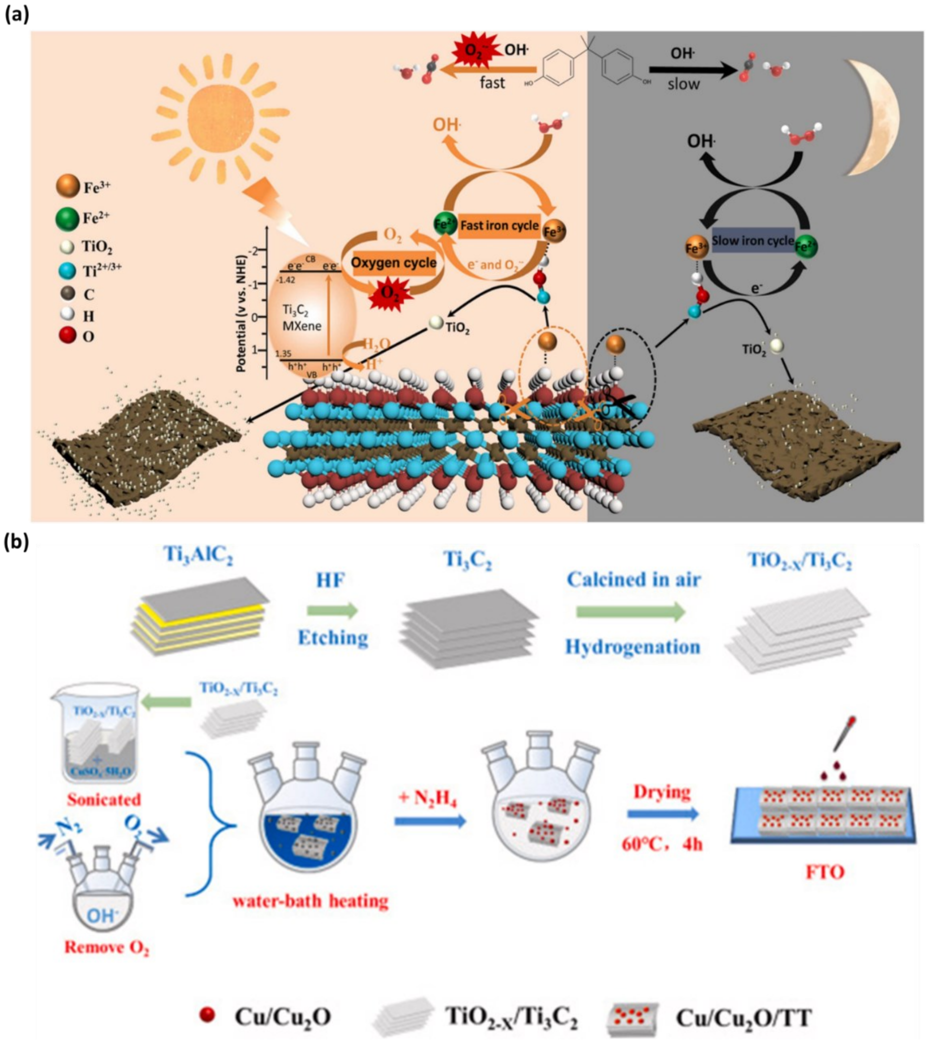

Figure 7. (a) Ti_3C_2 MXene promotes Fe^{3+}/H_2O_2 Fenton oxidation: comparison of the process under dark light and visible light [45]; **(b)** the fabrication process of the $Cu/Cu_2O/TiO_{2-X}$ electrode [46].

To detect H_2O_2, Li et al. [46] used in-situ produced TiO_{2-X} nanoparticles to modify Cu/Cu_2O nanoparticles on Ti_3C_2 MXene to form heterojunctions via a single-step hydrothermal process. The produced $Cu/Cu_2O/TiO_{2-X}/Ti_3C_2$(Cu/Cu2O/TT) was found to have a linear range of 28.328 mM, a sensitivity of 312 μA mM^{-1} cm^{-2} and detection limit of 0.42 μM. The synergistic effect of Cu/Cu_2O nanoparticles and TiO_{2-X}/Ti_3C_2 heterojunction not only improved the electron transfer and electrocatalytic activity but also increased the strength of the target molecules of the catalyst due to the abundance of extended catalytic sites. Therefore, compared to TiO_2X/Ti_3C_2, the detection limit of Cu/Cu_2O/TT was low, its reaction faster, and its sensitivity five times higher. Also, Cu/Cu_2O/TT exhibited excellent photoelectrochemical sensing performance in detecting H_2O_2 with a low detection limit, long-term stability, repeatability, and selectivity. The fabrication process of the Cu/Cu_2O/TT electrode followed by Li et al. [46] is shown in **Figure 7b**.

Iron particles deposited on the 2D MXene surface may exhibit multiple reaction zones. 2D MXene can facilitate the electrical transfer of magnetic materials. In addition, there are many hydrophilic functional groups (such as OH, COOH, and

CHO) on the surface of MXene/nanoscale zero-valent iron particle nanosheets, designed to promote H_2O_2 activation [43]. Zhu et al. [47] used $Ti_3C_2T_X$ to develop a sensitive and enzyme-free electrochemical sensing interface to detect H_2O_2 simply and practically. Prussian blue (PB) was electrochemically deposited on the surface of the glassy carbon electrode (GCE). Chitosan (CS) and MXene were degraded on the PB modified GCE surface. Simple MX/CS/PB/GCE detection interface demonstrated good electrochemical detection performance and good selection for H_2O_2 with a low limit (4 nM) and a wide linear range from 50 nM to 667 μM.

The light-driven magnetic MXene microrobot (MXeBOT) was developed as a moveable stage for the removal and degradation of bisphenol A (BPA) by Dekanovsky et al. [48]. A second control motor composed of embedded Fe_2O_3 nanoparticles (NPs) for magnetic push assisted the MXeBOT. Grafted bismuth nanoparticles acted as co-catalysts. It was investigated how BPA concentration and the chemical composition of the swimming environment affected the stability and reusability of MXeBOTs. MAXBOT could remove/degrade approximately 60% of BPA in just 10 minutes and approximately 100% in 1 hour. More than 86% of BPA mineralized within 1 h. Using Bi/Fe/MXeBOTs for the photocatalytic degradation of BPA demonstrated a significant advantage in converting BPA into CO_2 and H_2O [49].

5.2.2. Other advanced water remediation applications of MXenes

MXene and its compounds have also proven effective in other environmental applications such as membranes, capacitive deionization, and anti-bacterial agents. MXene is a promising product for water filtration due to its hydrophilicity, high surface area, and excellent electrical properties [48]. Molecules can be separated based on the size of the surface layer and the interaction with the MXene layer. In recent years, MXenes have been used in a variety of environmental applications for the treatment of contaminated groundwater and municipal wastewater, including desalination, outperforming the most widely used material in all regions [50]. MXene composites can adsorb a variety of organic and inorganic compounds and can undergo Faradaic capacitive deionization (CDI) when used in electrochemical applications. This method overcomes the concentration polarization limit of conventional CDI electrodes, greatly reducing the energy required and providing a solution for low-energy desalination of brackish water. Researchers provide an updated review of MXene and MXene mixtures for water purification and desalination applications. Kinetics and isotherms were examined, and the effects of water composition and activity discussed. Based on the literature review, the application of MXene in CDI, pervaporation desalination, and photothermal desalination have been studied. The impact of water composition and performance on recovery efficiency and long-term use has also been highlighted (see **Figure 8a**) [51].

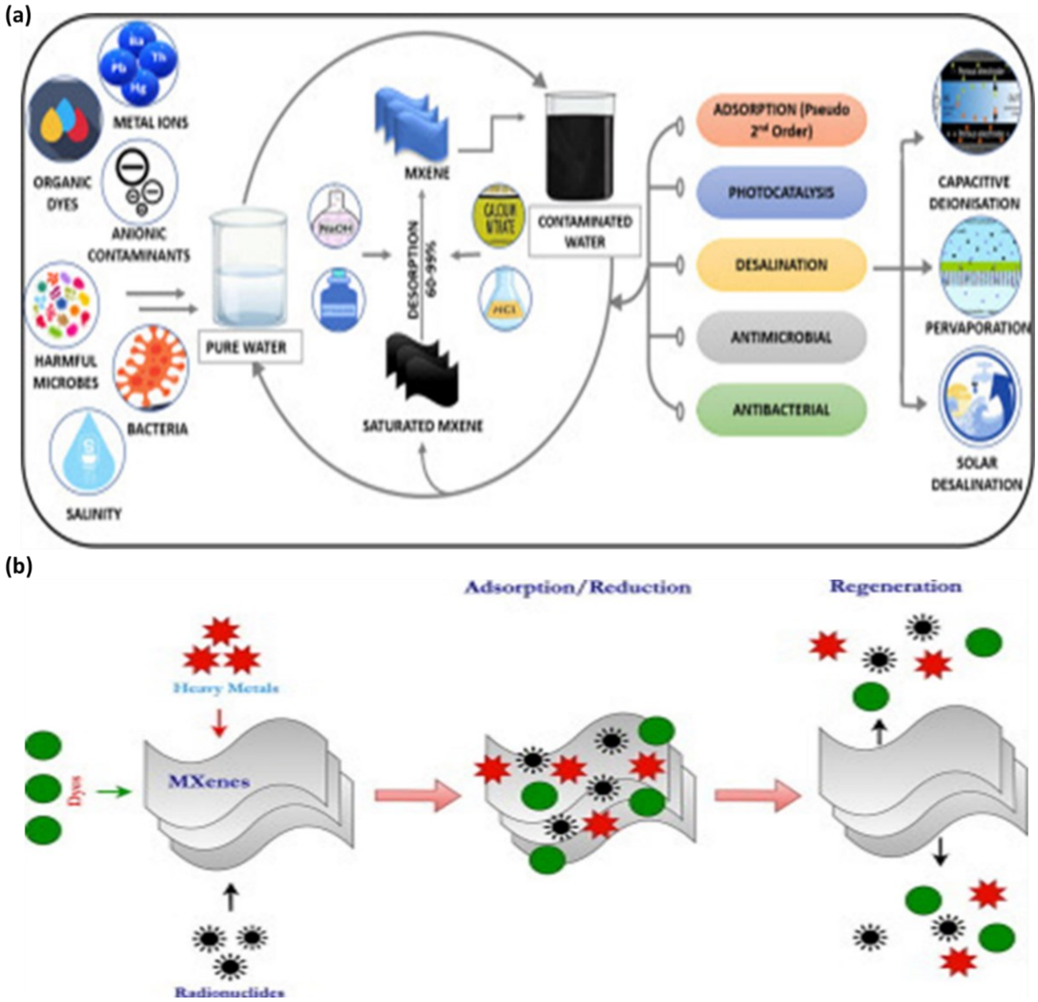

Figure 8. (a) Use of MXenes in water purification and energy-saving desalination [51]; **(b)** MXenes (2D metal carbides) as nanomaterials for water purification [49].

There is an interest in using MXene and its derivatives in water purification due to their unique properties. MXene has high electrical conductivity and hydrophilicity, as well as outstanding adsorption, reduction, and disinfection properties. In particular, $Ti_3C_2T_X$ and its compounds are widely used in water purification to remove various contaminants such as dyes, radionuclides, and heavy metals. Ihsanullah [49] evaluated the effectiveness of MXene and MXene-based mixtures in removing various pollutants from water, focusing on heavy metals, dyes, and radionuclides. The role of the MXene structure in the contaminant elimination process and the regeneration were reviewed and analyzed (see **Figure 8b**). The properties of MXene, such as high electricity, hydrophilicity, and catalytic activity, have attracted increasing research attention in environmental remediation and water purification applications [50]. Reports are available on recent advances in the synthesis and use of MXenes as adsorbents, desalination membranes, electrochemical deionization electrodes, and catalysts or antimicrobial agents for water purification and other environmental treatment. The challenges and opportunities have also been highlighted for advanced 2D materials by discussing experimental efforts to investigate MXenes for water use, biocompatibility, and environmental impact. Due to their unique mechanical, chemical, and electrical properties, many successful experiments have been carried out on the use of MXenes in water purification and environmental remediation applications. However, more efforts are needed to solve the stability, biocompatibility, and reusability issues of MXenes in aqueous environments. MXenes are reported to be used for pollutant adsorption/remediation, photodegradation, membrane separation, etc.

The increase in pollutants such as air pollution, organic dyes, chemicals, and pesticides released into the water due to population and the global economy has become the most important health problem in the world [51]. Magnetic MXene nanocomposites have many attractive and successful applications due to their unique properties, ease of production, cost-effective preparation, and excellent capability to degrade water and wastewater pollutants. These compounds offer exciting new opportunities for many applications, such as biosensors, cancer therapy, measurement systems, and especially water purification. Researchers are studying magnetic MXene nanocomposites to remove contaminants from ambient water. The use of magnetic nanomaterials for water treatment, the applications and implications of MXene in degrading water and wastewater pollutants, and the role of magnetic-MXene nanocomposites in water treatment have been studied and discussed (**Figure 9a**) [52].

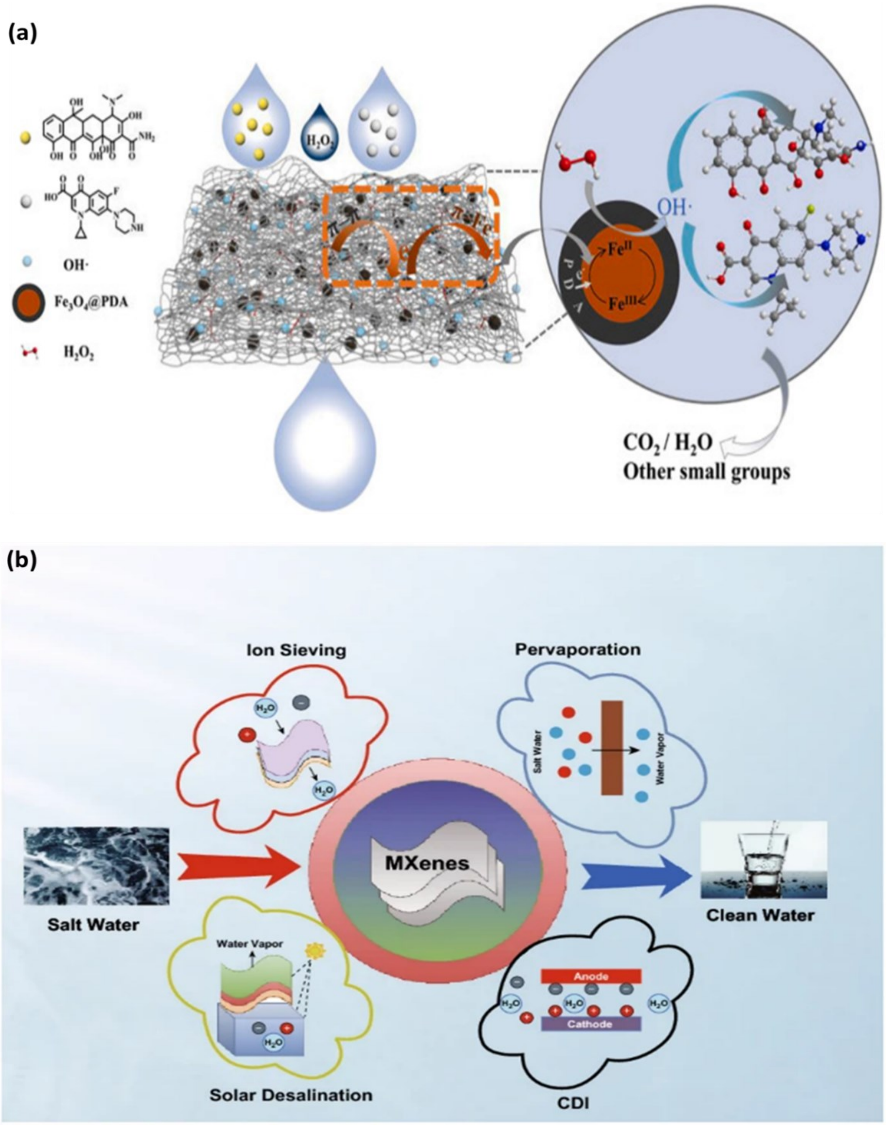

Figure 9. (a) Magnetic-MXene-based nanocomposites for water and wastewater treatment [52]; **(b)** advanced applications of Mxenes in CDI, solar desalination, ion sieving and pervaporation [53].

The advantages of MXene, such as high surface area, high metal conductivity, easy functionalization, biocompatibility, active metal hydroxide surface, and hydrophilicity, make it a good candidate for energy storage, catalysis, sensors, electronics, and environmental application. Due to their good physical and chemical properties and wide range of chemical properties, MXenes have attracted attention in water purification and desalination applications in recent years. Ihsanullah studied the advances in the synthesis of MXenes and MXene-based compounds for seawater desalination. The desalination potential of MXenes was described in detail, focusing on ion screen membranes, capacitive deionization, and solar desalination. The ion removal process and the recycling potential of MXene were also documented to provide insight into the process [53].

MXene has also emerged as a strong candidate for oil/water separation and photocatalytic environmental remediation applications (see **Figure 9b**) [53]. The ability to reduce organic molecules and some cations is a unique property that makes

MXene the best choice for future water purification applications [12]. Due to its hydrophilicity, high conductivity, high adsorption capacity for anions and cations, and tunable surface, MXene can also be used as a new electrode material for CDI applications [54]. The solar and evaporative desalination properties of MXene have also been investigated in various studies [55]. The rapid development of the economy causes serious water pollution and poses a threat to the environment. Currently, heterogeneous Fenton oxidation has attracted widespread attention due to its high efficiency and simple operation. Hydrogen peroxide and persulfate are two oxidants used in Fenton-like processes.

5.3. MXene-based battery

Significant efforts have been devoted to the development of electronic devices with excellent electrical properties and high energy density for energy storage and conversion. 2D materials show great potential in energy storage due to their unique properties. MXenes have excellent properties when used as electrodes for lithium-based batteries. Tang et al. have discussed the developments in MXene and MXene-based composites in terms of synthesis strategies, morphology engineering, physical/chemical attributes, and their use in lithium-ion batteries and lithium-sulfur batteries [56].

5.3.1. MXeneforlithiumbatteries

Lithium batteries are one of the most common types of batteries because they are the engines of modern electronic devices. Lithium batteries are currently used in mobile phones, computers, small cars, airplanes, and home appliances. Lithium’s high electropositivity and flexibility make it better than hydrogen [57]. Lithium-based cathodes have problems such as short life, low charge, toxicity, unstable electrolyte, high cost, high self-discharge, and poor specific energy. Anodes made of materials such as graphite, lithium, soft carbon, and tin have problems such as dendrites, low energy density, cracking/dissolution, and voltage fluctuations [58]. Therefore, it is necessary and urgent to produce good electrodes for these batteries. MXene is considered an effective material due to its large surface area, electrical conductivity, tunable thermal conductivity, and chemical stability. Rechargeable lithium-ion batteries (LIBs) have provided much-needed applications in electric vehicles and consumer electronics due to their high energy density and reduced storage capacity. In particular, research on LIBs focuses on their applications in small electronic devices by increasing energy density and reducing the footprint during fast charging [56]. MXene can not only produce lithium-ion batteries but also can produce lighter fuel than lithium ion.

Deng tested MXene as a LIB anode material and found it good due to its high specific surface area, weak interlayer strength, open structure, and surface functional groups [59]. Since MXene consists of functional groups M (when the substituted metal is), X (C and/or N), and T (functional groups O, OH, and F), it is possible to use many substituents for the treatment. goods. For example, the specific potential of different MXenes follows the order Ti_2C < Nb_2C < V_2C, with both Nb_2C and V_2C exhibiting higher activity [1]. In addition, the difference between different MXenes is also different. This shows the difference between MXenes for anodes or cathodes.

Additionally, work groups often have different characteristics; for example, bare MXene is magnetic, while active MXene is a semiconductor material. They may also interfere with lithium absorption and transport [54]. Nonnatural functional groups (e.g., chlorine) may be beneficial to MXene by hardening the surface and reducing the interaction of natural OH and F functional groups [55]. Even if the “M” stoichiometry is the same type and prepared by the manufacturing process, the capacity of the lithium-ion battery will be directly affected due to the difference in surface properties. Generally speaking, Ti2CTx has a higher surface energy than Ti3C2TX, which tends to reduce the lattice parameter k and thus inhibit the addition of lithium ions [59].

Lithium-ion MXene/metal electrodes:

The electrode material must have excellent electrical conductivity and be able to withstand high temperatures without cracking or breaking. Nowadays, metal electrodes such as titanium, aluminum, magnesium, copper, silver, zinc, and platinum face many problems. Corrosion, cracking, and low energy density are associated with intrinsic metallic electrodes. Due to the excellent properties of MXene, some researchers have mixed metal electrodes with MXene to improve its electrochemical behavior.

Mxene has a significant problem that affects its performance, such as the aggregation problem of MXene flakes [60]. A simple and effective way to solve this problem is to provide MXene hybrid composites produced with suitable materials such as silicon, tin, different nanocarbon fillers, metal oxides, phosphorus, metal sulfides, and double-layer oxides. The MXene surface is modified in many aspects, including decoration with silicon- and tin-based nanoparticles, bonding the network with carbon nanofillers, and creating heterostructures between graphene and MXene layers. These hybrid materials have high ion energy, high lithium-ion emissivity, and conductivity, in addition to extraordinary capacity. According to the current situation, lithium-ion battery electrode materials should help in improving the electrical properties of batteries, making them more efficient than before. MXene-based hybrid nanostructured materials provide insight into future challenges and guide in finding new materials to be used in future energy applications.

Since the discovery and development of graphene [60], 2D materials and the study of their properties have attracted widespread attention in materials science [34]. In recent years, 2D transition metal carbides, nitrides, and carbonitrides (MXenes for short) have been rapidly developed since the discovery of Ti_3C_2 in 2011 [35]. MXene is prepared by selectively etching individual atomic layers (called MAX phases) in a precursor layer [60].

The general structure of the MAX phase is $M_{n+1}AX_n$ (n = 1, 2, 3), where M represents the early transition metal (M = Ti, Sr, V, Cr, Ta, Nb, Zr, Mo, or Hf), and A represents group sp elements (IIIA or IVA only), X represents C or N, and both [39,61]. The MAX phase can be said to be a symbiotic structure in which tightly packed planar atom layers and hexagonal MX layers are stacked alternately. **Figure 10** shows the classical configuration of the MAX system (using Ti_2AlC as an example) [62]. In this structure, MX bonds are mostly ionic/covalent bonds, and all MA bonds are metal bonds [38]. Therefore, the MX bond is stronger than the MA bond and enables the removal of the A layer from the lamellar layer. However, unlike the weak van der Waals interlayer interactions between graphite and transition metal dichalcogenides, the MA bond is very strong, resulting in detachment of the MX layer from the MAX strength; this is not easily achieved by direct cleavage or ultrasonication techniques. Due to the different properties and strengths of M-X and MA bonds, it is possible to select the appropriate chemical in the process. This leaves a stable chemical structure of the volume near $M_{n+1}X_nT_x$ (T, F, OH, O, etc.), representing the functional group on the surface, near MXene (**Figure 10a**) [62]. The interactions between MXene layers are mainly hydrogen bonds and van der Waals bonds. Water, cations, DMSO, TBAOH, etc. are added to different parts of MXene. After sonication, the MXene layer becomes a suspension.

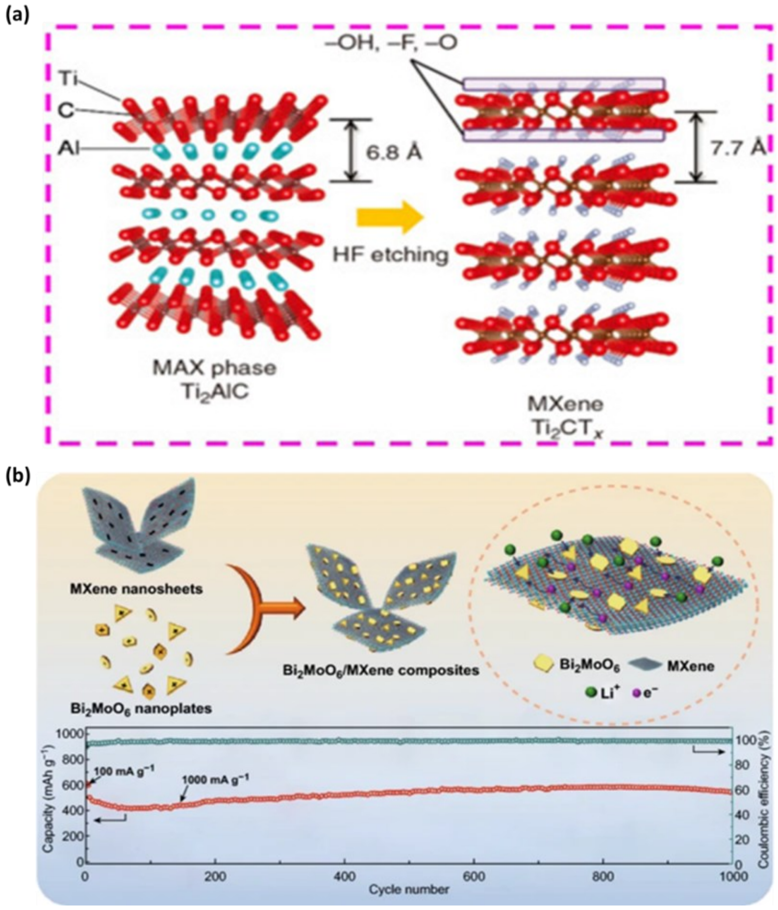

Figure 10. Schematic illustration for the formation of Ti_2CTx MXene from Ti_2AlC phase. **(a)** Reproduced with permission [61]; **(b)** plate-to-layer Bi_2MoO_6/MXene-heterostructured anode for lithium-ion batteries [62].

Due to the low electrical conductivity of Bi_2MoO_6 and the large volume expansion/contraction during charging and discharging, appropriate modification is essential to solve these problems. To overcome the issues, Zhang et al. [62] prepared the plate-to-layer Bi_2MoO_6/Ti_3C_2Tx (MXene) heterostructure by electrostatically assembling positively charged Bi_2MoO_6 nanosheets onto negatively charged MXene nanosheets. MXene nanosheets in heterostructure provided a highly conductive substrate to support and anchor Bi_2MoO_6 nanosheets, thereby increasing electrical conductivity and structure stability (see **Figure 10b**). When the mass fraction of

MXene was optimized to 30%, the Bi_2MoO_6/MXene heterostructure exhibited a specific capacity of 692 mAh g^{-1} at 100 mA g^{-1} after 200 cycles. A 99.6% Coulomb efficiency was achieved with 545.1 $mAhg^{-1}$ at 1 Ag^{-1} after 1000 cycles. The research resulted not only in providing high-performance lithium materials but also presented an idea to create heterostructures by modifying various metal oxides of MXene nanosheets and using them as lithium-ion batteries [62]. Zou et al. [63] synthesized a MXene/Ag composite product ($Ti_3C_2(OH)_{0.8}F_{1.2}$) by directly reducing $AgNO_3$ aqueous solution in the presence of MXene. The results demonstrated that the reduction of Ag in MXene solutions was associated with the presence of low-valence Ti. The recovery capacity at 1 ℃ was 310 $mAhg^{-1}$, at 10 ℃ it was 260 $mAhg^{-1}$ and the recovery capacity at 50 ℃ was 150 $mAhg^{-1}$. Moreover, the composite could withstand more than 5000 cycles at 1 to 50 ℃ without decay (see **Figure 11a**).

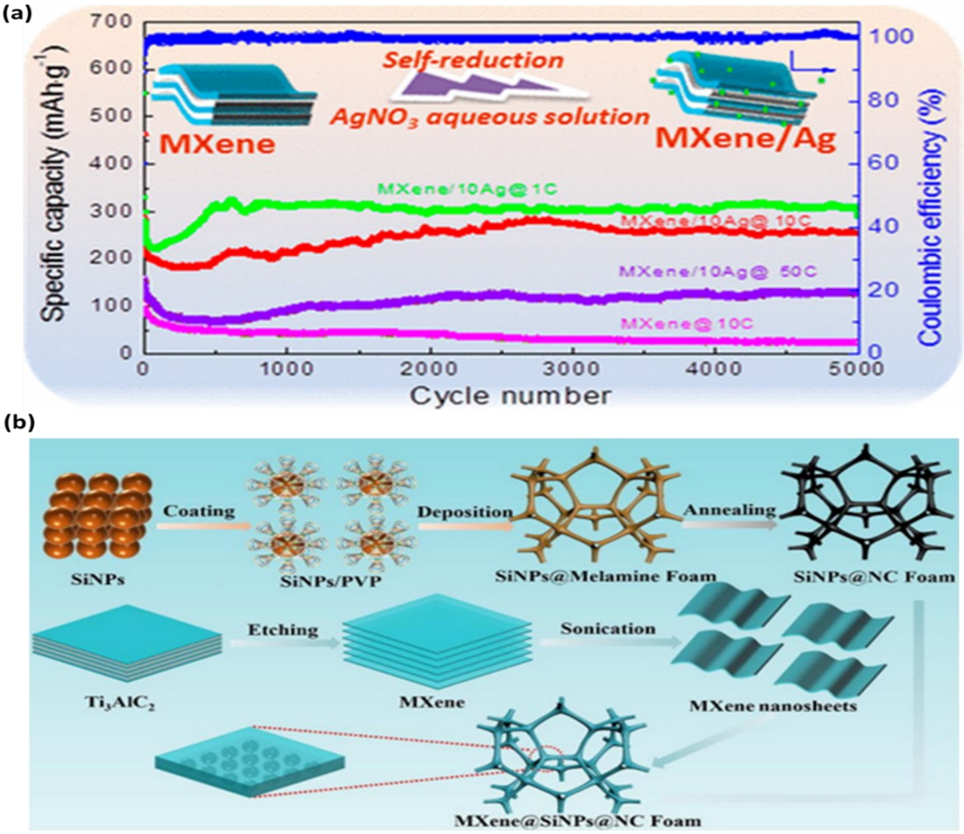

Figure 11. (a) Synthesis of MXene/Ag composites for high-speed lithium storage with ultra-long cycle life [63]; **(b)** schematic diagram of the preparation process of MXene@SiNPs@NC foam composites [64].

Metal-based anode materials such as Sb, Sn, and Bi have received great attention in battery applications due to their high electrical conductivity and high energy density. However, the large volume expansion during the alloying process makes the work very fast. Tian et al. synthesized Sb, Sn, and Bi on MXene sheets via a simple one-step electrodeposition process in a green ethylene glycol system. A strong, flexible, self-contained, and binder-free anode for potassium-ion batteries was prepared. The coating ensured a short diffusion for potassium ions and provided a buffer for the volume change during potassiumization/depotassiumization.

Efficient and flexible MXene materials could then be used as current generators, providing wide electrical paths to facilitate the transport of electricity while cycling and adapting to changing volumes. MXene@Sb resulted in a high reversible capacity of 516.8 $mAhg^{-1}$, a peak value of 270 $mAhg^{-1}$ at 500 $mA\ g^{-1}$, with the fading of only 0.042% per cycle [64].

Lithium-ion MXene/silicon electrode.

Organo-silicon electrodes are one of the best energy storage electrodes due to their unique capacity, non-toxicity, and raw materials. However, silicon expands in volume during cycling, resulting in poor electrochemical cycling performance [65]. The volume expansion that occurs during lithiation/delithiation is the cause of cracking and breakage in the electrode. The combination of silicon and MXene can be used to produce excellent electrochemical electrodes for lithium-ion batteries. The improved cycling performance of silicon/MXene electrodes can be attributed to the excellent thermal stability of MXene. Titanium-based MXene ($Ti_3C_2T_X$) nanosheets have become useful materials for low-voltage electronics (Si) due to their unique charge (lithium) storage capacity and rich abundance of silicon (Si). Si/$Ti_3C_2T_X$ composite material has been shown to have a wide and stable cycle time, good performance, and high economic value. To better understand and improve the electrochemical performance of composites, a review by Jiang et al. focused on the electrochemical processes occurring in Si/MXene composites [65]. Silicon (Si) is one of the most promising materials for lithium-ion batteries (LIB) due to its unique properties. However, low transmission efficiency and large voltage fluctuations block the development of silicon-based anodes. Zhang et al. [66] created a 3D structure containing silicon nanoparticles (SiNPs) anchored on nitrogen-doped carbon (NC) foam and coated with an MXene layer (MXene@SiNPs@NC foam) (see **Figure 11b**), which could act as a self-standing Si-based anode for high-performance LIBs. The design of the NC foam was based on the conductivity principle, and the MXene-based layer provided the advantage of electrons/ion diffusion while allowing the anode to adapt to large changes in Si volume during lithiation/desalination. The independent MXene@SiNPs@NC foam electrode had a capacity (1658 $mAhg^{-1}$ after 100 cycles at 0.1 ℃) and a residual capacity (857 $mAhg^{-1}$ after 500 cycles at 0.5 ℃). Moreover, the battery developed entirely using MXene@SiNPs@NC foam //NCM111 exhibited a high gravimetric energy density (433 Wh kg^{-1}). This MXene@SiNPs@NC foam anode demonstrated good electrical properties.

Silicon (Si) is considered one of the candidates that can replace graphite in anodes. Lithium-ion batteries store greater energy and, therefore, improve returns. However, the high mechanical stress caused by its high volumetric variation during charge and discharge cycles, added to its low electrical conductivity, has impeded its wide use. For this reason, silicon-based composites are studied to find out their commercial viability. MXene Ti_3C_2 is a two-dimensional material whose good mechanical resistance and conductivity can contribute to solving the problems of Si anodes. The results revealed that the addition of Ti_3C_2 particles to electrodes could reach 80% and 89% of their theoretical capacity when Ti_3C_2 represents 20% and 40% of the mass of the active electrode material, respectively, compared to the 56% achieved by the pure Si electrode. This improvement is explained by a reduction in the resistance to charge transfer observed in the EIS results. Finally, the electrode with 20% by weight of Ti_3C_2 (640 $mAhg^{-1}$) obtained the best specific capacity after 100 charge and discharge cycles than obtained by the pure Si electrode (572 $mAhg^{-1}$) [67].

Flexible pressure sensors are one of the most important sensors in electronic skin (e-skin), robotics, and medicine. However, sensors are still complex and expensive due to power consumption, unreliable operation, and manufacturing processes. $Ti_3C_2T_X$ is the most studied MXene in the field of pressure sensing, with good mechanical and electrical properties, excellent hydrophilicity, and flexibility. It increases the sensitivity of pressure sensors and the efficiency of the electrode process and continues to use pressure measurements in various areas, such as electrical skin elasticity. The MXene can be used in pressure sensors, which include piezoresistive, capacitive, piezoelectric, triboelectric, and potentiometric switching technologies. Integration of various devices is also possible [68].

5.3.2. MXene promoting beyond lithium battery

The lithium-based battery is undoubtedly the most studied and analyzed battery in scientific literature. However, lithium is not abundant in the earth's crust and will soon suffer the same fate as the overconsumption of fossil fuels, forcing us to look beyond lithium. Fortunately, research on other metal-ion batteries (sodium, potassium, aluminum, magnesium, zinc, etc.) has rapidly increased, and much has been borrowed from research on lithium-ion batteries. Although their theoretical capacity is lower than that of lithium [69], they can reduce the cost of lithium resources by serving as another energy store. The lithium-ion battery has been a leader in the electronics industry and research and development for nearly two decades. Due to concerns about the cost and future availability of lithium, sodium-ion batteries (SIBs) and other new technologies are emerging as candidates for sustainable energy. Research in this technology is increasing, with a focus on developing new cathode and anode materials that can improve cycle stability, operating costs, and energy. 2D materials are promising in many energy-related applications, especially energy storage, due to their ability to transport ions between layers and over large areas, enhanced ion adsorption, and rapid surface redox reactions [70]. Tang et al.'s [70] potassium metal batteries are considered attractive alternatives to lithium-ion batteries. However, uncontrollable dendrite growth of potassium metal anodes limits their practical applications. Functionalization of the potassium anode has been reported to be achieved by encapsulating the metal in a titanium-free, nitrogen-containing MXene/carbon nanotube freestanding scaffold. High and fast electrical conduction in the scaffold helps reduce density and current flow during coating/stripping. Additionally, theoretical calculations and experimental studies confirmed that the "potassium-loving" form of MXene can cause potassium nucleation and add potassium during exposure to stabilize the products. As a result, the produced potassium metal anode exhibits dendrite-free morphology, high Coulomb efficiency, and a long lifetime during the plating/stripping process. Such anodes also improve the electrochemical performance of potassium-sulfur batteries compared to bare metal anodes. The potential of Ti_2N monolayers and their Ti_2NT_2 derivatives (T = O, F, and OH) as anode materials for lithium-ion and ultra-lithium-ion batteries were investigated by first-principle calculations. The single layer exposed and removed is a very good metal material. The diffusion barriers of the bare Ti_2N monolayer were approximately Li^+ 21.5 meV, Na^+ 14.0 meV, K^+ 7.0 meV, Mg^{2+} 75.9 meV, and Ca^{2+} 38.0 meV. The 2D functional groups of Ti_2NT_2 increased the conduction effect by approximately 1-fold. The calculated capacity of single cations of Ti_2N and Ti_2NT_2 was close to conventional graphite anodes in lithium-ion batteries. In comparison, the Mg^{2+} capacity of Ti_2N and Ti_2NT_2 exceeded 2000 $mAhg^{-1}$ due to the two-electron reaction and multilayer adsorption of Mg^{2+}. A comparison of the electrical properties of Ti_2N and Ti_2C showed that Ti_2N is a better material than Ti_2C due to its sensitivity to various cations [24] (see **Figure 12a**).

The heavy reliance on LIBs has led to growing concerns about the sustainability of lithium and alternative metals and ethical issues in mining. Developing alternative energy storage technologies beyond lithium has become an important part of the world's energy research portfolio [71]. Other technologies, from electric transportation to renewable energy to large-scale energy storage, play an important role in developing energy storage for the future. Considering their chemical and economic benefits, potassium ion batteries (PIBs) are promising and are becoming strong competitors to LIBs and SIBs in many forms. However, many people do not understand the process by which potassium is deposited in materials and how it differs from lithium and sodium, and the material liquid interface chemistry in PIBs is also not fully understood. Therefore, there are still some important problems in the commercialization of PIB technology.

5.4. Supercapacitor

Supercapacitors have attracted significant attention as promising successors to traditional energy storage devices due to several key advantages like higher power density, faster charge-discharge cycles, and greater energy density over batteries and conventional dielectric capacitors [1,22]. There are two main types of supercapacitors based on their working principles: electrochemical double-layer capacitors (EDLC), pseudocapacitors, and hybrid capacitors. EDLCs store energy by the adsorption/desorption of ions on the surface through the electrical double layer, whereas pseudocapacitors store energy through surface redox reactions [4]. The energy density (E) of supercapacitors is governed by the formula $E = CV^2/2$, where C is capacitance and V is voltage. Therefore, enhancing capacitance and voltage window results in higher energy density supercapacitors. Voltage remains relatively constant for a specific electrolyte, so increasing capacitance is crucial for overall capacitor performance improvement [2,22]. As a result, there is significant research interest in enhancing capacitance to improve supercapacitor performance.

MXene exhibits significant potential as an electrode material for batteries and supercapacitors, due to its remarkable electrochemical properties resulting from the presence of transition metal carbide/nitride components and its high electrical conductivity [28]. MXenes typically originate from the MAX phase, which follows the general formula $M_{n+1}AX_n$. Here, M represents an early transition metal, A is a group of 13 or 14 elements, and X consists of C and/or N; n is generally 1–3. MXene formation occurs through the chemical etching of the A layer within the MAX phase using fluoride ion-containing solutions such as hydrofluoric acid (HF) [11]. Following the etching process, the configuration of MXene may exhibit significant variations, depending on the specific post-treatment method employed. After selectively etching the A layer with HF, the resultant powder manifests a multi-layered MXene structure [72]. In this structure, the atoms of the A layer, predominantly Al or Si, are substituted by terminal groups such as –O, –OH, and/or –F, leading to a phase denoted as $M_{n+1}X_nT_x$. Otherwise, when intercalants like Li^+ ions are used instead of etchants, sonication yields a colloidal phase comprising few-layered or monolayer-exfoliated MXene nanosheets. These exfoliated MXene nanosheets reveal a significantly expanded surface area due to the removal of the A layer spacing. Generally, the use of alkali metal ions as intercalants results in an enlargement of the surface area by at least a factor of two compared to that of the multilayered MXene [33,34,73]. Upon the exfoliation of MXene nanosheets, stacked layers will probably form in MXene films, driven by impromptu attractive interactions such as van der Waals forces and hydrogen bonding [36]. MXene films offer the benefits of flexibility, large conductivity, and surface hydrophilicity, making them favorable for enhanced electrochemical processes. Consequently, free-standing films based on MXene have been widely employed as active materials in supercapacitors and various electrochemical electrodes [37–38,74]. While MXene films possess numerous advantages, their applications are limited due to the lack of regulated film-forming processes [75]. While monolayer MXene nanosheets allow for the optimization of theoretical surface area and electrochemical surface activity, processes primarily involving layer-stacking film formation compromise the intrinsic properties anticipated from monolayers, thus affecting the performance of electrochemical applications [22,76].

Couly et al. proposed a simple approach to fabricate asymmetric micro-supercapacitors using MXene. These micro-supercapacitors are modifiable, free of binder, and current-collector-free. The method involved employing a customized mask and an expandable spray coating technique on a flexible and transparent substrate [77]. The electrode comprised titanium carbide MXene ($Ti_3C_2T_x$) and reduced graphene oxide, both possessing a 2D layered structure that facilitated rapid ion diffusion within the interdigitated electrode framework. This asymmetric micro-supercapacitor operated within a 1 *V* voltage window and retained 97% of its initial capacitance after ten thousand cycles. Furthermore, it demonstrated an energy density of 8.6 mW hcm^{-3} at a power density of 0.2 W cm^{-3}. Moreover, these micro-supercapacitors exhibited remarkable flexibility under mechanical bending. By leveraging the capacity of $Ti_3C_2T_x$—MXene electrodes to operate at negative potentials in aqueous electrolytes, it was demonstrated that employing $Ti_3C_2T_x$ as a negative electrode and reduced graphene oxide as a positive electrode in asymmetric configurations represented a viable approach to enhance both the energy and power densities of micro-supercapacitors.

Rakhi et al. [78] developed 2D Ti_2CT_x MXene nanosheets by selectively etching the Al layer from the Ti_2AlC MAX phase, utilizing HF. The hexagonal symmetry of the parent Ti_2AlC MAX phase was preserved in the MXene sheets. An extensive investigation was conducted to evaluate the influence of various post-etch annealing atmospheres, including argon (Ar), nitrogen (N_2), a combination of nitrogen and hydrogen (N_2/H_2), and air, on both the structure and electrochemical characteristics of the MXene nanosheets. It was found that the MXene sheets displayed changes in structure, morphology, and electrochemical behavior following annealing in air compared to the HF-treated MAX phase. In contrast, samples subjected to annealing in Ar, N_2, and N_2/H_2 atmospheres maintained their initial morphology. A substantial enhancement was observed in the supercapacitor performance of the annealed samples, particularly in those annealed in Ar, N_2, and N_2/H_2 atmospheres. In a symmetric two-electrode setup, the MXene sample annealed in an N_2/H_2 atmosphere exhibited superior capacitive performance, boasting a specific capacitance of 51 Fg^{-1} at 1 Ag^{-1} and an impressive rate performance of 86%. This notable enhancement in electrochemical performance post-annealing was attributed to several factors, including the increased carbon content, decreased fluorine content on the surface, and the preservation of the original two-dimensional layered morphology, ensuring optimal access of the aqueous electrolyte to the electrodes.

Wen et al. [79] introduced a novel electrode material for supercapacitors, nitrogen-doped two-dimensional MXene (N-$Ti_3C_2T_x$), through annealing of $Ti_3C_2T_x$ in ammonia post-etching. Through precise control of annealing temperatures within the range of 200 °C to 700 °C, the concentrations of nitrogen in N-$Ti_3C_2T_x$ materials were made ranging from 1.7% to 20.7%. The incorporation of nitrogen as a heteroatom into the $Ti_3C_2T_x$ structure led to an expansion of the c-lattice parameter in MXene sheets, from 1.92 nm in $Ti_3C_2T_x$ to 2.46 nm in N-doped counterparts after treatment with ammonia at 200 °C. The resultant doped MXene materials exhibited significantly enhanced electrochemical capacitance of 192 F/g in 1 M H_2SO_4 and 82 F/g in 1 M $MgSO_4$ electrolyte, under optimized conditions. These values represented a substantial rise in the capacitances, as observed for undoped $Ti_3C_2T_x$ materials, which recorded 34 F/g in 1 M H_2SO_4 and 52 F/g in 1 M $MgSO_4$ (see **Figure 12b**).

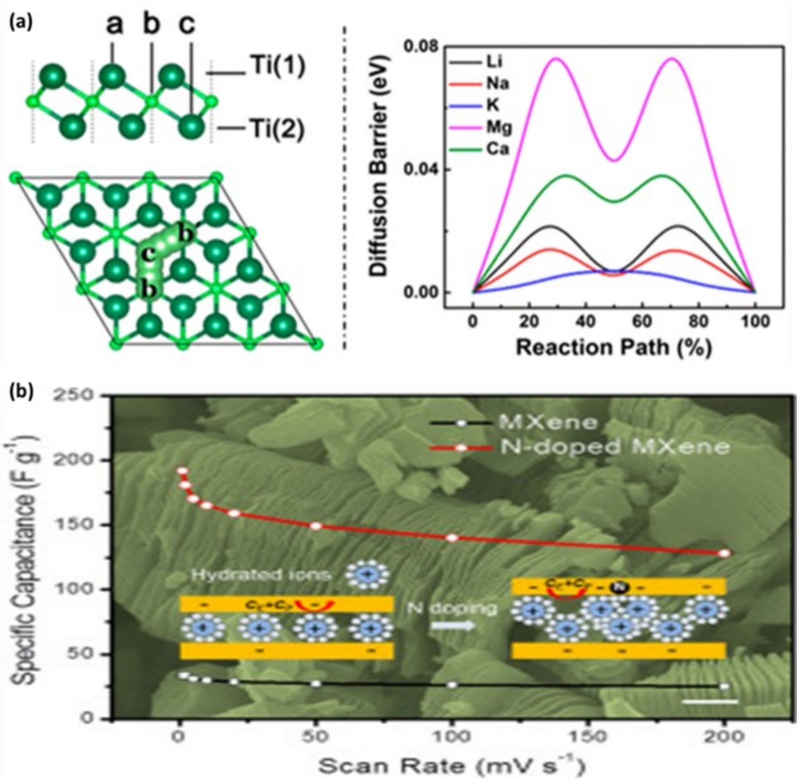

Figure 12. (a) First calculations of Ti_2N and Ti_2NT_2 (T=O, F, OH) monolayers as anode materials for lithium-ion batteries and other batteries [24]; **(b)** nitrogen-doped $Ti_3C_2T_x$ MXene electrodes for high-performance supercapacitors [79].

5.5. Biomedical applications

Levitt et al. [80] fabricated free-standing $Ti_3C_2T_x$ MXene/carbon nanofiber electrodes by electrospinning to combine $Ti_3C_2T_x$ MXene flakes with polyacrylonitrile (PAN), followed by carbonization. Through this approach, delaminated MXene flakes could be incorporated within carbon nanofibers, resulting in fiber mats that could be employed as electrodes. Notably, these composite electrodes exhibited superior sturdiness compared to their coated counterparts. In the spinning dope, MXene flakes were introduced into PAN solutions at a weight ratio of 2:1, resulting in fiber mats containing MXene up to 35 wt%. The resulting composite electrodes demonstrated an impressive areal capacitance of up to 205 mF cm^{-2} at 50 mV s^{-1}, nearly three times higher than that of pure carbonized PAN nanofibers, which registered at 70 mF cm^{-2} under the same conditions. Furthermore, in comparison to electrospun nanofibers spray-coated with $Ti_3C_2T_x$, these composite fibers exhibited a twofold increase in areal capacitance at 10 mV s^{-1} (refer to **Figure 13a**). This versatile technique holds promise beyond energy storage applications, as it can be extended to generate MXene composite fibers using a variety of polymers. Such applications may include filtration, adsorption, and electrocatalysis, where fibers with high aspect ratios, accessible surface areas, and porosity are highly desirable.

5.6. MXene as gas sensors

Kim et al. [81] introduced chemical sensors with exceptional gas-sensing characteristics through the synthesis of $Ti_3C_2T_x$ (see **Figure 13b**). These sensors exhibited remarkable selectivity towards hydrogen-bonding gases compared to acidic gases. Also, an empirical Limit of Detection (LOD) of 50 ppb was achieved and a theoretical LOD reaching the sub-ppb level for Volatile Organic Compounds (VOC), making the lowest detection limits among gas sensors utilizing 2D materials and functioning at room temperature without any pretreatment. Furthermore, the signal-to-noise ratio (SNR) of $Ti_3C_2T_x$ sensors surpassed that of all other 2D materials by up to two orders of magnitude. The remarkable sensitivity of $Ti_3C_2T_x$ sensors could be attributed to both the metallic conductivity of the core channels and the robust adsorption energy of the surface functional groups (**Figure 13b**) [82].

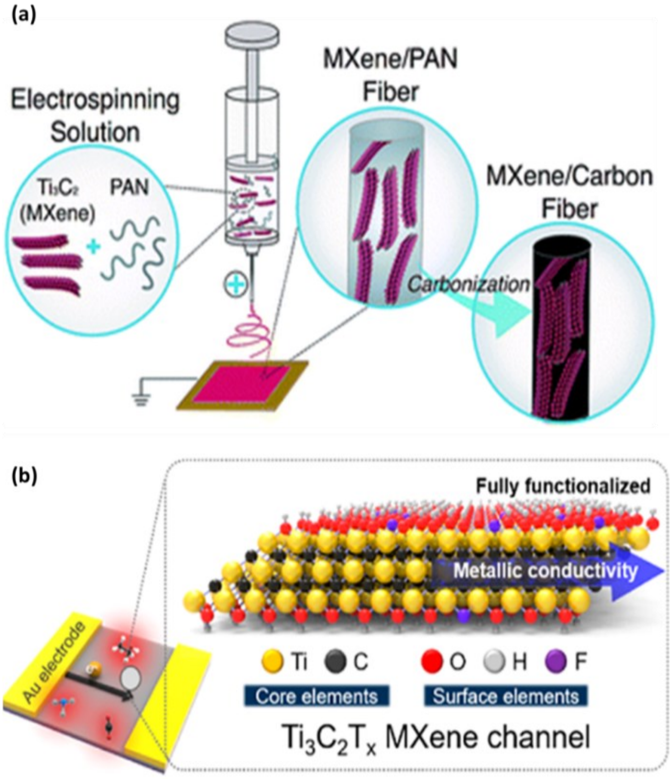

Figure 13. (a) Electrospun MXene/carbon nanofibers as supercapacitor electrodes [81]; **(b)**Schematic representation of $Ti_3C_2T_x$ films [82].

5.7. Sensors in biomedical applications

The distinctive 2D layered structure and remarkable array of physical and chemical attributes exhibited by MXenes, such as hydrophilic nature, biocompatibility, adeptness in light-to-heat conversion, and mechanical resilience, make them promising candidates across diverse biomedical domains. These applications encompass sensor technologies, bioimaging modalities, tissue engineering approaches, and advanced drug delivery systems.

Biosensors

Upon their discovery, MXenes swiftly ascended as a profoundly promising category of 2D materials. Their notable characteristics, including a substantial specific surface area, elevated conductivity, near-infrared absorption, and ease of functionalization, make them exceptionally well-suited for biomedical and environmental applications (**Tables 1** and **2**) [83]. In in-vitro experiments, MXenes exhibit toxicity against bacterial and animal cells, primarily due to mechanisms such as oxidative stress and the mechanical damage inflicted on cell membranes by the sharp edges of the nanosheets (**Figure 14a**).

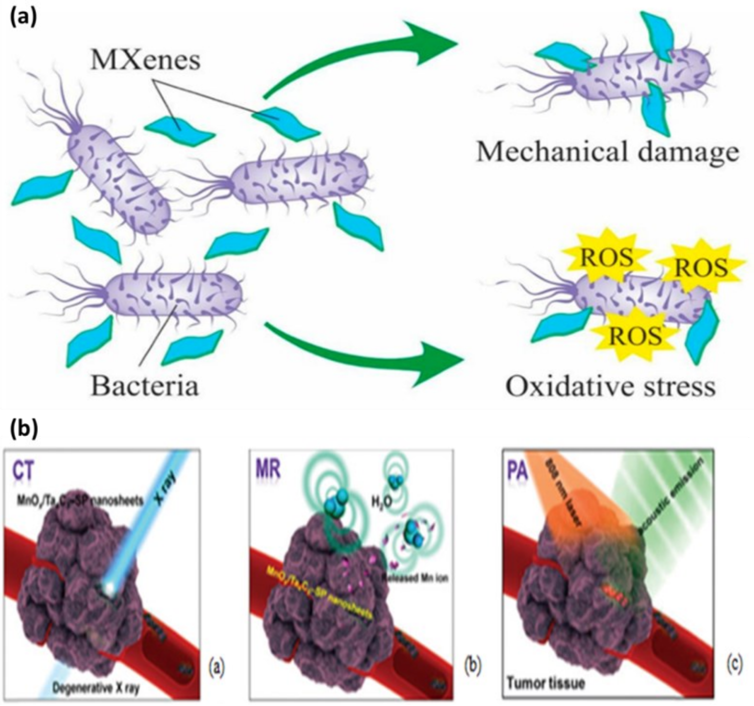

Figure 14. (a) Schematic representation of cytotoxic effects of MXene on bacterial cells [83]; **(b)** Schematic representation of **(a)** In vivo computed tomography Imaging of the Ta_4C_3 MXene composite **(b)** Disintegration of MnOx components from MnOx/Ta_4C_3 under a specific tumor microenvironment for contrast-enhanced T1-weighted magnetic resonance imaging **(c)** In vivo photoacoustic imaging [84].

Table 1. Biosensors for medicinal use [83].

Sensor Composition	**Detectable Analyte**	**Sensor Type**	**Sensor Efficiency**
MXene-Ti_3C_2	Hemoglobin	Electrochemical biosensors	detection limit of 20 nM
MXene-Ti_3C_2	Hemoglobin	Electrochemical biosensor	linear range of 0.5–11,800 µM, detection limit of 0.12 µM
GOx/Au/$Ti_3C_2T_x$-MXene/Nafion/GCE	Glucose	Electrochemical biosensor (amperometric)	detection limit of 5.9 µM
Ti_3C_2-MXene functionalized with aminosilane	Carcinoembryonic antigen (CEA)	Electrochemical biosensor	linear detection range of 0.0001–2000 ng mL^{-1} with sensitivity of 37.9 µA ng^{-1}mL cm^{-2} per decade
Ti_3C_2	Human papillomavirus (HPV)	Optical biosensor	detection limit of 100 pM
Ti_3C_2Tx MXene and phosphomolybdic acid embedded with polypyrrole	Osteopontin	Aptamer biosensor	0.98 µg/L
Ti_3C_2Tx/PtNP modified GCE	Ascorbic acid, dopamine, uric acid, acetaminophen	Electrochemical biosensor	nM level
OH-terminated Ti_3C_2	Label-free single-nucleotide in human urine	Electrochemiluminescence biosensor	Detection limit of 5 nM

Table 1. (*Continued*).

Sensor Composition	**Detectable Analyte**	**Sensor Type**	**Sensor Efficiency**
Ti_3C_2Tx/Prussian blue	Glucose and lactate in sweat	Electrochemical biosensor (amperometric)	Sensitivities of 35.3 µA $mm^{-1}cm^{-2}$ for glucose and 11.4 µA $mm^{-1}cm^{-2}$ for lactate
MXene-Ti_3C_2Tx incorporated with a dialysis microfluidic chip	Urea, uric acid, and creatinine	Electrochemical biosensor	
MXene-Ti_3C_2Tx modified screen-printed electrode	Acetaminophen (ACOP), isoniazid (INZ)	Electrochemical biosensor	Linear ranges from 0.25 to 2000 µM for ACOP and 0.1–4.6 mM for INZ. The detection limits of ACOP and INZ were 0.048 µM and 0.064 mM
Ti_3C_2Tx/ZIF-8	HIV-1 protein	Electrochemical biosensor	detection limit 0.3 fM
Au/Ti_3C_2T/HB5	HER2-positive cancer cells	Electrochemical cytosensor	linear range of 10^2–10^6 cells/mL, detection limit of 47 cells/mL
Chit/ChOx/Ti_3C_2Tx	Cholesterol	Electrochemical biosensor	concentration of cholesterol ranging from 0.3 to 4.5 nM, detection limit of 0.11 nM, sensitivity of 132.66 µA $nM^{-1}cm^{-2}$
Ti_3C_2Tx MXene/LBG/PDMS	Cortisol	Electrochemical impedimetric immunosensor	linearity 0.01–100 nM, detection limit 88 pM
PEI-Ru@Ti_3C_2@AuNPs	SARS-CoV-2 RdRp gene	Electrochemiluminescent biosensor	Detection limit of 12.8 aM
ZnO/Ti_3C_2	Glucose	Electrochemical enzymatic biosensor	Sensitivity 29 µA $mM^{-1}cm^{-2}$, limit of detection ≈ 17 µM, linear detection range 0.05–0.7 mM)

Table 2. Biosensors for environmental use [83].

Sensor Composition	**Detectable Analyte**	**Sensor Type**	**Sensor Efficiency**
$Mo_2Ti_2AlC_3$/MWCNT	Bisphenol A	Electrochemical biosensor (amperometric)	0.01–8.50 µM
MXene-Ti_3C_2	Tyrosinase	Electrochemical biosensor	linear range from 0.05 to 15.5 µM L^{-1}, detection limit of 12 nM L^{-1}
MXene-Ti_3C_2	$Ag^+$and Mn^{2+}	Optical sensors	Range of 0.1–40 µM for Ag^+, detection limits of 9.7 nM; 0.5–60 µM for Mn^{2+}ions,
Ti_3C_2Tx (MXene)-modified glassy carbon electrode	BrO^{3-}	Electrochemical biosensor	linear response from 50 nM to 5 µM, detection limit of 41 nM
Hydroxyl terminated alk-Ti_3C_2 modified GCE	Cd(II), Pb(II), Cu(II) and Hg(II)	Electrochemical biosensor	Detection limit of 0.098, 0.041, 0.032 and 0.130 µM for Cd(II), Pb(II), Cu(II) and Hg(II), respectively
AChE-Chit/Ti_3C_2-MXene/Au NPs/MnO_2/Mn_3O_4/GCE	Organophosphorus pesticides	Electrochemical biosensor	concentration range (10^{-12}–10^{-6}M), limit of detection (1.34×10^{-13}M)
AChE/CS-$Ti_3C_2T_x$/GCE	Organophosphorous pesticides (malathion)	Electrochemical biosensor	concentration range of 10^{-14}–10^{-8}M, limit of detection 0.3×10^{-14}M
AChE/Ag@$Ti_3C_2T_x$	Organophosphorous pesticides (malathion)	Electrochemical biosensor	concentration range of 10^{-14}–10^{-8} M
$Ti_3C_2T_x$	carbamate pesticides (methiocarb and diethofencarb)	Electrochemical biosensor	detection limits were 0.19 µg mL^{-1} and 0.46 µg mL^{-1} for methiocarb and diethofencarb respectively
CdS/MXene-NH_2/$ZnsnO_3$	Cd^{2+}, perfluorohexane	Photoelectrochemical biosensor	linear range of 0.008–100 nM, detection limit of 4.21 pM
$MnMoO_4$-MXene-GCE	Hydroquinone, catechol	electrochemical biosensor	linear response from 5 nM to 65 nM, detection limit of 0.26 nM for Hydroquinone and 0.30 nM for catechol

The interest in early detection of cancer has grown in the context of bioimaging and biosensing, owing to their capacity to unveil intricate cellular processes and a diverse array of diagnostic indicators. Ti_3C_2 is the most extensively researched MXene nanostructure in applications related to bioimaging and biosensing, while Ta_4C_3 MXene is commonly employed for multimodal imaging. The presence of tantalum (Ta) in the Ta_4C_3 MXene, characterized by a high atomic number and a notable X-ray attenuation coefficient, enables its utilization in CT imaging without requiring supplementary contrast agents. This streamlines the setting up of multimodal imaging. Regarding biosensing, platforms utilizing MXenes have been developed for various techniques, including electrochemistry, fluorescence, surface plasmon resonance, surface-enhanced Raman scattering, and colorimetric and chemiluminescence-based biosensing [84] (see **Figure 14b**).

Surface modification and functionalization are pivotal in augmenting the characteristics of materials based on MXene. Following surface modification, MXene-based materials have been propelled into the spotlight and have found widespread application in various fields, such as biomedicine, energy, and the environment. Specifically, this includes biosensing, drug delivery systems, bioimaging, photothermal therapy, antibacterial agents, and theragnostic nanoplatforms within the realm of biomedical applications [85].

5.8. Flexible pressure sensor

MXenes have found application in different sensing scenarios because of their adjustable surface functionalities. Sensors based on MXenes have proven effective in detecting a range of pollutants, exhibiting a lower detection limit and impressive selectivity/sensitivity [85,86]. The domains of electronic skin, human-machine interaction, and health monitoring demand pressure sensors that are both flexible and highly sensitive. However, most microstructure designs employed for creating pressure sensors with high performance involve intricate preparation processes. Yin et al. [87] obtained a 3D porous structure of MXene/polyaniline (PANI) foam through the application of a steam-induced foaming method. Utilizing this structure, a flexible piezoresistive sensor was manufactured. It demonstrated remarkable characteristics, including high sensitivity (690.91 kPa^{-1} quick response and recovery time of 106/95 ms, and excellent fatigue resistance (10,000 cycles). The pressure sensor, derived from MXene/PANI foam, could rapidly perceive subtle pressure changes. It was found suitable for applications in human activity and supervision of health [86,87].

As composite materials find extensive use in aeronautic structures, research on composite material repair methods is becoming increasingly comprehensive. However, owing to the unique nature of the composite materials, the visual efficacy of repairs and the service condition of the composite repaired structure is challenging, necessitating highly sensitive piezoresistive strain sensors. Wang et al. [88] introduced an innovative MXene film sensor technology capable of real-time and in-situ health monitoring of composite structures. The proposed method enabled the creation of MXene thin films with exceptional properties. MXene sensors were produced and organized into arrays and integrated into the composite repair structure to monitor strain across various points. The piezoresistive reaction of the MXene sensor was acquired, and the primary operational mechanism was elucidated. The strategic arrangement of MXene sensors in the repaired structure enhanced the monitoring process, offering a more thorough understanding of the failure mechanism. This monitoring approach, utilizing MXene sensors, can be used for investigating the health status of composite repair structures under both tensile and compression conditions [88] (see **Figure 15**).

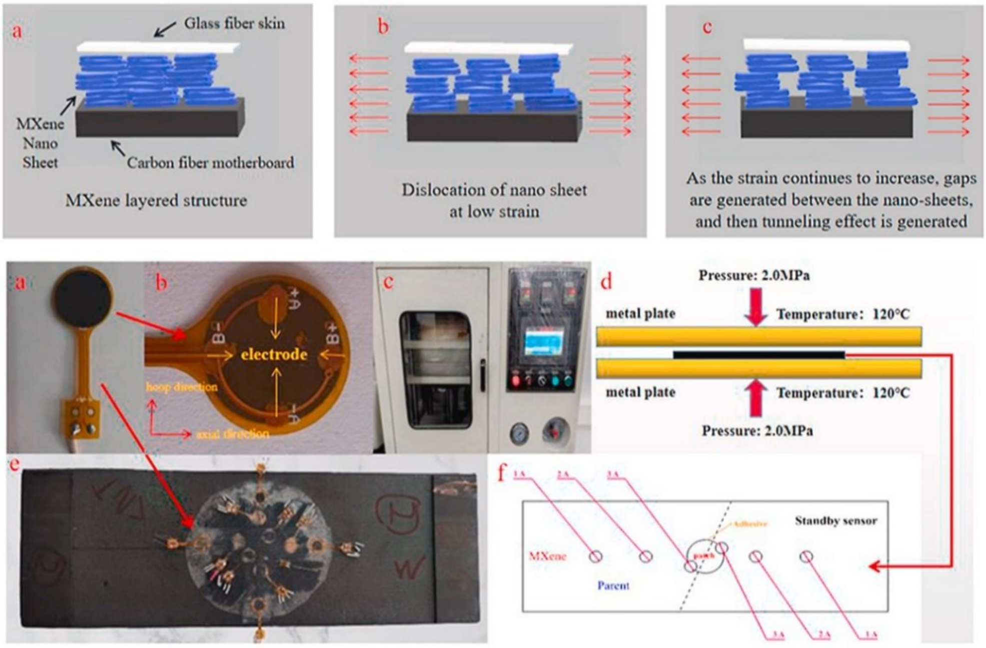

Figure 15. Monitoring of repaired composite structure [88].

Sen mechanism of MXene sensor and sensor array arrangement of composite material repair structure.

Despite possessing notable properties such as a large surface area, biocompatibility, metallic conductivity, hydrophilicity and tunable size, the application of MXene in biomedical settings is constrained by its limited stability in physiological environments, absence of sustained and controlled drug release, and low biodegradability. These challenges have prompted consideration for the adoption of MXene/polymer nanocomposites. The presence of functional groups on the MXene surface allows for polymer functionalization. Hence, these MXene nanocomposites functionalized with polymers showcase notable features such as high photothermal conversion efficiency, selectivity, responsiveness to stimuli, electron sensitivity, enhanced antibacterial properties, and more. These characteristics make them suitable for use in biomedical applications, including photothermal therapy, drug delivery, diagnostic imaging, biosensing, bone regeneration, and antibacterial activities [89] (see **Figure 16**).

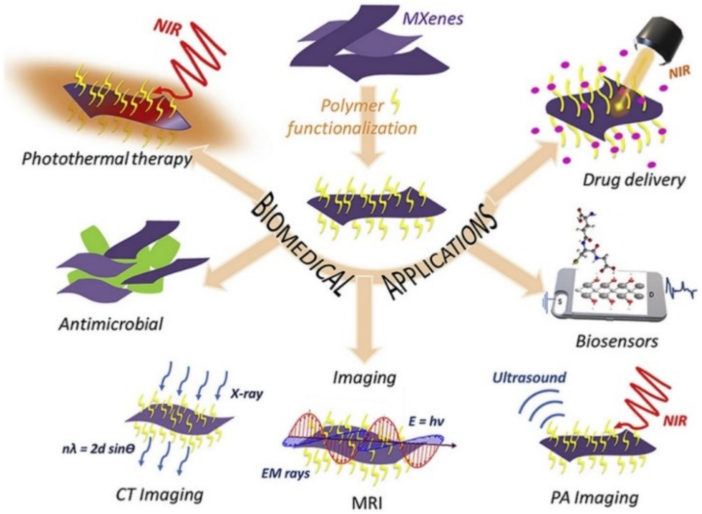

Figure 16. MXene-Polymer composites in biomedical applications [89].

5.9. Drug delivery system

The healing of chronic wounds is a fundamental and significant concern in medical and healthcare domains, and in recent times, hydrogel systems have emerged as promising carriers for drug delivery in the context of wound management, which is responsive to stimuli. Yang et al. [90] introduced a hydrogel system based on 2D MXene, designed for effective drug delivery with photo- and magnetic-responsive capabilities, specifically tailored for the treatment of deep chronic wounds. The smart and responsive drug delivery system using MXene consisted of magnetic colloids enveloped by MXene and dual-network hydrogels made from poly (N-isopropyl acrylamide) and alginate. It exhibited versatile responsiveness and precise drug release mechanisms, effectively mitigating the toxic side effects of drugs and enhancing the wound healing process. The real-world efficacy of the MXene-based hydrogel drug delivery system was validated through its application in treating full-thickness cutaneous wounds and subcutaneous infected wounds in a rat model, highlighting its substantial potential in clinical wound healing management and other relevant biomedical domains.

5.10. MXene in cancer treatment

Typical approaches to cancer treatment encompass surgical procedures, chemotherapy, and radiotherapy involving the use of anti-cancer medications. Recently, MXenes have generated considerable attention for their potential use as drug carriers. This is attributed to their planar structure, abundant surface functional groups, biocompatibility, and negatively charged surface. Even though nanosized Ti_3C_2, the pioneering MXene for drug delivery vehicles, exhibits an enhanced permeability and retention effect that allows it to accumulate at the tumor site, surface modification is essential. This is because it tends to restack under physiological conditions. The tumor microenvironment, which typically has a lower pH compared to normal tissues, offers an opportunity for controlled drug release, as the presence of H^+ ions can disrupt the electrostatic interaction between the drug and MXene. Additionally, controlled drug release can be achieved through near-infrared radiation stimulation [91].

Micro- and nanosystems incorporating MXene can be utilized for precise administration of anticancer drugs or therapeutic agents, offering the benefits of minimal toxicity and excellent biocompatibility. Confirming the effective uptake of therapeutic chemicals from the bloodstream to the intended site presents a significant challenge in systemic disposition. The vascular endothelial cell, serving as a barrier between organs and blood, emerges as a crucial focal point in this regard. By incorporating MXene into composites and subsequently functionalizing or modifying them with appropriate functional groups or agents, their loading capacity, biocompatibility, and bioavailability can be enhanced [92]. MXene-based micro- and nanosystems, following surface functionalization or modification with bioactive or biocompatible agents, have been employed for targeted delivery of anticancer drugs or therapeutic agents in cancer therapy (**Figure 17**) [92].

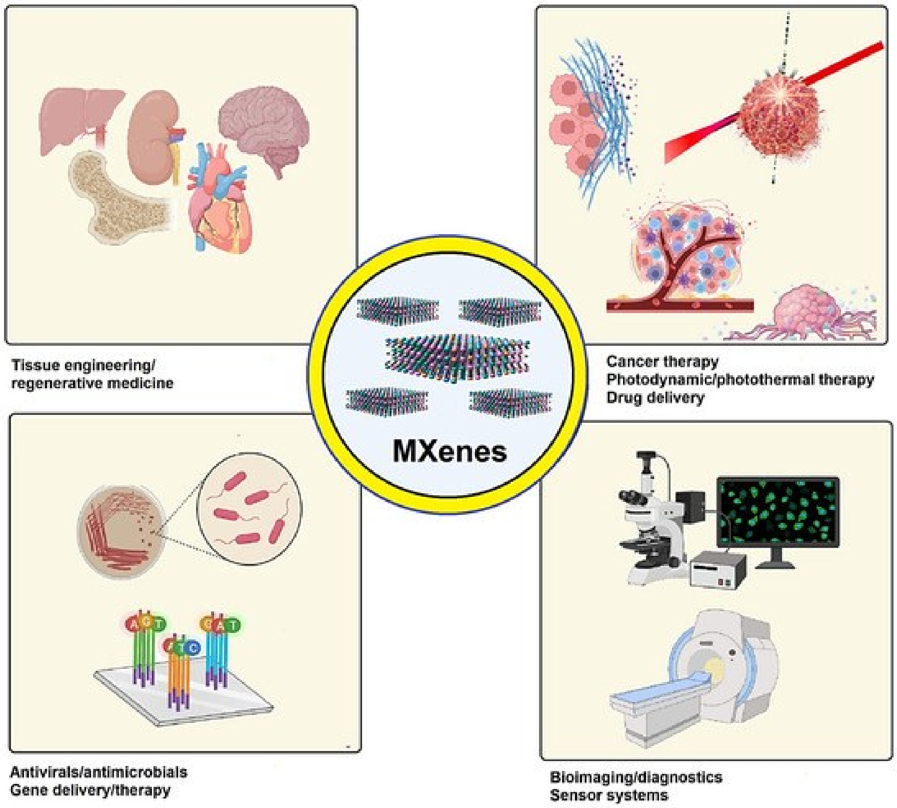

Figure 17. MXene with potential biomedical applications [92].

Liu et al. [93] described the creation of a drug delivery platform for the efficient loading of the chemotherapeutic doxorubicin (DOX) (see **Figure 18**). This platform exhibited dual drug release modes, responding to both near-infrared laser stimulation and variations in pH. Due to the surface modification involving thiol polyethene glycol aldehyde chains (SH-PEG-CHO) linked to the MXene through gold nanoparticles, the MXene@Au-PEG-DOX system exhibited favorable photothermal stability, biocompatibility, and tissue compatibility. Furthermore, using the effective photothermal conversion capabilities of both gold particles and MXene, it demonstrated a synergistic approach to combine photothermal ablation with chemotherapy to treat tumors. The enhancement of MXene through surface modification involving Au and PEG served not only to enhance the photothermal stability of the drug delivery system and the biocompatibility of the nanocomposites but also to regulate drug release through the formation of Schiff base bonds. Consequently, this, in turn, led to improved targeted therapeutic effects.

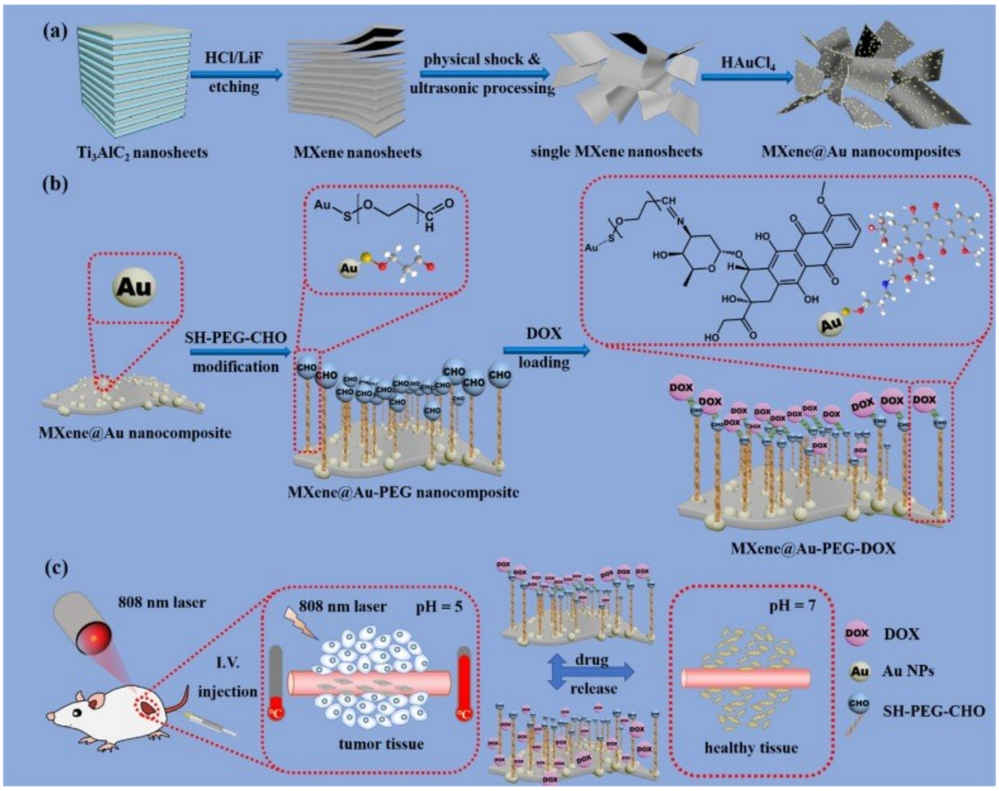

Figure 18. **(a)** Illustrative diagram of fabrication of MXene and MXene@Au nanosheets; **(b)** modification of MXene@Au surface using thiol polyethylene glycol aldehyde chains (SH-PEG-CHO), and DOX loading; **(c)** illustrative representation of MXene-based drug delivery system for near-infrared laser-triggered and pH-responsive drug release in tumor tissue [93].

A drug carrier with targeting capabilities for folate receptors was developed by Liu et al. [93], leveraging the plentiful surface functional groups and outstanding biocompatibility of MXenes. The drug carrier exhibited a drug-loading capacity of up to 69.9%, along with an extended drug release duration of up to 48 h. The findings indicated a substantial release of DOX in a pH 4.5 PBS solution. In comparison to the free drug, MXenes-FA-SP@DOX demonstrated increased cell inhibition and prolonged drug efficacy at lower concentrations (below 10 µg mg^{-1}). This drug delivery system can be used for the treatment of malignant tumors. Dong et al. [94] synthesized drug-loaded MXene/agarose hydrogel (MXene@Hydrogel). Initially, superior photothermal conversion efficiency and stability were achieved by preparing two-dimensional MXene nanosheets. Subsequently, these MXene nanosheets, along with the therapeutic drug, were integrated into a low-melting-point agarose hydrogel network to form the drug-loaded MXene/agarose hydrogel (MXene@Hydrogel). Incorporating a low concentration of MXene (20 ppm) facilitated rapid heating of the MXene@Hydrogel to 60 °C under near-infrared (NIR) irradiation, prompting its melting and subsequent release of encapsulated drugs. Control over drug release kinetics and on/off functionality could be easily modulated by adjusting agarose concentration, MXene concentration, light intensity, and exposure duration. Moreover, doxorubicin, an anticancer drug, maintained its efficacy upon release from the MXene@Hydrogel network under NIR irradiation. With its outstanding biocompatibility, this NIR-responsive MXene@Hydrogel represents a promising strategy for developing a smart hydrogel-based drug delivery system tailored for localized cancer therapy.

A nanoparticle system (MXene-TK-DOX@PDA) sensitive to reactive oxygen species (ROS) was engineered for efficient drug delivery in chemotherapy and applications in antibacterial therapy by Zhang et al. [95] (See **Figure 19**). The surface of (3-aminopropyl) triethoxysilane (APTES)-functionalized MXene served as a platform for conjugating DOX via a ROS-cleavable diacetyl thioketal (TK) linkage. Following this, the MXene nanosheets were coated with pH-responsive polydopamine (PDA) to serve as a gatekeeper. This incorporation of PDA enhanced the biocompatibility and stability of the MXene-TK-DOX@PDA nanoparticles. The ultrathin planar structure of MXene-TK-DOX@PDA nanoparticles, with a compact lateral size of around 180 nm, showcased exceptional photothermal conversion efficiency, superior stability in photothermal applications, and a notable extinction coefficient of 23.3 $Lg^{-1}cm^{-1}$ at 808 nm. The synthesized nanoparticles demonstrated effective release of DOX, responsive to both ROS and pH, attributed to the cleavage of the thioketal linker in MXene-TK-DOX@PDA. Furthermore, the MXene-TK-DOX@PDA nanoparticles exhibited potent antibacterial effects against both Gram-negative *Escherichia coli* (*E. coli*) and gram-positive *Bacillus subtilis* (*B. subtilis*) within a 5-hour timeframe.

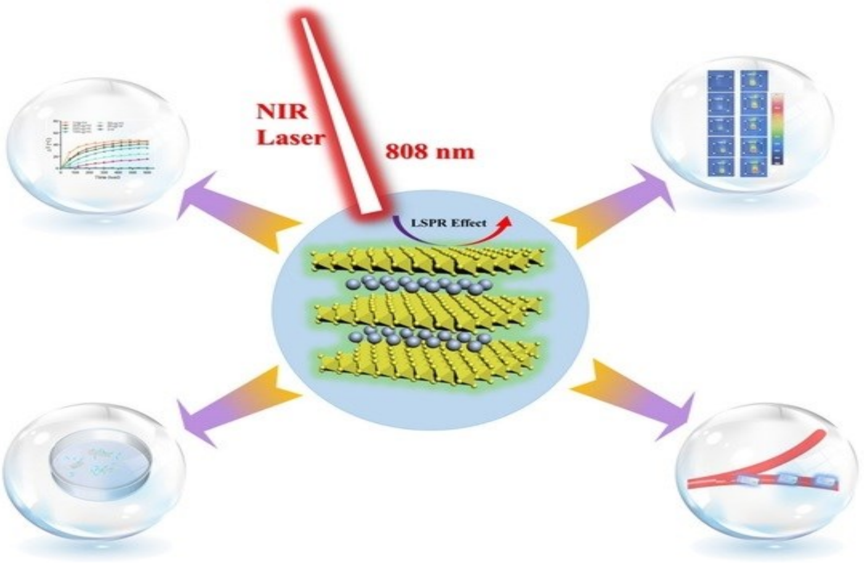

Figure 19. MXene-based nanoparticles as drug delivery carriers [95].

Using a layer-by-layer approach, a drug delivery system with pH/near-infrared responsiveness was created by Wu et al. [96]. This system is comprised of hollow hydroxyapatite (HAP), chitosan (CS)/hyaluronic acid (HA) multilayers, gold nanorods (AuNRs), and MXene. Multilayers of chitosan/hyaluronic acid were applied to the hollow hydroxyapatite (HAP) surface to mitigate the abrupt release of DOX during the initial delivery phase. Integration of MXenes and gold nanorods

(AuNRs) into the hybrid matrix notably enhanced the photothermal conversion efficiency of the microcapsules. The exceptional pH-/NIR-responsive drug delivery properties of HAP/CS/HA/MXene/AuNRs microcapsules were demonstrated through the disruption of electrostatic forces among chitosan/hyaluronic acid multilayers, the dissolution of HAP under acidic conditions, and the synergistically enhanced photothermal effect between MXene and AuNRs.

Liu et al. [97] developed a novel catalyst heterostructure (MXene/CoNWs) activated by NIR radiation, comprising 2D MXene and 1D cobalt nanowires (CoNWs), for combating bacteria without the use of drugs (see **Figure 20**). The incorporated CoNWs swiftly captured photogenerated electrons from Ti_3C_2 MXene nanosheets, thus mitigating the recombination of electron-hole pairs and enhancing carrier transfer under 808 nm NIR illumination, leading to increased reactive oxygen species (ROS) production. Moreover, the 2D/1D heterostructure exhibited a significantly amplified photothermal effect due to synergistic interactions between plasmonic CoNWs and the MXene semiconductor. Coatings of this heterostructure on orthopaedic implants demonstrated antibacterial efficacy exceeding 90% against both Gram-positive and Gram-negative bacteria within a mere 20-minute exposure period. Additionally, in vitro assessments indicated acceptable cytocompatibility of MXene/CoNWs heterojunctions.

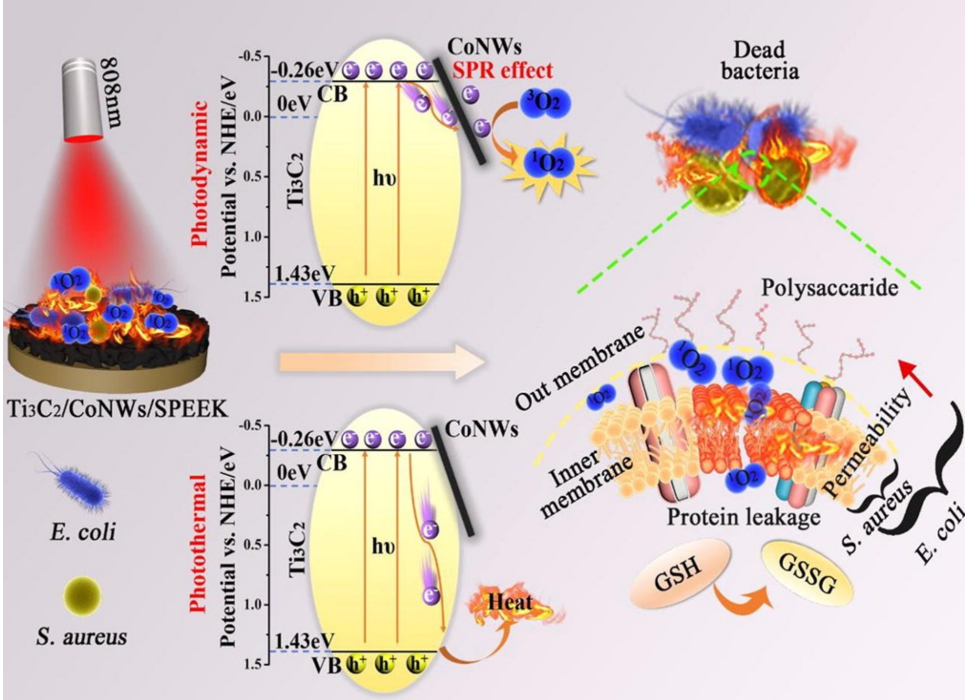

Figure 20. Schematic representation of MXene/CoWNs activation and action on bacteria [97].

5.11. Recent advanced progress in biomedical applications of MXenes

Owing to the captivating physicochemical attributes of MXenes, these materials and their blends have been engineered for diverse biomedical applications. $Ti_3C_2T_x$ was the first MXene to be identified, and it soon emerged as the most extensively researched MXenes. It demonstrated outstanding catalytic characteristics in the field of photocatalytic Hydrogen Evolution reaction. Nevertheless, the characteristics of $Ti_3C_2T_x$ were significantly influenced by its surface functional groups and associated materials. In particular, $Ti_3C_2T_x$ terminated with oxygen displayed the most optimal catalytic activity. Its efficacy could also be enhanced by combining it with other photoactive materials like TiO_2, ZnO, MoS_2, WS_2, CdS, and graphitic carbon nitride. These composite materials not only enhanced light absorption but also improved charge separation and active sites, thereby enhancing the overall performance of $Ti_3C_2T_x$ under UV-visible light irradiation [98] (See **Figure 21**). Koyappayil et al. [99] modified $Ti_3C_2T_x$ MXene nanosheets by incorporating *β*-hydroxybutyrate dehydrogenase to create a biosensor for amperometric detection of *β*-hydroxybutyrate. MXene demonstrated its excellence as an immobilization matrix, exhibiting strong compatibility with the enzyme *β*-hydroxybutyrate dehydrogenase. The biosensor utilizing MXene, working optimally at a potential of −0.35 V (vs. Ag/AgCl), exhibited a broad linear detection range (0.36 to 17.9 mM), a sensitivity of 0.480 $\mu A\ mM^{-1}\ cm^{-2}$, and a low detection limit (45 μM). Successful application of this biosensor was demonstrated in accurately determining *β*-hydroxybutyrate levels in real serum samples, even when spiked with additional compounds.

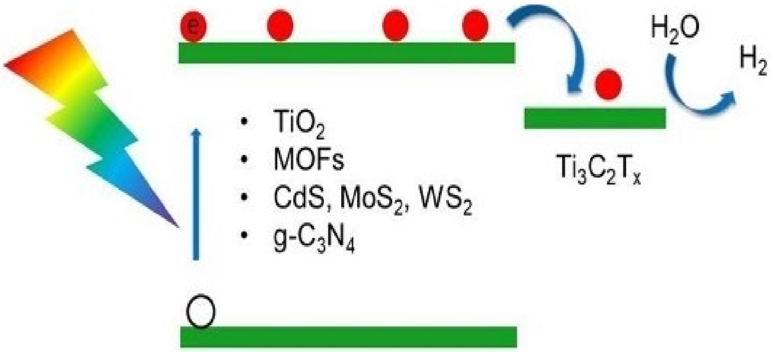

Figure 21. Titanium Carbide MXene in hydrogen production [98].

5.12. Cytocompatibility and cytotoxicity evaluations of MXenes

In contemporary biomedical research, MXene materials are increasingly employed. Zhang et al. [100] conducted experiments to assess the osteogenic potential of $Ti_3C_2T_x$ films, crucial for bone tissue engineering. Results from cellular studies revealed strong compatibility with cells and a propensity to stimulate osteogenic differentiation in vitro. Furthermore, the implantation of MXene films into rat subcutaneous and calvarial defect sites showcased remarkable biocompatibility, osteoinductive properties, and the ability to facilitate in vivo bone regeneration. Examining the potential risks associated with $Ti_3C_2T_x$ MXene exposure to the circulatory system, Huang et al. [101] investigated its cytocompatibility with red blood cells (RBCs) and human umbilical vein endothelial cells (HUVECs). Results indicated excellent compatibility even at high concentrations, with minimal hemolysis observed. Even at a high concentration of 200 μg/mL, $Ti_3C_2T_x$ induced minimal hemolysis at 0.8%, whereas GO at the same treatment concentration resulted in a considerably higher hemolysis rate of 50.8%. The structures of RBCs were left undisturbed. The presence of fully covered surface-terminating –O and –OH groups in $Ti_3C_2T_x$ resulted in a highly hydrophilic surface, impeding its influx into the inherently hydrophobic interior of the cell membrane (**Figure 22**). The remarkable compatibility of $Ti_3C_2T_x$ nanosheets with cell membranes and their minimal capacity to induce excessive reactive oxygen species (ROS) generation make them compatible with HUVECs.

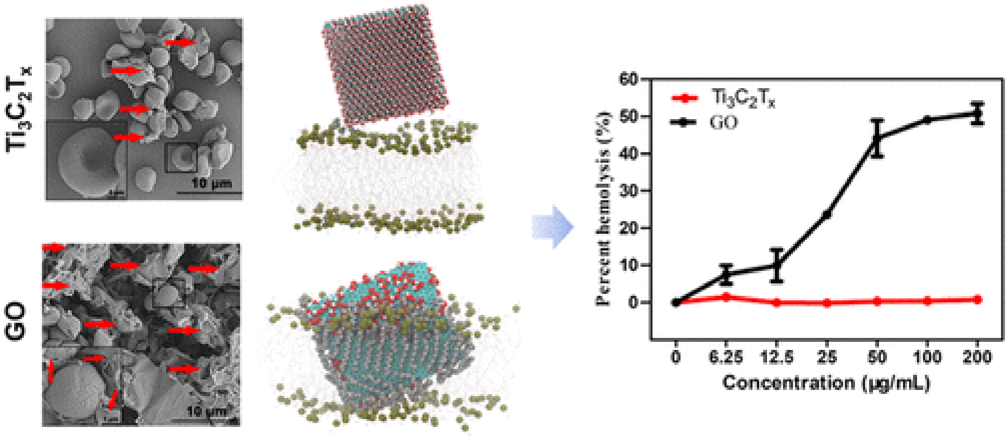

Figure 22. Cytocompatibility of $Ti_3C_2T_x$ MXene with red blood cells and human umbilical vein endothelial cells and the underlying mechanisms [101].

In the realm of flexible electronics and biomedical devices, MXene fibers hold promise due to their superior conductivity. Usman et al. [102] investigated the incorporation of silk fibroin biopolymer into MXene formulations to enhance fiber properties. The addition of silk fibroin led to improved durability, with fibres enduring up to 1 hour of high-frequency sonication. Also, fibers containing approximately 5 wt% silk fibroin demonstrated intriguing characteristics, such as high conductivity (approximately 3700 S cm^{-1}), elevated volumetric capacitance (approximately 910 F cm^{-3}), and non-cytotoxicity towards THP^{-1} monocytic cells. For the development of bioimaging tools, Neubertova et al. [103] suggested covalent functionalization of Ti_3C_2T flakes using the chelating agent diethylenetriaminepentaacetic acid (DTPA), followed by complexation with Gd^{3+} ions. This established functionalization technique endowed the inherently diamagnetic Ti_3C_2T flakes with a paramagnetic response, facilitating their utilization in T1-weighted magnetic resonance (MR) imaging. Additionally, a noticeable relationship between magnetic relaxation time and flake concentration was observed, enabling the estimation of the distribution of flakes in space. The covalent decoration approach applied to MXene resulted in safeguarding its surface against oxidation in phosphate buffered saline and blood serum while enhancing cytocompatibility simultaneously. Furthermore, the chelation of Gd^{3+} ions demonstrated superior prevention of leakage compared to electrostatic chemisorption. A high photothermal conversion efficiency of MXene-Gd was demonstrated, suggesting potential applications in photothermal therapy.

Yang et al. [104] highlighted the emergence of phototherapy as a promising strategy for combating bacterial infections without the associated risk of antibiotic resistance. However, the presence of endogenous antioxidative glutathione (GSH) in bacteria poses a challenge, as it hampers the desired antibacterial effects of externally generated reactive oxygen species (ROS) during phototherapy. A quad-channel synergistic antibacterial nanoplatform composed of Ti_3C_2 MXene/MoS_2 (MM) 2D bio-heterojunctions (2D bio-HJs) was fabricated. This platform exhibited photothermal, photodynamic, peroxidase-like (POD-like), and glutathione oxidase-like properties. Upon exposure to NIR laser, the 2D bio-HJs induced localized heating and elevated extracellular ROS levels, resulting in bacterial inactivation. Also, the Mo^{4+} ions released from the platform penetrated the bacterial membrane, triggering intracellular ROS generation and depletion of intracellular GSH, further contributing to bacterial eradication. The 2D bio-HJs produced localized heating and elevated extracellular ROS levels upon NIR laser irradiation, leading to bacterial deactivation. Simultaneously, Mo^{4+} ions easily penetrated the ruptured bacterial membrane, triggering intracellular ROS and depleting intracellular GSH.

In the "ROS Hurricane", bacteria faced substantial destruction from internal and external sources. However, when supplemented with fibroblast growth factor-21 (FGF21), 2D bio-hybrid junctions (bio-HJs) demonstrated favorable compatibility with cells and enhanced cell movement in vitro. Scheibe et al. [105] emphasized the necessity of conducting an in vitro examination to assess the impact of various types of MXenes and their precursors on human cell lines within the framework of nanomaterial safety. To this end, a range of multi-layered, few-layered, and single-layered $Ti_3C_2T_x$, alongside TiC, Ti_2AlC, and Ti_3AlC_2, were synthesized. Following the trends in nanomaterial safety assessment, thorough characterization encompassing morphology, size purity, and surface charge was conducted (**Figure 23**). Subsequently, various biological responses (including cytotoxicity, membrane permeability, reactive oxygen species generation, and mechanical stress) induced by MXenes, TiC, and parental MAX phases were investigated and compared using human fibroblasts (MSU1.1) and cervical cancer cells (HeLa) as model systems, reflecting differing tumorigenic properties.

The findings indicated that exposure to elevated concentrations (≥400 µg/mL) of TiC, Ti_2AlC, and Ti_3AlC_2 particles, sized < 44 µm, could pose significant harm, eliciting pronounced cytotoxic effects through oxidative and mechanical stress mechanisms. Conversely, all forms of $Ti_3C_2T_x$ were deemed safe for MSU1.1 cells, exhibiting only minor cytotoxic tendencies at the highest concentration levels. Furthermore, the observed cytotoxic behaviors were contingent upon cell type, with greater susceptibilities observed in cancer-derived cells.

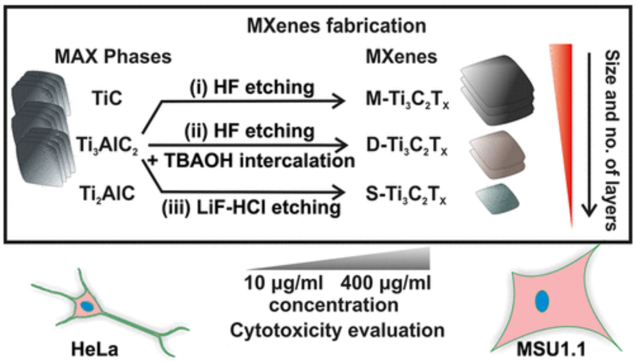

Figure 23. Cytotoxicity assessment of Ti-Al-C based MAX phases and $Ti_3C_2T_x$ MXenes on human fibroblasts and cervical cancer cells [105].

5.13. MXene-based materials for tissue engineering

2D MXenes are being used in the fields of tissue engineering and regenerative medicine. Also, because of their good electrical behavior, MXenes are used for neural tissue regeneration. Establishing artificial conduits to facilitate the growth of regenerating nerves and guide them through damaged areas is imperative for neuronal restoration. Despite the historical use of various natural and synthetic polymers in neural tissue engineering, certain drawbacks persist [106]. For instance, while poly (3,4-ethylene dioxythiophene) exhibits commendable biocompatibility and sufficient electrical and chemical stability, its proclivity towards chronic inflammation and limited degradability render it an unsuitable candidate.

Presently, MXenes are being incorporated as additives into polymeric nanofibers, fostering the growth of supportive cells and endowing them with sustained neurotrophic properties [107]. To validate the efficacy of MXene-modified polylactic acid nanofibers in facilitating nerve-guiding path formation, an experimental study was conducted. Integration of MXenes notably augmented the electrical conductivity of the material. The resultant current flow in the modified nanofiber membrane remained below 150 mA under an applied voltage of 5.5 V, although higher potentials induced dielectric behavior in the fabricated nanofibers. These findings underscore the potential of MXenes in conferring electroconductivity to polymer membranes for neural tissue engineering applications. Notably, the presence of polylactic acid membranes containing immobilized MXenes did not exhibit adverse effects on cellular viability, as evidenced by resazurin reduction assays. However, the outcomes were partially satisfactory due to challenges associated with MXene immobilization and handling during cell culture. Furthermore, the composite material demonstrated promising anti-adhesive properties against bacterial colonization, potentially disrupting cellular morphology and membrane integrity.

6. Challenges and future prospects

The numerous studies on MXenes and scientific reports, conferences, and articles are growing day by day, and the research in the right direction may address all challenges and issues. The possible right direction to the current state-of-art can open up new opportunities for innovations and developments of MXene-based devices. The current cutting-edge research on water-related issues can address the real problems, and the remarkable properties can make these efforts successful [3,9–13,73]. MXenes are mostly designed using the top-down approach, while very few reports on the bottom-up approaches are available in the literature [11,72]. Serious efforts are needed to explore the hidden potential in the bottom-up approaches to the synthesis of MXenes, to improve the characteristic properties of the MXenes, and to obtain desirable forms and structures of MXenes. After almost a decade of discovery of MXenes, this remarkable progress has been observed in the many fields and aspects related to MXenes, for example, synthesis, structural patterns, more applicability, and the discovery of new MXene compounds. But still, there are challenges left. The major challenges remain for MXenes and the application of MXene-based materials. Very few MAX phases have been experimentally exfoliated to date, while a few dozen possibilities are predicted. Theoretically, the MXenes can be the best possible cathode for high energy density 3458 Wh kg^{-1} Li-air batteries, but there is no successful report regarding this aspect [108,109]. Recently, Zn-air batteries have been successfully reported with promising performance, which proves the potential of MXenes [106,107].

Most of the reports are about coin-cell-based devices; it is just to see the actual potential of the material, while the pouch-type or large assembly of cells is needed to be tested for futuristic flexible, printable, or wearable applications of MXene-based batteries and supercapacitors. The performance of MXene-based devices with solid electrolytes needs to be tested to confirm the possibility of flexible and wearable MXene-based devices [61,110]. MXenes are proposed to be the future materials for absorption of toxic pollutants, but they need to be exploited fully [111]. For example, one of the promising MXene K_xMeO_2-based electrodes for batteries is under investigation, while the existing report shows lower operating potential and lower energy density in comparison to graphite/$LiMn_2O_4$-based LIBs [112] (**Figure 24**).

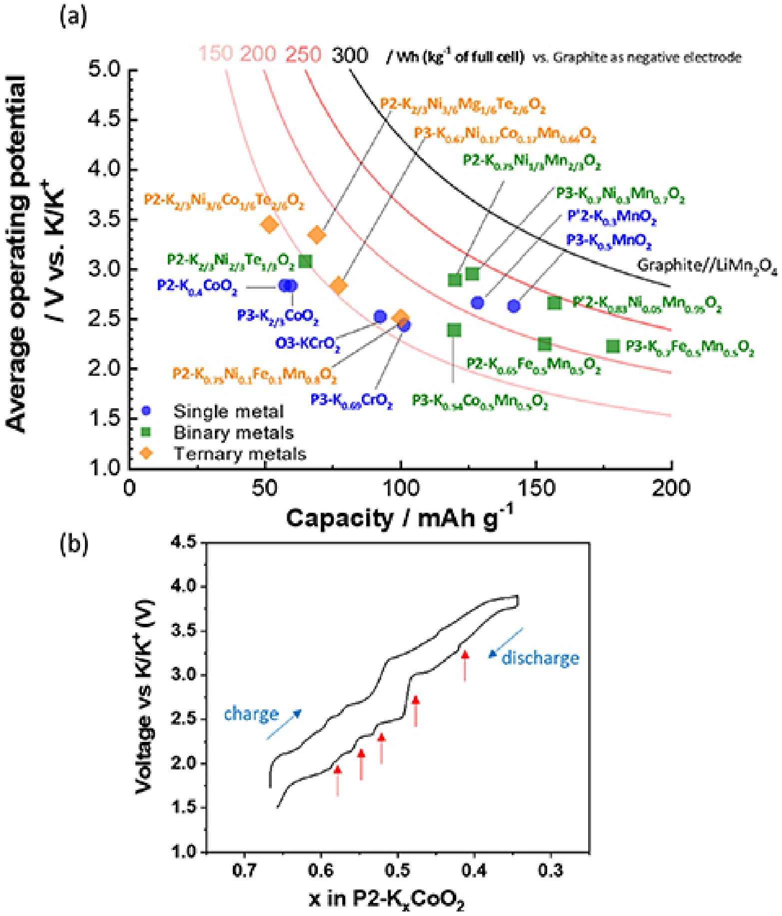

Figure 24. (a) Average operating potential versus gravimetric capacity plot for selected layered TMOs for PIBs; **(b)** typical charge/discharge curve for P2-type K_xCoO_2Xu [112].

The operating potential and capacity values reported for the various battery cells are derived from the potentiated state in half cells. While calculating the energy densities of full cells, graphite (with a capacity of 279 $mAhg^{-1}$ at 0.25 V vs. K/K^+) is employed as the negative electrode material in conjunction with various positive electrode materials. The key latest developments in MXene and MXene-based materials and devices are presented. Some key challenges and issues related to MXene-based materials for various applications need to be taken up [112].

7. Conclusion

MXene and MXene-based materials can be synthesized through various approaches and methodologies tailored to meet some specific properties and structural specification requirements. The exponential growth in the research articles and expansion of research groups around the world suggests expected tremendous improvement in the synthesis techniques soon. The specific properties of MXenes and MXene-based materials, e.g., specific surface area, chemical stability, hydrophilicity, thermal conductivity, and environmental compatibility, can be modified and customized according to the needs of applications. Water purification, absorption of impurities, metal removal, and degradation of impurities can be successfully done using MXenes-based materials in a better way. MXenes exhibit promising potential in diverse realms, including environmental remediation, biomedical applications, batteries, supercapacitors, and other advanced engineering fields. MXenes demonstrate excellent biocompatibility in biomedical applications. Nonetheless, there exist several challenges and unexplored research avenues that demand immediate attention to fully capitalize on the remarkable characteristics of these materials.

While numerous hurdles persist in translating research outputs into real-world applications, the growing research in many other fields with technological advancement is expected to conquer the existing challenges, and MXenes are anticipated to emerge as a pivotal component of futuristic applications, reflecting the continued evolution and integration of these intriguing materials into diverse domains.

Conflict of interest: The authors declare no conflict of interest.

References

1. Wang Y, Wang X, Li X, et al. Engineering 3D Ion Transport Channels for Flexible MXene Films with Superior Capacitive Performance. Advanced Functional Materials. 2019; 29(14). doi: 10.1002/adfm.201900326
2. Naguib M, Halim J, Lu J, et al. New two-dimensional niobium and vanadium carbides as promising materials for li-ion batteries. Journal of the American Chemical Society. 2013; 135(43): 15966–15969. doi: 10.1021/ja405735d
3. Okubo M, Sugahara A, Kajiyama S, Yamada A. MXene as a Charge Storage Host. Accounts of Chemical Research. 2018; 51(3): 591–599. doi: 10.1021/acs.accounts.7b00481
4. Wang H, Wu Y, Yuan X, et al. Clay-Inspired MXene-Based Electrochemical Devices and Photo-Electrocatalyst: State-of-the-Art Progresses and Challenges. Advanced Materials. 2018; 30(12). doi: 10.1002/adma.201704561
5. An H, Habib T, Shah S, et al. Surface-agnostic highly stretchable and bendable conductive MXene multilayers. Science Advances. 2018; 4(3). doi: 10.1126/sciadv.aaq0118
6. Zhan C, Naguib M, Lukatskaya M, et al. Understanding the MXene Pseudocapacitance. The Journal of Physical Chemistry Letters. 2018; 9(6): 1223–1228. doi: 10.1021/acs.jpclett.8b00200
7. Xiong D, Li X, Bai Z, et al. Recent Advances in Layered Ti_3C_2Tx MXene for Electrochemical Energy Storage. Small. 2018; 14(17). doi: 10.1002/smll.201703419

8. Anasori B, Xie Y, Beidaghi M, et al. Two-Dimensional, Ordered, Double Transition Metals Carbides (MXenes). ACS Nano. 2015; 9(10): 9507–9516. doi: 10.1021/acsnano.5b03591
9. Wang Y, Wang Y. MXene ink printing of high-performance micro-supercapacitors. Carbon Neutralization. 2021. doi: 10.1002/cnl2.165
10. Badawi N, Bhuyan M, Luqman M, et al. MXenes the future of solid-state supercapacitors: Status, challenges, prospects, and applicatio. The Arabian Journal of Chemistry .2024; 10(66). doi: 10.1016/j.arabjc.2024.105866
11. Kajiyama S, Szabova L, Sodeyama K, et al. Sodium-Ion Intercalation Mechanism in MXene Nanosheets. ACS Nano. 2016; 10(3): 3334–3341. doi: 10.1021/acsnano.5b06958
12. Vonlanthen D, Lazarev P, See KA, et al. A Stable Polyaniline-Benzoquinone-Hydroquinone Supercapacitor. Advanced Materials. 2014; 26(30): 5095–5100. doi: 10.1002/adma.201400966
13. Zhang C, Kremer MP, Seral-Ascaso A, et al. Stamping of Flexible, Coplanar Micro-Supercapacitors Using MXene Inks. Advanced Functional Materials. 2018; 28(9). doi: 10.1002/adfm.201705506
14. Kurra N, Ahmed B, Gogotsi Y, et al. MXene-on-Paper Coplanar Microsupercapacitors. Advanced Energy Materials. 2016; 6(24). doi: 10.1002/aenm.201601372
15. Xu S, Dall'Agnese Y, Wei G, et al. Screen-printable microscale hybrid device based on MXene and layered double hydroxide electrodes for powering force sensors. Nano Energy. 2018; 50: 479–488. doi: 10.1016/j.nanoen.2018.05.064
16. Zhang C, McKeon L, Kremer MP, et al. Additive-free MXene inks and direct printing of micro-supercapacitors. Nature Communications. 2019; 10(1). doi: 10.1038/s41467-019-09398-1
17. Jiao S, Zhou A, Wu M, et al. Kirigami Patterning of MXene/Bacterial Cellulose Composite Paper for All-Solid-State Stretchable Micro-Supercapacitor Arrays. Advanced Science. 2019; 6(12). doi: 10.1002/advs.201900529
18. Luo S, Xie L, Han F, et al. Nanoscale Parallel Circuitry Based on Interpenetrating Conductive Assembly for Flexible and High-Power Zinc Ion Battery. Advanced Functional Materials. 2019; 29(28). doi: 10.1002/adfm.201901336
19. Ma Y, Liu N, Li L, et al. A highly flexible and sensitive piezoresistive sensor based on MXene with greatly changed interlayer distances. Nature Communications. 2017; 8(1). doi: 10.1038/s41467-017-01136-9
20. Ronchi RM, Arantes JT, Santos SF. Synthesis, structure, properties and applications of MXenes: Current status and perspectives. Ceramics International. 2019; 45(15): 18167–18188. doi: 10.1016/j.ceramint.2019.06.114
21. Naguib M, Mashtalir O, Carle J, et al. Two-Dimensional Transition Metal Carbides. ACS Nano. 2012; 6(2): 1322–1331. doi: 10.1021/nn204153h
22. Naguib M, Mochalin VN, Barsoum MW, et al. 25th Anniversary Article: MXenes: A New Family of Two-Dimensional Materials. Advanced Materials. 2013; 26(7): 992–1005. doi: 10.1002/adma.201304138
23. Hemanth NR, Kandasubramanian B. Recent advances in 2D MXenes for enhanced cation intercalation in energy harvesting Applications: A review. Chemical Engineering Journal. 2020; 392: 123678. doi: 10.1016/j.cej.2019.123678
24. Mashtalir O, Naguib M, Mochalin VN, et al. Intercalation and delamination of layered carbides and carbonitrides. Nature Communications. 2013; 4(1). doi: 10.1038/ncomms2664
25. Shekhirev M, Shuck CE, Sarycheva A, et al. Characterization of MXenes at every step, from their precursors to single flakes and assembled films. Progress in Materials Science. 2021; 120: 100757. doi: 10.1016/j.pmatsci.2020.100757
26. Jain A, Ong S, Hautier G, et al. Commentary: The materials project: A materials genome approach to accelerating materials innovation. APL Materials.2013; 1(1). doi: 10.1063/1.4812323/119685
27. Lim GP, Soon CF, Ma NL, et al. Cytotoxicity of MXene-based nanomaterials for biomedical applications: A mini review. Environmental Research. 2021; 201: 111592. doi: 10.1016/j.envres.2021.111592
28. Shahmoradi S, Mirshafiei M, Zare I, et al. Two-Dimensional Nanomaterials-Based Polymer Nanocomposites for Tissue Engineering Applications. Scrivener Publishing LLC. 2024; 9781119904847. doi:10.1002/9781119905110.ch17
29. Sana SS, Santhamoorthy M, Haldar R, et al. Recent advances on MXene-based hydrogels for antibacterial and drug delivery applications. Process Biochemistry. 2023; 132: 200–220. doi: 10.1016/j.procbio.2023.06.022
30. Alyasi H, Wahib S, Gomez TA, et al. The power of MXene-based materials for emerging contaminant removal from water—A review. Desalinction. 2024, 117913. doi: 10.1016/j.desal.2024.117913
31. Ibrahim KB, Shifa TA, Zorzi S, et al. Emerging 2D materials beyond mxenes and TMDs: Transition metal carbo-chalcogenides. Progress in Materials Science. 2024, 101287. doi: 10.1016/j.pmatsci.2024.101287
32. Naguib M, Kurtoglu M, Presser V, et al. Two-Dimensional Nanocrystals Produced by Exfoliation of Ti_3AlC_2. Advanced Materials. 2011; 23(37): 4248–4253. doi: 10.1002/adma.201102306

33. Rafieerad A, Yan W, Sequiera GL, et al. Application of Ti_3C_2 MXene Quantum Dots for Immunomodulation and Regenerative Medicine. Advanced Healthcare Materials. 2019; 8(16). doi: 10.1002/adhm.201900569
34. Chen K, Chen Y, Deng Q, et al. Strong and biocompatible poly(lactic acid) membrane enhanced by Ti_3C_2Tz (MXene) nanosheets for Guided bone regeneration. Materials Letters. 2018; 229: 114–117. doi: 10.1016/j.matlet.2018.06.063
35. Pan S, Yin J, Yu L, et al. 2D MXene-Integrated 3D-Printing Scaffolds for Augmented Osteosarcoma Phototherapy and Accelerated Tissue Reconstruction. Advanced Science. 2019; 7(2). doi: 10.1002/advs.201901511
36. Cui Y, Liu M, Huang H, et al. A novel one-step strategy for preparation of Fe_3O_4-loaded Ti_3C_2 MXenes with high efficiency for removal organic dyes. Ceramics International. 2020; 46(8): 11593–11601. doi: 10.1016/j.ceramint.2020.01.188
37. Wychowaniec JK, Litowczenko J, Tadyszak K, et al. Unique cellular network formation guided by heterostructures based on reduced graphene oxide—Ti_3C_2Tx MXene hydrogels. Acta Biomaterialia. 2020; 115: 104–115. doi: 10.1016/j.actbio.2020.08.010
38. Wang H, Sun F, Zhao Y, et al. A highly luminescent organic crystal with the well-balanced charge transport property: The role of cyano-substitution in the terminal phenyl unit of distyrylbenzene. Organic Electronics. 2016; 28: 287–293. doi: 10.1016/j.orgel.2015.11.008
39. Rastin H, Zhang B, Mazinani A, et al. 3D bioprinting of cell-laden electroconductive MXene nanocomposite bioinks. Nanoscale. 2020; 12(30): 16069–16080. doi: 10.1039/d0nr02581j
40. He J, Yang J, Jiang F, et al. Photo-assisted peroxymonosulfate activation via 2D/2D heterostructure of Ti_3C_2/g-C_3N_4 for degradation of diclofenac. Chemosphere. 2020; 258: 127339. doi: 10.1016/j.chemosphere.2020.127339
41. Song H, Du R, Wang Y, et al. Anchoring single atom cobalt on two-dimensional MXene for activation of peroxymonosulfate. Applied Catalysis B: Environmental. 2021; 286: 119898. doi: 10.1016/j.apcatb.2021.119898
42. Ma Y, Xiong D, Lv X, et al. Rapid and long-lasting acceleration of zero-valent iron nanoparticles@Ti_3C_2-based MXene/peroxymonosulfate oxidation with bi-active centers toward ranitidine removal. Journal of Materials Chemistry A. 2021; 9(35): 19817–19833. doi: 10.1039/d1ta02046c
43. Wu Y, Xiong W, Wang Z, et al. Self-assembled MXene-based Schottky-junction upon Transition metal oxide for regulated tumor microenvironment and enhanced CDT/PTT/MRI activated by NIR irradiation. Chemical Engineering Journal. 2022; 427: 131925. doi: 10.1016/j.cej.2021.131925
44. Lee JB, Choi GH, Yoo PJ. Oxidized-co-crumpled multiscale porous architectures of MXene for high performance supercapacitors. Journal of Alloys and Compounds. 2021; 887: 161304. doi: 10.1016/j.jallcom.2021.161304
45. Xu S, Liu C, Jiang X, et al. Ti_3C_2 MXene promoted Fe_{3+}/H_2O_2 fenton oxidation: Comparison of mechanisms under dark and visible light conditions. Journal of Hazardous Materials. 2023; 444: 130450. doi: 10.1016/j.jhazmat.2022.130450
46. Li Q, Wang X, Chen L, et al. Cu/Cu_2O nanoparticles modified Ti_3C_2 MXene with in-situ formed TiO_{2-X} for detection of hydrogen peroxide. Ceramics International. 2023; 49(6): 9632–9641. doi: 10.1016/j.ceramint.2022.11.133
47. Zhu F, Wang X, Yang X, et al. Reasonable design of an MXene-based enzyme-free amperometric sensing interface for highly sensitive hydrogen peroxide detection. Analytical Methods. 2021; 13(22): 2512–2518. doi: 10.1039/d1ay00568e
48. Dekanovsky L, Huang H, Akir S, et al. Light-Driven MXene-Based Microrobots: Mineralization of Bisphenol A to CO_2 and H_2O. Small Methods. 2023; 7(8). doi: 10.1002/smtd.202201547
49. Ihsanullah I. MXenes (two-dimensional metal carbides) as emerging nanomaterials for water purification: Progress, challenges and prospects. Chemical Engineering Journal. 2020; 388: 124340. doi: 10.1016/j.cej.2020.124340
50. Dixit F, Zimmermann K, Dutta R, et al. Application of MXenes for water treatment and energy-efficient desalination: A review. Journal of Hazardous Materials. 2022; 423: 127050. doi: 10.1016/j.jhazmat.2021.127050
51. Rasool K, Pandey RP, Rasheed PA, et al. Water treatment and environmental remediation applications of two-dimensional metal carbides (MXenes). Materials Today. 2019; 30: 80–102. doi: 10.1016/j.mattod.2019.05.017
52. Hojjati-Najafabadi A, Mansoorianfar M, Liang T, et al. Magnetic-MXene-based nanocomposites for water and wastewater treatment: A review. Journal of Water Process Engineering. 2022; 47: 102696. doi: 10.1016/j.jwpe.2022.102696
53. Ihsanullah I. Potential of MXenes in Water Desalination: Current Status and Perspectives. Nano-Micro Letters. 2020; 12(1). doi: 10.1007/s40820-020-0411-9
54. Saththasivam J, Wang K, Yiming W, et al. A flexible Ti3C2Tx (MXene)/paper membrane for efficient oil/water separation. RSC Advances. 2019; 9(29): 16296–16304. doi: 10.1039/c9ra02129a
55. Bao W, Tang X, Guo X, et al. Porous Cryo-Dried MXene for Efficient Capacitive Deionization. Joule. 2018; 2(4): 778–787. doi: 10.1016/j.joule.2018.02.018

56. Tang X, Guo X, Wu W, et al. 2D Metal Carbides and Nitrides (MXenes) as High-Performance Electrode Materials for Lithium-Based Batteries. Advanced Energy Materials. 2018; 8(33). doi: 10.1002/aenm.201801897
57. Deng D. Li-ion batteries: basics, progress, and challenges. Energy Science & Engineering. 2015; 3(5): 385–418. doi: 10.1002/ese3.95
58. Goodenough JB. Evolution of Strategies for Modern Rechargeable Batteries. Accounts of Chemical Research. 2012; 46(5): 1053–1061. doi: 10.1021/ar2002705
59. Jyoti J, Singh BP, Sandhu M, et al. New insights on MXene and its advanced hybrid materials for lithium-ion batteries. Sustainable Energy & Fuels. 2022; 6(4): 971–1013. doi: 10.1039/d1se01681d
60. Wu X, Jovanović MR. Sparsity-promoting optimal control of systems with symmetries, consensus and synchronization networks. Systems & Control Letters. 2017; 103: 1–8. doi: 10.1016/j.sysconle.2017.02.007
61. Wang X, Kajiyama S, Iinuma H, et al. Pseudocapacitance of MXene nanosheets for high-power sodium-ion hybrid capacitors. Nature Communications. 2015; 6(1). doi: 10.1038/ncomms7544
62. Zhang P, Wang D, Zhu Q, et al. Plate-to-Layer Bi_2MoO_6/MXene-Heterostructured Anode for Lithium-Ion Batteries. Nano-Micro Letters. 2019; 11(1): 01.doi: 10.1007/s40820-019-0312-y
63. Zou G, Zhang Z, Guo J, et al. Synthesis of MXene/Ag Composites for Extraordinary Long Cycle Lifetime Lithium Storage at High Rates. ACS Applied Materials & Interfaces. 2016; 8(34): 22280–22286. doi: 10.1021/acsami.6b08089
64. Tian Y, An Y, Xiong S, et al. A general method for constructing robust, flexible and freestanding MXene@metal anodes for high-performance potassium-ion batteries. Journal of Materials Chemistry A. 2019; 7(16): 9716–9725. doi: 10.1039/c9ta02233c
65. Jiang T, Xiong Q, Yang H, et al. Performance and application of Si/Ti_3C_2T x (MXene) composites in lithium-ion battery. Journal of Physics: Energy. 2023; 5(1): 014020. doi: 10.1088/2515-7655/acb6b4
66. Zhang W, Shi H, Wang D, et al. Three-dimensional Ti_3C_2 MXene@silicon@nitrogen-doped carbon foam for high performance self-standing lithium-ion battery anodes. Journal of Electroanalytical Chemistry. 2022; 921: 116664. doi: 10.1016/j.jelechem.2022.116664
67. Rojas Dávalos CA. Chemomechanical study of silicon composite anodes for lithium-ion batteries. Available online: https://tesis.pucp.edu.pe/repositorio/handle/20.500.12404/21155 (accessed on 15 December 2021).
68. Lei D, Liu N, Su T, et al. Roles of MXene in Pressure Sensing: Preparation, Composite Structure Design, and Mechanism. Advanced Materials. 2022; 34(52). doi: 10.1002/adma.202110608
69. Peng L, Zhu Y, Chen D, et al. Two-Dimensional Materials for Beyond-Lithium-Ion Batteries. Advanced Energy Materials. 2016; 6(11). doi: 10.1002/aenm.201600025
70. Tang X, Zhou D, Li P, et al. MXene-Based Dendrite-Free Potassium Metal Batteries. Advanced Materials. 2019; 32(4). doi: 10.1002/adma.201906739
71. Wang D, Ga Y, LiuY, et al. First-Principles Calculations of Ti_2N and Ti_2NT_2 (T = O, F, OH) Monolayers as Potential Anode Materials for Lithium-Ion Batteries and Beyond. Journal of Physical Chemistry C. 2017; 121(24): 13025. doi: 10.1021/acs.jpcc.7b03057
72. Wang G, Zhang L, Zhang J. A review of electrode materials for electrochemical supercapacitors. Chem Soc Rev. 2012; 41(2): 797–828. doi: 10.1039/c1cs15060j
73. Alhabeb M, Maleski K, Anasori B, et al. Guidelines for Synthesis and Processing of Two-Dimensional Titanium Carbide (Ti3C2Tx MXene). Chemistry of Materials. 2017; 29(18): 7633–7644. doi: 10.1021/acs.chemmater.7b02847
74. Lukatskaya MR, Kota S, Lin Z, et al. Ultra-high-rate pseudocapacitive energy storage in two-dimensional transition metal carbides. Nature Energy. 2017; 2(8). doi: 10.1038/nenergy.2017.105
75. Ghidiu M, Lukatskaya MR, Zhao MQ, et al. Conductive Two-Dimensional Titanium Carbide ‘Clay’ with High Volumetric Capacitance. Available online: https://www.nature.com/articles/nature13970 (accessed on 2 September 2023).
76. Pomerantseva E, Bonaccorso F, Feng X, et al. Energy storage: The future enabled by nanomaterials. Science. 2019; 366(6468). doi: 10.1126/science.aan8285
77. Couly C, Alhabeb M, Van Aken KL, et al. Asymmetric Flexible MXene-Reduced Graphene Oxide Micro-Supercapacitor. Advanced Electronic Materials. 2017; 4(1). doi: 10.1002/aelm.201700339
78. Rakhi RB, Ahmed B, Hedhili MN, et al. Effect of Postetch Annealing Gas Composition on the Structural and Electrochemical Properties of Ti2CTx MXene Electrodes for Supercapacitor Applications. Chemistry of Materials. 2015; 27(15): 5314–5323. doi: 10.1021/acs.chemmater.5b01623

79. Wen Y, Rufford TE, Chen X, et al. Nitrogen-doped Ti3C2Tx MXene electrodes for high-performance supercapacitors. Nano Energy. 2017; 38: 368–376. doi: 10.1016/j.nanoen.2017.06.009
80. Levitt AS, Alhabeb M, Hatter CB, et al. Electrospun MXene/carbon nanofibers as supercapacitor electrodes. Journal of Materials Chemistry A. 2019; 7(1): 269-277. doi: 10.1039/c8ta09810g
81. Kim SJ, Koh HJ, Ren CE, et al. Metallic Ti3C2Tx MXene Gas Sensors with Ultrahigh Signal-to-Noise Ratio. ACS Nano. 2018; 12(2): 986–993. doi: 10.1021/acsnano.7b07460
82. Vasyukova IA, Zakharova OV, Kuznetsov DV, et al. Synthesis, Toxicity Assessment, Environmental and Biomedical Applications of MXenes: A Review. Nanomaterials. 2022; 12(11): 1797. doi: 10.3390/nano12111797
83. Huang M, Gu Z, Zhang J, et al. MXene and black phosphorus based 2D nanomaterials in bioimaging and biosensing: progress and perspectives. Journal of Materials Chemistry B. 2021; 9(26): 5195–5220. doi: 10.1039/d1tb00410g
84. Huang H, Jiang R, Feng Y, et al. Recent development and prospects of surface modification and biomedical applications of MXenes. Nanoscale. 2020; 12(3): 1325–1338. doi: 10.1039/c9nr07616f
85. Lee E, VahidMohammadi A, Prorok BC, et al. Room Temperature Gas Sensing of Two-Dimensional Titanium Carbide (MXene). ACS Applied Materials & Interfaces. 2017; 9(42): 37184–37190. doi: 10.1021/acsami.7b11055
86. Sinha A, Dhanjai, Zhao H, et al. MXene: An emerging material for sensing and biosensing. TrAC Trends in Analytical Chemistry. 2018; 105: 424–435. doi: 10.1016/j.trac.2018.05.021
87. Yin T, Cheng Y, Hou Y, et al. 3D Porous Structure in MXene/PANI Foam for a High-Performance Flexible Pressure Sensor. Small. 2022; 18(48). doi: 10.1002/smll.202204806
88. Wang X, Lu J, Lu S, et al. Health monitoring of repaired composite structure using MXene sensor. Composites Communications. 2021; 27: 100850. doi: 10.1016/j.coco.2021.100850
89. George SM, Kandasubramanian B. Advancements in MXene-Polymer composites for various biomedical applications. Ceramics International. 2020; 46(7): 8522–8535. doi: 10.1016/j.ceramint.2019.12.257
90. Yang X, Zhang C, Deng D, et al. Multiple Stimuli-Responsive MXene-Based Hydrogel as Intelligent Drug Delivery Carriers for Deep Chronic Wound Healing. Small. 2021; 18(5). doi: 10.1002/smll.202104368
91. Huang J, Li Z, Mao Y, et al. Progress and biomedical applications of MXenes. Nano Select. 2021; 2(8): 1480–1508. doi: 10.1002/nano.202000309
92. Mohajer F, Ziarani GM, Badiei A, et al. Advanced MXene-Based Micro- and Nanosystems for Targeted Drug Delivery in Cancer Therapy. Micromachines. 2022; 13(10): 1773. doi: 10.3390/mi13101773
93. Liu A, Liu Y, Liu G, et al. Engineering of surface modified Ti3C2Tx MXene based dually controlled drug release system for synergistic multi-therapies of cancer. Chemical Engineering Journal. 2022; 448: 137691. doi: 10.1016/j.cej.2022.137691
94. Dong Y, Li S, Li X, et al. Smart MXene/agarose hydrogel with photothermal property for controlled drug release. International Journal of Biological Macromolecules. 2021; 190: 693–699. doi: 10.1016/j.ijbiomac.2021.09.037
95. Zhang WJ, Li S, Vijayan V, et al. ROS- and pH-Responsive Polydopamine Functionalized Ti3C2Tx MXene-Based Nanoparticles as Drug Delivery Nanocarriers with High Antibacterial Activity. Nanomaterials. 2022; 12(24): 4392. doi: 10.3390/nano12244392
96. Wu Z, Shi J, Song P, et al. Chitosan/hyaluronic acid based hollow microcapsules equipped with MXene/gold nanorods for synergistically enhanced near infrared responsive drug delivery. International Journal of Biological Macromolecules. 2021; 183: 870–879. doi: 10.1016/j.ijbiomac.2021.04.164
97. Liu Y, Tian Y, Han Q, et al. Synergism of 2D/1D MXene/cobalt nanowire heterojunctions for boosted photo-activated antibacterial application. Chemical Engineering Journal. 2021; 410: 128209. doi: 10.1016/j.cej.2020.128209
98. Nguyen VH, Nguyen BS, Hu C, et al. Novel Architecture Titanium Carbide (Ti3C2Tx) MXene Cocatalysts toward Photocatalytic Hydrogen Production: A Mini-Review. Nanomaterials. 2020; 10(4): 602. doi: 10.3390/nano10040602
99. Koyappayil A, Chavan SG, Mohammadniaei M, et al. β-Hydroxybutyrate dehydrogenase decorated MXene nanosheets for the amperometric determination of β-hydroxybutyrate. Microchimica Acta. 2020; 187(5). doi: 10.1007/s00604-020-04258-y
100. Zhang J, Fu Y, Mo A. Multilayered Titanium Carbide MXene Film for Guided Bone Regeneration. International Journal of Nanomedicine. 2019; 14: 10091–10103. doi: 10.2147/ijn.s227830
101. Huang J, Su J, Hou Z, et al. The cytocompatibility of Ti3C2Tx MXene with Red Blood Cells and Human Umbilical Vein Endothelial Cells and the Underlying Mechanisms. Chemical Research in Toxicology. 2023; 36(3): 347–359. doi: 10.1021/acs.chemrestox.2c00154
102. Usman KAS, Yao Y, Bacal CJO, et al. Robust Biocompatible Fibers from Silk Fibroin Coated MXene Sheets. Advanced

Materials Interfaces. 2023; 10(9). doi: 10.1002/admi.202201634

103. Neubertova V, Guselnikova O, Yamauchi Y, et al. Covalent functionalization of Ti3C2T MXene flakes with Gd-DTPA complex for stable and biocompatible MRI contrast agent. Chemical Engineering Journal. 2022; 446: 136939. doi: 10.1016/j.cej.2022.136939
104. Yang Z, Fu X, Ma D, et al. Growth Factor-Decorated Ti3C2 MXene/MoS2 2D Bio-Heterojunctions with Quad-Channel Photonic Disinfection for Effective Regeneration of Bacteria-Invaded Cutaneous Tissue. Small. 2021; 17(50). doi: 10.1002/smll.202103993
105. Scheibe B, Wychowaniec JK, Scheibe M, et al. Cytotoxicity Assessment of Ti-Al-C Based MAX Phases and Ti3C2Tx MXenes on Human Fibroblasts and Cervical Cancer Cells. ACS Biomaterials Science & Engineering. 2019; 5(12): 6557–6569. doi: 10.1021/acsbiomaterials.9b01476
106. Amini S, Salehi H, Setayeshmehr M, et al. Natural and synthetic polymeric scaffolds used in peripheral nerve tissue engineering: Advantages and disadvantages. Polymers for Advanced Technologies. 2021; 32(6): 2267–2289. doi: 10.1002/pat.5263
107. Katz-Demyanetz A, Koptyug A, Popov VV. In-situ Alloying as a Novel Methodology in Additive Manufacturing. In: Proceedings of the 2020 IEEE 10th International Conference Nanomaterials: Applications & Properties (NAP). 2020. doi: 10.1109/nap51477.2020.9309652
108. Yi S, Liu G, Liu Z, et al. Theoretical insights into nitrogen fixation on Ti_2C and Ti_2CO_2 in a lithium-nitrogen battery. Journal of Materials Chemistry A. 2019; 7(34): 19950–19960. doi: 10.1039/c9ta06232g
109. Wei S, Wang C, Chen S, et al. Dial the Mechanism Switch of VN from Conversion to Intercalation toward Long Cycling Sodium-Ion Battery. Advanced Energy Materials. 2020; 10(12). doi: 10.1002/aenm.201903712
110. Wang C, Wei S, Chen S, et al. Delaminating Vanadium Carbides for Zinc-Ion Storage: Hydrate Precipitation and H_+/Zn_{2+} Co-Action Mechanism. Small Methods. 2019; 3(12). doi: 10.1002/smtd.201900495
111. Ming F, Liang H, Zhang W, et al. Porous MXenes enable high performance potassium ion capacitors. Nano Energy. 2019; 62: 853–860. doi: 10.1016/j.nanoen.2019.06.013
112. Zhong J, Sun W, Wei Q, et al. Efficient and scalable synthesis of highly aligned and compact two-dimensional nanosheet films with record performances. Nature Communications. 2018; 9(1). doi: 10.1038/s41467-018-05723-2

Characterization and Application of Nanomaterials 2024, 7(2), 8543.
https://doi.org/10.24294/can.v7i2.8543

Review

Carbon nanomaterials for efficient oxygen and hydrogen evolution reactions in water splitting: A review

Razu Shahazi[1], Amirul Islam Saddam[1], Md. Rakibul Islam[1], Md. Kawsar Mahamud[1],
Mohammed Muzibur Rahman[2,3], Md. Mahmud Alam[1,2,*]

[1] Department of Chemical Engineering, Z. H. Sikder University of Science and Technology (ZHSUST), Shariatpur 8024, Bangladesh
[2] Center of Excellence for Advanced Materials Research (CEAMR), King Abdulaziz University, Jeddah 80203, Saudi Arabia
[3] Chemistry Department, Faculty of Science, King Abdulaziz University, Jeddah 80203, Saudi Arabia
*** Corresponding author:** Md. Mahmud Alam, alam-mahmud@hotmail.com, mmalam@zhsust.ac.bd

CITATION

Shahazi R, Saddam AI, Islam MR, et al. Carbon nanomaterials for efficient oxygen and hydrogen evolution reactions in water splitting: A review. Characterization and Application of Nanomaterials. 2024. 7(2): 8543.
https://doi.org/10.24294/can.v7i2.8543

ARTICLE INFO

Received: 13 August 2024
Accepted: 10 October 2024
Available online: 28 October 2024

Abstract: Water splitting has gained significant attention as a means to produce clean and sustainable hydrogen fuel through the electrochemical or photoelectrochemical decomposition of water. Efficient and cost-effective water splitting requires the development of highly active and stable catalysts for the oxygen evolution reaction (OER) and hydrogen evolution reaction (HER). Carbon nanomaterials, including carbon nanotubes, graphene, and carbon nanofibers, etc., have emerged as promising candidates for catalyzing these reactions due to their unique properties, such as high surface area, excellent electrical conductivity, and chemical stability. This review article provides an overview of recent advancements in the utilization of carbon nanomaterials as catalysts or catalyst supports for the OER and HER in water splitting. It discusses various strategies employed to enhance the catalytic activity and stability of carbon nanomaterials, such as surface functionalization, hybridization with other active materials, and optimization of nanostructure and morphology. The influence of carbon nanomaterial properties, such as defect density, doping, and surface chemistry, on electrochemical performance is also explored. Furthermore, the article highlights the challenges and opportunities in the field, including scalability, long-term stability, and integration of carbon nanomaterials into practical water splitting devices. Overall, carbon nanomaterials show great potential for advancing the field of water splitting and enabling the realization of efficient and sustainable hydrogen production.

Keywords: oxygen evolution reaction (OER); hydrogen evolution reaction (HER); carbon nanomaterials; surface functionalization; optimization of nanostructure and morphology

1. Introduction

Water splitting, the process of converting water into oxygen and hydrogen gases, has emerged as a promising avenue for sustainable energy production and storage. It offers a pathway to generate clean and renewable hydrogen fuel, which can be used as a versatile energy carrier. The efficient catalysis of the oxygen evolution reaction (OER) and hydrogen evolution reaction (HER) remains a critical challenge in water splitting technologies [1,2]. Catalysts used in the oxygen evolution reaction frequently experience stability problems when exposed to harsh oxidative environments, resulting in degradation and a decrease in catalytic performance over time. The oxygen evolution reaction generally necessitates a high overpotential to achieve a substantial reaction rate, diminishing overall efficiency. Many of the best catalysts for OER and HER use noble metals such as platinum, iridium, and ruthenium, which are rare and costly. This restricts their widespread use and highlights the need for affordable and abundant alternatives. Achieving high efficiency and selectivity in both OER and HER is difficult because of competing side reactions and the necessity for precise control over the reaction environment and catalyst properties [3–5]. To address this challenge, researchers have turned their attention to carbon nanomaterials, which exhibit unique structural and electronic properties that make them attractive candidates for efficient catalysis in water splitting. Carbon nanomaterials, such as carbon nanotubes, graphene, and carbon nanofibers, possess exceptional characteristics, including high surface area, excellent electrical conductivity, and chemical stability [6,7]. The high surface area of carbon nanomaterials provides a large number of active sites for catalytic reactions, facilitating the adsorption and activation of reactant molecules. This leads to increased reaction kinetics and improved catalytic efficiency. Furthermore, the excellent electrical conductivity of carbon nanomaterials enables efficient charge transfer during electrochemical reactions, reducing energy losses and enhancing overall catalytic activity [8–10].

The chemical stability of carbon nanomaterials is another advantageous attribute for water splitting. Their robust nature allows them to withstand harsh reaction conditions, such as high temperatures and corrosive environments, ensuring long-term durability and catalytic performance [11,12]. In recent years, extensive research efforts have been dedicated to exploring the catalytic properties and performance of carbon nanomaterials in water splitting. Various strategies have been employed to optimize their catalytic activity, including surface functionalization, heteroatom doping, and incorporation of other active materials. These approaches aim to enhance the catalytic efficiency, selectivity, and stability of carbon-based catalysts for both the OER and HER [13,14].

This review aims to provide an overview of the recent advancements in the utilization of carbon nanomaterials for efficient OER and HER in water splitting. It will discuss the fundamental mechanisms underlying their catalytic activity, highlight the strategies employed to enhance their performance, and address the challenges associated with their implementation in practical water splitting systems. Additionally, future research directions and opportunities for the development of carbon nanomaterial-based catalysts will be explored.

2. Importance of water splitting for sustainable energy production

Water splitting is of paramount importance for sustainable energy production because it can harness and utilize hydrogen as a clean and renewable energy source.

2.1. Hydrogen fuel

Water splitting enables the production of hydrogen gas (H_2), which can be used as a fuel in various applications. Hydrogen is a versatile energy carrier that can be used in fuel cells to generate electricity or directly combusted. Unlike fossil fuels, hydrogen combustion or utilization in fuel cells produces only water as a byproduct, making it a clean and environmentally friendly energy option [15].

2.2. Renewable energy storage

One of the significant challenges with renewable energy sources like solar and wind is their intermittent nature. Water splitting offers a way to store excess renewable energy by converting it into hydrogen [16]. The generated hydrogen can be stored and used later when energy demand exceeds supply, providing a reliable and controllable energy storage option. This helps to balance the intermittent nature of renewables and ensures a consistent energy supply.

2.3. Decarbonization

Hydrogen produced through water splitting can play a vital role in decarbonizing various sectors of the economy. When hydrogen is produced using renewable electricity, the entire process becomes carbon-neutral or even carbon-free [17]. By substituting hydrogen for fossil fuels in transportation, heating, and industrial processes, we can significantly reduce greenhouse gas emissions and mitigate climate change.

2.4. Industrial applications

Water splitting and the production of hydrogen can revolutionize various industrial processes. Hydrogen can be used as a feedstock for producing chemicals, such as ammonia and methanol, replacing fossil fuel-based methods [18]. This enables the decarbonization of industries and promotes a more sustainable and environmentally friendly manufacturing sector.

2.5. Transportation

Water splitting enables the production of hydrogen fuel for transportation applications. Hydrogen fuel cells can power vehicles, including cars, buses, trucks, and trains [19]. Hydrogen fuel cell vehicles emit only water vapor, offering a zero-emission alternative to conventional fossil fuel-powered vehicles [20]. By transitioning to hydrogen-powered transportation, we can significantly reduce air pollution and dependence on fossil fuels.

2.6. Grid flexibility

Water splitting and hydrogen production contribute to grid flexibility and stability. By utilizing excess renewable energy to produce hydrogen, we can effectively store energy and balance the electricity grid. Hydrogen can be converted back to electricity during peak demand periods, ensuring a stable power supply and enhancing the resilience of the grid [21].

3. Potential of carbon nanomaterials as catalysts or catalyst supports

Carbon nanomaterials, such as carbon nanotubes (CNTs), graphene, and carbon nanofibers, show significant potential as catalysts or catalyst supports for water-splitting reactions. Here are some key reasons for their attractiveness in this field:

3.1. High surface area

Carbon nanomaterials possess a large surface area per unit mass or volume. This high surface area provides abundant active sites for catalytic reactions, allowing for efficient utilization of the catalyst and enhancing reaction rates [22,23].

3.2. Chemical stability

Carbon nanomaterials exhibit excellent chemical stability, which is crucial for withstanding the harsh conditions of water-splitting reactions. They are resistant to corrosion and degradation, ensuring long-term catalytic activity and durability [24,25].

3.3. Electrical conductivity

Several carbon nanomaterials, such as CNTs and graphene, exhibit excellent electrical conductivity. This property enables efficient charge transfer during electrochemical reactions, minimizing energy losses and improving overall catalytic performance [26,27].

3.4. Tailorable properties

Carbon nanomaterials offer versatility in terms of their structural and surface properties. Their morphology, surface chemistry, and functionalization can be tailored to optimize catalytic activity, selectivity, and stability for specific water-splitting reactions [28,29].

3.5. Catalyst support

Carbon nanomaterials can serve as excellent supports for other catalyst materials, such as metal nanoparticles or metal oxides. The high surface area and unique structural features of carbon nanomaterials facilitate the dispersion and stabilization of active catalyst particles, enhancing their catalytic performance [30,31]. **Figure 1** demonstrates the use of graphene sheets as catalyst supports.

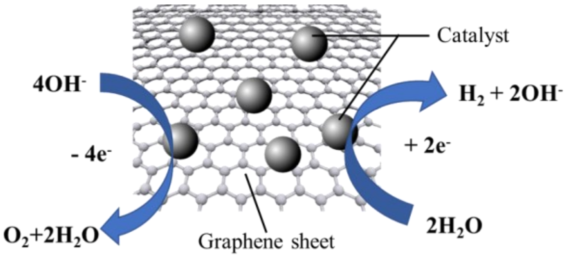

Figure 1. Graphene as catalyst support.

3.6. Abundance and low cost

Carbon is an abundant and relatively low-cost element. Carbon nanomaterials can be synthesized from various carbon sources, making them economically favorable for large-scale production and implementation in water splitting technologies [32,33].

3.7. Synergistic effects

Carbon nanomaterials can exhibit synergistic effects when combined with other catalyst materials. For example, the integration of carbon nanomaterials with transition metal-based catalysts can lead to enhanced catalytic activity and stability through synergistic interactions and improved electron transfer pathways [34,35].

While carbon nanomaterials hold great potential, challenges still exist. These include further enhancing catalytic activity, improving mass transport limitations, minimizing side reactions, and addressing potential issues such as catalyst poisoning or surface fouling. Continued research and development efforts are focused on optimizing carbon nanomaterials and harnessing their full potential as catalysts or catalyst supports for water splitting, contributing to the advancement of sustainable energy production.

4. Carbon nanomaterials for OER and HER

Carbon nanomaterials have shown great potential as catalysts for both the hydrogen evolution reaction (HER) and the oxygen evolution reaction (OER), which are essential processes in water splitting for hydrogen production and in various energy conversion and storage technologies. **Figure 2** depicts a range of carbon nanomaterials. Here's an overview of the potential of carbon nanomaterials for HER and OER:

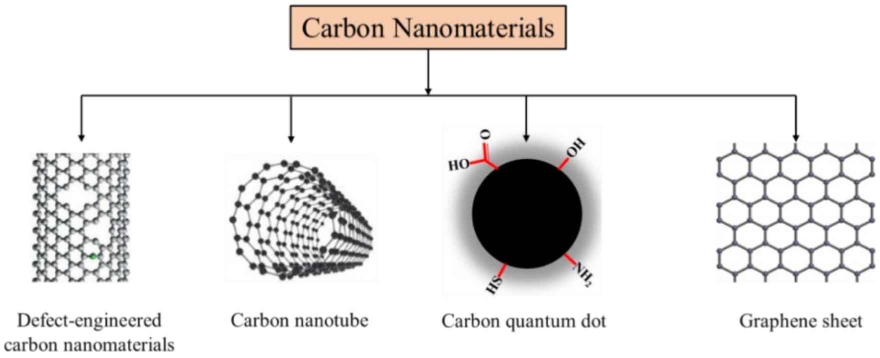

Figure 2. Various types of carbon nanomaterials.

4.1. Carbon nanotubes (CNTs)

CNTs possess high electrical conductivity, a large surface area, and unique tubular structures, making them attractive catalysts for both HER and OER. Their conductivity facilitates efficient charge transfer during the electrochemical reactions, while their high surface area provides abundant active sites. Functionalization of CNTs with metal nanoparticles or heteroatoms can further enhance their catalytic activity for both HER and OER [36–39].

4.2. Graphene

Graphene, a two-dimensional carbon material, exhibits excellent electrical conductivity and a large surface area, making it a promising catalyst for HER and OER. Pristine graphene itself has limited intrinsic activity. Strategies such as functionalization, doping, or hybridization with other materials have been explored to enhance its catalytic performance for both reactions [40,41].

4.3. Carbon nitride (C_3N_4)

Carbon nitride-based materials, such as graphitic carbon nitride (g-C_3N_4), have emerged as metal-free catalysts for both HER and OER. The structure of graphitic carbon nitride is demonstrated in **Figure 3**. These materials are abundant, low-cost, and environmentally friendly. Their unique electronic structure enables efficient charge transfer and catalytic activity during both reactions. Further modifications and optimization are required to improve their intrinsic activity and stability [42,43]. Modifications may include tailoring the shape and surface characteristics of g-C_3N_4, doping with other elements, or forming composites with other materials. These changes are intended to improve light absorption characteristics, expand the number of active sites accessible for catalytic reactions, and strengthen the material's overall resilience to operating conditions [44,45].

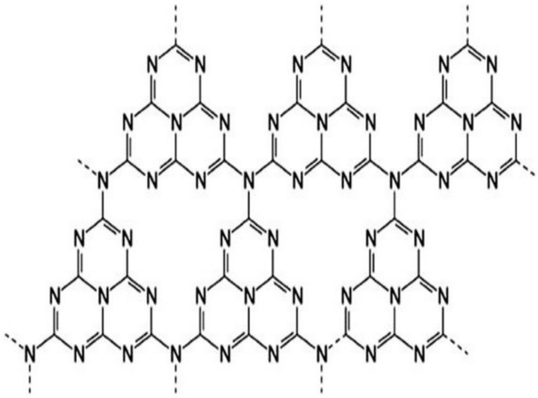

Figure 3. Structure of graphitic carbon nitride (g-C_3N_4).

4.4. Carbon quantum dots (CQDs)

Carbon quantum dots, small carbon nanoparticles, have shown promise as catalysts for both HER and OER. Their unique quantum confinement effects and tunable surface properties enable efficient charge transfer and catalytic activity. Surface functionalization or doping of CQDs with heteroatoms or metal species can further enhance their performance for both reactions [46–48].

4.5. Defect-engineered carbon materials

Introducing defects or heteroatoms into carbon nanomaterials can significantly influence their electronic structure and surface reactivity, enhancing their catalytic activity for both HER and OER. Defect engineering provides additional active sites and improves charge transfer kinetics. Tailoring the defect density and distribution can optimize the performance of carbon nanomaterials for both reactions [49,50].

While carbon nanomaterials hold promise for HER and OER catalysis, challenges remain in enhancing their intrinsic activity, stability, and mass transport properties. Additionally, understanding the underlying mechanisms and optimizing the catalyst design are ongoing research areas. Nonetheless, carbon nanomaterials offer exciting opportunities to advance HER and OER catalysis and enable efficient and sustainable energy conversion and storage technologies [51].

5. Carbon nanomaterial hybridization with other materials for enhanced catalysis

Hybridization of carbon nanomaterials with other materials has been extensively explored to enhance water splitting catalysis, particularly in the context of the hydrogen evolution reaction (HER) and the oxygen evolution reaction (OER). Here are some examples of carbon nanomaterials hybridized with other materials for enhanced water splitting catalysis.

5.1. Carbon nanotubes (CNTs) and metal nanoparticles

CNTs can be hybridized with metal nanoparticles, such as platinum (Pt), palladium (Pd), or nickel (Ni), to form composite catalysts. Metal nanoparticles may be applied to the surface of carbon nanotubes (CNTs) to create a composite material, as seen in **Figure 4**. The metal nanoparticles provide high catalytic activity, while the CNTs act as conductive supports, facilitating electron transfer during the reactions. The hybridization enhances the overall catalytic performance and stability [52,53].

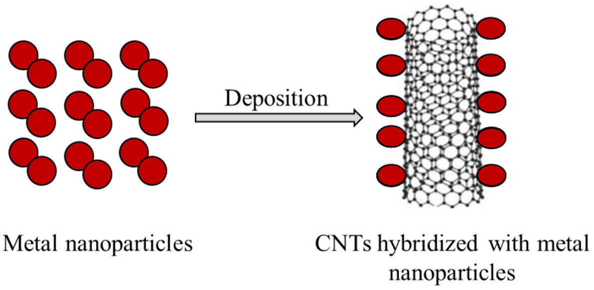

Figure 4. Deposition of metal nanoparticles on carbon nanotube.

5.2. Graphene and metal oxides

Graphene can be combined with metal oxides, such as titanium dioxide (TiO_2), iron oxide (Fe_2O_3), or cobalt oxide (Co_3O_4), to form composite catalysts. The metal oxides provide high catalytic activity, while graphene offers excellent electrical conductivity and large surface area. The hybrid structure promotes efficient charge transfer and provides additional active sites, enhancing the water splitting catalysis [54–56].

5.3. Carbon nitride (C_3N_4) and transition metal compounds

Carbon nitride-based materials, such as graphitic carbon nitride (g-C_3N_4), can be hybridized with transition metal compounds, including metal oxides or sulfides, to form composite catalysts. The transition metal compounds provide catalytic activity, while carbon nitride offers a stable and conductive support. The hybridization promotes synergistic effects, leading to enhanced water splitting catalysis [57–60].

5.4. Carbon quantum dots (CQDs) and semiconductor nanomaterials

Carbon quantum dots can be combined with semiconductor nanomaterials, such as metal chalcogenides (e.g., MoS_2, WS_2) or metal oxides (e.g., ZnO, WO_3), to form hybrid catalysts. The semiconductor nanomaterials provide light absorption and charge separation capabilities, while carbon quantum dots contribute to improved charge transfer and catalytic activity. The hybridization enables efficient utilization of solar energy for water splitting [61–65].

5.5. Carbon-based heterostructures

Carbon nanomaterials, such as CNTs or graphene, can be integrated with other functional materials, such as metal nanoparticles, metal oxides, or semiconductor nanomaterials, to form complex heterostructures. The combination of different materials in the heterostructures allows for synergistic effects, enhanced catalytic activity, and improved charge transfer kinetics [66–68].

Hybridization strategies enable the integration of the unique properties of carbon nanomaterials with those of other materials, leading to enhanced water splitting catalysis. The resulting hybrid catalysts can exhibit improved activity, stability, and efficiency, which are crucial for advancing water splitting technologies for sustainable hydrogen production and energy storage.

6. Challenges and future perspectives

Carbon nanomaterials have shown great potential for water splitting applications, but there are several challenges that need to be addressed for their effective implementation. Additionally, there are several future perspectives that can drive further advancements in this field. Here are the challenges and future perspectives of carbon nanomaterials in water splitting:

6.1. Challenges

Catalyzing the oxygen evolution reaction (OER) and hydrogen evolution reaction (HER) is crucial for efficient water splitting and sustainable energy production. Several challenges exist in developing effective catalysts for these reactions. Both OER and HER are kinetically sluggish processes, meaning that the reaction rates are relatively slow. This limits the overall efficiency and scalability of water splitting systems [69,70]. Catalysts need to accelerate the reaction rates and improve the kinetics to enhance the performance of the reactions. These reactions typically require a significant overpotential, which is the additional energy input needed to drive the reactions. High overpotentials result in increased energy losses and reduced overall efficiency [71–73]. Developing catalysts that can minimize the overpotential required for these reactions is a major challenge. Catalysts for OER and HER must be stable and durable under the harsh conditions of water splitting, including high temperatures, corrosive electrolytes, and repeated cycling. Many catalyst materials suffer from degradation, corrosion, particle detachment, or surface restructuring over time, leading to reduced activity and performance. An illustration of carbon corrosion and particle detachment is shown in **Figure 5**. Developing catalysts with high stability and durability is crucial for long-term and practical applications. The widespread adoption of water splitting technologies depends on the availability and affordability of catalyst materials. Some catalysts, such as those based on precious metals like platinum [74,75] and iridium [76,77], are expensive and scarce, limiting their large-scale deployment.

Developing catalysts based on Earth-abundant elements or low-cost materials is important for making water splitting economically viable.

Efficient water splitting systems require the integration of OER and HER catalysts with other components, such as electrodes, membranes, and electrolytes. Achieving optimal compatibility and synergy among these components is challenging. Catalyst designs that can facilitate effective coupling with other system components are crucial for maximizing overall performance. Achieving high selectivity for either OER or HER is desirable to minimize energy losses and maximize overall water splitting efficiency. Catalysts may exhibit side reactions or undesired reactions, leading to reduced selectivity. Developing catalysts that can selectively promote either OER or HER without significant crossover or side reactions is a challenge. For practical implementation, catalysts need to be scalable, meaning they should be easily synthesized, fabricated, and deployed at a large scale. Some catalyst materials may face limitations in terms of scalability due to complex synthesis methods or high-cost fabrication techniques. Developing scalable catalyst synthesis and manufacturing processes is important for commercialization.

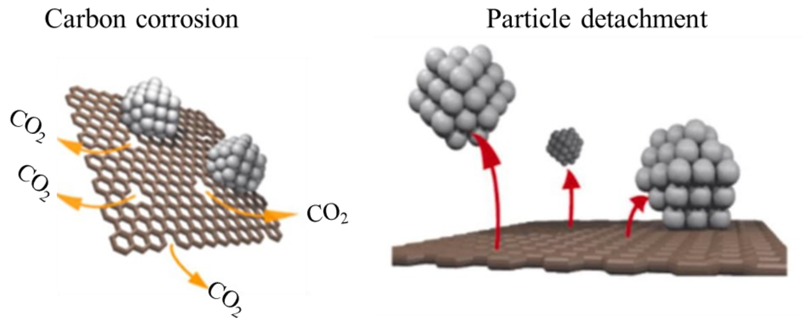

Figure 5. The reduction of catalyst activity through carbon corrosion and particle detachment.

Thus, addressing these challenges requires a multidisciplinary approach involving materials science, electrochemistry, catalysis, and engineering. Researchers are actively exploring new catalyst materials, nanostructured architectures, surface modifications, and advanced characterization techniques to overcome these hurdles and develop efficient and stable catalysts for OER and HER in water splitting systems. The key points are presented in the forthcoming paragraphs.

6.1.1. Limited catalytic activity

Carbon nanomaterials, such as carbon nanotubes and graphene, often exhibit limited intrinsic catalytic activity for water splitting reactions. Enhancing their catalytic performance is crucial for achieving efficient water splitting. Future research should focus on developing strategies to improve the catalytic activity of carbon nanomaterials through doping, functionalization, and structural modifications.

6.1.2. Stability and durability

Carbon nanomaterials can suffer from degradation and oxidation under harsh water splitting conditions, leading to reduced stability and durability. Improving the stability and durability of carbon nanomaterials is essential for long-term performance.

Future research should investigate protective coatings, surface modifications, and composite structures to enhance the stability and durability of carbon nanomaterials.

6.1.3. Mass transport limitations

Carbon nanomaterials often possess high surface area but limited porosity, which can hinder the mass transport of reactants to the catalytic sites. Improving mass transport is crucial for efficient water splitting. Future research should focus on optimizing the porous structure and surface morphology of carbon nanomaterials to enhance reactant diffusion and accessibility to active sites.

6.1.4. Cost and scalability

The cost-effective synthesis and large-scale production of carbon nanomaterials remain a challenge. Many carbon nanomaterials are still produced through complex and expensive methods. Future research should explore scalable synthesis routes and cost-effective fabrication techniques to enable the widespread implementation of carbon nanomaterials in water splitting technologies.

Integration with Other Components: Carbon nanomaterials often need to be integrated with other components, such as electrodes and membranes, in water splitting systems. Achieving effective integration and compatibility between carbon nanomaterials and other components is crucial for overall system performance. Future research should focus on developing suitable interfaces and interfacial engineering strategies to enable efficient integration of carbon nanomaterials with other functional components.

6.2. Future perspectives

6.2.1. Advanced catalyst design

Future research should focus on the rational design of carbon nanomaterial-based catalysts. This includes tailoring the morphology, structure, and composition of carbon nanomaterials to optimize their catalytic activity. Additionally, exploring novel carbon nanomaterials and hybrid systems can lead to breakthroughs in water splitting catalysis.

6.2.2. Synergistic hybrid materials

The combination of carbon nanomaterials with other functional materials, such as metal nanoparticles or metal oxides, can create synergistic effects and enhance water splitting performance. Future research should explore the development of hybrid materials that leverage the unique properties of carbon nanomaterials and other materials to achieve improved catalytic activity and stability.

6.2.3. Electrocatalysis and photocatalysis

Carbon nanomaterials can be employed in both electrocatalytic and photocatalytic water splitting systems. Future research should investigate the fundamental mechanisms and optimize the parameters for efficient electrocatalysis and photocatalysis using carbon nanomaterials. This includes exploring new carbon nanomaterial-based electrode architectures and tuning their band structures for enhanced performance.

6.2.4. Integration with renewable energy sources

Carbon nanomaterials can be integrated with renewable energy sources, such as solar energy or wind energy, to achieve sustainable and clean water splitting. Future research should explore the synergistic integration of carbon nanomaterials with renewable energy systems to develop efficient and environmentally friendly water splitting technologies.

6.2.5. Environmental impact assessment

As with any nanomaterial, it is essential to consider the potential environmental impact of carbon nanomaterials. Future research should focus on comprehensive environmental impact assessments to ensure the safe and sustainable implementation of carbon nanomaterials in water splitting technologies.

Addressing these challenges and exploring the future perspectives will drive the advancement of carbon nanomaterials in water splitting, enabling the development of efficient and sustainable hydrogen production systems. Continued research, collaboration, and innovation are crucial for realizing the full potential of carbon nanomaterials in this field.

7. Conclusion

In conclusion, carbon nanomaterials have emerged as promising catalysts for efficient oxygen and hydrogen evolution reactions in water splitting. They offer several advantages, including high surface area, tunable properties, and chemical stability. There are still challenges that need to be addressed to fully exploit their potential. Enhancing the catalytic activity and stability of carbon nanomaterials is a key focus for future research. Strategies such as doping, functionalization, and structural modifications can be employed to improve their intrinsic activity and durability. Additionally, optimizing the porous structure and surface morphology of carbon nanomaterials can enhance mass transport and reaction kinetics. The scalability and cost-effectiveness of carbon nanomaterials also require attention. Developing scalable synthesis methods and cost-effective fabrication techniques is essential for their large-scale production and practical implementation in water splitting technologies. Future perspectives include advanced catalyst design, exploring synergistic hybrid materials, and leveraging carbon nanomaterials in electrocatalytic and photocatalytic systems. The integration of carbon nanomaterials with renewable energy sources holds promise for sustainable water splitting. Additionally, comprehensive environmental impact assessments are crucial to ensuring the safe and responsible use of carbon nanomaterials. Overall, with continued research, innovation, and interdisciplinary collaborations, carbon nanomaterials have the potential to play a significant role in achieving efficient and sustainable water splitting, contributing to the development of clean energy systems, and addressing global energy challenges.

Conflict of interest: The authors declare no conflict of interest.

References

1. Liu Y, Zhou D, Deng T, et al. Research Progress of Oxygen Evolution Reaction Catalysts for Electrochemical Water Splitting. ChemSusChem. 2021; 14(24): 5359-5383. doi: 10.1002/cssc.202101898
2. Yu Z, Duan Y, Feng X, et al. Clean and Affordable Hydrogen Fuel from Alkaline Water Splitting: Past, Recent Progress, and Future Prospects. Advanced Materials. 2021; 33(31). doi: 10.1002/adma.202007100

3. Xie X, Du L, Yan L, et al. Oxygen Evolution Reaction in Alkaline Environment: Material Challenges and Solutions. Advanced Functional Materials. 2022; 32(21). doi: 10.1002/adfm.202110036
4. Thao NTT, Jang JU, Nayak AK, et al. Current Trends of Iridium-Based Catalysts for Oxygen Evolution Reaction in Acidic Water Electrolysis. Small Science. 2023; 4(1). doi: 10.1002/smsc.202300109
5. Raveendran A, Chandran M, Dhanusuraman R. A comprehensive review on the electrochemical parameters and recent material development of electrochemical water splitting electrocatalysts. RSC Advances. 2023; 13(6): 3843-3876. doi: 10.1039/d2ra07642j
6. Yadav D, Amini F, Ehrmann A. Recent advances in carbon nanofibers and their applications – A review. European Polymer Journal. 2020; 138: 109963. doi: 10.1016/j.eurpolymj.2020.109963
7. Gaur M, Misra C, Yadav AB, et al. Biomedical Applications of Carbon Nanomaterials: Fullerenes, Quantum Dots, Nanotubes, Nanofibers, and Graphene. Materials. 2021; 14(20): 5978. doi: 10.3390/ma14205978
8. Riyajuddin S, Azmi K, Pahuja M, et al. Super-Hydrophilic Hierarchical Ni-Foam-Graphene-Carbon Nanotubes-Ni_2P–CuP_2 Nano-Architecture as Efficient Electrocatalyst for Overall Water Splitting. ACS Nano. 2021; 15(3): 5586-5599. doi: 10.1021/acsnano.1c00647
9. Majeed A, Li X, Hou PX, et al. Monolayer carbon-encapsulated Mo-doped Ni nanoparticles anchored on single-wall carbon nanotube film for total water splitting. Applied Catalysis B: Environmental. 2020; 269: 118823. doi: 10.1016/j.apcatb.2020.118823
10. Xing X, Liu R, Anjass M, et al. Bimetallic manganese-vanadium functionalized N,S-doped carbon nanotubes as efficient oxygen evolution and oxygen reduction electrocatalysts. Applied Catalysis B: Environmental. 2020; 277: 119195. doi: 10.1016/j.apcatb.2020.119195
11. Li W, Wang C, Lu X. Integrated transition metal and compounds with carbon nanomaterials for electrochemical water splitting. Journal of Materials Chemistry A. 2021; 9(7): 3786-3827. doi: 10.1039/d0ta09495a
12. Yang D, Hou W, Lu Y, et al. Cobalt phosphide nanoparticles supported within network of N-doped carbon nanotubes as a multifunctional and scalable electrocatalyst for water splitting. Journal of Energy Chemistry. 2021; 52: 130-138. doi: 10.1016/j.jechem.2020.04.005
13. Noor T, Yaqoob L, Iqbal N. Recent Advances in Electrocatalysis of Oxygen Evolution Reaction using Noble-Metal, Transition-Metal, and Carbon-Based Materials. ChemElectroChem. 2020; 8(3): 447-483. doi: 10.1002/celc.202001441
14. Wang J, Kong H, Zhang J, et al. Carbon-based electrocatalysts for sustainable energy applications. Progress in Materials Science. 2021; 116: 100717. doi: 10.1016/j.pmatsci.2020.100717
15. Sharma S, Agarwal S, Jain A. Significance of Hydrogen as Economic and Environmentally Friendly Fuel. Energies. 2021; 14(21): 7389. doi: 10.3390/en14217389
16. Ikuerowo T, Bade SO, Akinmoladun A, et al. The integration of wind and solar power to water electrolyzer for green hydrogen production. International Journal of Hydrogen Energy. 2024; 76: 75-96. doi: 10.1016/j.ijhydene.2024.02.139
17. Aslam S, Rani S, Lal K, et al. Electrochemical hydrogen production: sustainable hydrogen economy. Green Chemistry. 2023; 25(23): 9543-9573. doi: 10.1039/d3gc02849f
18. Le PA, Trung VD, Nguyen PL, et al. The current status of hydrogen energy: an overview. RSC Advances. 2023; 13(40): 28262-28287. doi: 10.1039/d3ra05158g
19. Rajalakshmi N, Balaji R, Ramakrishnan S. Recent developments in hydrogen fuel cells: Strengths and weaknesses. Sustainable Fuel Technologies Handbook. Published online 2021: 431-456. doi: 10.1016/b978-0-12-822989-7.00015-9
20. Guilbert D, Vitale G. Hydrogen as a Clean and Sustainable Energy Vector for Global Transition from Fossil-Based to Zero-Carbon. Clean Technologies. 2021; 3(4): 881-909. doi: 10.3390/cleantechnol3040051
21. Wang J, Wen J, Wang J, et al. Water electrolyzer operation scheduling for green hydrogen production: A review. Renewable and Sustainable Energy Reviews. 2024; 203: 114779. doi: 10.1016/j.rser.2024.114779
22. Zhang L, Shi Y, Wang Y, et al. Nanocarbon Catalysts: Recent Understanding Regarding the Active Sites. Advanced Science. 2020; 7(5). doi: 10.1002/advs.201902126
23. Asefa T, Tang C, Ramírez-Hernández M. Nanostructured Carbon Electrocatalysts for Energy Conversions. Small. 2021; 17(48). doi: 10.1002/smll.202007136
24. Nemiwal M, Zhang TC, Kumar D. Graphene-based electrocatalysts: Hydrogen evolution reactions and overall water splitting. International Journal of Hydrogen Energy. 2021; 46(41): 21401-21418. doi: 10.1016/j.ijhydene.2021.04.008

25. Ali M, Pervaiz E, Sikandar U, et al. A review on the recent developments in zirconium and carbon-based catalysts for photoelectrochemical water-splitting. International Journal of Hydrogen Energy. 2021; 46(35): 18257-18283. doi: 10.1016/j.ijhydene.2021.02.202
26. Thamaraiselvan C, Wang J, James DK, et al. Laser-induced graphene and carbon nanotubes as conductive carbon-based materials in environmental technology. Materials Today. 2020; 34: 115-131. doi: 10.1016/j.mattod.2019.08.014
27. Eivazzadeh-Keihan R, Bahojb Noruzi E, Chidar E, et al. Applications of carbon-based conductive nanomaterials in biosensors. Chemical Engineering Journal. 2022; 442: 136183. doi: 10.1016/j.cej.2022.136183
28. Yi J, El-Alami W, Song Y, et al. Emerging surface strategies on graphitic carbon nitride for solar driven water splitting. Chemical Engineering Journal. 2020; 382: 122812. doi: 10.1016/j.cej.2019.122812
29. Shi LN, Cui LT, Ji YR, et al. Towards high-performance electrocatalysts: Activity optimization strategy of 2D MXenes-based nanomaterials for water-splitting. Coordination Chemistry Reviews. 2022; 469: 214668. doi: 10.1016/j.ccr.2022.214668
30. Cong Y, Huang S, Mei Y, et al. Metal–Organic Frameworks-Derived Self-Supported Carbon-Based Composites for Electrocatalytic Water Splitting. Chemistry – A European Journal. 2021; 27(64): 15866-15888. doi: 10.1002/chem.202102209
31. Zhang X, Zhang X, Yang P, et al. Transition metals decorated g-C3N4/N-doped carbon nanotube catalysts for water splitting: A review. Journal of Electroanalytical Chemistry. 2021; 895: 115510. doi: 10.1016/j.jelechem.2021.115510
32. Chen Z, Wei W, Chen H, et al. Eco-designed electrocatalysts for water splitting: A path toward carbon neutrality. International Journal of Hydrogen Energy. 2023; 48(16): 6288-6307. doi: 10.1016/j.ijhydene.2022.03.046
33. Ashok A, Kumar A, Ponraj J, et al. Synthesis and growth mechanism of bamboo like N-doped CNT/Graphene nanostructure incorporated with hybrid metal nanoparticles for overall water splitting. Carbon. 2020; 170: 452-463. doi: 10.1016/j.carbon.2020.08.047
34. Muzammil A, Haider R, Wei W, et al. Emerging transition metal and carbon nanomaterial hybrids as electrocatalysts for water splitting: a brief review. Materials Horizons. 2023; 10(8): 2764-2799. doi: 10.1039/d3mh00335c
35. Song W, Li M, Wang C, et al. Electronic modulation and interface engineering of electrospun nanomaterials-based electrocatalysts toward water splitting. Carbon Energy. 2020; 3(1): 101-128. doi: 10.1002/cey2.85
36. Fan M, Cui J, Wu J, et al. Improving the Catalytic Activity of Carbon-Supported Single Atom Catalysts by Polynary Metal or Heteroatom Doping. Small. 2020; 16(22). doi: 10.1002/smll.201906782
37. He Q, Qiao S, Zhou Y, et al. Carbon Nanotubes-Based Electrocatalysts: Structural Regulation, Support Effect, and Synchrotron-Based Characterization. Advanced Functional Materials. 2021; 32(11). doi: 10.1002/adfm.202106684
38. Tavakkoli M, Flahaut E, Peljo P, et al. Mesoporous Single-Atom-Doped Graphene–Carbon Nanotube Hybrid: Synthesis and Tunable Electrocatalytic Activity for Oxygen Evolution and Reduction Reactions. ACS Catalysis. 2020; 10(8): 4647-4658. doi: 10.1021/acscatal.0c00352
39. Shahazi R, Majumdar S, Saddam AI, et al. Carbon nanomaterials for biomedical applications: A comprehensive review. Nano Carbons. 2023; 1(1): 448. doi: 10.59400/n-c.v1i1.448
40. Chandrasekaran S, Ma D, Ge Y, et al. Electronic structure engineering on two-dimensional (2D) electrocatalytic materials for oxygen reduction, oxygen evolution, and hydrogen evolution reactions. Nano Energy. 2020; 77: 105080. doi: 10.1016/j.nanoen.2020.105080
41. Gusmão R, Veselý M, Sofer Z. Recent Developments on the Single Atom Supported at 2D Materials Beyond Graphene as Catalysts. ACS Catalysis. 2020; 10(16): 9634-9648. doi: 10.1021/acscatal.0c02388
42. Wang S, Zhang J, Li B, et al. Engineered Graphitic Carbon Nitride-Based Photocatalysts for Visible-Light-Driven Water Splitting: A Review. Energy & Fuels. 2021; 35(8): 6504-6526. doi: 10.1021/acs.energyfuels.1c00503
43. Malik R, Tomer VK. State-of-the-art review of morphological advancements in graphitic carbon nitride (g-CN) for sustainable hydrogen production. Renewable and Sustainable Energy Reviews. 2021; 135: 110235. doi: 10.1016/j.rser.2020.110235
44. Yuan S, Dai L, Xie M, et al. Modification optimization and application of graphitic carbon nitride in photocatalysis: Current progress and future prospects. Chemical Engineering Science. 2024; 296: 120245. doi: 10.1016/j.ces.2024.120245
45. Zhang Y, Wu G, Feng F, et al. Synergetic effects of in-plane and interlayer dual regulation on sandworm-like graphitic carbon nitride for high-efficiency photocatalytic performance. Optical Materials. 2024; 147: 114742. doi: 10.1016/j.optmat.2023.114742

46. Li W, Wei Z, Wang B, et al. Carbon quantum dots enhanced the activity for the hydrogen evolution reaction in ruthenium-based electrocatalysts. Materials Chemistry Frontiers. 2020; 4(1): 277-284. doi: 10.1039/c9qm00618d
47. Yang S, Du R, Yu Y, et al. One-step electrodeposition of carbon quantum dots and transition metal ions for N-doped carbon coupled with NiFe oxide clusters: A high-performance electrocatalyst for oxygen evolution. Nano Energy. 2020; 77: 105057. doi: 10.1016/j.nanoen.2020.105057
48. Sher F, Ziani I, Smith M, et al. Carbon quantum dots conjugated with metal hybrid nanoparticles as advanced electrocatalyst for energy applications – A review. Coordination Chemistry Reviews. 2024; 500: 215499. doi: 10.1016/j.ccr.2023.215499
49. Zhu J, Mu S. Defect Engineering in Carbon-Based Electrocatalysts: Insight into Intrinsic Carbon Defects. Advanced Functional Materials. 2020; 30(25). doi: 10.1002/adfm.202001097
50. Tao L, Wang Y, Zou Y, et al. Charge Transfer Modulated Activity of Carbon-Based Electrocatalysts. Advanced Energy Materials. 2019; 10(11). doi: 10.1002/aenm.201901227
51. Majumdar S, Shahazi R, Saddam AI, et al. Carbon nanomaterial-based electrochemical sensor in biomedical application, a comprehensive study. Characterization and Application of Nanomaterials. 2024; 7(1): 4654. doi: 10.24294/can.v7i1.4654
52. Cozzarini L, Bertolini G, Šuran-Brunelli ST, et al. Metal decorated carbon nanotubes for electrocatalytic water splitting. International Journal of Hydrogen Energy. 2017; 42(30): 18763-18773. doi: 10.1016/j.ijhydene.2017.06.101
53. Tafete GA, Thothadri G, Abera MK. A review on carbon nanotube-based composites for electrocatalyst applications. Fullerenes, Nanotubes and Carbon Nanostructures. 2022; 30(11): 1075-1083. doi: 10.1080/1536383x.2022.2028278
54. Singh N, Jana S, Singh GP, et al. Graphene-supported TiO2: study of promotion of charge carrier in photocatalytic water splitting and methylene blue dye degradation. Advanced Composites and Hybrid Materials. 2020; 3(1): 127-140. doi: 10.1007/s42114-020-00140-w
55. Zai SF, Zhou YT, Yang CC, et al. Al, Fe-codoped CoP nanoparticles anchored on reduced graphene oxide as bifunctional catalysts to enhance overall water splitting. Chemical Engineering Journal. 2021; 421: 127856. doi: 10.1016/j.cej.2020.127856
56. Zhao X, Fan Y, Wang H, et al. Cobalt Phosphide-Embedded Reduced Graphene Oxide as a Bifunctional Catalyst for Overall Water Splitting. ACS Omega. 2020; 5(12): 6516-6522. doi: 10.1021/acsomega.9b04143
57. Wang L, Si W, Tong Y, et al. Graphitic carbon nitride (g-C3N4)-based nanosized heteroarrays: Promising materials for photoelectrochemical water splitting. Carbon Energy. 2020; 2(2): 223-250. doi: 10.1002/cey2.48
58. Wu C, Xue S, Qin Z, et al. Making g-C3N4 ultra-thin nanosheets active for photocatalytic overall water splitting. Applied Catalysis B: Environmental. 2021; 282: 119557. doi: 10.1016/j.apcatb.2020.119557
59. Zhang X, Jiang SP. Layered g-C_3N_4/TiO_2 nanocomposites for efficient photocatalytic water splitting and CO2 reduction: a review. Materials Today Energy. 2022; 23: 100904. doi: 10.1016/j.mtener.2021.100904
60. Yu F, Wang L, Xing Q, et al. Functional groups to modify g-C3N4 for improved photocatalytic activity of hydrogen evolution from water splitting. Chinese Chemical Letters. 2020; 31(6): 1648-1653. doi: 10.1016/j.cclet.2019.08.020
61. Choubey P, Sharma MD, Basu M. Sulfur/Nitrogen-Codoped Carbon-Dot-Modified WO3 Nanosheets toward Enhanced Charge-Carrier Separation in a Saline Water-Splitting Reaction. ACS Applied Nano Materials. 2023; 7(16): 18251-18261. doi: 10.1021/acsanm.3c03203
62. Sial QA, Singh R, Duy LT, et al. Nitrogen-doped carbon dot anchored 1-D WO3 for enhanced solar water splitting: A nano surface imaging evidence of charge separation and accumulation. International Journal of Hydrogen Energy. 2021; 46(64): 32546-32558. doi: 10.1016/j.ijhydene.2021.07.115
63. Li G, Huang J, Wang N, et al. Carbon quantum dots functionalized g-C3N4 nanosheets as enhanced visible-light photocatalysts for water splitting. Diamond and Related Materials. 2021; 116: 108242. doi: 10.1016/j.diamond.2021.108242
64. Wang Q, Cai J, Biesold-McGee GV, et al. Silk fibroin-derived nitrogen-doped carbon quantum dots anchored on TiO2 nanotube arrays for heterogeneous photocatalytic degradation and water splitting. Nano Energy. 2020; 78: 105313. doi: 10.1016/j.nanoen.2020.105313
65. Shahazi R, Saddam AI, Majumdar S, et al. Advancements in water splitting for sustainable energy generation: A review. Characterization and Application of Nanomaterials. 2024; 7(1): 5834. doi: 10.24294/can.v7i1.5834
66. Dong Y, Han Q, Hu Q, et al. Carbon quantum dots enriching molecular nickel polyoxometalate over CdS semiconductor for photocatalytic water splitting. Applied Catalysis B: Environmental. 2021; 293: 120214. doi: 10.1016/j.apcatb.2021.120214

67. Xu H, Jia H, Fei B, et al. Charge Transfer Engineering via Multiple Heteroatom Doping in Dual Carbon-Coupled Cobalt Phosphides for Highly Efficient Overall Water Splitting. Applied Catalysis B: Environmental. 2020; 268: 118404. doi: 10.1016/j.apcatb.2019.118404
68. Liu J, Yang X, Si F, et al. Interfacial component coupling effects towards precise heterostructure design for efficient electrocatalytic water splitting. Nano Energy. 2022; 103: 107753. doi: 10.1016/j.nanoen.2022.107753
69. Xu Q, Zhang J, Zhang H, et al. Atomic heterointerface engineering overcomes the activity limitation of electrocatalysts and promises highly-efficient alkaline water splitting. Energy & Environmental Science. 2021; 14(10): 5228-5259. doi: 10.1039/d1ee02105b
70. Prats H, Chan K. The determination of the HOR/HER reaction mechanism from experimental kinetic data. Physical Chemistry Chemical Physics. 2021; 23(48): 27150-27158. doi: 10.1039/d1cp04134g
71. Zhang K, Zou R. Advanced Transition Metal-Based OER Electrocatalysts: Current Status, Opportunities, and Challenges. Small. 2021; 17(37). doi: 10.1002/smll.202100129
72. Jiang WJ, Tang T, Zhang Y, et al. Synergistic Modulation of Non-Precious-Metal Electrocatalysts for Advanced Water Splitting. Accounts of Chemical Research. 2020; 53(6): 1111-1123. doi: 10.1021/acs.accounts.0c00127
73. Li D, Liu H, Feng L. A Review on Advanced FeNi-Based Catalysts for Water Splitting Reaction. Energy & Fuels. 2020; 34(11): 13491-13522. doi: 10.1021/acs.energyfuels.0c03084
74. Ioroi T, Yasuda K. Highly reversal-tolerant anodes using Ti4O7-supported platinum with a very small amount of water-splitting catalyst. Journal of Power Sources. 2020; 450: 227656. doi: 10.1016/j.jpowsour.2019.227656
75. Jeong S, Mai HD, Nam KH, et al. Self-Healing Graphene-Templated Platinum–Nickel Oxide Heterostructures for Overall Water Splitting. ACS Nano. 2022; 16(1): 930-938. doi: 10.1021/acsnano.1c08506
76. Pi Y, Xu Y, Li L, et al. Selective Surface Reconstruction of a Defective Iridium-Based Catalyst for High-Efficiency Water Splitting. Advanced Functional Materials. 2020; 30(43). doi: 10.1002/adfm.202004375
77. Chen Z, Duan X, Wei W, et al. Iridium-based nanomaterials for electrochemical water splitting. Nano Energy. 2020; 78: 105270. doi: 10.1016/j.nanoen.2020.105270

Characterization and Application of Nanomaterials 2024, 7(2), 8205.
https://doi.org/10.24294/can.v7i2.8205

Review

Biosynthesis of gold nanoparticles via fungi: A review of their optimization, antibacterial action and applications

Asma Shahzad

Department of Biotechnology, Lahore College for Women University, Punjab 44444, Pakistan; asmashahzad87@gmail.com

CITATION

Shahzad A. Biosynthesis of gold nanoparticles via fungi: A review of their optimization, antibacterial action and applications. Characterization and Application of Nanomaterials. 2024. 7(2): 8205.
https://doi.org/10.24294/can.v7i2.8205

ARTICLE INFO

Received: 26 July 2024
Accepted: 12 October 2024
Available online: 28 October 2024

Abstract: Gold nanoparticles (AuNPs) have been known to possess exceptional electric, biochemical, and optical characteristics and are 'the topic of discussion' these days, especially relating to the field of biomedicine. Several plants, bacteria, and fungi have been utilized for the generation of AuNPs, besides other physical and chemical methods. While some studies have been reported with gold nanoparticles, less are aimed at fungi and its optimization factors. These parameters can allow us to design AuNPs of our choice depending on the use. The present review focuses on and inspects AuNPs with green synthesis through fungus optimization parameters followed by applications, aiming specifically at their antibacterial activity. Their antibacterial characteristics can open new doors for the pharmaceutical industry in the future.

Keywords: gold nanoparticles; green synthesis; optimization; fungi; antibacterial activity

1. Introduction

Nano-biotechnology is the subdivision of nanotechnology that is expanding day by day and includes the development and fabrication of nanomaterials [1]. Nanoparticles (NPs) can be generated by utilizing several plants, bacteria, and fungi by using different approaches comprising of physical, chemical, and biological methods. Various microorganisms can be employed for both extracellular and intracellular nanoparticles owing to their incomparable characteristics; however, separation of intracellular NPs is laborious and requires extra processes [2].

The credit for discovering AuNPs in particular goes to Michael Faraday, who in 1857 observed these small particles (<100 nm) radiating a red colour. This phenomenon is also known as the Tyndall effect, which is in fact dispersion of the light as a ray of light passes through a colloid. Although these particles were not visible at that time, they gave a 'golden-coloured glow'. It is known that light's wavelength is more in contrast to the gold nanoparticles owing to their size. This is the basis of present-day nanotechnology, and it has allowed a lot of researchers to work in this field [3].

The nanoparticles can easily be characterized using multiple instruments; their varying size and morphology in particular can be identified by using Transmission Electron Microscope (TEM), Scanning Electron Microscope (SEM), zeta sizer, or Atomic Force Microscope (AFM). Moreover, their Surface Plasmon Resonance (SPR) band can be detected by using UV-Vis spectrophotometer whereas their functional groups can be exposed using Fourier transform infrared spectroscopy (FTIR). In order to find out the nature of a certain nanoparticle, X-ray diffraction (XRD) is also carried out [4,5].

Additionally, the process of nanoparticle formation can be enhanced by altering a few factors like biomass weight of fungi, temperature, synthesis or incubation time, pH, and concentration of substrates, etc. Still further studies are necessary to regulate the size, assembly, conformation, and other physico-chemical characteristics of NPs developed by employing fungi [5,6].

2. Methods of nanoparticle development

There are three ways to generate nanoparticles: firstly, physical, then chemical, and finally biological. Physical techniques include ball milling, laser ablation, lithography, thermal evaporation, etc., which basically require the application of external force. These procedures are high maintenance and call for higher temperatures in addition to reaction time. On the other hand, chemical procedures are most commonly used to produce NPs but use and emit chemical and harmful gases along with contaminated end products. Additional steps like hydrolysis and reduction are also part of the chemical synthesis. Lastly, the biological technique has been gaining popularity these days and involves extracts from various plants, microbes like fungi, bacteria, algae, and viruses for its production.

Green synthesis of nanoparticles is not only harmless towards the environment and cost-effective but is known to have fewer inadequacies in contrast to the chemical and physical techniques discussed above; additionally, they are also excellent candidates for upscaling. Hence, fungi in particular have been selected for much research these days due to their easy availability, harmless nature, wide variety, and novel strains. Fungi are also known to produce natural metabolites and excrete enzymes and proteins that act as capping agents and support the reduction process during NP formation. Moreover, fungi itself have more surface area owing to their mycelial structure, releasing more proteins in return, forming NPs rapidly and effectively [7].

3. Attributes of gold nanoparticles

Many metals have been employed for the synthesis of NPs, but gold nanoparticles have amazed researchers due to their unmatched properties, which allow alterations on their surface. Gold nanoparticles, specifically, are known for their surface plasmon resonance (SPR) phenomenon and give out a range of colours, i.e., red, purple, and orange, as the size of NPs increases. Owing to this factor, the SPR band is formed between 500 and 550 nm, which is validated later by a UV-Vis spectrophotometer; moreover, highly charged particles have the ability to either be suspended or stay diffused in a solution, as Hammami and Alabdallah [5] described.

Gold NPs have enhanced adsorption capacity along with great biocompatibility, chemical, and opto-electronic capabilities, which also determine their morphology, permitting them to be used in various sectors, especially biomedical. Gold is a valuable metal known for its stability and for being inert henceforth allowing it to be used in many applications, specifically its role in antibacterial studies, which has gained popularity among researchers as microbe resistance towards antibiotics has become a dilemma these days [8].

4. Green technique by employing fungi

By using the green technique and choosing fungi over bacteria and plant extracts has more benefits, like they can withstand additional agitation along with pressure. Another important factor is temperature, which makes fungi a suitable candidate for biosynthesis; also, their scaling up is easy [8]. Quite a few inspections were aimed towards the biosynthesis of AuNPs by a variety of fungi giving off different sizes (**Figure 1),** such as *Candida albicans* (15 nm), *Aspergillus niger* (20 nm), *Fomes fomentarius* (50 nm), *Ganoderma lucidum* (30 nm), *Gliocladium roseum* (45 nm), *Lentinula edodes* (35 nm), *Myrothecium verrucaria* (40 nm), *Phanerochaete chrysosporium* (40 nm), *Pleurotus florida* (50 nm), *Schizophyllum commune* (45 nm), *Trichoderma harzianum* (40 nm), and *Tolypocladium ophioglossoides* (60 nm) [9]. After their generation, they were used in various applications like drug delivery, biosensors, preservation of paintings, effluent treatment and management, antifungal glazes, food preservation, optics, and environmental monitoring [8].

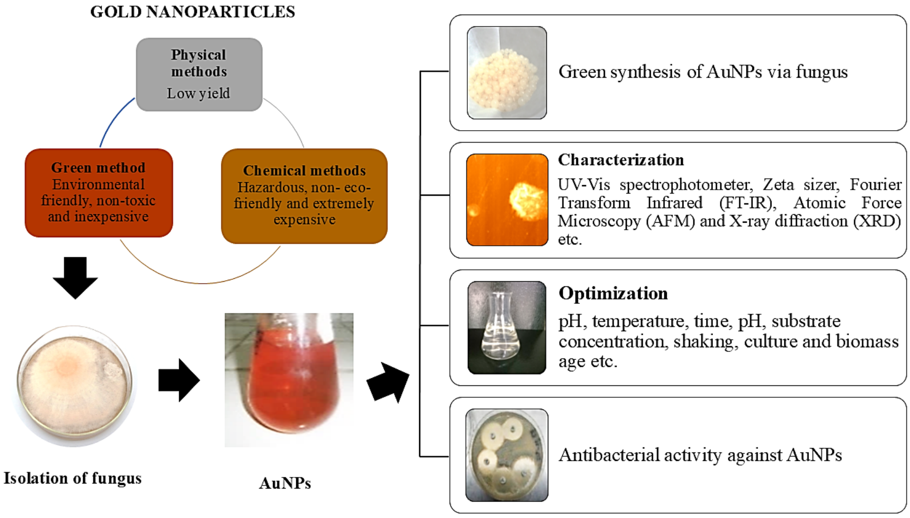

Figure 1. Overview of the fungi-mediated synthesis of gold nanoparticles.

Similarly, many more reports regarding AuNPs from fungi include *Pleurotus sajor-caju* [10], *Fusarium solani* [11], *Jahnula aquatica* [12], *Botryosphaeria rhodian* [13], *Aspergillus terreus* [14], *Pleurotus ostreatus* [15], *Aspergillus tamarii* [16], *Ganoderma neo-japonicum* [17], *Morchella esculenta* [18], *Cladosporium* sp. [19], and *Aspergillus flavus*, etc. [20]. Furthermore, AuNPs were also produced by employing some strains such as *Alternaria* sp. (9.5 nm), *Trichoderma viride* (24.7 nm), *Ganoderma sessile* (13.6 nm), *Trichoderma asperellum* (16.4 nm), and *Botrytis cinerea* (92.9 nm) [21]. Additionally, some more research on AuNPs was also conducted using *Helminthosporum solani, Neurospora crassa,* [22] *Penicillium citrinum*, *M. phaseolina,* [3] *Fusarium oxysporum, Colletotrichum* sp., *Fusarium semitectum, Phoma glomerata,* etc. with varying sizes and shapes. It was observed that AuNPs were generated both intracellularly and extracellularly by *Trichothecium* sp. with a variety of shapes consisting of triangular and spherical forms [23].

5. Mechanism of gold NPs

There are many benefits in the generation of gold NPs via fungi, such as little or no energy is required, additional supplements or agents are not needed, and they are highly functional. Furthermore, the process of production is quite simple, followed by purification. During research, several fungi have been utilized in the formation of gold NPs, as mentioned previously, and they can be both extracellular (outside the cell) and intracellular (inside the cell) with varying unique morphologies. It has been reported that phenols, peptides, and enzymes located on the outside of the fungal cell are mainly in charge of the extracellular production of gold NPs, whereas the intracellular process basically revolves around the concept of absorption through mostly proteins plus enzymes and reduction of gold ions occurring within the cytoplasm or in the cell wall through enzymes or proteins. We can attain NPs with varying sizes and forms along with unique characteristics by optimizing the parameters. In order to improve the function of NPs, we can also adjust substrate concentrations, pH, process time, temperature of incubation, biomass weight, etc. [24].

It was reported earlier that reduction within the AuNPs occurs within the cytoplasm or the surface of the cells due to the presence of Nicotinamide Adenine Dinucleotide Phosphate (NADPH) or Nicotinamide Adenine Dinucleotide (NADH). Additionally, it was exposed that reduction occurs firstly with Au^{+3} which is further reduced to Au^{+} and finally into its elemental form, i.e., Au^{0}, but the enzymes or proteins involved are yet to be investigated [25]. Moreover, it was also reported that other metabolites, i.e., flavin adenine dinucleotide (FAD)-dependent glutathione reductase alongside NADH, have performed a major task in the generation of AuNPs via fungi. Other than that, quinine was also involved in the process of reduction along with phytochelatin when substrate concentration was increased to a certain level [26].

Mainly, the development of nanoparticles involves two processes occurring side by side: first, reduction, which transforms Au^{+3} into Au^{0}; and second, particles' growth and equilibrium amongst them are monitored by capping agents. The NPs are guarded by these ligands, which prevent any form of aggregates and additional development with the assistance of electrostatic charges. It is also reported that some amino acids or chemical metabolites are capable of working as both reducing and capping agents. Proteins and enzymes use Van der Waals forces and adhere to the surface of gold NPs or alternatively attach by bonds among sulfur along with nitrogen atoms within the protein. They are known to bind even at points of zero charge, but it decreases their bonding capability [27].

6. Optimization factors

The AuNPs can be acquired by altering several parameters one at a time of our choice with varying physical and chemical properties. Some of the important factors are discussed below in **Table 1**.

Table 1. Synthesis of gold nanoparticles by various fungi and their characterization.

Fungi	Incubation conditions	Size (nm)	Zeta potential (mV)	SPR band (nm)	Functional groups	Shape	Antibacterial studies	References
Cladosporium sp.	1 mM, ($HAuCl_4$) Fungal extract/ $HAuCl_4$ (70 mL: 30 mL) Temperature 37 °C Agitation rate 180 rpm Reaction time 24/h	5–10	-	524	O-H C=O	Spherical, irregular	-	[19]
Epicoccum nigrum	1 mM, ($HAuCl_4$) Temperature 28 °C Dark condition Agitation rate 180 rpm Reaction time 24/h	2–30	-	550	O-H C=O C-H	Quasi-spherical	*Bacillus subtilis* with 100, 200, 300 mg/L (AuNPs)	[28]
Fusarium chlamydosporum	0.1 mM, ($HAuCl_4$) CFF (10 mL) Temperature 25 °C Dark condition 120 rpm agitation rate Reaction time 24 h 25 g biomass weight	22.1	37.6	530	-	Spherical	*Escherichia coli* and *Pseudomonas aeruginosa*	[29]
Fusarium solani	Temperature 25 °C Dark condition Concentration 1 mM ($HAuCl_4$) pH 8.5 Fungal extract/ $HAuCl_4$ (1: 99) Incubation time 48 h	40–45	2.5	551	C-N C-H	Needle, flower	-	[11]
Jahnula aquatica	Reaction time 48 h Reaction temperature 70–90 °C	8, 20, 60	−43.5	560	N-H O-H C=O C-H C-N C-C	Spherical	-	[12]
Aspergillus flavus	Filtrate concentration (10%) $HAuCl_4$ 1mM Tween 20 (0.1%) Incubation period 30 min with light Temperature (30 °C) Reaction time (15 min)	10–50	positive	530	C-O-O C=O C-N N-H O-H	Spherical, hexagonal, rectangular	*B. subtilis*, *S. aureus*, *E. coli*, *P. aeruginosa* yeast, *C. albicans* No ZOI observed	[20]
Pleurotus ostreatus	pH 5 Salt concentration (5mM) Agitation 200 rpm Incubation time 48 h Temperature 30 °C Ratio of salt and ECF (5:1)	10–30	−24.0	550	N-H	Spherical	*B. subtilis* (30 mm), *E. coli* (30 mm), *S. aureus* (30 mm), *C. albicans* (13 mm)	[15]
Morchella esculenta	1mM $HAuCl_4$ Extract: gold chloride solution ratio (1:5)	16.51	-	511	O-H C=C C-H C=O	Cubic	*S. aureus* *P. aeruginosa* (10 mm)	[18]
Fusarium oxysporum	Temperature 37 °C and 80 °C	50	−28	541	-	Spherical	-	[30]
Candida tropicalis	Temperature 37 °C CTAB	12.4	+57.5	482	-	Spherical	-	[31]

Table 1. (*Continued*).

Fungi	Incubation conditions	Size (nm)	Zeta potential (mV)	SPR band (nm)	Functional groups	Shape	Antibacterial studies	Refer-ences
Thermoascus thermophilus	pH (4.7) Temperature 35.0 °C, 45.0°C and 55.0 °C Reaction time 3–20 h Czapek-Dox medium	40	-	450–650	-	Spherical	-	[27]
Fusarium acuminatum	Acidic pH 1 mM (gold chloride) Temperature 37 °C	8–28	-	520–550	-	Spherical	-	[32]
Aspergillus Trinidadensis	2–12 pH 48 and 72 h culture ages 1 mM substrate concentration Shaking (160 rpm) Biomass weight (80–240 mg/mL)	35		530–570	N-H C-N C=O	Spherical		[33]
Bipolaris tetramera	1 mM substrate concentration	58.4–261.7		570		Spherical, triangular, hexagonal	*B. subtilis,* *B. cereus,* *S. aureus,* *E. coli,* *E. aerogenes*	[34]
Agaricus bisporus	1 mM of $HAuCl_4$ solution (10 mL) 1 ml of mushroom extract	25	−45.8	510–570	N-H C-N C-O-C C-OH	Spherical	-	[35]
Aspergillus terreus	$HAuCl_4$ solution (1mM) pH (4–12) Temperature (25°C to 60 °C) Fungal extract intensity (10–200 ppm) Shaking (150 rpm)	10–16	−28.2	536	O-H C-H C=O C-N	Spherical	*S. aureus,* *V. cholera,* *S.typhimurium*	[36]
	$HAuCl_4$ solution (1 mM) pH (5–10)	2–29	-	550	C-H, N-H −SH	elongated, triangular, rod	*Escherichia coli*	[37]
Candida rugopelliculosa	1 mM of $HAuCl_4$ solution Temperature (35 °C), Shaking (120 rpm)	10–30	-	550	C-H C=O C-N $-NH_2$	-	-	[38]
Pycnoporus sanguineus	Substrate concentration (0.5–2.0 mM) Temperature (30 °C), Shaking (165 rpm)	29.3–61.4	-	520–560	O-H C=O C-N C-H $-NH_2$	Spherical, pseudo-spherical, triangular, triangular, pentagonal hexagonal		[22]

6.1. Temperature and time of synthesis

NPs typically attain large-size to small-size during the synthesis at high temperatures. Usually, elevated temperatures favour bigger NPs as it is suitable for growth alongside the nucleation stage. In contrast to this, lower temperatures support ‘growth’ leading to an increase in the rate of reaction. Due to an alteration in temperature, NPs of many conformations are generated, and the number of substrates secreted is also affected, which also shifts the equilibrium between growth and nucleation. In order to obtain small-sized NPs, higher temperatures are needed, which will trigger the reduction rate, use up the metal ions, and obstruct secondary reduction progress, which can still take place [39].

Many studies have evaluated the AuNPs with varying temperatures. In a study with *Pleurotus ostreatus*, AuNPs were optimized by employing varying temperatures such as 30 °C, 37 °C and 40 °C. It was seen that 30 °C gave the highest yield of AuNPs [13]. *Aspergillus terreus* was also utilized for the generation of gold NPs, and temperature was optimized at 30 °C within a period of twelve hours [14]. Moreover, *Verticillium luteoalbum* was also used for the formation of gold nanoparticles, and varying temperatures of 25 °C, 35 °C and 50 °C were assessed. It was observed that rapid development of NPs occurred with rise of temperature in contrast to lower temperatures. Most of the growth and development was revealed in the first hour with a spherical shape and size of about 10 nm. At a temperature of 50 °C no further changes were detected [40]. In another study with *Fusarium oxysporum,* AuNPs were synthesized after incubation with two varying temperatures, one at 37 °C and subsequently at 80 °C. AuNPs slightly above 50 nm were generated, but it was also seen that at higher temperatures they are more suitable, taking less time, and it was realized that this also allows the formation of smaller nanoparticles [31].

Similarly, in a study with *Aspergillus flavus*, various temperature ranges were applied and AuNPs were monitored; temperatures from 20 °C to 100 °C were analyzed. In this study, 30 to 40 °C proved to be the most suitable for monodispersed AuNPs, whereas after 60 °C a decline was observed, and later at 80 °C clumping of the nanoparticles was noticed. No AuNPs were formed at lower temperatures of 20 °C [20], whereas the time of synthesis was observed from 25 min to 55 mins. It was detected that the gold NPs started forming right after 15 mins of mixing CFF and gold chloride solution. It is known that time of reaction plays a significant role in molding the shapes and sizes of any nanoparticles, together with the yield of NPs [41].

In the recent studies, many shapes have been revealed with the changes in temperatures with AuNPs, such as spherical, triangular, hexagonal, etc. It was stated that generation of NPs can be boosted by raising the temperature up to 50 °C and substrate concentration up to 0.7 mM. Hammami and Alabdallah [3] found that the ideal temperature for the production of AuNPs was between 28–55 °C by maintaining the incubation temperature of the fungal cell-free extract [3].

6.2. pH

During the synthesis of nanoparticles, a change in pH can play a significant role. It is reported that at a low pH, the biomass itself clutches onto more positive charges and produces small-sized nanoparticles rapidly due to the weakened reduction power and binding site being nearby. Moreover, pH plays a vital role in the initial stages of AuNP generation with respect to size and shape. It was described that gold NPs specifically do not form at lower pH, but greater pH values help establish extracellular AuNPs. Furthermore, an increase in pH means a higher rate of reaction along with a reducing rate, thus producing a variety of shapes and sizes [42].

In an interesting investigation with the fungus *Verticillium luteoalbum*, pH was adjusted several times using different levels, commencing from 3, 5, 7, and later 9. It was established that altering the pH greatly impacts the shape and size of NPs. A size of 10 nm AuNPs (spherical) was observed with a pH of 3, and a similar outcome was realized. Furthermore, a pH 5 exposed triangular-shaped or rod-shaped NPs as well after the synthesis. pH 7 and 9 revealed small-sized nanoparticles with spherical shapes [40]. A similar study with the fungus *Penicillium brevicompactum* was employed for the formation of gold NPs, and its pH was optimized by varying it between 5 and 8 [43].

Besides, *Aspergillus terreus* was also utilized for the formation of gold nanoparticles, and its pH was also optimized. No change was noted with pH 1 and 2, whereas at pH 3, pink to violet colour transformations were observed. Later, at pH 7, stable NPs were seen, and colour intensified at a pH of 10, with little or no synthesis at higher pH [14].

Likewise, in a study with *Aspergillus flavus*, various pHs commencing from 3 to 4 to 7, 9 and 12 were tested to enhance the functioning of gold NPs, but it was noted that alteration in pH did not influence the process of NP formation. Rapid synthesis was observed with the distilled water alone, and changes in pH only reduced the absorbance capacity, so it can be said that the reduction process was disturbed due to fluctuations in pH within the cell-free filtrate (CFF) [20]. Another experiment with *Pleurotus ostreatus* evaluated AuNPs; they were optimized by applying pH 5, 6, and 7. It was established that a pH of 5 gave a suitable outcome with AuNPs; however, little or no effect was felt on the nanoparticles themselves [15]. Moreover, another study with *Aspergillus trinidadensis* described the effect of pH on the stability of AuNPs. Varying pHs from 2 to 12 were applied to the AuNPs for a period of 12 h, and it was revealed that a pH of 7.4 enhanced the monodispersion and NPs were steady under all the tested pH ranges [33].

Another study states that the most optimum pH for AuNPs development is between 5 and 9 of the cell-free extract that can be easily maintained with the help of buffers. It was also stated that a change in pH can alter the conformation of AuNPs, like it was observed that a lower pH of 2 revealed rod-shaped (large) NPs, whereas a pH of 4 produced smaller rods. Likewise, it was noted that pH of 8 and 9 normally yielded spherical to oval-shaped NPs, while pH of 10 exposed rod-shaped morphology, though nanowires were exhibited at a pH of 11 [3].

In an examination of AuNPs with *Aspergillus terreus*, it was noted that NPs of varying sizes (20 to 29 nm) were developed with varying pH ranges. At a pH of 8, NPs were mostly polydispersed, establishing themselves with rod and spherical conformation, while at a pH of 5 to 7, NPs with triangular to rod-shaped shapes were attained along with broad SPR peaks. pH 9 and 10 showed monodispersed NPs, and size varied from 10 nm to 19 nm, and it can be stated that there was a reduction in size with the increasing pH towards alkalinity [37]. This also shows that the environment was ideal for the AuNPs and led towards small-sized nanoparticles.

6.3. Agitation rate

Optimizing the rate of agitation is important, as it plays a substantial part in the reduction of the nanoparticles. Static agitation will give low absorbance along with a low reaction rate during the process of the development of nanoparticles, resulting in low performance and efficiency in contrast to the experiment conducted with agitation [44].

However, in a study with *Pleurotus ostreatus,* AuNPs were optimized by using varying agitation rates, i.e., 100 rpm, 150 rpm, and 200 rpm; nevertheless, it was noted that the most suitable agitation rate was 200 rpm, which gave the greatest response [15]. Similarly, in a study with *Aspergillus flavus*, it was analyzed that the agitation speed of 120 rpm did not affect or boost the process of gold nanoparticle formation [20]. It was also noted in a study that *Trichothecium* sp. produced intracellular AuNPs quickly with a spherical shape with shaking. However, surprisingly, without agitation, it produced both intracellular and extracellular nanoparticles, giving rise to triangular and spherical NPs [23].

6.4. Substrate concentration

Metal salt concentration also leaves an impact on the size of the nanoparticles. It was described that nanoparticles may develop with very large sizes if the concentration is extremely high, as struggle between the capping agents and ions (metal) may possibly escalate to form NPs, and excess substrates may form aggregates [45]. Many studies were conducted to optimize the AuNPs with fungi, and interesting results were revealed in an investigation with *Aspergillus terreus.* 1 mM substrate concentration proved to be the most optimum even though $AuCl_3$ of many intensities was applied from 1 mM to 10 mM, but they simply failed to generate NPs [14]. Likewise, after investigation with *Penicillium brevicompactum*, it was seen that after 2 mM gold, NPs started to form aggregates and also increased in size, probably due to saturation of the environment [40]. In another study with *Pleurotus ostreatus*, AuNPs were optimized by using different substrate concentrations at 1 mM, 2.5 mM, and 5 mM. The most optimum substrate concentration was found to be 5 mM and showed a rapid reduction soon after its addition [15].

Similarly, in a study, *Aspergillus flavus* gold chloride solutions of varying molarities starting from 0.5 mM to 2 mM were applied to control the functionality of AuNPs. Results displayed that at 1 mM some synthesis took place, whereas at 0.5 mM a broad SPR band was revealed, while 2 mM exposed reduced absorbance [20]. It was also stated in an investigation that lower intensities of substrates along with reduced weight of biomass give rise to AuNPs with a smaller size, but on the other hand, their yield becomes restricted if upscaled [8].

6.5. Fungal filtrate

Fungal filtrate concentration clearly effects the formation of nanoparticles. In order to analyze fungal filtrates and the functionality of AuNPs, varying concentrations of 5% to 40% were applied in a study with *Aspergillus flavus*. It was seen that at a higher percentage of fungal filtrate, a broad SPR band was obtained in contrast to a reduced concentration of 5 to 10%, which probably occurred due to the presence of exceedingly reducing agents [20]. In a study with *Agaricus bisporus*, it was seen that fungal filtrate of '1 mL' generated AuNPs of approximately 25 nm with great stability of −45.8 mV by Zeta sizer [35].

6.6. Biomass weight

Biomass weight is another important factor that must be kept in mind while optimizing nanoparticles. It was reported that if the biomass quantity is increased during the synthesis of NPs, its size begins to modify, and if the enzymes become saturated while the process is taking place, researchers may have to deal with large-sized NPs as the enzymes are secreted in excess, which might lead to aggregation later [46]. Another study was conducted using *Aspergillus terreus* to produce NPs with varying biomass weights, such as 10 g/100 mL to 30 g/100 mL. It was noted that the increase in the biomass weight did not work for the biosynthesis of gold NPs, probably due to the occurrence of additional reducing agents; however, at a weight of 10 g/100 mL, NP formation was observed as the environment must be in equilibrium and not saturated with enzymes [14].

Furthermore, *Aspergillus Trinidadensis* was also studied with varying biomass intensities until optimization was achieved. Initially, experiments were conducted with biomass of 160 mg/mL; later, more ranges were introduced, starting from 40–240 mg/mL with 1 mM of $HAuCl_4$ solution. Finally, 4 g (160 mg/mL) of biomass was found to be ideal along with the rest of the optimization variables like culture, temperature of incubation, pH, etc. [33].

6.7. Fungal culture age

In an inspection with the fungus *Verticillium luteoalbum*, different time periods, i.e., 24 h, 48 h, and 72 h, were applied and AuNPs were monitored. Initially it was observed the fungal culture age did not seem to affect the AuNPs, but it was perceived that as the reaction time progressed and culture grew old, generation of the NPs was reduced, which probably means the rapid development occurred in the exponential phase, reducing the gold ions right away. The older culture hence has a low rate of reduction and reaction and is less active, declining the production of NPs. At low reaction rates, spherical particles were formed in contrast to high rates, which yielded rods and a platelet-like appearance [40]. Furthermore, in an investigation with *Aspergillus trinidadensis*, the effect of different fungal cultures was examined with gold nanoparticles. Cultures of 36 h, 48 h, 72 h, and 96 h were employed with 160 mg/mL intensity, and it was observed that 72 h produced the best results and was optimized using these conditions [33].

6.8. Supplementation with surfactants

Microbes such as bacteria, fungi, and yeast are known to produce extracellular bio-surfactants comprising both hydrophobic and hydrophilic elements. Stabilization of the nanoparticles is usually established by the addition of surfactants during the generation of NPs that consist of mostly fats and sugar. Due to the addition of surfactants, an even distribution occurs with the NPs colloidal solution; moreover, it is eco-friendly and non-hazardous. They are also utilized for designing NPs with varying shapes and sizes [47].

Likewise, in a study with *Aspergillus flavus*, surfactants were added to enhance the performance of gold NPs. Various surfactants such as sodium dodecyl sulphate (SDS) 0.1% along with Tween 20, 0.1% were used in the experiment with AuNPs. It was observed that Tween 20 stabilized the AuNPs, and the SPR band persisted and remained unaffected for approximately three months, whereas others were able to keep them steady for less. It was also reported earlier that surfactants like Tween 20 are biocompatible; moreover, they are utilized for surface modifications [20].

7. Antimicrobial activity

Antimicrobial resistance has become a major problem all over the globe these days. It is basically the capability of the microbes to resist a variety of antibiotics, hence making the medicine ineffective [48]. The entire concept of antimicrobial activity of gold nanoparticles revolves around the gram-negative and gram-positive bacteria occurring on the surface of the membrane. It was previously described that the reduction of adenosine triphosphate (ATP) is perceived, along with obstruction of ribosomal structures and an increase in oxidative stress, in the presence of AuNPs; hence, they are successful antimicrobial agents. After interaction between microbes and NPs, an increase is felt in the production of ROS, which initiates degeneration together with degradation in the cell membrane and overall cell structure, proving their antibacterial nature (**Figure 2**) [41]. It was reported earlier that small nanoparticles approximately 20 nm are able to penetrate the cell wall of bacteria and cause degradation in organelles, hence leading towards death, which makes AuNPs a good contender for antibiotics [49].

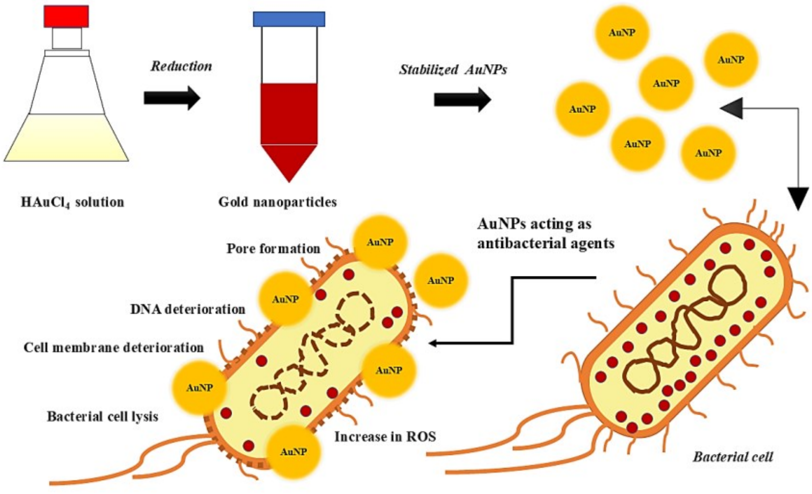

Figure 2. Antibacterial activity of gold nanoparticles.

Size and dimensions both play a significant role in determining the efficiency of the antibacterial properties of nanoparticles. Consequently, gold nanoparticles with smaller sizes usually demonstrate a substantial amount of antibacterial activity [50]. Thus, a study with *Inonotus obliquus* showed antibacterial properties of gold NPs against various stains like *S. aureus*, *E. coli*, and *B. subtilis*. After analysis, ZOI were noted down for the afore mentioned strains. A zone of 14 nm was observed with *E. coli*, whereas *S. aureus* displayed 16 mm while *B. subtilis* established a ZOI at 12 mm.

In earlier studies, it was reported that the positive charge occurring within the gold ion directs the antimicrobial activity of any microbe. The cell membrane supporting a negative charge along with NPs carrying a positive charge makes the whole mechanism work. It was also proposed that cell death occurs when the NPs creates perforations within the cell walls elevating its penetrability, forcing the cellular environment to change and contents to leak, hence another idea towards mechanism [18].

Likewise, in another recent investigation with *Aspergillus terreus*, antibacterial activities were revealed, showing maximum ZOI against *Vibrio cholerae* (9.31 ± 0.14) and *Staphylococcus aureus* (8.58 ± 0.28) with AuNPs at 400 µg/mL. The antibacterial activities are again thought to be using processes affiliated with ROS or deterioration of enzymes or cell membranes to kill bacteria [43].

Similarly, in another evaluation with *Bipolaris tetramera*, antibacterial activity was also assessed. The bacterial pathogens like *B. subtilis*, *B. cereus*, *S. aureus*, *E. coli*, and *E. aerogenes* were tested against AuNPs with varying concentrations from 10 µM to 150 µM. The highest ZOI of 1.3 cm was formed against *S. aureus* at a concentration of 100 µM, whereas the lowest was observed with *E. coli* at 0.5 cm with 100 µM intensity. Overall, 10 µM formed the lowest ZOI of less than 0.5 cm with all the pathogens, and it was noted that as the intensities of the AuNPs were increased, the antibacterial activities also increased, which could be due to its small size [34].

Another study with *Aspergillus terreus* exposed the antibacterial abilities of gold NPs against some stains like *S. aureus*, *V. cholera*, and *S. typhimurium* with concentrations ranging from 100 to 400 µg/mL. After investigation, it was revealed that maximum ZOI appeared at 400 µg/mL with *S. aureus* and *V. cholera*, i.e., 8.58 ± 0.28 mm and 9.31 ± 0.14 mm, respectively. Other concentrations did not reveal any significant results [36].

8. Applications

AuNPs are known to have many applications in different fields of life as they occur in their natural form (**Figure 3**). Firstly, as the gold NPs are biology compatible and less harmless, they are utilized in drug deliveries and are used in early detection for various ailments related to cancer and heart along with gene therapies [42] and photoacoustic imaging [48]. The anti-tumor activities with the AuNPs are being carried out by employing varying categories of NPs, which include nanoshells, nanotubes, nanostars [51], nanocages, etc. These are inserted in the body, which then incorporate themselves into the tumor; later, they are subjected to infrared followed by heat, which destroys the cancerous cells after raising the temperature, avoiding the healthy cells. It is an efficient tool for the treatment of cancer without comprising any more healthy cells. Two of these successful methods include thermo-chemotherapy (TCT) and gene therapy (GT), which are worth mentioning. AuNPs have also proved themselves in immunotherapy, where these small-sized NPs can pass through and penetrate various tissues, such as lymphoid tissue, and harm the immune cells [3].

Also, they are being used as reliable antimicrobial agents against various infections [52].

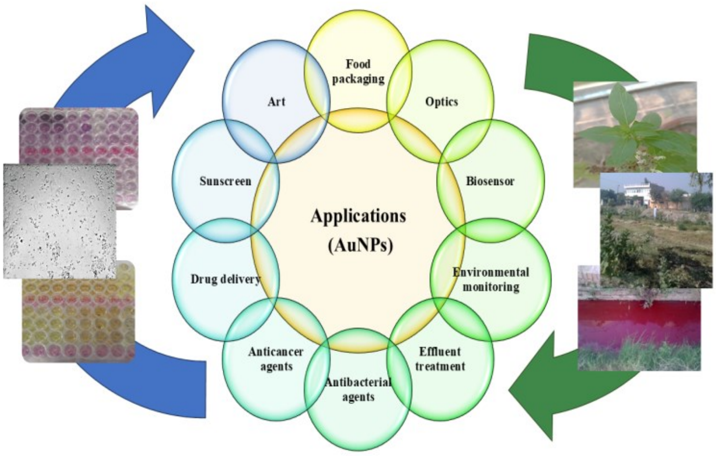

Figure 3. Some applications of gold nanoparticles.

Gold nanoparticles have also been used in drug delivery in which they were coupled up with the medicine or antibiotics using simple covalent or ionic bonds or by absorption approach. For instance, an anti-cancer treatment involved the coupling of folic acid with 13 nm AuNPs to interrupt the cancer cells during folate metabolism [53]. AuNPs have also been applied in the treatment of various skin diseases like psoriasis, pemphigus, hives, etc., and illnesses related to joints such as Lupus, etc.

Secondly, AuNPs have good chemical and thermal properties, which enable them to act as sensors. They have also been utilized in cleaning of the air, like removing carbon monoxide or any odour from an enclosed space [3]. Thirdly, gold nanoparticles can be controlled, their size and shapes can be varied according to your requirements, permitting them to be used in various processes, like food preservation. Additionally, they are consumed in some food items as ‘nano-capsules that transfer varying nutrients without comprising the taste or its presence [3].

Other applications include optics, conservation of paintings, environmental assessment, waste water treatment, and control. When fungal extract is revealed to metals, they usually generate nanoparticles from it, and it overpowers the toxic elements present within the wastewater by reducing it; hence, it develops into a less harmful form and persists the metal toxicity. In this way, the metal toxicity is reduced from varying sources, ensuring a better and cleaner environment through the use of gold nanoparticles. Some species of fungi have developed high tolerance towards heavy metal pollution, like *Penicillium* sp. and *Aspergillus* sp. [54], but their mechanisms still need to be studied further to develop new techniques [55–58].

Moreover, during the production of AuNPs via green synthesis, no external agent is required, so no capping agents are added, which stabilizes the NPs by themselves, allowing researchers to alter their form easily [41]. Besides, they can also be used as an insecticide [39] and in agriculture too [48,59]. The agriculture sector is also suffering due to depletion of nutrients and increasing human population; thus, new techniques must be developed for increasing the productivity of the crops. Hence, NPs are employed as agro-chemical ‘agents’ and have been introduced to eradicate pesticides. Moreover, they are designed to enhance crop productivity and are being utilized as fertilizers as well. Some biosensors have also been introduced to protect the crops and detect various diseases occurring in a specific crop. Additionally, they are also being employed as growth regulators for the plants and help improve the overall yield of the crops [60].

9. Future perspectives and challenges

Even though the gold nanoparticles have proven to be non-toxic and have great potential as antibiotics, further research is required, and doses need to be administered before they can actually be used in the biomedicine field on a larger scale. Experiments are essential to make sure that they are safe and can be used as drugs alone. We need to indulge in this notion a bit more, as the antimicrobial resistance and its overuse are growing day by day, and it is becoming challenging for the pharmaceutical companies to come up with novel strains for this purpose; therefore, we need to find treatments that are innovative [49].

10. Conclusion

The green technique of synthesizing gold nanoparticles is an interesting approach as it is simple, safe, economical, stable, and biocompatible in contrast to old methods. After synthesis, unique shapes and sizes can be expected and controlled, which can be utilized in many applications, specifically biomedical. These intriguing AuNPs can be optimized according to the need by altering various parameters like temperature, pH, amount of biomass, agitation rate, surfactants or enhancers, metal concentration, etc. The gold NPs are unique due to their antimicrobial properties, and their small size and large surface area are another plus, which makes them excellent candidates for future antibiotic investigations.

Conflict of interest: The author declares no conflict of interest.

References

1. Iranmanesh S, Shahidi Bonjar GH, Baghizadeh A. Study of the biosynthesis of gold nanoparticles by using several saprophytic fungi. SN Applied Sciences. 2020; 2(11). doi: 10.1007/s42452-020-03704-z
2. Karnwal A, Kumar Sachan RS, Devgon I, et al. Gold Nanoparticles in Nanobiotechnology: From Synthesis to Biosensing Applications. ACS Omega. 2024; 9(28): 29966-29982. doi: 10.1021/acsomega.3c10352
3. Hammami I, Alabdallah NM, jomaa AA, et al. Gold nanoparticles: Synthesis properties and applications. Journal of King Saud University–Science. 2021; 33(7): 101560. doi: 10.1016/j.jksus.2021.101560
4. Soltani Nejad M, Samandari Najafabadi N, Aghighi S, et al. Evaluation of Phoma sp. Biomass as an Endophytic Fungus for Synthesis of Extracellular Gold Nanoparticles with Antibacterial and Antifungal Properties. Molecules. 2022; 27(4): 1181. doi: 10.3390/molecules27041181
5. Ali S, Iqbal M, Naseer A, et al. State of the art of gold (Au) nanoparticles synthesis via green routes and applications: A review. Environmental Nanotechnology, Monitoring & Management. 2021; 16: 100511. doi: 10.1016/j.enmm.2021.100511
6. Mostafazade R, Arabi L, Tazik Z, et al. Fungal endophytes: Treasure trove for green synthesis of metallic nanoparticles and their biological applications. Biocatalysis and Agricultural Biotechnology. 2024; 60: 103307. doi: 10.1016/j.bcab.2024.103307

7. Andrade F, Jenipher C, Gurav N, et al. Endophytic fungi-assisted biomass synthesis of eco-friendly formulated silver nanoparticles for enhanced antibacterial, antioxidant, and antidiabetic activities. Journal of Drug Delivery Science and Technology. 2024; 97: 105749. doi:10.1016/j.jddst.2024.105749
8. Xu F, Li Y, Zhao X, et al. Diversity of fungus-mediated synthesis of gold nanoparticles: properties, mechanisms, challenges, and solving methods. Critical Reviews in Biotechnology. 2023; 44(5): 924-940. doi: 10.1080/07388551.2023.2225131
9. Naimi-Shamel N, Pourali P, Dolatabadi S. Green synthesis of gold nanoparticles using Fusarium oxysporum and antibacterial activity of its tetracycline conjugant. Journal de Mycologie Médicale. 2019; 29(1): 7-13. doi: 10.1016/j.mycmed.2019.01.005
10. Chaturvedi VK, Yadav N, Rai NK, et al. Pleurotus sajor-caju-Mediated Synthesis of Silver and Gold Nanoparticles Active against Colon Cancer Cell Lines: A New Era of Herbonanoceutics. Molecules. 2020; 25(13): 3091. doi: 10.3390/molecules25133091
11. Clarance P, Luvankar B, Sales J, et al. Green synthesis and characterization of gold nanoparticles using endophytic fungi Fusarium solani and its in-vitro anticancer and biomedical applications. Saudi Journal of Biological Sciences. 2020; 27(2): 706-712. doi: 10.1016/j.sjbs.2019.12.026
12. Mohamed MA. Myco-engineered gold nanoparticles from Jahnula aquatica coated with ampicillin/amoxicillin and their antibacterial and anticancer activity against cancer cells. Biotechnology Letters. 2019; 42(1): 151-170. doi: 10.1007/s10529-019-02764-5
13. Mohamed HI, Fawzi EM, Abd-Elsalam KA, et al. Endophytic fungi-derived biogenic nanoparticles: mechanisms and applications, 1st ed. Elsevier; 2023. pp. 361-391.
14. BalaKumaran MD, Ramachandran R, Balashanmugam P, et al. Comparative analysis of antifungal, antioxidant and cytotoxic activities of mycosynthesized silver nanoparticles and gold nanoparticles. Materials Technology. 2020; 37(6): 411-421. doi: 10.1080/10667857.2020.1854518
15. El Domany EB, Essam TM, Ahmed AE, et al. Biosynthesis physico-chemical optimization of gold nanoparticles as anti-cancer and synergetic antimicrobial activity using Pleurotus ostreatus fungus. Journal of Applied Pharmaceutical Science. 2018; 8(5): 119-128. doi: 10.7324/JAPS.2018.8516
16. Radhakrishnan R, Mani U, Gnanamani A, et al. Myco-Fabricated Gold Nanoparticles from Aspergillus tamarii MTCC5152, its Characterization and Dye Biodegradation. Applied Microbiology: Theory & Technology. 2021; 1: 52-62. doi: https://doi.org/10.37256/amtt.222021792
17. Smirnov O, Dzhagan V, Yeshchenko O, et al. Effect of pH of Ganoderma lucidum aqueous extract on green synthesis of silver nanoparticles. Advances in Natural Sciences: Nanoscience and Nanotechnology. 2023; 14 (3): 1-9.
18. Hilal A. Utilization of Morchella esculenta-mediated green synthesis golden nanoparticles in biomedicine applications. Preparative Biochemistry & Biotechnology. 2020; 51(2): 127-136. doi: 10.1080/10826068.2020.1799390
19. Munawer U, Raghavendra VB, Ningaraju S, et al. Biofabrication of gold nanoparticles mediated by the endophytic Cladosporium species: Photodegradation, in vitro anticancer activity and in vivo antitumor studies. International Journal of Pharmaceutics. 2020; 588: 119729. doi: 10.1016/j.ijpharm.2020.119729
20. El-Bendary MA, Moharam ME, Hamed SR, et al. Myco-synthesis of gold nanoparticles using Aspergillus flavus: Characterization, optimization and cytotoxic activity. Microbiology. 2018; 12: 1- 14.
21. Olvera-Aripez J, Camacho-López S, Flores-Castañeda M, et al. Biosynthesis of gold nanoparticles by fungi and its potential in SERS. Bioprocess and Biosystems Engineering. 2024; 47(9): 1585-1593. doi: 10.1007/s00449-024-03053-w
22. Mikhailova EO. Gold Nanoparticles: Biosynthesis and Potential of Biomedical Application. Journal of Functional Biomaterials. 2021; 12(4): 70. doi: 10.3390/jfb12040070
23. Roy A, Pandit C, Gacem A, et al. Biologically Derived Gold Nanoparticles and Their Applications. Aruni W, ed. Bioinorganic Chemistry and Applications. 2022; 2022(1). doi: 10.1155/2022/8184217
24. Abu-Elghait M, Soliman MKY, Azab MS, et al. Response surface methodology: Optimization of myco-synthesized gold and silver nanoparticles by Trichoderma saturnisporum. Biomass Conversion and Biorefinery. 2023. doi: 10.1007/s13399-023-05188-4
25. Banerjee K, Ravishankar Rai V. A Review on Mycosynthesis, Mechanism, and Characterization of Silver and Gold Nanoparticles. BioNanoScience. 2017; 8(1): 17-31. doi: 10.1007/s12668-017-0437-8
26. Adebayo EA, Azeez MA, Alao MB, et al. Fungi as veritable tool in current advances in nanobiotechnology. Heliyon. 2021; 7(11): e08480. doi: 10.1016/j.heliyon.2021.e08480

27. Kitching M, Ramani M, Marsili E. Fungal biosynthesis of gold nanoparticles: mechanism and scale up. Microbial Biotechnology. 2014; 8(6): 904-917. doi: 10.1111/1751-7915.12151
28. Molnár Z, Bódai V, Szakacs G, et al. Green synthesis of gold nanoparticles by thermophilic filamentous fungi. Scientific Reports. 2018; 8(1). doi: 10.1038/s41598-018-22112-3
29. Guzmán-Moreno J, Ramírez-Santoyo RM, Ortega-Sigala JJ, et al. Fungal biosynthesis of gold nanoparticles with sporicidal activity against bacterial endospores. Green Chemistry Letters and Reviews. 2024; 17(1): doi: 10.1080/17518253.2024.2360489
30. Hammad SE, El-Rouby MN, Abdel-Aziz MM, et al. Endophytic fungi–assisted biomass synthesis of gold, and zinc oxide nanoparticles for increasing antibacterial, and anticancer activities. Biomass Conversion and Biorefinery. 2023. doi: 10.1007/s13399-023-04954-8
31. Pourali P, Svoboda M, Benada O, et al. Biological Production of Gold Nanoparticles at Different Temperatures: Efficiency Assessment. Particle & Particle Systems Characterization. 2023; 40(12). doi: 10.1002/ppsc.202200182
32. Dasilva MA, Andrada KFC, Torales MM, et al. Synergistic activity of gold nanoparticles with amphotericin B on persister cells of Candida tropicalis biofilms. Journal of Nanobiotechnology. 2024; 22(1). doi: 10.1186/s12951-024-02415-6
33. Deshmukh AG, Mistry V, Sharma A, et al. Green and sustainable bio-synthesis of gold nanoparticles using Aspergillus Trinidadensis VM ST01: Heterogeneous catalyst for nitro reduction in water. Tetrahedron Green Chem. 2023; 2: 100021. doi: 10.1016/j.tgchem.2023.100021
34. Fatima F, Bajpai P, Pathak N, et al. Antimicrobial and immunomodulatory efficacy of extracellularly synthesized silver and gold nanoparticles by a novel phosphate solubilizing fungus Bipolaris tetramera. BMC Microbiology. 2015; 15(1). doi: 10.1186/s12866-015-0391-y
35. Eskandari-Nojedehi M, Jafarizadeh-Malmiri H, Rahbar-Shahrouzi J. Hydrothermal green synthesis of gold nanoparticles using mushroom (Agaricus bisporus) extract: physico-chemical characteristics and antifungal activity studies. Green Processing and Synthesis. 2018; 7(1): 38-47. doi: 10.1515/gps-2017-0004
36. Mishra RC, Kalra R, Dilawari R, et al. Bio-Synthesis of Aspergillus terreus Mediated Gold Nanoparticle: Antimicrobial, Antioxidant, Antifungal and In Vitro Cytotoxicity Studies. Materials. 2022; 15(11): 3877. doi: 10.3390/ma15113877
37. Santhosh PB, Genova J, Chamati H. Green Synthesis of Gold Nanoparticles: An Eco-Friendly Approach. Chemistry. 2022; 4(2): 345-369. doi: 10.3390/chemistry4020026
38. Zhao X, Hou N, Wan C, et al. Gold nanoparticles synthesis mediated by fungus isolated from aerobic granular sludge: Process and mechanisms. Heliyon. 2024; 10(6): e28281. doi: 10.1016/j.heliyon.2024.e28281
39. Patil S, Chandrasekaran R. Biogenic nanoparticles: a comprehensive perspective in synthesis, characterization, application and its challenges. Journal of Genetic Engineering and Biotechnology. 2020; 18(1): 67. doi: 10.1186/s43141-020-00081-3
40. Gericke M, Pinches A. Microbial production of gold nanoparticles. Gold Bulletin. 2006; 39(1): 22-28. doi: 10.1007/bf03215529
41. Kaval U, Hoşgören H. Biosynthesis, Characterization, and Biomedical Applications of Gold Nanoparticles with Cucurbita moschata Duchesne Ex Poiret Peel Aqueous Extracts. Molecules. 2024; 29(5): 923. doi: 10.3390/molecules29050923
42. Gupta R, Padmanabhan P. Biogenic synthesis and characterization of gold nanoparticles by a novel marine bacteria marinobacter Algicola: Progression from nanospheres to various geometrical shapes. Journal of microbiology, biotechnology and food sciences. 2018; 8(1): 732-737. doi: 10.15414/jmbfs.2018.8.1.732-737
43. Mishra A, Tripathy SK, Wahab R, et al. Microbial synthesis of gold nanoparticles using the fungus Penicillium brevicompactum and their cytotoxic effects against mouse mayo blast cancer C2C12 cells. Applied Microbiology and Biotechnology. 2011; 92(3): 617-630. doi: 10.1007/s00253-011-3556-0
44. Tidke PR, Gupta I, Gade AK, et al. Fungus-Mediated Synthesis of Gold Nanoparticles and Standardization of Parameters for its Biosynthesis. IEEE Transactions on NanoBioscience. 2014; 13(4): 397-402. doi: 10.1109/tnb.2014.2347803
45. do Nascimento JM, Cruz ND, de Oliveira GR, et al. Evaluation of the kinetics of gold biosorption processes and consequent biogenic synthesis of AuNPs mediated by the fungus Trichoderma harzianum. Environmental Technology & Innovation. 2021; 21: 101238. doi: 10.1016/j.eti.2020.101238
46. Singh A, Gautam PK, Verma A, et al. Green synthesis of metallic nanoparticles as effective alternatives to treat antibiotics resistant bacterial infections: A review. Biotechnology Reports. 2020; 25: e00427. doi: 10.1016/j.btre.2020.e00427
47. Saleem SS, Saleem S, Nazar MF. Role of Biosurfactants in Nanoparticles Synthesis and their Stabilization, 1st ed. Springer International Publishing; 2023. pp. 191-213.

48. Aly Khalil AM, Saied E, Mekky AE, et al. Green biosynthesis of bimetallic selenium–gold nanoparticles using Pluchea indica leaves and their biological applications. Frontiers in Bioengineering and Biotechnology. 2024; 11. doi: 10.3389/fbioe.2023.1294170
49. Chauhan A, Anand J, Parkash V, et al. Biogenic synthesis: a sustainable approach for nanoparticles synthesis mediated by fungi. Inorganic and Nano-Metal Chemistry. 2022; 53(5): 460-473. doi: 10.1080/24701556.2021.2025078
50. Aljarba NH, Imtiaz S, Anwar N, et al. Anticancer and microbial activities of gold nanoparticles: A mechanistic review. Journal of King Saud University - Science. 2022; 34(4): 101907. doi: 10.1016/j.jksus.2022.101907
51. Kalimuthu K, Cha BS, Kim S, et al. Eco-friendly synthesis and biomedical applications of gold nanoparticles: A review. Microchemical Journal. 2020; 152: 104296. doi: 10.1016/j.microc.2019.104296
52. Lee KX, Shameli K, Yew YP, et al. Recent Developments in the Facile Bio-Synthesis of Gold Nanoparticles (AuNPs) and Their Biomedical Applications International Journal of Nanomedicine. 2020; 15: 275-300. doi: 10.2147/ijn.s233789
53. Amina SJ, Guo B. A Review on the Synthesis and Functionalization of Gold Nanoparticles as a Drug Delivery Vehicle International Journal of Nanomedicine. 2020; 15: 9823-9857. doi: 10.2147/ijn.s279094
54. Priyadarshini E, Priyadarshini SS, Cousins BG, et al. Metal-Fungus interaction: Review on cellular processes underlying heavy metal detoxification and synthesis of metal nanoparticles. Chemosphere. 2021; 274: 129976. doi: 10.1016/j.chemosphere.2021.129976
55. Qamar SUR, Ahmad JN. Nanoparticles: Mechanism of biosynthesis using plant extracts, bacteria, fungi, and their applications. Journal of Molecular Liquids. 2021; 334: 116040. doi: 10.1016/j.molliq.2021.116040
56. Taha RH. Green synthesis of silver and gold nanoparticles and their potential applications as therapeutics in cancer therapy; a review. Inorganic Chemistry Communications. 2022; 143: 109610. doi: 10.1016/j.inoche.2022.109610
57. Mughal B, Zaidi SZJ, Zhang X, et al. Biogenic Nanoparticles: Synthesis, Characterisation and Applications. Applied Sciences. 2021; 11(6): 2598. doi: 10.3390/app11062598
58. Jadoun S, Chauhan NPS, Zarrintaj P, et al. Synthesis of nanoparticles using microorganisms and their applications: A review. Environmental Chemistry Letters. 2022; 20(5): 3153-3197.
59. Chowdhury NK, Choudhury R, Gogoi B, et al. Microbial Synthesis of Gold Nanoparticles and their Application. Current Drug Targets. 2022; 23(7): 752-760. doi: 10.2174/1389450123666220128152408
60. Rai M, Bonde S, Golinska P, et al. Fusarium as a Novel Fungus for the Synthesis of Nanoparticles: Mechanism and Applications. Journal of Fungi. 2021; 7(2): 139. doi: 10.3390/jof7020139

EnPress Publisher, LLC

Add: 9650 Telstar Avenue, Unit A, Suite 121, El Monte, CA 91731
Email: contact@enpress-publisher.com